Physiochemical Principles for the Design of Functional Materials based on Liquid Crystalline Droplets

By

Daniel S. Miller

A dissertation submitted in partial fulfillment of

the requirements for the degree of

Doctor of Philosophy

(Chemical Engineering)

at the

UNIVERSITY OF WISCONSIN-MADISON

2014

Date of final oral examination: 8/6/2014

The dissertation is approved by the following members of the Final Oral Committee:

Nicholas L. Abbott, Professor, Chemical and Biological Engineering
Eric V. Shusta, Professor, Chemical and Biological Engineering
Daniel J. Klingenberg, Professor, Chemical and Biological Engineering
Sean P. Palecek, Professor, Chemical and Biological Engineering
Arun Yethiraj, Professor, Chemistry

Physiochemical Principles for the Design of Functional Materials based on Liquid Crystalline Droplets

Daniel S. Miller

Under the supervision of Professor Nicholas L. Abbott

at the University of Wisconsin-Madison

Abstract

The research described in this thesis elucidates physiochemical principles for the design of functional materials based on water-dispersed microdroplets of thermotropic liquid crystal (LC). The materials can be grouped into two categories: (i) LC-in-water emulsion-based biological sensors; and (ii) spherical and non-spherical microparticles with chemical patches synthesized from the droplets of LC-in-water emulsions. Accordingly, the presentation of the research is organized into two parts.

In the first part, principles for the design of biosensors based on nematic LC-in-water emulsions are described. Whereas past designs have relied on transformations in the configuration of LC confined within emulsion droplets (ordering transitions) triggered by adsorbate-driven changes in their surface energies, this thesis reports on a fundamentally new mechanism for such ordering transitions. Specifically, bacterial endotoxins are found to trigger ordering transitions when added to the aqueous medium surrounding LC droplets at picogram per milliliter concentrations (concentrations that are six orders of magnitude lower than the aforementioned adsorbates) *via* a localized interaction with topological defects present within the

droplets. The ordering transitions give rise to distinct changes in the optical appearances of the LC droplets when viewed under a polarized light microscope, thus allowing the presence of endotoxins to be transduced. The exquisite sensitivity of LC droplets to endotoxins is found to depend on droplet size and solution conditions both of which perturb the delectate balance of energetics necessary for the ordering transitions.

A novel methodology for rapid determination of configurations of water-dispersed LC microdroplets (rates of up to 10,000 droplets per second) based on measurement of light scattered by droplets as they are passed through a flow focusing device is also reported in the first part. Application of the technique is demonstrated for detection of both endotoxins and cell-shed microvesicles, which are thought to be released at elevated rates in diseased states of cells. For both of these systems, the rapid nature of the technique enables insights into the underlying phenomena that govern the responsiveness of LC droplets to the two biological species.

The second part builds on a recent discovery that the droplets of LC-in-water emulsions can be utilized as templates for synthesis of spherical and non-spherical microparticles with chemical surface patches. First, an added level of control over particle synthesis is demonstrated by using reversible adsorbate-driven ordering transitions of the LC droplets to manipulate the positions of chemical patches. The utility of the approach is illustrated through synthesis of both “Janus-like” microparticles and magnetically-responsive patchy microdroplets of LC with either dipolar or quadrupolar symmetry that exhibit distinct optical responses upon application of an external magnetic field. Next, the forces that underlie organized assemblies formed by colloids at the surfaces of water-dispersed LC microdroplets in a bipolar configuration are revealed. Finally, it is shown that remarkable control over the shape and surface morphology of polymer particles

templated from LC microdroplets can be achieved through chemical manipulation of the configuration of the droplets.

Overall, the advances reported in this thesis reveal physiochemical principles which will enable design of not only LC droplet-based biosensors or polymer microparticles, but also a broad range of functional soft materials based on liquid crystalline microdroplets.

This thesis is dedicated to both my wife for her endless support and my parents for providing me with the education that made this work possible.

Acknowledgements

I would like to take this opportunity to thank all of the people that contributed to this thesis both directly and indirectly. First, I would like to thank my advisor, Professor Nicholas L. Abbott. His intellectual curiosity allowed me to accomplish much more academically than I ever dreamed possible. I hope that I can maintain the high standards of scientific reasoning and critical thinking that I learned during my time in his research group. Second, I would like to thank the members of the Abbott group both past and present. In particular, I would like to thank Xiaoguang Wang for our numerous collaborative research projects, the results of which form the basis for several chapters presented in this thesis. He brought out the best of me as a scientific researcher, and I know that he will one day make an excellent professor. From the Abbott group, I would also like to thank Dr. I-Hsin Lin, Dr. Rebecca J. Carlton, Dr. Jacob T. Hunter, Reza Abbasi, Peter C. Mushenheim, Dr. Lie Na Tan, Dr. Gregory J. Wiepz, Arturo G. Guadarrama, James Buchen, Dr. Frédéric Mondiot, Dr. Abhijit Dan, Travis W. Nelson, Emre Bukusoglu, and Marco A. Bedolla Pantoja for their contributions to research reported in this thesis, Derek Ma for research to be reported elsewhere, and Dr. Aaron Lowe, Dr. Claribel Acevedo-Velez, Dr. Yiqun Bai, Dr. John Muller, and Maggie Budianto for moral support. Third, I would like to thank my other collaborators from outside of the Abbott group: Professor Juan J. de Pablo, Professor David M. Lynn, Professor Eric V. Shusta, Professor Daniel J. Klingenberg, Professor Michael D. Graham, Professor Douglas B. Weibel, Professor Paul J. Bertics, Professor Christopher J. Murphy, Professor Loren C. Denlinger, Professor Oleg D. Lavrentovich, Professor Samo Kralj, Professor Slobodan Žumer, Dr. Uttam Manna, Dr. Jonathan K. Whitmer, Tine Porenta, Tyler F. Roberts, Abhijeet Joshi, Matthew C. D. Carter, and Manohary Rajendram. Fourth, I would like to thank the undergraduates that I had the pleasure of mentoring: James Buchen, Jose Alberto

Gómez Roldán, Jinlu Liu, Long Lin, Shuting Zhang, Fernando Borges, and Thaddeus Brown. Fifth, I would like to thank the agencies that funded the research reported in this thesis: the National Science Foundation (NSF), the Materials Research Science and Engineering Center (MRSEC) at the University of Wisconsin–Madison, the Army Research Office, the National Institute of Health (NIH), and the Department of Energy (DOE). Sixth, I would like to thank my Final Oral Committee: Professor Nicholas L. Abbott, Professor Eric V. Shusta, Professor Daniel J. Klingenberg, Professor Sean P. Palecek, and Professor Arun Yethiraj. Seventh, I would like to thank my previous advisor Professor Abraham M. Lenhoff and his student and my mentor Dr. Kelley Kearns for allowing me to start my research career. Finally, I would like to thank all of my friends and family for moral support, especially my wife Elizabeth L. Miller, my parents, Stephen and Ella Miller, my sisters, Amanda and Elizabeth H. Miller, my grandparents, Francis and Rose Miller, my parents-in-law, Mark and Jennifer Byrd, my brothers-in-law, Adam Byrd and Thomas Gull, and my sister-in-law, Brandi Gull. This accomplishment is not individual, but rather the result of contributions from an amazing group of people.

Table of Contents

List of Figures, Schemes, and Tables

Chapter 1. Introduction and Overview

1.1 Introduction

The primary goal of the research described in this thesis was elucidation of physiochemical principles for the design of functional materials based on water-dispersed microdroplets of thermotropic liquid crystal (LC). This goal was accomplished through the study of two experimental systems, both of which involved LC-in-water emulsions (*i.e.*, oil-in-water emulsions in which the oil phase confined to the droplets possesses long-range orientational molecular order; see below). The first system involved addition of amphiphiles (surface active molecules) to the aqueous medium surrounding the micrometer-sized droplets (hundreds of nanometers to tens of micrometers-in-diameter) of the emulsions. The amphiphiles spontaneously adsorb at the surfaces and interact with the LC droplets to trigger transformations in the internal structure of the LC confined within (a so-called ordering transition). The presence of the amphiphiles in solution is readily transduced by the changes in the optical appearances of the droplets that result from the amphiphile-induced ordering transition when viewed under a polarized light microscope. Whereas these principles have been exploited for the design of chemical and biological sensors based on LC droplets in the past,[1-5] this thesis reports on a new mechanism for such ordering transitions (driven by ~10^3 molecules/droplet) which is anticipated to enable the design of extremely sensitive LC droplet-based sensors. Specifically, it is revealed that bacterial endotoxins trigger an ordering transition in LC microdroplets through a localized interaction with topological defects present in the droplets. Previously, amphiphiles were only

known to trigger the transitions by spontaneous adsorption of a near monolayer of molecules (~10^7 molecules/droplet) to the surfaces of the droplets.

The second experimental system involved adsorption of solid colloids (1 to 4 μm-in-diameter) at the surfaces of the LC microdroplets. In two main respects, this system was inspired by insights gleaned through study of the first system. First, although useful for chemical and biological sensing applications, the droplets of LC-in-water emulsions are unstable and readily coalesce over the course of several hours. Motivated by this observation, experiments were initiated to explore adsorption of colloids at the surfaces of the droplets for emulsion stabilization, which lower the surface energy penalty associated with droplet formation by replacement of aqueous—LC interface (Pickering emulsion[6, 7]). Second, the observation that endotoxin localizes at the defects contained in LC droplets, along with reports of partitioning of colloids to defects in other geometries of LCs,[8-16] led to the hypothesis that colloids adsorbed at the surfaces of LC microdroplets would partition to topological defects present on the surface, thus allowing manipulation of the positions of colloids. Indeed, this was observed by my colleagues in a preliminary investigation.[17] Furthermore, they showed that the droplets could be doped with a small amount of reactive mesogenic monomer and photopolymerized with LC either left within or extracted to synthesize spherical or non-spherical microparticles with chemical patches, respectively. Because particle shape has been shown to influence the efficiency of intracellular delivery of particles,[18] colloidal interactions between particles either adsorbed at liquid—liquid interfaces or dispersed in liquid crystalline (LC) solvents,[17, 19-22] and Brownian motion[23] this synthetic methodology could enable the design of several functional soft materials.

The research reported in this thesis provides a deeper understanding of the molecular level mechanisms that both lead to partitioning of colloids to surface defects and govern the assemblies formed by the colloids, and reveals a methodology to control the shape of the polymer microparticles through manipulations of the order within the droplets. The outcome of the experimental investigations will further enable design of functional soft materials based on colloid-decorated LC microdroplets. I note here that curvature-induced stresses in the membranes of bacteria lead to phase separation of phospholipids within the lipid bilayers. Specifically, lipids with the most negative spontaneous curvature partition to the two poles of the capped cylindrically-shaped cells (corresponding to the regions of highest membrane curvature),[24, 25] and proteins have also been observed to localize within these regions.[26] Thus, the second system also provides important insights into these complex biological phenomena, and a combination of the first and second systems might be used as a biomimetic material for bacterial cells.

1.2 Introduction to Liquid Crystals

An extensive introduction to optical characterization of LCs and a literature review of applications of LCs, in which both the internal configurations and conditions which lead to the configurations of LC droplets are described, follow this chapter. To prepare the reader, the present section provides an introduction to LCs and highlights some important properties of LCs that make them useful in the design of functional materials. A brief history of LCs is also provided.

1.2.1 Properties of Liquid Crystals

LCs are unique phases of matter that combine properties commonly associated with crystalline solids (long-range order) and isotropic liquids (high levels of molecular mobility, Figure 1-1A).[27-30] The combination of these two attributes causes colloids and amphiphiles to behave differently at LC interfaces than at the interfaces of isotropic liquids. Specifically, LC phases exhibit three main features that differentiate them from isotropic liquids:

(i) surface-induced ordering (surface anchoring) that can extend as far as 100 μm away from an interface[30](Figure 1-1B),

(ii) elastic mechanical properties that can lead to new classes of amphiphilic or colloidal interactions[31-36] (Figure 1-1C), and

(iii) topological defects (localized regions in which confinement of the LC causes the molecules to become sufficiently strained that the local order is diminished (analogous to "melting" to an isotropic phase)) that although only represent a minor contribution to the overall free energy of a bulk liquid crystalline phase can play an important role in interfacial phenomena[36-42] (Figure 1-1D).

These features, when combined with the optical birefringence of LCs, makes LC phases ideal for chemical and biological sensing applications or design of novel soft materials. For the case of LC-based sensors, the confining geometry and interfacial chemistry of a LC phase can be engineered such that interaction of a target specie (analyte) with the LC triggers an ordering transition that leads to changes in birefringence, which can be detected by polarized light microscopy (see Chapters 2 and 3).[1-5] These principles have been exploited for design of LC-based sensors for surfactants,[33, 43-49] phospholipids,[31, 50-54] bile acids,[55] proteins,[50, 56, 57] and

synthetic polymers.[48, 58-65] The features can also be exploited to control the positions of colloids adsorbed at a LC interface for material design. As was shown previously[66] and extensively in the research reported in this thesis, the strain within LC microdroplets can be manipulated to control the positions of colloids adsorbed at the surface and surface defects can be used as kinetic traps to lock the colloids in place.

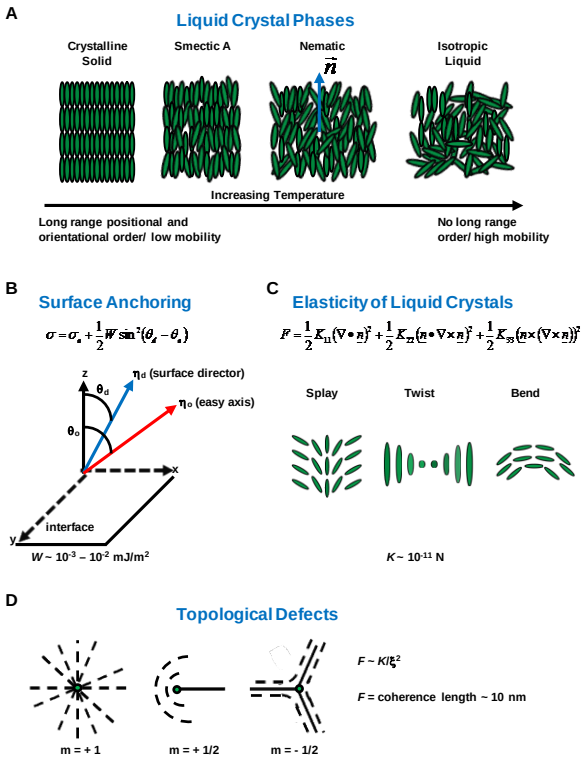

Figure 1-1. Properties of LC phases.

(A) Schematic illustration of the temperature-dependent phases of materials. (B) Orientation of a director and an easy axis of a LC at a surface. (C) Schematic illustration of three modes of strain in LCs: (i) splay, (ii) twist, and (iii) bend. (D) Schematic illustration of three types of topological defects.

1.2.2 Brief History of Liquid Crystal[1, 28, 67]

In 1888, Austrian botanist and chemist Friedrich Reinitzer discovered the existence of two melting points for the compound cholesterol benzoate.[1, 28, 67] Upon heating the solid form of the compound, he first observed an opaque optical appearance that after further heating became transparent. He later sent samples of various derivatives of cholesterol to a German physicist named Otto Lehman who was experienced in polarized light microscopy of crystalline materials. Lehman exploited his experience to analyze the samples after which he concluded that the opaque fluid was a distinct phase of matter with properties of both liquids and solids. Thus, the concept of a liquid crystal was born.[68] While fundamentally intriguing, no immediate application of this new phase of mater was envisioned causing research on LCs to be mainly limited to synthesis of new liquid crystalline materials for about 80 years (such as those synthesized by Daniel Vorländer,[69] George William Gray,[70] and Glenn H. Brown[71]).[72] This all changed in the 1960s when it was discovered by Richard Williams that the orientations of LCs can be manipulated *via* application of an electric field.[73] The discovery marked the advent of the development of modern liquid crystal displays (LCDs). Since the development of this now ubiquitous display technology, LC research remains extremely active as LCs have found use in chemical and biological sensing,[1-5] as active fluids for the manipulation of colloids,[33, 35, 36, 38, 42, 74, 75] and in numerous other optical devices.[76, 77]

1.3 Thesis Overview

Chapters 2-11 were prepared as separate publications and thus can be read independently. Chapter 2 introduces the reader to optical properties of LCs and the methods utilized for their

characterization in the research reported in this thesis. Chapter 3 is a literature review of chemical and biological sensing using LCs and the templated synthesis of polymer microparticles from LC droplets. The remainder of the chapters report on experimental investigations completed over the course of this thesis and can be grouped into the two experimental systems described above. Chapters 4 through 8 focus on principles for the design of LC droplet-based biological sensors, and Chapters 9 through 11 report principles for the design of novel soft materials based on LC microdroplets with colloids adsorbed at the surface. Below highlights of the experimental accomplishments reported in these chapters are provided.

Chapter 4 reports that picogram per milliliter (pg/mL) concentrations of endotoxin from the gram-negative bacteria *Escherichia coli* in water trigger an ordering transition in micrometer-size LC droplets from a bipolar state of the droplets to a radial state. The ordering transition, which occurs at surface concentrations of endotoxin that are less than 10^{-5} Langmuir, are not due to adsorbate-induced changes in the interfacial energy of the LC. The sensitivity of the LC to endotoxin was measured to change by six orders of magnitude with the geometry of the LC (droplet versus slab), supporting the hypothesis that interactions of endotoxin with topological defects in the LC mediate the response of the droplets. The LC ordering transition was also found to depend strongly on glycophospholipid structure.

Chapter 5 reveals that the ordering transition induced by endotoxin is strongly dependent on the size of the LC droplets. Specifically, as the diameters of the LC droplets increase from 2 μm to above 10 μm (in phosphate buffered saline with an ionic strength of 90 mM and a pH of 7.2), the percentage of droplets exhibiting a radial configuration in the presence of 100 pg/mL endotoxin is measured to decrease from 98 ± 1% to 3 ± 2%. A decrease in either the ionic strength or pH of the aqueous phase is also measured to reduce the percentage of droplets

exhibiting a radial configuration in the presence of endotoxin. These results, when interpreted within the context of a simple thermodynamic model that incorporates the contributions of elasticity and surface anchoring to the free energies of the LC droplets, lead to the conclusion that (i) the elastic constant K_{24} plays a central role in determining the size-dependent response of the LC droplets to endotoxin, and (ii) the endotoxin-triggered ordering transition occurs only under solution conditions (pH, ionic strength) where the combined contributions of elasticity and surface anchoring to the free energies of the bipolar and radial configurations of the LC droplets are similar in magnitude. The analysis also suggests that the presence of endotoxin perturbs the free energies of the LC droplets by $\sim 10^{-17}$ J per droplet, which is comparable to the standard free energy of self-association of $\sim 10^{3}$ endotoxin molecules. The results presented in Chapter 5, when combined with those reported in Chapter 4 of localization of endotoxin at the center of LC droplets, are consistent with the hypothesis that self-assembly of endotoxin within micrometer-sized LC droplets provides the driving force for the ordering transition. Overall, the results advance understanding of ordering transitions triggered by the interactions of analytes with LC droplets and, more broadly, provide guidance to the design of LC droplet systems as the basis of stimuli-responsive soft materials.

While past studies[1-5] and Chapters 4 and 5 of this thesis demonstrate the utility of LC-in-water emulsions for chemical and biological sensing, assays based on such emulsions can be hindered by the difficulty of characterizing the LC droplets using polarized light microscopy (which stems from high droplet mobility, sedimentation, and droplet—substrate interactions that influence both droplet shape and configuration). To address the need for a better methodology, Chapter 6 reports the use of flow cytometry to identify the internal ordering (director

configurations) of micrometer-sized droplets of thermotropic LCs dispersed in aqueous solutions of adsorbates (surfactants and phospholipids). It reveals that changes in the configurations of the LC droplets induced by the adsorbates generate distinct changes in light scattering plots (side versus forward scattering). Specifically, when compared to bipolar droplets, radial droplets generate a narrower distribution of side scattering intensities (SSC, large angle light scattering) for a given intensity of forward scattering (FSC, small angle light scattering). This difference is shown to arise from the rotational symmetry of a radial LC droplet which is absent for the bipolar configuration of the LC droplet. In addition, the scatter plots for radial droplets possess a characteristic “S-shape”, with two or more SSC intensities observed for each intensity of FSC. The origin of the experimentally observed S-shape is investigated *via* calculation of form factors and established to be due to size-dependent interference effects that differ for the forward and side scattered light. Finally, by analyzing emulsions composed of mixtures of bipolar and radial droplets at rates of up to 10,000 droplets per second, it is demonstrated that flow cytometry permits precise determination of the percentage of radial droplets within the mixture with a coefficient of determination of 0.98 (as validated by optical microscopy). Overall, the results presented in Chapter 6 demonstrate that flow cytometry provides a promising approach for high throughput quantification of the internal configurations of LC emulsion microdroplets. Because large numbers of droplets can be characterized, it enables statistically robust analyses of LC droplets.

In Chapter 7 the flow cytometry approach developed in Chapter 6 is used for rapid detection of bacterial endotoxins. Specifically, the methodology is used to demonstrate quantification of endotoxin in solution in the pg/mL range and that endotoxin from *Escherichia coli*, *Salmonella minnesota* or *Pseudomonas aeruginosa* all lead to quantitatively similar

responses in the LC droplets. Significantly, by varying the number of LC droplets in the dispersion containing the endotoxin, it is demonstrated that the LC droplets respond to the state of aggregation of the endotoxin in solution, which has been proposed previously to play a role in mediating cellular responses to endotoxin. Whereas a commercial flow cytometer was used for the experiments reported in Chapter 7, the principles defined by the study are applicable to microfluidic chip-based flow cytometers, thus potentially providing low cost methods for analysis of endotoxin that do not require biologically-derived reagents.

Chapter 8 moves away from detection of bacterial endotoxins to exploit LC-based flow cytometry for detection of membrane-derived microvesicles (MVs) shed by cells that are selectively captured *via* antibody-mediated interactions. Detection of MVs is important because they are being investigated for their role in intercellular communication and as potential biomarkers of disease. The methodology reported in the chapter was developed using MVs shed by epidermoid carcinoma A431 cells that contain epidermal growth factor receptor (EGFR) as an important and representative example of MVs containing signaling proteins that play a central role in cancer. The LC droplets were found to be sensitive to 10^6 MVs containing EGFR (relative to controls using isotype control antibody) and to possess a dynamic range of response across several orders of magnitude. Because the 100 nm-sized MVs captured *via* EGFR generate an optical response in the micrometer-sized LC droplets that can be readily detected by flow cytometry in light scattering mode, the approach possesses significant advantages over direct detection of MVs by flow cytometry. The LC droplets are also substantially more sensitive than techniques such as immunoblotting because the lipid-component of the MVs serves to amplify the antibody-mediated capture of the target proteins in the MVs.

As stated above, Chapter 9 represents a shift in the experimental system to LC-in-water emulsions that contain droplets to which colloids are adsorbed at the surface. The research reported in the chapter demonstrates that adsorbate-driven switching of the internal configurations of LC droplets can be used to sweep colloids to a single location on the LC droplet surfaces, thus resulting in the synthesis of homogeneous populations of patchy microparticles. The project was motivated by the desire to overcome the existence of multiple local energetic minima at the sites of surface defects, which can generate kinetic traps for colloids on the surfaces of the LC droplets and result in heterogeneous populations of patchy microparticles. The surface-driven switching of the LC can be triggered by addition of surfactant or salts, and permits the synthesis of dipolar microparticles as well as "Janus-like" microparticles. By using magnetic colloids, the utility of the approach is illustrated by synthesizing magnetically-responsive patchy microdroplets of LC with either dipolar or quadrupolar symmetry that exhibit distinct optical responses upon application of an external magnetic field.

Chapter 10 reports on the formation of organized assemblies of 1 μm-in-diameter colloids (polystyrene (PS)) at the poles of water-dispersed droplets (diameters 7 - 20 μm) of nematic liquid crystal (LC). For 4-cyano-4'-pentylbiphenyl droplets decorated with two to five PS colloids, 32 distinct arrangements of the colloids were found to form at the boojums of bipolar droplet configurations. Significantly, all but one of these configurations (a ring comprised of five PS colloids) could be mapped onto a local (non-close packed) hexagonal lattice. To provide insight into the origin of the hexagonal lattice, planar aqueous—LC interfaces were investigated, and it was found that organized assemblies of PS colloids did not form at these interfaces. Additional experiments involving the addition of salts revealed that a repulsive

interaction of electrostatic origin prevented formation of assemblies at planar interfaces, and that regions of high splay near the poles of the LC droplets generated cohesive interactions between colloids that could overcome the repulsion. Support for this interpretation was obtained from a model that included (i) a long-range attraction between adsorbed colloids and the boojum due to the increasing rate of strain (splay) of LC near the boojum (splay attraction), (ii) an attractive inter-colloid interaction that reflects the quadrupolar symmetry of the strain in the LC around the colloids, and (iii) electrostatic repulsion between colloids. The model predicted that electrostatic repulsion between colloids can lead to a ~1,000 k_BT energy barrier at planar interfaces of LC films, and that the repulsive interaction can be overcome by splay attraction of the colloids to the boojums of the LC droplets. Overall, the results reported in Chapter 10 provide insights into the directed assembly of colloids at interfaces of LC droplets.

Finally, Chapter 11 describes a collaborative research project in which the configurations of LC droplets doped with a reactive mesogenic monomer are manipulated (both in the presence and absence of colloids on the droplet surfaces) prior to photopolymerization of the droplets to synthesize polymer microparticles of different shape. After photopolymerization and subsequent extraction of the LC, bipolar, radial, axial, or preradial configurations of the droplets led to lemon-shaped, spherical, rod-shaped, or pear-shaped particles, respectively. The aspect ratio of the lemon-shaped particles can be controlled by the amount of reactive monomer initially doped into the LC (higher concentrations resulted in lower aspect ratios). Overall, the results of Chapter 11 reveal that water-dispersed LC microdroplets represent a rich palette of templates for synthesis polymer particles.

1.4 References

1. Bai, Y.; Abbott, N. L., Recent Advances in Colloidal and Interfacial Phenomena Involving Liquid Crystals. *Langmuir* **2011**, 27, 5719-5738.
2. Carlton, R. J.; Hunter, J. T.; Miller, D. S.; Abbasi, R.; Mushenheim, P. C.; Tan, L.; Abbott, N. L., Chemical and Biological Sensing Using Liquid Crystals. *Liquid Crystal Reviews* **2013**, 1, 1-23.
3. Lockwood, N. A.; Gupta, J. K.; Abbott, N. L., Self-Assembly of Amphiphiles, Polymers and Proteins at Interfaces between Thermotropic Liquid Crystals and Aqueous Phases. *Surface Science Reports* **2008**, 63, 255-293.
4. Lowe, A. M.; Abbott, N. L., Liquid Crystalline Materials for Biological Applications. *Chemistry of Materials* **2012**, 24, 746-758.
5. Miller, D. S.; Wang, X.; Abbott, N. L., Design of Functional Materials Based on Liquid Crystalline Droplets. *Chemistry of Materials* **2013**, 26, 496–506.
6. Madivala, B.; Vandebril, S.; Fransaer, J.; Vermant, J., Exploiting Particle Shape in Solid Stabilized Emulsions. *Soft Matter* **2009**, 5, 1717-1727.
7. Aveyard, R.; Binks, B. P.; Clint, J. H., Emulsions Stabilised Solely by Colloidal Particles. *Advances in Colloid and Interface Science* **2003**, 100, 503-546.
8. Rozic, B.; Tzitzios, V.; Karatairi, E.; Tkalec, U.; Nounesis, G.; Kutnjak, Z.; Cordoyiannis, G.; Rosso, R.; Virga, E. G.; Musevic, I.; Kralj, S., Theoretical and Experimental Study of the Nanoparticle-Driven Blue Phase Stabilisation. *European Physical Journal E* **2011**, 34, 1-11.
9. Muševič, I.; Škarabot, M.; Babič, D.; Osterman, N.; Poberaj, I.; Nazarenko, V.; Nych, A., Laser Trapping of Small Colloidal Particles in a Nematic Liquid Crystal: Clouds and Ghosts. *Physical Review Letters* **2004**, 93, 187801.
10. Pires, D.; Fleury, J.-B.; Galerne, Y., Colloid Particles in the Interaction Field of a Disclination Line in a Nematic Phase. *Physical Review Letters* **2007**, 98, 247801.
11. Ravnik, M.; Alexander, G. P.; Yeomans, J. M.; Zumer, S., Mesoscopic Modelling of Colloids in Chiral Nematics. *Faraday Discussions* **2010**, 144, 159-169.
12. Ravnik, M.; Alexander, G. P.; Yeomans, J. M.; Žumer, S., Three-Dimensional Colloidal Crystals in Liquid Crystalline Blue Phases. *Proceedings of the National Academy of Sciences* **2011**, 108, 5188-5192.
13. Škarabot, M.; Ravnik, M.; Babič, D.; Osterman, N.; Poberaj, I.; Žumer, S.; Muševič, I.; Nych, A.; Ognysta, U.; Nazarenko, V., Laser Trapping of Low Refractive Index Colloids in a Nematic Liquid Crystal. *Physical Review E* **2006**, 73, 021705.
14. Voloschenko, D.; Pishnyak, O. P.; Shiyanovskii, S. V.; Lavrentovich, O., Effect of Director Distortions on Morphologies of Phase Separation in Liquid Crystals. *Physical Review E* **2002**, 65, 060701.
15. Coursault, D.; Grand, J.; Zappone, B.; Ayeb, H.; Lévi, G.; Félidj, N.; Lacaze, E., Linear Self-Assembly of Nanoparticles Within Liquid Crystal Defect Arrays. *Advanced Materials* **2012**, 24, 1461-1465.
16. Fleury, J.-B.; Pires, D.; Galerne, Y., Self-Connected 3D Architecture of Microwires. *Physical Review Letters* **2009**, 103, 267801.

17. Mondiot, F.; Chandran, S. P.; Mondain-Monval, O.; Loudet, J.-C., Shape-Induced Dispersion of Colloids in Anisotropic Fluids. *Physical Review Letters* **2009**, 103, 238303.
18. Muro, S.; Garnacho, C.; Champion, J. A.; Leferovich, J.; Gajewski, C.; Schuchman, E. H.; Mitragotri, S.; Muzykantov, V. R., Control of Endothelial Targeting and Intracellular Delivery of Therapeutic Enzymes by Modulating the Size and Shape of ICAM-1-Targeted Carriers. *Molecular Therapy* **2008**, 16, 1450-1458.
19. Botto, L.; Lewandowski, E. P.; Cavallaro, M.; Stebe, K. J., Capillary Interactions between Anisotropic Particles. *Soft Matter* **2012**, 8, 9957-9971.
20. Lapointe, C. P.; Mason, T. G.; Smalyukh, I. I., Shape-Controlled Colloidal Interactions in Nematic Liquid Crystals. *Science* **2009**, 326, 1083-1086.
21. Loudet, J.-C.; Alsayed, A. M.; Zhang, J.; Yodh, A. G., Capillary Interactions between Anisotropic Colloidal Particles. *Physical Review Letters* **2005**, 94, 018301.
22. Yao, L.; Botto, L.; Cavallaro Jr, M.; Bleier, B. J.; Garbin, V.; Stebe, K. J., Near Field Capillary Repulsion. *Soft Matter* **2013**, 9, 779-786.
23. Han, Y.; Alsayed, A.; Nobili, M.; Zhang, J.; Lubensky, T. C.; Yodh, A. G., Brownian Motion of an Ellipsoid. *Science* **2006**, 314, 626-630.
24. Renner, L. D.; Weibel, D. B., Cardiolipin Microdomains Localize to Negatively Curved Regions of Escherichia Coli Membranes. *Proceedings of the National Academy of Sciences* **2011**, 108, 6264-6269.
25. Oliver, P. M.; Crooks, J. A.; Leidl, M.; Yoon, E. J.; Saghatelian, A.; Weibel, D. B., Localization of Anionic Phospholipids in Escherichia Coli Cells. *Journal of Bacteriology* **2014**, JB. 01877-14.
26. Renner, L. D.; Weibel, D. B., MinD and MinE Interact with Anionic Phospholipids and Regulate Division Plane Formation in Escherichia Coli. *Journal of Biological Chemistry* **2012**, 287, 38835-38844.
27. Chandrasekhar, S., *Liquid Crystals*. 2nd ed.; Cambridge University Press: New York, NY, USA, 1992.
28. Collings, P. J.; Hird, M., *Introduction to Liquid Crystals Chemistry and Physics*. Taylor & Francis: Bristol, PA, USA, 1997.
29. Collings, P. J., *Liquid Crystals : Nature's Delicate Phase of Matter*. 2nd ed.; Princeton University Press: Princeton, NJ, USA, 2002.
30. Gennes, P.-G. d.; Prost, J., *The Physics of Liquid Crystals*. 2nd ed.; Clarendon Press: New York, NY, USA, 1993.
31. Gupta, J.; Meli, M.; Teren, S.; Abbott, N., Elastic Energy-Driven Phase Separation of Phospholipid Monolayers at the Nematic Liquid-Crystal-Aqueous Interface. *Physical Review Letters* **2008**, 048301.
32. Gupta, J.; Abbott, N., Principles for Manipulation of the Lateral Organization of Aqueous-Soluble Surface-Active Molecules at the Liquid Crystal-Aqueous Interface. *Langmuir* **2009**, 2026-2033.
33. Poulin, P.; Stark, H.; Lubensky, T.; Weitz, D., Novel Colloidal Interactions in Anisotropic Fluids. *Science* **1997**, 1770-1773.
34. Smalyukh, I.; Chernyshuk, S.; Lev, B.; Nych, A.; Ognysta, U.; Nazarenko, V.; Lavrentovich, O., Ordered Droplet Structures at the Liquid Crystal Surface and Elastic-Capillary Colloidal Interactions. *Physical Review Letters* **2004**, 117801.

35. Smalyukh, I.; Lavrentovich, O.; Kuzmin, A.; Kachynski, A.; Prasad, P., Elasticity-Mediated Self-Organization and Colloidal Interactions of Solid Spheres with Tangential Anchoring in a Nematic Liquid Crystal. *Physical Review Letters* **2005**, 157801.
36. Nych, A.; Ognysta, U.; Pergamenshchik, V.; Lev, B.; Nazarenko, V.; Musevic, I.; Skarabot, M.; Lavrentovich, O., Coexistence of Two Colloidal Crystals at the Nematic-Liquid-Crystal-Air Interface. *Physical Review Letters* **2007**, 057801.
37. Lin, I.; Koenig, G.; de Pablo, J.; Abbott, N., Ordering of Solid Microparticles at Liquid Crystal-Water Interfaces. *Journal of Physical Chemistry B* **2008**, 16552-16558.
38. Musevic, I.; Skarabot, M.; Tkalec, U.; Ravnik, M.; Zumer, S., Two-Dimensional Nematic Colloidal Crystals Self-Assembled by Topological Defects. *Science* **2006**, 954-958.
39. Fernandez-Nieves, A.; Link, D.; Marquez, M.; Weitz, D., Topological Changes in Bipolar Nematic Droplets under Flow. *Physical Review Letters* **2007**, 157801.
40. Gupta, J.; Zimmerman, J.; de Pablo, J.; Caruso, F.; Abbott, N., Characterization of Adsorbate-Induced Ordering Transitions of Liquid Crystals within Monodisperse Droplets. *Langmuir* **2009**, 9016-9024.
41. Gupta, J.; Sivakumar, S.; Caruso, F.; Abbott, N., Size-Dependent Ordering of Liquid Crystals Observed in Polymeric Capsules with Micrometer and Smaller Diameter. *Angewandte Chemie, International Edition* **2009**, 1652-1655.
42. Nazarenko, V.; Nych, A.; Lev, B., Crystal Structure in Nematic Emulsion. *Physical Review Letters* **2001**, -.
43. Brake, J.; Abbott, N., An Experimental System for Imaging the Reversible Adsorption of Amphiphiles at Aqueous-Liquid Crystal Interfaces. *Langmuir* **2002**, 6101-6109.
44. Brake, J.; Mezera, A.; Abbott, N., Active Control of the Anchoring of 4 '-pentyl-4-cyanobiphenyl (5CB) at an Aqueous-Liquid Crystal Interface by using a Redox-Active Ferrocenyl Surfactant. *Langmuir* **2003**, 8629-8637.
45. Brake, J.; Mezera, A.; Abbott, N., Effect of Surfactant Structure on the Orientation of Liquid Crystals at Aqueous-Liquid Crystal Interfaces. *Langmuir* **2003**, 6436-6442.
46. Lockwood, N.; de Pablo, J.; Abbott, N., Influence of Surfactant Tail Branching and Organization on the Orientation of Liquid Crystals at Aqueous-Liquid Crystal Interfaces. *Langmuir* **2005**, 6805-6814.
47. Price, A.; Schwartz, D., Fatty-Acid Monolayers at the Nematic/Water Interface: Phases and Liquid-Crystal Alignment. *Journal of Physical Chemistry B* **2007**, 1007-1015.
48. Bahr, C., Surfactant-Induced Nematic Wetting Layer at a Thermotropic Liquid Crystal/Water Interface. *Physical Review E* **2006**, 030702.
49. Fletcher, P.; Kang, N.; Paunov, V., UV Polymerisation of Surfactants Adsorbed at the Nematic Liquid Crystal-Water Interface Produces an Optical Response. *ChemPhysChem* **2009**, 3046-3053.
50. Brake, J.; Daschner, M.; Luk, Y.; Abbott, N., Biomolecular Interactions at Phospholipid-Decorated Surfaces of Liquid Crystals. *Science* **2003**, 2094-2097.
51. Brake, J.; Daschner, M.; Abbott, N., Formation and Characterization of Phospholipid Monolayers Spontaneously Assembled at Interfaces Between Aqueous Phases and Thermotropic Liquid Crystals. *Langmuir* **2005**, 2218-2228.
52. Brake, J.; Abbott, N., Coupling of the Orientations of Thermotropic Liquid Crystals to Protein Binding Events at Lipid-Decorated Interfaces. *Langmuir* **2007**, 8497-8507.

53. Hartono, D.; Bi, X.; Yang, K.; Yung, L., An Air-Supported Liquid Crystal System for Real-Time and Label-Free Characterization of Phospholipases and Their Inhibitors. *Advanced Functional Materials* **2008**, 2938-2945.
54. Meli, M.; Lin, I.; Abbott, N., Preparation of Microscopic and Planar Oil-Water Interfaces that are Decorated with Prescribed Densities of Insoluble Amphiphiles. *Journal of the American Chemical Society* **2008**, 4326-4333.
55. Bera, T.; Fang, J. Y., Optical Detection of Lithocholic Acid with Liquid Crystal Emulsions. *Langmuir* **2013**, 29, 387-392.
56. Park, J.; Abbott, N., Ordering Transitions in Thermotropic Liquid Crystals Induced by the Interfacial Assembly and Enzymatic Processing of Oligopeptide Amphiphiles. *Advanced Materials* **2008**, 1185-1190.
57. Xue, C.; Yang, K., Dark-to-Bright Optical Responses of Liquid Crystals Supported on Solid Surfaces Decorated with Proteins. *Langmuir* **2008**, 563-567.
58. Gupta, J.; Tjipto, E.; Zelikin, A.; Caruso, F.; Abbott, N., Characterization of the Growth of Polyelectrolyte Multilayers Formed at Interfaces between Aqueous Phases and Thermotropic Liquid Crystals. *Langmuir* **2008**, 5534-5542.
59. Kinsinger, M.; Sun, B.; Abbott, N.; Lynn, D., Reversible Control of Ordering Transitions at Aqueous/Liquid Crystal Interfaces using Functional Amphiphilic Polymers. *Advanced Materials* **2007**, 4208-4212.
60. Kinsinger, M.; Buck, M.; Campos, F.; Lynn, D.; Abbott, N., Dynamic Ordering Transitions of Liquid Crystals Driven by Interfacial Complexes Formed between Polyanions and Amphiphilic Polyamines. *Langmuir* **2008**, 13231-13236.
61. Kinsinger, M.; Buck, M.; Meli, M.; Abbott, N.; Lynn, D., Langmuir Films of Flexible Polymers Transferred to Aqueous/Liquid Crystal Interfaces Induce Uniform Azimuthal Alignment of the Liquid Crystal. *Journal of Colloid and Interface Science* **2010**, 124-135.
62. Lockwood, N.; Cadwell, K.; Caruso, F.; Abbott, N., Formation of Polyelectrolyte Multilayer Films at Interfaces Between Thermotropic Liquid Crystals and Aqueous Phases. *Advanced Materials* **2006**, 850-854.
63. Price, A.; Schwartz, D., DNA Hybridization-Induced Reorientation of Liquid Crystal Anchoring at the Nematic Liquid Crystal/Aqueous Interface. *Journal of the American Chemical Society* **2008**, 8188-8194.
64. Sivakumar, S.; Gupta, J.; Abbott, N.; Caruso, F., Monodisperse Emulsions Through Templating Polyelectrolyte Multilayer Capsules. *Chemistry of Materials* **2008**, 2063-2065.
65. Tjipto, E.; Cadwell, K.; Quinn, J.; Johnston, A.; Abbott, N.; Caruso, F., Tailoring the Interfaces Between Nematic Liquid Crystal Emulsions and Aqueous Phases via Layer-by-Layer Assembly. *Nano Letters* **2006**, 2243-2248.
66. Mondiot, F. d. r.; Wang, X.; de Pablo, J. J.; Abbott, N. L., Liquid Crystal-Based Emulsions for Synthesis of Spherical and Non-Spherical Particles with Chemical Patches. *Journal of the American Chemical Society* **2013**, 135, 9972-9975.
67. Liquid Crystals. http://www.nobelprize.org/educational/physics/liquid_crystals/history/ (30 Jun 2014).
68. Lehmann, O., Über Fliessende Krystalle. *Zeitschrift für Physikalische Chemie* **1889**, 4, 462-472.
69. Vorlaender, D., *Chemische Kristallographie der Flüssigkeiten*. Akad. Verlagsges.: 1924.

70. Gray, G. W., *Molecular Structure and the Properties of Liquid Crystals*. Academic Press: London, England, 1962.
71. Brown, G. H.; Shaw, W. G., The Mesomorphic State-Liquid Crystals. *Chemical Reviews* **1957**, 57, 1049-1157.
72. Sluckin, T. J.; Dunmur, D. A.; Stegemeyer, H.; Press, C., *Crystals that Flow: Classic Papers from the History of Liquid Crystals*. Taylor & Francis: London, England, 2004.
73. Williams, R., Domains in Liquid Crystals. *The Journal of Chemical Physics* **1963**, 39, 384-388.
74. Sengupta, A.; Bahr, C.; Herminghaus, S., Topological Microfluidics for Flexible Micro-Cargo Concepts. *Soft Matter* **2013**, 9, 7251-7260.
75. Stark, H., Physics of Colloidal Dispersions in Nematic Liquid Crystals. *Physics Reports* **2001**, 351, 387-474.
76. Bahadur, B.; Tilton, M., *Liquid Crystals: Applications and Uses*. World Scientific: River Edge, NJ, USA, 1992.
77. Drzaic, P. S., *Liquid Crystal Dispersions*. World Scientific Publishing Company: River Edge, NJ, USA, 1995.

Chapter 2. Introduction to Optical Methods for Characterizing Liquid Crystals at Interfaces Used in the Experiments Reported in this Thesis*

2.1 Introduction

Liquid crystals (LCs) near interfaces enable fundamental studies of biological materials (*e.g.*, lipid droplets found in certain types of mammalian cells),[1, 2] the design of electro-optical devices (such as liquid crystal displays),[3] strategies for the hierarchical design of nanoscale materials (*e.g.*, semiconducting nanorods),[4, 5] and the creation of LC-based materials that respond to specific chemical and biological cues.[6-8] The intent of this chapter is not to dig deeply into fundamental questions specific to any one of these contexts, but rather this chapter seeks to enable new researchers to study interfacial phenomena involving LCs by providing instruction in key experimental methods. We focus in particular on the use of optical methods because these are accessible in many research and teaching laboratories, and they can provide broadly useful information on both the average orientations of LCs and the strengths with which LCs are held in preferred orientations at interfaces. In this chapter, we also avoid providing extensive details regarding the preparation of experimental systems because they tend to be specific to a particular line of investigation and are described elsewhere.[6-26]

2.2 Organization of this Chapter

This chapter covers three classes of LC interfaces (where the LCs are formed from molecules such as those shown in Figure 2-1A). We briefly describe these LC interfaces below

and refer to them in subsequent sections of this chapter.

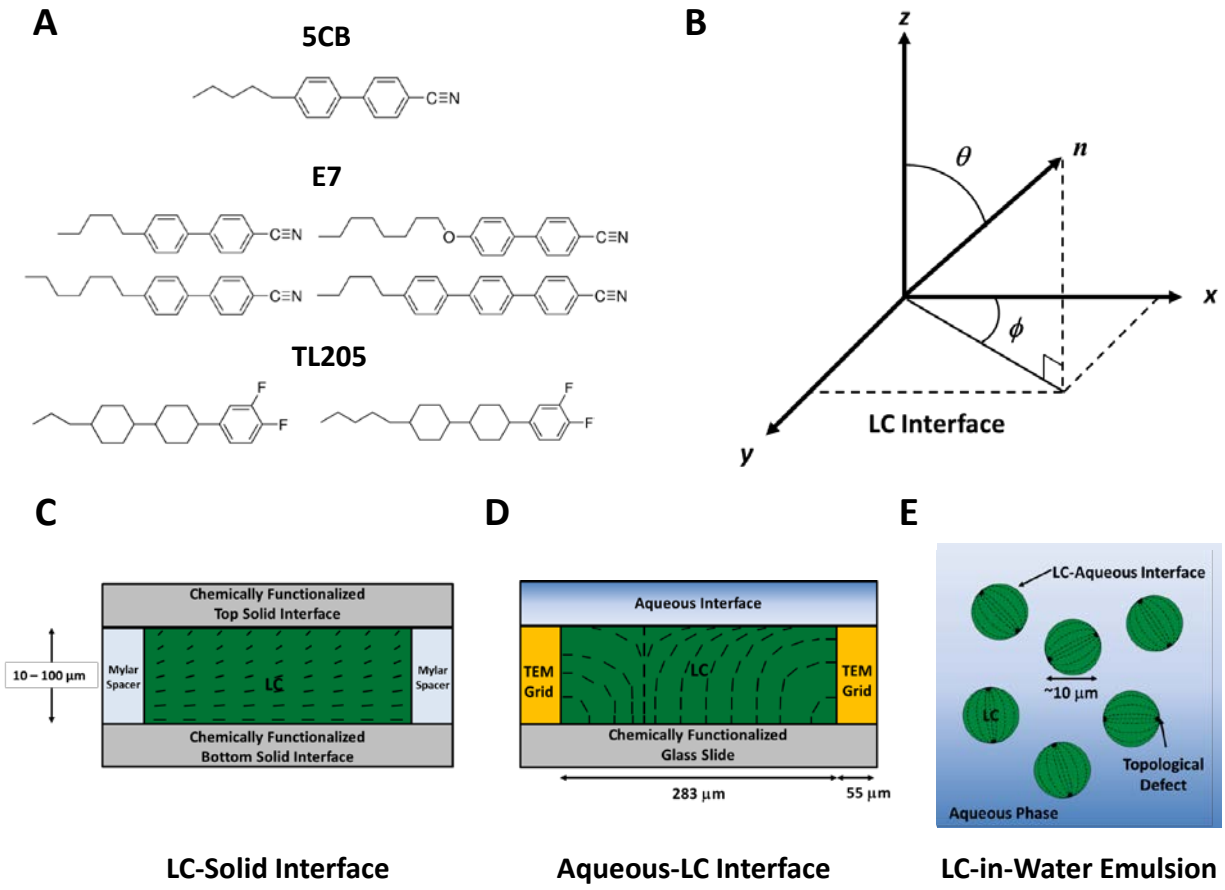

Figure 2-1. Common LC interfaces.

(A) Molecular structures of three common mesogens or mixtures of mesogens that form room-temperature nematic LC phases: 4-cyano-4′-pentylbiphenyl (5CB), E7, and TL205. The physical properties of these LCs are shown in Table 2-S1 of the SI. (B) Definition of angles used to characterize the average orientation of a LC (director, ***n***) near a flat interface. The azimuthal orientation is characterized by the azimuthal angle (ϕ), and the zenithal orientation is characterized by the zenithal angle (θ). (C−E) Schematic illustrations of three classes of LC interfaces that are discussed in this chapter. (C) LC−solid interface: LC is sandwiched between two chemically functionalized solid surfaces, each of which anchors the LC in a preferred orientation. (D) Aqueous—LC interface: LC is hosted within the pores of a grid supported on a chemically functionalized glass slide and submerged in an aqueous solution to create a stable aqueous—LC interface. (E) LC-in-water emulsion: LC droplets are dispersed in an aqueous phase. Dashed lines indicate the director of the LC. Modified and reproduced with permission.[7]

The first class of LC interfaces is formed between a LC and a solid (Figure 2-1C). This is the most widely explored class of LC interfaces because of its use in electro-optical devices. (The planar solid surface typically comprises an electrode that is used to switch the orientation of the LC.) Materials that are commonly used to prepare such solid interfaces include polymers (*e.g.*, sheared mechanically to align the polymer such that it serves as a molecular template that directs the orientation of the LC)[27, 28] and inorganic compounds prepared by physical vapor deposition (such as silicon oxide or gold).[29, 30] In the case of gold, the surface can be chemically functionalized using organosulfur compounds to generate a wide range of intermolecular interactions between the LC and the solid interface.[14, 23, 24, 31, 32] This latter system is particularly versatile and suitable for fundamental studies of the ordering of LCs at solid surfaces. At solid surfaces, the preferred orientation of the LC (easy axis) is defined by an azimuthal angle and a zenithal angle (Figure 2-1B). Typically, the azimuthal angle, ϕ, is defined with respect to a symmetry axis within the solid surface (*e.g.*, the direction of deposition of an inorganic layer deposited by physical vapor deposition at an oblique angle of incidence). The zenithal angle, θ, is reported with respect to the surface normal.

We note that a common occurrence in an experiment involving a film of LC confined between two solid surfaces is that the easy axes of the LC differ at the two surfaces. In this situation (often referred to as a "hybrid" LC system), the orientation of the LC between the two surfaces is determined by the minimization of the anchoring and elastic energies of the film of LC (Figure 2-1C). The strains experienced by a LC include splay, bend, and twist, and an elastic constant (K) for each mode of deformation connects the strain to the free energy density. (See equation 2-2 and associated text below for additional detail.[3, 33, 34]) In this situation, it is common to consider a so-called extrapolation length, defined as $L \approx K/W$ for the case of planar films,

where W is the orientation-dependent surface energy or anchoring energy per unit area.[34] In a planar film of LC, the extent to which the LC departs from the orientation of the easy axis depends on the ratio of the extrapolation length to the thickness of the LC film (d). For sufficiently thick films ($L/d \ll 1$), the orientation of the LC near an interface is close to the easy axis. Unless indicated otherwise, the planar films of LC discussed in this chapter satisfy this criterion.

The second class of planar interfaces involving LCs that can be characterized using the methods described in this chapter are those formed between LCs and aqueous phases.[7] As depicted in Figure 2-1D, the stabilization of this type of LC interface has to date been commonly achieved by using capillary forces generated by the placement of a grid onto a solid surface.[10] Within the pores of the grid, which have a width (typically ∼300 μm) that is much larger than the thickness of the LC film (5−50 μm), an approximately planar interface can be formed between the LC and the aqueous phase. Particular experimental protocols must be followed, however, to obtain an approximately planar interface. For example, if excess LC is deposited within the pores of the grid, then the resulting LC interface will be curved due to formation of a meniscus, which will impact the optical characterization of the interface (see below). Similar to the case of a LC−solid interface, the orientation of the LC at the aqueous interface is defined by azimuthal and zenithal angles (see above).

Finally, we comment that this chapter also addresses the characterization of LC droplets (Figure 2-1E), including LC droplets dispersed in an aqueous phase. This spherical geometry has particular relevance to the development of stimuli-responsive LC materials because confinement can lead to configurations of LC within the droplet that reflect a delicate balance of interfacial and elastic contributions to the free energy. One additional common feature of the droplet

geometry is the formation of so-called topological defects in the LC. In brief, when LCs are confined within the approximately spherical volume of a droplet, in many instances it is not possible for the LC to satisfy the anchoring conditions at the droplet interface through the continuous strain of the LC (such as by some combination of twist, splay, and bend). In these situations, localized regions of the LC partially "melt" (*i.e.*, exhibit low levels of orientational order relative to that of the bulk LC) to generate defects in the LC. The "cores" of the defects, although nanoscopic in size, possess refractive indices that differ substantially from that of the surrounding LC and thus can be characterized using optical methods. Common defects encountered in the droplet geometry include point defects and line defects, where the latter are frequently referred to as disclination lines. Additional discussion regarding defects in LCs can be found later in this chapter.

The remainder of this chapter is organized into four sections. First, we briefly outline procedures that can be used to prepare each of the three classes of experimental systems mentioned above. For details, we refer the reader to past publications. [6-26] Second, we describe the use of polarized light microscopy to provide qualitative information regarding the orientations of LCs near interfaces. Third, we report optical methods that permit the quantitation of optical properties of LCs that in turn provide a quantitative measurement of, for example, the zenithal angle assumed by a LC at an interface. Fourth, we describe methods that permit the measurement of the anchoring energies of LCs. Finally, we briefly describe some unresolved challenges related to the preparation and characterization of LC interfaces. In each of these sections, we address the characterization of the three classes of experimental systems shown in Figure 2-1C−E.

2.3 Preparation of Experimental Systems

2.3.1 LC–Solid Interfaces

To study the orientation of a LC at a solid surface, it is common to form an optical cell within which the LC is confined between two solid surfaces (as shown in Figure 2-1C). The preparation of the system typically begins by the placement of thin sheets of a polymer film, often Mylar, of known thickness (typically 2−100 μm) along two edges of the bottom solid surface. Next, the top surface is inverted, aligned with the bottom surface, and placed on the spacers in a manner such that a cavity is defined between the two surfaces of interest. The edges that have the spacers are then clipped together (using “bulldog” or “binder” clips); alternatively, the cell can be sealed and held together using epoxy after the introduction of the LC. Next, both the LC in a glass syringe and the sample cell are heated to above the nematic-to-isotropic transition temperature (clearing temperature) of the LC, which can be achieved, for example, by the placement of the sample on a hot plate. The LC is then introduced into the cell by capillary action. We note that it is generally preferred to introduce the LC into an optical cell after heating it above the clearing temperature to avoid flow-induced alignment and “surface-memory” effects that occur if the material is introduced while in the LC phase. If using labile organic interfaces (*e.g.*, self-assembled monolayers formed on gold films), however, one also has to be careful that the heating of the system does not cause thermal degradation. Finally, the sample is moved to an optical microscope for characterization.

2.3.2 Aqueous—LC Interfaces

The preparation of an interface between an aqueous phase and a LC can be achieved by first adding a small amount (~0.2 μL) of a nematic LC to the pores of a copper- or gold-coated transmission electron microscopy (TEM) grid supported on a glass substrate.[10] The glass substrate is usually chemically functionalized to induce a preferential zenithal orientation of the contacting LC. Common treatments of the glass employ one of two silanes, octadecyltrichlorosilane (OTS) or dimethyloctadecyl[3- (trimethoxysilyl)propyl]ammonium chloride (DMOAP), either of which causes perpendicular (homeotropic) anchoring of most nematic LCs.[7, 10, 35] As mentioned above, the grids are used to generate capillary forces that lead to the formation of stable aqueous—LC interfaces. A typical grid used in such an experiment will have a lateral pore size of ~300 μm and a known thickness ranging from 5 to 50 μm. Prior to use, the grids should be rinsed sequentially with ethanol, methanol, and chloroform and dried overnight in an oven. After a grid is placed on the glass substrate, it is filled with LC to form a film with approximately the same thickness as the grid. Excess LC (which will create a curved interface) can be removed from the grid by touching the LC with an empty capillary tube. The glass substrate supporting the LC-filled grid is then held at a slight angle from the horizontal and immersed in an aqueous solution to form the interface between the LC and the aqueous solution. As noted above, curved aqueous—LC interfaces will be generated if the grid is significantly overfilled or underfilled with LC. These situations are easily recognized by rings of interference colors that are observed upon imaging the sample between crossed polarizers using white light (described below). Finally, we note that the gold- and copper-coated surfaces of the TEM grids cause a homeotropic orientation of the LCs. However, the extent of this alignment (~10 μm) is

small compared to the lateral size of the grid pores typically used in these experiments (~300 μm, Figure 2-3C).

2.3.3 LC-in-Water Emulsions

The simplest method for preparing a LC-in-water emulsion involves the use of sonication and vortex mixing to disperse LC added to a bulk aqueous phase (*e.g.*, 2 μL of LC in 1 mL of water).[21, 25] When using conditions detailed in our past publication, this simple procedure results in a polydisperse population of LC droplets with diameters ranging from 1 to 20 μm.[25] A measurement of turbidity (using a UV−vis spectrophotometer) is a useful way to assess the end point of the sonication because, for a given volume of LC added to the bulk aqueous phase, emulsions with similar turbidities will possess similar size distributions of LC droplets. If precise control over the size of the LC droplets in the LC-in-water emulsion is desired, then one of several alternative methods of preparation can be employed. For example, monodisperse LC-in-water emulsions have been prepared by using polyelectrolyte multilayer capsules as templates[26] or by using microfluidics.[19] Finally, for optical characterization of a LC-in-water emulsion, a small volume of the emulsion (several microliters is usually sufficient) can be dispersed onto a supporting substrate (*e.g.*, a glass microscope slide) and the sample can be placed onto the stage of a microscope. We note that glycerol is often added to the aqueous phase of LC-in-water emulsions in order to increase the viscosity of the aqueous phase and thereby slow the diffusion of the LC droplets (for ease of observation by microscopy).

2.4 Qualitative Optical Characterization of LCs at Interfaces

Most LCs possess anisotropic optical properties, and thus many methods used to characterize the orientations of LCs revolve around the interaction of polarized light with the LCs. As detailed below, measurements of the polarization of light transmitted through LCs are commonly performed by placing a polarizer before and after a LC sample in the optical path of a microscope (Figure 2-2). To enable a discussion of polarized light microscopy, below we briefly describe how polarized light interacts with (uniaxial) LCs.

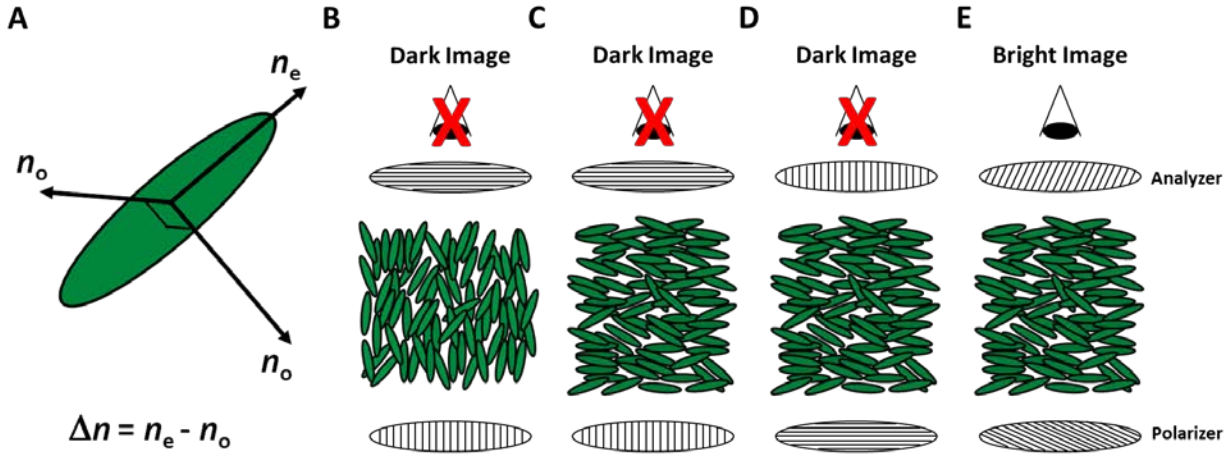

Figure 2-2. Polarized light microscopy of nematic LCs using orthoscopic illumination.
(A) Schematic illustration of the index ellipsoid of a uniaxial nematic LC. Two distinct refractive indices are evident: a refractive index parallel to the nematic director (n_e) and a refractive index perpendicular to the director (n_o). The difference between these refractive indices is known as birefringence ($\Delta n = n_e - n_o$). (B−D) Examples of orientations of LCs that, when viewed between crossed polarizers, exhibit a dark optical appearance. In B, the director of the LC is oriented parallel to the direction of the propagation of light through the LC. In C and D, the director of the LC is oriented in the plane of the sample with an azimuthal alignment that is either perpendicular (C) or parallel (D) to the incident polarizer. (E) When the director of the LC is oriented in the plane of the sample but with an azimuthal orientation that lies between the polarizer and analyzer, the light transmitted through the LC gains an elliptical polarization. This leads to a bright optical appearance of the LC.

Polarized light propagating through a LC in a uniaxial nematic phase can experience two distinct refractive indices depending on the polarization of the light relative to the director of the LC (the direction the molecules of the LC tend to align on average): a refractive index parallel to the nematic director (n_e, extraordinary refractive index) and a refractive index perpendicular to the director (n_o, ordinary refractive index) (Figure 2-2A).[33] The difference between these direction-dependent refractive indices is known as birefringence ($\Delta n = n_e - n_o$) and leads to two possible scenarios when a nematic LC is placed between a polarizer and an analyzer (oriented 90° with respect to the polarizer; crossed polarizers) and viewed in transmission mode using white light (Figure 2-2B−E). First, if the LC is oriented perpendicular to the bottom surface of the sample (Figure 2-2B) or if the azimuthal orientation of the LC is either 90° (Figure 2-2C) or 0° (Figure 2-2D) relative to the plane of polarization of the light passing through the bottom polarizer, then the light propagating through the LC will experience only one index of refraction (n_o or n_e) and the polarization of the light passing through the LC will remain unchanged. Thus, upon exiting the LC, light will not pass through the crossed analyzer, resulting in a dark optical appearance of the material (Figure 2-2B−D). Second, if the azimuthal orientation of the LC is neither parallel nor perpendicular to the bottom polarizer (Figure 2-2E), then the light propagating through the LC will experience two indices of refraction and split into so-called ordinary and extraordinary rays with electric field vectors vibrating in different planes. The different refractive indices experienced by the two rays causes them to travel at different velocities, inducing a phase shift. In general, the rays are phase shifted such that the light emerges from the LC with an elliptical polarization. Thus, some light will pass through the analyzer, resulting in a bright optical appearance of the LC (Figure 2-2E). As will be discussed in

detail below, the specific orientations of the LCs in the second scenario can give rise to a range of optical appearances of the LC samples.

2.4.1 Orthoscopic Polarized Light Microscopy of LCs

2.4.1.1 Orthoscopic Polarized Light Microscopy of Planar Films of LC

An important consequence of the above-described birefringence of nematic LCs is that orthoscopic polarized light microscopy can be employed to characterize the orientational ordering of nematic LCs at interfaces.[6, 7] This technique probes a LC sample with a beam of near-parallel rays of polarized light. To illustrate its utility in characterizing the orientational ordering of nematic LCs at interfaces, we focus on a system in which a thin planar film (slab geometry) of LC, tens of micrometers in thickness, is confined between a solid substrate and an aqueous phase (Figure 2-3). At the aqueous—LC interface, the zenithal orientation of the LC can be either homeotropic (perpendicular to the interface), planar (parallel to the interface), or tilted (at an acute angle to the interface). The bottom interface in Figure 2-3 is a reference interface, where the zenithal orientation of the LC is homeotropic (caused by treatment of a glass surface with a silane, see above). Each of the three zenithal orientations of the LC at the top interface will lead to distinct optical appearances of the LC film when viewed using polarized light microscopy. Below, we describe the optical appearance of the film for each of these zenithal orientations. We also comment that this discussion, although presented in the context of aqueous—LC interfaces, applies also to analysis of LCs between two solid surfaces.

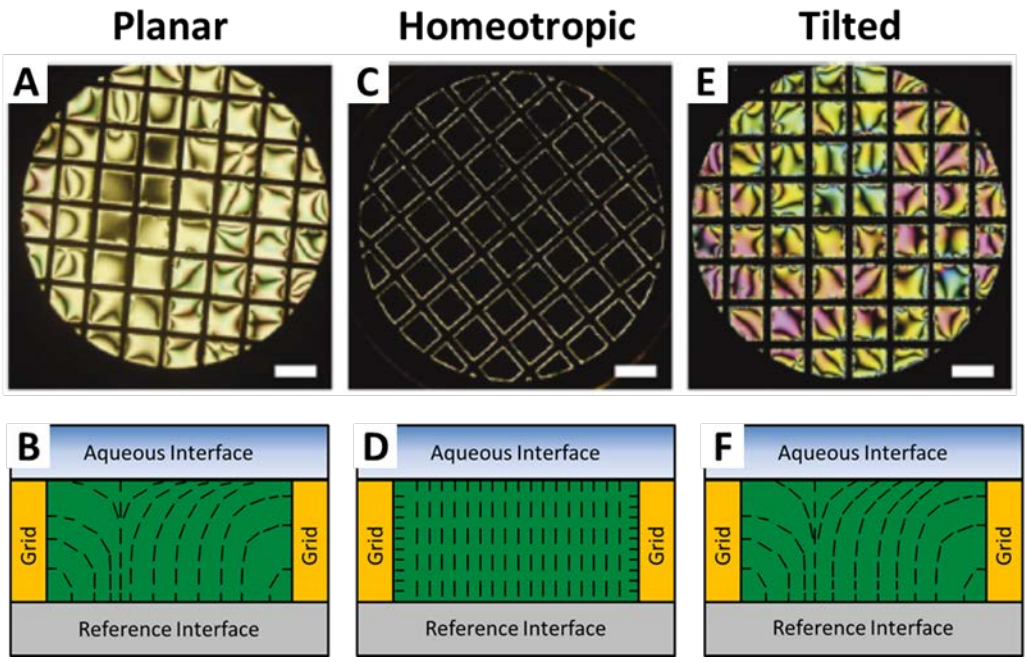

Figure 2-3. Polarized light micrographs (orthoscopic illumination) of micrometer-thick films of nematic 5CB anchored in three distinct orientations at aqueous—LC interfaces.

Optical images (crossed polarizers; A, C, and E) and schematic illustrations of the director profiles (B, D, and F) are shown. A and B correspond to planar anchoring, C and D correspond to homeotropic anchoring, and E and F correspond to tilted anchoring of the LC at the aqueous—LC interface. Scale bars are 300 μm. Reproduced with permission.[†,7]

When the zenithal orientation of the LC is parallel at the aqueous interface (so-called planar anchoring), the LC confined in the film will undergo splay and bend distortions (Figure 2-3B) to accommodate the competing anchoring conditions at opposing interfaces. This configuration of the LC leads to a bright optical appearance of the film as a result of the in-plane birefringence of the LC (Figure 2-3A). It is important to note that, although the zenithal orientation of the LC is well-defined at the aqueous—LC interface in Figure 2-3A, the azimuthal orientation (preferred orientation of the LC in the plane of the interface) of the LC is influenced by interactions with the vertical surfaces of the TEM grid. As a result of the anchoring on the

TEM grid, dark brushes that emanate from the edges of the film as well as defects (described in further detail below) are evident in the optical appearance of the LC film. The LC appears dark when the azimuthal orientation of the LC is locally parallel to either the polarizer or analyzer and bright when the LC adopts an intermediate azimuthal orientation. When the azimuthal orientation of a LC is degenerate, the appearance of the LC is often referred to as having a Schlieren texture.[33, 36, 37] Outside of the dark brushes, if the sample is illuminated using white light, the colors of the film of the LC are typically faint yellow, pink, or green (Figure 2-3A). These colors depend on the optical retardance of the LC film, which in turn is a function of the thickness of the film of LC as well as the LC orientation (also discussed in more detail below).

In contrast to the case of a planar orientation at the aqueous—LC interface, when the zenithal orientation of the LC is homeotropic, the orientation of the LC is uniformly perpendicular except near the vertical surfaces of the grid (Figure 2-3D). The perpendicular configuration of the majority of the LC leads to a dark optical appearance when the LC film is viewed between crossed polarizers (Figure 2-3C). The sample appears dark because, as described above, polarized light transmitted through the LC experiences only one index of refraction of the LC (the so-called ordinary refractive index). Thus, the polarization of the incident light will be preserved upon transmission through the sample, and the light will not be able to pass through the crossed analyzer. As noted above, the bright regions of the LC evident near the surfaces of the grid are caused by a homeotropic orientation of the LC on the vertical surfaces of the grid. The influence of the grid on the LC only extends a distance horizontally from the grid surface that is comparable to the thickness of the LC film (~10 μm in Figure 2-3C).

Finally, similar to the case of a planar orientation, when the orientation of the LC is tilted at the aqueous—LC interface, both splay and bend distortions will be present in the LC film

(Figure 2-3F). In the regions of the LC where the azimuthal orientation of the LC is not influenced by the grid, the LC exhibits an appearance that is similar to a Schlieren texture(Figure 2-3E). However, as compared to the case of a planar orientation, a tilted orientation at the top interface leads to a lower optical retardance. This lower retardance leads to intense coloration in regions outside of the dark brushes (Figure 2-3E). An analysis of the interference colors can provide quantitative information regarding the tilt angles of the LC at the interface (see below).

The experimental situation addressed in Figure 2-3 did not involve a twist deformation of the thin film of the LC. If a sample, when viewed between crossed polarizers, does not appear dark at some orientation between crossed polarizers, it is likely that a twist distortion is present in the sample. This situation can occur if the orientation of the LC is parallel to both the top and bottom interfaces yet the azimuthal orientation of the LC is different at both interfaces (Figure 2-9A). In this situation, if the azimuthal orientation of the LC at the bottom surface is aligned with the plane of polarization of the light passing through the bottom polarizer, then the LC will serve as a waveguide where the polarization of the light follows the twist of the nematic director. In later sections, we describe in detail how the rotation of a sample cell with a twist distortion can be used to quantify the azimuthal orientation of the LC at each interface (and thus also the twist angle of the LC in the sample).

As briefly mentioned above, the optical texture of a thin film of LC between crossed polarizers often possesses dark brush-like features (Figure 2-3A,E). These brushes typically emanate from defects present in the film. The defects can be either line defects (disclinations) extending throughout the bulk of the LC film or isolated point defects confined to the plane of observation. Under conditions that lead to a degenerate azimuthal orientation at the top interface of a thin film of LC (Figure 2-4A), two dark brushes emanate from the cores of disclinations

whereas four dark brushes will emanate from the cores of isolated point defects.[36] The presence of disclinations in areas where two brushes originate can be confirmed by displacing either the top or bottom confining surface of the LC film. When either of the surfaces is shifted, the centers with two brushes will leave a clear singular trace and the centers with four brushes will not.[36]

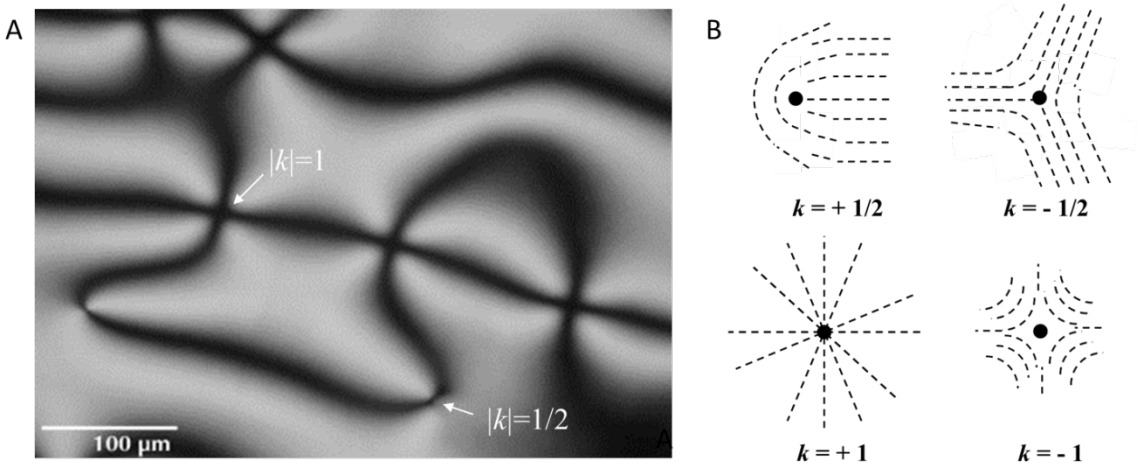

Figure 2-4. Topological defects in LCs.

(A) Polarized light micrograph of a Schlieren texture characteristic of a micrometer-thick film of LC with a degenerate planar alignment. Arrows indicate the positions of topological defects. (B) Schematic illustrations of director profiles around topological defects of indicated strength (k). (A) Modified and reproduced with permission.[‡,38]

The number of brushes (B) emanating from the core of a defect can be used to assign the magnitude of the strength of a defect ($|k|$) according to the relationship $|k| = B/4$.[36] Physically, $|k|$ defines the number of times the orientation of the nematic director rotates by $\pm 2\pi$ around the core of the defect (Figure 2-4B). In addition, the direction that the brushes rotate around a defect during an in-plane rotation of the film of LC can be used to define the sign of the defect. Clockwise rotation of the brushes around a defect corresponds to a positive defect, and counterclockwise rotation of the brushes corresponds to a negative defect. Figure 2-4B shows the director profiles around defects with different signs and strengths. Finally, we note that the type

of defect can provide insight into the orientation of the LC at an interface. For example, in a film formed by spreading LC onto a solid substrate in air (with a perpendicular orientation of the LC at the air—LC interface), the observation of a disclination line running through the central region of the film indicates that the zenithal orientation at the LC−solid interface is planar and the azimuthal orientation is uniform.[39] Furthermore, the direction that the disclination traverses the film is perpendicular to the azimuthal orientation of the LC at the LC−solid interface.

2.4.1.2 Orthoscopic Polarized Light Microscopy of LC-in-Water Emulsions

The example presented above illustrates how orthoscopic polarized light microscopy can be used to make qualitative statements regarding the orientational ordering of nematic LCs at the flat interface of a micrometer-thick film. Although the orientational ordering of LCs at the interface of micrometer-sized droplets in a LC-in-water emulsion can also be elucidated through the use of orthoscopic polarized light microscopy,[3, 6, 7, 18, 21, 25, 33] key differences exist between the approaches typically used to determine the orientations of LCs at the interfaces of droplets as compared to planar films. In particular, the confinement of LCs to micrometer-sized droplets generates well-defined patterns of topological defects within the LCs.[3, 40] The observation of these defects can be very useful when determining the orientations of the LC within droplets with light microscopy. As shown in Figure 2-5, the positions of topological defects in LC droplets and the organizations of the LC director around these defects (so-called “director configurations”) result in distinct optical signatures when the LC droplets are viewed between crossed polarizers.

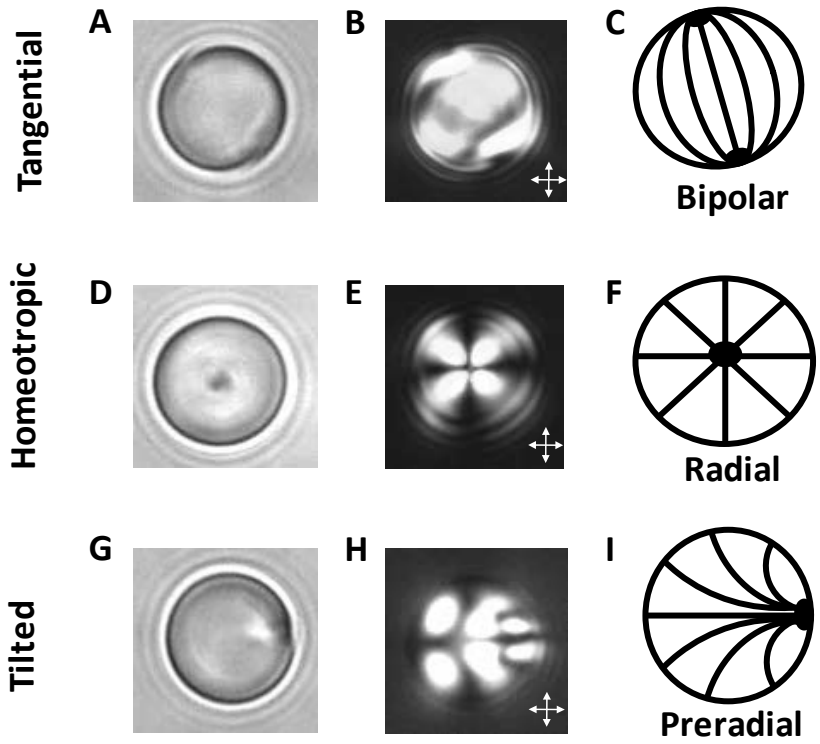

Figure 2-5. Orthoscopic bright field and polarized light micrographs of 8-μm-diameter droplets of nematic 5CB, shown as a function of the anchoring of the LC at the droplet interface.
Bright field micrographs (A, D, G), polarized light micrographs (crossed polarizer, B, E, H), and schematic illustrations of the director configurations (C, F, I) are shown for tangential (A−C), homeotropic (D−F), and tilted (G−I) anchoring of the LC at the droplet interface. Reproduced with permission.[21]

The positions of topological defects within the bulk or at the interfaces of LC droplets are governed by a subtle balance of surface anchoring and bulk elastic energies of the LC.[3, 16, 40] The relative importance of the two contributions to the droplet free energy is size-dependent, with the anchoring energy scaling with the square of the droplet radius and the elastic energy scaling in proportion to the droplet radius. For the purpose of this chapter, we focus on the characterization of large LC droplets (>1 μm) with strong anchoring. The term strong anchoring implies that the surface chemistry at the droplet interface sets the orientation of the LC at this interface and the

LC within the bulk of the droplet relaxes to a director configuration that minimizes the elastic energy of the LC. For a discussion of the influence of droplet size and weak anchoring on defect structures encountered in LC droplets, the reader is directed elsewhere (see also Chapter 3).[3, 16, 40]

In contrast to systems containing flat films of LC, LC-in-water emulsions contain LC droplets that are diffusing (translating and rotating), resulting in the time-varying optical appearance of LC droplets. When LC droplets are characterized, it is useful to obtain multiple images of each LC droplet by using video microscopy. By imaging LC droplets in many different orientations, the full director profile of the LC confined within the droplet can be determined. In addition to diffusion, when the LC is denser than the confining aqueous medium (such as in the case of nematic 5CB in water), a second complication is that the LC droplets undergo sedimentation. Our past studies have established that the sedimentation of LC droplets onto solid surfaces (*e.g.*, a glass microscope slide) can result in changes in the orientational ordering of the LC within the droplets.[20] Imaging of LC droplets should, therefore, be performed before a majority of the LC droplets contained in the emulsion have sedimented onto the supporting substrate (which often occurs within a few minutes of preparing a sample for observation). Finally, to ensure that the LC droplets were not perturbed by the supporting substrate, LC droplets that were at least 50 μm above the surface of the substrate and translating with velocities greater than 1 μm s^{-1} were selected for characterization in our past experiments. This distance (50 μm) is a conservative estimate based on our experimental observations and knowledge of the sizes of the LC droplets in the LC-in-water emulsions used in our studies (diameters of 1 to 20 μm).[20, 21, 25] Hydrodynamic interactions between diffusing LC droplets and surfaces have not been studied in detail, although it is likely that the distance over which

interactions occur will depend on the sizes of the droplets. As noted above, glycerol can also be added to the aqueous phases to increase the viscosity and slow sedimentation.

If the orientation of the LC at a droplet interface is tangential (*i.e.*, locally planar), then the director may exhibit a so-called bipolar configuration within the droplet (Figure 2-5A−C). In a bipolar configuration, the droplet possesses two diametrically opposed point defects (called boojums; Figure 2-5A,B).[3] These point defects can be identified by their dark appearance in polarized light images (Figure 2-5B) but are more readily identified when the droplets are viewed using bright field microcopy because they scatter light, resulting in areas of high contrast compared to defect-free regions (Figure 2-5A).[18] Therefore, bright field microscopy is a useful and complementary tool to polarized light microscopy when characterizing the orientational ordering of LCs confined within micrometer-sized droplets. In brief, bright field microscopy is performed by imaging the sample following the removal of the analyzer in a polarized light microscope.

In regions of a droplet where the projected orientation of the LC is uniform along the optical path and either parallel or perpendicular to the polarizer or analyzer (crossed polarizers), the LC will appear dark. In other regions of the LC droplet, the LC will appear bright. Thus, in the polarized light micrograph of the bipolar droplet shown in Figure 2-5B the majority of the LC within the droplet appears bright. However, Figure 2-5B is only one of many appearances that a bipolar droplet can exhibit between crossed polarizers because the ordering of the LC within the bipolar configuration is not spherically symmetric. Polarized light micrographs of bipolar droplets viewed in many different orientations can be found in reference [3].

When the orientation at a LC droplet interface is homeotropic, one possible director configuration is a so-called radial configuration (Figure 2-5D−F). The radial configuration is

characterized by a single point defect (or a very small disclination line in the shape of a ring) located at the center of the droplet.[3] A radial droplet possesses spherical symmetry, and thus its optical appearance is invariant upon rotation of the droplet. Finally, a polarized light micrograph of a radial droplet is characterized by a dark crosslike pattern as generated by the regions of the LC that are oriented either parallel or perpendicular to a polarizer (Figure 2-5E).

When the orientation of the LC at a droplet interface is tilted, one possible director configuration is the so-called preradial configuration (Figure 2-5G−I). Similar to a radial configuration, the preradial configuration possesses a single point defect. However, this defect is located at the surface of the droplet rather than in the core of the droplet. Similar to a bipolar droplet, a preradial droplet does not possess the spherical symmetry characteristic of a droplet in a radial configuration, and thus many possible optical appearances are exhibited by preradial droplets, dependent on the plane of rotation of the droplets. Again, by imaging preradial droplets oriented in many different planes of rotation, the full director profile within the droplet can be characterized (Figure 2-5I).

Finally, we note that the LC droplet configurations described above represent one of many possible director configurations induced by a tangential, homeotropic, or tilted orientation of the LC at a droplet interface. The most stable director configuration for a given preferred orientation is dictated by the relative magnitudes of the elastic constants that characterize the different modes of strain within the LC droplets. The elastic constant for twist is typically smaller than the other elastic constants (for splay and bend), and thus twisted configurations of LC droplets are not uncommon. For an extensive catalog of possible director configurations for each anchoring condition, the reader is directed elsewhere.[3] Finally, in contrast to defects in planar films of LC, defects present in LC droplets are typically classified by a topological

charge. This classification is somewhat more complex than assigning a strength to a defect in a planar film.[40]

2.4.2 Conoscopic Polarized Light Microscopy of Planar Films of LCs

The above sections describe how orthoscopic polarized light microscopy can be used to characterize the orientational ordering of nematic LCs at interfaces. Oftentimes, however, a complementary technique is necessary to provide an unambiguous determination of the orientation of the LC. For example, in the slab geometry, either a LC film with a uniform homeotropic orientation between confining interfaces (Figure 2-3D) or a film containing an isotropic phase of mesogens will appear dark when viewed using orthoscopic polarized light microscopy (Figure 2-6C,E). If the LC film is formed within the pores of a TEM grid, then a simple method to distinguish between these two states of a LC film is to observe the regions near the grid. As discussed in section 2.4.1.1, the regions of the LC films near the surfaces of the grids will appear bright (Figure 2-6C). In contrast to LC films with a uniform homeotropic alignment, an isotropic phase of mesogens will appear dark near the surfaces of the grids. More generally, however, conoscopic polarized light microscopy can be performed in conjunction with the orthoscopic examination to distinguish between homeotropic and isotropic states of a sample.

Figure 2-6A and 2-6B shows schematic illustrations of a polarized light microscope configured for orthoscopic and conoscopic observations, respectively. In contrast to orthoscopic examination, conoscopic examination requires, in addition to crossed polarizers, the insertion of a Bertrand lens and a substage condensing lens.[41] The substage condenser causes the sample to be illuminated by a cone of light rather than a column of light, and the Bertrand lens brings

interference patterns resulting from the interaction of this cone of light with the LC film into the focal plane of the ocular lens of the microscope. The conoscopic examination of a thin film of LC in a uniform homeotropic alignment between confining interfaces will lead to an interference pattern consisting of a dark cross overlying concentric rings (Figure 2-6D). In contrast, the conoscopic examination of an isotropic phase of mesogens will not generate an interference figure but rather will give rise to a dark optical appearance of the film (Figure 2-6F) because the polarization of the light transmitted though the isotropic film remains unchanged. If the LC is tilted slightly away from homeotropic, then the cross shown in Figure 2-6D will be displaced from the center of the image. Below we return to the analysis of conoscopic figures to provide quantitative information regarding the tilt of a LC away from the surface normal.

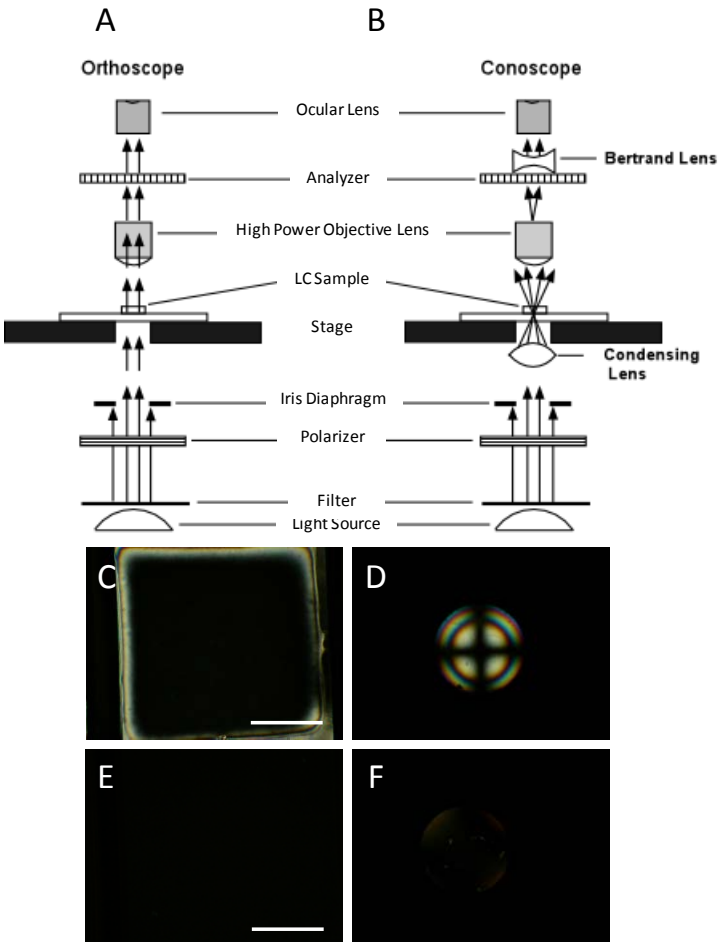

Figure 2-6. Orthoscopic and conoscopic polarized light microscopy.
Schematic illustrations (cross-sectional view) of the optical elements in a polarized light microscope when using (A) orthoscopic and (B) conoscopic illumination. (C) Orthoscopic and (D) conoscopic polarized light micrographs (crossed polarizers) of a LC film with a uniform homeotropic orientation. (E) Orthoscopic and (F) conoscopic polarized light micrographs (crossed polarizers) of a film of an isotropic phase of mesogens. Scale bars are 100 μm. (A, B) Modified and reproduced with permission.[42]

We conclude this section by reminding the reader that a film of LC oriented in a uniform planar alignment between confining interfaces can also give rise to a dark optical appearance during orthoscopic examination with crossed polarizers. However, conoscopic examination is not necessary to distinguish between this situation and the previous two scenarios described above.

Instead, if the film of LC is rotated at an angle between 0 and 90° relative to the polarizer, then the LC will exhibit a bright optical appearance (brightest at 45°). In contrast to a film containing LC in a uniform planar alignment, both a film with a uniform homeotropic alignment of the LC and a film of an isotropic material will remain dark at all angles of rotation of the sample.

2.5 Quantitation of the Orientations of LCs at Planar Interfaces

The experimental methods described above lead to qualitative information regarding the orientations of LCs at interfaces. (For example, they can indicate the presence of a tilt but do not provide the tilt angle.) In this section, we discuss optical methods that permit the quantitation of the orientations of LCs at interfaces. Obtaining quantitative information regarding the orientation of a LC at a surface, in general, requires a consideration of the director profile in a sample (that is, a description of the variation of the nematic director as a function of position throughout the sample). In this section, we will discuss the experimental methods that are used to infer both the zenithal and azimuthal orientations of LCs in thin films.

2.5.1 Quantitation of the Zenithal Orientations of LCs

First we consider the case of a LC film that exhibits a homeotropic orientation at a bottom (reference) surface. In this situation, as was shown in section 2.4.1.1, the zenithal orientation of the LC at the opposing top interface (*i.e.*, planar, homeotropic, or tilted) determines the optical appearance of the LC film (Figure 2-3). To quantify the orientation of the LC at the top interface of the LC film (θ_{top}, zenithal tilt angle), it is first necessary to determine

both the thickness, *d*, and the optical retardance, Δr, of the LC film. Methods used to measure these two quantities are described below.

2.5.1.1 Measurement of LC Film Thickness, d

In some circumstances, where a precise measurement of θ_{top} is not required, it may be sufficient to approximate the thickness of a LC film by, for example, the thickness of a Mylar spacer[43] (slab geometry) or by the thickness of a TEM grid (aqueous—LC interface).[10] To obtain a precise measurement of the tilt angle of the LC, however, a measurement of LC film thickness will likely be required. As described below, the thickness of the LC film within a LC optical cell can be obtained through the use of a UV−vis spectrophotometer.

In the situation where a LC film is to be confined between two semireflective solid surfaces, the thickness can be measured using the interferogram generated when the cell is inserted into the light path in a UV−vis spectrophotometer (before the cell is filled with the LC or when the LC is heated to an isotropic phase). Once within the light path, the constructive and destructive interference of light partially reflected from the internal surfaces of the optical cell leads to the formation of a pattern of interference fringes. Specifically, the thickness is calculated by identifying the wavelengths of adjacent peaks (λ_i) in the interference pattern using the following equation

$$d = \frac{1}{2n}\left(\frac{1}{\frac{1}{\lambda_2} - \frac{1}{\lambda_1}}\right) \qquad (2 - 1)$$

where *n* is the index of refraction of the medium in the optical cell (for the case of an air-filled cell, $n = 1$).

When a LC film has a free interface (*e.g.*, an aqueous—LC interface), measuring the thickness of the LC film is not as straightforward as in the case of a LC film confined between two solid surfaces. In the former situation, one approach is to measure the LC film thickness by decorating the aqueous interface of the LC with a few microparticles and by scratching the surface of the supporting solid substrate (before contacting the LC with the surface).[21] By locating the focal plane of the microscope on the features on both interfaces of the LC and by calibrating the notches on the fine focus knob of the microscope, the distance between the two interfaces of the LC can be determined by moving the focus from the bottom surface to the top interface of the LC film. The theoretical accuracy of this method is limited by the numerical aperture (NA) of the objective used. (The limit of the out-of-plane resolution of a microscope objective is proportional to $1/NA^2$.) We estimate, in practice, that this method permits the determination of the LC film thickness within ±1 μm when using a 50× objective with NA = 0.5 (on an Olympus BX60 microscope).

2.5.1.2 Measurement of LC Film Optical Retardance, Δr

The optical retardance, Δr, of a LC film is the integrated effect of the LC birefringence and the optical path length experienced by light transmitted through the film. As described in section 2.4.1.1, upon entering a LC film with hybrid boundary conditions, light refracts into two components (ordinary and extraordinary rays) that travel at different velocities through the film. The relative phase shift between these two rays upon exiting the LC medium is referred to as the optical retardance. As described below, this quantity can be measured through the use of a compensator, a Polscope, or it may also be estimated through the use of a Michel-Levy chart.

Compensators are instruments that shift the phase of light to exactly offset, or compensate for, the retardance of a birefringent sample. Although many different types of compensators exist and can be used to determine the retardance of a sample, here we discuss the Berek U-CTB compensator because it is a commonly used compensator. A Berek compensator consists of a birefringent calcite plate that can be precisely tilted to generate a desired (compensating) optical retardance (Figure 2-7). To use this instrument to determine the retardance of a LC film, one must first place the sample on a circular stage and examine the film between crossed polarizers using a polarized light microscope. It is then necessary to identify and focus on a region of the film where the LCs locally exhibit a uniform azimuthal orientation. The stage is then rotated until the observed region of the film attains extinction (*i.e.*, appears dark). Note that if the confining interface does not give rise to an overall preferred azimuthal orientation, as is the case for the interface between a LC and water, then regions of local uniform azimuthal alignment can be conveniently identified by the location of dark brushes. Next, the stage is rotated clockwise 45° and clamped into place (Figure 2-7C). The Berek compensator crystal is then inserted into the optical path above the sample but beneath the analyzer with its drum initially set to 30°. Subsequently, the angle adjustment dial of the compensator is slowly rotated in one direction, which leads to the appearance of a number of brightly colored fringes passing through the sample. The dial should continue to be rotated until a single black fringe intersects the center of the field of view (Figure 2-7D). This angle (θ_1) is recorded from the compensator. The dial is then rotated in the opposite direction, past 30°, until a second black fringe appears at θ_2 (Figure 2-7E). If no colored fringes are observed during this process, then rotate the stage counterclockwise 90°, reclamp it, and repeat the procedure described above. If a black fringe is still not observed to intersect the center of the field of view, it is possible that the

retardation of the LC film exceeds that which is measurable by the Berek compensator. After the measurement of these angles, the angle $\theta = |\theta_1 - \theta_2|/2$ is calculated and used to determine the retardance of the LC film (each compensator is accompanied by a reference table that reports the retardance as a function of this angle, Figure 2-7B).

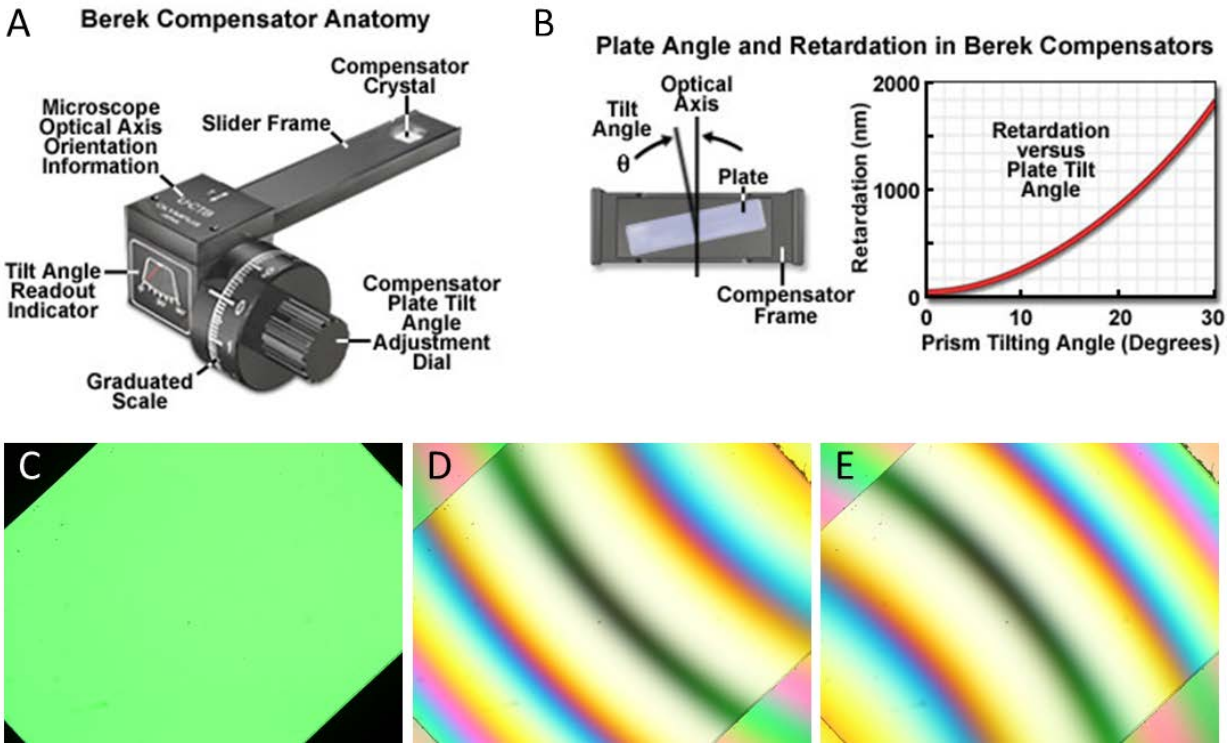

Figure 2-7. Measurement of optical retardance using a Berek compensator.
(A) Schematic illustration of a Berek compensator. (B) Illustration of the calcite crystal within a Berek compensator and the tilting of the crystal to introduce compensating retardance into the optical path. (C) Polarized white light micrograph of a birefringent reference sample viewed between crossed polarizers when rotated by 45° from extinction. (D, E) Optical images following the insertion of a Berek compensator into the optical path and subsequent rotation of the compensator dial, both forward (D) and backward (E), to locate a black fringe in the middle of the image. (A, B) Reproduced with permission.[44]

An alternative way to measure the optical retardance of a LC film is through the use of a retardance mapping instrument such as the CRI PolScope.[15] This instrument operates by

illuminating a sample with circularly polarized light (λ = 546.5 nm). After passing through the sample, the light is collected by a LC compensator and imaged through the use of a CCD camera. This instrument is capable of mapping the retardance of a sample over a large spatial area and can determine retardance values of between 0 and 273 nm (*i.e.*, $\lambda/2$) to a precision of 0.02 nm. A limitation of this technique is that it cannot be used to measure the absolute value of the retardance of a sample when the retardance exceeds 273 nm. (The Polscope reports retardances above 273 nm with an ambiguity on the order of the retardation.) The Polscope is best utilized either for analyzing small spatial variations in the retardance of a sample or for calculating exact retardance values in cases when the approximate retardance of the sample is already known.

Finally, we comment that a comparison of the interference colors observed in a LC sample (when imaged between crossed polarizers using white light) with those found in a Michel-Levy chart (Figure 2-8) can be used to estimate the retardance of a thin film of LC. However, the precision of this method can be low, especially for high optical retardances (>1500 nm), because individual interference colors can correspond to broad ranges (~300 nm) of retardance values. The interference colors also become increasingly washed out at high orders. We note that the Michel-Levy chart can also be utilized to estimate the thickness of a LC film when the orientation of the LC is known.

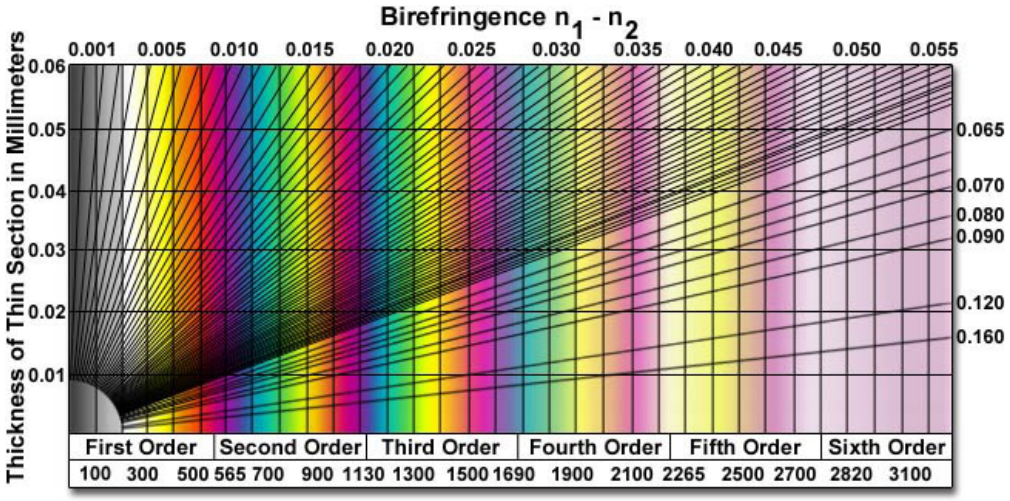

Figure 2-8. Michel-Levy color chart.

The chart relates the sample thickness, optical retardance, and effective birefringence of optically anisotropic materials to colors observed when using crossed polarizers and white light illumination. The optical retardance (in nm) is given at the bottom of the chart. Reproduced with permission.[45]

2.5.1.3 Determination of the Zenithal (Tilt) Angle

As mentioned above, the zenithal orientation of a LC (θ_{top}) at the upper interface of a LC film can be determined from the measurements of the retardance and film thickness. The evaluation of θ_{top} is based on a model of the director profile across the thickness of the LC film, which is typically determined by the minimization of an expression for the elastic free energy of the thin LC film.[7, 11, 15] The elastic free energy density of a LC, as described by the Frank−Oseen expression, is

$$F_{\text{elastic}} = \frac{1}{2}\left[K_{11}(\nabla \cdot n)^2 + K_{22}(n \cdot \nabla \times n)^2 + K_{33}(n \times \nabla \times n)^2 - K_{24}\nabla \cdot \left(n \times \nabla \times n + n(\nabla \cdot n)\right)\right] \quad (2\text{-}2)$$

where n is the director of the LC and K_{11}, K_{22}, K_{33}, and K_{24} are the elastic constants for splay, twist, bend, and saddle-splay deformations, respectively.[34] An additional term containing K_{13}, the

splay−bend elastic constant, is not included in equation 2-2 because it contains higher-order derivatives of n.[46, 47] The term containing K_{24} is also often neglected, although it clearly plays an important role in some geometries, including spherical LC droplets.[3, 16, 21, 25] Finally, a one elastic constant approximation ($K_{11} = K_{22} = K_{33} = K$) of the full Frank−Oseen expression[3, 34] is often used to simplify equation 2-2 further, although we note that there are instances where this simplification does not capture the experimental behavior of the LC.[16, 25] The use of the one-constant approximation reduces the expression for the elastic free energy density of the film to

$$F_{\text{elastic}}\left(\theta, \dot{\theta}\right) = \frac{1}{2} K \dot{\theta}^2 \qquad (2\text{-}3)$$

Minimization of the elastic free energy of the LC slab geometry leads to the result that the tilt of the LC varies linearly with position across the film

$$\theta(z) = \frac{z}{d}\left(\theta_{\text{top}} - \theta_{\text{bottom}}\right) + \theta_{\text{bottom}} \qquad (2\text{-}4)$$

For the situation where the orientation of the LC on the bottom substrate is strong and homeotropic ($\theta_{\text{bottom}} = 0°$), the relationship between the optical retardance of the LC film of thickness d and the tilt angle at the top interface (θ_{top}, measured from the surface normal) is given by

$$\Delta r \approx \int_0^d \left(\frac{n_{\text{o}} n_{\text{e}}}{\sqrt{n_{\text{o}}^2 \sin^2\left(\frac{z}{d}\theta_{\text{top}}\right) + n_{\text{e}}^2 \cos^2\left(\frac{z}{d}\theta_{\text{top}}\right)}} - n_{\text{o}} \right) \mathrm{d}z \qquad (2\text{-}5)$$

in which n_{o} and n_{e} are the indices of refraction perpendicular and parallel to the optical axis of the LC, respectively.[7, 11, 15] The solution of this equation to obtain the experimentally measured value of Δr yields θ_{top}. The interested reader is referred elsewhere to a detailed derivation of the equations for Δr and $\theta(z)$.[7]

To illustrate the relative precision of estimates of θ_{top} obtained using a compensator versus the Michel-Levy chart, we consider the following example. The retardance of a sample composed of a 20-μm-thick film of nematic 5CB (n_e = 1.711 and n_o = 1.5296)[22] with strong homeotropic orientation on the bottom reference surface was measured using a compensator in our laboratory to be Δr = 1,055 ± 14 nm. The solution of equation 2-5 for θ_{top} yields θt_{op} = 63.0 ± 0.5°. For comparison, from the Michel-Levy chart (Figure 2-8), it can be seen that such a film would possess pink interference colors when imaged between crossed polarizers using white light. However, the chart also shows that the pink interference color will be observed for all Δr values between ~1,020 and 1,100 nm. Therefore, if only the Michel-Levy chart was used to estimate θ_{top} in this particular sample, then θ_{top} could only be determined to lie between 61.7 and 64.6°.

Finally, we note that conoscopy can also be used to determine θ_{top}, particularly when the director is tilted only slightly from a homeotropic orientation. As noted above, the conoscopic examination of a thin LC film with uniform homeotropic alignment yields an interference figure consisting of a dark extinction cross overlying concentric rings in the center of the field of view. In the case of a LC film that tilts slightly from the homeotropic orientation, the dark cross will be shifted from the center of the field of view. The measurement of the position of the cross, when combined with a knowledge of the refractive indices of the LC, can be used to obtain α_o, the angle between the surface normal and the center of the interference figure through use of Mallard's equation

$$\frac{r}{R}\mathrm{NA} = \langle n \rangle \sin \alpha_o \qquad (2\text{-}6)$$

where *r* is the distance between the center of the field of view and the center of the cross, *R* is the radius of the field of view, NA is the numerical aperture of the objective, and ⟨*n*⟩ is the average refractive index of the sample.[48] The tilt angle is then given by

$$\theta_{\mathrm{top}} = 90° - \alpha_{\mathrm{o}} \qquad (2\text{-}7)$$

We refer the reader to a prior publication for a complete description of this method.[48]

2.5.2 Quantitation of Azimuthal Orientations of LCs

In this section, we describe how the azimuthal orientation of a LC can be quantified for the experimental situation in which the LC film is sandwiched between two contacting solid surfaces, each of which induces different azimuthal orientations in the LC. The distinct azimuthal orientation of the nematic LC at each of the two confining surfaces will lead, in general, to the formation of a twist distortion within the LC (Figure 2-9A). Depending on the azimuthal anchoring energy (W_{a}) at each of the confining surfaces and the elastic energy stored in the bulk resulting from the twist deformation, the LC director at one or both surfaces may depart from the easy axis.[14] Figure 2-9A depicts a case in which the easy axes of the LC at the two confining surfaces are aligned orthogonal to one another and a strong azimuthal orientation of the LC on the bottom reference surface prevents the LC director from deviating from the easy axis on the bottom surface.[6] However, weak anchoring of the director to the top surface allows the LC director to deviate from the top easy axis, decreasing the twist distortion across the film (characterized by the twist angle, Ψ).

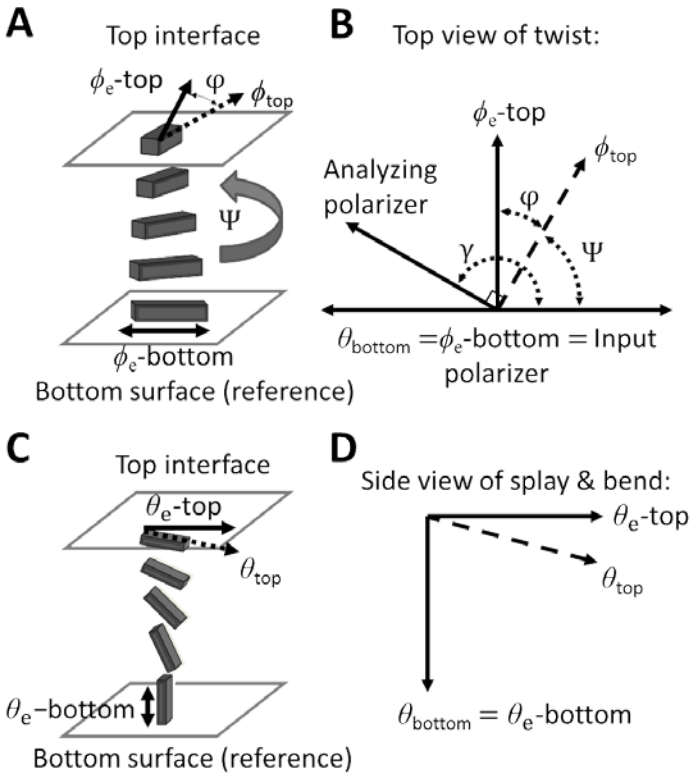

Figure 2-9. Experimental setups and angle diagrams used to determine azimuthal (A, B) and zenithal (C, D) anchoring energies.

(A) Schematic illustration of a twisted nematic LC (TNLC). (B) Diagram depicting the angles used to characterize the TNLC between two polarizers. The azimuthal orientation of the easy axis of the LC (defined by ϕ_e) and the azimuthal orientation of the LC director (defined by ϕ) are shown for both the top and bottom surfaces. Modified and reproduced with permission.[14] (C, D) Schematic illustrations and corresponding definitions of angular displacements of the director in a LC film with planar−homeotropic hybrid anchoring conditions. The bottom surface is assumed to cause strong homeotropic anchoring and is used as a reference surface. The orientation of the easy axis of the LC on the top surface is characterized by the zenithal angle θ_e, and the orientation of the LC director is characterized by θ.

The twisted nematic LC (TNLC) described above acts as a waveguide. Thus, polarized light propagating through the LC film follows the twist of the LC director provided the Mauguin condition, $\lambda \ll (n_e - n_o)P$, is satisfied,[34] where P, the pitch of the LC, is equivalent to $4d$ and d is

the thickness of the film for a 90° twist.[34] This condition is satisfied in LC films that are tens of micrometers in thickness.

With reference to Figure 2-9B, to determine Ψ, it is first necessary to determine the angle between the analyzer and source polarizer corresponding to the minimal transmission of polarized light (angle γ). A determination of γ requires that the easy axis of the LC on the bottom reference surface be aligned parallel to the input polarizer. This can be accomplished by the use of reference regions within the TNLC cell, corresponding to regions of the upper substrate that have been patterned such that the easy axis is parallel to that of the reference surface.[24] Within these regions, the LC film will have a uniform zenithal and azimuthal alignment. However, even in the absence of these reference regions, the reference surface of a TNLC cell can be properly aligned because the complete extinction of transmitted light will be observed upon the rotation of the analyzer only when the easy axis of the reference surface is aligned parallel to the input polarizer. In this situation, the TNLC cell is placed on a microscope stage between crossed polarizers with the input polarizer facing the reference surface, and the sample is subsequently rotated between the stationary polarizers to minimize light transmitted through the sample. Subsequently, the analyzer is rotated to further minimize the light transmitted through the sample. Three iterations of this procedure are typically sufficient to obtain extinction.[24] This procedure can be conveniently performed by capturing optical images of the TNLC at regularly spaced intervals of the sample or analyzer orientation (Figure 2-10A). Image processing is then used to determine the mean luminosity of the LC in each image, and this data can be plotted as a function of analyzer position (Figure 2-10B). The magnitude of light transmitted through the twisted LC film can be fit to a function of the form[14, 49]

$$f(x) = A\cos^2(x - x_o) \qquad (2\text{-}8)$$

to determine γ. The twist angle, Ψ, can then be obtained from γ using the angle diagram depicted in Figure 2-9B. For the case of interest, when the easy axes of the two confining substrates are orthogonal to one another, the relationship is

$$\Psi = \gamma - 90° \qquad (2\text{-}9)$$

where Ψ is constrained to be between −90 and +90°.[14, 49] A generalization of this expression for TNLC cells in which the easy axes are not orthogonal can be found elsewhere.[14, 49]

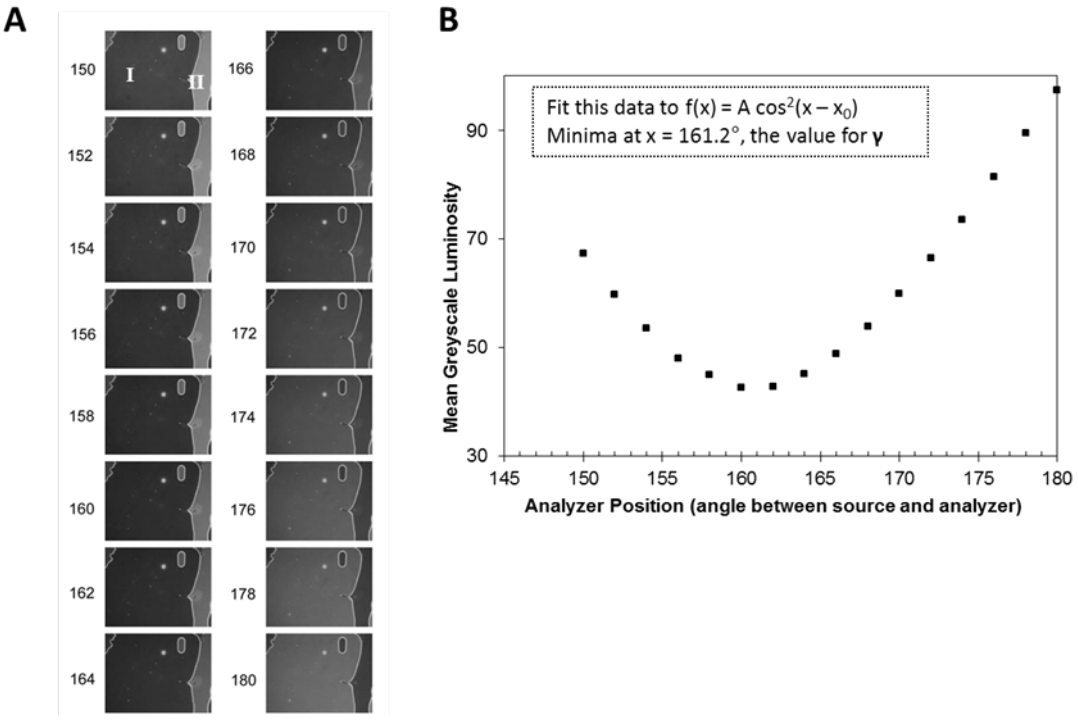

Figure 2-10. Measurement and analysis of the intensity of light transmitted through a twisted LC to determine the angle γ (definition in the text).

(A) Optical images (polarized white light) captured for the TNLC cell as a function of analyzer position (*i.e.*, crossed polarizers correspond to 90°). (B) Mean luminosity of a domain within the LC sample, plotted as a function of analyzer position. The data were fit to a cosine squared function (inset) to provide an accurate determination of the minimum. The angle at which the minimum occurs corresponds to γ. Reproduced with permission.[14]

Finally, we note that a pixel-by-pixel quantitation of the twist angle within a TNLC cell (*i.e.*, azimuthal orientation of LC on the top surface relative to the bottom surface) can also be performed using methods adapted from those described above.[23] For example, Figure 2-11 shows a high-resolution map of the twist angle within a TNLC cell.[23] We also note that the quantification of the orientations of LCs in spherical geometries (*i.e.*, LC-in-water emulsions) is more difficult than in the slab geometry described above. In general, quantitative information about the orientations of LCs at the interfaces of LC droplets is obtained by comparing the optical textures of droplets calculated from simulations to experimentally obtained polarized light micrographs.[3] We caution that the procedure is laborious and can be ambiguous.

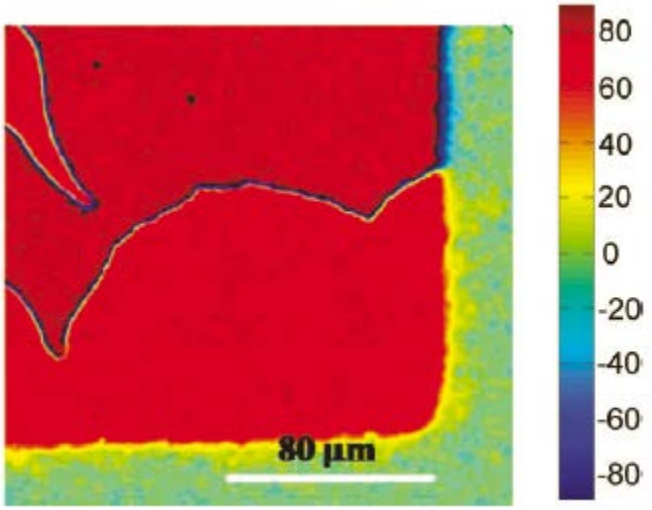

Figure 2-11. Optical map depicting the spatial variation of the twist angle within a LC that is anchored on a chemically patterned surface.

The color chart shown on the right side indicates the twist angle. The measurement of the position-dependent twist angle of the LC can be used to image chemical patterns on surfaces (details in the text). Reproduced with permission.[23]

2.6 Measurements of Anchoring Energies[§]

The measurement of the anchoring energy of a LC can provide fundamental insight into the intermolecular interactions responsible for the orientations of a LC at a particular interface, and it is also a technologically important quantity because it often determines the response of a LC to a stimulus (*e.g.*, electric field) or adsorbate. In the context of using LCs to report interfacial phenomena, measurements of changes in the anchoring energy can be substantially more sensitive than measurements of changes in the easy axis.[9, 14, 23] Below, we describe methods that permit the measurement of anchoring energies at a variety of LC interfaces.

2.6.1 Quantification of Anchoring Energies of LCs at Planar Interfaces

A number of methods exist to measure the anchoring energy of a LC at an interface.[3, 7, 14, 21-25, 34] In general, the methods involve the application of a perturbation to the LC and the measurement of a response that is dictated by the anchoring energy. One common approach is to design the LC to be elastically strained (deformed in the bulk) such that the torque generated by the strain in the LC causes the LC to deviate from the easy axis at the surface of interest. The magnitude of the angular deviation of the LC from the easy axis permits an evaluation of the anchoring energy. We note that this approach requires a knowledge of the orientation of the easy axis of the LC. When characterizing LCs in slab geometries, the torque generated by a thick film will be small, and thus experiments performed with thick LC films (*i.e.*, $d \approx 50$ μm) are typically used to determine the orientation of the easy axis of the LC. Conversely, measurements using thin LC films will yield orientations of the LC at the confining surfaces that deviate from the

easy axes (because of the torque associated with the strain of the LC) and thus provide access to anchoring energies of LCs.

2.6.1.1 Governing Equations Used to Determine Anchoring Energies

The orientation-dependent interfacial energy, f_S, of a LC is often described by the Rapini−Papoular expression,[7, 50] namely,

$$f_S = \frac{1}{2} W_z \sin^2(\theta - \theta_e) + \frac{1}{2} W_a \sin^2(\phi - \phi_e) \qquad (2\text{-}10)$$

where subscripts z and a denote zenithal and azimuthal quantities, respectively. We consider first an experiment performed in a thin film geometry that is designed to provide values for W_z. We then generalize the result to allow the determination of W_a. For simplicity, we assume that the magnitude of the elastic constants for splay, bend, and twist are equal (the so-called one-constant approximation discussed above). The experimental system comprises a bottom confining surface (reference surface with strong anchoring) and a top surface at which the anchoring energy is to be determined. As described below, minimization of the free energy of the system using the one elastic constant expression for the elastic energy and the Rapini−Papoular expression for the interfacial energy at the top surface results in a simple expression for W on the top surface. In brief, equations 2-3, 2-4, and 2-10 are inserted into the expression for the free energy of the LC film

$$F = \int_0^d F_{elastic}(\theta, \dot{\theta}) dz + \underbrace{f_{S1} + f_{S2}}_{F_{Surface}} \qquad (2\text{-}11)$$

to yield

$$F(\theta_{\text{top}}) = \int_0^d \frac{K}{2}\left(\frac{\theta_{\text{top}} - \theta_{\text{bottom}}}{d}\right)^2 \mathrm{d}z + \frac{1}{2}W_{\text{z}} \sin^2(\theta_{\text{top}} - \theta_{\text{e}}) + f_{\text{S2}} \quad (2\text{ - }12)$$

where θ_{top} and θ_{bottom} are the zenithal angles defined by the director at the top and bottom interfaces, respectively (Figure 2-9), and θ_{e} defines the orientation of the easy axis of the LC at the top interface. The minimization of this free energy with respect to the orientation of the LC at the top interface yields the expression

$$W_{\text{z}} = \frac{2K(\theta_{\text{top}} - \theta_{\text{bottom}})}{d \sin\left(2(\theta_{\text{e}} - \theta_{\text{top}})\right)} \quad (2\text{ - }13)$$

For the measurement of the azimuthal anchoring energy, a twisted nematic LC cell is used. By using the twist elastic constant (*i.e.*, $K = K_{22}$) and by redefining the angles in the system, we reach the commonly used torque balance expression ($\phi_{\text{top}} - \phi_{\text{bottom}} = \psi$ and $\phi_{\text{e}} - \phi_{\text{top}} = \varphi$, see Figure 2-9):[14, 23]

$$W_{\text{a}} = \frac{2K_{22}\psi}{d \sin(2\varphi)} \quad (2\text{ - }14)$$

2.6.1.2 Measurement Technique

To use equation 2-14 to determine the azimuthal anchoring energy at a LC−solid interface, the thickness of the LC film (section 2.5.1.1) and the twist angle of the LC (section 2.5.2) are measured. Figure 2-12 shows the relationship among the LC film thickness, twist angle, and anchoring energy calculated using equation 2-14 (using $K_{22} \approx 3.8$ pN).[24, 51] From Figure 2-12, we make a couple of observations. First, the twist angle varies significantly with anchoring energy for values of W that are less than ~0.5 μJ/m^2 for thick films (d = 50 μm) and less than ~2 μJ/m^2 for thin films (d = 4 μm). For larger values of the anchoring energy, the

torque generated by the elastic energy stored in the LC film is insufficient to cause easily measured deviations of the LC orientation from the easy axis at the interface. The range of anchoring energies that can be measured by this method is therefore relatively limited (0.5−2.0 $\mu J/m^2$). Outside of this range of anchoring energies, the uncertainty associated with the measured anchoring energies will be larger because small changes in the twist angle correspond to large changes in the anchoring energy (Figure 2-12B).[24] Specifically, for a surface with an anchoring energy of 5 $\mu J/m^2$, if characterized with a LC film with a thickness of 50 μm and a LC orientation measured with a precision of ±0.5°, the uncertainty in the anchoring energy would be approximately ±2 $\mu J/m^2$.

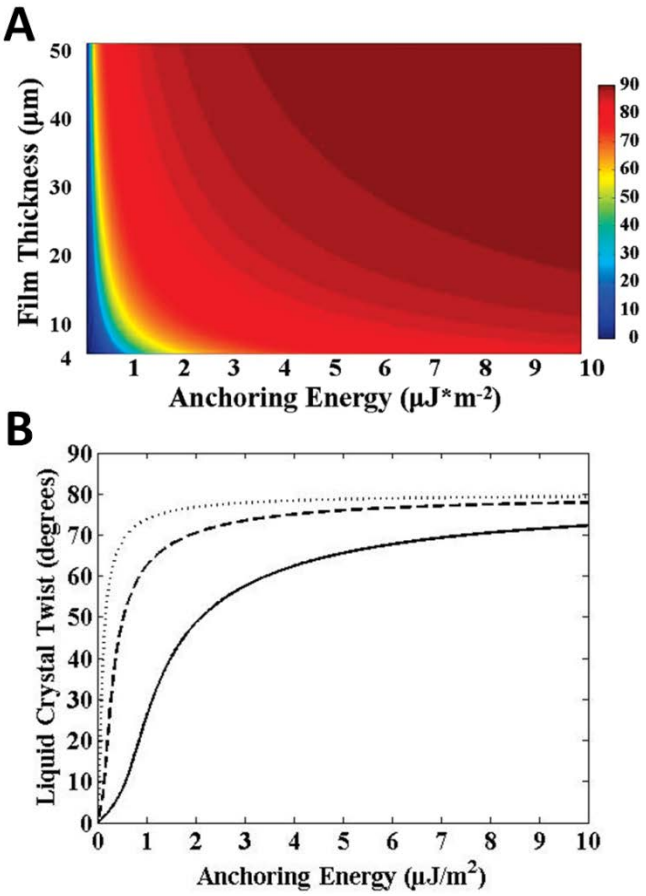

Figure 2-12. Twist angles of LCs calculated from the torque-balance equation (details in the text). Results shown are for 5CB and assume that the orientations of the easy axes (in the plane of the surface) at the confining surfaces are separated by 80°. (A) LC twist angles plotted as a function of anchoring energy and LC film thickness. (B) Plots of LC twist vs azimuthal anchoring energy for LC films with thicknesses of 50 μm (···), 16 μm (---), and 4 μm (−). Reproduced with permission.[24]

An implementation of equation 2-13 forms the basis of the measurement of the zenithal anchoring energy. To illustrate this method, we describe the measurement of the zenithal anchoring energy at a free interface of a LC film, such as the aqueous—LC interface. Here we assume that the anchoring of the LC at the bottom reference surface is strong and homeotropic. As with the example described above, it is first necessary to determine the thickness of the LC film (details in section 2.5.1.1). Next, the measurement of the retardance of the LC film is

performed using a compensator (section 2.5.1.2.). By solving equation 2.5, it is possible to determine the tilt of the LC at the aqueous—LC interface and, using equation 2-13, to determine the zenithal anchoring energy. The challenges associated with this method include the measurement of the thicknesses of LC films with free interfaces (such as an aqueous—LC interface). For example, a LC film of thickness 7 ± 1 μm and measured retardance of 475 ± 10 nm leads to an estimate of W that lies between 2 and 16 μJ/m^2 (using K = 6 pN). When performing measurements of the anchoring energies of LCs at aqueous—LC interfaces, it is also important to understand that the pH and the ionic content of the aqueous phase play important roles in determining the anchoring energy.[12, 13]

We end this section by commenting that the above analysis assumes that the film thickness (d) is large compared to the extrapolation length ($L/d \ll 1$, where L is the extrapolation length, defined in section 2.2, at the top surface). As described earlier, this means that the LC film thickness is large enough that it leads to relatively small deviations of the director from the easy axis. In experiments in which the LC film thickness is comparable to the extrapolation length at the top surface ($L/d \approx 1$) and the anchoring of the LC on the bottom surface is strong and homeotropic, the determination of the film thickness at which the entire film becomes homeotropic provides the basis of another method to estimate the anchoring energy of the LC at the top surface.

2.7 Unresolved Challenges and Cautions

Before concluding this chapter, we briefly discuss some unresolved challenges and cautions related to the optical characterization of LC interfaces. We present the challenges with

the hope that they might define topics of research for new researchers entering the field. The cautions are presented with the goal of alerting new researchers to some of the potential pitfalls when characterizing LC interfaces.

Our first comments involve the characterization of LC droplets. As discussed above, this area of research is a fertile one (for example, as the basis of biological sensors), yet the characterization of the interfaces of LC droplets remains relatively difficult. As noted in section 2.4.1.2, micrometer-sized LC droplets in LC-in-water emulsions typically translate with velocities greater than 1 μm s^{-1} both in and out of the focal plane of a microscope. This makes the imaging of LC droplets a challenge.[20, 21, 25] Past attempts by us and others to address this issue include the immobilization of LC droplets on chemically tailored solid surfaces.[20] The immobilization of the LC droplets, however, perturbs the ordering of the LC within the droplets.[20] An alternative approach (as described above) is to add glycerol to the aqueous phase to increase the viscosity of the aqueous phase and thus slow the motion of the LC droplets. Although this approach does decrease the velocity of the droplets, it also has the potential to change interfacial phenomena occurring in LC-in-water emulsion systems (*e.g.*, adsorbate-induced ordering transitions involving biological molecules; see also Chapter 11) substantially. In addition, we emphasize that in general it is particularly difficult to obtain quantitative information about the orientations of LCs at the interfaces of droplets. Current procedures typically involve calculations of the optical appearance of droplets from the results of simulations and comparisons of the calculated optical appearance to experimentally obtained polarized light micrographs. These procedures are laborious and can be ambiguous.[3] Overall, there exists an unmet need for the development of general and facile optical methods that permit the quantitative characterization of LC-in-water droplets. Advances in microfluidic technologies

and associated single-particle optical techniques (*e.g.*, flow cytometry) might form the basis of such techniques (see Chapter 6).

We also offer a few cautions for new researchers working in this field. The first caution relates to the purity (and stability) of LCs. LCs, although often provided by manufacturers at high purity, can degrade if not handled correctly (*e.g.*, exposed to sunlight from a window).[52] The degradation of a small fraction of the molecules within a LC sample can quickly change the interfacial ordering of the LC if the degradation products are surface-active. Therefore, care must be taken to avoid the degradation of the LC or the introduction of impurities from materials that contact the LC (*e.g.*, water that forms the basis of an aqueous—LC interface). A second caution that we offer here relates to the characterization of aqueous—LC interfaces. This is a so-called buried interface that is relatively difficult to characterize when decorated, for example, by a biological analyte such as a lipid that triggers an anchoring transition within the LC. A common approach is to add to the adsorbate a small amount of a fluorescent marker and perform fluorescence microscopy in parallel with both bright field and polarized light optical microscopy.[6, 7, 18, 20, 21] We and others have observed that the presence of fluorophores at the LC interface can substantially change the ordering of the LC.[7] The development of spectroscopic methods that do not require the use of labels and can be used to characterize buried interfaces (*e.g.*, nonlinear optical methods) is a promising area of ongoing research.

2.8 Conclusions

This chapter presents an introductory-level description of widely accessible optical methods that can be used to characterize the orientations of LCs at interfaces. These methods can

be used to characterize the orientations of LCs at planar interfaces (LC−solid and aqueous—LC) as well as the curved interfaces of LC-in-water emulsion droplets. All of the methods described in this chapter can be performed on a standard polarized light microscope with white-light illumination and a Bertrand lens. In addition, we describe optical methods that permit the measurement of the anchoring energies of LCs at interfaces. Such measurements can provide important insights into interfacial phenomena occurring at LC interfaces that do not give rise to changes in the easy axes of LCs. Overall, the methods described in this chapter enable studies of LC interfaces relevant to electro-optical devices, materials synthesis, biological liquid crystals, and the design of stimuli-responsive LC systems suitable for chemical and biological sensing.

Acknowledgements

This 1121288 (Materials Research Science and Engineering Center) and DMR-0425880, the Army Research Office (W911NF-11-1-0251 and W911NF-10-1-0181), and the National Institutes of Health (CA108467, CA105730, and 5T32GM08349). N.L.A. also acknowledges the support of research relevant to this review from the Department of Energy, Basic Energy Sciences, Biomaterials Program (DESC0004025).

2.9 Supporting Information

Physical properties of liquid crystals

Table 2-S1 shows physical properties of the liquid crystals (LCs) presented in Figure 2-1A of the main text (4-cyano-4'-pentylbiphenyl (5CB), E7 and TL205).

Table 2-S1. Physical properties of the LCs displayed in Figure 2-1A of the main text[a]

Property	5CB[b]	E7[c]	TL205[d]
K_{11} (pN)	6.3	11.7	17.3
K_{22} (pN)	3.9	8.8	-
K_{33} (pN)	8.3	19.5	20.4
T_{NI} (°C)	35	58	87.4
Δn	0.212	0.2255	0.2175
n_e	1.742	1.7472	1.7445
n_o	1.53	1.5217	1.527
Δε	20.1	14.1	5

[a]Notation: K_{11}, splay elastic constant; K_{22}, twist elastic constant; K_{33}, bend elastic constant; T_{NI}, nematic–to-isotropic clearing temperature; Δn, birefringence; n_e, extraordinary refractive index; n_o, ordinary refractive index; Δε, dielectric anisotropy.
[b]elastic constants from [53]; T_{NI} from [43, 54].
[c]elastic constants from [55, 56]; T_{NI} from [54].
[d]elastic constants courtesy of EMD group, ***Merck*** KGaA.; T_{NI} from [54].
[b,c,d]Δn, n_e, n_o, and Δε courtesy of EMD group, ***Merck*** KGaA.

2.10 References

*This chapter was originally published as an Instructional Review in the journal *Langmuir*. My contribution to this review was in writing sections 2.2-2.4, 2.7, and 2.9, discussing content of other sections, and assisting my co-authors in the proof reading of the manuscript and preparation of some of the figures.

†Figure 2-3:

‡Figure 2-4:

§The published version of this chapter included another subsection under this section titled Anchoring Energies in LC-in-Water Emulsions. The methods presented in this subsection were developed during the course of my Ph.D. research and are presented in Chapter 5 of this thesis.

1. Rothblat, G. H.; Rosen, J. M.; Insull, W.; Yau, A. O.; Small, D. M., Production of Cholesteryl Ester-Rich, Anisotropic Inclusions by Mammalian-Cells in Culture. *Experimental and Molecular Pathology* **1977,** 26, 318-324.
2. Stewart, G. T., Liquid Crystals of Lipid in Normal and Atheromatous Tissue. *Nature* **1959,** 183, 873-875.
3. Drzaic, P. S., *Liquid Crystal Dispersions*. World Scientific: River Edge, NJ, USA, 1995.
4. Karanikolos, G. N.; Alexandridis, P.; Mallory, R.; Petrou, A.; Mountziaris, T. J., Templated Synthesis of ZnSe Nanostructures Using Lyotropic Liquid Crystals. *Nanotechnology* **2005,** 16, 2372-2380.
5. Yang, C. S.; Awschalom, D. D.; Stucky, G. D., Growth of CdS Nanorods in Nonionic AmphiphilicTriblock Copolymer Systems. *Chemistry of Materials* **2002,** 14, 1277-1284.
6. Bai, Y.; Abbott, N. L., Recent Advances in Colloidal and Interfacial Phenomena Involving Liquid Crystals. *Langmuir* **2011,** 27, 5719-5738.
7. Lockwood, N. A.; Abbott, N. L., Self-Assembly of Surfactants and Phospholipids at Interfaces Between Aqueous Phases and Thermotropic Liquid Crystals. *Current Opinion in Colloid & Interface Science* **2005,** 10, 111-120.
8. Lowe, A. M.; Abbott, N. L., Liquid Crystalline Materials for Biological Applications. *Chemistry of Materials* **2012,** 24, 746-758.
9. Bai, Y.; Abbott, N. L., Enantiomeric Interactions Between Liquid Crystals and Organized Monolayers of Tyrosine-Containing Dipeptides. *Journal of the American Chemical Society* **2012,** 134, 548-558.

10. Brake, J. M.; Abbott, N. L., An Experimental System for Imaging the Reversible Adsorption of Amphiphiles at Aqueous-Liquid Crystal Interfaces. *Langmuir* **2002,** 18, 6101-6109.
11. Brake, J. M.; Mezera, A. D.; Abbott, N. L., Effect of Surfactant Structure on the Orientation of Liquid Crystals at Aqueous-Liquid Crystal Interfaces. *Langmuir* **2003,** 19, 6436-6442.
12. Carlton, R. J.; Gupta, J. K.; Swift, C. L.; Abbott, N. L., Influence of Simple Electrolytes on the Orientational Ordering of Thermotropic Liquid Crystals at Aqueous Interfaces. *Langmuir* **2012,** 28, 31-36.
13. Carlton, R. J.; Ma, C. D.; Gupta, J. K.; Abbott, N. L., Influence of Specific Anions on the Orientational Ordering of Thermotropic Liquid Crystals at Aqueous Interfaces. *Langmuir* **2012,** 28, 12796-12805.
14. Clare, B. H.; Guzman, O.; de Pablo, J. J.; Abbott, N. L., Measurement of the Azimuthal Anchoring Energy of Liquid Crystals in Contact with Oligo(ethylene glycol)-Terminated Self-Assembled Monolayers Supported on Obliquely Deposited Gold Films. *Langmuir* **2006,** 22, 4654-4659.
15. Gupta, J. K.; Abbott, N. L., Principles for Manipulation of the Lateral Organization of Aqueous-Soluble Surface-Active Molecules at the Liquid Crystal-Aqueous Interface. *Langmuir* **2009,** 25, 2026-2033.
16. Gupta, J. K.; Sivakumar, S.; Caruso, F.; Abbott, N. L., Size-Dependent Ordering of Liquid Crystals Observed in Polymeric Capsules with Micrometer and Smaller Diameter. *Angewandte Chemie-International Edition* **2009,** 48, 1652-1655.
17. Gupta, J. K.; Tjipto, E.; Zelikin, A. N.; Caruso, F.; Abbott, N. L., Characterization of the Growth of Polyelectrolyte Multilayers Formed at Interfaces Between Aqueous Phases and Thermotropic Liquid Crystals. *Langmuir* **2008,** 24, 5534-5542.
18. Gupta, J. K.; Zimmerman, J. S.; de Pablo, J. J.; Caruso, F.; Abbott, N. L., Characterization of Adsorbate-Induced Ordering Transitions of Liquid Crystals within Monodisperse Droplets. *Langmuir* **2009,** 25, 9016-9024.
19. Khan, W.; Choi, J. H.; Kim, G. M.; Park, S. Y., Microfluidic Formation of pH Responsive 5CB Droplets Decorated with PAA-b-LCP. *Lab on a Chip* **2011,** 11, 3493-3498.
20. Kinsinger, M. I.; Buck, M. E.; Abbott, N. L.; Lynn, D. M., Immobilization of Polymer-Decorated Liquid Crystal Droplets on Chemically Tailored Surfaces. *Langmuir* **2010,** 26, 10234-10242.
21. Lin, I. H.; Miller, D. S.; Bertics, P. J.; Murphy, C. J.; de Pablo, J. J.; Abbott, N. L., Endotoxin-Induced Structural Transformations in Liquid Crystalline Droplets. *Science* **2011,** 332, 1297-1300.
22. Lockwood, N. A.; de Pablo, J. J.; Abbott, N. L., Influence of Surfactant Tail Branching and Organization on the Orientation of Liquid Crystals at Aqueous-Liquid Crystal Interfaces. *Langmuir* **2005,** 21, 6805-6814.
23. Lowe, A. M.; Bertics, P. J.; Abbott, N. L., Quantitative Methods Based on Twisted Nematic Liquid Crystals for Mapping Surfaces Patterned with Bio/chemical Functionality Relevant to Bioanalytical Assays. *Analytical Chemistry* **2008,** 80, 2637-2645.
24. Lowe, A. M.; Ozer, B. H.; Bai, Y.; Bertics, P. J.; Abbott, N. L., Design of Surfaces for Liquid Crystal-Based Bioanalytical Assays. *ACS Applied Materials & Interfaces* **2010,** 2, 722-731.

25. Miller, D. S.; Abbott, N. L., Influence of Droplet Size, pH and Ionic Strength on Endotoxin-Triggered Ordering Transitions in Liquid Crystalline Droplets. *Soft Matter* **2013,** 9, 374–382.
26. Sivakumar, S.; Gupta, J. K.; Abbott, N. L.; Caruso, F., Monodisperse Emulsions through Templating Polyelectrolyte Multilayer Capsules. *Chemistry of Materials* **2008,** 20, 2063-2065.
27. Chen, W.; Feller, M. B.; Shen, Y. R., Investigation of Anisotropic Molecular Orientational Distributions of Liquid-Crystal Monolayers by Optical 2nd-Harmonic Generation. *Physical Review Letters* **1989,** 63, 2665-2668.
28. Jerome, B., Surface Effects and Anchoring in Liquid-Crystals. *Reports on Progress in Physics* **1991,** 54, 391-451.
29. Goodman, L. A.; Mcginn, J. T.; Anderson, C. H.; Digeronimo, F., Topography of Obliquely Evaporated Silicon-Oxide Films and Its Effect on Liquid-Crystal Orientation. *IEEE Transactions on Electron Devices* **1977,** 24, 795-804.
30. Skaife, J. J.; Brake, J. M.; Abbott, N. L., Influence of Nanometer-Scale Topography of Surfaces on the Orientational Response of Liquid Crystals to Proteins Specifically Bound to Surface-Immobilized Receptors. *Langmuir* **2001,** 17, 5448-5457.
31. Gupta, V. K.; Abbott, N. L., Azimuthal Anchoring Transition of Nematic Liquid Crystals on Self-Assembled Monolayers Formed from Odd and Even Alkanethiols. *Physical Review E* **1996,** 54, R4540-R4543.
32. Luk, Y. Y.; Tingey, M. L.; Hall, D. J.; Israel, B. A.; Murphy, C. J.; Bertics, P. J.; Abbott, N. L., Using Liquid Crystals to Amplify Protein-Receptor Interactions: Design of Surfaces with Nanometer-Scale Topography that Present Histidine-Tagged Protein Receptors. *Langmuir* **2003,** 19, 1671-1680.
33. Collings, P. J., *Liquid Crystals : Nature's Delicate Phase of Matter*. 2nd ed.; Princeton University Press: Princeton, NJ, USA, 2002.
34. Gennes, P.-G. d., *The Physics of Liquid Crystals*. Clarendon Press: Oxford, England, 1974.
35. Mullin, C. S.; Guyotsionnest, P.; Shen, Y. R., Properties of Liquid-Crystal Monolayers on Silane Surfaces. *Physical Review A* **1989,** 39, 3745-3747.
36. Lavrentovich, O. D.; Buschow, K. H. J., Nematic Liquid Crystals: Defects. In *Encyclopedia of Materials Science and Technology*, Elsevier: New York, NY, USA, 2001; Vol. 6, pp 6071-6076.
37. Nehring, J.; Saupe, A., Schlieren Texture in Nematic and Smectic Liquid-Crystals. *Journal of the Chemical Society-Faraday Transactions* **1972,** 68, 1-15.
38. Lagerwall, J. P. F.; Scalia, G., A New Era for Liquid Crystal Research: Applications of Liquid Crystals in Soft Matter Nano-, Bio- and Microtechnology. *Current Applied Physics* **2012,** 12, 1387-1412.
39. Lay, E. H.; Kirakosian, A.; Lin, J. L.; Petrovykh, D. Y.; Crain, J. N.; Himpsel, F. J.; Shah, R. R.; Abbott, N. L., Alignment of Liquid Crystals on Stepped and Passivated Silicon Templates Prepared in Ultrahigh Vacuum. *Langmuir* **2000,** 16, 6731-6738.
40. Lavrentovich, O. D., Topological Defects in Dispersed Liquid Crystals, or Words and Worlds Around Liquid Crystal Drops. *Liquid Crystals* **1998,** 24, 117-125.
41. Bloss, F. D., *An Introduction to the Methods of Optical Crystallography*. Holt: New York, NY, USA, 1961.

42. Perkins, D.; Henke, K. R., *Minerals in Thin Section*. Prentice Hall: Upper Saddle River, NJ, USA, 2000.
43. Shah, R. R.; Abbott, N. L., Coupling of the Orientations of Liquid Crystals to Electrical Double Layers Formed by the Dissociation of Surface-Immobilized Salts. *Journal of Physical Chemistry B* **2001,** 105, 4936-4950.
44. Davidson, M. W. The Berek Compensator. http://www.olympusmicro.com/primer/techniques/polarized/berekcompensator.html (November 5, 2012),
45. Hoffman, R.; Davidson, M. W. Michel-Levy Birefringence Chart. http://www.olympusmicro.com/primer/techniques/polarized/michel.html (November 5, 2012),
46. Allender, D. W.; Crawford, G. P.; Doane, J. W., Determination of the Liquid-Crystal Surface Elastic-Constant K_{24}. *Physical Review Letters* **1991,** 67, 1442-1445.
47. Goyal, R. K.; Denn, M. M., Orientational Multiplicity and Transitions in Liquid Crystalline Droplets. *Physical Review E* **2007,** 75, 021704-1-021704-10.
48. Van Horn, B. L.; Winter, H. H., Analysis of the Conoscopic Measurement for Uniaxial Liquid-Crystal Tilt Angles. *Applied Optics* **2001,** 40, 2089-2094.
49. Fonseca, J. G.; Galerne, Y., Simple Method for Measuring the Azimuthal Anchoring Strength of Nematic Liquid Crystals. *Applied Physics Letters* **2001,** 79, 2910-2912.
50. Rapini, A.; Papoular, M., Distortion d'une Lamelle Nematique sous champ Magnetique Conditions d'Ancrage aux Parois. *Journal de Physique* **1969,** 30, 54–56.
51. Toyooka, T.; Chen, G.; Takezoe, H.; Fukuda, A., Determination of Twist Elastic-Constant K-22 in 5cb by 4 Independent Light-Scattering Techniques. *Japanese Journal of Applied Physics Part 1-Regular Papers Short Notes & Review Papers* **1987,** 26, 1959-1966.
52. Park, J. S.; Jang, C. H.; Tingey, M. L.; Lowe, A. M.; Abbott, N. L., Influence of 4-cyano-4 '-biphenylcarboxylic acid on the orientational ordering of cyanobiphenyl liquid crystals at chemically functionalized surfaces. *Journal of Colloid and Interface Science* **2006,** 304, 459-473.
53. Bradshaw, M. J.; Raynes, E. P.; Bunning, J. D.; Faber, T. E., The Frank Constants of Some Nematic Liquid-Crystals. *Journal de Physique* **1985,** 46, 1513-1520.
54. Luk, Y. Y.; Campbell, S. F.; Abbott, N. L.; Murphy, C. J., Non-toxic thermotropic liquid crystals for use with mammalian cells. *Liquid Crystals* **2004,** 31, 611-621.
55. Ambrozic, M.; Formoso, P.; Golemme, A.; Zumer, S., Anchoring and droplet deformation in polymer dispersed liquid crystals: NMR study in an electric field. *Physical Review E* **1997,** 56, 1825-1832.
56. Wu, S. T.; Smith, W. H.; Lackner, A. M., Diamagnetic Anisotropy Measurements of Nematic Liquid-Crystals. *Molecular Crystals and Liquid Crystals* **1986,** 140, 83-93.

Chapter 3. Literature Review: Liquid Crystalline Materials for Chemical and Biological Sensing or Templated Synthesis of Polymer Microparticles*

3.1 Introduction

Liquid crystals (LCs) have a long history of being used as responsive materials in a range of technologies, perhaps most obviously in the now-ubiquitous LC display. In a LC display, an electric field of predetermined strength is applied to the LC to drive it through a change in orientation and thus optical appearance. Although LC display technology is based on fundamental studies performed in 1927, it is only in the past 20 years that it has been widely adopted. In those studies, it was discovered that the orientations of rod-shaped LCs (and intensity of light transmitted through the LCs) could be changed by application of an electric field across the LCs.[1, 2] This phenomenon can be viewed as an example of the use of a LC as an actuator (light-shutter).[3-7] Elastomeric materials made with LC components have also been used as mechanical actuators that undergo a change in shape in response to a predefined stimulus (*e.g.*, change of temperature).[8] Conversely, LCs can be used as sensors. In this context, the responsive nature of the LC remains important, but the response of the LC is used to indicate the appearance of a stimulus. Past studies have demonstrated that LC-based sensors can be designed to report a range of physical stimuli, including mechanical shear, temperature, electric and magnetic fields, and light. For example, Marcos *et al.*[9] reported the use of LCs to sense shear and temperature fields, Herzer *et al.*[10] reported printable cholesteric LC films as temperature and humidity sensors, and Chatterjee *et al.*[11] examined the influence of shear fields on defects in LCs. In addition, Chanishvili *et al.*[12] reported cholesteric LC mixtures that are sensitive to different

wavelengths of solar UV radiation. Nematic LCs have also been doped with light-driven chiral switches that can be used to tune the pitch of the chiral phase.[13]

While the paragraph above indicates that the responsive nature of LCs has been leveraged in the past to create actuators and sensors of a range of physical phenomena, the majority of this chapter moves to address a more recent effort that has been focused on the design of LCs as materials that respond to targeted chemical and biological species. As described in various sections of this chapter, a series of recent publications have demonstrated the use of LCs to amplify molecular events into macroscopic signals, and thus provide the basis of new classes of cheap, rapid, and label-free sensors. This chapter is primarily focused on the use of interfacial phenomena for the creation of LC-based chemical and biological sensors, but, prior to detailing those studies, we note that several research groups have also reported the design of LC-based sensors for chemical and biological species based on changes in the bulk properties of LCs. For example, cholesteric LC phases have been used to detect ethanol,[14] water vapor (*via* hydrolysis of a cholesteric dopant),[15] and vaporous analytes[16-18] such as amines.[19, 20] This latter class of LC-based sensors lies outside the scope of this chapter, and the interested reader is referred to the above-listed references for additional details.

We comment that the use of LCs for chemical and biological sensing defines a range of fundamental and technical challenges. For example, relative to LC display technologies, the interfacial phenomena encountered in the design of LC-based sensors are far more varied, complex and challenging. The diversity of chemical functional groups that are presented by targeted chemical and biological analytes is substantially greater than the relatively simple polymeric surfaces that are typically used in LC display technologies (compare the complexity of a protein to a polyimide). This makes *a priori* prediction of the orientations that LCs assume on

surfaces decorated with targeted analytes a particular (and largely unresolved) challenge. In addition, charges (*e.g.*, ionic species) are ubiquitous in gas and liquid phases of relevance to sensing (*e.g.*, a sample of water), and thus the interfaces of LCs charge as a consequence of ion adsorption/dissociation leading, for example, to the formation of electrical double layers at the interface of the LC which influence the ordering of the LC.[21, 22] Finally, because LC sensors must be open systems in order to interact with analytes, design of mechanically stable, open, microsystems containing LCs requires additional investigation and optimization. For example, mechanical stabilization of micrometer-thick films of LC remains a challenge under the conditions relevant to many practical sensing environments, although recent advances on this front appear promising.[23]

While the primary focus of this chapter is a review of LC-based chemical and biological sensors, a subsection is dedicated to an exciting new application of LC-in-water emulsions. Specifically, it was recently demonstrated that the orientational order of LCs confined to the microdroplets of these emulsions that makes them useful for sensing applications can also be exploited for templated synthesis of spherical or non-spherical microparticles with chemical surface patches.[24] As will be reviewed below, LC droplets provide a unique and facile methodology to simultaneously engineer multiple properties of the microparticles which could enable design of many functional soft materials (*e.g.*, see Chapter 9 of this thesis).

The remainder of this chapter is organized into additional five sections and a conclusion. The first section describes the detection of gas-phase analytes using thin-film, LC-based sensors. Second, we examine the use of LCs for the imaging of biomolecules displayed at solid surfaces. Next, we move to a discussion of biomolecular sensing at the dynamic aqueous—LC interface. Fourth, we address the use of LC emulsion droplets dispersed in water as a sensing platform and

as templates for polymer particle synthesis. As this topic is the primary focus of research presented in this thesis, special care is taken to highlight fundamental design principles for these two applications of LC-in-water emulsions. The last section (section 5) of this literature review focuses on progress related to the use of LCs as sensors of viruses, bacteria and mammalian cells. In each of the above-described sections, we highlight unresolved fundamental and technical challenges, and suggest areas for future research.

3.2 Gas Sensing Based on LCs

The first topic that we address in this chapter involves the use of LCs to create sensors for targeted chemical species present in a gas phase. Examples of important gas phase analytes include: (i) organophosphonates (OP) that are the basis of many nerve agents and pesticides; (ii) chlorine and ammonia, which are representative of a wide range of toxic industrial chemicals (TICs); (iii) chemicals found in exhaled breath that are associated with the health of a patient, including nitric oxide for asthma and ketones for diabetes; (iv) organoamines that indicate the freshness of foods; and (v) hazardous gases found in workplaces such as aldehydes and volatile organic compounds (VOCs). Because of the broad importance of detection of these and other gases, a large investment has been made in development of gas sensing technologies such as ion-mobility spectrometry (IMS), surface acoustic wave (SAW) devices, quartz crystal microbalances (QCM), and metal oxide-based sensors. Each existing technology, however, has attributes that limit its utility. A common disadvantage of these techniques, for example, is that they are limited in the range of species that can be detected. This is true, in particular, for IMS, where the length of the drift-tube must be matched to the targeted analytes. A second common challenge is instrumental sensitivity. A sensor for sarin needs, for example, to detect the nerve

agent with a concentration that is under the CDC airborne exposure limit, which is approximately 20 ppb.[25] This concentration range is a challenge for many sensing technologies, and significantly, for other gases considered occupational hazards in the workplace (*e.g.*, NO_2 from vehicle exhaust). We also note that evolving regulatory requirements are placing exposure limits at even lower concentrations. Finally, we comment that water (*i.e.*, relative humidity) is a common interfering agent in gas sensing technologies. Dealing with variations in humidity and the chemical complexity of industrial workplaces and homes (*e.g.*, a kitchen) remains a central challenge for many sensing technologies.[26] In the sections below, we describe efforts to develop LC-based gas sensors that are motivated, in large part, by the goal of addressing the above-listed limitations of existing gas sensing technologies.

A schematic illustration of the principle of operation of a surface-based LC sensor for gas-phase chemicals is shown in Figure 3-1.[27] The sensor comprises a micrometer-thick film of LC that is supported on a chemically functionalized solid surface. The supported film of LC is exposed to a gas (*e.g.*, air) that contains the vapor-phase analyte to be detected. The analyte diffuses across the LC film and binds to the chemically functionalized solid surface, leading to a change in the alignment of the LC at the solid surface, as shown in Figure 3-1A. A key element of the gas sensor is the design of the interface between the LC and the solid. In the examples shown in Figure 3-1, the chemically functionalized solid surface is selected to align the LC in a preferred azimuthal (Figure 3-1B) or zenithal alignment (Figure 3-1D) in the absence of the analyte. Upon binding of the analyte to the chemically functionalized surface, the molecular interactions between the solid surface and the LC are perturbed. This exchange of molecular interactions (*i.e.*, competitive binding of the LC and targeted analyte for the surface) leads to a

change in the azimuthal (Figure 3-1C) or zenithal alignment (Figure 3-1E) of the LC, thus reporting the presence of the vapor analyte.[27]

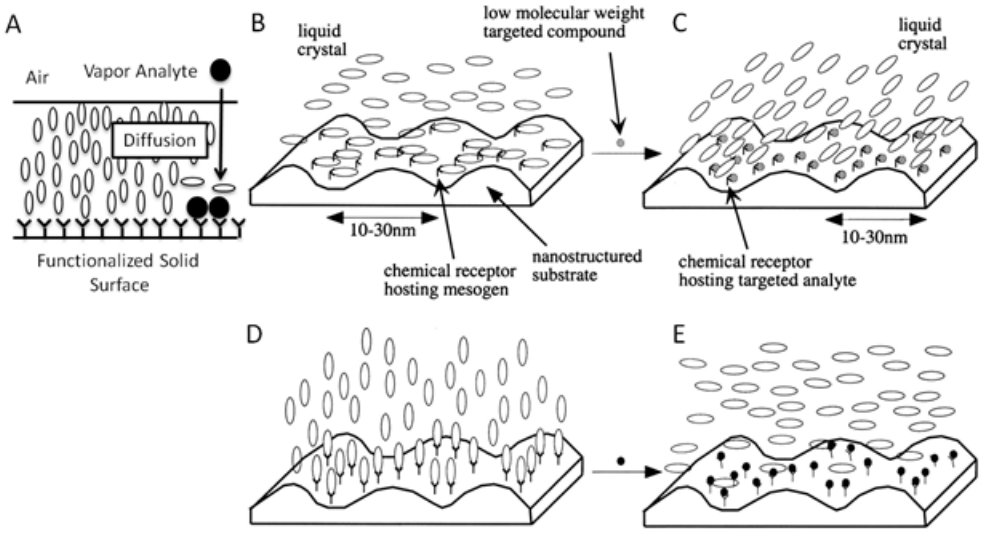

Figure 3-1. Surface-based LC sensors for gas-phase chemicals.

(A) Schematic illustration of a LC-based sensor. A thin film of LC is exposed to air containing an analyte that diffuses across the LC film and binds with the solid surface to change the anchoring of the LC. (B, C) Schematic illustration of a LC sensor for the detection of organoamines from a gas phase. The initial alignment of nematic 5CB supported on a carboxylic acid-terminated SAM is perpendicular to the anisotropic grooves of the solid substrate, as shown in (B). In the presence of organoamines that bind with the carboxylic acid groups on the surface more favorably than nematic 5CB, the orientation of the 5CB is dictated by the topography of the surface (resulting in an azimuthal alignment along the anisotropic grooves) (C). (D, E) Schematic illustration of a LC sensor that detects organophosphonate molecules. Prior to exposure to the analyte, the interaction of nematic 5CB with the copper perchlorate-decorated surfaces aligns the LC homeotropically, as shown in (D). The homeotropic orientation of the 5CB is lost in the presence of an organophosphonate (E). Reproduced with permission.[27]

As noted above, the design principles underlying LC gas sensors are based on the engineering of competitive interactions between the chemical functional groups of the mesogens and the vapor analyte for the solid surface. Manipulation of the chemically functionalized solid surface can, therefore, be used to change the selectivity of the LC-based sensor (*i.e.*, which

compound is detected by the sensor).[27-30] To date, this approach has been exploited to develop LC-based sensors that can detect organophosphonate compounds,[27, 31] organoamines,[32] aldehydes[33] and organosulfur[34] compounds. Below we focus on two of these examples to illustrate some of the attributes of LC-based gas sensors.

The first example that we describe below addresses detection of organophosphonates using surfaces decorated with metal perchlorate salts. The design of the sensor is based on the observation that LCs comprised of mesogens with nitrile groups (*e.g.*, 5CB, 8CB, or E7) will assume a homeotropic (perpendicular) alignment on surfaces decorated with metal perchlorate salts with cations that have a high electron affinity. For example, and as illustrated in Figure 3-2A-C, copper (II) perchlorate forms a coordination complex with nitrile-containing mesogens (*e.g.*, 5CB), causing a homeotropic alignment of nematic phases of 5CB. Because the LC also assumes a homeotropic alignment in contact with air, such a LC film exhibits a dark appearance when viewed between crossed polarizers.[27] Evidence of formation of the coordination complex between the nitrile groups of LCs and the Cu (II) ions on the surface has been obtained using infrared spectroscopy (Figure 3-2D). Inspection of Figure 3-2D-i reveals a nitrile-stretch absorption peak at 2227 cm^{-1}, which corresponds to free nitrile groups, and a second peak at 2287 cm^{-1} that corresponds to the nitrile groups of 8CB in coordination with Cu (II). As reported elsewhere,[28, 35] by changing the metal cation in the perchlorate salt, it has been demonstrated that the presence of a coordination interaction between the nitrile group and the metal cation is correlated to the observation of homeotropic alignment of the LC. This observation supports the hypothesis that the orientation of the LCs can be predictably manipulated based on metal-ligand coordination interactions at surfaces.

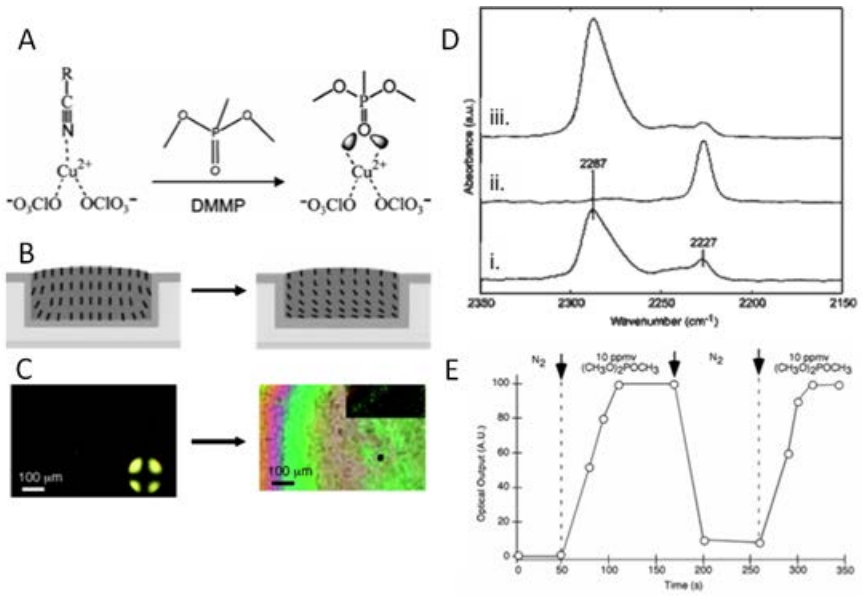

Figure 3-2. LC-based sensor for DMMP detection.

(A) Schematic illustration of DMMP-triggered disruption of a coordination interaction between the nitrile group of 5CB and copper (II) perchlorate. (B) Illustration of the orientation of nematic 5CB in a microwell, before and after the ligand exchange depicted in (A). The copper (II) perchlorate is deposited on the bottom of the well. (C) Optical micrographs (crossed polarizers) of micrometer-thick films of 5CB supported on copper (II) perchlorate before (left) and after (right) exposure to DMMP. (D) PM-IRRAS spectrum corresponding to the nitrile stretch vibration (i) in the presence of air, (ii) in the presence of 10 ppm DMMP, (iii) after a 30 min purge of DMMP by air (see text for details). (E) The optical response of the thin films of 5CB exposed sequentially to nitrogen and 10 ppm DMMP. Reproduced with permission.[27, 35]

As described above, the initial orientation of a LC in a sensor based on the use of metal salts is determined by metal ion-ligand coordination interactions between the LC and metal salt on the surface. When using Cu (II) as the metal ion in the salt, the introduction of dimethyl methylphosphonate (DMMP) into the gas phase overlying the supported LC film has been shown to result in the preferential binding of DMMP to the Cu (II) ions (and displacement of the nitrile groups of the LC from the coordination interaction with the Cu(II)). This change in interfacial interaction is evidenced by a change in the alignment of the LC from homeotropic to planar, with

an associated increase in the amount of light transmitted through the LC film when viewed between crossed polarizers (Figure 3-2A-C).[27] The molecular basis of the change in orientation of the LC has also been supported by infrared measurements. Specifically, upon exposure to a vapor phase containing 10 ppm DMMP, as shown in Figure 3-2D-ii, the absorption peak corresponding to the metal ion-coordinated state of the nitrile group of 8CB (at 2287 cm^{-1}) was observed to disappear.[35] In addition, the response of the LC to DMMP was found to be reversible, meaning that the orientation of the LC returns to the homeotropic state after the DMMP is removed from the vapor space above the LC film (see Figure 3-2E). This return of the LC to the homeotropic state was accompanied by the reappearance of the peak corresponding to the coordinated nitrile group in the infrared spectrum (Figure 3-2D-iii).[27] Here we also note that exposure of the Cu(II)-based LC sensors to vapors of water, alkanes and various other organic compounds (alcohols, ketones *etc.*) does not lead to a response (*i.e.*, change in orientation of the LC) because these compounds cannot displace the nitrile groups of the LC from coordination with the Cu (II) at the surface.

The molecular engineering principles described above – a LC sensor based on competitive coordination interactions at metal ion-decorated surfaces – is a general one, as a range of different metal ions (or more broadly, chemical functional groups) can be presented at the surfaces of solids to manipulate the selectivity of the sensor. As an example, Figure 3-3 shows results obtained with surfaces that presented aluminium (III), zinc (II), or iron (III) perchlorate salts. Although LCs supported on surfaces presenting Al (III) salts responded to four organophosphonate nerve agents (GB, GD, GA and VX), the surfaces with Zn (II) reported only GB and VX, and the surfaces with Fe (III) reported GB but not VX.[31] An additional design parameter that can be used to tune the response of a LC sensor is the chemical structure of the

mesogens used to form the LC phase. For example, mesogens that possess two nitrile groups have been synthesized, and LC phases containing these tailored mesogens exhibited homeotropic alignments on metal ion-decorated surfaces under conditions that LCs containing a single nitrile group do not. Specifically, bivalent mesogens were measured to align on surfaces presenting very low concentrations of Al (III) ions.[36]

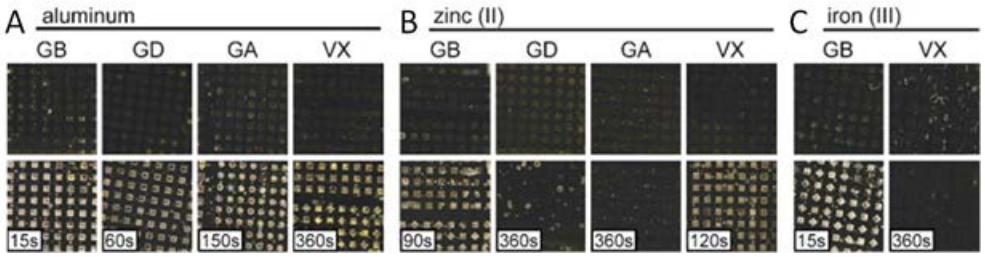

Figure 3-3. LC-based sensors for sarin (GB), soman (GD), tabun (GA), and VX using different perchlorate salts.

Optical micrographs (crossed polarizers) of nematic E7 supported within microwells containing perchlorate salts of (A) aluminium (III), (B) zinc (II), and (C) iron (III), before (top row) and after (bottom row) exposure to organophosphonate nerve agents (GB, GD, GA, and VX). The duration of exposure is indicated. The images areas are approximately 7.5 mm by 7.5 mm. Reproduced with permission.[†,31]

While the studies described above highlight the role that coordination interactions can play in the design of gas sensors based on LCs, we also note that surfaces decorated with metal salts are complex and remain to be fully understood. For example, it has recently been established that metal salts on surfaces can dissolve partially into the LC, leading to the formation of electrical double layers. The presence of the electrical double layers can influence the alignment of the LC and thus the response of the sensors to targeted compounds.[22, 36] Additional aspects of the interfacial designs of these sensors that remain to be fully understood include the role of the counter-ions (the above described results were based on perchlorate salts) and various properties of the surface that support the metal salts.[30, 37]

The second example of chemical sensing using LCs that we describe in this chapter involves detection of organoamines. In this example, the sensors are based on surfaces that possess anisotropic topography and present carboxylic acid groups. The design of the sensor exploits competitive topographic and molecular-level interactions to drive anchoring transitions upon exposure to targeted analytes. The topographic interactions were engineered into the surfaces *via* the presence of statistical "grooves" that possessed amplitudes of 1-2 nm and wavelengths of 10-30 nm. This topography causes the LC to align in an azimuthal orientation that is parallel to the grooves (Figure 3-1C). However, when the surfaces were decorated with an organized monolayer presenting oriented carboxylic acids groups, hydrogen bonding of the mesogens to the acid groups displayed by the surface causes the LC to assume an orientation that is perpendicular to the grooves (Figure 3-1B).[38] The role of hydrogen bonding in determining the orientations of LCs on these surfaces is supported by the results of infrared spectroscopy. Figure 3-4A-i shows the infrared spectrum of a carboxylic acid-terminated monolayer. The absorbance peaks indicate the presence of a mixture of non-hydrogen-bonded carbonyl groups (peak at 1736 cm^{-1}) and hydrogen-bonded carbonyl groups (peak at 1716 cm^{-1}). A schematic illustration of such a surface is shown in Figure 3-4B-i. When the surface is contacted with 8CB, as shown in Figure 3-4A-ii, the absorption peak in the infrared spectrum corresponding to intra-monolayer hydrogen bonding is observed to decrease in intensity, consistent with competitive formation of hydrogen bonds between the nitrile group of the mesogen and the carboxylic acid groups on the surface (Figure 3-4B-ii).[38]

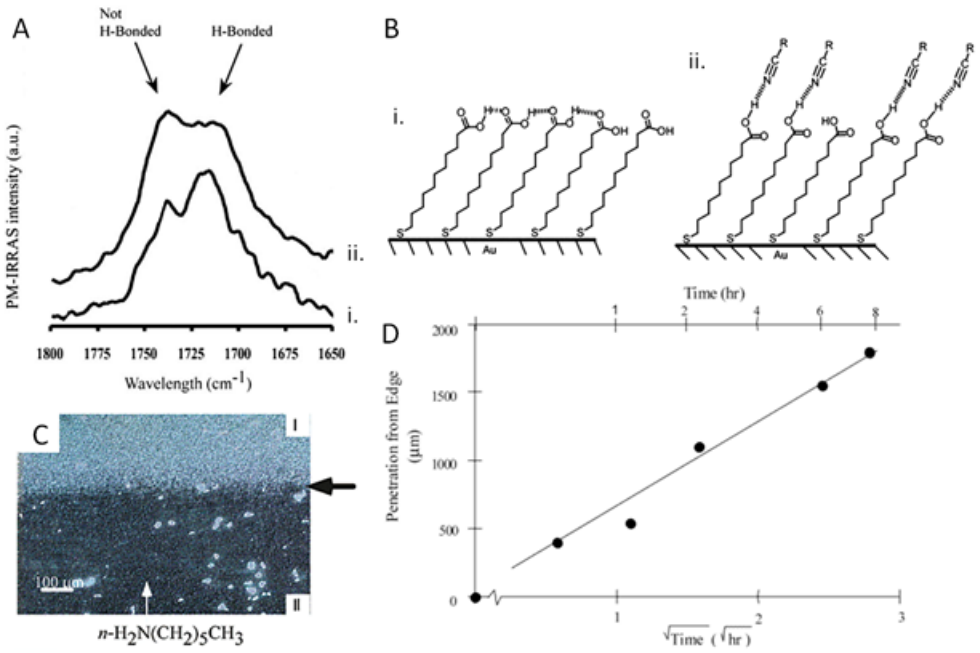

Figure 3-4. Role of hydrogen bonding between 8CB and carboxylic-acid terminated SAMs formed on grooved substrates in defining the surface alignment of 8CB.

(A) PM-IRRAS spectra of carboxylic-acid terminated SAMs (i) before and (ii) after contact with 8CB. (B) Schematic illustration of hydrogen bonding within a carboxylic acid-terminated SAM before (left) and after (right) contact with 8CB. (C) An optical image (between cross polarizers) of a LC cell (thickness ~12 μm) with surfaces formed from carboxylic acid-terminated SAMs. The edge of the cell was exposed to 750 ppm of *n*-$H_2N(CH_2)_5CH_3$. In region I, the presentation of the carboxylic acid on the surface (and hydrogen bonding with the LC) causes a twist distortion of the LC. However, in the presence of the amine in region II, the LC relaxes to the azimuthal alignment of the film dictated by the anisotropic topography of the surface. (D) The penetration distance (from the open edge of the LC cell) of *n*-$H_2N(CH_2)_5CH_3$ plotted as a function of the square root of exposure time. Reproduced with permission.[‡,32, 38]

Upon introduction of an amine compound into the gas phase overlying the above-described LC film, an acid-base reaction occurs between the carboxylic acid and the amine (resulting in the formation of an ammonium carboxylate salt), thus disrupting the hydrogen bonding between the LC and the surface, as described above. In the absence of the hydrogen-bonding interaction, the LC relaxes to an orientation on the surface that is dictated by the

topography of the surface. The change in the azimuthal alignment of the LC can be optically detected through crossed polarizers, as shown in Figure 3-4C. Here we end our discussion of this LC sensor design by noting that it is possible to design systems that quantify the diffusion of an analyte *laterally* through a thin film of LC confined between two solid surfaces. Figure 3-4D shows the distance that hexylamine has diffused laterally across a film of LC, revealing that the penetration distance of the analyte is proportional to the square root of the exposure time (consistent with passive transport of the amine *via* diffusion).[32] This geometry of the LC sensor is a promising one for quantification of cumulative exposure to a targeted analyte (*e.g.*, for measurement of personal exposure to potentially hazardous chemical environments).

3.3 LC-Based Sensing of Biomolecules Displayed on Surfaces

The second class of LC-based sensors that we address in this chapter is aimed at reporting the presence of biological molecules, such as proteins, oligopeptides, and nucleic acids, displayed on the surfaces of solids.[39-42] While technologies for reporting biomolecules at surfaces (in contexts such as environmental monitoring, medical diagnostics, food safety and biosecurity) have been developed, existing approaches typically involve the use of complex instrumentation (*e.g.*, mass spectroscopy and evanescent optical methods such as surface plasmon resonance) or schemes that involve the labelling of molecules with fluorescent, redox-active, or radio-active tags. LC-based approaches, in contrast, do not require the use of labels and do not require complex instrumentation for read-out.

In the approaches described below for LC-based detection of biomolecules, the surfaces of solids are designed with carefully selected chemical functionality and nanoscopic topography. Following capture of the targeted biomolecular species on the solid surface (typically *via* a

specific binding event), the surface is contacted with LC. The surface is designed such that the captured biomolecules change either the energy of interaction of the LC with the surface (anchoring energy, *W*) or the preferred orientation of the LC (easy axis). In this section, we will highlight several studies that illustrate the potential utility of LCs for imaging surfaces decorated by proteins, oligopeptides, or DNA.

3.3.1 Proteins

The first examples that we address involve the LC-based imaging of proteins displayed on the surfaces of solids. Past studies have demonstrated that LCs can be used to image proteins captured on solid surfaces *via* specific protein—small molecule or protein—protein interactions. In addition, as described below, LCs can also be used to image proteins that have been printed (non-specifically adsorbed) onto a surface in the context of analytic schemes based on affinity contact printing (with a spatial resolution of tens of micrometers). These results suggest that LCs may offer the basis of label-free and highly multiplexed methods for protein analysis.[39, 43-45] The first report of the use of chemically functionalized surfaces for LC-based protein detection was published by Gupta *et al.*.[40] Specifically, this report demonstrated that nematic LCs can be used to amplify and transduce receptor-mediated binding of proteins at surfaces into readily observable optical responses. Organized monolayers (so-called self-assembled monolayers or SAMs) of ligands capable of binding targeted proteins were formed on the surfaces of obliquely deposited gold films. Ordinarily, as noted above, such obliquely deposited gold films impart a uniform azimuthal alignment to LCs. However, when either avidin or anti-biotin antibodies (IgG) were incubated against SAMs presenting the binding group called biotin, the anisotropic topography of the obliquely deposited gold films was masked by the bound protein layer such

that the LCs exhibited non-uniform orientations on the surfaces. In addition, the authors demonstrated that it was possible to tune the surface topography of the gold films (by changing the angle of deposition of the gold during physical vapor deposition) such that the capture of an antibody by a surface immobilized protein resulted in a measurable change in the alignment of the LC.[40]

Building from the results of the above study, Skaife and Abbott[44] demonstrated that it was possible to quantify the optical response of LCs, and thus the amount of protein captured at a surface, by measuring the fraction of polarized light transmitted through the LC. The optical response (quantified as a gray-scale brightness) was observed to be a continuous function of the amount of bound protein. Because the amount of bound IgG was largely determined by mass transfer of antibody to the surface, quantification of the LC optical response allowed for determination of the bulk IgG concentration over two orders of magnitude (1-100nM).[44]

In contrast to many other methods used for imaging biomolecules at surfaces, a distinguishing feature of LC-based methods is that the LCs can probe the structure of the biomolecules displayed at the surface. This attribute is illustrated by a study by Luk *et al.*[46] who investigated the immobilization of ribonuclease A (RNase A) on surfaces. Although ellipsometry reported the effective optical thickness of RNase A to be identical for two methods of immobilization, the anchoring of the 5CB on the surface with RNase A immobilized in random orientations was different from that observed when 5CB was anchored on the surface with RNase A immobilized in a preferred orientation. This result indicates that the orientational states of proteins immobilized on surfaces can be distinguished by examining the optical response of the LC.[46]

An additional useful attribute of LC-based imaging of biomolecules on surfaces is that LCs can be used to detect proteins captured on surfaces *via* a wide range of binding groups. For example, Clare and Abbott[47] investigated the orientations of 5CB in contact with surfaces that presented oligopeptides for specific binding of proteins. In particular, surfaces functionalized with the oligopeptide-substrate for the Src protein kinase (Src-tide) and its phosphorylated synthetic equivalent (p-Src-tide) were studied (Figure 3-5A, see Figure 3-5B for oligopeptide structures). The time required for a contacting film of 5CB to adopt a uniform homeotropic orientation on the surface was demonstrated to increase with increasing areal densities of immobilized peptides. Furthermore, it was demonstrated that specific binding between anti-phosphotyrosine IgG and the surface-immobilized phosphopeptide (p-Src-tide) slowed the dynamic reorganization of the LC such that the system did not achieve uniform anchoring within experimentally accessible time scales (Figure 3-5B). This report suggests that the measurement of line defect densities and relaxation times of LCs can be used as a means to quantify areal densities of surface immobilized peptides and also to report protein binding events at such interfaces.[47]

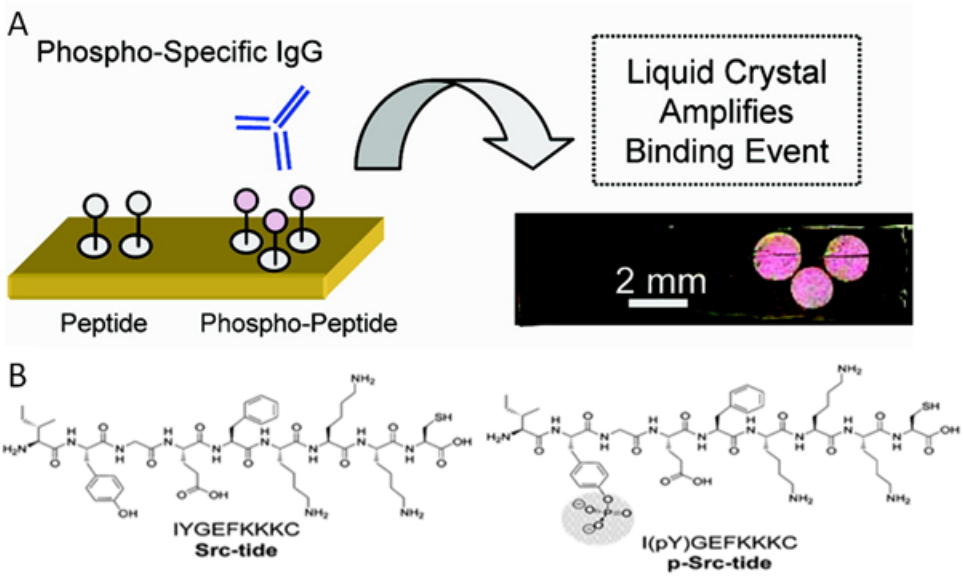

Figure 3-5. LC-based methodology for detection of specific binding of proteins.
(A) Schematic illustration and optical images (polarized light microscopy) demonstrating the use of LCs to amplify and report protein binding events occurring on a surface displaying a spatially resolved peptide array. (B) Oligopeptide substrate of the Src kinase protein and synthetic peptide equivalent to the phosphorylated peptide product after Src kinase modification. Reproduced with permission.[47]

While the studies described above address changes in the orientations of LCs that are triggered by the capture of targeted proteins *via* binding groups presented at surfaces, more recent studies have demonstrated that measurement of the anchoring energies of LCs at surfaces offers a highly sensitive and quantitative method to report the presence of captured proteins. For example, Govindaraju *et al.*[39] utilized such anchoring energy measurements to quantify proteins captured on surfaces decorated with oligopeptides. The presence of bound antibody caused the anchoring energy (W) of 5CB to decrease systematically from 4.4 to 1.4 $\mu J/m^2$ as the antibody concentration increased from 10 pM to 100 nM (Figure 3-6). Over the same range of experimental conditions, ellipsometry was not sufficiently sensitive to permit detection of the captured antibody.[39]

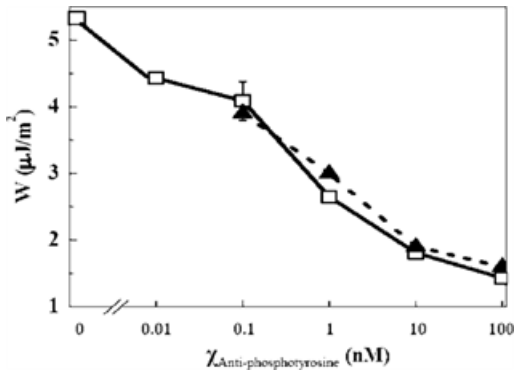

Figure 3-6. Plot of anchoring energy (*W*) of nematic LC (5CB) on an oligopeptide-presenting surface as a function of the solution concentration of monoclonal anti-phosphotyrosine antibody (IgG) that was incubated with the surface before LC cell assembly.

Two independent data sets are shown with a standard error calculated from five repeat measurements at 100 pM antibody. Reproduced with permission.[39]

Finally, we comment that LCs can be combined with affinity contact printing to report the presence of proteins captured on surfaces. As an example of this approach, Lowe *et al.*[48] covalently functionalized polydimethylsiloxane (PDMS) stamps with an antibody to the trans-membrane protein called epidermal growth factor receptor (EGFR). The anti-EGFR functionalized PDMS stamps were then used to capture EGFR and transfer it to amino-tetra(ethylene glycol)-terminated alkanethiol (EG4N) functionalized gold films by affinity contact printing. The EGFR printed onto these surfaces changed the orientation of the LC through a decrease in the anchoring energy. These effects were interpreted to be the result of the presence of EGFR on the surface masking interactions between the EG4N SAM and the 5CB. This study also demonstrated that mass densities of EGFR as low as 30-40 pg/mm^2 could be detected using the above mentioned method.[48, 49]

3.3.2 Oligopeptides

The preceding section focused on the use of LCs to report the presence of macromolecular biomolecules (*i.e.*, proteins) at surfaces. Additionally, LCs can be used to detect the presence and state of small biomolecules displayed at surfaces. This point is illustrated in this section by describing LC ordering on surfaces presenting oligopeptides. Here we also note that, although LCs can report proteins on surfaces, the complexity of proteins has hindered identification of the intermolecular forces acting between the proteins and LCs.[42, 50] The simpler structure of oligopeptides as compared to full proteins, as well as the ability to make systematic modifications to oligopeptide structure and stereochemistry has led to fundamental insight into the intermolecular interactions underlying the ordering of LCs at biomolecular interfaces.[42]

We refer the reader elsewhere for a detailed description of the anchoring of LCs on surfaces decorated with oligopepides such as IYGEFKKKC (which is a substrate for Src kinase protein, see above)[51] and focus here on insights that have emerged from studies of the orientations of LCs on surfaces decorated with dipeptides possessing different chirality (L-C-L-Y vs. L-C-D-Y vs. D-C-D-Y) and phosphorylation status.[42] A particularly significant finding was that the ordering of nematic 5CB and TL205 on the dipeptide-decorated surfaces was influenced strongly by the chirality of the dipeptides (Figure 3-7). A series of experiments revealed that the influence of the chirality of the dipeptides on the LC was, at least in part, due to patterns of hydrogen bonds formed between the LCs and the surfaces (these results also hint at the fundamental origins of the above-mentioned influence of the orientations of immobilized proteins on the ordering of LCs). In addition, phosphorylation of the tyrosine residue in the dipeptides led to markedly different orientations of the LCs compared to their orientations on surfaces decorated with non-phosphorylated dipeptides. This difference between interactions of

phosphorylated and non-phosphorylated dipeptides with LCs suggests a means to detect the phosphorylation state of dipeptides through measurements of the easy axis of LCs.[42]

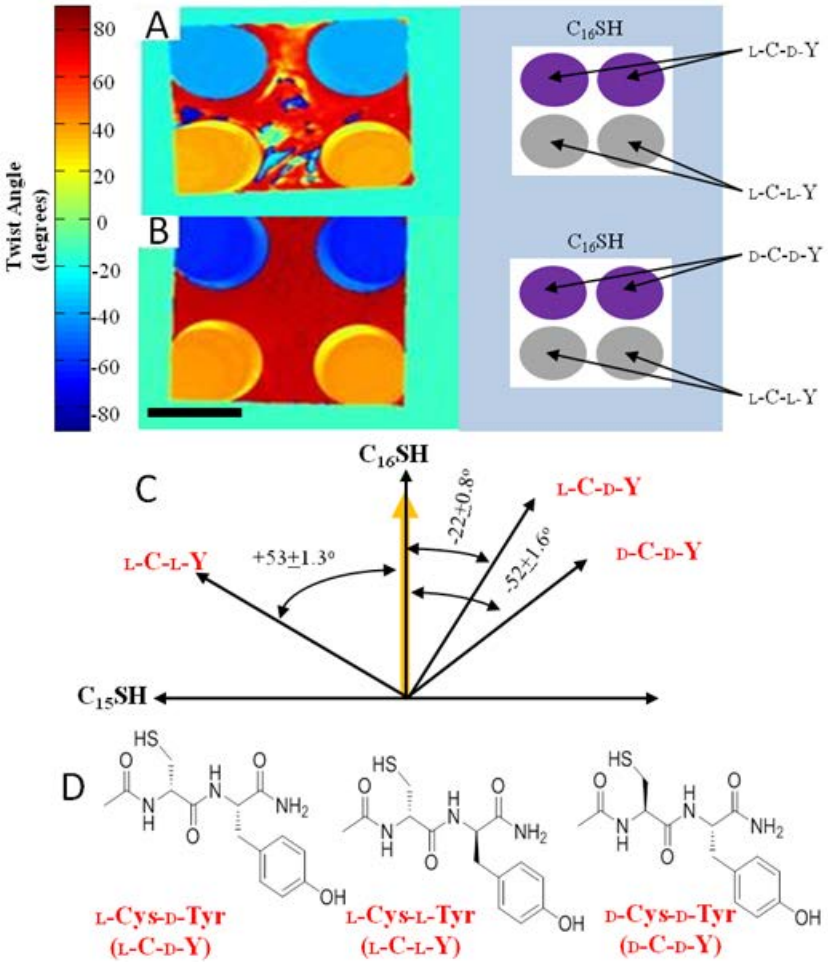

Figure 3-7. Enantiomeric interactions between LCs and organized monolayers of tyrosine-containing dipeptides.

(A) Map of twist angles of nematic 5CB on gold films decorated with monolayers of L-C-D-Y or L-C-L-Y. (B) Map of twist angles of nematic 5CB on gold films decorated with monolayers of D-C-D-Y or L-C-L-Y. The scale bar is 2 mm. (C) Angle diagram and quantitative analysis of the easy axes of 5CB on L-C-L-Y, L-C-D-Y-, and D-C-D-Y-decorated surfaces relative to the direction of gold deposition (yellow arrow) and reference surfaces ($C_{15}SH$ and $C_{16}SH$). (D) Chemical structures of these dipeptides. Reproduced with permission.[42]

3.3.3 DNA

A third class of biomolecules that have been imaged on surfaces using LCs is DNA. As noted above, LCs are promising probes of biomolecules on surfaces because they are sensitive to the orientational and configurational states of the biomolecules. This attribute is evident also in recent studies of the anchoring of LCs on surfaces presenting DNA. As described below, LCs have been successfully used to detect and quantify single and double stranded DNA (ssDNA and dsDNA) molecules at solid surfaces.[52-54]

First, Nakata *et al.* [52] reported on the alignment of various achiral LCs (both nematic (MBBA) and smectic A (8CB) phases) on mechanically sheared dsDNA gels. An angular offset between the mean DNA orientation and the LC alignment was observed, the magnitude of which differed for 8CB and MBBA. Building from these observations, Malone and Schwartz[41] investigated the alignment of nematic LCs on isolated DNA molecules extended on a surface. They observed that the LC was aligned in the direction of ssDNA extension, whereas dsDNA caused alignment at an oblique angle (Figure 3-8), similar to that reported by Nikata *et al.* In contrast to Nikata *et al.*,[52] however, this study[41] demonstrated that the alignment of two different LCs (MBBA and 5CB) by dsDNA were the same within experimental error. Malone and Schwartz suggest these differences in LC alignment might arise from LC mesogens interacting with parts of the stretched dsDNA helix that are not accessible when the dsDNA molecules are instead organized into closely packed DNA gels. Key conclusions of their study are that LCs can be used to image DNA on surfaces at extraordinary low densities (at an area fraction occupied by DNA of 10^{-6}) and that the orientations assumed by LCs can, in principle, form the basis of sensitive sensors of DNA hybridization (*i.e.*, indicating whether or not dsDNA or ssDNA is

presented on the surface). Before ending this section, we refer the interested reader to another report of the use of LCs to detect DNA (including specific sequences) at solid surfaces.[53]

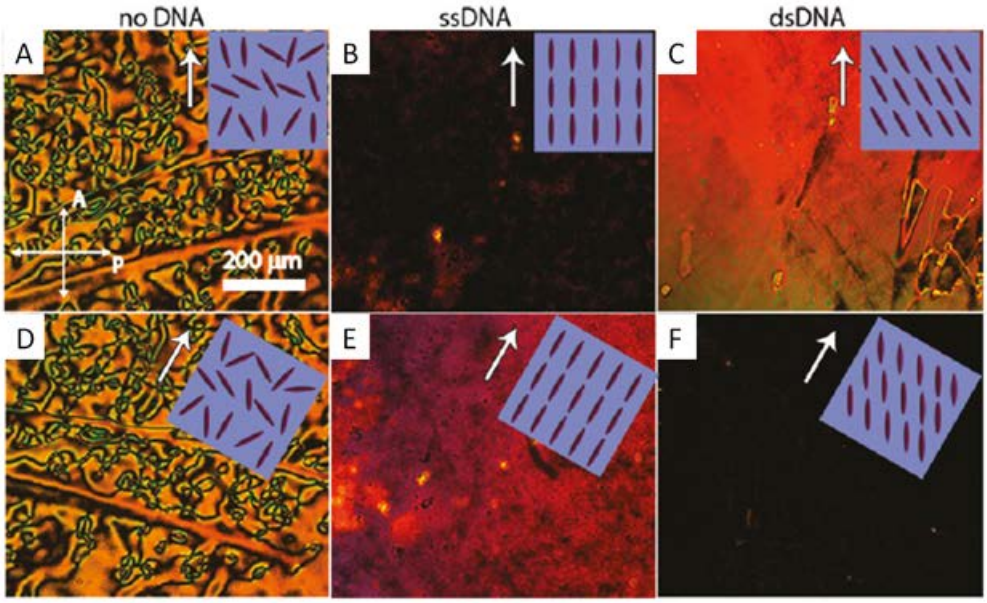

Figure 3-8. Polarized light micrographs of LC (representative of either 5CB or MBBA, which had roughly the same surface orientation) on DNA-decorated surfaces.

Crossed white arrows (in A) indicated the directions of the analyzer and polarizer. White arrows indicate the direction of DNA extension where surfaces in (A-C) are aligned with the analyzer (*i.e.*, 0° rotation) and surfaces in (D-F) are rotated by 30°. A dark micrograph indicates LC alignment in the direction of the polarizer or analyzer (not homeotropic ordering). The cartoons in the inset show the alignment of the LC consistent with the respective micrographs. (A, D) Control sample contacted with buffer that did not contain DNA at 0° and 30° rotation, respectively. (B, E) ssDNA-decorated surface at 0° and 30° rotation, respectively. (C, F) dsDNA-decorated surface at 0° and 30° rotation, respectively. Reproduced with permission.[41]

3.4 Biomolecular Sensing at Aqueous—LC Interfaces

Water plays a key role in preserving the structure and functionality of many biomolecules. The recent series of publications characterizing interfaces formed between thermotropic (oily) LCs and aqueous phases thus provides new opportunities to create biological

sensors based on LCs.[55, 56] We begin this section by noting some key conceptual differences between aqueous—LC interfaces and the more extensively studied LC—solid interface (as described above). Specifically, we comment that (i) the aqueous—LC interface is soft and deformable relative to LC—solid interfaces, (ii) the mobility of molecules at aqueous—LC interfaces is high as compared to solid surfaces, thus enabling lateral reorganization of biomolecules upon binding to aqueous—LC interface, and (iii) the organization of molecules at aqueous—LC interfaces is influenced by the elasticity of the LC, leading to interfacial phase states of molecules that are not realized at LC—solid interfaces.[56] As illustrated below, these various attributes of aqueous—LC interfaces lead to a rich range of phenomena that promise the realization of biosensors with attributes not found in other sensing technologies.

The geometry of a typical experiment performed to report biomolecular interactions at the aqueous—LC interface is shown in Figure 3-9.[56] The LC is hosted in the pores of an electron microscopy grid that is supported on a glass microscope slide treated with a self-assembled monolayer of octadecyltrichlorosilane (OTS). Immersion of the supported film of LC into an aqueous phase leads to the formation of a stable interface between the aqueous phase and LC (Figure 3-9A). The capture of adsorbates at this interface (typically from the aqueous phase) can trigger anchoring transitions in the LC films, resulting in a range of different orientations (Figure 3-9B-D) and thus optical appearances of LC films (Figure 3-9E-G).

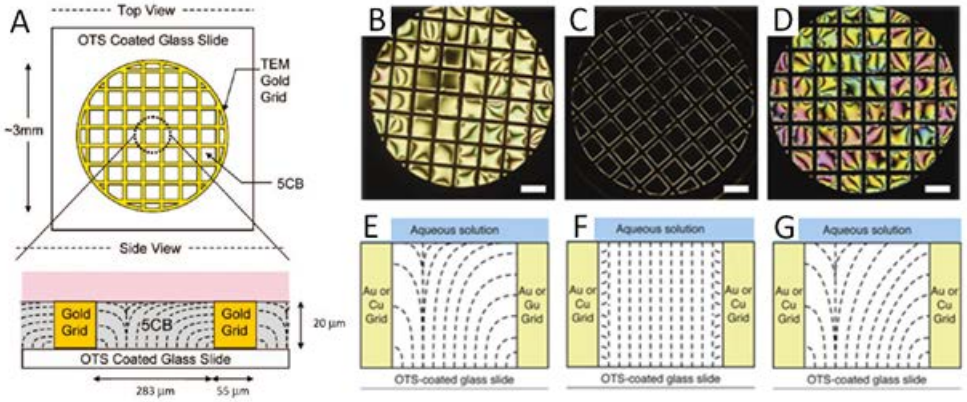

Figure 3-9. Geometry of a typical experiment performed to report biomolecular interactions at the aqueous—LC interface.

Illustration of a LC film hosted in a TEM grid supported on an OTS-treated slide (A) and interpretations of the optical appearances of the LC films in terms of the orientation of the LC at the aqueous—LC interface: planar (B, E); homeotropic (C, F); or tilted (D, G). Reproduced with permission.[§,56]

3.4.1 Phospholipid-Decorated Aqueous—LC Interfaces

The first example of biosensing at the aqueous—LC interface involves the use of phospholipids of the type found in biological membranes.[58, 59] In this example, aqueous suspensions of dilaurylphosphatidylcholine (DLPC) in the form of small unilamellar vesicles were placed into contact with a film of LC. Fusion of the vesicles with the interface of the LC triggered the anchoring of 5CB at the interface to change discontinuously from a planar to homeotropic orientation (Figure 3-10A-C). The density of lipid present on the aqueous—LC interface was subsequently characterized using quantitative epifluorescence microscopy and it was found that at saturation coverage, a monolayer of DLPC was adsorbed at the interface (0.45 nm^2/ molecule). Fluorescence recovery after photobleaching (FRAP) experiments also revealed that the phospholipids at the interface were laterally mobile, exhibiting diffusion coefficients that were comparable to those measured within lipid bilayers. The homeotropic orientation assumed

by the LC at the lipid-decorated interface was interpreted to be due to molecular interdigitation of the tails of the phospholipids and the mesogens forming the LC, a conclusion that is supported by a number of early studies on the interactions of LCs and lipids supported on solid surfaces (Langmuir-Blodgett films of lipids).[57]

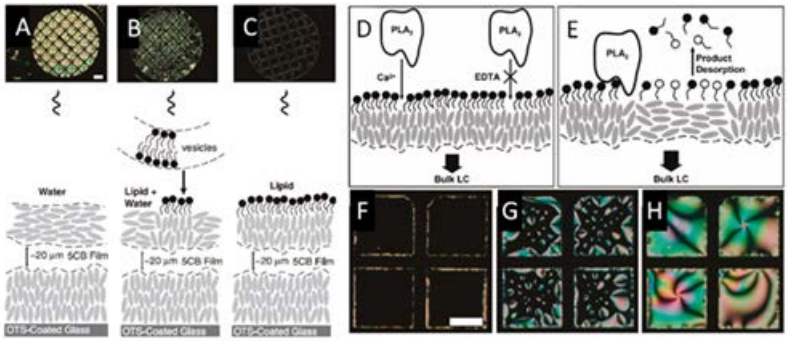

Figure 3-10. Biomolecular interactions at phospholipid-decorated surfaces of LCs.
Illustrations and optical micrographs (crossed polarizers) of (A-C) the formation of a phospholipid monolayer at an aqueous—LC interface and (D-H) enzymatic reaction occurring at the interface, leading to hydrolysis of the monolayer of phospholipid at the interface. Reproduced with permission.[58, 59]

Lipid-decorated aqueous—LC interfaces, as described above, were used by Brake and co-workers to report protein binding and enzymatic events.[59] Brake showed that both specific binding interactions between the enzyme phospholipase A_2 and lipids, as well as subsequent enzymatic hydrolysis of the lipids (binding and/or hydrolysis), led to the reorganization of the lipids in a manner that was optically reported as a dynamic orientational transition in the LC. In contrast, non-specific interactions between proteins (*e.g.*, albumin, lysozyme, and cytochrome-*c*) and the lipid-laden interface of the LC did not trigger orientational transitions in the LCs. When reporting enzymatic hydrolysis of the lipids, concurrent epifluorescence and polarized light imaging of the lipids and proteins labelled with fluorophores at the aqueous—LC interface showed that spatially patterned orientations of the LCs reflected the lateral organization

(micrometer-sized domains) of the proteins and lipids, respectively, at the aqueous—LC interface (Figure 3-10D-H). Closely related to this observation, beta-bungarotoxin, which exhibits Ca^{2+}-dependent phospholipase A_2 activity, has also been shown to induce an anchoring transition in the LC when it hydrolyzed a phospholipid monolayer assembled at the aqueous—LC interface.[60] The selectivity was demonstrated by the lack of response of the phospholipid-decorated LC to alpha-bungarotoxin and myotoxin II, both of which do not exhibit any phospholipase activity.

Although the examples above involve specific interactions between lipids and proteins at the LC interface, we note also that the aqueous—LC interface provides an opportunity to report the interactions between biomolecules that are non-specific in nature. For example, De Tercero *et al.*[61] reported on non-specific interactions of proteins with aqueous—LC interfaces decorated with *partial* monolayer coverage of DLPC. Although non-specific interactions of four proteins (cytochrome *c*, bovine serum albumin, immunoglobulins, and neutravidin) do not perturb the ordering of the LC when a *full* monolayer of DLPC is assembled at the aqueous—LC interface, patterned orientations of the LC that reflect penetration and subsequent lateral organization of proteins into the interface of the LC were observed with *partial* monolayer coverage of DLPC. The shapes of the protein domains in the lipid layer (ellipsoidal domains in the case of BSA or elongated networks in the case of IgGs) hint at the relative strength and directionality of the lipid—lipid, lipid—protein and protein—protein interactions at these interfaces. These results indicate that phospholipid-decorated interfaces formed between LC and aqueous phases offer the basis of a simple tool with which to study the spatial organization and dynamics of protein networks formed at mobile, lipid-decorated interfaces.

We note also the use of phospholipid-decorated aqueous—LC interfaces to report non-specific interactions involving protein-coated nanoparticles.[62] This approach was motivated by the goal of providing new methods to assess the potential cytotoxicity of nanomaterials, where interactions between nanoparticles and cell membranes are thought, in some cases, to underlie cytotoxicity. In these studies, it was observed that interactions between protein-coated gold nanoparticles (AuNPs) and phospholipid monolayers assembled at aqueous—LC interfaces triggered orientational transitions of the LCs.

Finally, we comment that aqueous—LC interfaces have also been used to report the interaction of cationic anti-microbial peptides with anionic lipids.[63] Prior to contact with the antimicrobial peptides, the LC interfaces decorated with the anionic lipids exhibited homeotropic orientations. However, bright domains were observed in the LC (corresponding to tilted orientations of the LC) when antimicrobial peptides were introduced into the aqueous phase. In contrast, no change in the optical appearance of the LC was reported (*i.e.*, a homeotropic orientation was maintained) when antimicrobial peptides were incubated against a LC interface presenting a monolayer of zwitterionic phospholipids. The LC anchoring transition observed in the presence of the anionic lipid and antimicrobial peptide was interpreted to be due to formation of a complex between the two species at the interface of the LC. This approach hints at the potential utility of LCs in studies of membrane disruption or permeabilization caused by antimicrobial agents.

In the examples described above, the phospholipids were fused spontaneously with the aqueous interface of the LCs, a result of so-called hydrophobic interactions between LC and the phospholipids. In additional studies, s*pecific* capture of ligand-functionalized phospholipid vesicles has been reported at aqueous—LC interfaces that were decorated with a monolayer of

adsorbed protein (streptavidin or anti-biotin antibody) (Figure 3-11A).[64] The specific binding of the vesicles to the proteins was demonstrated to trigger a continuous anchoring transition (continuous change in the tilt) in the LC, which was quantified by measurement of the optical retardance of the LC (Figure 3-11B-D). The observation of a continuous change in the ordering of the LC contrasts with prior reports of fusion of lipid vesicles with protein-free interfaces of LCs, where discontinuous transitions and the appearance of micrometer-sized domains of lipid were observed. This difference was interpreted to indicate that the presence of the protein on the interface limits the size of lipid domains to the sub-optical range, resulting in a far-field tilt of the LC (which changes with the fraction of the interface decorated with lipids and proteins). Overall, these results demonstrate that LC ordering transitions have the potential to be useful for reporting specific binding events involving vesicles and proteins. Here we note that detection and quantification of microvesicles shed by cells is an area of growing significance in biology and medicine because analysis of the microvesicles can provide information about the states of the cells.

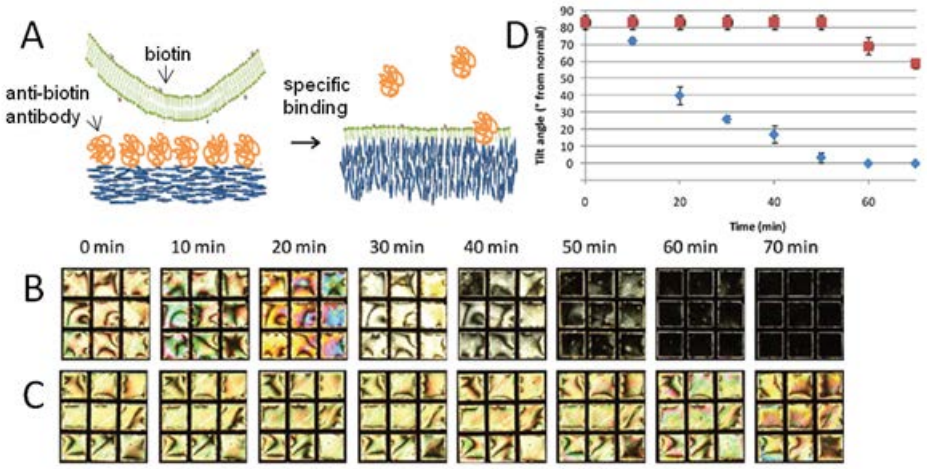

Figure 3-11. Anchoring transitions induced in films of 5CB by specific binding of biotinylated phospholipid vesicles to anti-biotin antibody-decorated aqueous−5CB interfaces.
(A) Schematic illustration of the specific capture of phospholipid on protein-decorated aqueous—LC interface. (B-C) Optical images (crossed polarizers) of 5CB that result from incubation of anti-biotin antibody-decorated interfaces against dispersions of vesicles containing (B) 5 mol % and (C) 0 mol % biotin-DOPE. (D) Tilt angle of 5CB at the aqueous—LC interfaces corresponding to (B) diamonds and (C) squares. Reproduced with permission.[64]

3.4.2 Molecules Tailored for Biosensing at the Aqueous—LC Interface

The examples presented above reveal that a key challenge underlying the use of aqueous—LC interfaces for biosensing is the functionalization of the interface of the LC such that anchoring transitions of the LCs are triggered by a targeted biomolecular interaction. Although phospholipids have proved effective for that purpose, an opportunity exists to functionalize aqueous—LC interfaces with non-natural molecules that present biologically-relevant chemical functionality and thereby cause the LC to undergo well-defined anchoring transitions in the presence of targeted analytes. Below we summarize several recent studies that have tailored the interfacial properties of LCs using synthetic and semi-synthetic molecules.

The first example addresses the use of conjugates formed between synthetic surfactants and oligopeptides, and the interaction of these conjugates with enzymes.[65, 66] Park and Abbott showed that oligopeptide-decorated interfaces of LCs can be prepared by covalently attaching an oligopeptide (with 17 amino-acid residues) to the terminal carboxylic acid groups of surfactants adsorbed at the aqueous interface of the LC (Figure 3-12A). Conjugation of the oligopeptides to the surfactants led to an anchoring transition in the LC due to the reorganization of the monolayer. In contrast, physical adsorption of oligopeptides onto the surfactant-laden interface of the LC did not cause an anchoring transition, thus highlighting the role of covalent bond formation. Significantly, the authors also demonstrated that introduction of a protease, which catalyzed the hydrolysis of the oligopeptide-surfactant conjugate, released the surfactants from the oligopeptide-induced organization, thus resulting in an anchoring transition that returned the LC to the orientation exhibited prior to conjugate with the oligopeptide (Figure 3-12B-C). This result suggests that oligopeptide-decorated LCs provide a convenient and simple method to selectively report protease activity.

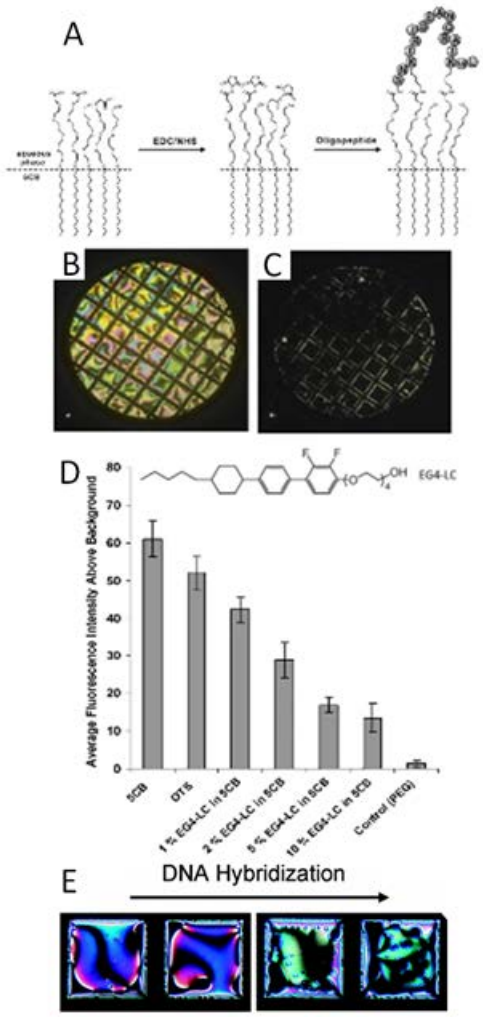

Figure 3-12. Designs for LC-based biosensors at the aqueous—LC interface.

(A) Schematic illustration of the formation of a surfactant-oligopeptide conjugate at the aqueous—LC interface; (B-C) Optical images of LC before (B) and after (C) enzymatic hydrolysis of the oligopeptide-surfactant conjugate at the interface (as shown in A). (D) Molecular structure of EG4-LC and measurements of non-specific adsorption of proteins to the interfaces of various materials, including 5CB doped with EG4-LC. (E) Ordering transition in a LC (E7) triggered by DNA hybridization at the surface of the LC (see text for details). Reproduced with permission.[65, 67, 68]

As a second example of the design of a synthetic modifier of LC interfaces, we briefly mention the use of nitrilotriacetic acid-terminated amphiphiles. When adsorbed at aqueous—LC interfaces and primed with Ni^{2+} ions, these amphiphiles were used to bind histidine-tagged

ubiquitin through binding of the Ni^{2+} to the histidine tag.[60] When the LC interfaces presenting immobilized histidine-tagged ubiquitin were exposed to an aqueous solution of anti-ubiquitin antibody, an orientational transition was induced in the LC, presumably also due to a change in organization of the amphiphiles at the interface.

A third example involves the use of LC interfaces decorated with cationic surfactants to report hybridization of oligonucleotides.[67, 69, 70] This approach builds from past studies that have demonstrated that cationic amphiphiles form organized assemblies with DNA in bulk solution.[67, 69, 70] Although a complex formed between octadecyltrimethylammoniurn bromide (OTAB) and single-stranded DNA (ssDNA) at the aqueous interface of nematic 5CB caused a tilted orientation of the LC, exposure of the ssDNA/OTAB interfacial complex to its ssDNA complement resulted in the nucleation, growth, and coalescence of regions that caused homeotropic LC alignment (Figure 3-12E). Fluorescence microscopy revealed that the complement was co-localized in the same regions as the homeotropic domains, and that exposure to non-complementary ssDNA caused no such response. These results support the conclusion that the homeotropic regions were due to DNA hybridization.

Finally, we comment that block copolymers containing liquid crystalline blocks (LCP) are an additional class of molecules that have been used to functionalize interfaces of LCs for detection of proteins.[71, 72] Although this approach appears promising, to date, however, the detection of proteins has been non-selective. For example, Seo *et al.*[72] adsorbed an amphiphilic block copolymer of PAA-*b*-LCP and demonstrated that adsorption of several different proteins in the μM-range caused a transition from homeotropic to planar anchoring of 5CB. These authors also demonstrated that they could detect proteins in human urine from a patient having albuminuria (with a detection limit of 0.032 mg/mL).

3.4.3 pH-Based Biosensors

Many enzymatic events lead to the consumption or generation of a proton, and thus detection of pH is a common method to detect enzymatic activity. Building from this observation, a series of studies have reported the design of pH-sensitive aqueous—LC interfaces for the purpose of reporting enzymatic activities that lead to changes in pH.

As first example, we comment that it has been reported that 5CB, when doped with 4'-pentyl-biphenyl-4-carboxylic acid (PBA), undergoes an anchoring transition in response to protonation and deprotonation of PBA at the aqueous—LC interface. Building from this observation, the PBA-doped LC was used to monitor local pH changes triggered by enzymatic reactions. As a proof of concept, the hydrolysis of penicillin G by surface-immobilized penicillinase was reported through a pH-induced anchoring transition.[73] A second example involves the detection of catalase activity based on doping of the aldehyde dodecanal into 5CB. In brief, hydrogen peroxide was generated by the catalytic oxidation of dodecanal into dodecanoic acid, thus leading to homeotropic anchoring as the dodecanoic acid formed carboxylate anions at the aqueous interface.[74] Finally, we note that urease has been detected *via* changes in pH that were induced by the reaction product ammonia.[75] This method was successfully used to detect urease belonging to the family of amidohydrolase, which hydrolyzes urea into ammonia and carbon dioxide. This ammonia-based LC biosensor may be useful for sensitive detection of other amidohydrolases.

3.4.4 Tailored Mesogens for Biosensing

Finally, we note that a largely untapped opportunity exists to design mesogens tailored for biosensing at the aqueous—LC interface. As a first step in this direction, mesogens have been designed containing oligomeric ethylene glycol (Figure 3-12D).[68] The approach was inspired by

past studies that have demonstrated that monolayers of oligomeric ethylene glycol can passivate surfaces to strong, non-specific adsorption of proteins. To explore if a similar strategy could be used at the surface of a LC film, miscible mixtures of 5CB and EG4-LC (a mesogen with a tetra(ethylene glycol) tail) were contacted with an aqueous phase. LC mixtures containing 1-5% wt/wt of EG4-LC triggered an anchoring transition to a homeotropic orientation, consistent with partitioning of EG4-LC from the bulk of the LC to its aqueous interface. Significantly, the interfacial partitioning of the EG4-LC also lowered the level of non-specific adsorption of BSA to the interface of the LC. Minimization of non-specific adsorption of proteins to the interfaces of synthetic materials represents a key challenge in the design of biotic–abiotic interface. The results demonstrate a general and facile approach to the design of LC interfaces that present biologically relevant chemical functional groups, exhibit well-defined anchoring at aqueous interfaces, and exhibit minimal non-specific adsorption of proteins.

3.5 LC-in-Water Emulsions for Sensing or Templated Synthesis of Polymer Particles

Whereas the sensors described above employ LC confined to planar films with thicknesses of several micrometers, droplets of LC dispersed in water (*i.e.*, LC-in-water emulsions) are rapidly emerging as promising candidates for LC-based sensing. Specifically, LC emulsions have now been utilized to report the presence of surfactants,[76-78] lipids,[76, 79-81] charged macromolecules,[82] bacteria,[83] viruses,[83] and proteins[76, 84] in aqueous solution.

In many of the past studies that have employed LC emulsions as sensors, a target analyte adsorbs to the surfaces of the LC droplets, triggering a change in the surface anchoring of the LC and thus the configuration of the LC within the droplet (*i.e.*, the so-called director configuration,

where the director (***n***) describes the average orientation of the LC; Figure 3-13 shows schematic illustrations of several possible director configurations). Recent studies of LC emulsion-based sensors have been motivated by several advantages that they offer relative to sensors based on planar films of LC (described above). First, in contrast to the sensors based on planar films of LC, sensors based on LC emulsions do not require surface treatment of solid substrates to define the initial orientation of the LC.[85] Instead, the initial director configuration within the droplets of a LC emulsion is defined by the chemistry of the droplet interfaces. Second, as will be discussed in detail below, the ordering of the LC confined within the droplets of LC emulsions is sensitive to the size of the droplets, thus providing an additional means to tune the response of the LC droplets to the presence of target analytes or changes to bulk solution conditions (*i.e.*, by controlling the size of the droplets; see also Chapter 5).[77, 86] Finally, droplets contained in LC emulsions are highly mobile, thereby providing advantages in terms of sample handling (*e.g.*, using microfluidics; see Chapter 6), reagent mixing, and detection.[87]

It has recently been revealed that many of the properties that make LC-in-water emulsions effective sensors can also be exploited for their use in templated synthesis of polymer microparticles. Specifically, the droplets of LC-in-water emulsions can be doped with a small amount of reactive mesogenic monomer, the orientation of which follows the director configuration of the LC droplet, and photopolymerized with LC either left within or extracted to synthesize spherical or non-spherical microparticles.[24] Chemically functionalized solid colloids can be adsorbed at the surfaces of the droplets prior to polymerization to yield polymer particles with chemical surface patches.

The remainder of this section is organized into four subsections. To provide the reader with a basic understanding of the fundamental properties of LC droplets which make them useful

as sensors or templates for soft material synthesis, the first subsection provides a common formulation of the free energy of a LC droplet and several key predictions to which the formulation leads. The second subsection builds from the first and details recent studies that have revealed size-dependent ordering of LCs within micrometer-sized droplets that possess precisely defined sizes and interfacial chemistry. In the third subsection, we highlight how these observations underlie new, emerging designs of LC-in-water emulsion based biological sensors. The final subsection addresses the use of LC droplets as templates for synthesis of spherical and non-spherical polymeric particles with chemical patches, highlighting the diversity of functional properties that can be engineered based on the presence of defects in LCs. We note here that LC droplets confined within polymer matrices (so-called polymer dispersed liquid crystals (PDLCs)) have been extensively studied for their use in display applications,[88-90] and where appropriate below we provide key insights gained from these studies which are relevant to LC-in-water emulsion based sensors or synthetic templates.

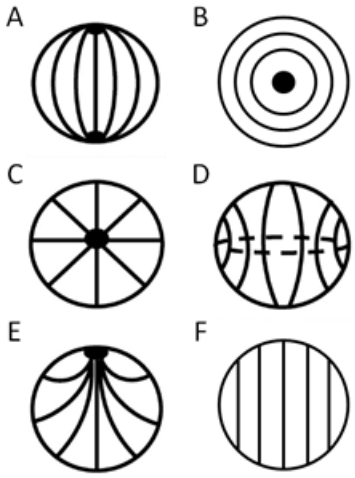

Figure 3-13. Schematic illustrations of possible director configurations within nematic LC droplets under different anchoring conditions of the LC at the droplet surface.
The solid black lines within the droplet boundaries represent the orientation of the director. Under planar (tangential) anchoring conditions the droplets can adopt (A) a bipolar configuration with two diametrically opposed surface point defects (boojums) at the poles of the droplet, or (B) a concentric (*i.e.*, tordial or axial) configuration with a disclination line that traverses the diameter of the droplet, passing through the center of the sphere. Under normal anchoring conditions the droplets can adopt (C) a radial configuration possessing a central point defect at the core of the droplet, or (D) an axial (*i.e.*, equatorial) configuration with a disclination line along the equator of the droplet. Under anchoring conditions between normal and tangential the droplets can adopt (E) a preradial configuration. Another possible droplet configuration is (F) a uniform director profile.

3.5.1 Free Energy of a LC Droplet

As background to the recent observations of size-dependent ordering of LCs in droplets that are detailed below, here we briefly introduce a common formulation of the free energy of a LC droplet and then summarize key predictions that follow from the description. In short, the equilibrium director configuration within a LC droplet is governed by a delicate energetic

balance that involves surface and volumetric contributions. The free energy (F) of a LC droplet can be expressed as:

$$F = F_{\text{homogeneous}} + \int_A f_s dA + \int_V f_e dV + \int_V f_{\text{field}} dV + \int_{V_d} f_d dV_d \quad (3-1)$$

where $F_{\text{homogeneous}}$ is the free energy of an unstrained bulk LC (typically expressed as a function of the orientational order parameter of the LC, and neglected in analytical models of relative energies of two director configurations), A is the surface area of a droplet, V the volume of a droplet, f_s and f_e are the surface anchoring energy and elastic free energy densities, respectively, and f_{field} is the free energy density due to external fields (*e.g.*, an electric field).[89] The last term in equation 3-1 describes the contribution of defects to the free energy, as discussed in detail below. We note that in the discussion below we assume the LC droplet shape to be spherical and independent of the internal ordering of the LC. This approximation is a good one for thermotropic LCs dispersed in water as the interfacial tensions are high (typically 10^{-3} to 10^{-2} J/m^2).

The surface anchoring energy of the LC droplet (second term in equation 3-1) characterizes the energetic penalty associated with deviations of the nematic director from its preferred alignment at the droplet interface (easy axis; set by the interfacial chemistry). The surface anchoring energy density (f_s) is often approximated using the single-constant Rapini and Papoular equation:

$$f_s = \frac{1}{2} W \sin^2 \varphi \quad (3-2)$$

where φ is the angle between the director ($\boldsymbol{n}$) and easy axis, and W is surface anchoring energy per unit area.[91] Typical values of W range from 10^{-6} to 10^{-5} J/m^2,[89, 92] a range that is at least two

orders of magnitude smaller than common values of interfacial tension for LC droplets dispersed in water (see above).[93, 94]

The elastic free energy of the LC droplet (third term in equation 3-1) is the energetic penalty associated with strain of the LC. The elastic free energy density (f_e) can be described by the Frank-Oseen equation:

$$f_e = \frac{1}{2}\begin{bmatrix} K_{11}(\nabla \cdot \boldsymbol{n})^2 + K_{22}(\boldsymbol{n} \cdot \nabla \times \boldsymbol{n})^2 + K_{33}(\boldsymbol{n} \times \nabla \times \boldsymbol{n})^2 \\ -K_{24}\nabla \cdot \left(\boldsymbol{n} \times \nabla \times \boldsymbol{n} + \boldsymbol{n}(\nabla \cdot \boldsymbol{n})\right) \end{bmatrix} \qquad (3\text{-}3)$$

where K_{11}, K_{22}, K_{33} (which are sometimes also labeled as K_1, K_2, and K_3[95-97]) and K_{24} are elastic constants associated with splay, twist, bend, and saddle-splay strain, respectively.[98-100] We also comment that a fifth elastic constant not shown in equation 3-3 is the splay-bend elastic constant (K_{13}), which is typically neglected because it involves higher order derivatives of $\boldsymbol{n}$.[101, 102]

Two external fields frequently applied to LC droplets are electric and magnetic fields. The free energy density due to these two external fields (f_{field}; fourth term in equation 3-1) can be expressed as:

$$f_{field} = -\frac{1}{2}\varepsilon_o \Delta\varepsilon[\boldsymbol{E} \cdot \boldsymbol{n}]^2 - \frac{1}{2}\frac{\Delta\chi}{\mu_o}[\boldsymbol{B} \cdot \boldsymbol{n}]^2 \qquad (3\text{-}4)$$

where the first term is the energy density due to an applied electric field, and ε_o is the free space permittivity, $\Delta\varepsilon$ is the nematic dielectric anisotropy, and $\boldsymbol{E}$ is the local electric field inside a droplet (usually different from the applied field).[89, 99, 103, 104] The second term in equation 3-4 is the energy density due to an applied magnetic field, and μ_o is the free space permeability, $\Delta\chi$ is diamagnetic anisotropy, and $\boldsymbol{B}$ is the local magnetic field inside a droplet.

The fifth term in equation 3-1 is the free energy contribution from topological defects, where f_d and V_d are the free energy density and volume of defects, respectively. Defects are localized regions of LC that partially "melt" in response to a high local elastic free energy

density of the LC. Specifically, the cores of defects, which are typically about 10 nm in size, possess levels of orientational order that are lower than that of the bulk LC.[105, 106] In general, defects are easily identified in bright field micrographs of LC droplets because the defect cores, although nanoscopic in size, possess refractive indices that differ substantially from that of the surrounding LC and strongly scatter light (see Chapter 2). Defects, therefore, are frequently used to aid in characterization of the director configuration of LC droplet.[107] As discussed below, the contribution of defects to the free energy of a droplet is typically two orders of magnitude lower than the surface anchoring and elastic energies and, therefore, often neglected in the evaluation of equation 3-1.[108] Despite their small "core" energies, however, defects appear to play an important role in mediating the interactions of LC droplets with some biological amphiphiles (see Chapters 4, 5, and 7)[81, 108] as well as colloidal species in LC-templated material synthesis[24] (see below).

The above formulation of the free energy of a LC droplet has been widely used to predict the size-dependent ordering of nematic LC within droplets. Historical descriptions have typically neglected the contribution saddle-splay strain (K_{24}) to the elastic energy (although more recent studies indicate that it can play a role in the relative stability of droplet director configurations, a point that we expand on below)[77, 81, 89, 108] and applied the "one elastic constant approximation" (*i.e.*, $K = K_{11} = K_{22} = K_{33}$).[89, 100] With these approximations, equations 3-1 through 3-3 predict that the elastic energy of a LC droplet scales with the droplet radius (~ KR) and the surface anchoring energy scales with the square of the droplet radius (~ WR^2). In the absence of applied fields and neglecting defect energies, these two contributions to the free energy lead to the expectation that droplets with $R << K/W$ will exhibit a uniform director profile free of strain (see Figure 3-16B below) although larger droplets will satisfy the surface anchoring and incur a free

energy penalty associated with strain.[92, 109] Because typical elastic constants and surface anchoring energies per unit area are 10^{-11} N and 10^{-5} J/m^2, respectively,[81, 95] this scaling argument predicts a cross-over in free energy/droplet configuration for droplets with sizes of ~1 μm. As will be discussed below, recent experimental measurements have led to observations of size-dependent order that are not consistent with these historical predictions, thus leading to a reexamination of the energetics that control the size-dependent ordering of LC droplets.[77, 110]

3.5.2 Recent Observations of Size-Dependent Ordering of LCs in Micrometer-Sized Droplets

3.5.2.1 Size-Dependent Ordering of LCs in the Droplets of PDLCs

Here we briefly discuss past observations of size-dependent ordering of LCs in droplets of PDLCs to provide a historical perspective and highlight gaps in knowledge addressed by the more recent experimental studies that are the focus of this subsection. Size-dependent changes in the director configuration of micrometer-sized droplets of LC dispersed in polymer matrices have been characterized both experimentally[103, 111] and predicted theoretically.[99, 104] For example, Figure 3-14A shows an experimentally measured phase diagram for droplets of a nematic LC called E7 dispersed in a polyurethane matrix that causes homeotropic anchoring of the LC.[103] It was observed that a decrease in LC droplet size below a critical value caused a spontaneous radial-to-axial ordering transition. A second transition from an axial to a uniform director was predicted but was not observed in experiments (Figure 3-14B). We also comment here that past studies have demonstrated that application of an electric field can trigger a radial-to-axial

ordering transition within the LC droplets. The strength of the applied field needed to trigger the transitions is dependent on the size of the LC droplets in the PDLC.[99, 103, 104, 111]

While the studies summarized above report size-dependent ordering of LCs in PDLCs, we comment that the processes of phase separation leading to formation of LC droplets in PDLCs impact the composition of the LC (note that the nematic-to-isotropic clearing temperature of the LC in Figure 3-14 is 303 K although the clearing temperature of pure E7 is 30 K higher). This compositional uncertainty is resolved in more recent experiments performed using water-dispersed LC droplets (see below). We also note that recent experiments also permit precise control over the interfacial anchoring of the LC.[77, 110]

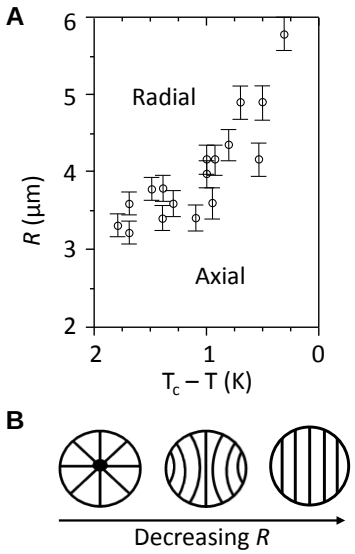

Figure 3-14. Preferred director configuration of E7 droplets in a PDLC as a function of temperature (T) and droplet radius (*R*).

(A) Experimental phase diagram of the preferred configuration of nematic droplets of E7 dispersed in a polyurethane matrix as a function of T and *R*. T_c is the nematic-to-isotropic clearing temperature (303 K for this system). (B) Schematic illustrations of the director configuration predicted as a function of decreasing *R*. Reproduced with permission.[103]

3.5.2.2 Preparation of LC Droplets with Precise Size and Interfacial Chemistry

In addition to the phase separation processes described above in the context of PDLCs, methods that permit preparation of dispersions of LC droplets include sonication,[81, 107-109 112, 113] microfluidics,[82, 87, 114] homogenization,[24] shearing of droplets and subsequent crystallization fractionation,[112, 113] and dispersion polymerization.[115-117] These methods, while generally effective for the preparation of LC droplets larger than 10 μm, do not work well at the 1 μm-scale. Recently, however, a new technique, which involves the templated synthesis of polyelectrolyte multilayer (PEM) capsules using sacrificial silica micro or nanoparticles and

subsequent filling of the capsules with LC, has provided the necessary level of control to explore size-dependent ordering of LC droplets with sizes around 1 μm (Figure 3-15).[77, 110]

Here we briefly summarize the methodology. First, PEMs were formed on the surfaces of silica (template) particles of predetermined size *via* layer-by-layer adsorption of polyelectrolytes from aqueous solution. In the studies summarized below, the PEMs were prepared from the anionic polyelectrolyte poly(sodium 4-styrene-sulfonate) (PSS) and the cationic polyelectrolyte poly(allylamine hydrochloride) (PAH) (Figure 3-15C and 3-15D, respectively).[77] Following formation of the PEMs, the silica template particles were selectively etched using hydrofluoric acid, resulting in formation of hollow PEM capsules. The hollow capsules were then infiltrated with an isotropic mixture of ethanol (5 wt%) and 4'-pentyl-4-cyanobiphenyl (5CB, Figure 3-15B). Finally, the ethanol was evaporated from the mixture, and the monodisperse nematic LC-filled PEM capsules were extracted into a bulk aqueous phase thus forming LC droplets of precise size that were encapsulated in PEMs of pre-determined chemical composition. Because a range of polymers can be incorporated into PEMs, this technique provides a level of control over both the interfacial chemistry of the LC droplets and the size of the LC droplets (as determined by the silica template particle; see Figure 3-15) that is difficult to achieve with other methods of preparing LC droplets. We end this section by noting that removal of the multilayers from the LC droplets to prepare "bare" droplets is possible using hydrogen bonded polymeric multilayers (*e.g.*, poly-(methacrylic acid)/poly(vinylpyrrolidone)).[76]

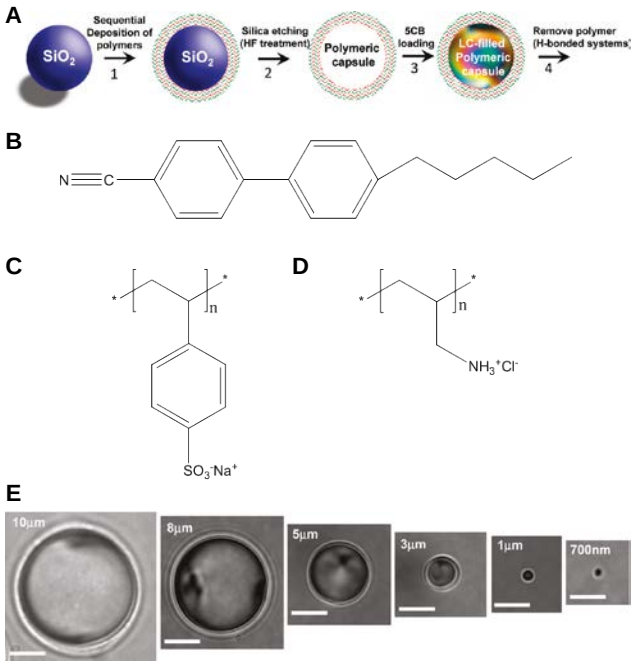

Figure 3-15. Procedure used to prepare LC droplets of predetermined sizes within polymeric multilayer capsules.

(A) Polymeric capsules were prepared by the sequential deposition of polyelectrolytes onto silica particles and the subsequent etching of silica. The resulting polymeric capsules were filled with LCs (see the text for details). (B-D) Chemical structures of the (B) 5CB and the polyelectrolytes used to create polymeric multilayer capsules ((C) PSS and (D) PAH). (E) Bright field micrographs of polymer-encapsulated 5CB droplets obtained using silica templates with diameters of 10 ± 0.22, 8 ± 0.20, 5 ± 0.19, 3 ± 0.18, 1 ± 0.04, and 0.7 ± 0.08 μm, respectively. All scale bars are 3 μm. Reproduced with permission.[77]

3.5.2.3 Observation of Size-Dependent Ordering

Using the synthetic methodology described above, micrometer-sized droplets of nematic 5CB were prepared to study the size-dependent ordering in the droplets and thereby test prior theoretical predictions (see above).[77] In the studies described below, the LC droplets were coated with PEMs prepared from PSS/PAH (Figure 3-15C and 3-15D). For encapsulated 5CB droplets with diameters larger than 3 μm, the LC was observed to exhibit a bipolar configuration (Figure

3-16C and 3-16D). This configuration is consistent with tangential anchoring of the LC on the PEM. Surprisingly, however, droplets with diameters of ~ 1 μm and 700 nm were observed to assume so-called preradial (Figure 3-16F-I) and radial (Figure 3-16K and 3-16L) configurations, respectively. In a radial configuration, the LC director is aligned normal to the droplet surface and a single point defect (or a very small disclination line in the shape of a ring)[111, 118-120] is present at the core of each droplet (Figure 3-16M).[77, 79, 80, 89] Similar to a radial configuration, the preradial configuration possesses a single point defect. However, this defect is located at the surface of the droplet rather than in the center of the droplet and the LC director is tilted at the droplet interface (Figure 3-16J).[79, 80, 89, 107, 121] These results, obtained with the PEM-coated LC, thus revealed that polymer-coated LC droplets transition from a bipolar to the radial configuration (a so-called “bipolar-to-radial ordering transition”) with decreasing droplet size. Specifically, the LC droplets were not observed to transition to a homogeneous internal director configuration, as previously predicted on the basis of scaling arguments (see above).

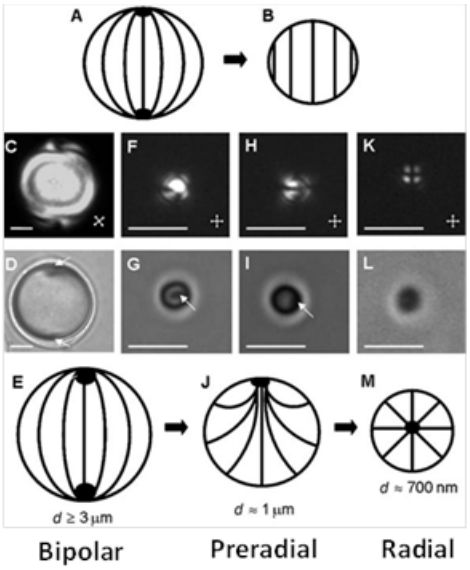

Figure 3-16. Size-dependent ordering within LC droplets.
(A and B) Schematic illustrations of the bipolar (A) and uniform (B) ordering of LCs predicted from scaling arguments. (C, F, H, K) Polarized light and (D, G, I, L) bright field optical micrographs of polymer-encapsulated 5CB droplets with (C, D) diameters of 8.0 ± 0.2 μm and bipolar LC ordering, (F–I) diameters of 1.0 ± 0.2 μm and preradial LC ordering ((F and G) show the end on views of the preradial ordering; (H and I) show side views), and (K, L) diameters of 0.70 ± 0.08 μm and radial LC ordering. Point defects in the LCs are indicated by white arrows. Schematic illustrations (E, J, and M) show bipolar, preradial, and radial ordering of the LC droplets, respectively. The scale bars are 2 μm for (C, D, and F–I), and 1 μm for (K, L). Reproduced with permission.[77]

The experimental results described above (and others that confirm the size-dependent ordering)[108] have led to a reexamination of the relative importance of contributions to the LC droplet free energy, as described by equation 3-1. Specifically, by relaxing the one constant approximation[89, 100] and including the contribution of the saddle-splay elastic constant (K_{24}), it was shown that the above-described stabilization of the radial configuration relative to the uniform configuration could be predicted.[77] In this revised treatment, the free energy of the radial configuration (F_r) is described as:[122]

$$F_r = 8\pi K_{11} R - 4\pi K_{24} R + 2\pi W R^2 \qquad (3\text{-}5)$$

where the first term is associated with splay deformation within the LC droplet, and the third term is the energetic penalty associated with a homeotropic orientation of the LC at the droplet interface (note that the easy axis is tangential to the droplet interface).[77] The second term is associated with saddle-splay deformation of the LC, and favors the radial configuration.[77, 99] In contrast to a radial configuration, a droplet with a uniform director profile is free of elastic strain. Thus, the only contribution to the free energy of a uniform LC droplet (F_{uniform}) is an anchoring energy penalty: [77]

$$F_{\text{uniform}} = \frac{2}{3}\pi W R^2 \qquad (3\text{-}6)$$

By comparing equations 3-5 and 3-6, it is possible to predict that a radial configuration will be favored over a uniform director profile for droplets with $R < 6K^*/W$, where $K^* = K_{24}/2 - K_{11}$.[77] While this analysis of the free energy can, in principle, provide an account for the stabilization of the radial configuration, it requires that K_{24} be greater than $2K_{11}$, which violates one of the Ericksen inequalities ($K_{24} \leq 2K_{11}$).[123, 124] However, we note that more detail and quantitative numerical models have concluded that elastic constants that satisfy the Ericksen stability limits can predict stabilization of the radial configuration.[125] We end by noting that experimental estimates of K_{24} vary widely and range up to $3.1K_{11}$.[124] Thus, while it appears likely that K_{24} plays an important role in determining the configurations of the LC droplets, additional investigations are needed to provide a full account of the experimental observations.

3.5.3 LC Emulsion-Based Biosensors: Ordering Transitions in LC Droplets Triggered Interactions with Biomolecular Species

3.5.3.1 Interactions between Lecithin and LC Droplets of PDLCs

The observations of size-dependent ordering of LCs within droplets, as outlined above, have inspired and aided in the interpretation of a series of investigations of LC droplet systems that respond to the presence of biological species that assemble at the aqueous interface of the LC.[126] Prior to discussing these investigations, here we mention briefly an early study that reported on the effects of incorporation of lecithin into the polymer matrix of a PDLC. Figure 3-17 shows a series of configurational states observed for 5CB droplets contained in a poly(vinyl butyral) matrix doped with increasing amounts of lecithin.[79] Overall, these studies revealed configurations of the LC that corresponded to the bipolar, monopolar, preradial and radial states (each of which possess a single defect). In this study, however, the sizes of the LC droplets were not maintained constant (see scale bars in Figure 3-17). As described below, more recent studies with LC-in-water emulsions with LC droplets of well-defined size have revealed that the effects of adsorbates on LC configurations within droplets are size-dependent. In addition, observations of the dynamic transition pathways observed during the interaction of the adsorbate from the aqueous phase provide new insights into two distinct mechanisms by which adsorbates trigger LC ordering transitions (adsorption at the aqueous—LC interface or formation of self-assembled structures within LC droplets). The first mechanism will be described below, and the second will be described in Chapter 4.

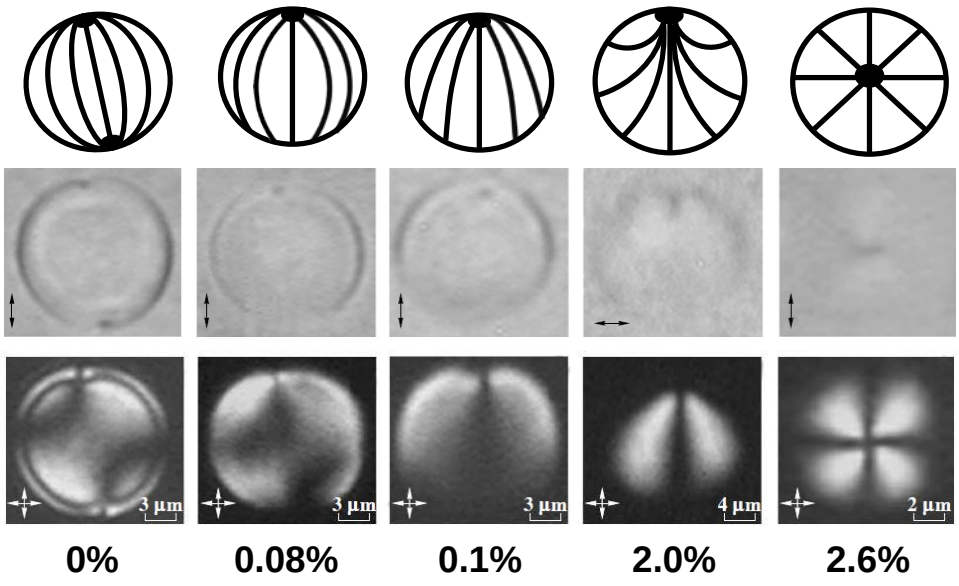

Figure 3-17. Equilibrium director configurations observed in nematic LC droplets dispersed in a poly(vinyl butyral) matrix containing lecithin.

The top row shows schematic illustrations of the configuration of the LC within each droplet, and the middle and bottom rows, respectively, show the corresponding bright field and polarized light micrographs of the 5CB droplets. The weight percent of lecithin doped into the polymeric matrix is indicated below each polarized light micrograph. Note that the scale-bar differs between figures. Double headed arrows in bright field micrographs indicate the orientation of the single polarizer, while double headed arrows in polarized light micrographs indicate the orientation of the crossed polarizers. Reproduced with permission.[79]

3.5.3.2 Adsorption of Amphiphiles at the Aqueous—LC Interface

The aqueous environment of LC-in-water emulsions provides a means of delivery of biomolecules to LC interfaces and also influences the interfacial adsorption process (*e.g.*, through water mediated interactions such as those associated with hydrophobic hydration).[126-128] As noted above, recent interest in aqueous dispersions of LCs has been motivated by prior reports that amphiphiles adsorb to and alter the orientational ordering of LCs at aqueous—LC

interfaces.[56, 58, 129] This phenomenon is commonly referred to as an "adsorbate-induced anchoring transition"[76] and involves a change in the LC anchoring energy induced by the amphiphile (the second term in equation 3-1 for LC droplets). To change the anchoring energy to an extent that an ordering transition is triggered from the interface, a coverage of the interface by adsorbate of 0.1 to 1 Langmuir is typically required.[58, 79, 80, 83, 130]

Figure 3-18 shows an adsorbate-induced bipolar-to-radial ordering transition in water-dispersed droplets of nematic 5CB, where the adsorbate is sodium dodecyl sulfate (SDS).[76] This figure demonstrates that an increasing concentration of adsorbate leads to a series of stable director configurations that are driven by changes in the anchoring of the LC at the droplet interface. The first transition shown in Figure 3-18 is a bipolar-to-axial transition, evidenced by the disappearance of the two point defects (boojums) at the diametric ends of the bipolar droplet and simultaneous appearance of a disclination ring near the droplet equator. With further increase in bulk surfactant concentration (and thus concentration of the SDS at the aqueous—LC interface), this ring defect moved towards a pole and shrank to a surface point defect, forming a preradial configuration. Finally, the point defect migrated from the surface of the droplet to the center, forming the radial structure. The above-described sequence of configurational states of the LC droplets observed with SDS is similar to that reported previously in a study of the effect of temperature on glycerol-dispersed 5CB droplets in the presence of a fixed concentration of lecithin.[80] Although changes in temperature are expected to impact all terms in equation 3-1 (including elastic energies), the results reported recently with SDS clearly define the role of surface anchoring in dictating the series of configurational states shown in Figure 3-18. We comment that the sequence of configurational states observed in these two studies is distinct from that observed for polymer-dispersed 5CB droplets doped with lecithin (Figure 3-17). The

reasons for these differences are not fully understood, but it is possible that they reflect differences in the uniformity of the distribution of adsorbates on the surfaces of the LC droplets.

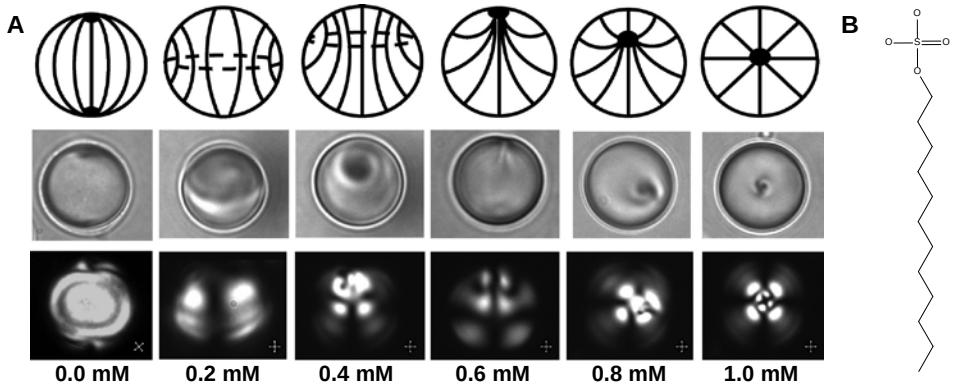

Figure 3-18. Adsorbate-induced ordering transitions of LCs within monodisperse droplets. (A) Concentration-dependent equilibrium director configurations induced by an adsorbate-driven change in the anchoring energy of LC droplets coated by polymeric multilayer capsules composed of alternating layers of PSS and PAH (Figure 3C and D respectively). The change in surface anchoring of the LC droplet (from tangential to perpendicular) was achieved by equilibrating 8.0 ± 0.2-μm-diameter, polymer-encapsulated 5CB droplets with aqueous solutions containing SDS at concentrations that ranged from 0 to 1 mM (as indicated). The top row shows schematic illustrations of the configuration of the LC within each droplet, and the middle and bottom rows, respectively, show the corresponding bright field and polarized light micrographs of the 5CB droplets. (B) Molecular structure of sodium dodecyl sulfate (SDS). Reproduced with permission.[76]

Importantly, and as outlined above, the concentration of SDS that triggers the various internal configurations of LC droplets shown in Figure 3-18 can be tailored by taking advantage of the size-dependent energetics of the LC droplets. Specifically, Figure 3-19 shows one set of results obtained with LC droplets with diameters between 1 and 10 μm.[77] The observations of both a family of equilibrium director configurations as a function of interfacial concentration of adsorbate and the size-dependence of the responsiveness of LC droplets to adsorbates have initiated studies aimed at elucidation of general design principles for LC-in-water emulsion-based biosensors.[126] Specifically, as mentioned above, LC droplets have been shown to undergo

ordering transitions in response to the presence of lipids,[76, 81] surfactants,[77, 78] proteins,[76, 84, 131, 132] bile acids,[133] and bacteria and viruses (see below).[83] Finally, we note that size-dependent ordering of LC droplets has also been exploited to design LC materials that respond to changes in ionic strength[134] and pH[87] of aqueous solutions and the presence of charged macromolecules.[82]

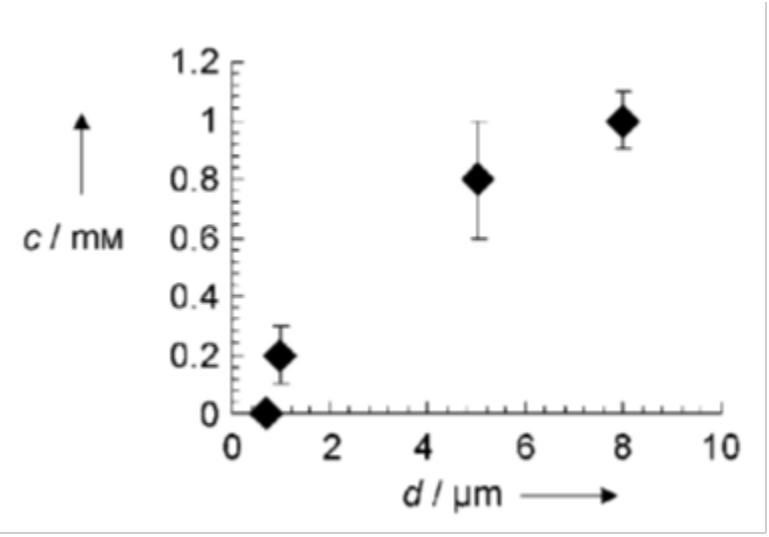

Figure 3-19. SDS concentrations (*c*) in aqueous solution that caused LC droplets of the indicated size (*d*) to assume a radial configuration.
Reproduced with permission.[77]

3.5.4 Templated Synthesis of Polymer Particles with Chemical Patches Using LC Droplets

In addition to providing designs of biosensors, LC droplets have recently been explored as the basis of a general and facile class of templates for the synthesis of spherical and non-spherical polymer particles with chemical patches. The work was motivated by the observation that particles with either anisotropic shape or patterned surface chemistry are enabling new scientific and technological advances (*e.g.*, intracellular delivery of particles;[135] tuning of colloidal interactions between particles;[136-140] stabilization of Pickering emulsions;[141]

manipulation of Brownian motion;[142] and design of hierarchical structures using particles as building blocks[143, 144]). While non-spherical and chemically patterned particles represent an exciting frontier in materials science, the synthesis of such particles remains challenging.[143-145] It is this challenge that has recently been addressed by particle synthesis templated using LC droplets.

A number of past studies have revealed that colloids can localize at defects in bulk LCs to decrease the free energy cost associated with both elastic deformations of LCs near defects and diminished orientational ordering of molecules in the core of the defects.[146-149] Building from these prior observations, recent studies have used the defects associated with the bipolar configuration of LC droplets (the boojums) to localize the association of colloids with the LC droplets.[24, 76, 79, 89, 150-152] Figure 3-20 shows a schematic illustration of the synthetic scheme. First, 5CB-in-water emulsions were prepared by homogenizing 5CB in the presence of fluorescent polystyrene (PS) colloids (Figure 3-20A). After emulsification (Figure 3-20B), bipolar nematic droplets were obtained. Inspection of combined fluorescence and bright field micrographs (Figure 3-20E and G) revealed that the PS colloids adsorbed at the droplet surface and localized at the boojums of the bipolar droplets. Bipolar droplets possessing two boojums were used to direct the self-assembly of organic or inorganic colloids to the poles of droplets independent of the type of anchoring of the LC at the colloid surface.[24]

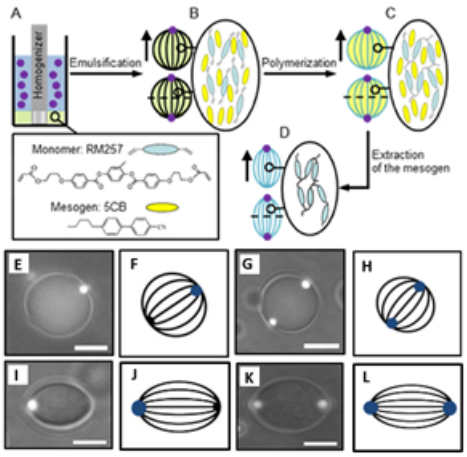

Figure 3-20. Synthesis of non-spherical and chemical-patterned particles.
(A) Emulsification of LC. (B) After emulsification, formation of bipolar nematic droplets with either one or two fluorescent PS colloids located at the poles. (C) After polymerization of the monomer within the droplets, formation of spherical particles. (D) Upon the extraction of the LC from the polymerized droplets, formation of non-spherical particles. (E, G) Combined fluorescence and bright field micrographs of bipolar nematic droplets exhibiting one or two fluorescent PS colloids adsorbed at their surfaces. (I, K) Combined fluorescence and bright field, of non-spherical particles exhibiting one or two fluorescent PS particles. Scale bars: 5 μm. (F, H, J, L) The corresponding schematic illustrations of the director field configuration (dark lines) within spherical nematic droplets and non-spherical particles; the blue spots represent the PS colloids (at the poles). Reproduced with permission.[24]

While the scheme reported above leads to the formation of LC droplets with chemical patches at their poles (defined by the colloids), it was also demonstrated that photo-polymerization of reactive liquid crystalline mesogens could be performed to preserve the initial assembly (Figure 3-20C).[153, 154] This procedure leads to spherical particles comprised of a cross-linked polymeric network that is swollen with 5CB. One or two poles of the particles were decorated with chemical patches defined by the colloids. Finally, it was also demonstrated that non-spherical particles could be obtained by extraction of LC from the above described particles (Figure 3-20D). Extraction of the 5CB resulted in contraction (de-swelling) of the polymerized particles in a direction perpendicular to the line joining the poles of the nematic droplets, as

shown in Figure 3-20I-L. These observations indicated that the polymer network had been templated by the mesogens in the initial bipolar configuration of the nematic droplets. Overall, this study defines the basis of a general method for the synthesis of spherical and non-spherical particles possessing well-organized chemically distinct domains from LC-in-water emulsions. Ongoing efforts are aimed at using other configurations of LC droplets as templates for particle synthesis, including the size-dependent configurations of LC droplets described earlier in this subsection (see Chapter 11 of this thesis).

3.6 LCs as Sensors of Viruses, Bacteria and Mammalian Cells

As discussed above, past studies have shown that interactions between phospholipids and mesogens of LC phases can trigger LC orientational transitions. Because many viruses, bacteria as well as mammalian cells are encapsulated by lipid membranes, recent studies have been performed to investigate their interactions with LCs. These studies have demonstrated that contact between LCs and lipid-encapsulated viruses[83, 155, 156] and gram-negative bacteria[83, 157] can drive ordering transitions within the LC, implicating LCs as potentially useful sensors of these virions and microorganisms. This is a promising capability, as the rapid and sensitive detection of harmful microorganisms and infectious agents is important for upholding public health and safety in areas including food processing, water and environmental monitoring, and clinical diagnostics.[158] Additionally, several studies have investigated the impact that contact with various LCs has on the viability of cells [159-161] and microorgansisms.[161, 162] In particular, it was found that LC interfaces can be used to support the growth of cells.[163, 164] Such LC-based substrates may have utility in reporting interactions with cells. In the following section, we detail

the progress that has been made in understanding the interactions between viruses, bacteria, and mammalian cells with LCs.

3.6.1 Viruses

Espinoza *et al.*[155] first demonstrated that LCs can be utilized for the detection of lipid-encapsulated viruses. Solutions of vesicular stomatitis virus (VSV) were incubated on the surface of gold slides treated with poly-L-lysine. Electrostatic attractions between the VSV outer membrane and the polycation film led to immobilization of the VSV at the surface. Next, LC optical cells were created by sandwiching 5CB between the VSV-decorated slides and reference slides which induced homeotropic anchoring. It was shown that interactions between the LCs and the VSV-treated surface induced homeotropic LC ordering when a critical density of the virus was captured on the slide.

Jang *et al.* [156] extended the study described above by examining the LC anchoring properties of surfaces treated with additional viruses besides VSV, including adenovirus, influenza, and La Crosse virus. It was discovered that only surfaces upon which sufficient densities of lipid-encapsulated viruses were captured induced homeotropic anchoring of a contacting LC film (Figure 3-21). Adenovirus, which lacks an outer lipid envelope, did not give rise to homeotropic anchoring at any virus concentration tested. Thus, the authors proposed that physical interaction between the lipid envelope of viruses and the LC was responsible for giving rise to the homeotropic alignment of 5CB.

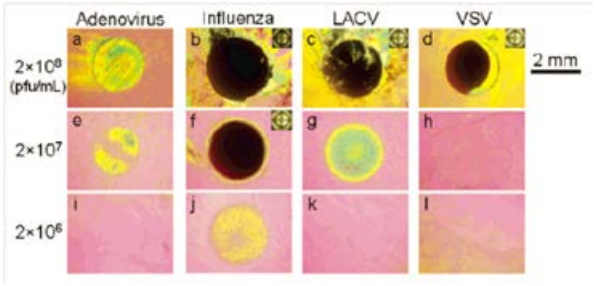

Figure 3-21. Detection of lipid-encapsulated viruses using LCs.
Poly-L-lysine treated gold slides were spotted with various virus-containing solutions to capture the virus on the surface. The virus bound on the surface was then contacted with nematic 5CB. The numbers on the left indicate the concentration of each virus suspension. Conoscopic images of the samples are provided in the insets in (b-d, f). All images were obtained immediately after the assembly of the liquid crystal cell. Reproduced with permission.[156]

As discussed in the preceding section of this chapter, LC emulsion droplets have been employed recently for a variety of sensing applications. For example, it has been shown that, following the transfer and assembly of a monolayer of lipids at the aqueous—LC interface, LC droplets undergo a bipolar-to-radial ordering transition. Sivakumar *et al.*[83] exploited this phenomenon in extending the use of these LC droplets to the detection and differentiation of various strains of viruses in aqueous solutions. It was demonstrated that incubation of LC droplets with a lipid-encapsulated virus, *A/NWS/Tokyo/67*, gave rise to the bipolar-to-radial ordering transition. This likely occurred following adsorption of viral lipids at the aqueous—LC interface. No such transition was observed following incubation of droplets with *M13 helper phage*, a non-enveloped virus. The divergent responses of the LC droplets to these two viruses suggest another means through which lipid-encapsulated viral strains can be differentiated from non-enveloped strains.

3.6.2 Bacteria

In addition to viruses, Sivakumar *et al.*[83] explored the interactions between LC droplets and various bacterial strains. Bacteria are generally classified as either gram-negative or gram-positive based on the presence or absence, respectively, of an outer lipid membrane. The study found that, when a solution containing gram-negative bacteria, such as *E. coli*, was added to the LC emulsion, transfer of membrane lipids was observed to drive a bipolar-to-radial ordering transition in the droplets (Figure 3-22A and 3-22B). No such transition, however, occurred following incubation of droplets with a gram-positive bacterium, *B. subtilis* (Figure 3-22C and 3-22D).

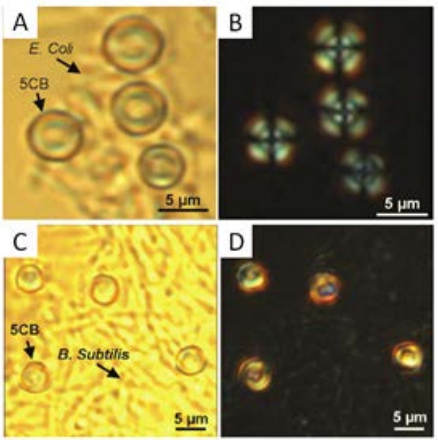

Figure 3-22. Influence of gram-negative and gram-positive bacteria on the ordering within monodisperse micrometer-sized droplets of 5CB.

(A) Bright-field and (B) corresponding polarized light (crossed polarizers) micrographs of 5CB droplets dispersed in an aqueous solution containing the gram-negative bacterium *E. coli* at a concentration of 5×10^5 cells/mL. The presence of *E. coli* caused a bipolar-to-radial ordering transition. (C) Bright-field and (D) corresponding polarized light (crossed polarizers) micrographs of 5CB droplets dispersed in an aqueous solution containing the gram-positive bacterium *B. subtilis* at a concentration of 6×10^5 cells/mL. The droplets remained in a bipolar configuration. Reproduced with permission.[83]

3.6.3 Mammalian Cells

Before discussing experimental results that demonstrate that LCs can be used as engineered materials that support the attachment and growth of mammalian cells, we comment first on enabling studies that were performed to identify thermotropic LCs with limited toxicity towards living cells. Specifically, Luk *et al.*[159] found that although 5CB and several other LCs exhibited toxicity when added above cultures of mammalian cells (3T3 fibroblasts and corneal epithelial cells), LCs containing fluorocarbon functionalities, including TL205 and the C-series (see Figure 3-23A), did not cause pronounced cell death. In a subsequent study performed by Lockwood *et al.*,[160] 5CB was found to partition to a much greater extent than TL205 into multi-lamellar DPPC vesicles, which served as simple models for cell membranes (Figure 3-23B). The authors suggested that the physical mechanisms behind the dissimilar partitioning of TL205 and 5CB into the DPPC bilayers might also underlie the observed difference in toxicity of cells contacted with 5CB and TL205.

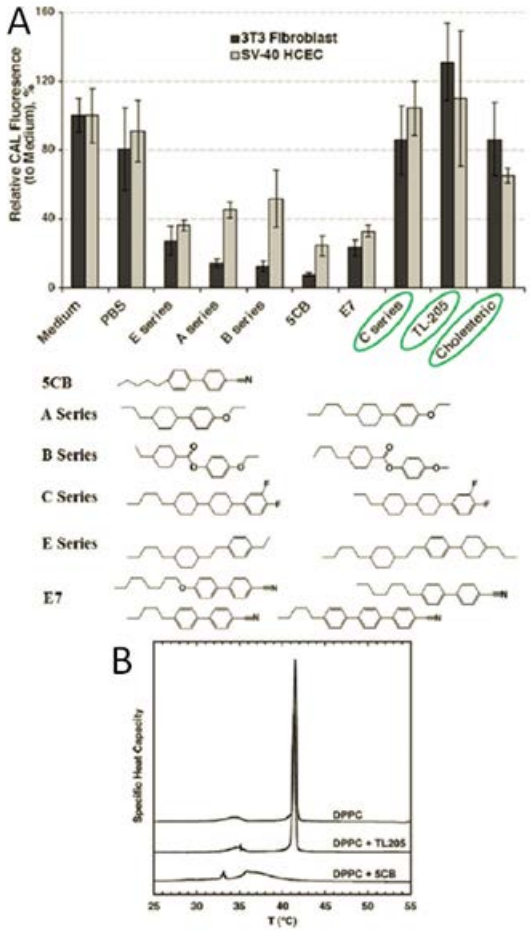

Figure 3-23. Toxicity of thermotropic LCs towards living cells.

(A) Relative intensities of fluorescence from CAL-AM added to 3T3 fibroblasts (black bars) and SV-40 HCECs (gray bars) following 4 h of contact of the cells with each LC indicated below the plot. The CAL fluorescence indicates the presence of living cells. (B) Endotherms (from differential scanning calorimetry) of DPPC multi-lamellar vesicle suspensions following seven days of incubation at 37 °C in the absence or presence of either TL205 or 5CB (as indicated). Reproduced with permission.[159, 160]

Additional studies have investigated the compatibility of various lyotropic LCs with cells. Specifically, Cheng *et al.*[161] reported that contact with the lyotropic LC disodium cromoglycate (DSCG) is not toxic to human epitheloid cervical carcinoma (HeLa) cells. Also, it was shown that VSV can still successfully infect HeLa cells in the presence of the DSCG. Woolverton *et*

al.[162] additionally found that various species of bacteria remained viable following suspension within volumes of four different lyotropic chromonic LCs (Neutral Grey, Red 14, Blue 27, and DSCG). Following the identification of particular LCs which are not toxic to mammalian cells, subsequent reports demonstrated successful use of LC substrates for the attachment and proliferation of mammalian cells. Lockwood *et al.*[163] found that human embryonic stem cells (hESCs) can survive and grow on a protein (Matrigel)-decorated aqueous—LC interface in which TL205 was used as the LC (Figure 3-24A). Cell-driven reorganization of the Matrigel layer was observed over the course of a week, which allowed regions of the TL205 film to come into contact with the aqueous cell media. The LC at this interface adopted a homeotropic orientation, which was concluded to be a consequence of the adsorption of lipids present in the cell media solution onto the LC-media interface (see Figure 3-24).

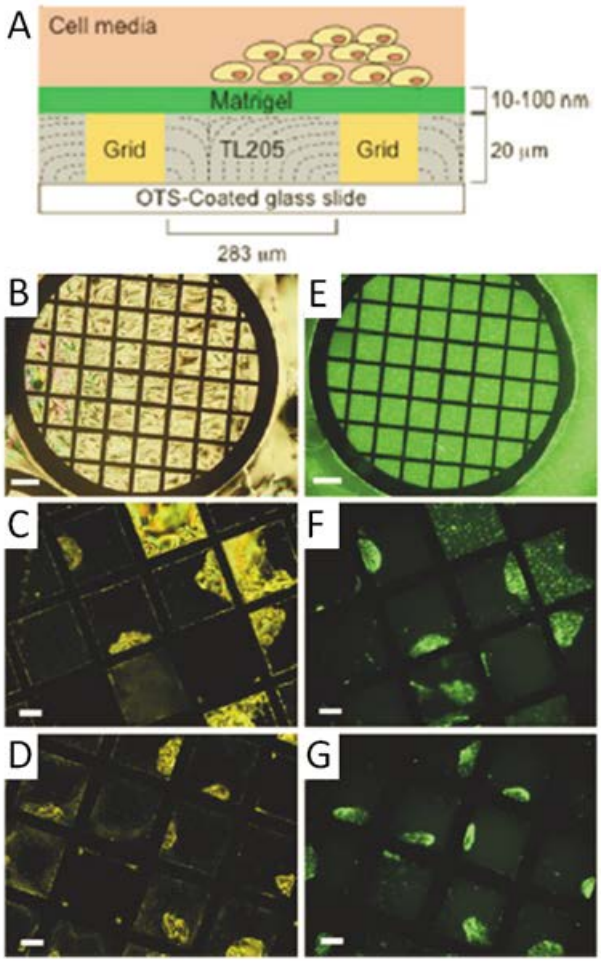

Figure 3-24. Growth of human embryonic stem cells (hESCs) on a Matrigel-decorated aqueous—LC interface.

(A) Schematic illustration of human embryonic stem cells (hESCs) cultured at the interface between aqueous phases and nematic TL205. (B-D) Polarized light and (E-G) epifluorescence images of hESCs before the seeding of cells (B, E), 3 days following seeding (C, F) and 7 days following seeding (D, G). The Matrigel was labelled with Alexa Fluor 430. Scale bars are 300 μm for (B, E); all others are 100 μm. Reproduced with permission.[163]

Agarwal *et al.*[164] found that cells such as fibroblasts, in contrast to hESCs, were unable to grow at the aqueous—LC interface (Figure 3-25A and 3-25B). This was attributed to the fact that fibroblasts require more rigid substrates for successful attachment and growth. The investigators

found that instead, a LC composite material, a colloid-in-LC (CLC) gel, could be successfully utilized as a substrate for fibroblast growth (Figure 3-25C and 3-25D). The LC domains within these CLC gels were shown to still be responsive to changes in surface anchoring, suggesting these gels could also potentially be exploited in the future for reporting biomolecular interactions with the LC.

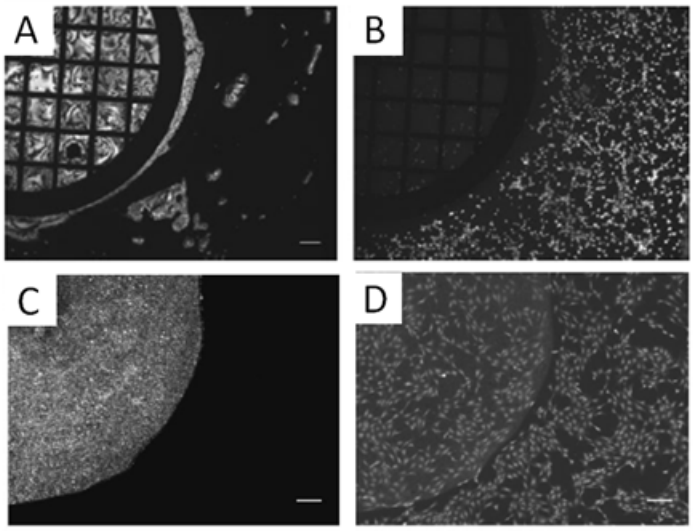

Figure 3-25. Growth of fibroblast cells on a colloid-in-LC gel.
Fibroblast cells seeded on both a TEM grid containing nematic phase E7 (A, B) and a colloid-in-LC gel formed with E7 (C, D) were stained with Calcein AM and imaged using polarized light (A, C) and epifluorescence (B, D). Cells were only able to grow on the CLC gel. Scale bar is 200 μm in (A) and 100 μm in (C, D). Reproduced with permission.[164]

In summary, LCs have been successfully used to sense and detect bacteria and viruses. Additionally, non-toxic LCs have been identified and utilized for supporting the growth of mammalian cells and for reporting interfacial cell-protein interactions. This research, when combined, shows that LCs are promising candidates for use in these biological contexts. A number of questions, however, remain to be addressed. For example, there exists a great

diversity of lipids within the membranes of bacteria, viruses, and cells. Tail length, multiplicity, and degree of unsaturation, in addition to lipid phase behavior, can all vary greatly amongst biological lipids. There remains an incomplete understanding of how all of these parameters impact the way in which these lipids organize at the LC interface and impact the ordering of the LC. Also, biological buffers and media are fairly complex and typically include salts, proteins and lipids; all of which may also influence the ordering of LC films. Thus, given this complex environment, the challenge is to design LC interfaces that respond solely to the biological targets of interest.

3.7 Conclusion

A range of examples presented in this chapter demonstrates that surface-induced ordering of LCs can be exploited in diverse contexts to create LC-based sensors of chemical and biological species. The fundamental challenge for sensing applications is that of understanding how the structure and organization of molecules at LC interfaces impacts the ordering of LCs. While this challenge has been addressed in the context of development of LC-based technologies for displays, the diversity and complexity of the interfaces that form the basis of chemical and biological sensors far exceeds that encountered in electrooptical devices such as LC displays. In some examples presented in this chapter, such as the use of LCs for chemical sensors, substantial progress has been made in understanding the molecular interactions responsible for the functioning of the sensor. For example, IR spectroscopic evidence supports the central role of metal ion-ligand coordination interactions in controlling the orientation of LCs in sensors for organophosphonate-based compounds (*e.g.*, nerve agents). However, in many of the other examples described in this chapter, our understanding of the molecular-level interactions

responsible for the functioning of the sensors remains to be fully developed. This is particularly true of LC-based sensors of biological molecules. For example, whereas LC-based methods for reporting proteins show substantial promise (*e.g.*, reporting antibody-antigen interactions), the underlying intermolecular interactions responsible for the changes measured in anchoring energies of LCs on protein-decorated surfaces have not been identified. The use of small fragments of proteins (oligopeptides) has, in recent studies, provided the basis of some useful insights (*e.g.*, role of chirality and hydrogen bonding), and additional studies in this direction will likely yield additional knowledge that will permit, in the long term, rational design of LC interfaces for biological sensing.

The examples of sensors described in this chapter also highlight the potential utility of interfaces formed between aqueous phases and thermotropic LCs for biological sensing. Although a great deal of past effort has been devoted to understanding the orientational ordering of LCs at the surfaces of solids, aqueous interfaces of LCs are fundamentally different from LC—solid interfaces in that they are soft and deformable interfaces, at which interfacial adsorbates exhibit high lateral mobility, and where the elasticity of the LC can drive the organization of adsorbates. In this respect, the LC is not a passive reporter of the presence of targeted analytes at its interface, but rather the LC participates in directing the formation of interfacial assemblies of relevance to biological sensing. As will be shown in the following chapter this fundamental phenomenon underlies the sensitivity and selectivity of the response of LC droplets (dispersed in water) to bacterial endotoxin.

Finally, we note that the diversity of configurations which LCs adopt when confined to micrometer-sized droplets and the influence of elastic stresses on the positions of colloids adsorbed at the surfaces of the droplets make LC-in-water emulsions promising templates for

synthesis of spherical or non-spherical microparticles with chemical surface patches. This scalable synthetic methodology represents a new frontier in the design of functional soft materials and will be studied from both a fundamental and applied standpoint in Chapters 9 through 11 of this thesis.

Acknowledgements:

This work was primarily supported by NSF through DMR-1121288 (Materials Research Science and Engineering Center), the Army Research Office (W911NF-11-1-0251 and W911NF-10-1-0181), and the National Institutes of Health (CA108467, CA105730, 5T32GM08349 and AI092004). Acknowledgment of support is also made to the Department of Energy, Basic Energy Sciences, Biomaterials Program (DESC0004025). NLA thanks Frank Caruso and Juan de Pablo for collaborations that enabled aspects of the work reported in this chapter. The authors would like to thank Rebecca J. Carlton and Emre Bukusoglu for discussions that were helpful in the writing of section 3.5 of this chapter.

3.8 References

*This chapter was originally prepared as two separate publications. The first was an invited review in the journal *Liquid Crystals Reviews*. My contribution to this review was in writing the section on LC-in-water emulsions as sensors and assisting my co-authors in the proof reading of the manuscript and preparation of some of the figures. The second publication was a perspective in the journal *Chemistry of Materials.* My contribution to this perspective was in writing the first four sections, guiding the preparation of sections written by my co-authors, proof reading the manuscript, and preparing everything for submission.

1. Fréedericksz, V.; Repiewa, A., Theoretisches und Experimentelles zur Frage nach der Natur der anisotropen Flüssigkeiten [Theoretical and Experimental Work on the Question of the Nature of Anisotropic Fluids]. *Zeitschrift für Physik A Hadrons and Nuclei* **1927**, 42, 532-546. German.
2. Fréedericksz, V.; Zolina, V., Forces Causing the Orientation of an Anisotropic Liquid. *Transactions of the Faraday Society* **1933**, 29, 919-930.
3. Kawamoto, H., The History of Liquid-Crystal Displays. *Proceedings of the IEEE* **2002**, 90, 460-500.
4. Gray, G. W.; Kelly, S. M., Liquid Crystals for Twisted Nematic Display Devices. *Journal of Materials Chemistry* **1999**, 9, 2037-2050.
5. Schadt, M., Liquid Crystal Materials and Liquid Crystal Displays. *Annual Review of Materials Science* **1997**, 27, 305-379.
6. Goodby, J. W., The Nanoscale Engineering of Nematic Liquid Crystals for Displays. *Liquid Crystals* **2011**, 38, 1363-1387.
7. Clark, M. G.; Harrison, K. J.; Raynes, E. P., Liquid-Crystal Materials and Devices. *Physics in Technology* **1980**, 11, 232-240.

8. Ohm, C.; Brehmer, M.; Zentel, R., Liquid Crystalline Elastomers as Actuators and Sensors. *Adv. Mater.* **2010**, 22, 3366-3387.
9. Marcos, C.; Pena, J. M. S.; Torres, J. C.; Santos, J. I., Temperature-Frequency Converter using a Liquid Crystal Cell as a Sensing Element. *Sensors* **2012**, 12, 3204-3214.
10. Herzer, N.; Guneysu, H.; Davies, D. J. D.; Yildirim, D.; Vaccaro, A. R.; Broer, D. J.; Bastiaansen, C. W. M.; Schenning, A., Printable Optical Sensors Based on H-Bonded Supramolecular Cholesteric Liquid Crystal Networks. *Journal of the American Chemical Society* **2012**, 134, 7608-7611.
11. Chatterjee, S.; Anna, S. L., Formation and Ordering of Topological Defect Arrays Produced by Dilatational Strain and Shear Flow in Smectic-A Liquid Crystals. *Physical Review E* **2012**, 85, 011701.
12. Chanishvili, A.; Chilaya, G.; Petriashvili, G.; Barberi, R.; Bartolino, R.; De Santo, M. P., Cholesteric Liquid Crystal Mixtures Sensitive to Different Ranges of Solar UV Irradiation. *Molecular Crystals and Liquid Crystals* **2005**, 434, 353-366.
13. Wang, Y.; Li, Q., Light-Driven Chiral Molecular Switches or Motors in Liquid Crystals. *Advanced Materials* **2012**, 24, 1926-1945.
14. Sutarlie, L.; Yang, K. L., Monitoring Spatial Distribution of Ethanol in Microfluidic Channels by Using a Thin Layer of Cholesteric Liquid Crystal. *Lab on a Chip* **2011**, 11, 4093-4098.
15. Saha, A.; Tanaka, Y.; Han, Y.; Bastiaansen, C. M. W.; Broer, D. J.; Sijbesma, R. P., Irreversible Visual Sensing of Humidity using a Cholesteric Liquid Crystal. *Chemical Communications* **2012**, 48, 4579-4581.
16. Winterbottom, D. A.; Narayanaswamy, R.; Raimundo, I. M., Cholesteric Liquid Crystals for Detection of Organic Vapours. *Sensors and Actuators, B: Chemical* **2003**, 90, 52-57.
17. Dickert, F. L.; Haunschild, A.; Hofmann, P., Cholesteric Liquid Crystals for Solvent Vapour Detection — Elimination of Cross Sensitivity by Band Shape Analysis and Pattern Recognition. *Fresenius' Journal of Analytical Chemistry* **1994**, 350, 577-581.
18. Poziomek, E. J.; Novak, T. J.; Mackay, R. A., Use of Liquid Crystals as Vapor Detectors. *Molecular Crystals and Liquid Crystals* **1974**, 27, 175-185.
19. Kirchner, N.; Zedler, L.; Mayerhofer, T. G.; Mohr, G. J., Functional Liquid Crystal Films Selectively Recognize Amine Vapours and Simultaneously Change their Colour. *Chemical Communications* **2006**, (14), 1512-1514.
20. Sutarlie, L.; Qin, H.; Yang, K. L., Polymer Stabilized Cholesteric Liquid Crystal Arrays for Detecting Vaporous Amines. *Analyst* **2010**, 135, 1691-1696.
21. Carlton, R. J.; Gupta, J. K.; Swift, C. L.; Abbott, N. L., Influence of Simple Electrolytes on the Orientational Ordering of Thermotropic Liquid Crystals at Aqueous Interfaces. *Langmuir* **2012**, 28, 31-36.
22. Shah, R. R.; Abbott, N. L., Coupling of the Orientations of Liquid Crystals to Electrical Double Layers Formed by the Dissociation of Surface-Immobilized Salts. *Journal of Physical Chemistry B* **2001**, 105, 4936-4950.
23. Liu, Y.; Cheng, D.; Lin, I.-H.; Abbott, N. L.; Jiang, H., Microfluidic Sensing Devices Employing in situ-Formed Liquid Crystal Thin Film for Detection of Biochemical Interactions. *Lab on a Chip* **2012**, 12, 3746-3753.
24. Mondiot, F.; Wang, X.; de Pablo, J. J.; Abbott, N. L., Liquid Crystal-Based Emulsions for Synthesis of Spherical and Non-Spherical Particles with Chemical Patches. *Journal of the American Chemical Society* **2013**, 135, 9972-9975.

25. Stewart, C. E., *Weapons of Mass Casualties and Terrorism Response Handbook*. Jones & Bartlett Learning: Sudbury, MA, USA, 2006.
26. Cantalini, C.; Valentini, L.; Armentano, I.; Lozzi, L.; Kenny, J. M.; Santucci, S., Sensitivity to NO_2 and Cross-Sensitivity Analysis to NH_3, Ethanol and Humidity of Carbon Nanotubes Thin Film Prepared by PECVD. *Sensors and Actuators, B: Chemical* **2003**, 95, 195-202.
27. Shah, R. R.; Abbott, N. L., Principles for Measurement of Chemical Exposure Based on Recognition-Driven Anchoring Transitions in Liquid Crystals. *Science* **2001**, 293, 1296-1299.
28. Yang, K. L.; Cadwell, K.; Abbott, N. L., Mechanistic Study of the Anchoring Behavior of Liquid Crystals Supported on Metal Salts and their Orientational Responses to Dimethyl Methylphosphonate. *Journal of Physical Chemistry B* **2004**, 108, 20180-20186.
29. Yang, K. L.; Cadwell, K.; Abbott, N. L., Use of Self-Assembled Monolayers, Metal Ions and Smectic Liquid Crystals to Detect Organophosphonates. *Sensors and Actuators, B: Chemical* **2005**, 104, 50-56.
30. Wang, P. H.; Yu, J. H.; Zhao, Y. B.; Li, Z. J.; Li, G. Q., A Novel Liquid Crystal-Based Sensor for the Real-Time Identification of Organophosphonate Vapors. *Sensors and Actuators, B: Chemical* **2011**, 160, 929-935.
31. Cadwell, K. D.; Lockwood, N. A.; Nellis, B. A.; Alf, M. E.; Willis, C. R.; Abbott, N. L., Detection of Organophosphorous Nerve Agents Using Liquid Crystals Supported on Chemically Functionalized Surfaces. *Sensors and Actuators, B: Chemical* **2007**, 128, 91-98.
32. Shah, R. R.; Abbott, N. L., Orientational Transitions of Liquid Crystals Driven by Binding of Organoamines to Carboxylic Acids Presented at Surfaces with Nanometer-Scale Topography. *Langmuir* **2003**, 19, 275-284.
33. Bi, X.; Yang, K. L., Real-Time Liquid Crystal-Based Glutaraldehyde Sensor. *Sensors and Actuators, B: Chemical* **2008**, 134, 432-437.
34. Xu, H.; Bi, X.; Ngo, X.; Yang, K.-L., Principles of Detecting Vaporous Thiols Using Liquid Crystals and Metal Ion Microarrays. *Analyst* **2009**, 134, 911-915.
35. Cadwell, K. D.; Alf, M. E.; Abbott, N. L., Infrared Spectroscopy of Competitive Interactions between Liquid Crystals, Metal Salts, and Dimethyl Methylphosphonate at Surfaces. *Journal of Physical Chemistry B* **2006**, 110, 26081-26088.
36. Pal, S. K.; Acevedo-Vélez, C.; Hunter, J. T.; Abbott, N. L., Effects of Divalent Ligand Interactions on Surface-Induced Ordering of Liquid Crystals. *Chemistry of Materials* **2010**, 22, 5474-5482.
37. Bungabong, M. L.; Ong, P. B.; Yang, K. L., Using Copper Perchlorate Doped Liquid Crystals for the Detection of Organophosphonate Vapor. *Sensors and Actuators, B: Chemical* **2010**, 148, 420-426.
38. Luk, Y. Y.; Yang, K. L.; Cadwell, K.; Abbott, N. L., Deciphering the Interactions between Liquid Crystals and Chemically Functionalized Surfaces: Role of Hydrogen Bonding on Orientations of Liquid Crystals. *Surface Science* **2004**, 570, 43-56.
39. Govindaraju, T.; Bertics, P. J.; Raines, R. T.; Abbott, N. L., Using Measurements of Anchoring Energies of Liquid Crystals on Surfaces to Quantify Proteins Captured by Immobilized Ligands. *Journal of the American Chemical Society* **2007**, 129, 11223–11231.
40. Gupta, V. K.; Skaife, J. J.; Dubrovsky, T. B.; Abbott, N. L., Optical Amplification of Ligand-Receptor Binding using Liquid Crystals. *Science* **1998**, 279, 2077-2080.
41. Malone, S. M.; Schwartz, D. K., Macroscopic Liquid Crystal Response to Isolated DNA Helices. *Langmuir* **2011**, 27, 11767-11772.

42. Bai, Y. Q.; Abbott, N. L., Enantiomeric Interactions Between Liquid Crystals and Organized Monolayers of Tyrosine-Containing Dipeptides. *Journal of the American Chemical Society* **2012**, 134, 548-558.
43. Jang, C. H.; Tingey, M. L.; Korpi, N. L.; Wiepz, G. J.; Schiller, J. H.; Bertics, P. J.; Abbott, N. L., Using Liquid Crystals to Report Membrane Proteins Captured by Affinity Microcontact Printing from Cell Lysates and Membrane Extracts. *Journal of the American Chemical Society* **2005**, 127, 8912-8913.
44. Skaife, J. J.; Abbott, N. L., Quantitative Interpretation of the Optical Textures of Liquid Crystals Caused by Specific Binding of Immunoglobulins to Surface-Bound Antigens. *Langmuir* **2000**, 16, 3529-3536.
45. Skaife, J. J.; Abbott, N. L., Influence of Molecular-Level Interactions on the Orientations of Liquid Crystals Supported on Nanostructured Surfaces Presenting Specifically Bound Proteins. *Langmuir* **2001**, 17, 5595-5604.
46. Luk, Y. Y.; Tingey, M. L.; Dickson, K. A.; Raines, R. T.; Abbott, N. L., Imaging the Binding Ability of Proteins Immobilized on Surfaces with Different Orientations by Using Liquid Crystals. *Journal of the American Chemical Society* **2004**, 126, 9024-9032.
47. Clare, B. H.; Abbott, N. L., Orientations of Nematic Liquid Crystals on Surfaces Presenting Controlled Densities of Peptides: Amplification of Protein-Peptide Binding Events. *Langmuir* **2005**, 21, 6451-6461.
48. Lowe, A. M.; Ozer, B. H.; Bai, Y. Q.; Bertics, P. J.; Abbott, N. L., Design of Surfaces for Liquid Crystal-Based Bioanalytical Assays. *ACS Applied Materials & Interfaces* **2010**, 2, 722-731.
49. Lowe, A. M.; Bertics, P. J.; Abbott, N. L., Quantitative Methods Based on Twisted Nematic Liquid Crystals for Mapping Surfaces Patterned with Bio/Chemical Functionality Relevant to Bioanalytical Assays. *Analytical Chemistry* **2008**, 80, 2637-2645.
50. Tingey, M. L.; Snodgrass, E. J.; Abbott, N. L., Patterned Orientations of Liquid Crystals on Affinity Microcontact Printed Proteins. *Advanced Materials* **2004**, 16, 1331-1336.
51. Clare, B. H.; Guzman, O.; de Pablo, J.; Abbott, N. L., Anchoring Energies of Liquid Crystals Measured on Surfaces Presenting Oligopeptides. *Langmuir* **2006**, 22, 7776-7782.
52. Nakata, M.; Zanchetta, G.; Buscaglia, M.; Bellini, T.; Clark, N. A., Liquid Crystal Alignment on a Chiral Surface: Interfacial Interaction with Sheared DNA Films. *Langmuir* **2008**, 24, 10390-10394.
53. Chen, C. H.; Yang, K. L., Detection and Quantification of DNA Adsorbed on Solid Surfaces by using Liquid Crystals. *Langmuir* **2010**, 26, 1427-1430.
54. Lai, S. L.; Tan, W. L.; Yang, K. L., Detection of DNA Targets Hybridized to Solid Surfaces Using Optical Images of Liquid Crystals. *ACS Applied Materials & Interfaces* **2011**, 3, 3389-3395.
55. Brake, J. M.; Abbott, N. L., An Experimental System for Imaging the Reversible Adsorption of Amphiphiles at Aqueous-Liquid Crystal Interfaces. *Langmuir* **2002**, 18, 6101-6109.
56. Lockwood, N. A.; Gupta, J. K.; Abbott, N. L., Self-Assembly of Amphiphiles, Polymers and Proteins at Interfaces between Thermotropic Liquid Crystals and Aqueous Phases. *Surface Science Reports* **2008**, 63, 255-293.
57. Hiltrop, K.; Stegemeyer, H., Alignment of Liquid-Crystals by Amphiphilic Monolayers. *Berichte der Bunsengesellschaft f˙ur Physikalische Chemie* **1978**, 82, 884-889.

58. Brake, J. M.; Daschner, M. K.; Luk, Y. Y.; Abbott, N. L., Biomolecular Interactions at Phospholipid-Decorated Surfaces of Liquid Crystals. *Science* **2003**, 302, 2094-2097.
59. Brake, J. M.; Abbott, N. L., Coupling of the Orientations of Thermotropic Liquid Crystals to Protein Binding Events at Lipid-Decorated Interfaces. *Langmuir* **2007**, 23, 8497-8507.
60. Hartono, D.; Lai, S. L.; Yang, K. L.; Yung, L. Y. L., A Liquid Crystal-Based Sensor for Real-Time and Label-Free Identification of Phospholipase-Like Toxins and their Inhibitors. *Biosensors & Bioelectronics* **2009**, 24, 2289-2293.
61. De Tercero, M. D.; Abbott, N. L., Ordering Transitions in Liquid Crystals Permit Imaging of Spatial and Temporal Patterns Formed by Proteins Penetrating into Lipid-Laden Interfaces. *Chemical Engineering Communications* **2008**, 196, 234-251.
62. Hartono, D.; Qin, W. J.; Yang, K. L.; Yung, L. Y. L., Imaging the Disruption of Phospholipid Monolayer by Protein-Coated Nanoparticles using Ordering Transitions of Liquid Crystals. *Biomaterials* **2009**, 30, 843-849.
63. Hu, Q. Z.; Jang, C. H., Using Liquid Crystals to Report Molecular Interactions between Cationic Antimicrobial Peptides and Lipid Membranes. *Analyst* **2012**, 137, 567-570.
64. Tan, L. N.; Orler, V. J.; Abbott, N. L., Ordering Transitions Triggered by Specific Binding of Vesicles to Protein-Decorated Interfaces of Thermotropic Liquid Crystals. *Langmuir* **2012**, 28, 6364-6376.
65. Park, J. S.; Abbott, N. L., Ordering Transitions in Thermotropic Liquid Crystals Induced by the Interfacial Assembly and Enzymatic Processing of Oligopeptide Amphiphiles. *Advanced Materials* **2008**, 20, 1185-1190.
66. Hu, Q. Z.; Jang, C. H., Liquid Crystal-Based Imaging of Enzymatic Reactions at Aqueous-Liquid Crystal Interfaces Decorated with Oligopeptide Amphiphiles. *Bulletin of the Korean Chemical Society* **2010**, 31, 1262-1266.
67. Price, A. D.; Schwartz, D. K., DNA Hybridization-Induced Reorientation of Liquid Crystal Anchoring at the Nematic Liquid Crystal/Aqueous Interface. *Journal of the American Chemical Society* **2008**, 130, 8188-8194.
68. Yang, Z.; Gupta, J. K.; Kishimoto, K.; Shoji, Y.; Kato, T.; Abbott, N. L., Design of Biomolecular Interfaces Using Liquid Crystals Containing Oligomeric Ethylene Glycol. *Advanced Functional Materials* **2010**, 20, 2098-2106.
69. McUmber, A. C.; Noonan, P. S.; Schwartz, D. K., Surfactant-DNA Interactions at the Liquid Crystal-Aqueous Interface. *Soft Matter* **2012**, 8, 4335-4342.
70. Lai, S. L.; Hartono, D.; Yang, K. L., Self-Assembly of Cholesterol DNA at Liquid Crystal/Aqueous Interface and its Application for DNA Detection. *Applied Physics Letters* **2009**, 95, 153702.
71. Park, J. S.; Teren, S.; Tepp, W. H.; Beebe, D. J.; Johnson, E. A.; Abbott, N. L., Formation of Oligopeptide-Based Polymeric Membranes at Interfaces between Aqueous Phases and Thermotropic Liquid Crystals. *Chemistry of Materials* **2006**, 18, 6147-6151.
72. Seo, J. M.; Khan, W.; Park, S. Y., Protein Detection using Aqueous/LC Interfaces Decorated with a Novel Polyacrylic Acid Block Liquid Crystalline Polymer. *Soft Matter* **2012**, 8, 198-203.
73. Bi, X.; Hartono, D.; Yang, K. L., Real Time Liquid Crystal pH Sensor for Monitoring Enzymatic Activities of Penicillinase. *Advanced Functional Materials* **2009**, 19, 3760-3765.
74. Hu, Q. Z.; Jang, C. H., Using Liquid Crystals for the Label-Free Detection of Catalase at Aqueous-LC Interfaces. *Journal of Biotechnology* **2012**, 157, 223-227.

75. Hu, Q. Z.; Jang, C. H., Using Liquid Crystals for the Real-Time Detection of Urease at Aqueous/Liquid Crystal Interfaces. *Journal of Materials Science* **2012**, 47, 969-975.
76. Gupta, J. K.; Zimmerman, J. S.; de Pablo, J. J.; Caruso, F.; Abbott, N. L., Characterization of Adsorbate-Induced Ordering Transitions of Liquid Crystals within Monodisperse Droplets. *Langmuir* **2009**, 25, 9016-9024.
77. Gupta, J. K.; Sivakumar, S.; Caruso, F.; Abbott, N. L., Size-Dependent Ordering of Liquid Crystals Observed in Polymeric Capsules with Micrometer and Smaller Diameter. *Angewandte Chemie, International Edition* **2009**, 48, 1652-1655.
78. Tjipto, E.; Cadwell, K. D.; Quinn, J. F.; Johnston, A. P. R.; Abbott, N. L.; Caruso, F., Tailoring the Interfaces between Nematic Liquid Crystal Emulsions and Aqueous Phases via Layer-by-Layer Assembly. *Nano Letters* **2006**, 6, 2243-2248.
79. Prischepa, O. O.; Shabanov, A. V.; Zyryanov, V. Y., Transformation of Director Configuration upon Changing Boundary Conditions in Droplets of Nematic Liquid Crystal. *JETP Letters* **2004**, 79, 257-261.
80. Volovik, G. E.; Lavrentovich, O. D., The Topological Dynamics of Defects - Boojums in Nematic Drops. *Zhurnal Eksperimental'noi i Teoreticheskoi Fiziki* **1983**, 85, 1997-2010.
81. Lin, I. H.; Miller, D. S.; Bertics, P. J.; Murphy, C. J.; de Pablo, J. J.; Abbott, N. L., Endotoxin-Induced Structural Transformations in Liquid Crystalline Droplets. *Science* **2011**, 332, 1297-1300.
82. Bera, T.; Fang, J. Y., Polyelectrolyte-Coated Liquid Crystal Droplets for Detecting Charged Macromolecules. *Journal of Materials Chemistry* **2012**, 22, 6807-6812.
83. Sivakumar, S.; Wark, K. L.; Gupta, J. K.; Abbott, N. L.; Caruso, F., Liquid Crystal Emulsions as the Basis of Biological Sensors for the Optical Detection of Bacteria and Viruses. *Advanced Functional Materials* **2009**, 19, 2260-2265.
84. Alino, V. J.; Pang, J.; Yang, K. L., Liquid Crystal Droplets as a Hosting and Sensing Platform for Developing Immunoassays. *Langmuir* **2011**, 27, 11784-11789.
85. Kinsinger, M. I.; Buck, M. E.; Abbott, N. L.; Lynn, D. M., Immobilization of Polymer-Decorated Liquid Crystal Droplets on Chemically Tailored Surfaces. *Langmuir* **2010**, 26, 10234-10242.
86. Zou, J. H.; Fang, J. Y., Director Configuration of Liquid-Crystal Droplets Encapsulated by Polyelectrolytes. *Langmuir* **2010**, 26, 7025-7028.
87. Khan, W.; Choi, J. H.; Kim, G. M.; Park, S. Y., Microfluidic Formation of pH Responsive 5CB Droplets Decorated with PAA-b-LCP. *Lab on a Chip* **2011**, 11, 3493-3498.
88. Craighead, H.; Cheng, J.; Hackwood, S., New Display Based on Electrically Induced Index-Matching in an Inhomogeneous Medium. *Applied Physics Letters* **1982**, 40, 22-24.
89. Drzaic, P. S., *Liquid Crystal Dispersions*. World Scientific: River Edge, NJ, USA, 1995.
90. Fergason, J. L. In *Polymer Encapsulated Nematic Liquid Crystals for Display and Light Control Applications*, Digest of Technical Papers - Society for Information Display International Symposium, 1985; 1985; pp 268-270.
91. Rapini, A.; Papoular, M., Distortion d'une Lamelle Nematique sous Champ Magnetique Conditions d'Ancrage aux Parois. *Journal de Physique Colloques* **1969**, 30, C4-54-C4-56.
92. Lavrentovich, O. D., Topological Defects in Dispersed Liquid Crystals, or Words and Worlds Around Liquid Crystal Drops. *Liquid Crystals* **1998**, 24, 117-125.
93. Hiemenz, P. C.; Rajagopalan, R., *Principles of Colloid and Surface Chemistry*. 3rd ed.; Marcel Dekker: New York, NY, USA, 1997.

94. Israelachvili, J. N., *Intermolecular and Surface Forces*. 2nd ed.; Academic Press London: San Diego, CA, USA, 1991.
95. Kléman, M.; Lavrentovich, O. D., *Soft Matter Physics : An Introduction*. Springer: New York, NY, USA, 2003.
96. Napoli, G.; Vergori, L., Extrinsic Curvature Effects on Nematic Shells. *Physical Review Letters* **2012**, 108, 207803-1-207803-5.
97. Prinsen, P.; van der Schoot, P., Shape and Director-Field Transformation of Tactoids. *Physical Review E* **2003**, 68, 021701-1-021701-11.
98. Frank, F. C., I. Liquid Crystals. On the Theory of Liquid Crystals. *Discussions of the Faraday Society* **1958**, 25, 19-28.
99. Zumer, S.; Kralj, S., Influence of K_{24} on the Structure of Nematic Liquid-Crystal Droplets. *Liquid Crystals* **1992**, 12, 613-624.
100. Gennes, P.-G. d.; Prost, J., *The Physics of Liquid Crystals*. 2nd ed.; Clarendon Press ; Oxford University Press: New York, NY, USA, 1993.
101. Allender, D. W.; Crawford, G. P.; Doane, J. W., Determination of the Liquid-Crystal Surface Elastic-Constant K_{24}. *Physical Review Letters* **1991**, 67, 1442-1445.
102. Goyal, R. K.; Denn, M. M., Orientational Multiplicity and Transitions in Liquid Crystalline Droplets. *Physical Review E* **2007**, 75, 021704-1-021704-10.
103. Erdmann, J. H.; Zumer, S.; Doane, J. W., Configuration Transition in a Nematic Liquid-Crystal Confined to a Small Spherical Cavity. *Physical Review Letters* **1990**, 64, 1907-1910.
104. Kralj, S.; Zumer, S., Freedericksz Transitions in Supra-μm Nematic Droplets. *Physical Review A* **1992**, 45, 2461-2470.
105. Ruhwandl, R. W.; Terentjev, E. M., Monte Carlo Simulation of Topological Defects in the Nematic Liquid Crystal Matrix around a Spherical Colloid Particle. *Physical Review E* **1997**, 56, 5561-5565.
106. Zhang, Z. X.; van Duijneveldt, J. S., Effect of Suspended Clay Particles on Isotropic-Nematic Phase Transition of Liquid Crystal. *Soft Matter* **2007**, 3, 596-604.
107. Miller, D. S.; Carlton, R. J.; Mushenheim, P. C.; Abbott, N. L., Introduction to Optical Methods for Characterizing Liquid Crystals at Interfaces. *Langmuir* **2013**, 29, 3154−3169.
108. Miller, D. S.; Abbott, N. L., Influence of Droplet Size, pH and Ionic Strength on Endotoxin-Triggered Ordering Transitions in Liquid Crystalline Droplets. *Soft Matter* **2013**, 9, 374-382.
109. Tixier, T.; Heppenstall-Butler, M.; Terentjev, E. M., Spontaneous Size Selection in Cholesteric and Nematic Emulsions. *Langmuir* **2006**, 22, 2365-2370.
110. Sivakumar, S.; Gupta, J. K.; Abbott, N. L.; Caruso, F., Monodisperse Emulsions through Templating Polyelectrolyte Multilayer Capsules. *Chemistry of Materials* **2008**, 20, 2063-2065.
111. Bodnar, V. G.; Lavrentovich, O. D.; Pergamenshchik, V. M., The Threshold for the Hedgehog - Ring Structural Transition in Nematic Drops in an Alternating Electric-Field. *Zhurnal Eksperimentalnoi I Teoreticheskoi Fiziki* **1992**, 101, 111-125.
112. Bibette, J., Depletion Interactions and Fractionated Crystallization for Polydisperse Emulsion Purification. *Journal of Colloid and Interface Science* **1991**, 147, 474-478.
113. Hsu, P.; Poulin, P.; Weitz, D. A., Rotational Diffusion of Monodisperse Liquid Crystal Droplets. *Journal of Colloid and Interface Science* **1998**, 200, 182-184.
114. Fernandez-Nieves, A.; Cristobal, G.; Garces-Chavez, V.; Spalding, G. C.; Dholakia, K.; Weitz, D. A., Optically Anisotropic Colloids of Controllable Shape. *Advanced Materials* **2005**, 17, 680-684.

115. Sandomirski, K.; Martin, S.; Maret, G.; Stark, H.; Gisler, T., Highly Birefringent Colloidal Particles for Tracer Studies. *Journal of Physics: Condensed Matter* **2004**, 16, S4137-S4144.
116. Vennes, M.; Martin, S.; Gisler, T.; Zentel, R., Anisotropic Particles from LC Polymers for Optical Manipulation. *Macromolecules* **2006**, 39, 8326-8333.
117. Vennes, M.; Zentel, R., Liquid-Crystalline Colloidal Particles. *Macromolecular Chemistry and Physics* **2004**, 205, 2303-2311.
118. Gartland, E. C.; Mkaddem, S., Instability of Radial Hedgehog Configurations in Nematic Liquid Crystals under Landau-de Gennes Free-Energy Models. *Physical Review E* **1999**, 59, 563-567.
119. Mkaddem, S.; Gartland, E. C., Fine Structure of Defects in Radial Nematic Droplets. *Physical Review E* **2000**, 62, 6694-6705.
120. Lavrentovich, O. D.; Terentiev, E. M., Phase-Transition with the Change of Symmetry of Topological Point-Defects (Hedgehogs) in a Nematic Liquid-Crystal. *Zhurnal Eksperimentalnoi I Teoreticheskoi Fiziki* **1986**, 91, 2084-2096.
121. Prishchepa, O. O.; Zyryanov, V. Y.; Gardymova, A. P.; Shabanov, V. F., Optical Textures and Orientational Structures of Nematic and Cholesteric Droplets with Heterogeneous Boundary Conditions. *Molecular Crystals and Liquid Crystals* **2008**, 489, 84-93.
122. Dubois-Violette, E.; Parodi, E., Emulsions Nematiques. Effects de Champ Magnetiques et Effects Piezoelectriques. *Journal de Physique, Colloque* **1969**, 30, 57-64.
123. Ericksen, J. L., Inequalities in Liquid Crystal Theory. *Physics of Fluids* **1966**, 9, 1205-1207.
124. Polak, R. D.; Crawford, G. P.; Kostival, B. C.; Doane, J. W.; Zumer, S., Optical Determination of the Saddle-Splay Elastic-Constant K_{24} in Nematic Liquid-Crystals. *Physical Review E* **1994**, 49, R978-R981.
125. Tomar, V.; Hernandez, S. I.; Abbott, N. L.; Hernandez-Ortiz, J. P.; de Pablo, J. J., Morphological Transitions in Liquid Crystal Nanodroplets. *Soft Matter* **2012**, 8, 8679-8689.
126. Carlton, R. J.; Hunter, J. T.; Miller, D. S.; Abbasi, R.; Mushenheim, P. C.; Tan, L.; Abbott, N. L., Chemical and Biological Sensing Using Liquid Crystals. *Liquid Crystal Reviews* **2013**, 1, 1-23.
127. Bai, Y.; Abbott, N. L., Recent Advances in Colloidal and Interfacial Phenomena Involving Liquid Crystals. *Langmuir* **2011**, 27, 5719-5738.
128. Lowe, A. M.; Abbott, N. L., Liquid Crystalline Materials for Biological Applications. *Chemistry of Materials* **2012**, 24, 746-758.
129. Brake, J. M.; Daschner, M. K.; Abbott, N. L., Formation and Characterization of Phospholipid Monolayers Spontaneously Assembled at Interfaces Between Aqueous Phases and Thermotropic Liquid Crystals. *Langmuir* **2005**, 21, 2218-2228.
130. Meli, M. V.; Lin, I. H.; Abbott, N. L., Preparation of Microscopic and Planar Oil-Water Interfaces that are Decorated with Prescribed Densities of Insoluble Amphiphiles. *Journal of the American Chemical Society* **2008**, 130, 4326-4333.
131. Alino, V. J.; Sim, P. H.; Choy, W. T.; Fraser, A.; Yang, K. L., Detecting Proteins in Microfluidic Channels Decorated with Liquid Crystal Sensing Dots. *Langmuir* **2012**, 28, 17571-17577.
132. Alino, V. J.; Tay, K. X.; Khan, S. A.; Yang, K. L., Inkjet Printing and Release of Monodisperse Liquid Crystal Droplets from Solid Surfaces. *Langmuir* **2012**, 28, 14540-14546.

133. Bera, T.; Fang, J. Y., Optical Detection of Lithocholic Acid with Liquid Crystal Emulsions. *Langmuir* **2013**, 29, 387-392.
134. Zou, J. H.; Bera, T.; Davis, A. A.; Liang, W. L.; Fang, J. Y., Director Configuration Transitions of Polyelectrolyte Coated Liquid-Crystal Droplets. *Journal of Physical Chemistry B* **2011**, 115, 8970-8974.
135. Muro, S.; Garnacho, C.; Champion, J. A.; Leferovich, J.; Gajewski, C.; Schuchman, E. H.; Mitragotri, S.; Muzykantov, V. R., Control of Endothelial Targeting and Intracellular Delivery of Therapeutic Enzymes by Modulating the Size and Shape of ICAM-1-Targeted Carriers. *Molecular Therapy* **2008**, 16, 1450-1458.
136. Botto, L.; Lewandowski, E. P.; Cavallaro, M.; Stebe, K. J., Capillary Interactions between Anisotropic Particles. *Soft Matter* **2012**, 8, 9957-9971.
137. Lapointe, C. P.; Mason, T. G.; Smalyukh, I. I., Shape-Controlled Colloidal Interactions in Nematic Liquid Crystals. *Science* **2009**, 326, 1083-1086.
138. Loudet, J.-C.; Alsayed, A. M.; Zhang, J.; Yodh, A. G., Capillary Interactions between Anisotropic Colloidal Particles. *Physical Review Letters* **2005**, 94, 018301-1-018301-4.
139. Mondiot, F.; Chandran, S. P.; Mondain-Monval, O.; Loudet, J. C., Shape-Induced Dispersion of Colloids in Anisotropic Fluids. *Physical Review Letters* **2009**, 103, 238303-1-238303-4.
140. Yao, L.; Botto, L.; Cavallaro, M.; Bleier, B. J.; Garbin, V.; Stebe, K. J., Near Field Capillary Repulsion. *Soft Matter* **2013**, 9, 779-786.
141. Madivala, B.; Vandebril, S.; Fransaer, J.; Vermant, J., Exploiting Particle Shape in Solid Stabilized Emulsions. *Soft Matter* **2009**, 5, 1717-1727.
142. Han, Y.; Alsayed, A. M.; Nobili, M.; Zhang, J.; Lubensky, T. C.; Yodh, A. G., Brownian Motion of an Ellipsoid. *Science* **2006**, 314, 626-630.
143. Costi, R.; Saunders, A. E.; Banin, U., Colloidal Hybrid Nanostructures: A New Type of Functional Materials. *Angewandte Chemie, International Edition* **2010**, 49, 4878-4897.
144. Glotzer, S. C.; Solomon, M. J., Anisotropy of Building Blocks and Their Assembly into Complex Structures. *Nature Materials* **2007**, 6, 557-562.
145. Duguet, E.; Desert, A.; Perro, A.; Ravaine, S., Design and Elaboration of Colloidal Molecules: An Overview. *Chemical Society Reviews* **2011**, 40, 941-960.
146. Fleury, J. B.; Pires, D.; Galerne, Y., Self-Connected 3D Architecture of Microwires. *Physical Review Letters* **2009**, 103, 267801-1-267801-4.
147. Pires, D.; Fleury, J. B.; Galerne, Y., Colloid Particles in the Interaction Field of a Disclination Line in a Nematic Phase. *Physical Review Letters* **2007**, 98, 247801-1-247801-4.
148. Ravnik, M.; Alexander, G. P.; Yeomans, J. M.; Zumer, S., Mesoscopic Modelling of Colloids in Chiral Nematics. *Faraday Discussions* **2010**, 144, 159-169.
149. Skarabot, M.; Ravnik, M.; Zumer, S.; Tkalec, U.; Poberaj, I.; Babic, D.; Musevic, I., Hierarchical Self-Assembly of Nematic Colloidal Superstructures. *Physical Review E* **2008**, 77, 061706-1-061706-4.
150. Berggren, E.; Zannoni, C.; Chiccoli, C.; Pasini, P.; Semeria, F., Computer-Simulations of Nematic Droplets with Bipolar Boundary-Conditions. *Physical Review E* **1994**, 50, 2929-2939.
151. Meyer, R. B., Piezoelectric Effects in Liquid Crystals. *Physical Review Letters* **1969**, 22, 918-921.
152. Ondris-Crawford, R.; Boyko, E. P.; Wagner, B. G.; Erdmann, J. H.; Zumer, S.; Doane, J. W., Microscope Textures of Nematic Droplets in Polymer Dispersed Liquid-Crystals. *Journal of Applied Physics* **1991**, 69, 6380-6386.

153. Crawford, G. P.; Polak, R. D.; Scharkowski, A.; Chien, L. C.; Doane, J. W.; Zumer, S., Nematic Director-Fields Captured in Polymer Networks Confined to Spherical Droplets. *Journal of Applied Physics* **1994**, 75, 1968-1971.
154. Fernandez-Nieves, A., Engineering Colloids with Optical and Geometrical Anisotropies: De-Coupling Size Monodispersity and Particle Properties. *Soft Matter* **2006**, 2, 105-108.
155. Espinoza, L. A. T.; Schumann, K. R.; Luk, Y. Y.; Israel, B. A.; Abbott, N. L., Orientational Behavior of Thermotropic Liquid Crystals on Surfaces Presenting Electrostatically Bound Vesicular Stomatitis Virus. *Langmuir* **2004**, 20, 2375-2385.
156. Jang, C. H.; Cheng, L. L.; Olsen, C. W.; Abbott, N. L., Anchoring of Nematic Liquid Crystals on Viruses with Different Envelope Structures. *Nano Letters* **2006**, 6, 1053-1058.
157. Xu, H.; Hartono, D.; Yang, K. L., Detecting and Differentiating Escherichia Coli Strain TOP10 Using Optical Textures of Liquid Crystals. *Liquid Crystals* **2010**, 37, 1269-1274.
158. Lazcka, O.; Del Campo, F. J.; Muñoz, F. X., Pathogen Detection: A Perspective of Traditional Methods and Biosensors. *Biosensors & Bioelectronics* **2007**, 22, 1205-1217.
159. Luk, Y. Y.; Campbell, S. F.; Abbott, N. L.; Murphy, C. J., Non-Toxic Thermotropic Liquid Crystals for Use with Mammalian Cells. *Liquid Crystals* **2004**, 31, 611-621.
160. Lockwood, N. A.; Meli, M. V.; Surjosantoso, A.; Kim, E. B.; de Pablo, J. J.; Abbott, N. L., Characterization of the Interactions between Synthetic Nematic LCs and Model Cell Membranes. *Liquid Crystals* **2007**, 34, 1387-1396.
161. Cheng, L. L.; Luk, Y. Y.; Murphy, C. J.; Israel, B. A.; Abbott, N. L., Compatibility of Lyotropic Liquid Crystals with Viruses and Mammalian Cells that Support the Replication of Viruses. *Biomaterials* **2005**, 26, 7173-7182.
162. Woolverton, C. J.; Gustely, E.; Li, L.; Lavrentovich, O. D., Liquid Crystal Effects on Bacterial Viability. *Liquid Crystals* **2005**, 32, 417-423.
163. Lockwood, N. A.; Mohr, J. C.; Ji, L.; Murphy, C. J.; Palecek, S. P.; de Pablo, J. J.; Abbott, N. L., Thermotropic Liquid Crystals as Substrates for Imaging the Reorganization of Matrigel by Human Embryonic Stem Cells. *Advanced Functional Materials* **2006**, 16, 618-624.
164. Agarwal, A.; Huang, E.; Palecek, S.; Abbott, N. L., Optically Responsive and Mechanically Tunable Colloid-in-Liquid Crystal Gels that Support Growth of Fibroblasts. *Advanced Materials* **2008**, 20, 4804-4809.

Chapter 4. Endotoxin-Induced Structural Transformations in Liquid Crystalline Droplets*

4.1 Introduction

The functional properties of inorganic and organic materials have been manipulated through the deliberate introduction of defects and grain boundaries, as well as through the partitioning of low concentrations of dopant species to these localized regions of the materials.[1-4] For soft materials, such as liquid crystals (LCs), geometrical confinement within micrometer-sized systems has been shown to lead to the formation of a range of thermodynamically stable defects with nanoscopic dimensions and varied topologies (points, lines, rings).[5-11] In this chapter, we report that confinement of LCs within micrometer-sized droplets dispersed in water can lead to ordering transitions in the LC droplets that are highly specific and sensitive to a particular bacterial glycophospholipid. These ordering transitions occur at concentrations of lipid that are six orders of magnitude lower than previously reported adsorbate driven ordering transitions in LC systems.[9, 10, 12, 13]

4.2 Experimental Section

Materials. Endotoxin (from *E. coli* O127:B8), lipid A, and sodium dodecyl sulfate (SDS) were purchased from Sigma-Aldrich (St. Louis, MO). 1,2-Dilauroyl-*sn*-glycero-3-phosphatidylcholine (DLPC) and 1,2-dioleoyl-sn-glycero-3-phosphatidylcholine (DOPC) were purchased from Avanti Polar Lipids, Inc. (Alabaster, AL). Octadecyltrichlorosilane (OTS), methanol, methylene

chloride, sulfuric acid, hydrogen peroxide (30% w/v), and heptane were obtained from Fisher Scientific (Pittsburgh, PA). Ethanol was obtained from Pharmco-Aaper (Brookfield, CT). The 4'-pentyl-4-cyanobiphenyl (5CB) was obtained from EM Sciences (New York, NY). *Limulus* amoebocyte lysate (LAL) reagent water was purchased from Associates of Cape Cod, Inc. (East Falmouth, MA). EndoTrap® Red Equilibration Buffer (described below as PBS buffer; 10 mM Na_2HPO_4/NaH_2PO_4, 80 mM NaCl, pH 7.4; certified to contain a concentration of endotoxin of less than 0.02 EU/mL (~2 pg/mL)) was purchased from Hyglos GmbH (Regensburg, Germany). Neptune pipette tips (no detectable endotoxin) were purchased from Continental Lab Product, Inc (San Diego, CA). Polystyrene tubes (certificated nonpyrogenic tubes) were purchased from Becton Dickinson Labware (Franklin Lakes, NJ). Fisher's Finest Premium Grade glass microscope slides and cover glass were obtained from Fisher Scientific (Pittsburgh, PA). Gold specimen grids (20 μm thickness, 50 μm wide bars, and 283 μm grid spacing) were obtained from Electron Microscopy Sciences (Fort Washington, PA).

Preparation of LC Emulsions. The emulsions were formed by sequential sonication and vortex mixing of 2 μL of nematic 5CB in 1 mL of LAL reagent water or PBS at 25°C. Twelve cycles comprising 10 seconds of vortex mixing (at 2,500 rpm) and 10 seconds of sonication yielded milky white emulsions. The LC droplets were confirmed to exhibit bipolar configurations following sonication. The size distributions of the LC emulsion droplets were determined from optical micrographs using Image J (NIH, Bethesda, MD) software. The majority of the LC emulsion droplets possessed diameters that ranged from 4 μm to 8 μm, and were observed visually to be stable against coalescence at least for 3 hours. The LC emulsions were used within 3 hours of preparation.

Preparation of Aqueous Dispersion of Endotoxin or Lipid A. Powdered endotoxin or lipid A was dissolved in LAL reagent water at room temperature. After addition of the endotoxin or lipid A powder to obtain a concentration of either 1 mg/mL or 20 μg/mL, each solution was mixed by vortexing at 2,500 rpm for 4 minutes. After dilution, each solution was vortexed for an additional 45 seconds. Concentrations of endotoxin were verified by a kinetic turbidimetric LAL assay (Charles River Laboratories International, Inc.; Wilmington, MA) performed in the Waisman Clinical Biomanufacturing Facility Laboratory, University of Wisconsin-Madison.

Preparation of Aqueous Dispersions of DLPC, DOPC and SDS. Briefly, DLPC or DOPC were dissolved in chloroform and dispensed into glass vials. The phospholipid-containing chloroform solution was evaporated under a stream of nitrogen gas (N_2), and the vial containing lipid was then placed under vacuum for at least 2 hours. The dried lipid was resuspended in aqueous solution and subsequently sonicated using a probe ultrasonicator which resulted in a clear solution (60 Sonic Dismembrator from Fisher Scientific (Pittsburgh, PA); 3 times at 15W for 5 minutes each in a water bath). The phospholipid solution was then extruded through a 0.22 μm pore filter (Millipore; Billerica, MA) before use.

Preparation of Planar LC Films. Detailed descriptions of procedures used to prepare planar LC films (stabilized by hosting the LC within metallic grids) can be found in past publications.[14, 15] Briefly, glass microscope slides were cleaned according to published procedures and coated with OTS. The quality of the OTS layer was assessed by checking the alignment of 5CB confined between two OTS-coated glass slides. Any surface not causing homeotropic anchoring

(perpendicular alignment) of 5CB was discarded. Gold specimen grids that were cleaned sequentially in methylene chloride, ethanol, and methanol were placed onto the surface of OTS-coated glass slides. Approximately 1 μL of 5CB was dispensed onto each grid and then excess LC was removed by contacting a capillary tube with the droplet of 5CB. As described in previous publications, the thickness of the LC film is set by the thickness of the metallic grid.[14, 15] Each LC-filled grid was equilibrated at ambient temperature and subsequently immersed into the aqueous solution of interest at 25°C.

Optical Characterization of Liquid Crystal in the Presence of Lipid by Polarized Light Microscopy. A volume of 40 μL of an aqueous dispersion of lipid (in LAL reagent water or PBS) was dispensed onto a cover glass. A volume of LC emulsion, prepared as described above, was added to the lipid dispersion to produce a sample containing the desired number of LC droplets. The configurations of the LCs within the emulsion droplets were determined by observation of the optical appearance of the droplets under an Olympus IX71 inverted microscope (Center Valley, PA) using an objective power of 100x (an oil lens). Bright field and polarized light micrographs of the LC emulsions were collected with a Hamamatsu 1394 ORCA-ER CCD camera (Bridgewater, NJ) connected to a computer and controlled through SimplePCI imaging software (Compix, Inc., Cranberry Twp., NJ). As described in detail elsewhere, we characterized LC droplets that were translating with a velocity greater than 1 μm/s to avoid observation of droplets interacting with the surfaces of the cover slips.[16] The droplets were diffusing (translating and rotating) – thus a radial droplet has an optical appearance that is invariant with time when viewed between crossed polars whereas the bipolar droplet has a distinct, time-varying optical appearance.

The orientations of the LCs within Au grids were determined by using an Olympus BX60 microscope with crossed polars (transmission mode). Orthoscopic examinations were performed with the source light intensity set to 50% of full illumination and the aperture set to 10% to collimate the incident light. Homeotropic (perpendicular) alignment of LC was determined by insertion of a condenser below the stage and a Bertrand lens above the stage to allow conoscopic examination of the specimen. Observation of an optical pattern consisting of two crossed isogyres confirmed the homeotropic alignment. Images were captured with a microscope-mounted digital camera (Olympus C-4000 Zoom) set to an f-stop of 2.8 and a shutter speed of 1/320 seconds.

Confocal Microscopy of BODIPY-Labeled Endotoxin Adsorbed to LC Droplets. Confocal fluorescence imaging was performed using a Leica SP2 confocal system and Leica DMIRE2 inverted microscope at Northwestern University (Illinois). The BODIPY was excited at 488 nm using an argon laser, and the detector collected light with wavelengths from 499 nm to 634 nm. The thickness of the equator focal plane was 40.7 nm. The images were obtained with an exposure time of ~6 seconds.

4.3 Results and Discussion

Endotoxin is a bacterial lipopolysaccharide comprised of a glycophospholipid (called lipid A) (Figure 4-1A) in addition to two polysaccharide domains. Lipid A has six tails, and thus it is structurally distinct from all other lipids.[17] We investigated the interactions of endotoxin from *Escherichia coli*, the lipid A portion of endotoxin, and the other phospholipids and surfactants shown in Figure 4-1B to 4-1D, with micrometer-sized droplets of the nematic LC 4′-

pentyl-4-cyanobiphenyl (5CB) (Figure 4-1E) that were dispersed initially in endotoxin free water. In the absence of endotoxin, bright field (Figure 4-1F) and polarized light micrographs (Figure 4-1G) revealed the presence of two point defects (surface defects, called boojums) located at the "poles" of the LC droplets, corresponding to a so-called bipolar configuration of the droplet where the LC assumes a tangential orientation at the droplet surface (Figure 4-1H).[5] After the addition of endotoxin to the water at a concentration of 1 mg/mL, both bright field (Figure 4-1I) and polarized light imaging (Figure 4-1J) revealed a reordering of the LC within the droplet to a so-called radial configuration, corresponding to a single defect located at the droplet center and LC oriented perpendicular to the droplet surface (Figure 4-1K).[5] Upon measuring the fraction of LC droplets within a solution of endotoxin that exhibited the radial configuration (Figure 4-1L), we found that remarkably low concentrations of endotoxin (< 1 pg/mL) trigger the ordering transition. Consistent with our conclusion that the interaction of the LC droplets and endotoxin was responsible for the ordering transition, the fraction of LC droplets in the radial configuration increased with the concentration of endotoxin (Figure 4-1L). The response of the LC droplets to endotoxin was dependent on the total number of LC droplets in solution, allowing the ordering transition to be tuned over a range of endotoxin concentrations (*e.g.*, 1 to 10 pg/mL or 1 to 100 pg/mL) (Figure 4-1L). The lipid A portion of endotoxin caused similar ordering transitions in the LC droplets.

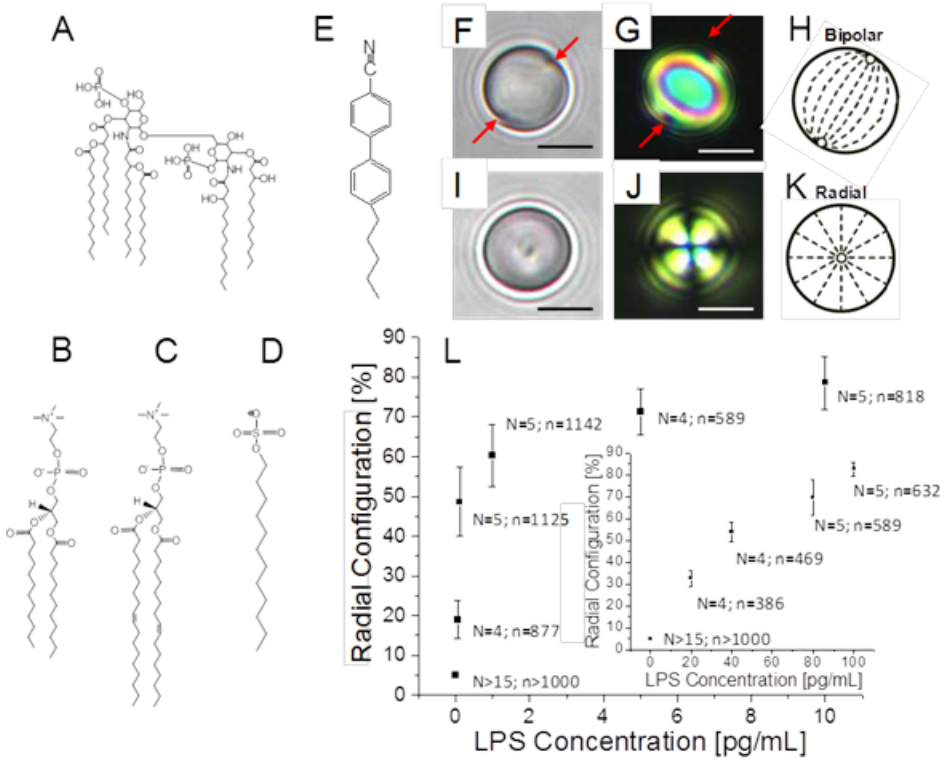

Figure 4-1. Endotoxin-induced structural transformations in liquid crystalline droplets.
(A) Lipid A portion of endotoxin. (B) DLPC. (C) DOPC. (D) SDS. (E) 5CB. (F and G) Bright field (F) and polarized light (G, crossed polars) micrographs of a LC droplet in endotoxin free water. The red arrows indicate boojums at the aqueous—LC interface of the droplet. (H) Schematic illustration of the bipolar configuration of the LC droplet corresponding to (F) and (G). (I and J) Bright field (I) and polarized light (J, crossed polars) micrographs of a LC droplet after exposure to endotoxin from E. coli (O127:B8; 1 mg/mL) in water. (K) Schematic illustration of the radial configuration of the LC droplet corresponding to (I) and (J). (L) Percentage of 8,300 LC droplets in 40 µL of water that exhibited a radial configuration, plotted as a function of endotoxin concentration. The inset shows the response of the LC droplets when 94,000 droplets were used. The LC-in-water emulsion droplets (diameters of ~4 to 8 µm) were prepared by sonication of nematic 5CB in water that was free of endotoxin. The droplet numbers were determined using flow cytometry. Endotoxin concentrations were validated using an independently performed *Limulus* amoebocyte lysate assay. N indicates the number of independent experiments, and n indicates the total number of LC emulsion droplets that were analyzed. Scale bars, 5 µm.

The simplest continuum description of the ordering of LCs within droplets considers the free energy, F, of each droplet to be influenced by an orientation-dependent surface free energy

and an elastic strain free energy, namely $F = \int W dA + \frac{K}{2}\int (\nabla \boldsymbol{n})^2 dV$, where W is the so-called surface anchoring energy per unit area, A is the surface area of the droplet, K is the elastic modulus for strain of the LC,[18] $\boldsymbol{n}$ is the director of the LC,[18] and V is the volume of the LC droplet.[5, 8-10] Past studies have demonstrated that lipids and synthetic surfactants can induce ordering transitions at aqueous—LC interfaces through a mechanism that involves an adsorbate-induced change in W.[12, 13, 19] However, to change W to induce an ordering transition requires near saturation coverage of the interface by the adsorbate (0.1 to 1 Langmuir), typically corresponding to solution concentrations of lipids of at least ~10 mg/mL.[9, 10, 12, 13, 20] Consistent with a mechanism involving changes in W, we observed that double-tailed lipids such as 1,2-dilauroyl-*sn*-glycero-3-phosphatidylcholine (DLPC) and 1,2-dioleoyl-*sn*-glycero-3-phosphatidylcholine (DOPC) (Figure 4-1B and 4-1C) and single-tailed synthetic surfactants such as sodium dodecyl sulfate (SDS) (Figure 4-1D) induced ordering transitions in the LC droplets only at concentrations greater than 10 mg/mL (Figure 4-2A). These results contrast to lipid A where ordering transitions are induced in the LC droplets at concentrations of lipid A that are at least six orders of magnitude lower (picograms per milliliter). We calculated that if all of the endotoxin in 40 µL of a 1 pg/mL solution adsorbed uniformly over the aqueous—LC interface of ~10^4 LC droplets (radius 3 µm) in one of our experiments (Figure 4-1L), the interfacial density of endotoxin would be ~1 molecule/ 10^6 nm^2 or ~10^{-5} of saturation monolayer coverage (~10^{-5} Langmuir).[21] In contrast, the double-tailed lipids mentioned above (Figure 4-1B and C) trigger ordering transitions at interfacial concentrations that correspond to ~1 molecule/0.6 nm^2 (saturation coverage is ~1molecule/0.4 nm^2). This pronounced difference in surface density of lipid (5 to 6 orders of magnitude) required to trigger ordering transitions within LC droplets led us to propose that, at pg/mL concentrations, endotoxin and lipid A do not trigger ordering

transitions in the LC droplets through changes in W (as is the case for DLPC and DOPC) but instead trigger the ordering transitions through interaction with localized regions of the LC droplets.We hypothesized that the local regions of interaction were defined by the defects in the LC (Figure 4-1H and K).

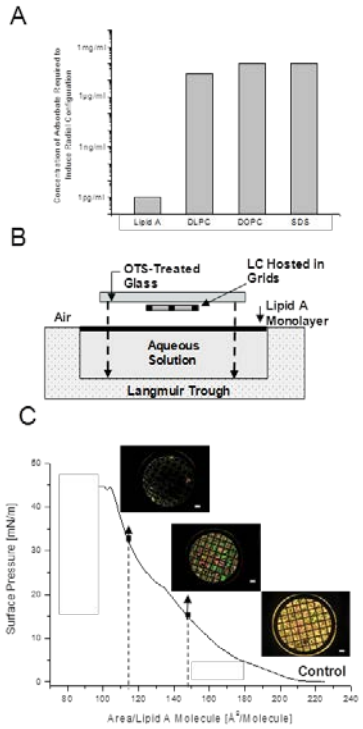

Figure 4-2. Areal density of endotoxin required to trigger an ordering transition at a planar aqueous—LC interface.

(A) Bulk concentrations of lipids or surfactants in solution (40 µL) required to cause at least 50% of 8,300 LC droplets added to each solution to adopt a radial configuration. (B) Schematic illustration of the experimental apparatus used to transfer Langmuir monolayers of lipid A at prescribed surface densities from an air-water interface onto a planar aqueous—LC interface.[13] In brief, micrometer-thick films of nematic 5CB (with planar interfaces) were prepared within the pores of Au grids supported on glass slides treated with octadecyltrichlorosilane (to cause perpendicular ordering of the LC). The supported LC was then immersed downward through the lipid A monolayer at the surface of the water to transfer the monolayer onto the planar aqueous—LC interface. (C) Surface pressure-area isotherm measured for a Langmuir monolayer of lipid A and the optical appearance (between crossed polars) of films of 5CB with planar interfaces (hosted within the metallic grids) after transfer of Langmuir films of lipid A at the indicated interfacial density onto the aqueous—5CB interface (see (B) for details). The control corresponds to LC passed into endotoxin free water. The bright optical appearance of the control indicates an orientation of the LC that is parallel to the aqueous—LC interface. The optical appearance of the sample prepared at an area per molecule of lipid A of 148 $Å^2$/molecule indicates a tilted state of the LC. The dark optical appearance of the sample prepared at 115 $Å^2$/molecule indicates a perpendicular orientation of the LC at the aqueous interface. Scale bars, 300 µm.

Past studies have established that nematic LCs, when confined in certain geometries, cannot satisfy the boundary conditions of the system through continuous strain (splay, bend, and twist) of the LC.[5, 7-10] Instead, the LC satisfies the boundary conditions through the generation of nanoscopic regions within which the molecules comprising the LC possess low levels of orientational order, namely, defects such as the point defects shown in Figure 4-1H and K. We tested the role of defects in the LC ordering transitions induced by endotoxin and lipid A by changing the geometry of the LC system. First, we measured ordering transitions induced by spontaneous adsorption of endotoxin or lipid A at planar interfaces of LC that lack the defects generated by the spherical geometry of the droplets. At these planar interfaces, neither lipid A nor endotoxin triggered an ordering transition in the LC until the concentration exceeded ~1 mg/mL (Figure 4-S1 of Supporting Information).[12, 22, 23] Second, we formed Langmuir monolayers of lipid A of known density at the surface of water and transferred the lipid A monolayers onto planar aqueous—LC interfaces using the Langmuir-Schaefer transfer method (as illustrated in Figure 4-2B).[13] These measurements revealed that a surface concentration of lipid A of ~1 molecule/1.15 nm^2 was required to cause an ordering transition at the planar LC interface (Figure 4-2C), a surface concentration that is six orders of magnitude greater than the surface concentration driving the ordering transition of the LC droplets. These observations, when combined with the results reported above, support our hypothesis that endotoxin and lipid A trigger ordering transitions in micrometer-sized LC droplets through interaction with defects in the LC that are induced by the spherical geometry of the LC droplets.

To provide further insight into the interaction of endotoxin with the defects of the LC droplets, we performed confocal fluorescence microscopy using boron dipyrromethene (BODIPY)–labeled endotoxin (Figure 4-3A). These measurements confirmed that endotoxin was

localized at the point defect formed at the center of each LC droplet with a radial configuration. Interestingly, after deliberate photobleaching of the BODIPY-labeled endotoxin at the point defect, we measured a time-dependent recovery of the fluorescence (Figure 4-3B), indicating an exchange of lipid between the center and surface of the droplet that occurred over tens of seconds. We also heated an emulsion of 5CB free of endotoxin above the clearing temperature of the nematic phase (T_{iso} = 35°C; experiments were performed at 50°C), added 10 pg/mL of endotoxin, and then cooled the sample through the isotropic-to-nematic phase transition. We measured the characteristic time interval between the formation of the nematic phase during cooling and the establishment of radial ordering (Figure 4-3C).[24, 25] The time interval was found to scale with the square of the droplet radius, consistent with a physical process underlying the ordering transition that involved diffusion of the lipid. We calculated the time for diffusion of lipid across the surface of the LC droplet (calculated as $t_1 = L_A^2/4D_s$, where L_A corresponds to $\pi R/2$, the distance along the surface from the equator to the pole) to be in good agreement with the data in Figure 4-3C (using D_s ~ 10 × 10^{-12} m^2/s)[12]. The surface diffusion time for a droplet with a radius of 3 μm was calculated to be ~0.6 seconds; the experimentally measured characteristic time was ~1 seconds (Figure 4-3C).[24, 25] This result suggests a physical process in which the dynamics of the ordering transition induced by endotoxin are governed by the lateral transport of endotoxin across the surface of the LC droplet, a process that would be necessary to localize endotoxin at surface defects (boojums) to initiate the ordering transition. We note that past studies have reported observations of the localization of inorganic colloids at defects generated in LC systems,[26, 27] including stabilization of blue phases.[28] We also observed 10 pg/mL of endotoxin to trigger the ordering transition from the bipolar to the radial configuration through a kinetic pathway that was distinct from that observed during the surface-driven ordering

transitions caused by DLPC, SDS, lecithins and concentrations of endotoxin (50 μg/mL) that were sufficient to saturate the LC interface (see Figures 4-S2 through 4-S4 of Supporting Information for the kinetic pathway of the transition between the bipolar and radial configurational states of the LC droplets).[9, 10] The distinct kinetic pathway triggered by 10 pg/mL of endotoxin provides further support for our conclusion that the ordering transitions at low concentrations of endotoxin are not caused by changes in surface anchoring energy (W).

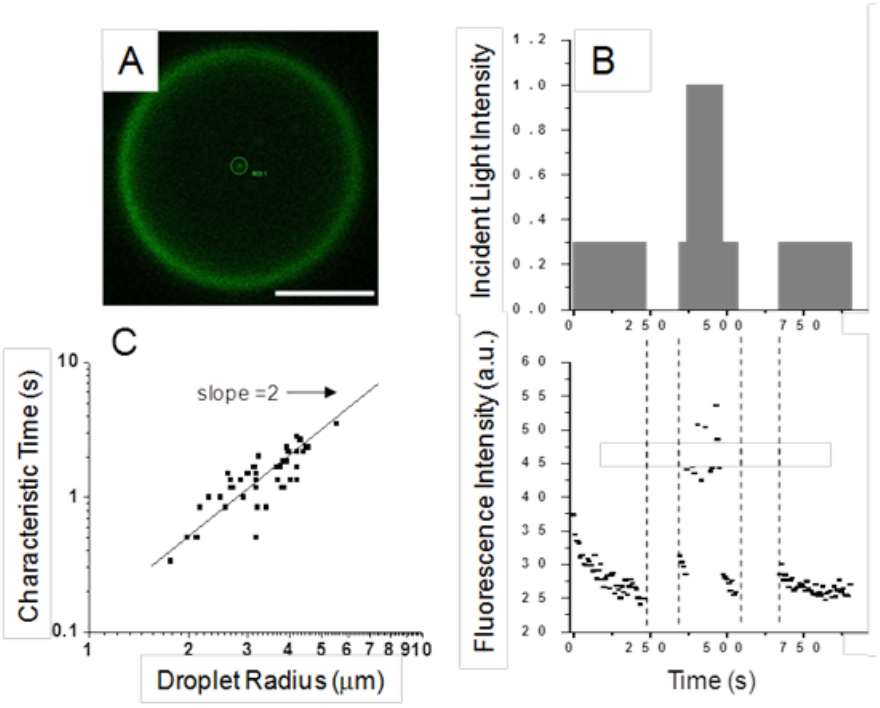

Figure 4-3. Localization of endotoxin at defects within LC droplets.

(A) Confocal fluorescence micrograph of a LC droplet in contact with a solution of BODIPY-labeled endotoxin. The point defect at the center of the droplet with a radial configuration exhibits a strong fluorescence signal. The concentration of endotoxin in solution was 20 μg/mL in order to achieve a sufficient signal intensity to image the droplets. Imaging was performed using an argon laser at an excitation wavelength of 488 nm, and the detector collected the emission with wavelengths from 499 to 634 nm. Scale bar, 5 μm. (B) Photobleaching of the BODIPY-labeled endotoxin at the center of the LC droplet. The upper panel shows the intensity of the excitation laser, and the lower panel shows the corresponding fluorescence intensity. Loss of fluorescence signal is apparent during the periods of sample illumination (*e.g.*, 0 to 230 s), and recovery of fluorescence is apparent in the periods of time when the laser incident on the sample was blocked (*e.g.*, 230 to 350 s); a.u. indicates arbitrary units. The incident light intensity is indicated as a fraction of the maximum laser power. (C) Time taken for LC droplets to exhibit radial ordering after a thermal quench from the isotropic to nematic phase, plotted as a function of the droplet radius. The experiment was performed with 21,500 LC droplets dispersed in 100 μL of solution containing 10 pg/mL endotoxin. The line shown in the figure has a slope of 2.

4.4 Conclusions

In summary, the experiments in this chapter establish that the effect of endotoxin at concentrations of ~1 pg/mL on the surface anchoring energy of LCs is negligible; ordering transitions in LC droplets driven by changes in surface anchoring energy require six orders of magnitude higher surface concentrations of lipid than are present in the experiments with endotoxin. Furthermore, we do not expect the endotoxin to change the elastic moduli of the LC and thus drive the ordering transition through a lowering of the elastic energy. Instead, the experimental results reported in this chapter are consistent with the proposition that the ordering transitions in micrometer-sized LC droplets are driven by the interactions of endotoxin with topological defects induced by the geometry of the LC droplets. The observation that the ordering transitions of the LC droplets are specific to the lipid structure of endotoxin suggests that endotoxin may be forming organized assemblies within the cores of the defects to change the defect energies to favor stabilization of the radial configuration over the bipolar structure. In comparison with previously reported ordering transitions involving planar LC films, we find that endotoxin driven ordering transitions in LC droplets are ~10^6 times more sensitive. This sensitivity and structure-based selectivity of ordering transitions in LC droplets suggests new principles for the design of responsive LC systems, particularly for the design of sensors that respond to targeted biological analytes.[29, 30]

Acknowledgements

This work was primarily supported by NSF through DMR-0520527 (MRSEC), the ARO (W911NF-07-1-0446 and W911NF-06-1-0314) and the National Institutes of Health (CA108467 and CA105730). The technical assistance of Rebecca J. Carlton is gratefully acknowledged.

4.5 Supporting Information

Anchoring Energy of Nematic 5CB at the Aqueous-Nematic Interface

We determined the magnitude of the anchoring energy of nematic 5CB at the aqueous—nematic interface by preparing planar films of 5CB of known thickness within metallic grids on OTS-treated glass slides (see Experimental Section for details; the thicknesses of the metallic grids were 5 μm and 20 μm). We confirmed the thicknesses of the LC films by quantifying the displacement of the focal plane when imaging the two interfaces of each LC film. We measured the optical retardance of the LC films, and calculated the anchoring energy assuming (i) the elastic constant of nematic 5CB to be 5 pN, (ii) the anchoring energy per unit area to be described by $W=1/2\sin^2\Theta$, and (iii) the anchoring of the 5CB at the OTS-treated glass interface to be homeotropic and strong. From these measurements, we determined the magnitude of the anchoring energy to be ~ 10 $\mu J/m^2$.

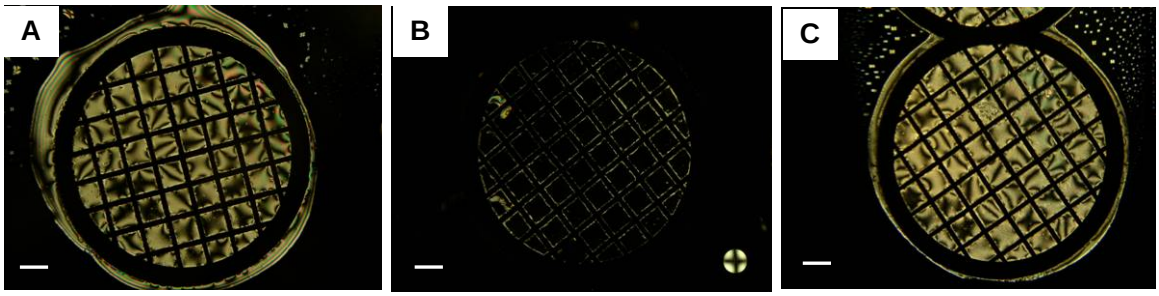

Figure 4-S1. Polarized light micrographs (crossed polars) of 20 μm-thick LC films with planar interfaces in contact with aqueous solutions.

(A) Endotoxin free water for 1 day; (B) 1 mg/mL endotoxin for less than 2 minutes; (C) 1 μg/mL endotoxin for 1 day. The bright appearance of the optical micrographs in A and C indicate that the orientation of the LC is parallel to the aqueous—LC interface in these samples. In contrast, the dark optical appearance in B indicates an orientation of the LC that is perpendicular to the aqueous—LC interface, a result that is confirmed by a conoscopic image (inset, lower right). Scale bars are 300 μm.

Characterization of the Kinetic Pathway of the Endotoxin-Induced Ordering Transition

We used video microscopy to identify the kinetic pathways underlying the endotoxin-induced ordering transitions between the bipolar and radial configurations of the LC droplets. The LC droplets dispersed in water were translating and rotating during imaging. Because the LC droplets rotated between the times at which we obtained the polarized light and bright field images for each droplet, in Figure 4-S2 and 4-S3, we rotated the bright field images to align them with the polarized light images.

First, we performed experiments using high concentrations of endotoxin (50 μg/mL) to characterize the kinetic pathway of LC droplets going through a *surface-driven* ordering transition in the presence of endotoxin (Figure 4-S2). We note that a concentration of 50 μg/mL of endotoxin is sufficient to saturate the interface of the LC droplets in these experiments.

Inspection of Figure 4-S2 reveals that the kinetic pathway observed at high endotoxin concentrations involves transitions states that comprise (i) a disclination loop, (ii) a preradial configuration, and (iii) an escaped radial configuration. We note also that the kinetic pathway shown in Figure 4-S2 is similar to past observations by us (using SDS and L-DLPC[31]) and others (using lecithin[10]) in which *adsorbate-induced changes in the easy axis* were observed to drive the ordering transitions of the LC droplets.

Second, we performed experiments in which we recorded the transition states assumed by the LC droplets during an ordering transition triggered by the presence of 10 pg/mL of endotoxin (Figure 4-S3). Inspection of Figure 4-S3 reveals that the LC droplets were initially in a bipolar configuration. The onset of the transition was first evidenced by the disappearance of one of the point defects (boojums) at a pole of the droplet. The remaining point defect transformed to a hedgehog corresponding to a preradial configuration. Finally, the point defect migrated from the droplet surface, corresponding to an escaped radial configuration, to the core of the droplet forming a radial configuration. In contrast to the surface-driven ordering transition induced by 50 μg/mL of endotoxin (Figure 4-S2), the ordering transition triggered by 10 pg/mL did not involve a transition state with a disclination loop, an observation that is consistent with our conclusion that the ordering transition in the LC droplets caused by 10 pg/mL of endotoxin is not caused by a change in surface anchoring energy. In summary, these results establish that the kinetic pathway of the *surface-driven* transition caused by 50 μg/mL of endotoxin is different from the kinetic pathway when using 10 pg/mL of endotoxin. This result supports our conclusion that the ordering transition induced by 10 pg/mL of endotoxin is not due to a change in the surface anchoring energy.

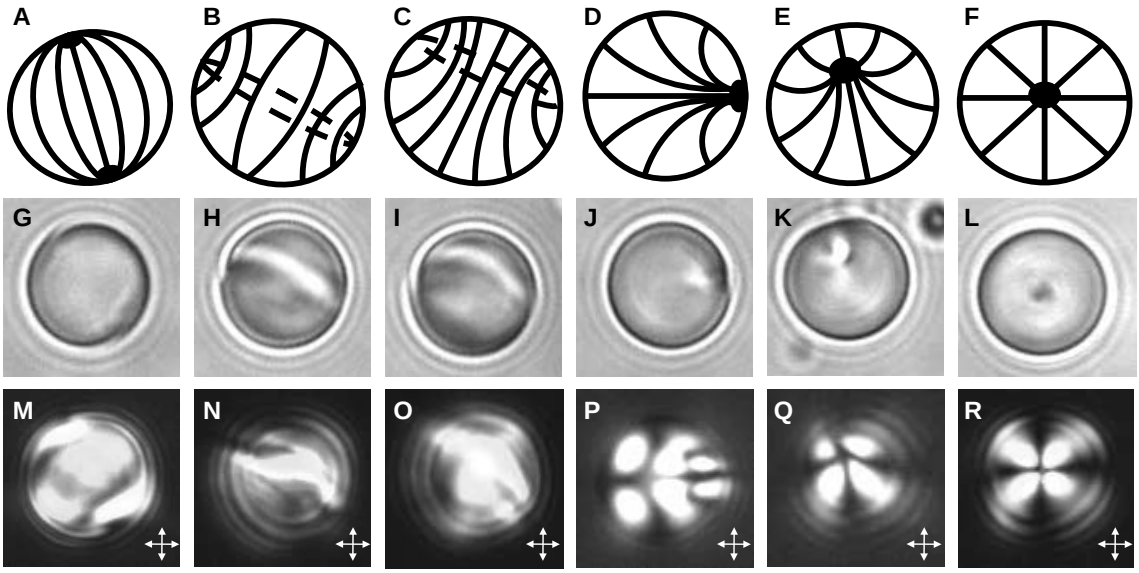

Figure 4-S2. Transition states for an ordering transition in LC droplets triggered by adsorption of endotoxin.

(A-F) Schematic illustrations, (G-L) bright field micrographs, and (M-R) polarized light micrographs (crossed polars) of 8-μm-diameter 5CB droplets following exposure of the droplets to 50 μg/mL of endotoxin. Initially, the droplets were in a bipolar configuration (A, G, M). As the boundary conditions transitioned from tangential to normal, the two point defects (boojums) at the diametric ends of the bipole disappeared, and a disclination loop appeared near the droplet equator (B, H, N). The disclination loop subsequently moved towards a pole of the droplet (C, I, O) and shrank to a surface point defect (hedgehog) corresponding to a preradial configuration (D, J, P). Finally, the point defect moved from the surface of the droplet, corresponding to an escaped radial configuration (E, K, Q), to the droplet center forming a radial configuration (F, L, R).

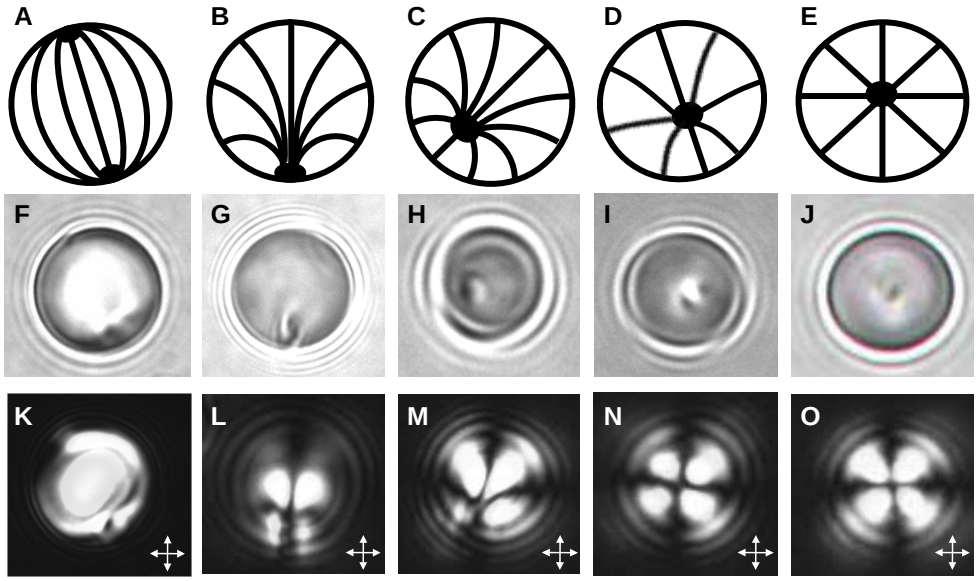

Figure 4-S3. Transition states for an ordering transition in LC droplets triggered by localized interaction of endotoxin with defects within the droplets.

(A-E) Schematic illustrations, (F-J) bright field micrographs, and (K-O) polarized light micrographs (crossed polars) of 8-μm-diameter 5CB droplets following exposure of the LC droplets to 10 pg/mL of endotoxin. Initially, the droplets are in a bipolar configuration (A, F, K). One of the boojums of the bipolar state was observed to disperse whereas the other boojum was observed to form a hedgehog defect, thus forming a preradial configuration (B, G, L). Next, the point defect migrated off the droplet surface, forming an escaped radial configuration (C, H, M and D, I, N). Ultimately, the defect arrived at the core of the droplet forming a radial configuration (E, J, O). Contrary to the pathway observed at an endotoxin concentration of 50 μg/mL, no disclination rings were observed during the transition of the droplets from bipolar to radial configurations in the presence of 10 pg/mL of endotoxin.

We also place the observations described above into the context of past observations of ordering transitions reported by Volovik *et al.*[10] and Prichepa *et al.*.[9] First, when endotoxin is present at high concentrations (50 μg/mL), we observed an intermediate state that exhibited the distinct optical signature of a disclination loop (Figure 4-S2). A kinetic pathway involving a disclination ring has also by reported by Volovik *et al.*.[10] Second, in contrast to the above studies by ourselves [31] and Volovik *et al.*,[10] we observed LC droplets to transform from bipolar to radial

configurations in the presence of 10 pg/mL of endotoxin without exhibiting a disclination line as an intermediate state. We note that Prischepa *et al.*[9] have reported a kinetic pathway for a bipolar-to-radial ordering transition for LC droplets (embedded in a solid polymer matrix) that does not involve an intermediate disclination loop. However, key differences also exist between our observations and those reported by Prischepa *et al.*.[9] In particular, Prischepa *et al.*[9] report that the intermediate states (*e.g.*, escaped radial) observed during a bipolar-to-radial transition correspond to equilibrium states of the system that can be accessed by varying the concentration of lipid dissolved into the solid, polymeric matrix. In our experiments, we do not observe the intermediate states (*e.g.*, escaped radial) to be stable equilibrium states of the system that are encountered with increasing endotoxin concentration (in the pg/mL range) in the aqueous solution. In contrast, we observe the droplets to exhibit only transient intermediate states between bipolar and radial configurations, and at equilibrium, with increasing concentration of endotoxin in the pg/mL range, we observe an increasing fraction of radial droplets in solution (see Figure 4-1L). This point is illustrated in Figure 4-S4, where the fractions of emulsion droplets in the bipolar, preradial/escaped radial, or radial configurations were recorded each minute after exposure to 10 pg/mL of endotoxin. Inspection of Figure 4-S4 reveals that prior to addition of the endotoxin, the majority of the LC droplets were determined to be in a bipolar configuration. In the first minute following addition of the endotoxin, a transient rise in the percentage of droplets exhibiting the preradial/escaped radial configuration was observed. A maximum in the fraction of preradial/escaped radial droplets in solution was observed after ~3-4 minutes. The final state of the system was comprised of radial LC droplets.

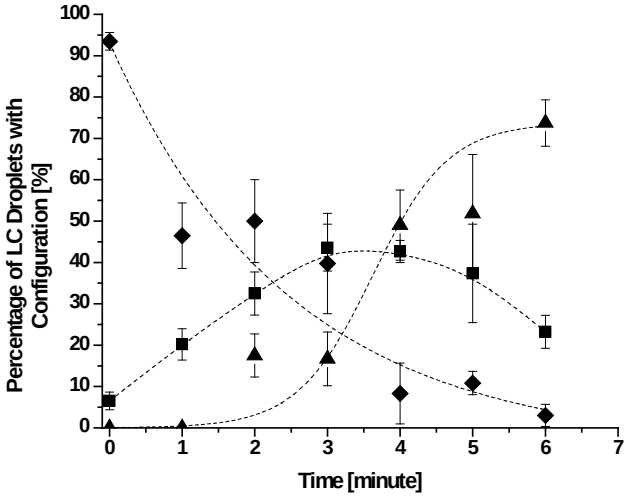

Figure 4-S4. Percentage of LC droplets that exhibited bipolar (♦), preradial/escaped radial (■), and radial (▲) configurations following the addition of 10 pg/mL endotoxin.

The lines are drawn to guide the eye. Each data point represents the average of 3 independent experiments.

4.6 References

*This chapter was prepared as a Full Paper reporting original research in the journal *Science*. My co-authors contributed to the initial development of the project and preliminary experiments. Reprinted (adapted) with permission from: Lin, I-H.; Miller, D. S.; Bertics, P. J.; Murphy, C. J.; de Pablo, J. J.; Abbott, N. L. Endotoxin-Induced Structural Transformations in Liquid Crystalline Droplets. *Science* **2011**, 332, 1297-1300. Copyright 2011 American Association for the Advancement of Science.

1. Hu, D.; Yu, J.; Wong, K.; Bagchi, B.; Rossky, P. J.; Barbara, P. F., Collapse of Stiff Conjugated Polymers with Chemical Defects into Ordered, Cylindrical Conformations. *Nature* **2000**, 405, 1030-1033.
2. Queisser, H. J.; Haller, E. E., Defects in Semiconductors: Some Fatal, Some Vital. *Science* **1998**, 281, 945-950.
3. Romalis, M., Applied Physics - Virtues of Diamond Defects. *Nature* **2008**, 455, 606-607.
4. Simon, J.; Protasenko, V.; Lian, C. X.; Xing, H. L.; Jena, D., Polarization-Induced Hole Doping in Wide-Band-Gap Uniaxial Semiconductor Heterostructures. *Science* **2010**, 327, 60-64.
5. Lavrentovich, O. D., Topological Defects in Dispersed Liquid Crystals, or Words and Worlds around Liquid Crystal Droplets. *Liquid Crystals* **1998**, 24, 117-125.
6. Lee, B. W.; Clark, N. A., Alignment of Liquid Crystals on Patterned Isotropic Surfaces. *Science* **2001**, 291, 2576-2580.
7. Musevic, I.; Skarabot, M.; Tkalec, U.; Ravnik, M.; Zumer, S., Two-Dimensional Nametic Colloidal Crystals Self-Assembled by Topological Defects. *Science* **2006**, 313, 954-958.
8. Poulin, P.; Stark, H.; Lubensky, T. C.; Weitz, D. A., Novel Colloidal Interactions in Anisotropic Fluids. *Science* **1997**, 275, 1770-1773.
9. Prischepa, O. O.; Shabanov, A. V.; Zyryanov, V. Y., Transformation of Director Configuration Upon Changing Boundary Conditions in Droplets of Nematic Liquid Crystal. *JETP Letters* **2004**, 79, 257-261.
10. Volovik, G. E.; Lavrentovich, O. D., The Topological Dynamics of Defects - Boojums in Nematic Drops. *Soviet Physics JETP* **1983**, 58, 1159-1165.
11. Zapotocky, M.; Ramos, L.; Poulin, P.; Lubensky, T. C.; Weitz, D. A., Particle-Stabilized Defect Gel in Cholesteric Liquid Crystals. *Science* **1999**, 283, 209-212.
12. Brake, J. M.; Daschner, M. K.; Luk, Y. Y.; Abbott, N. L., Biomolecular Interactions at Phospholipid-Decorated Surfaces of Liquid Crystals. *Science* **2003**, 302, 2094-2097.
13. Meli, M. V.; Lin, I. H.; Abbott, N. L., Preparation of Microscopic and Planar Oil-Water Interfaces That Are Decorated with Prescribed Densities of Insoluble Amphiphiles. *Journal of the American Chemical Society* **2008**, 130, 4326-4333.
14. Brake, J. M.; Daschner, M. K.; Abbott, N. L., Formation and Characterization of Phospholipid Monolayers Spontaneously Assembled at Interfaces between Aqueous Phases and Thermotropic Liquid Crystals. *Langmuir* **2005**, 21, 2218-2228.
15. Brake, J. M.; Daschner, M. K.; Luk, Y. Y.; Abbott, N. L., Biomolecular Interactions at Phospholipid-Decorated Surfaces of Liquid Crystals. *Science* **2003**, 302, 2094-2097.
16. Kinsinger, M. I.; Buck, M. E.; Abbott, N. L.; Lynn, D. M., Immobilization of Polymer-Decorated Liquid Crystal Droplets on Chemically Tailored Surfaces. *Langmuir* **2010**, 26, 10234-10242.
17. Raetz, C. R. H.; Whitfield, C., Lipopolysaccharide Endotoxins. *Annual Review of Biochemistry* **2002**, 71, 635-700.
18. *This simple model assumes the elastic modulus for splay, bend and twist of the LC to be equal in magnitude. The director is a vector that is used to describe the average orientation of molecules within a LC.*

19. Gupta, J. K.; Sivakumar, S.; Caruso, F.; Abbott, N. L., Size-Dependent Ordering of Liquid Crystals Observed in Polymeric Capsules with Micrometer and Smaller Diameter. *Angewandte Chemie, International Edition* **2009**, 48, 1652-1655.
20. Sivakumar, S.; Wark, K. L.; Gupta, J. K.; Abbott, N. L.; Caruso, F., Liquid Crystal Emulsions as the Basis of Biological Sensors for the Optical Detection of Bacteria and Viruses. *Advanced Functional Materials* **2009**, 19, 2260-2265.
21. *Assumptions underlying the calculation: (i) the molecular weight of endotoxin is 50 kDa, (ii) the emulsion droplets have radii of 3 μm, and (iii) endotoxin in solution adsorbs uniformly over the interface of all LC droplets.*
22. McCamley, M. K.; Artenstein, A. W.; Opal, S. M.; Crawford, G. P., Optical Detection of Sepsis Markers Using Liquid Crystal-Based Biosensors. *Proceedings of SPIE* **2007**, 6441, 64411Y1-64411Y8.
23. McCamley, M. K.; Ravnik, M.; Artenstein, A. W.; Opal, S. M.; Zumer, S.; Crawford, G. P., Detection of Alignment Changes at the Open Surface of a Confined Nematic Liquid Crystal Sensor *Journal of Applied Physics* **2009**, 105, 123504.
24. *For LC droplets with diameters smaller than 10 μm, the kinetics of formation of the nematic phase are fast (< 50ms) compared to the dynamics of the transformation leading to the appearance of the radial configuration of the nematic phase.*
25. Chen, X. C.; Hamlington, D.; Shen, A. Q., Isotropic-to-Nematic Phase Transition in a Liquid-Crystal Droplet. *Langmuir* **2008**, 24, 541-546.
26. Fernandez-Nieves, A.; Vitelli, V.; Utada, A. S.; Link, D. R.; Marquez, M.; Nelson, D. R.; Weitz, D. A., Novel Defect Structures in Nematic Liquid Crystal Shells. *Physical Review Letters* **2007**, 99, 4.
27. Skarabot, M.; Ravnik, M.; Zumer, S.; Tkalec, U.; Poberaj, I.; Babic, D.; Musevic, I., Hierarchical Self-Assembly of Nematic Colloidal Superstructures. *Physical Review E* **2008**, 77, 4.
28. Ravnik, M.; Alexander, G. P.; Yeomans, J. M.; Zumer, S., Mesoscopic Modelling of Colloids in Chiral Nematics *Faraday Discussions* **2010**, 144, 159-169.
29. *Endotoxin is an indicator of bacterial contamination. Detection of endotoxin in purified water (in the 1-100 pg/mL range) is widely performed during manufacturing processes for pharmaceutical products (including validation of water used in such processes) and biomedical devices, in a variety of public health contexts (particularly analysis of aerosols in industrial and indoor environments) and for biological research.*
30. Cohen, J., The Immunopathogenesis of Sepsis. *Nature* **2002**, 420, 885-891.
31. Gupta, J. K.; Zimmerman, J. S.; de Pablo, J. J.; Caruso, F.; Abbott, N. L., Characterization of Adsorbate-Induced Ordering Transitions of Liquid Crystals within Monodisperse Droplets. *Langmuir* **2009**, 25, 9016-9024.

Chapter 5. Influence of Droplet Size, pH and Ionic Strength on Endotoxin-Triggered Ordering Transitions in Liquid Crystalline Droplets*

5.1 Introduction

Past studies have established that the presence and organization of amphiphiles at interfaces formed between liquid crystals (LCs) and immiscible aqueous phases can influence the orientational ordering of the LCs.[1, 2] For example, in systems containing LC confined to micrometer-sized droplets, it has been demonstrated that spontaneous adsorption of synthetic surfactants or lipids to the interfaces of the LC droplets can induce a bipolar-to-radial ordering transition, where the preferred alignment of the LC at the interface changes from planar (parallel, Figure 5-1A) to homeotropic (perpendicular, Figure 5-1B).[3-6] These ordering transitions within LC droplets have been attributed to adsorbate-induced changes in the orientation-dependent part of the interfacial energy of the LCs (so-called anchoring energy).[3-6] To change the anchoring energy to induce such an ordering transition, a coverage of the interface by adsorbate of 0.1 to 1 Langmuir is typically required.[3, 4, 7-9] More recently, however, we have reported on bipolar-to-radial ordering transitions within micrometer-sized droplets of nematic 4'-pentyl-4-cyanobiphenyl (5CB) dispersed in aqueous solutions that are driven by the presence of the bacterial lipopolysaccharide endotoxin at interfacial concentrations that are at least five orders of magnitude lower than the concentration required for saturation coverage (10^{-5} Langmuir)(Chapter 4).[10] Such surface concentrations are well below those that lead to ordering transitions through uniform changes in anchoring energies.

The endotoxin used in the experiments reported above is comprised of a six-tailed glycophospholipid (called lipid A) in addition to two polysaccharide domains.[11] Several observations reported in our prior study hint at the origins of the endotoxin-triggered ordering transitions in the LC droplets.[10] First, the ordering transitions induced by endotoxin at pg/mL concentrations were observed only when the LC was confined within micrometer-sized droplets. Specifically, ordering transitions were not observed when using planar, micrometer-thick films of 5CB (slab geometry) at comparable concentrations (pg/mL) of endotoxin. Second, the characteristic time-scales of the endotoxin-triggered ordering transitions were measured to be comparable to the times required for diffusion of endotoxin across the surfaces of the 5CB droplets, as would be required for localized association of the endotoxin on the droplet. Third, we observed pg/mL concentrations of endotoxin to induce the ordering transitions in the LC droplets through a kinetic pathway (series of transition states) that was different from that observed with adsorbates that induce changes in the anchoring energy of the LC droplets, thus providing further support for our conclusion that the ordering transitions in the LC droplets caused by pg/mL concentrations of endotoxin are not driven by uniform changes in anchoring energy.[3-5] Finally, we demonstrated that endotoxin partitions to the center of LC droplets in the radial configuration (through the use of confocal microscopy with a fluorescently labelled endotoxin molecule), suggesting that endotoxin may be self-assembling at the locations of defects that form in LC droplets with radial configurations.[12-14] While these past observations provide insight into the origins of endotoxin-triggered ordering transitions, a full understanding of the phenomenon is yet to be established. Herein we report an investigation that advances this understanding by examining the role of LC droplet size and aqueous solution conditions on the ordering transitions.

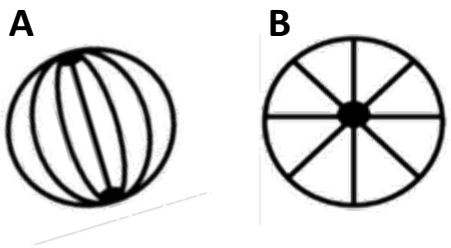

Figure 5-1. Schematic illustrations of the orientational ordering of LC within a droplet in a (A) bipolar configuration and the (B) radial configuration.
In a bipolar configuration LC is oriented parallel to the interface of the droplet and two diametrically opposite surface point defects (called boojums) are present at the poles of the droplet, whereas in the radial configuration LC is oriented perpendicular to the interface of the droplet and a defect is present at the core of the droplet.

A number of past publications have reported analyses of the energetics of LC droplets by considering the equilibrium director configuration to be governed by surface anchoring and bulk elastic energies.[14] When the easy axis of the LC is tangential to the droplet surface and the bulk elastic energy density is modelled using splay (K_{11}), twist (K_{22}), and bend (K_{33}) elastic constants[15], the contributions of surface anchoring and bulk elastic energies to the overall free energy of the LC droplet stabilizes the bipolar configuration relative to the radial configuration, independent of droplet size. However, recent experimental and theoretical studies have also revealed the saddle-splay elastic constant (K_{24}) to play an important role in determining the equilibrium director configuration of LC droplets.[6, 16, 17] For example, polymer-encapsulated 5CB droplets were observed to change from bipolar to radial configurations as the diameters of the droplets decreased, consistent with the effects of K_{24}.[6] This result is important because it indicates that there exists a narrow range of LC droplet sizes in which K_{24} causes radial and bipolar droplets to be almost energetically degenerate (see below for additional details). As

reported below, it is for LC droplets close to this size range that we observe endotoxin-driven ordering transitions in the pg/mL concentration range.

In this chapter, motivated by the above considerations, we first report a series of experiments that investigated the influence of LC drop size on the endotoxin-triggered ordering transitions. These studies reveal a strong dependence on LC droplet size, consistent with the influence of K_{24} on the elastic energies of the LC droplets. In addition, we investigated the effects of changes in the ionic strength and pH of the aqueous phase in which the LC droplets were dispersed, which we interpret in terms of changes in anchoring energies.[18] We place these results within the context of a simple thermodynamic model that leads to an estimate of the extent to which the association of endotoxin with LC droplets perturbs the energetics of the droplets.

5.2 Experimental Section

Materials. Endotoxin (from *E.coli* O127:B8) was purchased from Sigma-Aldrich (St. Louis, MO). Sodium hydroxide (NaOH) and 85 wt% phosphoric acid (H_3PO_4) were obtained from Fisher Scientific (Pittsburgh, PA). The 4'-pentyl-4-cyanobiphenyl (5CB) was obtained from EM Sciences (New York, NY). *Limulus* amoebocyte lysate (LAL) reagent water was purchased from Associates of Cape Cod, Inc. (East Falmouth, MA). EndoTrap® Red Equilibration Buffer (described below as PBS buffer; 10 mM Na_2HPO_4/NaH_2PO_4, 80 mM NaCl, pH7.2; certified to contain a concentration of endotoxin of less than 0.02 EU/mL (~2 pg/mL)) and EndoTrap® Red 1/1 chromatography columns for endotoxin removal were purchased from Hyglos GmbH (Regensburg, Germany). Neptune pipette tips (no detectable endotoxin) were purchased from Continental Lab Product, Inc. (San Diego, CA). Polystyrene tubes (certificated nonpyrogenic

tubes) were purchased from Becton Dickinson Labware (Franklin Lakes, NJ). Fisher's Finest Premium Grade glass microscope slides and cover glass, and Wheaton glass 20 mL scintillation vials were obtained from Fisher Scientific (Pittsburgh, PA). Deionization of a distilled water source was performed with a Milli-Q system (Millipore, Bedford, MA) to give water with a resistivity of 18.2 MΩ•cm.

Preparation of LC Emulsions. The emulsions were formed by sequential sonication and vortex mixing of 2 μL of nematic 5CB in 1mL of PBS at 25°C. Three cycles each comprising 10 seconds of vortex mixing (at 2,500 rpm) and 10 seconds of sonication yielded milky white emulsions. The LC droplets were confirmed to exhibit bipolar configurations following sonication. The size distributions of the LC emulsion droplets were determined from optical micrographs using Image J (NIH, Bethesda, MD) software. The LC emulsions were observed visually to be stable against coalescence at least for 3 hours. The LC emulsions were used within 3 hours of preparation.

Preparation of Buffers. PBS buffers of different ionic strength were prepared by diluting PBS with LAL reagent water. Following dilution, the PBS was mixed with a vortex mixer at 2,500 rpm. Buffers of different pH were prepared by adjusting the pH of PBS with 1.0 and 0.1 M H_3PO_4 and NaOH solutions. The 1.0 and 0.1 M H_3PO_4 solutions were prepared by diluting the 85 wt% H_3PO_4 stock solution into Milli-Q water. The 1.0 and 0.1 M NaOH solutions were prepared by dissolving NaOH in Milli-Q water. After the pH adjustment and vortex mixing at 2,500 rpm, the buffers were passed three times through an EndoTrap® Red 1/1 chromatography column to remove endotoxin.

Preparation of Aqueous Dispersions of Endotoxin. Powdered endotoxin was dissolved in PBS at room temperature. After addition of the endotoxin powder to obtain a concentration of 20 μg/mL, each solution was mixed by vortexing at 2,500 rpm for 4 minutes. Serial dilutions were performed to reach a final concentration of either 10 pg/mL or 100 pg/mL. After dilution, each solution was vortexed for an additional 45 seconds. For experiments measuring the effect of ionic strength on the response of LC droplets to the presence of endotoxin, the final dilution step, to reach 10 pg/mL endotoxin, was performed in PBS of different ionic strengths. Similarly, for experiments measuring the effect of pH, the final dilution step, to reach 100 pg/mL endotoxin, was performed in PBS buffers of different pH.

Optical Characterization of LC Droplets by Polarized Light Microscopy. A volume of 40 μL of an aqueous dispersion of endotoxin in PBS was dispensed onto a glass coverslip. A volume of 4 μL of an LC emulsion, prepared as described above, was added to the endotoxin dispersion to produce a sample containing 94,000 LC droplets. The ordering within the LC droplets was characterized 2 minutes after introducing the LC emulsion to the 100 pg/mL endotoxin solution to allow observation of larger droplets before the droplets sedimented to the bottom of the sample. The configurations of the LCs within the emulsion droplets were determined by observation of the droplets under an Olympus IX71 inverted microscope (Center Valley, PA) using an objective power of 100x (an oil lens). Polarized light micrographs of the LC emulsions were collected with a Hamamatsu 1394 ORCAER CCD camera (Bridgewater, NJ) connected to a computer and controlled through SimplePCI imaging software (Compix, Inc., Cranberry Twp., NJ). As described in detail elsewhere, we characterized LC droplets that were at least 50 μm

above the surface of the coverslip and translating with velocities greater than 1 μm/s to avoid observation of droplets interacting with the surfaces of the coverslips.[19] The droplets were diffusing (translating and rotating) – thus a radial droplet has an optical appearance that is invariant with time when viewed between crossed polars, whereas the bipolar droplet has a distinct, time-varying optical appearance. Multiple images of each droplet were taken to determine the time-dependent optical texture of the droplet, and thus the director configuration.

Zeta Potential Measurements of LC Droplets. Zeta potential measurements required a larger sample volume than optical characterization of the LC droplets. Therefore, 0.5 mL of an LC emulsion was added to 5 mL of PBS to maintain the 1:10 emulsion to sample ratio employed during optical characterization (see above). Following sample preparation, the zeta potential of the LC droplets was measured using a Malvern Instruments Zetasizer 3000 HSa (Malvern, Worcestershire, UK).

5.3 Results

In our first set of experiments, we investigated the influence of LC droplet size on the director configuration of droplets of 4'-pentyl-4-cyanobiphenyl (5CB) dispersed in an immiscible aqueous phase, both in the absence and presence of endotoxin. In the experiments reported below, we added to the aqueous phase a concentration of endotoxin of 100 pg/mL and characterized droplets with diameters ranging from 2 μm to 20 μm. If it is assumed that all of the endotoxin present in the aqueous solution associates with the LC droplets in our experiments, 100 pg/mL of endotoxin corresponds to roughly 10^3 endotoxin molecules per LC droplet (for additional details see *Size Distribution of the LC Droplets* in the Supporting Information).

Furthermore, if the endotoxin was to adsorb to the surface of the LC droplets, a concentration of 100 pg/mL would lead to 10^{-5} of saturation coverage of the LC surfaces (saturation requires μg/mL concentrations of an adsorbate[3, 4, 7, 9, 10, 19]).

Our experiments were initiated by emulsifying (see above for details) nematic 5CB in a phosphate buffered saline solution (PBS buffer), certified to have < 2 pg/mL of endotoxin. The PBS contained 10 mM sodium hydrogen phosphate (Na_2HPO_4), and 80 mM sodium chloride (NaCl) with a pH of 7.2. In each experiment, 4 μL of the 5CB emulsion was added to a 40 μL volume of 100 pg/mL endotoxin in PBS supported on a coverslip for observation.[10] In the experiments reported below, we limited our observations to freely diffusing (rotating and translating) droplets that were located at least 50 μm above the surface of the coverslip to avoid the perturbing effects of interactions with the coverslip on the LC droplet configuration. These droplets possessed velocities of at least 1 μm/s.

We observed droplets with diameters larger than 2 μm to exhibit a bipolar configuration in the absence of endotoxin in solution.[10] For example, Figures 5-2A through 5-2D show bright field and polarized light micrographs of bipolar droplets with diameters of 6.5 ± 0.5 μm (Figures 5-2A and 5-2B) and 10.5 ± 0.5 μm (Figures 5-2C and 5-2D). A bipolar configuration is characterized by 5CB oriented tangentially to the droplet interface and two diametrically opposite surface point defects (called boojums) at the poles of the droplet (Figure 5-1A).[5, 20-22] Following the procedures employed in several previous reports, we identified droplets to be in a bipolar configuration by locating the boojums at the poles of the droplets (as indicated by the single-headed arrows in Figure 5-2).[5, 6, 10, 19] We emphasize that the droplets characterized in our study were diffusing (translating and rotating) in the aqueous solutions, resulting in a time varying optical appearance for droplets in the bipolar configuration (due to their lack of spherical

symmetry).[14] Therefore, the bright field and polarized light micrographs of bipolar droplets displayed in Figure 5-2 represent one of many possible optical textures, and were selected to demonstrate the presence of both boojums. Boojums scatter light, and thus they can be easily identified in bright field images (Figures 5-2A and 5-2C). The boojums can also be identified by their dark appearance when viewed between crossed polars (Figures 5-2B and 5-2D). Finally, we comment that under boundary conditions that impose a tangential alignment of LC at a droplet interface, two commonly observed director configurations are the bipolar and axial configurations.[20, 23] It has been demonstrated that the bipolar configuration is favored over an axial configuration when the ratio of the bend elastic constant (K_{33}) to the splay elastic constant (K_{11}) exceeds unity ($K_{33}/K_{11} > 1$).[23] Therefore, our observation of the bipolar configuration in the absence of endotoxin is consistent with the values of K_{33}/K_{11} reported in literature for 5CB, which range from 1.3 to 1.6.[24-26]

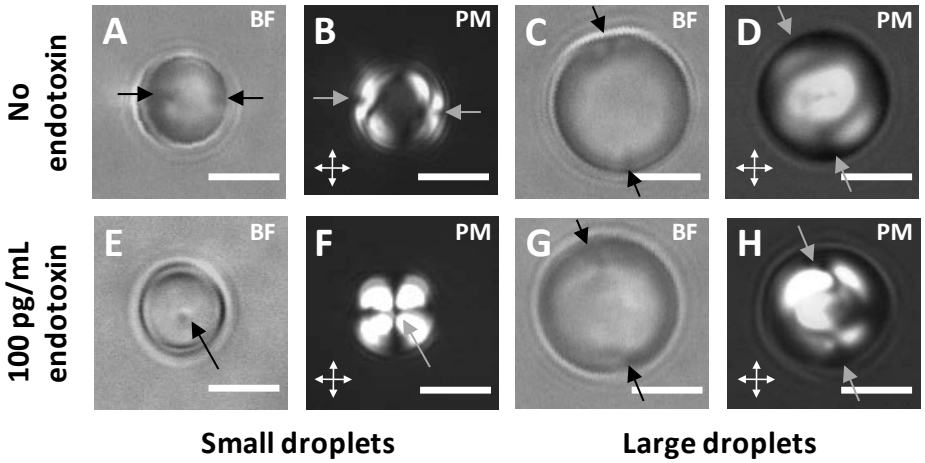

Figure 5-2. Influence of the size of 5CB droplets dispersed in PBS buffer (pH = 7.2) on the response of the droplets to the presence of 100 pg/mL endotoxin in solution.

(A-D) In the absence of endotoxin, droplets with diameters of 6.5 ± 0.5 μm (A and B) and 10.5 ± 0.5 μm (C and D) exhibit a bipolar configuration. (E-F) Upon addition of endotoxin, droplets with diameters of 6.5 ± 0.5 μm (E and F) undergo a bipolar-to-radial ordering transition, whereas a majority of droplets with diameters of 10.5 ± 0.5 μm (G and H) remain in the bipolar configuration. BF indicates a bright field micrograph and PM indicates a polarized light micrograph (crossed polars). The single headed arrows indicate the position of defects in the droplets and the double headed arrows indicated the orientation of the crossed polars. Scale bars, 5 μm.

In the presence of 100 pg/mL endotoxin, we observed a majority of LC droplets with diameters between 4 and 8 μm to undergo an ordering transition from a bipolar configuration to a configuration possessing radial (or close-to-radial, see below) symmetry, as characterized by optical microscopy. For example, Figures 5-2E and 5-2F show bright field and polarized light micrographs of droplets with diameters of 6.5 ± 0.5 μm that exhibit a radial configuration (Figure 5-1B).[3-5, 13] In contrast to droplets in the bipolar configuration, droplets in the radial configuration exhibited an optical appearance that was invariant (as the droplets undergo rotational diffusion) over time.[14] We make three additional comments regarding the radial configurations of the LC droplets. First, while the observations by optical microscopy revealed

the configuration of the LC droplets to be radial, past simulation-based studies have reported that defects with various structures (*e.g.*, point defect or disclination ring) can form at the centers of droplets that exhibit overall radial configurations.[27, 28] The sizes of these defects, however, are smaller than the resolution of our microscope, and thus we do not resolve the structure of these defects in our measurements.[29, 30] Second, consistent with previous studies, we observed many of the droplets in our experiments to exhibit optical appearances that indicated the presence of distorted radial configurations. This was particularly true for larger droplets (see Supporting Information Figure 5-S2[†]).[27-30] For example, when the diameters of the droplets exceeded 5 μm, we observed the extinction bands present in polarized light micrographs of several droplets to exhibit a slight twist relative to the orientation of the crossed polars, indicating the formation of twist deformations in the LC emanating from the centers of the droplets. Third, and most significantly, we observed that a majority of the LC droplets with diameters larger than 10 μm did not undergo an ordering transition in the presence of 100 pg/mL endotoxin (they remained in a bipolar configuration). Figures 5-2G and 5-2H show bright field and polarized light micrographs of 10.5 ± 0.5-μm-diameter 5CB droplets in the presence of 100 pg/mL endotoxin.

To provide insight into the origin of the key, third observation reported above, we quantified the percentage of droplets exhibiting the radial (or near-radial) configuration, in the presence of 100 pg/mL endotoxin, as a function of droplet diameter by creating a histogram with a bin width of 2 μm for droplets with diameters ranging from 2 μm to 10 μm (Figure 5-3). Droplets with a diameter larger than 10 μm were grouped together into the final bin. Droplets that were not observed to exhibit the radial configuration were mainly observed to exhibit the bipolar configuration (see Supporting Information Figure 5-S3[†]). Inspection of Figure 5-3 reveals that 98 ± 1 % of the droplets with diameters between 2 and 4 μm exhibit radial ordering.

However, as the diameter of the droplets increased, we observed the percentage of droplets with a radial configuration to decrease from 95 ± 3 % to 43 ± 12 % for droplets with diameters of 5 ± 1 μm and 9 ± 1 μm, respectively. Droplets with diameters greater than 10 μm were insensitive to the presence of endotoxin (less than 5 % of the droplets underwent an ordering transition to a radial configuration). As discussed in detail below, this dependence on droplet size is consistent with our hypothesis that endotoxin-triggered ordering transitions occur in a size regime where the contributions of the elastic and surface anchoring energies to the free energies of the bipolar and radial droplets are nearly balanced. Specifically, the absence of the ordering transition in droplets with sizes larger than 10 μm suggests that, for droplets in this size range, the effects of the surface anchoring energy (which promote the bipolar configuration) cannot be overcome by the interactions of endotoxin with the LC droplets.

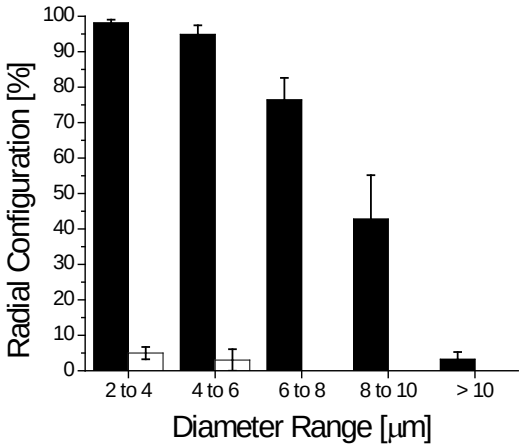

Figure 5-3. Histogram of the size-dependent response of 5CB droplets to the presence of 100 pg/mL endotoxin in PBS buffer, pH = 7.2.

The percentage of 5CB droplets that exhibited a radial configuration both in the presence (solid bar) and absence (open bar) of 100 pg/mL endotoxin is plotted for each droplet diameter range. No 5CB droplets were observed to exhibit a radial configuration in the absence of 100 pg/mL endotoxin above a diameter of 6 μm.

As discussed in the Introduction (and detailed below), the size-dependent scaling of elastic and surface anchoring energies leads to the prediction that there should also be a spontaneous transition to a radial configuration *in the limit of small droplet size in the absence of endotoxin*.[6] As shown in Figure 5-3, when 5CB droplets were dispersed in PBS buffer with pH = 7.2, however, we did not observe droplets within the experimentally observable size range (sizes as small as 2 μm) to exhibit a spontaneous transition to a radial configuration in the absence of endotoxin. This result suggests that the size-dependent transition to the radial configuration (in absence of endotoxin) for LC droplets dispersed in PBS at pH 7.2 occurs at a size below 2 μm. When the pH of the buffer was raised to 12.8, however, we did observe LC droplets with diameters less than approximately 3 ± 1 μm to exhibit the radial configuration and LC droplets with sizes greater than 3 ± 1 μm to exhibit the bipolar configuration (see Supporting Information Figure 5-S4[†]). This result is discussed further in the context of a simple thermodynamic model that is presented below.

In light of the influence of LC droplet size on the endotoxin-triggered ordering transitions, we hypothesized that changes in the surface anchoring energy of the 5CB droplets should also lead to changes in the fraction of droplets that undergo endotoxin-induced ordering transitions. In the experiments reported in this chapter, we tested this hypothesis by exploiting the results of a recent study that demonstrated that the presence of simple electrolytes in bulk aqueous solution can generate an electrical double layer on the LC-side of the aqueous—LC interface to change the anchoring energy of the LC.[18] Specifically, the electric field associated with the double layer exerts a torque on the LC to promote an alignment of the axis of the molecules with the highest dielectric constant (the long axis in the case of 5CB) parallel to the field. Previously, it has been shown that as the ionic strength or pH of the bulk aqueous solution

is increased, the torque changes the surface anchoring energy, leading ultimately to a transition from tangential to homeotropic ordering at the aqueous—5CB interface.[18] In the experiments reported below, we altered the anchoring energy of the 5CB droplets by changing the ionic strength and pH of the PBS buffer.

First, we investigated the role of the ionic strength of the buffer on the ability of 5CB droplets to undergo an ordering transition in the presence of endotoxin. To initiate our investigation, we dispersed 5CB droplets in increasingly dilute solutions of PBS buffer containing endotoxin, and measured the percentage of the droplets in the radial configuration. Upon dilution, we confirmed that the pH of each solution remained at 7.2. We limited our observations to droplets with diameters between 4 and 6 μm because, as reported in Figure 5-3, this size range leads to endotoxin-triggered ordering transitions in PBS at pH 7.2 with an ionic strength of 90 mM. The total ionic strength of each dilution, as well as the ionic strength of each component in the PBS buffer is shown in the Supporting Information (see Supporting Information Table 5-S1[†]). Inspection of Figure 5-4 reveals that the percentage of 5CB droplets observed to undergo an endotoxin-triggered ordering transition to a radial configuration decreased with decreasing ionic strength. For example, the fraction of droplets exhibiting the radial configuration was 80 ± 2 % at an ionic strength of 90 mM, and it was measured to decrease to 2 ± 2 % at an ionic strength of 9 mM.

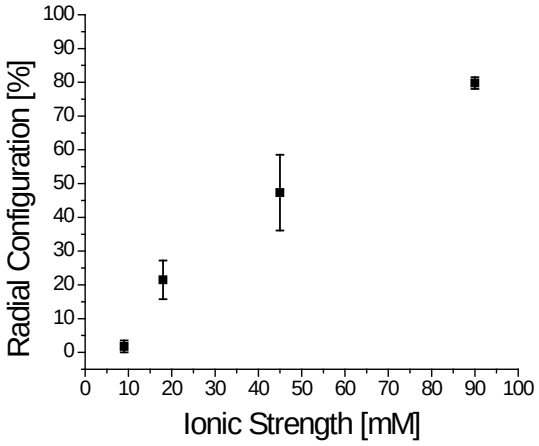

Figure 5-4. Percentage of 5CB droplets that exhibited a radial configuration in 40 μL of PBS buffer containing 10 pg/mL of endotoxin, plotted as a function of the total ionic strength of the PBS buffer solution.

The droplets analyzed had diameters of 4 to 6 μm. Note that we demonstrated previously that LC droplets in PBS at pH 7.2 (ionic strength of 90 mM) exhibit a radial configuration in the presence of 10 pg/mL of endotoxin.[10]

The results shown in Figure 5-4 are consistent with the predicted effect of ionic strength on the anchoring energy of the 5CB at the aqueous—LC interface. Specifically, our prior study demonstrated that a decrease in the ionic strength of the aqueous phase increases the Debye screening length of the electrical double layer on the LC-side of an aqueous—LC interface.[18] This increase in Debye screening length weakens the extent to which the double layer promotes the homeotropic orientation. The loss of the endotoxin-induced ordering transition upon decrease in the ionic strength of the buffer is consistent with an increase in strength of the anchoring of LC in an orientation that is tangential to the surface of the LC droplet.

Next, we investigated the effect of the pH of the buffer on the endotoxin-induced ordering transitions. Droplets of 5CB were dispersed in PBS buffer containing 100 pg/mL of

endotoxin with pH values of 5.0, 6.0, 7.0, 7.2, and 8.0. Again, we characterized the ordering of LC within droplets with diameters ranging between 4 and 6 μm. In endotoxin solutions with pH values between 7.0 and 8.0, we observed ~95 % of the droplets to undergo an ordering transition to a radial configuration (Figure 5-5). However, we observed the fraction of droplets in the radial configuration to decrease with pH below 7.0. For example, in endotoxin solutions with a pH of 6.0 and 5.0, we observed 85 ± 3 % and 52 ± 1 % of the droplets to undergo an ordering transition to a radial configuration, respectively. These results can also be interpreted in terms of the impact of pH on the charging of the aqueous—LC interface, and thus the contribution of an associated electrical double layer to the anchoring energy of the 5CB at the interface. Consistent with this interpretation, Figure 5-6A shows that the aqueous—LC interface acquired a less negative potential at the aqueous shear-plane as a function of decreasing pH. Over the range of ionic strengths reported in Figure 5-4, however, the change in the zeta-potential was small compared to the uncertainty in the experimental measurement (Figure 5-6B). We also comment that the zeta potential characterizes the electrical double layer on the aqueous side of the interface whereas the anchoring energy of the LC is influenced by the electrical double layer on the LC side of the interface.[18] We refer the reader to a past publication that discusses this point in detail.[18]

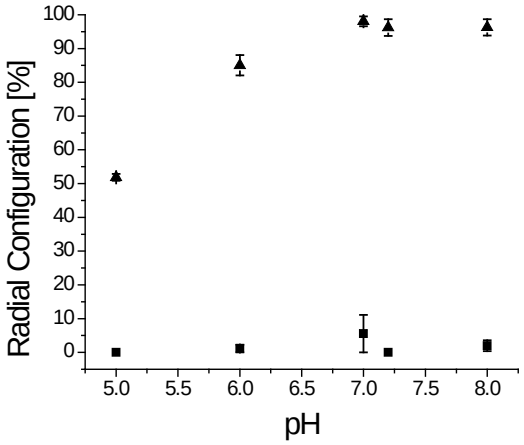

Figure 5-5. Percentage of 5CB droplets that exhibited a radial configuration in 40 µL of PBS buffer containing either (♦) 100 pg/mL of endotoxin or (■) no endotoxin, plotted as a function of the pH of the PBS buffer solution.

The droplets analyzed had diameters of 4 to 6 µm.

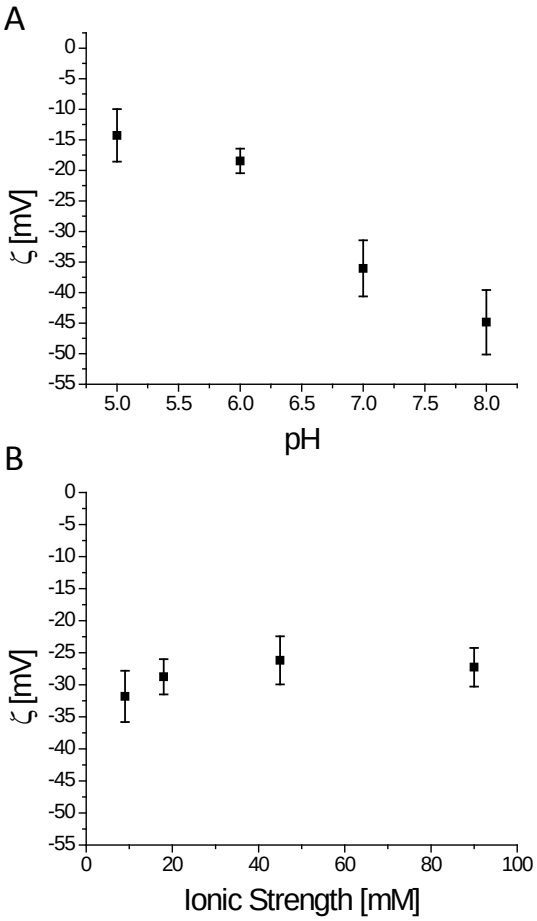

Figure 5-6. Zeta potential (ζ) potential of 5CB droplets in PBS buffer as function of the pH or ionic strength of the buffer.

(A) Zeta potential of 5CB droplets in PBS buffer with an ionic strength of 90 mM plotted as a function of the pH of the buffer. (B) Zeta potential of 5CB droplets in PBS buffer with pH = 7.2 plotted as a function of the percentage of the total ionic strength of the PBS buffer.

5.4 Discussion

The results presented above reveal that the percentage of water-dispersed, micrometer-sized droplets of 5CB that undergo an ordering transition from a bipolar to a radial configuration in the presence of pg/mL concentrations of endotoxin decreases with increasing droplet size.

Additionally, decreasing the ionic strength or pH of the aqueous phase also causes a decrease in the fraction of droplets that undergo the ordering transition in response to pg/mL concentrations of endotoxin; an effect that we associate with changes in the surface anchoring energy of the droplets. Below, we discuss these results in the context of a simple thermodynamic model for the endotoxin-triggered bipolar-to-radial ordering transitions in micrometer-sized LC droplets. We discuss the impact of droplet size, and the ionic strength and pH of the aqueous phase on the various contributions to the free energies of the LC droplets.

We consider the free energy of a LC droplet (F) to be described as

$$F = \int_S f_\mathrm{s} dA + \int_V f_\mathrm{e} dV + \int_{V_\mathrm{d}} f_\mathrm{d} dV_\mathrm{d} \qquad (5\text{-}1)$$

where A is the surface area of a droplet, V is the volume of a droplet, and f_s and f_e are the surface anchoring energy and elastic free energy densities, respectively.[14] We also note that we include a term in equation 5-1 that describes the self-association of endotoxin with the LC droplet (f_d),[10] where V_d is a volume that encompasses the endotoxin (see below for additional details). In the above expression, the surface anchoring energy density can be approximated using the single-constant Rapini and Papoular form

$$f_s = \frac{1}{2} W \sin^2 \varphi \qquad (5\text{-}2)$$

where φ is the angle between the director ($\boldsymbol{n}$) and the preferred orientation of the LC at the interface (easy axis), and W is surface anchoring energy per unit area.[31] The elastic free energy density is given by the Frank-Oseen equation

$$f_\mathrm{e} = \frac{1}{2}\big[K_{11}(\nabla \cdot \boldsymbol{n})^2 + K_{22}(\boldsymbol{n} \cdot \nabla \times \boldsymbol{n})^2 + K_{33}(\boldsymbol{n} \times \nabla \times \boldsymbol{n})^2 - K_{24}\nabla \cdot \big(\boldsymbol{n} \times \nabla \times \boldsymbol{n} + \boldsymbol{n}(\nabla \cdot \boldsymbol{n})\big)\big] \qquad (5\text{-}3)$$

where K_{11}, K_{22}, K_{33} and K_{24} are the splay, twist, bend, and saddle-splay elastic constants, respectively.[15, 17, 32] In the above expression, we have neglected the contribution from the splay-bend elastic constant (K_{13}) because it involves higher order derivatives of $\boldsymbol{n}$.[33, 34]

First we consider the energetics of the LC droplets in the absence of endotoxin. Recent theoretical studies predict that K_{24} is important in determining the equilibrium director configuration of LC droplets.[6, 16, 17] Specifically, the free energy of a droplet in a radial configuration (F_{r}) can be approximated using equations 5-1 through 5-3 as

$$F_{\mathrm{r}} = 8\pi K_{11} R - 4\pi K_{24} R + 2\pi W R^2 \qquad (5\text{-}4)$$

The first term is associated with splay deformation within the LC droplet, and the third term is the energetic penalty associated with a homeotropic orientation of the LC at the droplet interface (when the easy axis is tangential).[6] The second term is associated with saddle-splay deformation of the LC, and favors the radial configuration.[6, 17] The tendency of K_{24} to lower the elastic free energy penalty associated with the radial configuration gives K_{24} a central role in determining the relative stability of radial and bipolar configurations.[6, 16, 17]

Adding the contribution of K_{24} to the expression derived by Dubois-Violette and Parodi,[13] the free energy of a droplet with a bipolar configuration (F_{bp}) can be approximated as

$$F_{\mathrm{bp}} = 5\pi K_{11} R - 2\pi K_{24} R \qquad (5\text{-}5)$$

where K_{11} and K_{33} are assumed to be approximately equal in magnitude. In equation 5-5, there is no contribution from the anchoring energy because in aqueous solutions free of adsorbates the preferred orientation of the LC is tangential to the interface ($\varphi = 0$).[5, 6, 10]

The change in free energy upon transforming a LC droplet from a bipolar configuration to a radial configuration ($\Delta F^{\mathrm{bp}\rightarrow\mathrm{r}}$) can be obtained from equations 5-4 and 5-5 as

$$\Delta F^{\mathrm{bp}\rightarrow\mathrm{r}} = 3\pi K_{11}R - 2\pi K_{24}R + 2\pi WR^2 \qquad (5\text{-}6)$$

The model predicts several key behaviors consistent with our experimental observations in the absence of endotoxin. First, when the value of K_{24} exceeds 1.5 times the value of K_{11} ($K_{24} > 1.5K_{11}$), the contribution of the elastic energy to $\Delta F^{\mathrm{bp}\rightarrow\mathrm{r}}$ favors the radial configuration over the bipolar configuration. Experimental measurements of K_{24} for 5CB suggest it is possible to meet this criterion.[25, 35-37] For example, through the use of polarized light microscopy, Polak *et al*. optically determined an apparent value of K_{24} to be 3.1 times the value of K_{11} in systems containing 5CB confined to capillary tubes.[25] Although this value exceeds the so-called Ericksen limit ($K_{24} \leq 2K_{11}$),[38] we note that a value of $1.5K_{11} < K_{24} \leq 2K_{11}$ stabilizes the radial configuration. We also note that equation 5-6 is approximate (see above) and should not be expected to quantitatively predict the behavior of the system.

When the contribution of the elastic energy to $\Delta F^{\mathrm{bp}\rightarrow\mathrm{r}}$ favors the radial configuration, adoption of the radial configuration by the LC droplet requires that it overcome the anchoring energy (equation 5-6). The model predicts, therefore, that the contributions of the elastic and anchoring energy to $\Delta F^{\mathrm{bp}\rightarrow\mathrm{r}}$ will balance at a critical radius defined by $R_c = (K_{24} - 1.5K_{11})/W$. Below R_c, the radial configuration possesses a lower free energy whereas above R_c, the bipolar configuration corresponds to the lower free energy configuration. This prediction of the model is consistent with our previous observation of a bipolar-to-radial ordering transition within polymer-encapsulated 5CB droplets when the diameters of the droplets were below approximately 800 nm.[6] Using this value of the critical radius and a value of $K_{24} = 1.53K_{11}$, we calculate $W \approx 5.0 * 10^{-7}$ J/m^2 for polymer-encapsulated 5CB droplets. We note that this value of W corresponds to relatively weak anchoring conditions at the surfaces of the droplets.[14, 39, 40] In the present system, our results indicate that R_c falls below 1 μm for 5CB droplets dispersed in

PBS buffer at pH = 7.2 (Figure 5-3). However, when the pH of the buffer was raised to 12.8, a value of R_c of approximately 1.5 μm was observed (see Supporting Information Figure 5-S4). Similar to the polymer-coated 5CB droplets, this value of R_c results in an estimate of $W \approx 1.3 * 10^{-7}$ J/m^2.[6]

To describe the influence of endotoxin on the relative stability of the radial and bipolar configurations of the LC droplets, we modified equation 5-6 to

$$\Delta F^{\mathrm{bp}\rightarrow\mathrm{r}} = 3\pi K_{11}R - 2\pi K_{24}R + 2\pi W R^2 + \Delta F_{\mathrm{endotoxin}} \qquad (5\text{-}7)$$

where $\Delta F_{\mathrm{endotoxin}}$ describes the relative influence of endotoxin on the free energies of the radial and bipolar droplets (see equation 5-1). While very simple, this model yields several significant conclusions. First, as the size of the 5CB droplets increases above a threshold value of R, the balance between the elastic and anchoring energies will be lost because the contribution of the anchoring energy (proportional to R^2) will become dominant over the contribution of the elastic energy (proportional to R). Under these conditions, changes in the free energy due to the interactions of the LC droplets with endotoxin ($\Delta F_{\mathrm{endotoxin}}$) will no longer be sufficiently large to drive the ordering transition. Our observations presented in Figure 5-3 are consistent with this prediction, as droplets above a diameter of 10 μm did not undergo an ordering transition from a bipolar to a radial configuration in the presence of 100 pg/mL endotoxin (threshold radius of ~ 5 μm). Second, equation 5-6 can be combined with our experimental observations to estimate the magnitude of $\Delta F_{\mathrm{endotoxin}}$. At the threshold radius defined above (5 μm), the magnitude of $\Delta F_{\mathrm{endotoxin}}$ should be approximately equal to the combined contributions of the elastic and anchoring energies in equation 5-6. Insertion of this threshold radius into equation 5-6 along with $K_{24} = 1.53K_{11}$ and $W = 4.0 * 10^{-7}$ J/m^2 (corresponding to R_c = 500 nm) results in an estimate of $|\Delta F_{\mathrm{endotoxin}}|$ of approximately 10^{-17} J.

The above-described estimate of $|\Delta F_{\mathrm{endotoxin}}|$ is interesting to consider in light of past observations of accumulation of endotoxin at the center of LC droplets in the radial configuration.[10] Indeed, past studies with colloidal particles and blue phases of LCs have reached the conclusion that it is possible to stabilize blue phases *via* a "defect core replacement" mechanism.[41] The nanoparticles stabilize blue phases by displacing LC from the cores of topological defects, effectively reducing the large energetic penalty associated with the defects.[41] To determine if such a mechanism might give rise to an effect of order 10^{-17} J with endotoxin, we estimated the energy of a point defect as $E_{\mathrm{core}} \sim 4\pi/3\, r_{\mathrm{c}}^3 \varepsilon_{\mathrm{c}}$, where r_{c} is the radius of the core of the defect and ε_{c} is the free energy of melting a nematic phase to an isotropic phase.[42, 43] The size of the core can be calculated from the competing effects of the elastic energy density and melting energy density as $r_{\mathrm{c}} \sim (K/\varepsilon_{\mathrm{c}})^{0.5}$, resulting in $E_{\mathrm{core}} \sim 4\pi/3\, \varepsilon_{\mathrm{c}}^{-0.5} K^{1.5}$.[43] By approximating ε_{c} to be the same magnitude as the enthalpy of the nematic to isotropic transition (~10^6 J/m^3),[44] E_{core} is calculated to be on the order of 10^{-19} J, which is two orders of magnitude lower than the above-described experimental estimate of $|\Delta F_{\mathrm{endotoxin}}|$. This result suggests that the influence of endotoxin, if through localization at defects, is not simply *via* a "core replacement" mechanism, as has been proposed for the colloidal stabilization of blue phases of LCs over broad temperature ranges.[41, 45-47]

To provide further insight into the possible origin of the above-described experimental estimate of $|\Delta F_{\mathrm{endotoxin}}|$, we consider two observations from a previous study.[10] First, ordering transitions in LC droplets are triggered by pg/mL concentrations of endotoxin but not pg/mL concentrations of 1,2-dilauroyl-*sn*-glycero-3-phosphatidylcholine (DLPC), 1,2-dioleoyl-*sn*-glycero-3-phosphatidylcholine (DOPC), or synthetic surfactants such as sodium dodecyl sulfate (SDS).[10] The dependence of the ordering transitions on the lipid architecture of endotoxin leads

us to the hypothesis that self-assembly of endotoxin with the LC droplet drives the ordering transitions. Consistent with this hypothesis, we calculate the magnitude of the standard free energy of the self-association of 10^3 endotoxin molecules to be on the order of 10^{-17} J.[48, 49] Second, although occupation of the core of defects by endotoxin is insufficient to account for the magnitude of $|\Delta F_{\text{endotoxin}}|$, as noted above, accumulation of endotoxin at the location of the central defect in the LC droplets has been observed.[10] The magnitude of $\Delta F_{\text{endotoxin}}$, when combined with this past imaging, is consistent with the hypothesis that endotoxin lowers the energy of the radial configuration relative to the bipolar configuration through formation of an organized lipid assembly located at the center of the radial configuration. We note also, however, that the nanoscopic organization of the endotoxin at the center of the LC droplet is currently unknown, and that additional investigations are needed to validate this hypothesis.

A recent theoretical study predicts that the flexoelectricity of nematic LCs can induce an electrostatic potential at topological defects contained within LC droplets.[50] The presence of a positive electrostatic potential near the core of topological defects might provide some of the driving force for the localization of negatively charged endotoxin molecules at these defects.[10] The testing of this hypothesis is the focus of an ongoing investigation.

Finally, we note that the predictions of the above-described model for endotoxin-induced changes to the free energy of LC droplets are dependent on the LC anchoring energy. An increase in anchoring energy will decrease R_c, and thus for a given size of LC droplets, the fraction of droplets that undergo an ordering transition to the radial configuration in the presence of pg/mL concentrations of endotoxin is predicted to decrease. Our observations (Figures 5-4 and 5-5) are consistent with this prediction, as decreases in both the ionic strength and pH of PBS buffer led to a decreased fraction of 5CB droplets that undergo an ordering transition from a

bipolar to a radial configuration. As discussed in detail above, decreasing the ionic strength and pH of PBS buffer has been shown previously to increase the strength of anchoring of LC at the aqueous—LC interface in an orientation that is tangential to the interface due to a reduction in electrical double layer forces on the LC-side of the aqueous—5CB interface.[18] Overall, the results in Figures 5-4 and 5-5 are consistent with the prediction that the stronger anchoring of the LC in an orientation tangent to the aqueous—LC interface disrupts the near balance of elastic and anchoring energies necessary to observe an endotoxin-triggered ordering transition.

5.5 Conclusions

In summary, the experiments reported in this chapter advance our understanding of the origins of endotoxin-induced ordering transitions in micrometer-sized LC droplets that are triggered by pg/mL concentrations of endotoxin. Several key experimental results reported in this chapter support the proposition that the ordering transitions are observed under conditions where the contributions of the bulk elastic and surface anchoring energies to the free energy of LC droplets in the bipolar and radial configurations are close to degenerate. Specifically, we observe the ordering transitions induced by endotoxin to be strongly dependent on the size of the LC droplets and solution conditions that are expected to influence the surface anchoring energy of the LC at the aqueous interface (pH and ionic strength). These observations are consistent with a simple (order of magnitude) thermodynamic model that describes elastic and surface anchoring contributions to the LC droplet configurations. This model also yields an estimate of the endotoxin-induced change in the droplet free energy (approximately 10^{-17} J) required to cause an ordering transition. The magnitude of this term is much larger than a core defect energy but similar to the change in free energy associated with self-assembly of ~10^3 endotoxin molecules

with each LC droplet. When combined with prior reports of localization of endotoxin at the centers of LC droplets, these results are consistent with the proposition that self-assembly of endotoxin at the centers of LC droplets (of a narrow size range) can provide the driving force for the ordering transitions. In a broader context, the insights reported in this chapter advance the design of LC droplet systems as stimuli-responsive soft materials.

Acknowledgements

This work was primarily supported by NSF through DMR-1121288 (Materials Research Science and Engineering Center), the Army Research Office (W911NF-11-1-0251 and W911NF-10-1-0181), and the National Institutes of Health (CA108467 and CA105730). The authors would like to thank Samo Kralj, Slobodan Žumer, Tine Porenta and Oleg Lavrentovich for helpful discussions.

5.6 Supporting Information

Size Distribution of LC Droplets

We quantified the size distribution of the 5CB droplets used to obtain the results shown in Figure 5-3 by creating a histogram of the percentage of the droplets appearing in each size range (Figure 5-S1). The average diameter of the LC droplets was determined from our experiments to be 5.9 ± 0.4 μm. To calculate the average number of endotoxin molecules per LC droplet, we assumed a LC droplet diameter of 6 μm.

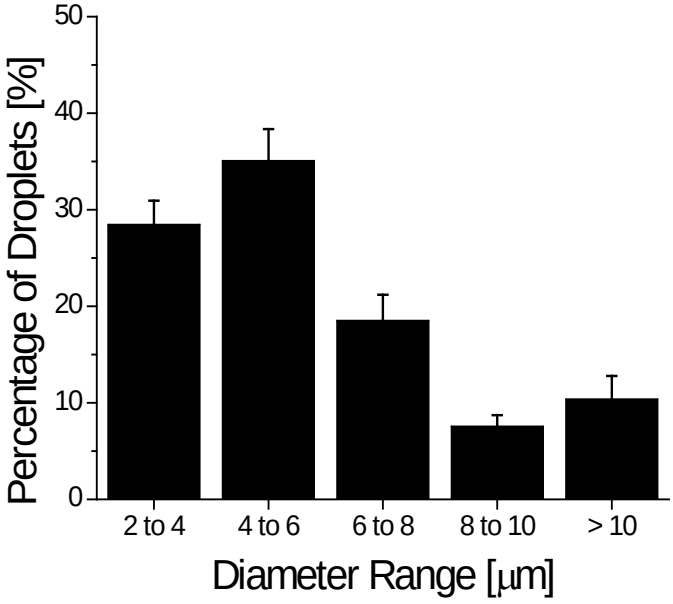

Figure 5-S1. Size distribution of the 5CB droplets used to obtain the results shown in Figure 5-3 of the main text.

The droplets were dispersed in PBS buffer, pH = 7.2.

Size-Dependent Changes in the Configurations of LC Droplets Induced by Endotoxin

Although LC droplets with diameters less than 10 μm exhibited configurations that were close to radial (outside of the central defect region that could not be imaged) in the presence of endotoxin, we also observed the precise ordering of the droplets to depart from an exact radial configuration. For example, Figure 5-S2 shows polarized light micrographs of 5CB droplets with different diameters in the presence of 100 pg/mL endotoxin in a phosphate buffered saline solution (PBS buffer) with an ionic strength of 90 mM and pH 7.2. Radial droplets with diameters as large as ~5 μm (Figures 5-S2A and 5-S2B) yielded polarized light micrographs with extinction bands approximately in line with the orientation of the crossed polars mounted on the microscope, suggesting radial symmetry of the LC confined within the droplets. However, the droplets with diameters above 5 μm gave rise to polarized light micrographs with extinction bands that were twisted with respect to the crossed polars, indicating the presence of a slightly twisted, radial configuration (Figure 5-S2C and D). When the diameters of the droplets were above 7 μm, polarized light micrographs of droplets revealed the formation of a small (~2 μm) region surrounding the core of the droplet with extinction bands that were twisted relative to the crossed polars (again indicating a twisting of the LC within this region) (Figure 5-S2E). Outside of this small region containing LC in a twisted configuration, the extinction bands in the polarized light micrographs were in line with the crossed polars, consistent with a radial symmetry of the LC within this region. The optical texture of the droplet displayed in Figure 5-S2E is similar to a texture reported in a study conducted by Lavrentovich and Terentjev for a LC droplet suspended in a glycerin matrix containing 10 wt% lecithin.[30] We also note that the optical appearance of the larger droplets is influenced by the relative location of the focal plane

and the equatorial plane of the droplets (the two are slightly displaced in D and E below). We refer the reader to references [3-5, 10, 27-30] for additional past studies of LC droplets.

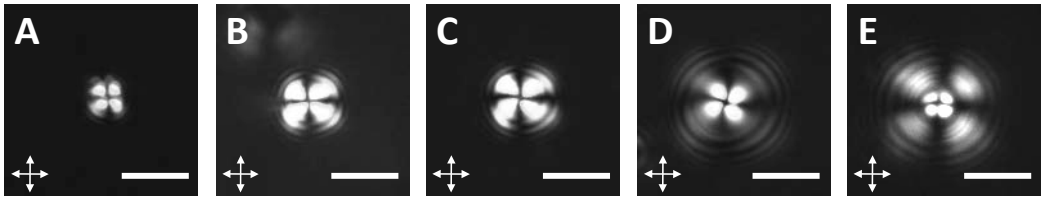

Figure 5-S2. Polarized light micrographs of radial 5CB droplets of different diameters in the presence of 100 pg/mL endotoxin in PBS buffer, pH = 7.2.

The diameters of the droplets are: (A) 2.6 μm, (B) 4.4 μm, (C) 5.2 μm, (D) 7.0 μm, and (E) 8.1 μm. The double-headed arrows indicate the orientation of the crossed polars. Scale bars, 5 μm.

Characterization of the Ordering within LC Droplets Dispersed in a 100 pg/mL Endotoxin Solution

Previously, we demonstrated that both preradial and escaped radial director configurations are observed transiently during the transition of a 5CB droplet from a bipolar to a radial configuration in the presence of pg/mL concentrations of endotoxin in solution.[10] Figure 5-S3 reports the percentages of droplets exhibiting the bipolar, transitional (either preradial or escaped radial), or radial configurations in the presence of 100 pg/mL endotoxin in PBS buffer with an ionic strength of 90 mM and pH 7.2 for the five diameter ranges presented in Figure 5-3 of the main text. The data presented in Figure 5-S3 corresponds directly to the solid black bars in Figure 5-3 of the main text. A majority of the droplets in each diameter range existed in either a bipolar or a radial configuration. Less than 20 % of the droplets in each size range were observed to exist in the transition states (preradial or escaped radial configuration). This result is consistent with our previous study and confirms that the preradial and escaped radial configurations are indeed transient intermediate states.[10]

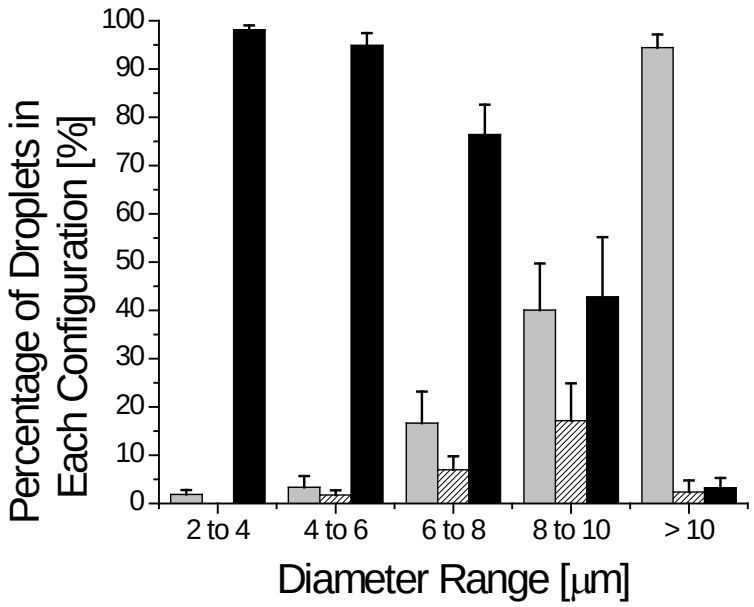

Figure 5-S3. Histogram of the size-dependent response of 5CB droplets to the presence of 100 pg/mL endotoxin in PBS buffer, pH = 7.2.

The percentages of 5CB droplets that exhibited a bipolar (grey bar), transition (preradial or escaped radial, striped bar), and radial (black bar) configuration in the presence of 100 pg/mL endotoxin are plotted for each droplet diameter range. The data corresponds to the solid black bars in Figure 5-3 of the main text.

Size-Dependent Ordering of LC Droplets as a Function of the pH of the Bulk Aqueous Phase

The percentage of 5CB droplets exhibiting a radial configuration when dispersed in PBS buffers, certified to contain < 2 pg/mL of endotoxin, was characterized at pH values ranging from 5.0 to 12.8 for droplets with diameters ranging from just below 1 μm to 10 μm (Figure 5-S4A). Below pH = 12.8, a majority of the droplets were not observed to exhibit a radial configuration. However, at pH = 12.8, 51 ± 10 % of the droplets were observed to exhibit a radial configuration. Additionally, at a pH of 12.8, the percentage of droplets exhibiting a radial configuration was quantified as a function of droplet diameter by creating a histogram with a bin width of 2 μm for droplets with diameters ranging from below 1 μm to 10 μm (Figure 5-S4B). Above a droplet diameter of 5 ± 1 μm, no droplets were observed to exhibit a radial configuration. In contrast, as the diameter of droplets was lowered from 5 ± 1 μm to 1 ± 1 μm, the percentage of droplets exhibiting a radial configuration was observed to increase from 29 ± 11 % to 97 ± 3 %.

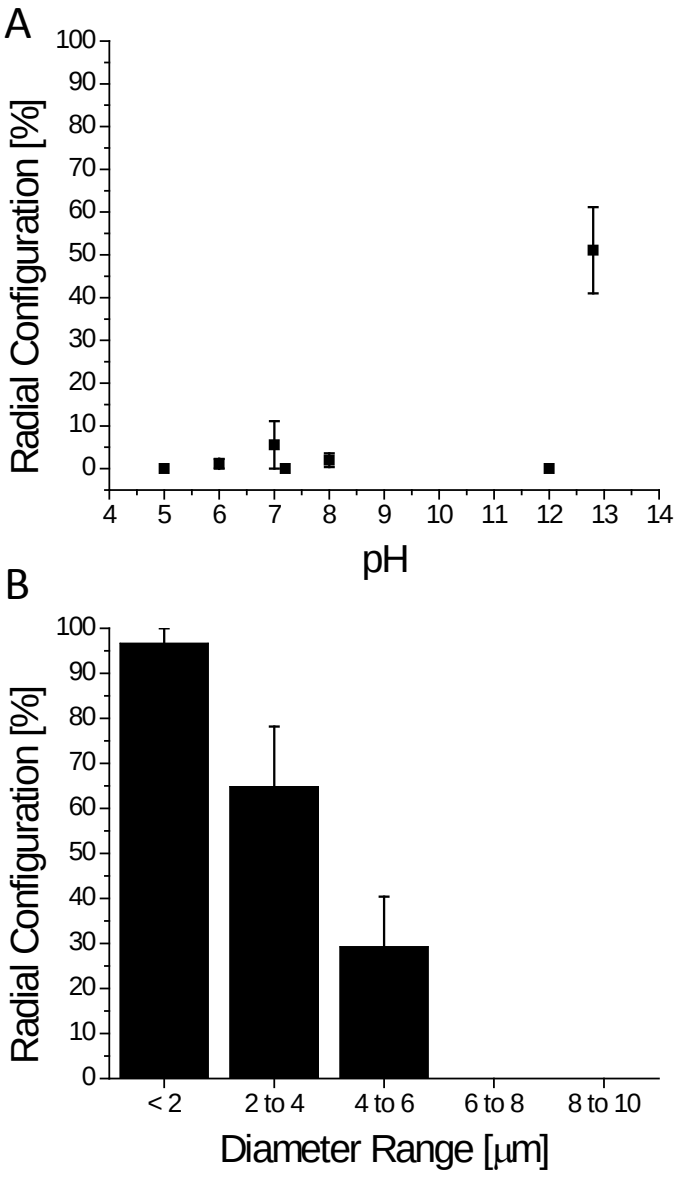

Figure 5-S4. Size-dependent ordering of 5CB droplets under alkaline solution conditions.

(A) Percentage of 5CB droplets in 40 μL of PBS buffer that exhibited a radial configuration in the absence of any added endotoxin, plotted as a function of the pH of the PBS buffer solution. (B) Histogram of the size-dependent ordering of 5CB droplets in PBS buffer with a pH = 12.8.

Ionic Strengths of the Components of PBS Buffer after Dilution

Table 5-S1 displays the total ionic strength of each dilution, as well as the ionic strength of each component in the PBS buffer for the data presented in Figure 5-4 of the main text.

Table 5-S1. Ionic strengths of the components of PBS buffer after dilution

Percentage of Initial Ionic Strength [%]	Ionic Strength of Na_2HPO_4 [mM]	Ionic Strength of NaCl [mM]	Total Ionic Strength [mM]
100	10	80	90
50	5	40	45
20	2	16	18
10	1	8	9

5.7 References

*This chapter was prepared as a Full Paper reporting original research in the journal *Soft Matter*. Reprinted (adapted) with permission from: Miller, D. S.; Abbott, N. L. Influence of Droplet Size, pH and Ionic Strength on Endotoxin-Triggered Ordering Transitions in Liquid Crystalline Droplets. *Soft Matter* **2013**, 9, 374-382. Copyright 2013 The Royal Society of Chemistry.

1. Lockwood, N. A.; Gupta, J. K.; Abbott, N. L., Self-Assembly of Amphiphiles, Polymers and Proteins at Interfaces between Thermotropic Liquid Crystals and Aqueous Phases. *Surface Science Reports* **2008**, 63, 255-293.
2. Bai, Y.; Abbott, N. L., Recent Advances in Colloidal and Interfacial Phenomena Involving Liquid Crystals. *Langmuir* **2011**, 27, 5719-5738.
3. Prischepa, O. O.; Shabanov, A. V.; Zyryanov, V. Y., Transformation of Director Configuration Upon Changing Boundary Conditions in Droplets of Nematic Liquid Crystal. *JETP Letters* **2004**, 79, 257-261.
4. Volovik, G. E.; Lavrentovich, O. D., The Topological Dynamics of Defects - Boojums in Nematic Drops. *Zhurnal Eksperimentalnoi I Teoreticheskoi Fiziki* **1983**, 85, 1997-2010.
5. Gupta, J. K.; Zimmerman, J. S.; de Pablo, J. J.; Caruso, F.; Abbott, N. L., Characterization of Adsorbate-Induced Ordering Transitions of Liquid Crystals within Monodisperse Droplets. *Langmuir* **2009**, 25, 9016-9024.
6. Gupta, J. K.; Sivakumar, S.; Caruso, F.; Abbott, N. L., Size-Dependent Ordering of Liquid Crystals Observed in Polymeric Capsules with Micrometer and Smaller Diameter. *Angewandte Chemie, nternational Edition* **2009**, 48, 1652-1655.
7. Brake, J. M.; Daschner, M. K.; Luk, Y. Y.; Abbott, N. L., Biomolecular Interactions at Phospholipid-Decorated Surfaces of Liquid Crystals. *Science* **2003**, 302, 2094-2097.
8. Rothblat, G. H.; Rosen, J. M.; Insull, W.; Yau, A. O.; Small, D. M., Production of Cholesteryl Ester-Rich, Anisotropic Inclusions by Mammalian-Cells in Culture. *Exp. Mol. Pathol.* **1977**, 26, 318-324.
9. Sivakumar, S.; Wark, K. L.; Gupta, J. K.; Abbott, N. L.; Caruso, F., Liquid Crystal Emulsions as the Basis of Biological Sensors for the Optical Detection of Bacteria and Viruses. *Advanced Functional Materials* **2009**, 19, 2260-2265.
10. Lin, I. H.; Miller, D. S.; Bertics, P. J.; Murphy, C. J.; de Pablo, J. J.; Abbott, N. L., Endotoxin-Induced Structural Transformations in Liquid Crystalline Droplets. *Science* **2011**, 332, 1297-1300.
11. Raetz, C. R. H.; Whitfield, C., Lipopolysaccharide Endotoxins. *Annual Review of Biochemistry* **2002**, 71, 635-700.
12. Lavrentovich, O. D., Topological Defects in Dispersed Liquid Crystals, or Words and Worlds around Liquid Crystal Drops. *Liquid Crystals* **1998**, 24, 117-125.
13. Dubois-Violette, E.; Parodi, E., Emulsions Nematiques. Effects De Champ Magnetiques Et Effects Piezoelectriques. *Journal de Physique (Paris)* **1969**, 30, 57-64.
14. Drzaic, P. S., *Liquid Crystal Dispersions*. World Scientific Publishing Company: River Edge, NJ, USA, 1995.
15. Frank, F. C., I. Liquid Crystals. On the Theory of Liquid Crystals. *Discussions of the Faraday Society* **1958**, 25, 19-28.

16. Kralj, S.; Zumer, S., Freedericksz Transitions in Supra-Mm Nematic Droplets. *Physical Review A* **1992**, 45, 2461-2470.
17. Zumer, S.; Kralj, S., Influence of K_{24} on the Structure of Nematic Liquid-Crystal Droplets. *Liquid Crystals* **1992**, 12, 613-624.
18. Carlton, R. J.; Gupta, J. K.; Swift, C. L.; Abbott, N. L., Influence of Simple Electrolytes on the Orientational Ordering of Thermotropic Liquid Crystals at Aqueous Interfaces. *Langmuir* **2012**, 28, 31-36.
19. Kinsinger, M. I.; Buck, M. E.; Abbott, N. L.; Lynn, D. M., Immobilization of Polymer-Decorated Liquid Crystal Droplets on Chemically Tailored Surfaces. *Langmuir* **2010**, 26, 10234-10242.
20. Meyer, R. B., Piezoelectric Effects in Liquid Crystals. *Physical Review Letters* **1969**, 22, 918-921.
21. Berggren, E.; Zannoni, C.; Chiccoli, C.; Pasini, P.; Semeria, F., Computer-Simulations of Nematic Droplets with Bipolar Boundary-Conditions. *Physical Review E* **1994**, 50, 2929-2939.
22. Ondriscrawford, R.; Boyko, E. P.; Wagner, B. G.; Erdmann, J. H.; Zumer, S.; Doane, J. W., Microscope Textures of Nematic Droplets in Polymer Dispersed Liquid-Crystals. *Journal of Applied Physics* **1991**, 69, 6380-6386.
23. Drzaic, P., A New Director Alignment for Droplets of Nematic Liquid-Crystal with Low Bend-to-Splay Ratio. *Molecular Crystals and Liquid Crystals* **1988**, 154, 289-306.
24. Kléman, M.; Lavrentovich, O. D., *Soft Matter Physics: An Introduction*. Springer: New York, NY, USA, 2003.
25. Polak, R. D.; Crawford, G. P.; Kostival, B. C.; Doane, J. W.; Zumer, S., Optical Determination of the Saddle-Splay Elastic-Constant K_{24} in Nematic Liquid-Crystals. *Physical Review E* **1994**, 49, R978-R981.
26. Karat, P. P.; Madhusudana, N. V., Elastic and Optical-Properties of Some 4'-N-Alkyl-4-Cyanobiphenyls. *Molecular Crystals and Liquid Crystals* **1976**, 36, 51-64.
27. Gartland, E. C.; Mkaddem, S., Instability of Radial Hedgehog Configurations in Nematic Liquid Crystals under Landau-De Gennes Free-Energy Models. *Physical Review E* **1999**, 59, 563-567.
28. Mkaddem, S.; Gartland, E. C., Fine Structure of Defects in Radial Nematic Droplets. *Physical Review E* **2000**, 62, 6694-6705.
29. Bodnar, V. G.; Lavrentovich, O. D.; Pergamenshchik, V. M., The Threshold for the Hedgehog - Ring Structural Transition in Nematic Drops in an Alternating Electric-Field. *Zhurnal Eksperimentalnoi I Teoreticheskoi Fiziki* **1992**, 101, 111-125.
30. Lavrentovich, O. D.; Terentiev, E. M., Phase-Transition with the Change of Symmetry of Topological Point-Defects (Hedgehogs) in a Nematic Liquid-Crystal. *Zhurnal Eksperimentalnoi I Teoreticheskoi Fiziki* **1986**, 91, 2084-2096.
31. Rapini, A.; Papoular, M., Distortion D'une Lamelle Nematique Sous Champ Magnetique Conditions D'ancrage Aux Parois. *Journal de Physique (Paris)* **1969**, 30, C4-54-C4-56.
32. Gennes, P.-G. d.; Prost, J., *The Physics of Liquid Crystals*. 2nd ed.; Oxford University Press: New York, NY, USA, 1993.
33. Allender, D. W.; Crawford, G. P.; Doane, J. W., Determination of the Liquid-Crystal Surface Elastic-Constant K_{24}. *Physical Review Letters* **1991**, 67, 1442-1445.
34. Goyal, R. K.; Denn, M. M., Orientational Multiplicity and Transitions in Liquid Crystalline Droplets. *Physical Review E* **2007**, 75, 021704-1-021704-10.

35. Crawford, G. P.; Allender, D. W.; Doane, J. W., Surface Elastic and Molecular-Anchoring Properties of Nematic Liquid-Crystals Confined to Cylindrical Cavities. *Physical Review A* **1992**, 45, 8693-8708.
36. Ondriscrawford, R. J.; Crawford, G. P.; Zumer, S.; Doane, J. W., Curvature-Induced Configuration Transition in Confined Nematic Liquid-Crystals. *Physical Review Letters* **1993**, 70, 194-197.
37. Sparavigna, A.; Lavrentovich, O. D.; Strigazzi, A., Periodic Stripe Domains and Hybrid-Alignment Regime in Nematic Liquid-Crystals - Threshold Analysis. *Physical Review E* **1994**, 49, 1344-1352.
38. Ericksen, J. L., Inequalities in Liquid Crystal Theory. *Physics of Fluids* **1966**, 9, 1205-1207.
39. Fukuda, J.; Zumer, S., Novel Defect Structures in a Strongly Confined Liquid-Crystalline Blue Phase. *Physical Review Letters* **2010**, 104, 017801-1-017801-4.
40. Ravnik, M.; Alexander, G. P.; Yeomans, J. M.; Zumer, S., Three-Dimensional Colloidal Crystals in Liquid Crystalline Blue Phases. *Proceedings of the National Academy of Sciences of the United States of America* **2011**, 108, 5188-5192.
41. Rozic, B.; Tzitzios, V.; Karatairi, E.; Tkalec, U.; Nounesis, G.; Kutnjak, Z.; Cordoyiannis, G.; Rosso, R.; Virga, E. G.; Musevic, I.; Kralj, S., Theoretical and Experimental Study of the Nanoparticle-Driven Blue Phase Stabilisation. *European Physical Journal E* **2011**, 34, 1-11.
42. Kleman, M.; Lavrentovich, O. D., Topological Point Defects in Nematic Liquid Crystals. *Philosophical Magazine* **2006**, 86, 4117-4137.
43. Ruhwandl, R. W.; Terentjev, E. M., Monte Carlo Simulation of Topological Defects in the Nematic Liquid Crystal Matrix around a Spherical Colloid Particle. *Physical Review E* **1997**, 56, 5561-5565.
44. Zhang, Z. X.; van Duijneveldt, J. S., Effect of Suspended Clay Particles on Isotropic-Nematic Phase Transition of Liquid Crystal. *Soft Matter* **2007**, 3, 596-604.
45. Coles, H. J.; Pivnenko, M. N., Liquid Crystal 'Blue Phases' with a Wide Temperature Range. *Nature* **2005**, 436, 997-1000.
46. Kikuchi, H.; Yokota, M.; Hisakado, Y.; Yang, H.; Kajiyama, T., Polymer-Stabilized Liquid Crystal Blue Phases. *Nature Materials* **2002**, 1, 64-68.
47. Nakata, M.; Takanishi, Y.; Watanabe, J.; Takezoe, H., Blue Phases Induced by Doping Chiral Nematic Liquid Crystals with Nonchiral Molecules. *Physical Review E* **2003**, 68, 041710-1-041710-6.
48. Israelachvili, J. N., *Intermolecular and Surface Forces*. 2nd ed.; Academic Press London: San Diego, CA, USA, 1991.
49. Hiemenz, P. C.; Rajagopalan, R., *Principles of Colloid and Surface Chemistry*. 3rd ed.; Marcel Dekker: New York, NY, USA, 1997.
50. Porenta, T.; Ravnik, M.; Zumer, S., Effect of Flexoelectricity and Order Electricity on Defect Cores in Nematic Droplets. *Soft Matter* **2011**, 7, 132-136.

Chapter 6. Analysis of the Internal Configurations of Droplets of Liquid Crystal Using Flow Cytometry*

6.1 Introduction

Recent studies demonstrate that micrometer-sized liquid crystalline droplets dispersed in water (*i.e.*, liquid crystal (LC)-in-water emulsions) can be employed to report the presence of a variety of different analytes based on adsorption of the analytes at the droplet interface and/or the self-assembly of analytes within the droplets.[1-4] For example, LC emulsions have been shown to form the basis of analytical methods for detection of lipids,[5-7] surfactants,[5, 8, 9] proteins,[5, 10-13] bile acids,[14] charged macromolecules,[15] bacteria,[16] and viruses[16] in aqueous solutions. Upon interaction with LC droplets, these analytes trigger changes in the configurations of the LC within the droplets (a so-called "ordering transition"), which results in changes in the optical properties of the droplets (*e.g.*, the LC droplets appear different when observed using polarized light microscopy before and after interaction with the analyte). One example of this phenomenon is an analyte-triggered bipolar-to-radial ordering transition. Prior to the transition, the LC droplets are dispersed in water in the absence of analyte and assume a bipolar director configuration.[5-9, 16] In this configuration, the LC (director) is aligned tangential to the droplet interface and two diametrically opposite point defects (so-called "boojums") are present at the poles of each LC droplet (Figure 6-1A,C).[5, 17-21] Upon interaction with an analyte such as a surfactant, the LC droplets transform to a radial director configuration,[5-9, 16] with the LC director aligned normal to the droplet surface, and a single point defect (hedgehog) is present at the core of each droplet (Figure 6-1B,D).[5, 18, 21, 22] Between these limiting conditions, LC droplets can

adopt a range of director configurations and defect types.[5, 6, 21-24] Here, we investigate the potential utility of flow cytometry for characterization of the configurations of LC droplets using model systems that contain mixtures of bipolar and radial droplets.

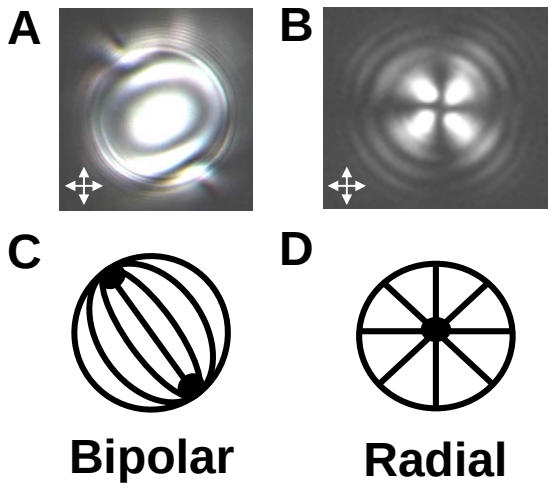

Figure 6-1. 4'-pentyl-4-cyanobiphenyl (5CB) droplets in a bipolar or radial configuration.
(A and B) Polarized light micrographs of a droplet of nematic 5CB dispersed in either (A) water or (B) aqueous 5 mM SDS. (C and D) Schematic illustrations of the director configurations within the (C) bipolar LC droplet imaged in (A), and the (D) radial LC droplet imaged in (B). The solid black lines within the droplet boundaries in (C) and (D) represent the orientation of the LC director and the black spots represent defects. Double headed arrows indicate the orientation of the crossed polars.

Although LC-in-water emulsions have been shown to possess attributes that make them promising systems for the detection and quantitation of a range of aqueous analytes, current methods for quantitation of the configurational states of the LC droplets are not optimal. Typically, quantitation has involved analysis of a large number of polarized light micrographs to determine the ordering within hundreds of LC droplets contained in emulsions.[6-8, 14, 15] This process is not well suited as the basis of an analytical method for three reasons. First, optical imaging and analysis of images of individual LC droplets is laborious (typically, hundreds of LC droplets must be analyzed to obtain statistically robust results). Second, obtaining easily

interpreted micrographs of water-dispersed LC droplets is difficult because the droplets are mobile, often translating at velocities greater than 1 μm/s (they quickly move out of the plane of focus).[25] Finally, LC droplets in water undergo sedimentation.[7, 25] A past study has observed that droplet—surface interactions that result from sedimentation of droplets onto surfaces can influence the configurations of LC droplets. [25] These challenges, when combined, motivated the study reported in this chapter in which flow cytometry is investigated as the basis of a high throughput method for characterization of the ordering of LCs within the droplets of LC-in-water emulsions.

Flow cytometry is widely used for analysis of mammalian and bacterial cells.[26-32] Typical analysis rates are thousands of cells per second. In flow cytometry, the objects to be characterized are focused hydrodynamically along the center-line of a capillary by injecting an aqueous dispersion of the objects into the center of a co-flowing stream of sheath fluid under laminar flow conditions.[28, 30, 31] After flow focusing, the objects pass through a beam of polarized light from a laser, and the intensity of light scattered by each object at both small (0.5−15°, so-called “forward scattering”; FSC) and large scattering angles (15−150°, “side-scattering”; SSC) is measured.[28, 30, 31] The light scattered by the objects (and the internal structure of the objects) gives rise to interference effects that are generally described by a form factor.[33, 34] At small detection angles, the form factor is nearly unity, and the intensity of the scattered light (*i.e.*, FSC) is approximately proportional to the volume of the object. At large detection angles (SSC), the scattering of light is more sensitive to interference effects arising from multiple scattering centers within the object and the form factor is nonunity. Thus, SSC in flow cytometry is generally viewed as being strongly influenced by the internal complexity of an object (*e.g.*, the granularity of a cell).[28, 30, 31]

Unlike biological cells, LC droplets are largely homogeneous in terms of material composition. However, LC droplets are strongly inhomogeneous optically. The director ***n*** that indicates the average orientation of molecules within the LC is also the local optic axis. Since LCs are birefringent, different internal configurations of the droplets result in different patterns of the optic axis and effective refractive indices. These differences manifest themselves in the scattering of light from micrometer and larger-sized LC droplets. Specifically, previous studies have established that bipolar and radial LC droplets exhibit different light scattering properties.[18, 35, 36] We hypothesized, therefore, that flow cytometry could be used to rapidly analyze director configurations of LC droplets contained in LC-in-water emulsions.

6.2 Experimental Section

Materials. 1,2-dilauroyl-*sn*-glycero-3-phosphocholine (DLPC) and 1,2-dipalmitoyl-*sn*-glycero-3-phosphocholine (DPPC) were purchased from Avanti Polar Lipids, Inc. Sodium dodecyl sulfate (SDS), cetyltrimethylammonium bromide (CTAB), endotoxin from *E. coli* O127:B8, chloroform, heptane, dodecane, benzonitrile, and the photo initiator 2-dimethoxy-2-phenyl acetophenone (DMPAP) were purchased from Sigma-Aldrich (St. Louis, MO). 4'-pentyl-4-cyanobiphenyl (5CB), octylcyanobiphenyl (8CB), and the reactive mesogenic monomer, 4-(3-acryloyloxypropyloxy) benzoic acid 2-methyl-1,4-phenylene ester (RM257) were obtained from EM Sciences (New York, NY). Neptune pipette tips were purchased from Continental Lab Product, Inc. (San Diego, CA). Polystyrene tubes (certificated nonpyrogenic tubes) were purchased from Becton Dickinson Labware (Franklin Lakes, NJ). Cargille immersion oil B, glass Hamilton syringes, 2 mL polypropylene graduated microcentrifuge tubes, 3 mL blunt syringes, Fisher's Finest Premium Grade glass microscope slides and cover glass, and Wheaton

glass 20 mL scintillation vials were obtained from Fisher Scientific (Pittsburgh, PA). EndoTrap® Red Equilibration Buffer (described below as PBS buffer; 10 mM Na_2HPO_4/NaH_2PO_4, 80 mM NaCl, pH 7.2) was purchased from Hyglos GmbH (Regensburg, Germany). Deionization of a distilled water source was performed with a Milli-Q system (Millipore, Bedford, MA) to give water with a resistivity of 18.2 MΩ cm.

Preparation of LC Emulsions. LC-in-water emulsions were prepared according to previously published procedures.[6, 7, 25] Briefly, the emulsions were formed by sequential sonication and vortex mixing of 4 μL of nematic 5CB in 1 mL of deionized, distilled water (referred to as Milli-Q water below) at 25°C. Five cycles each comprising 10 seconds of vortex mixing (at 2,500 rpm) and 10 seconds of sonication yielded milky white emulsions. This procedure results in a polydisperse population of LC droplets with diameters ranging from 1 to 15 μm (see Figure 6-S1 of the Supporting Information).[7, 37] To ensure that differences in polydispersity did not interfere with our characterization of the response of the LC droplets to analytes, we prepared a "stock" LC-in-water emulsion and divided it into aliquots. The aliquots were then added to solutions containing different analytes/concentrations. This ensured that the distribution of sizes of the droplets were similar in the comparative studies reported in this chapter.

Preparation of Isotropic Oil-in-Water Emulsions. Oil-in-water emulsions formed from isotropic oils were prepared by dispersing 4 μL of the isotropic oil in 1 mL of a 5.5 mM aqueous solution of SDS at 25°C. Note that the emulsions were formed in the presence of 5.5 mM SDS because bare isotropic oil droplets were observed to coalesce at a faster rate than the LC-in-water emulsions (several minutes compared to ~3 hours for LC-in-water emulsions;[6, 7, 37] unlike LC

droplets, droplets of isotropic oils do not possess an energy barrier associated with internal reorganization of LC during the process of coalescence,[38] and thus, they rapidly coalesce in the absence of surfactant). Five cycles each comprising 10 seconds of vortex mixing (at 2,500 rpm) and 10 seconds of sonication yielded isotropic oil-in-water emulsions.

Preparation of Aqueous Dispersions of Lipids. Aqueous dispersions of phospholipids (DLPC and DPPC) were prepared according to previously published methods.[5, 39] Briefly, the chloroform in which the phospholipids were initially dispersed was evaporated under a stream of nitrogen (N_2). Next, the vial containing the phospholipid was immediately placed under a vacuum for at least 1 hour. The dried lipid was then re-suspended in Milli-Q water to achieve a final concentration of 1.4 mM, and sonicated for 5 cycles of 1 minute at 12 W.

Aqueous dispersions of endotoxin were also prepared according to previous published methods.[6, 7] Powdered endotoxin was dissolved in PBS at 25°C. After addition of the endotoxin powder to obtain a concentration of 20 μg/mL, each solution was mixed by vortexing at 2,500 rpm for 4 minutes.

Preparation of Phospholipid-Coated LC Emulsions. The interfaces of LC droplets were decorated with phospholipid (1,2-dilauroyl-*sn*-glycero-3-phosphocholine (DLPC) or 1,2-dipalmitoyl-*sn*-glycero-3-phosphocholine (DPPC)) by equilibrating the LC droplets in an aqueous dispersion of vesicles for 1 hour. Prior to characterization of the resulting phospholipid-coated LC emulsions using flow cytometry, the droplets were rinsed three times in Milli-Q water to remove excess phospholipid from the bulk aqueous phase. The rinsing steps involved

sedimenting the coated LC droplets using centrifugation (5,000 rpm for 5 minutes), removing the resulting supernatant, and re-suspending the droplets in fresh Milli-Q water.

Optical Characterization and Flow Cytometry of Emulsions. Prior to characterization by flow cytometry, the LC emulsions were examined using a combination of bright field and polarized light microscopy to determine the ordering of the LC within the droplets. First, a 20 μL volume of the LC emulsion was dispensed onto a glass coverslip. Next, the configurations of the LCs within the emulsion droplets were determined by observation of the droplets under an Olympus IX71 inverted microscope (Center Valley, PA) using an objective magnification power of 100x (an oil-immersion lens).[6, 7, 37] Polarized light micrographs of the LC emulsions were collected with a Hamamatsu 1394 ORCAER CCD camera (Bridgewater, NJ) connected to a computer and controlled through SimplePCI imaging software (Compix, Inc., Cranberry Twp., NJ). Bright field micrographs were collected by removing the polarizer from the optical path of the microscope. We characterized LC droplets that were located at least 50 μm above the surface of the coverslip and translating with velocities greater than 1 μm/s to avoid observation of LC droplets interacting with the surfaces of the coverslips.[25] Because the droplets were diffusing (translating and rotating), radial droplets exhibited an optical appearance that was invariant with time when viewed between crossed polars, whereas bipolar droplets had a distinct, time-varying optical appearance.[37] Multiple images of each droplet were taken to determine the time-dependent optical appearance of the droplet, and thus the director configuration.

Following optical characterization, light scattering plots of the intensity of side light scattering (SSC) plotted against the intensity of forward light scattering (FSC) were obtained for both LC-in-water and isotropic oil-in-water emulsions using a BD Accuri C6 flow cytometer

(Ann Arbor, MI). FSC was measured at a detection angle of 0° ± 15°, and SSC was measured at a fixed detection angle of 90° ± 15°.[40] All flow cytometry measurements were performed at room temperature, and we are confident that any local heating of the LC droplets in the flow cytometer (*e.g.*, by the laser) did not disrupt the nematic phase of the droplets (see Supporting Information for more details). Unless indicated otherwise, in the experiments below, the emulsions were pumped through the flow cytometer at a flow rate of 14 μL/min and the scatter plots were constructed from the measurement of 50,000 LC droplets.

Flow Cytometry of LC Emulsions Containing Polymerized Droplets. As described previously,[41] 5CB was first doped with the reactive monomer, RM257 at 10% wt/wt and the photo initiator DMPAP at 5% wt/wt based on the mass of RM257. This mixture was used to prepare a LC-in-water emulsion following the procedure outlined above. Next, 100 μL of the emulsion was added to 1 mL of either Milli-Q water for bipolar droplets or a 5.5 mM aqueous solution of SDS for radial droplets. Then, light scattering plots of the intensity of side light scattering (SSC) plotted against the intensity of forward light scattering (FSC) were obtained for both LC-in-water emulsions (see above).

Following flow cytometry, the LC emulsions were photopolymerized using a UV lamp (365 nm) that delivered 2.5 mW/cm^2. Three cycles of exposure to UV light for 10 minutes followed by incubation in the dark for 10 minutes were performed. After photopolymerization, we again measured light scatter plots of the emulsions using the flow cytometer.

6.3 Results and Discussion

We performed flow cytometry using droplets of nematic 4′-pentyl-4-cyanobiphenyl (5CB) dispersed in either water or an aqueous solution of 5 mM sodium dodecyl sulfate (SDS) because these two solution conditions have been demonstrated previously to promote either bipolar or radial configurations of the LC droplets, respectively.[1, 3-8, 16] The concentration of SDS was selected to avoid formation of surfactant micelles (the critical micelle concentration (CMC) of SDS is 8.1 mM;[42] solutions of SDS only (no LC) were confirmed to not contribute to a significant number of light scattering events detectable by the flow cytometer). Prior to flow cytometry, we used polarized light microscopy to confirm that the 5CB droplets dispersed in water exhibited bipolar configurations (Figure 6-1A) and that the LC droplets in aqueous 5 mM SDS adopted radial (or near radial, see below) configurations (Figure 6-1B). Subsequently, the two LC emulsions were pumped through the flow cytometer at a rate of 14 μL/min, and the intensities of both forward and side scattered light (FSC and SSC, respectively) were measured for 50,000 LC droplets in ~2 μL of emulsion. In the analysis below, the data is presented according to the standard flow cytometry convention of plotting SSC as a function of FSC.[28, 30, 31] Such a plot is referred to as a "scatter plot" in the remainder of this chapter. From the scatter plots displayed in Figure 6-2, we make several qualitative observations. First, the scatter plot obtained using the LC droplets in the bipolar configuration (Figure 6-2A) exhibits a broad distribution of SSCs at each FSC value. In contrast, the scatter plot measured for the LC droplets in the radial configuration (Figure 6-2B) exhibits a narrower distribution of SSCs at each FSC value. In addition, we note that the scatter plot of radial LC droplets exhibits a characteristic "S-shape", with two or more values of SSC observed for each value of FSC that lies between ~30,000 and ~60,000 arbitrary units (a.u.). The physical origins of these qualitative features will

be discussed in detail below. Overall, we note that the scatter plots obtained for the two configurations of the LC droplets are strikingly different.

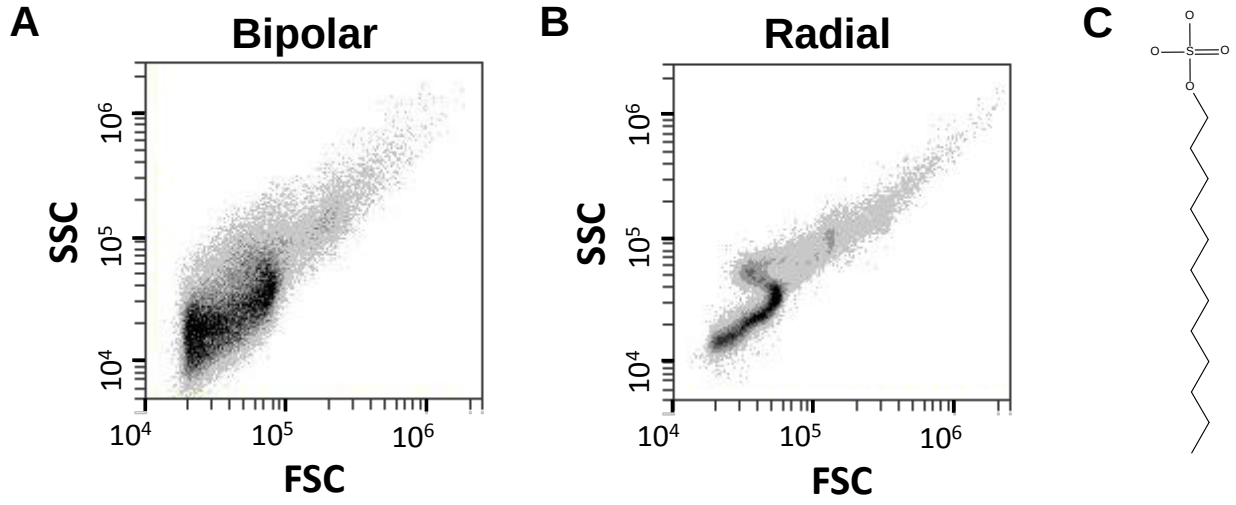

Figure 6-2. Scatter plots for aqueous dispersions of bipolar or radial 5CB droplets.
(A and B) Scatter plots obtained by flowing aqueous dispersions of nematic 5CB droplets in either bipolar (A) or radial (B) configurations through a flow cytometer. The 5CB droplets in (A) were suspended in water; whereas the 5CB droplets in (B) were suspended in an aqueous solution of 5 mM sodium dodecyl sulfate (SDS). Both scatter plots show 50,000 events recorded at a flow rate of 14 μL/min. (C) Molecular structure of SDS.

We performed three additional experiments to provide support for our conclusion that the differences in the abovementioned features of the scatter plots shown in Figure 6-2 arise from differences in the internal configuration of the LC within the droplets (and not other factors, as discussed below). First, we measured the characteristic features of the scatter plots of the bipolar and radial droplets (as described above) to be largely preserved over the operating range of flow rates of the flow cytometer (14−66 μL/min; see Figure 6-S2 of the Supporting Information). From this result, we conclude that the scatter plots displayed in Figure 6-2 were not influenced

by shear stresses imposed on the droplets during flow focusing in the cytometer. Next, we measured scatter plots for LC-in-water emulsions that contained radial 5CB droplets induced by different molecular amphiphiles (see Figure 6-S12 of the Supporting Information) to determine the extent to which the different amphiphiles would influence the scatter plots. The amphiphiles tested were the cationic surfactant cetyltrimethylammonium bromide (CTAB), the phospholipids 1,2-dilauroyl-*sn*-glycero-3-phosphocholine (DLPC) and 1,2-dipalmitoyl-*sn*-glycero-3-phosphocholine (DPPC), and the bacterial lipopolysaccharide endotoxin. All four amphiphiles generated scatter plots with qualitative features similar to the LC emulsions containing SDS-coated radial droplets (Figure 6-2B), further supporting our conclusion that the major features of the scatter plots are determined by the internal configuration of the LC within the droplets, independent of the choice of amphiphile (for the five amphiphiles investigated).

Past studies have established that micrometer-sized 5CB droplets can possess increasingly complex internal configurations as a function of increasing droplet size.[7, 43-46] For example, Figure 6-3A demonstrates that, when the diameters of nematic 5CB droplets in 5 mM SDS exceed 5 μm, the extinction bands present in polarized light micrographs of the LC droplets begin to twist relative to the orientation of the crossed polars, indicating the presence of twist deformation of the LC within the droplets. In contrast, LC-in-water emulsions with droplets of smectic octylcyanobiphenyl (8CB) exhibit radial configurations that do not permit the presence of twist (Figure 6-3B). To determine if size-dependent configurations of LC droplets (*e.g.*, twist within large (>5 μm) droplets) might be influencing the qualitative features of scatter plots of the LC droplets, in the third experiment, we measured a scatter plot for a LC-in-water emulsion that contained radial 8CB droplets coated by SDS (Figure 6-3D) and compared it to a scatter plot measured for radial 5CB droplets (Figure 6-3C). Inspection of Figure 6-3 reveals that the

qualitative features of the scatter plot obtained from radial 8CB droplets (narrow distribution of SSCs at a fixed FSC and a S-shape) were similar to the features of the scatter plots obtained from 5CB droplets. We comment that the higher level of structural detail evident in the scatter plot for 8CB droplets at high FSC values (Figure 6-3D) is likely due to a bigger population of large droplets in the 8CB emulsion (see below for more detail). We conclude, therefore, that scatter plots of emulsions containing radial nematic LC droplets are not significantly influenced by the presence of any twist near the cores of droplets exceeding 5 μm in diameter (likely reflecting that fact that the majority of the volume of LC within the droplets is not twisted; see Figure 6-3A). We note that ~33% percent of the droplets contained in a typical 5CB-in-water emulsion used in this study have diameters larger than 5 μm (see Figure 6-S1 of the Supporting Information).

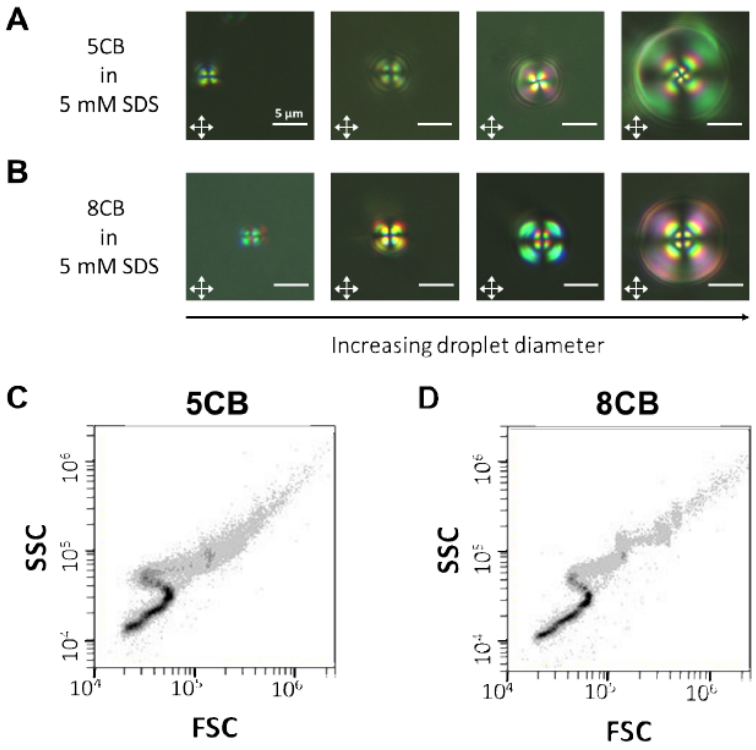

Figure 6-3. Comparison of scatter plots measured for aqueous dispersions of 5CB and 8CB droplets.

(A and B) Polarized light micrographs of (A) the radial or twisted-radial configuration exhibited by nematic 5CB droplets dispersed in an aqueous solution of 5 mM SDS and (B) the radial configuration exhibited by smectic 8CB droplets in an aqueous solution of 5 mM SDS. Double headed arrows indicate the orientation of the crossed polars. Scale bars, 5 µm. (C and D) Scatter plots obtained by flowing either (C) nematic 5CB droplets or (D) smectic 8CB droplets suspended in a 5 mM aqueous solution of SDS through a flow cytometer. The scatter plots comprise 50,000 events recorded at a flow rate of 14 µL/min.

The results presented above suggest that the differences observed in the scatter plots of emulsions containing either bipolar or radial LC droplets (Figure 6-2) arise largely from differences in the symmetry of the two droplet director configurations.[18] Specifically, because LC droplets in a radial configuration are centrosymmetric, the droplets present a rotationally invariant distribution of refractive indices (n) to an incident beam of light.[47] In contrast, LC droplets in the bipolar configuration present refractive indices to an incident beam of light that

depend on the orientation of the symmetry axes of the bipolar droplets relative to the polarization of the incident light. The broad distribution of SSC intensities at a fixed FSC intensity observed for bipolar droplets (Figure 6-2A) suggests the droplets are not substantially aligned along the direction of flow (also, see comments above and in the Supporting Information related to the effects of flow rate). To test further the role of the symmetry of the LC droplets in determining the scatter plots, we performed flow cytometry on several isotropic oil-in-water emulsions (Figure 6-4). The isotropic oils tested were heptane, dodecane, immersion oil B, and benzonitrile (refractive indices at 25°C shown in Figure 6-4). The oil-in-water emulsions were formed using 5.5 mM SDS to stabilize the emulsions.[34, 42] Two important results emerged from our measurements of the scatter plots of these isotropic oils. First, the scatter plots for each of these four emulsions possessed a narrower distribution of SSCs at each FSC than the scatter plots obtained from LC-in-water emulsions that contained bipolar droplets (see Figure 6-S14 of the Supporting Information). Second, as the refractive index of the oil in the emulsions approached the average refractive index of nematic 5CB ($n_{av} = (2n_o + n_e)/3 = 1.597$), the scatter plot measured by flow cytometry exhibited the S-shape characteristic of the radial LC droplets. Specifically, the scatter plot obtained using benzonitrile (which has a refractive index closest to the average refractive index of nematic 5CB) closely resembles the scatter plot obtained for radial 5CB droplets (compare Figure 6-4D,E). This result demonstrates that the S-shaped scatter plot characteristic of radial LC droplets is not unique to LC droplets but is also observed with isotropic droplets.

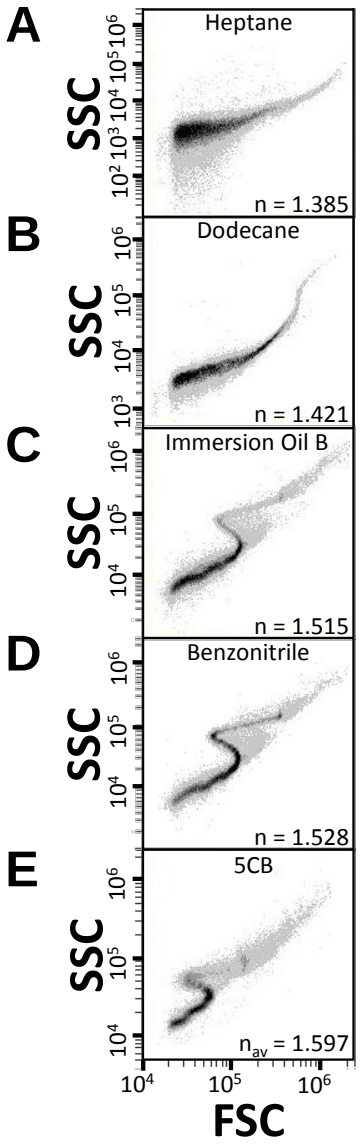

Figure 6-4. Scatter plots measured for aqueous dispersions of droplets of different isotropic oils. (A-D) Scatter plots obtained by flowing (A) heptane, (B) dodecane, (C) immersion oil B, (D) benzonitrile droplets, or (E) nematic 5CB droplets dispersed in a 5.5 mM aqueous solution of SDS through a flow cytometer. The refractive indices of each isotropic oil at 25°C and the average refractive index of nematic 5CB at 25°C is displayed in the bottom right corner of each respective scatter plot. Note that different SSC axis scales were used for the isotropic oil-in-water emulsions because these emulsions led to lower values of SSC. Each scatter plot represents 50,000 events recorded at a flow rate of 14 µL/min.

To provide further insight into the physical origin of the S-shaped scatter plots displayed in Figure 6-4, we considered the intensity of light scattered by a droplet of isotropic oil to be described by:

$$I = \Delta\rho^2 V^2 P(R, q) \qquad (6 - 1)$$

where $\Delta\rho$ is the difference in scattering length density between the droplet and the solvent ($\rho_{\text{droplet}} - \rho_{\text{solvent}}$), V is the volume of the droplet, and $P(R, q)$ is a form factor that depends on both the size and shape of the droplet and accounts for interference effects arising from multiple scattering centers within the droplet.[33, 34, 48] The form factor is a function of both the radius of the droplet (R) and the magnitude of the scattering vector (q), which is dependent on the angle of detection (θ) and λ, and is expressed as $q = 4\pi\sin\theta/\lambda$. As shown in equation 6-1, the intensity of light scattered is proportional to $P(R, q)$ which we discuss below.

We treat the droplets of isotropic oil contained in the emulsions as isotropic spheres. The form factor of an isotropic sphere is given as:[48]

$$P(R, q) = \left(3\frac{\sin qR - qR\cos qR}{(qR)^3}\right)^2 \qquad (6 - 2)$$

Inspection of equation 6-2 shows that the form factor is unity for $q = 0$, and thus, the intensity of forward scattered light is proportional to the square of the volume of a droplet ($I \propto V^2$).[30, 31] However, the angle of detection of FSC in a flow cytometer is nonzero because, at a detection angle of 0°, the intensity of the transmitted light would damage the detector.[34] The exact forward scattering angle of the BD Accuri C6 flow cytometer used in our experiments is not disclosed by the manufacturer but is stated to be between 0° and 15°.[40] For the purposes of the calculations presented below, we assume a forward scattering angle of 5°. The conclusions of our analysis do not depend strongly on the exact forward scattering angle. When a droplet

passing through the flow cytometer has a radius that exceeds a critical value, interference effects lead to size-dependent intensities of forward scattered light ($V^2P(R)$ for $\theta = 5°$; Figure 6-5A). A similar effect is seen for SSC ($75° < \theta < 105°$ in the flow cytometer used in our study), but the period of the interference bands is much shorter ($V^2P(R)$ for $\theta = 90°$; Figure 6-5B). Past studies of X-ray scattering from homogeneous spherical particles have demonstrated that when, the period of interference bands becomes sufficiently small, a continuous curve connecting the maxima of each predicted band is measured.[48] We propose that the SSC measured in our flow cytometer is also a curve that connects the maxima of the intensity bands predicted by light scattering theory (red line, Figure 6-5B).

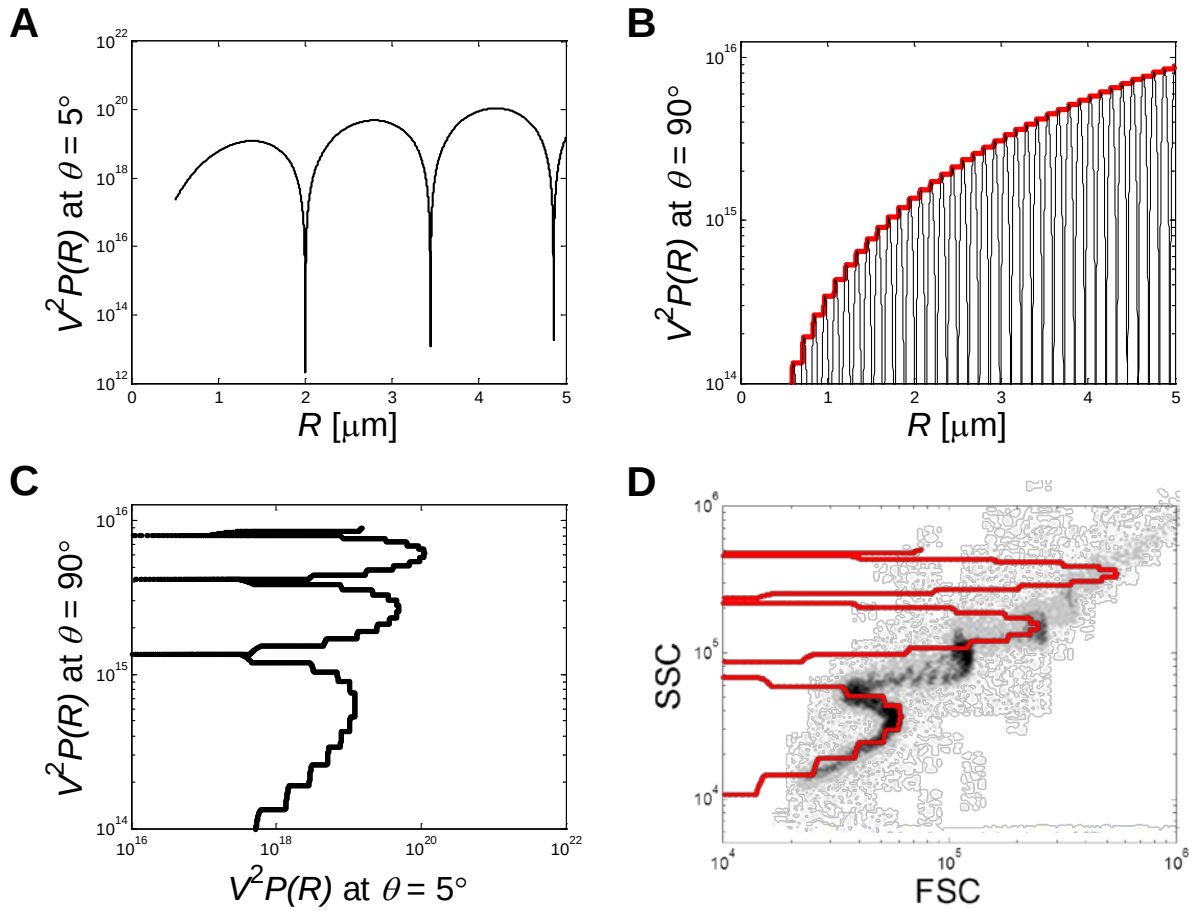

Figure 6-5. Calculated effect of droplet size on the intensity of light scattered ($V^2P(R)$) at detection angles (θ) of 5° and 90°.

(A) Detection angle of 5°. (B) Detection angle of 90°. (C) $V^2P(R)$ at $\theta = 90°$ plotted against $V^2P(R)$ at $\theta = 5°$. (D) Fit of the predicted scatter plot (red line) to the experimentally observed scatter plot for radial 5CB droplets coated by DLPC (as shown in Figure 6-S12D of SI).

An important consequence of the above prediction regarding SSC in our experiments is that SSC is expected to be strongly correlated to droplet size. We comment that this interpretation differs from the conventional interpretation of flow cytometry scatter plots measured for mammalian cells, where FSC is used to characterize cell size and SSC is used as a measure of the internal granularity of a cell (see Introduction for further detail).

Figure 6-5C shows $V^2P(R)$ calculated at $\theta = 90°$ plotted against the same quantity at $\theta = 5°$. Comparison of Figure 6-5C to experimentally determined scatter plots for both radial LC droplets and droplets composed of isotropic oils (Figures 6-2−6-4) reveals qualitative similarity. Specifically, Figure 6-5C predicts the characteristic S-shape of the experimental plots, where two or more intensities of SSCs are observed for a given value of FSC. In addition, we note that the calculated scatter plot can be fit to an experimentally measured scatter plot for radial LC droplets (Figure 6-5D) by rescaling the axes of the calculated scatter plot by factors of $10^{-10.3}$ for $\theta = 90°$ and $10^{-14.3}$ for $\theta = 5°$. These constants account for the excess scattering length density of the droplets ($\Delta\rho$), as well as several instrument parameters that influence the detector output (*e.g.*, differences in the calibration of the forward and side light scattering detectors). While quantitative calculation of the scatter plots lies beyond the scope of this study, the results above provide key insight into the origins of the difference of the qualitative features of the scatter plots for bipolar and radial LC droplets. Specifically, the characteristic S-shaped plot that allows us to identify the radial configuration of the LC droplets arises because of size-dependent interference effects. We emphasize that the S-shaped curve would not be observed for a sample of monodisperse LC droplets, and thus, the use of polydisperse samples can be used as an advantage in identifying radial droplets in a mixture of radial and bipolar droplets (see below).

To be a useful tool for analyte quantification using LCs, a flow cytometer must be able to report the percentage of LC droplets contained in an emulsion that exhibit the director configuration induced by the analyte.[5-8, 14, 15] Because the analytes used in this study induce a bipolar-to-radial ordering transition, we measured scatter plots for 5CB-in-water emulsions containing different percentages of radial LC droplets. The emulsions were prepared by mixing bipolar LC droplets (bare aqueous—LC interfaces) with DPPC-coated radial droplets. DPPC was

used to induce the radial configuration because DPPC monomers are essentially insoluble in aqueous solutions,[49] and thus, they were not expected to redistribute between the two populations of LC droplets after mixing. In the analysis below, Φ_{DPPC}^{PM} indicates the percentage of radial LC droplets contained in an emulsion, as determined from analysis of polarized light micrographs.[6-8, 15]

Figure 6-6 shows that an increase in Φ_{DPPC}^{PM} resulted in a continuous evolution of the scatter plots from those with features characteristic of bipolar droplets to those with features characteristic of radial droplets. Because the S-shaped region of the scatter plots of the radial droplets occurred between FSC values of 30,000 and 60,000 a.u. (red dashed lines in Figure 6-6G), we hypothesized that the total number of light scattering events measured within this range of FSC intensities would increase with an increase in the percentage of radial droplets. To test this hypothesis, we plotted frequency histograms of FSC for each Φ_{DPPC}^{PM} displayed in Figure 6-6 (Figure 6-7A). The frequency histograms reveal that a peak located between ~30,000 and ~60,000 a.u. indeed grows in intensity with an increase in Φ_{DPPC}^{PM} (red dashed lines in Figure 6-7A). To quantify this growth, we integrated the area under each peak. The area under the peak at Φ_{DPPC}^{PM} = 0% was subtracted from each peak as a baseline (see Supporting Information for more details), and the resulting area was normalized by the area under the peak for Φ_{DPPC}^{PM} = 100% (Φ_{DPPC}^{FC}). Figure 6-7B demonstrates that this metric of the scatter plot correlates closely with the percentage of radial droplets, as determined from polarized light micrographs of the same emulsions (Φ_{DPPC}^{PM}). A linear regression of the data in Figure 6-7B with Φ_{DPPC}^{FC} = 0% set as the intercept results in a slope of 1.01 and a coefficient of determination (R^2) of 0.98. This result leads us to conclude that flow cytometry can be used to quantify the percentage of radial droplets contained in a LC-in-water emulsion composed of a mixture of bipolar and radial droplets.

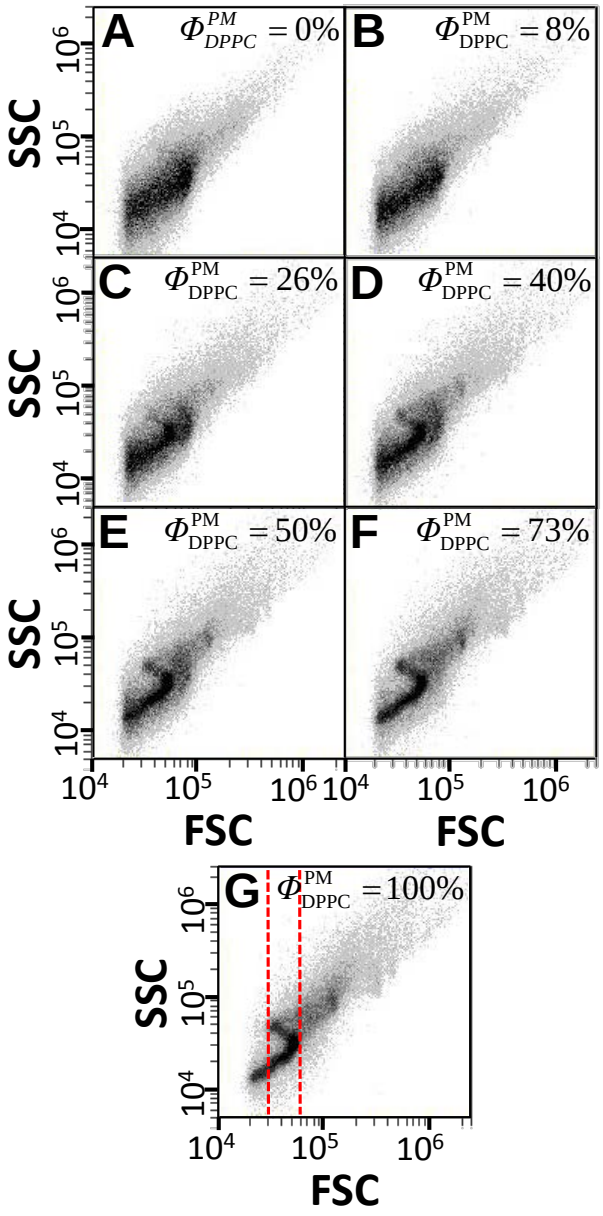

Figure 6-6. Scatter plots obtained by flowing nematic 5CB-in-water emulsions containing mixtures of bipolar and radial 5CB droplets through a flow cytometer.

The percentage of radial droplets in the mixture, as determined by optical microcopy (Φ_{DPPC}^{PM}), is indicated. Each scatter plot represents 50,000 events recorded at a flow rate of 14 μL/min. The red dashed lines in (G) highlight the area of the scatter plot used to calculate the percentage of radial LC droplets in LC-in-water emulsions (Φ_{DPPC}^{FC}, see Figure 6-7 and text for details).

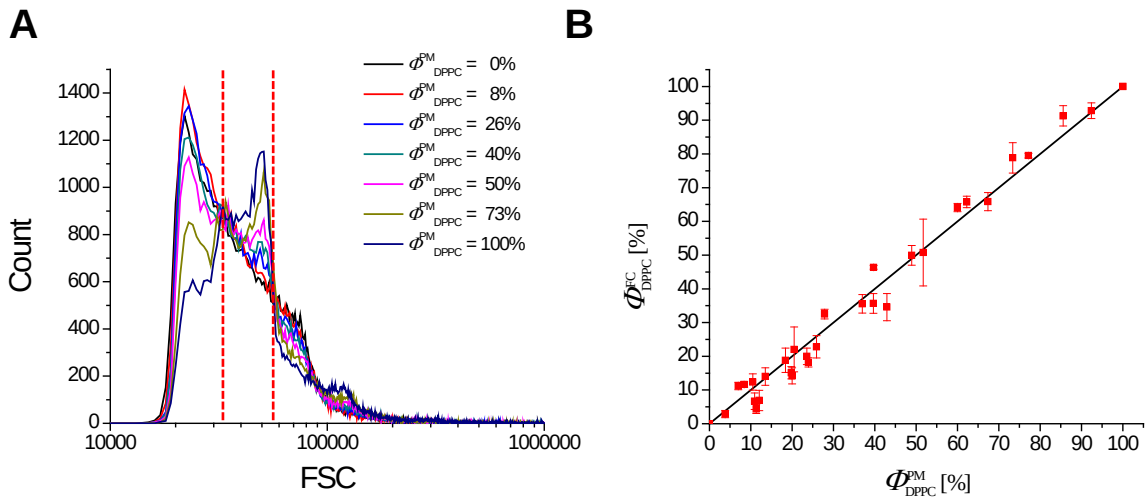

Figure 6-7. Correlation between the percentages of radial droplets as calculated from flow cytometry and those calculated from polarized light micrographs of the same emulsions.

(A) Frequency histogram for FSC obtained from Figure 6. Bin size, 1,000 a.u. (B) Percentage of radial LC droplets in a mixture of radial and bipolar droplets, as calculated from flow cytometry (Φ^{FC}_{DPPC}), plotted against the percentage of radial LC droplets calculated from polarized light micrographs of the same emulsions (Φ^{PM}_{DPPC}). The red dashed lines in (A) highlight the peak analyzed to calculate Φ^{FC}_{DPPC}.

Here, we emphasize the capability to quantify the fraction of radial droplets in a mixture of radial and bipolar droplets is a useful one as our past studies have demonstrated that important biological analytes, such as bacterial endotoxin, lead to LC droplets that assume either bipolar and or radial configurations (configurations other than radial and bipolar do not appear to be stable in the presence of endotoxin; see Chapters 4 and 5).[6, 7] Our results suggest that quantification of the percentage or radial droplets contained in these systems is possible using a flow cytometer. In addition, however, we note that other analytes can lead to LC droplet configurations other than radial and bipolar.[5, 21-24] In future studies, to enable analysis of such systems, we will explore methods of analysis of scatter plots that lead to identification of these other LC droplet configurations.

We end this study by briefly comparing flow cytometry to optical microscopy as an analytical methodology to quantify the number of droplets contained in a LC emulsion that exhibit a particular director configuration. First, flow cytometry requires a lower sample volume than optical microscopy. For example, the scatter plots used to determine Φ_{DPPC}^{FC} in Figure 6-7B were obtained using 50,000 droplets and required a sample volume of 2 μL. In contrast, determination of Φ_{DPPC}^{PM} for each data point displayed in Figure 6-7B required the analysis of at least 100 LC droplets in 20 μL of sample. Second, the rate of data acquisition is much faster for flow cytometry (up to 10,000 droplets/second) than for optical microscopy (~20 droplets/minute in the present study). Third, calculation of Φ_{DPPC}^{FC} from flow cytometry data can be accomplished in several minutes, which is much faster than the hours of image analysis required to calculate Φ_{DPPC}^{PM} from optical micrographs. Fourth, flow cytometry does not suffer from the challenges associated with droplet sedimentation which can influence the number of droplets observed as well as lead to droplet—surface interactions that change LC droplet director configurations while making observations using an optical microscope.[25] Finally, the cost of a flow cytometer is comparable to the cost of a polarized light microscope (the cost of the flow cytometer used in the present study was ~$20,000). Overall, we conclude that flow cytometry has a number of advantages relative to optical microscopy for characterization of the internal configurations of LC emulsions.

6.4 Conclusions

The results presented in this chapter demonstrate that flow cytometry can be used to characterize the internal configuration of LC droplets contained in LC-in-water emulsions. Specifically, LC droplets with rotational symmetry, such as droplets in the radial configuration,

generate a characteristic S-shaped scatter plot. The S-shape was shown (by calculation of form factors) to arise from size-dependent interference effects that differ for the two detection angles in a flow cytometer. The different light scattering properties of bipolar versus radial LC droplets leads to systematic differences in scatter plots measured for LC-in-water emulsions containing mixtures of droplets in these two director configurations. This permits the use of flow cytometry as an analytical method to quantify the percentage of droplets in an emulsion that exhibit a radial director configuration with high precision (in a mixture of radial and bipolar droplets). When compared to optical microscopy for such analyses, flow cytometry is faster and more statistically robust (it involves the analysis of >10,000 droplets compared to ~100 droplets for optical microscopy). Overall, these results suggest that flow cytometry can be used as a high throughput alternative to microscopy for read-out of chemical and biological assays based on stimuli-induced ordering transitions within LC droplets.[1-4] The results also suggest that flow cytometry could be utilized to sort LC droplets based on their different director configurations. In future studies, we will explore this possibility.

Acknowledgements

This work was primarily supported by NSF through DMR- 1121288 (Materials Research Science and Engineering Center), the Army Research Office (W911NF-11-1-0251 andW911NF- 10-1-0181), and the National Institutes of Health (AI092004 and CA108467). The authors thank Peter C. Mushenheim, Frédéric Mondiot, and LieNa Tan for helpful discussions.

6.5 Supporting Information

Distribution of Droplet Sizes Measured by Optical Microscopy

To determine the distribution of LC droplet sizes contained in a typical LC-in-water emulsion used in experiments reported in this chapter we measured the diameters of radial LC droplets in optical micrographs of the same emulsion used to obtain the scatter plot displayed in Figure 6-2B of the main text. The results of this analysis are displayed in Figure 6-S1.

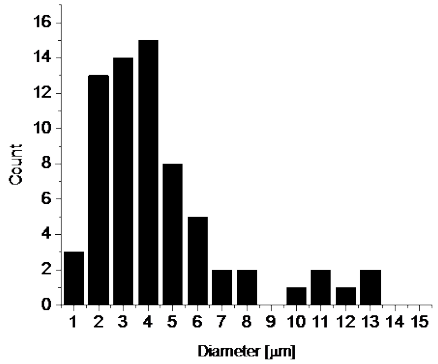

Figure 6-S1. Histogram of the distribution of 5CB droplet sizes measured from optical micrographs of the same emulsion used to obtain the scatter plot displayed in Figure 6-2B of the main text.

Influence of Sample Volumetric Flow Rate on Light Scatter Plots

We investigated the influence of the rate at which the droplets were pumped through the flow cytometer on the scatter plots to confirm that the plots displayed in Figure 6-2 of the main text were not influenced by shear stresses imposed on the droplets during flow focusing in the cytometer (Figure 6-S2). We observed that the characteristic features of the scatter plots of the bipolar and radial droplets (as described in the main text) were largely preserved over the operating range of flow rates of the flow cytometer (14 – 66 μL/min). We note that at a flow rate 66 μL/min, the distribution of SSC values broadened slightly for a given value of FSC (Figure 6-S2E and F). Droplets of the isotropic oil benzonitrile, polymerized LC droplets, and solid

polystyrene microbeads all showed a comparable change in their scatter plots with increase in flow rate (see below), leading us to conclude that these changes are not the result of shear-induced changes in the director configuration of the LC droplets. We comment here that we estimate the shear-induced deformation of the spherical shape of the emulsion droplets in the flow cytometer to be small (~0.02 %; see also below),[50-52] and thus unlikely to bias the orientation of the bipolar configuration in the flow cytometer (a result that is consistent with our experimental conclusion based on changes in flow rate). We also comment that past studies have reported shear-induced changes in director configurations, but only under conditions of extreme confinement.[53]

The scatter plots shown in Figure 6-S2 demonstrate that the distribution of side scattering intensities (SSC) becomes broader at a fixed value of forward light scattering (FSC) with an increase in the volumetric flow rate of a LC-in-water emulsion through the flow cytometer. To further analyze the influence of sample flow rate on the features of the scatter plots, we show the corresponding frequency histograms of FSC and SSC in Figure 6-S3. The frequency histograms S-7 of FSC measured for bipolar or radial 5CB droplets at 14 and 35 μL/min are qualitatively similar (Figure 6-S3A). However, at 66 μL/min the histograms of FSC measured for both bipolar and radial droplets are shifted to lower FSC values relative to the respective histograms measured at the two lower flow rates. The histogram for radial droplets underwent a larger shift and is noticeably broader (*i.e.*, the sharp peaks evident at the lower flow rates are nearly lost at 66 μL/min) than the histogram for bipolar droplets. Similar to the histograms of FSC, the frequency histograms of SSC (Figure 6-S3B) measured for both bipolar and radial 5CB droplets shift to lower SSC values with an increase in flow rate. Consistent with our above conclusion from the analysis of the corresponding scatter plots (Figure 6-S2), the histograms of SSC

measured for both bipolar and radial droplets also broaden with an increase in flow rate. Below we test several hypotheses for the origin of these changes in the scatter plots measured for LC-in-water emulsions with an increase in flow rate.

First, we hypothesized that the changes were the result of shear-induced alterations in the director configuration of the LC droplets. To test this hypothesis we measured flow cytometry scatter plots for benzonitrile droplets at the three flow rates tested in Figure 6-S2 (Figure 6-S4). A comparison of Figure 6-S4A through 6-S4C to Figure 6-S2B, 6-S2D, and 6-S2F reveals that similar changes in the scatter plots were observed for both benzonitrile and radial LC droplets. Similar changes were also observed in the frequency histograms of FSC and SSC (Figure 6-S4D and 6-S4E compared to Figure 6-S3). From this result, we conclude that changes in the features of the scatter plots measured for LC-in-water emulsions with an increase in flow rate are not the result of shear-induced alterations in the director configuration of the LC droplets.

Second, we hypothesized that the changes were caused by deformations in the shape of the LC droplets. Therefore, we polymerized bipolar and radial LC droplets to prevent shape deformations under flow, and measured scatter plots for the polymerized droplets (Figures 6-S5 and 6-S6). Polymerized droplets were fabricated by mixing 5CB with 10% wt /wt of the mesogenic monomer 4-(3-acryloyloxypropyloxy) benzoic acid 2-methyl-1,4-phenylene ester (RM257) (see above for more details).[41, 54] Figures 6-S5 and 6-S6 show that the scatter plots pre- and post-polymerization are similar, and that polymerization does not prevent the transformations in the plots with an increase in flow rate. From these results, we conclude that the changes in the scatter plots with an increase in flow rate are not caused by shear-induced alterations in the shape of the LC droplets. In addition, the results displayed in Figures 6-S5 and 6-S6 further support the conclusion that the changes in the scatter plots are not the result of

shear-induced alterations in the director configuration of the LC droplets because polymerization of LC droplets effectively traps them in the director configuration they exhibited prior to polymerization,[41, 54] thus preventing reorientation of the director configuration under flow.

Third, we hypothesized that the changes were caused by either contact of consecutive LC droplets during measurement of the scattered light or droplet coalescence. The impact of these possible causes would be reduced by using a more dilute LC-in-water emulsion. However, Figure 6-S7 shows that measurement of LC-in-water emulsions that were 10-fold more dilute than the emulsions measured in Figure 6-S2 did not significantly reduce the changes in the scatter plots that occur with an increase in flow rate. Therefore, we conclude that these changes are not caused by contact of consecutive LC droplets or coalescence.

Finally, we hypothesized that the changes are the result of a parameter of the flow cytometer that varies with flow rate. To test this hypothesis, we measured scatter plots for both 1 μm and 4 μm-in-diameter, water-dispersed polystyrene beads (Figure 6-S8). Consistent with the scatter plots displayed in Figure 6-S2 though 6-S7, we observed a shift in the distribution both FSC and SSC (Figures 6-S8G and 6-S8H, respectively) to lower values and a broadening of the distribution of SSC values with an increase in the flow rate for both bead sizes.

We speculate that the size of the fluid core containing the sample, which is dependent on flow rate, may influence the scatter plots. For example, an increase in flow rate from 14 to 66 μL/min causes the core size to increase from 10 to 22 μm.[40] Figure 6-S9 displays a proposed mechanism for the influence of an increase in core size on the position of a flowing 10 μm-in diameter LC droplet relative to the centerline of the capillary. At a sample flow rate of 14 μL/min the droplet is the size of the sample core and flows along the centerline of the capillary. Therefore, the position of the droplets is the same for each droplet struck by the laser of the flow

cytometer. At 35 μL/min the core size is 16 μm, the droplet begins to migrate away from the centerline, and the position of each droplet is slightly different when it is struck by the laser. Finally, at 66 μL/min the core is twice the size of the diameter of the droplet, and thus the droplet can be further away from the centerline when it is struck by the laser. We speculate that the variable position of each droplet at 66 μL/min results in the observed broader distribution of SSC values at each value of FSC. In addition, when a droplet is away from the centerline, the laser effectively strikes a smaller droplet resulting in a lower intensity of scattered light (see equation 6-1 of the main text). This leads to the observed shift in the histograms of FSC and SSC to lower values with an increase in flow rate.

We end this section by discussing the impact of sample volumetric flow rate on the use of flow cytometry to quantify of the internal configurations of LC emulsion microdroplets. In the main text we showed that the percentage of droplets exhibiting a radial configuration in an emulsion containing a mixed population of bipolar and radial droplets can be quantified by analyzing a peak in the frequency histogram of FSC that occurs between ~30,000 and ~60,000 a.u. (see Figure 6-7 of the main text). Therefore, we plotted the percentage of the droplets in each scatter plot displayed in Figure 6-S2 with FSC values between these two bounds in Figure 6-S10. Figure 6-S10 shows that the percentages at 14 and 35 μL/min for both bipolar and radial LC droplets are in close agreement. However, at 66 μL/min the percentage for bipolar droplets increases and the percentage for radial droplets decreases. From this result, we conclude that a flow rate of 66 μL/min should not be used to quantify of the internal configurations of LC emulsion microdroplets. Accordingly, 14 μL/min was used to quantify droplet configurations in the present study.

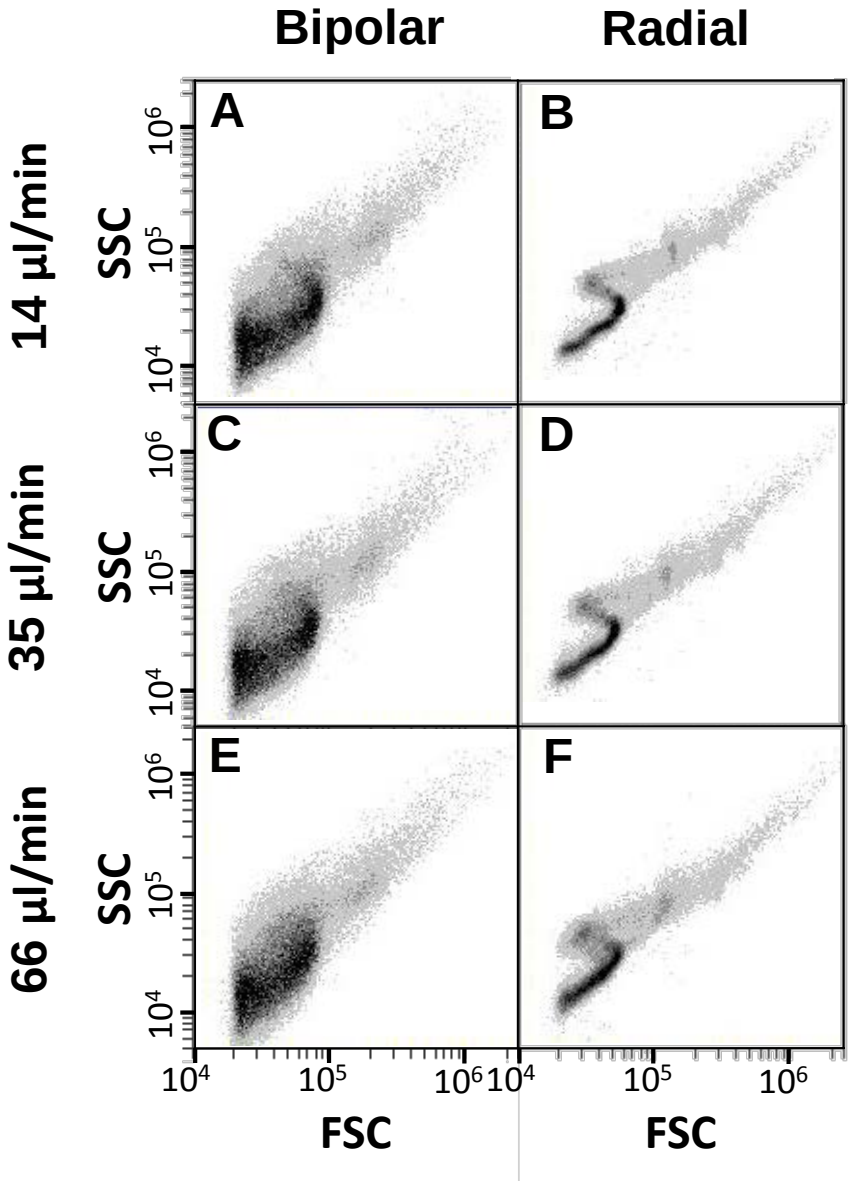

Figure 6-S2. Influence of the flow rate of 5CB emulsions through the flow cytometer on the measured scatter plots.

Scatter plots obtained by flowing aqueous dispersions of nematic 5CB droplets in either bipolar (A, C, and E) or radial (B, D, and F) configurations through a flow cytometer at various sample flow rates. The 5CB droplets shown in (A, C, and E) were suspended in water; whereas the 5CB droplets shown in (B, D, and F) were suspended in a 5 mM aqueous solution of SDS. The samples were pumped through the flow cytometer at a flow rate of 14 µL/min (A and B), 35 µL/min (C and D), or 66 µL/min (E and F). Each scatter plot contains 50,000 events.

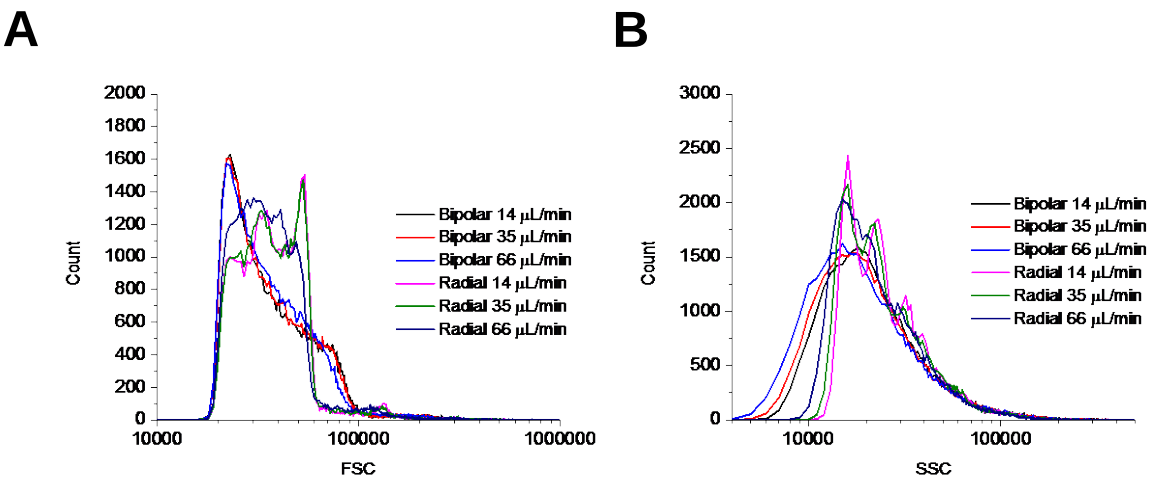

Figure 6-S3. Frequency histograms of the intensity of (A) forward (FSC) and (B) side (SSC) light scattering corresponding to the scatter plots displayed in Figure 6-S2.

Bin size, 1,000 a.u.

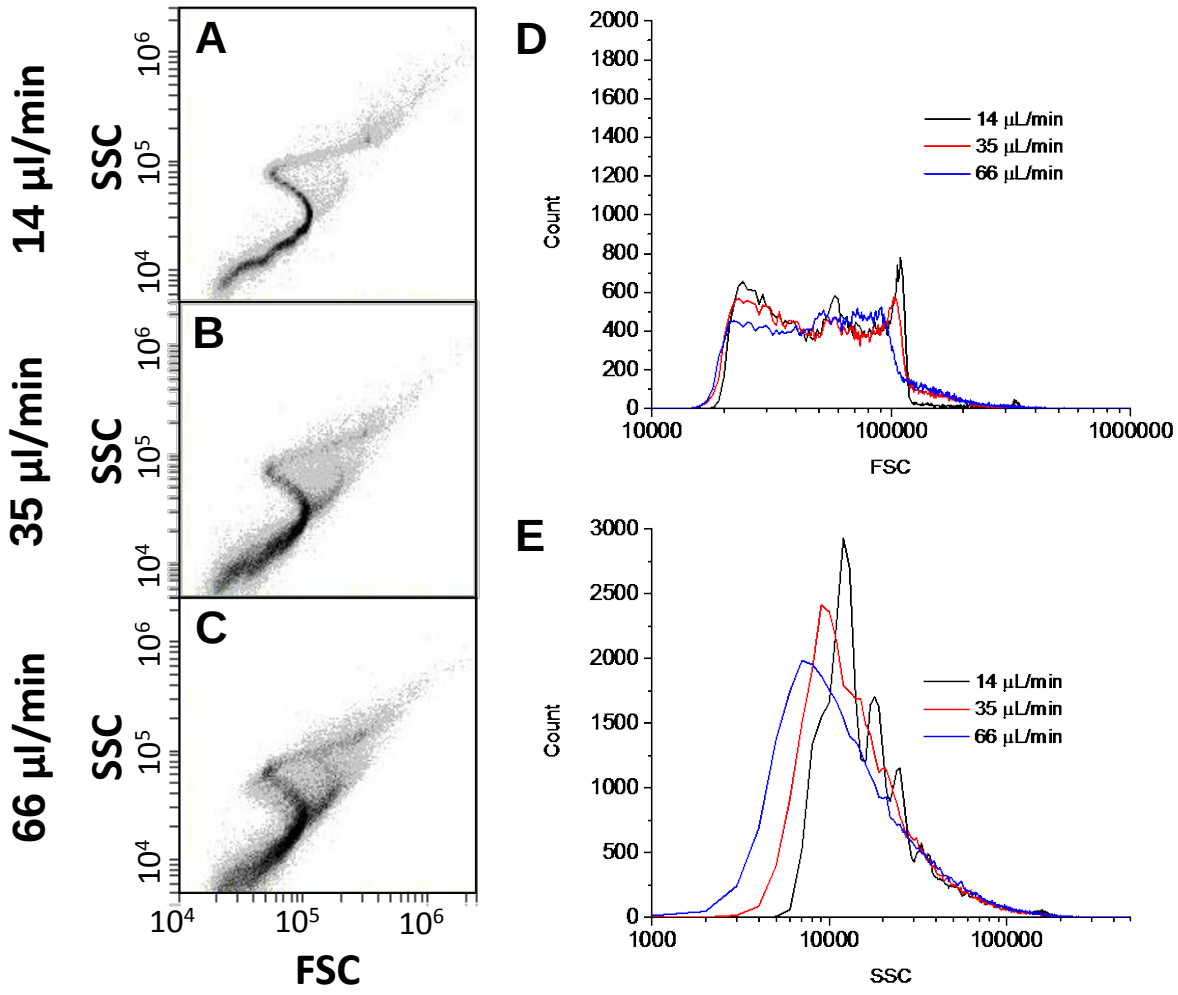

Figure 6-S4. Influence of the flow rate of benzonitrile emulsions through the flow cytometer on the measured scatter plots.

(A-C) Scatter plots obtained by flowing benzonitrile droplets dispersed in a 5.5 mM aqueous solution of SDS through a flow cytometer at various sample flow rates. The samples were pumped through the flow cytometer at a flow rate of 14 µL/min (A), 35 µL/min (B), or 66 µL/min (C). Each scatter plot contains 50,000 events. (D and E) Frequency histograms of (D) FSC and (E) SSC corresponding to the scatter plots displayed in A-C. Bin size, 1,000 a.u.

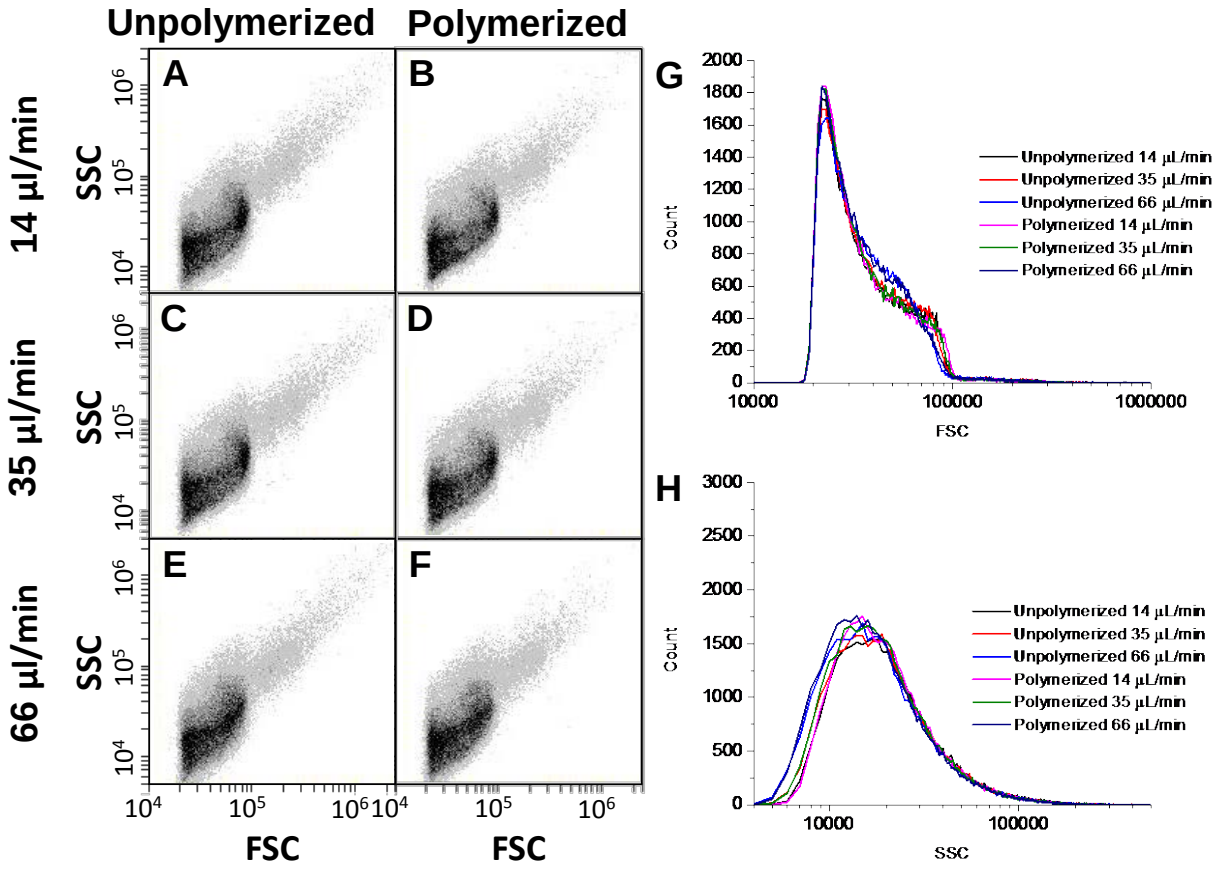

Figure 6-S5. Scatter plots measured for aqueous dispersions of polymerized bipolar droplets at different flow rates.

(A-F) Scatter plots obtained by flowing either (A, C, and E) unpolymerized or (B, D, and F) polymerized nematic 5CB droplets through a flow cytometer at various sample flow rates. The droplets were suspended in water which resulted in a bipolar configuration. The samples were pumped through the flow cytometer at a flow rate of 14 µL/min (A and B), 35 µL/min (C and D), or 66 µL/min (E and F). Each scatter plot contains 50,000 events. (G and H) Frequency histograms of (G) FSC and (H) SSC corresponding to the scatter plots displayed in A-F. Bin size, 1,000 a.u.

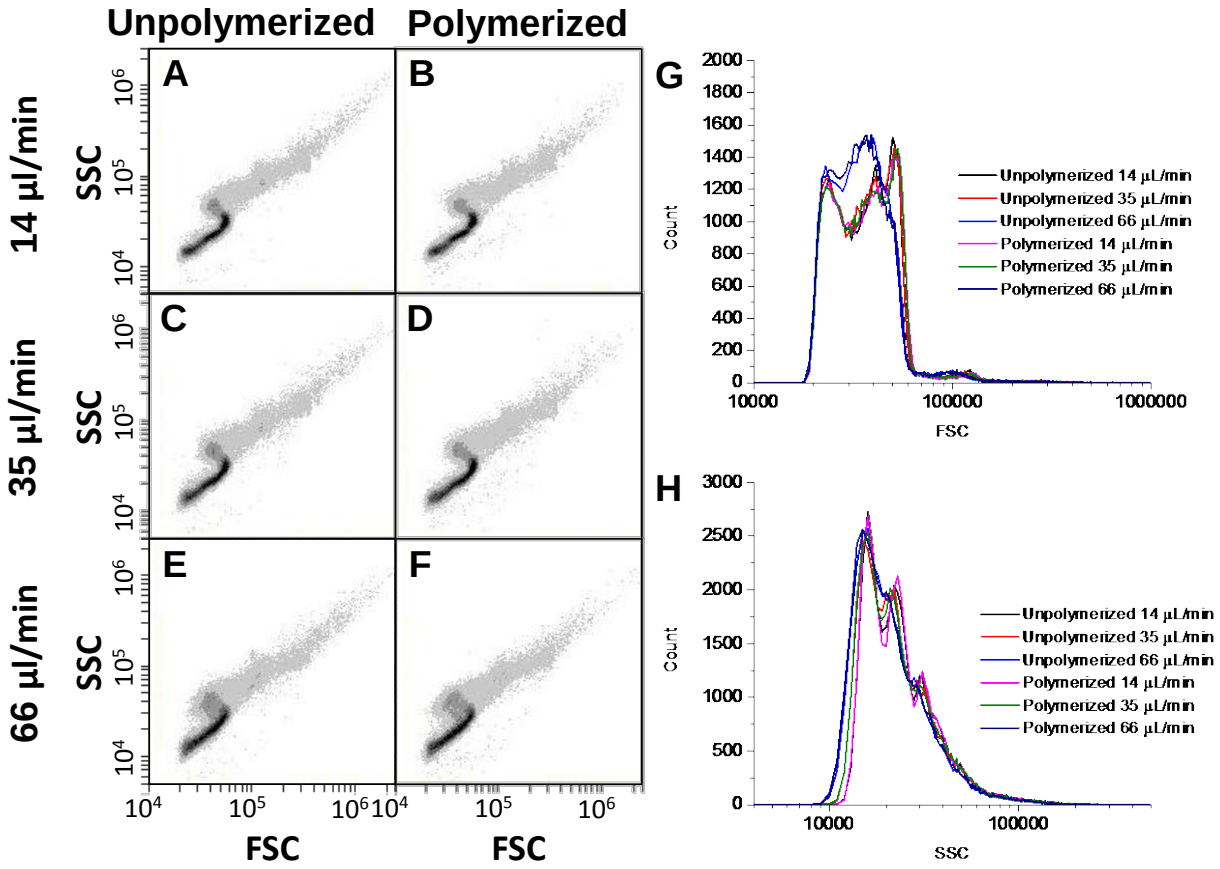

Figure 6-S6. Scatter plots measured for aqueous dispersions of polymerized radial droplets at different flow rates.

(A-F) Scatter plots obtained by flowing either (A,C, and E) unpolymerized or (B,D, and F) polymerized nematic 5CB droplets through a flow cytometer at various sample flow rates. The droplets were suspended in a 5 mM aqueous solution of SDS which resulted in a radial configuration. The samples were pumped through the flow cytometer at a flow rate of 14 µL/min (A and B), 35 µL/min (C and D), or 66 µL/min (E and F). Each scatter plot contains 50,000 events. (G and H) Frequency histograms of (G) FSC and (H) SSC corresponding to the scatter plots displayed in A-F. Bin size, 1,000 a.u.

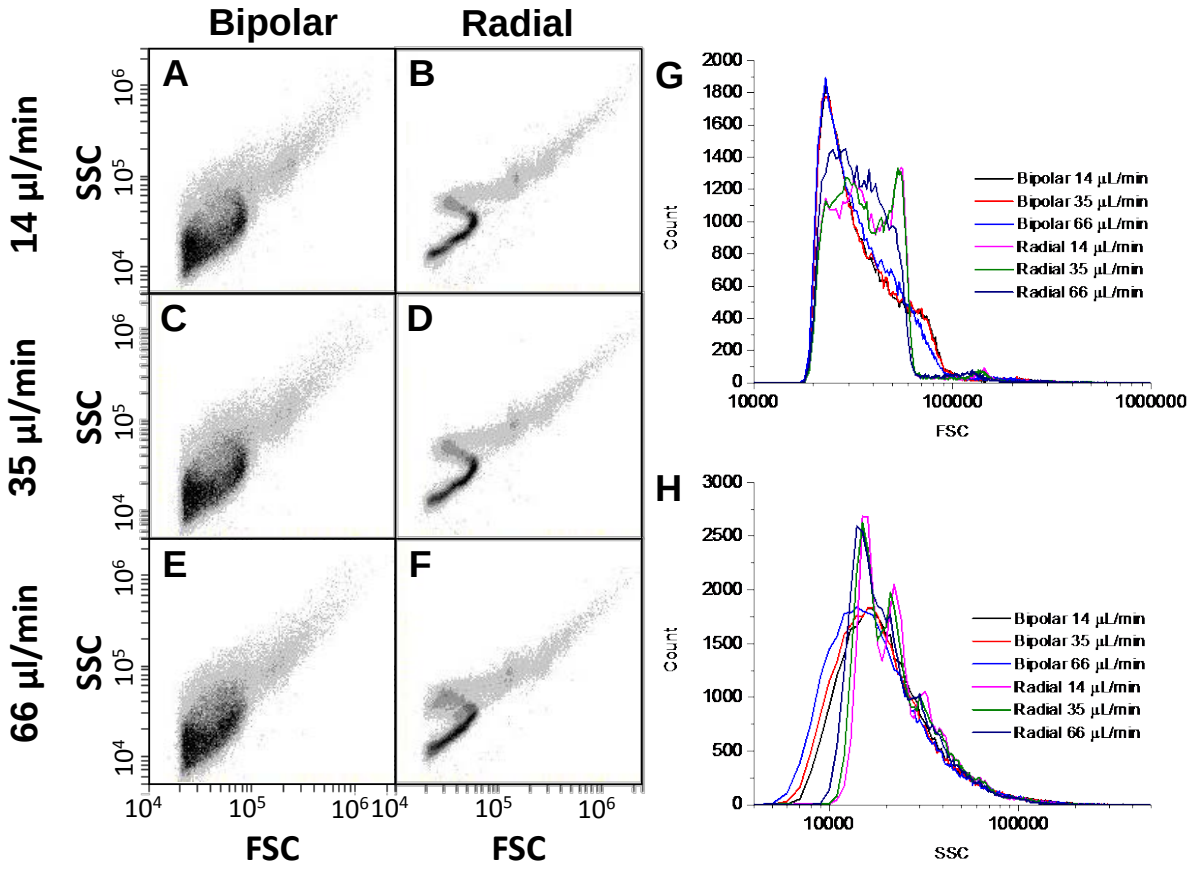

Figure 6-S7. Scatter plots measured for 5CB emulsions that were10 times more dilute.

(A-F) Scatter plots obtained by flowing nematic 5CB-in-water emulsions that were 10 times more dilute than the emulsions measured in Figure 6-S2 through a flow cytometer at various sample flow rates. The 5CB droplets shown in (A, C, and E) were suspended in water which resulted in a bipolar configuration; whereas the 5CB droplets shown in (B, D, and F) were suspended in a 5 mM aqueous solution of SDS which resulted in a radial configuration. The samples were pumped through the flow cytometer at a flow rate of 14 µL/min (A and B), 35 µL/min (C and D), or 66 µL/min (E and F). Each scatter plot contains 50,000 events. (G and H) Frequency histograms of (G) FSC and (H) SSC corresponding to the scatter plots displayed in A-F. Bin size, 1,000 a.u.

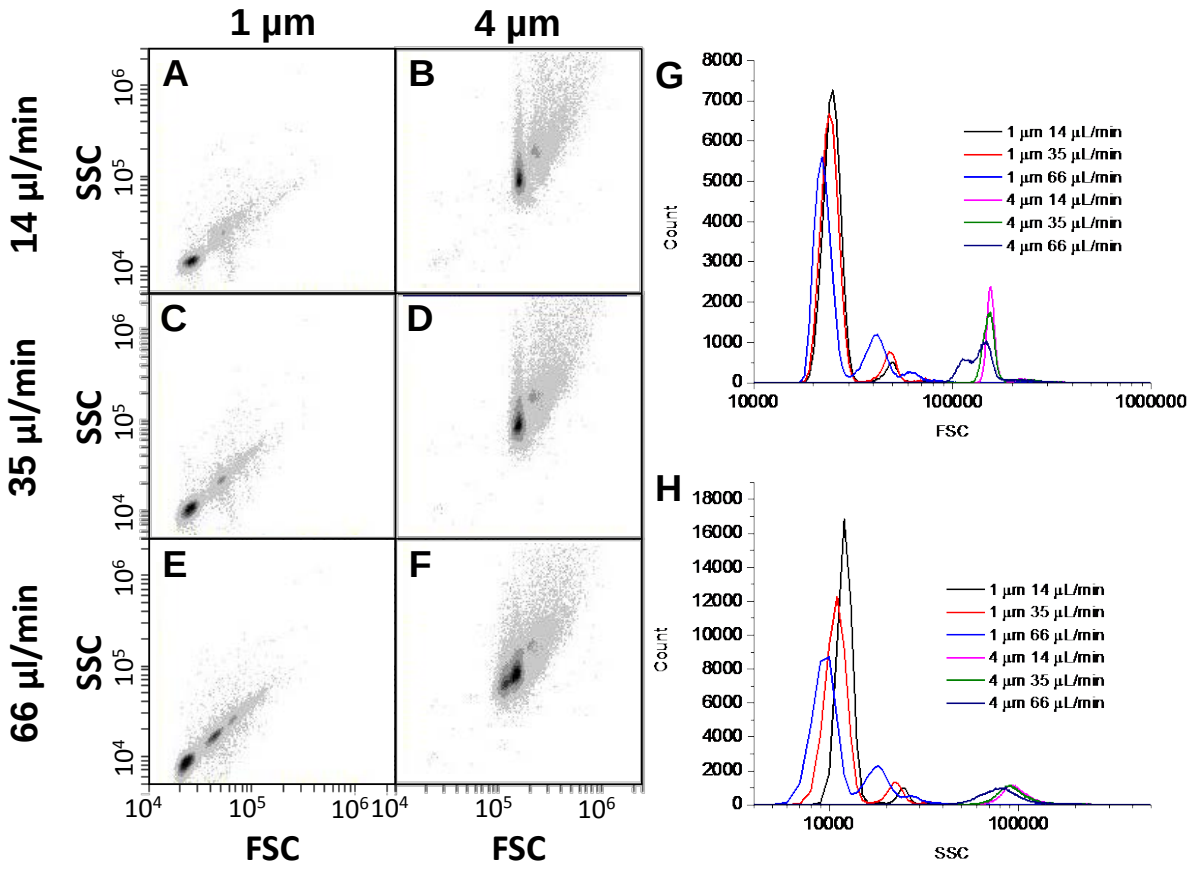

Figure 6-S8. Scatter plots measured for1 µm- or 4 µm-in-diameter polystyrene beads dispersed in water at different flow rates.

(A-F) Scatter plots obtained by flowing either (A, C, and E) 1 µm- or (B, D, and F) 4 µm-in-diameter polystyrene beads suspended in water through a flow cytometer at various sample flow rates. The samples were pumped through the flow cytometer at a flow rate of 14 µL/min (A and B), 35 µL/min (C and D), or 66 µL/min (E and F). Each scatter plot contains 50,000 events. (G and H) Frequency histograms of (G) FSC and (H) SSC corresponding to the scatter plots displayed in A-F. Bin size, 1,000 a.u.

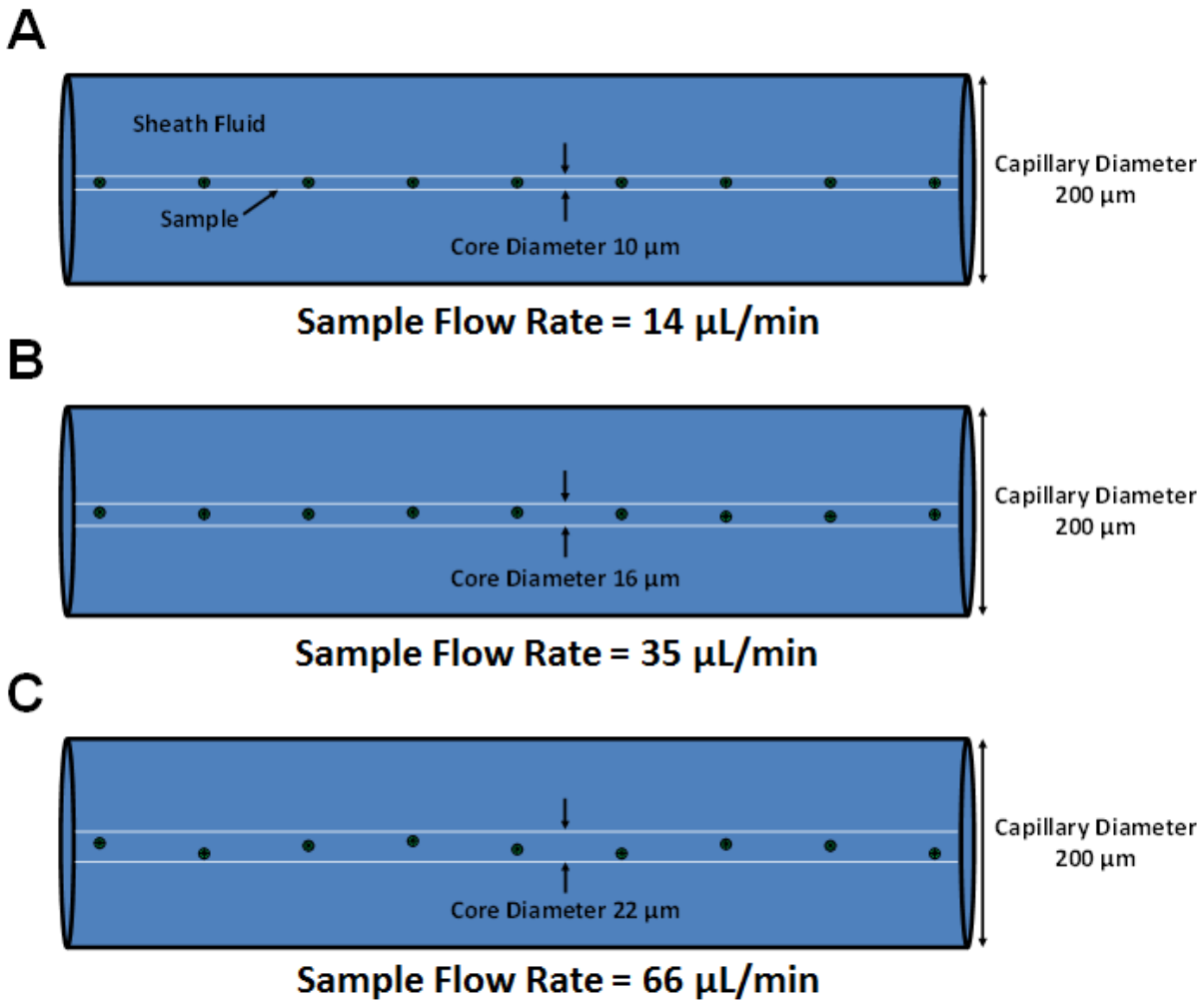

Figure 6-S9. Possible mechanism for the influence of an increase in core size on the position of a 10 µm-in-diameter LC droplet flowing through the main capillary of a flow cytometer relative to the centerline of the capillary.

(A) At a sample flow rate of 14 µL/min the droplet is the size of the sample core and flows along the centerline of the capillary. (B) At 35 µL/min the core size is 16 µm, and the droplet begins to migrate away from the centerline. (C) At 66 µL/min the core is twice the size of the diameter of the droplet, and thus the droplet can be further away from the centerline.

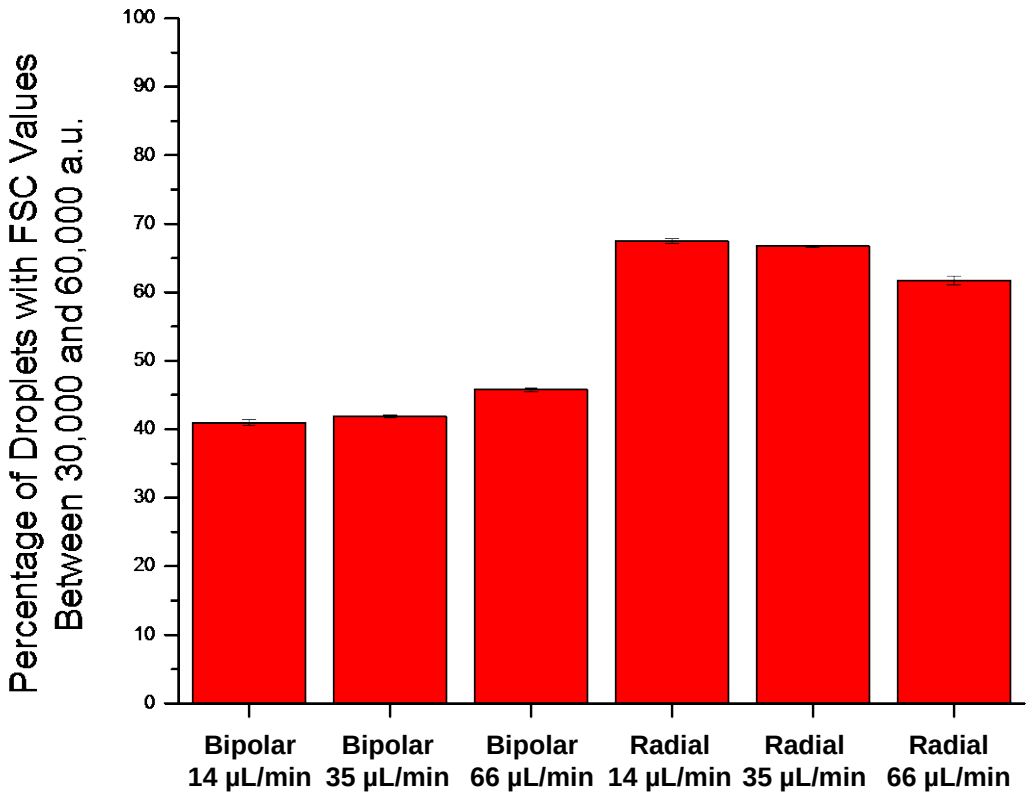

Figure 6-S10. Percentage of the droplets measured in each scatter plot displayed in Figure 6-S2 with FSC values between 30,000 and 60,000 a.u..

The plot was constructed from the frequency histograms displayed in Figure 6-S3A.

Estimation of the Shape Deformation Experienced by 5CB Droplets in a Flow Cytometer

Here we estimate the deformation experienced by 5CB droplets in the microfluidic channel of the flow cytometer used in experiments reported in this chapter.[51, 52] In our estimate, we consider the region of the channel in which the flow profile is fully developed and light scattering measurements are conducted (Figure 6-S11). The Reynold's number (Re), which is a dimensionless quantity that relates the inertial to viscous forces, is calculated as:

$$\mathrm{Re} = \frac{\rho_{\mathrm{H_2O}} U D}{\mu_{\mathrm{H_2O}}} \qquad (6\text{-}3)$$

where $\rho_{\mathrm{H_2O}}$ is the density of water (1,000 kg/m^3), U is the average velocity in the channel**,** D is the channel diameter, and $\mu_{\mathrm{H_2O}}$ is the viscosity of water (0.001 Pa s).[50] To calculate U, we note that the flow cell in a BD Accuri C6 flow cytometer consists of a 200 μm inner diameter (D) round quartz capillary, giving a cross-sectional area (A_{xs}) of 3.14×10^{-8} m^2.[40] The volumetric flow rate (Q) of the sheath fluid (*i.e.*, Milli-Q water) in the flow cytometer is typically 1 mL/min.[30] This results in a U of ($U = Q/A_{\mathrm{xs}}$) 0.53 m/s. Using this U, we calculate Re = 53, which is below the critical Reynold's number ($\mathrm{Re_{crit}}$) of 2,300, above which the flow is no longer laminar. Therefore, we conclude that the flow in the capillary is laminar.

For laminar flow in a tube, the velocity profile as function of a radial distance (r) from tube axis is parabolic (Figure 6-S11B), and is expressed as:

$$v_{\mathrm{z}}(r) = 2U\left(1 - \frac{r^2}{R^2}\right) \qquad (6\text{-}4)$$

where R is the radius of the tube (D/2 = 100 μm).[30, 50] By applying Newton's law of viscosity to equation 6-4, we calculate the radial shear stress to be given by:[50]

$$\tau_{\mathrm{rz}} = -\mu_{\mathrm{H_2O}} \frac{dv_{\mathrm{z}}}{dr} = \frac{4\mu_{\mathrm{H_2O}} U r}{R^2} \qquad (6\text{-}5)$$

From equation 6-5, we estimate the shear stress at the surface of a LC droplet with a radius of r_{droplet} flowing along the center-line of the microfluidic channel of the cytometer to be:

$$\tau_{\mathrm{rz}}|_{r_{\mathrm{droplet}}} = \frac{4\mu_{\mathrm{H_2O}} U r_{\mathrm{droplet}}}{R^2} \qquad (6\text{-}6)$$

The capillary number (Ca), which is a dimensionless quantity that relates the flow-induced viscous forces at the surface of a 5CB droplet to the surface tension (γ_{5CB}) of the droplet, is calculated as:[50]

$$\mathrm{Ca} = \frac{\tau_{\mathrm{rz}}|_{r_{\mathrm{droplet}}}}{2\gamma_{\mathrm{5CB}}/r_{\mathrm{droplet}}} = \frac{2\mu_{\mathrm{H_2O}} U r_{\mathrm{droplet}}^2}{\gamma_{\mathrm{5CB}} R^2} \qquad (6\text{-}7)$$

Using U = 0.53 m/s, γ_{5CB} = 25 mN/m,[55, 56] and $r_{droplet}$ = 5 μm, we calculate Ca = 10^{-4}. This value of Ca indicates that the flow-induced viscous forces at the surface of a 5CB droplet are small compared to the surface tension of the droplet.

The deformation (*Def*) of a spherical droplet in laminar flow can be calculated from the following equation:[51, 52]

$$Def = \frac{A_{\mathrm{r}} - 1}{A_{\mathrm{r}} + 1} = f(V_{\mathrm{r}})\mathrm{Ca} \qquad (6\text{-}8)$$

where A_{r} is defined as the major-to-minor axis length ratio of an ellipse, and $f(V_{\mathrm{r}})$ was measured by Tayor to be:[51]

$$f(V_{\mathrm{r}}) = \frac{1 + 19V_{\mathrm{r}}/16}{1 + V_{\mathrm{r}}} \qquad (6\text{-}9)$$

In equations 6-8 and 6-9, V_{r} is:

$$\mathrm{V_r} = \frac{\mu_{\mathrm{5CB}}}{\mu_{\mathrm{H_2O}}} \qquad (6\text{-}10)$$

where μ_{5CB} is the viscosity of 5CB (0.025 Pa s), and thus $\mathrm{V_r}$ = 25. Combining equations 6-8 through 6-10, and using the value of the capillary number calculated above, Ca = 10^{-4}, we calculate *Def* = 1.2 × 10^{-4} and A_{r}= 1.0002. From this analysis, we conclude that the shear experienced by the spherical 5CB droplets in the flow cytometer will not cause the LC droplets to significantly deform from their original shape.

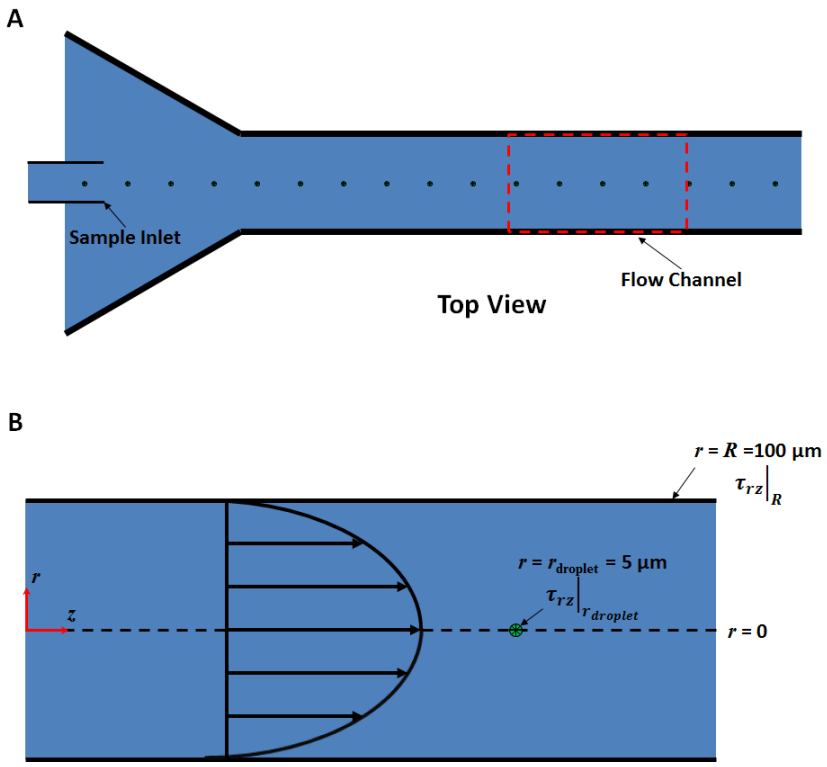

Figure 6-S11. Schematic illustration of the flow cell in a flow cytometer.
(A) Top view of hydrodynamic flow focusing in a flow cytometer. An object is focused to flow along the centerline of a capillary by injecting an aqueous dispersion of the object into the center of a co-flowing stream of sheath fluid under laminar flow conditions. (B) Side view of the area indicated by the red dashed line in (A). Within this region, the laminar flow profile is fully developed and light scattering measurements are conducted. This is the region considered for our estimation of the deformation of the shape of a LC droplet in our flow cytometer (see text).

Influence of Different Molecular Amphiphiles on Light Scatter Plots

We measured scatter plots for LC-in-water emulsions that contained radial 5CB droplets induced by different molecular amphiphiles (Figure 6-S12) to determine the extent to which the different amphiphiles would influence the scatter plots. The amphiphiles tested were the cationic surfactant cetyltrimethylammonium bromide (CTAB, Figure 6-S12A), the phospholipids 1,2-dilauroyl-*sn*-glycero-3-phosphocholine (DLPC, Figure 6-S12C) and 1,2-dipalmitoyl-*sn*-glycero-

3-phosphocholine (DPPC, Figure 6-S12E), and the bacterial lipopolysaccharide endotoxin. Endotoxin is comprised of a six-tailed glycophospholipid (called lipid A, Figure 6-S12G) in addition to two polysaccharide domains.[57] The concentrations of CTAB and LPS were 0.5 mM (CMC ≈ 0.9 mM) and 1.5 μM (CMC as low as 10 pg/mL; see Chapter 7), respectively, in the samples flowed through the cytometer.[42, 58] In contrast, the DLPC- and DPPC-coated LC droplets were obtained by incubating the droplets in an aqueous dispersion of phospholipid vesicles at a lipid concentration of 1.4 mM, and subsequently removing the excess lipid through a series of rinsing steps (see Experimental Section of the main text for further detail). Inspection of Figure 6-S12 reveals that all four amphiphiles generated scatter plots with qualitative features similar to the LC emulsions containing SDS-coated radial droplets (Figure 6-2B of the main text). We note, however, that there are minor quantitative differences between the scatter plots for each of the amphiphiles. For example, the DLPC- and DPPC-coated radial LC droplets are characterized by greater SSC intensities (above 30,000 a.u.; Figure 6-S12D and 6-S12F) than the radial droplets decorated by the other three amphiphiles (Figure 6-2B of the main text and Figure 6-S12B and 6-S12H). However, we also note that the emulsions used in our study are polydisperse with diameters ranging from 1 to 15 μm (see Figure 6-S1 of SI), and that the size distribution of droplets within each emulsion may vary with the amphiphile.[7, 37] Indeed, a comparison of the frequency histograms of SSC for radial droplets coated by each of the five amphiphiles tested in this study (Figure 6-S13) supports our hypothesis that the minor differences in the scatter plots in Figure 6-S12 arise from differences size distributions of the LC emulsions. Specifically, the DLPC- and DPPC-coated droplets have histograms shifted to larger SSC values. Overall, the results in Figure 6-S12 support our conclusion that the major features of the scatter plots are

determined by the internal configuration of the LC within the droplets, independent of the choice of amphiphile (for the five amphiphiles investigated).

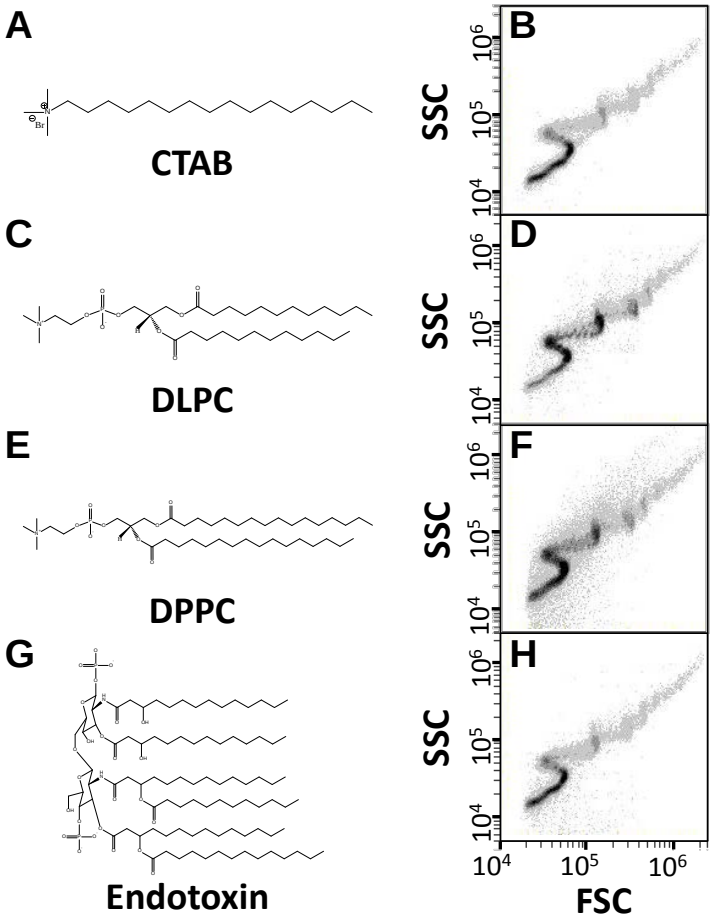

Figure 6-S12. Scatter plots measured for radial 5CB droplets dispersed in aqueous solutions of different amphiphiles.

(A, C, E, and G) Molecular structures of (A) cetyl trimethyl ammonium bromide (CTAB), (C) 1,2-dilauroyl-*sn*-glycero-3-phosphocholine (DLPC), (E) 1,2-dipalmitoyl-*sn*-glycero-3-phosphocholine (DPPC), and (G) the six-tailed glycophospholipid portion of endotoxin from *E. coli*, lipid A. (B, D, F, and H) Scatter plots obtained by flowing amphiphile-coated nematic 5CB droplets in a radial configuration through a flow cytometer. Decoration of the aqueous—LC droplet interfaces by each amphiphile was achieved by either suspending the droplets in aqueous solutions of (B) 0.5 mM CTAB or (H) 1.5 μM endotoxin, or by incubating the droplets in aqueous dispersions of 1.4 mM (D) DLPC or (F) DPPC and subsequently removing the excess phospholipid. Each scatter plot represents 50,000 events recorded at a flow rate of 14 μL/min.

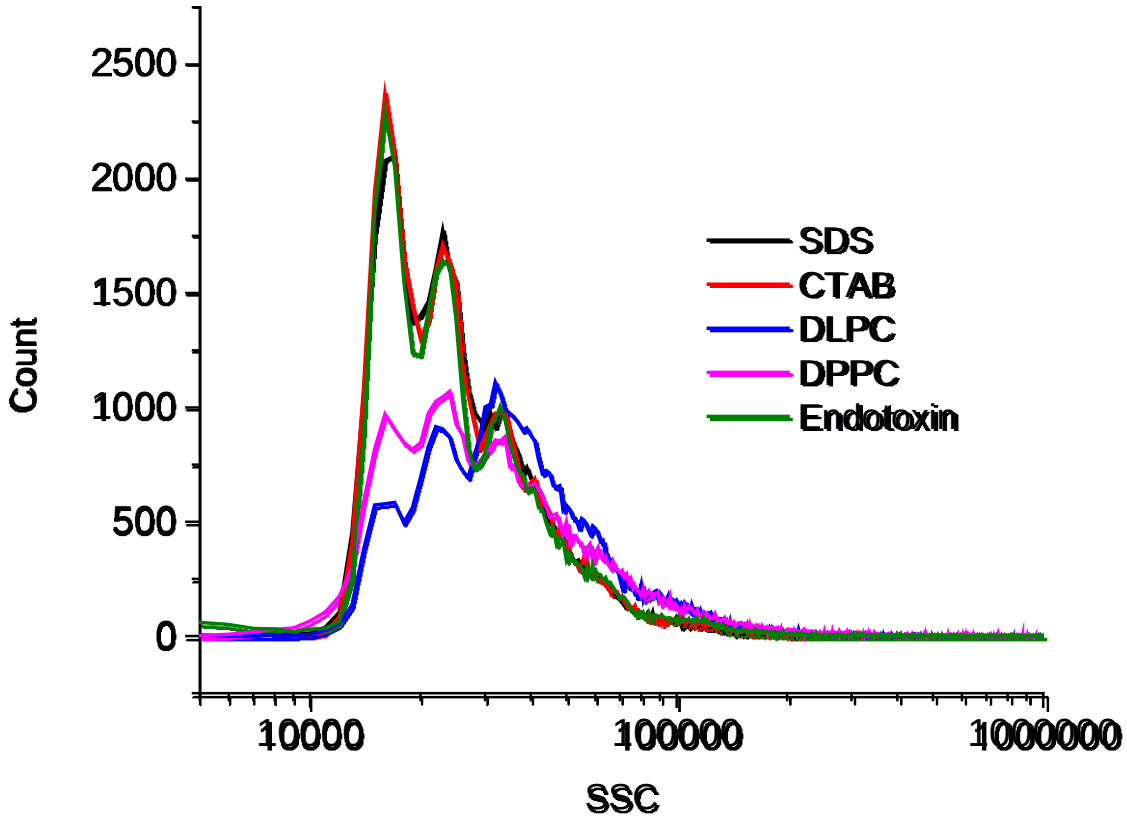

Figure 6-S13. Frequency histogram of SSC corresponding to the scatter plots measured for radial 5CB droplets decorated by either SDS (Figure 6-2B of the main text) or each of the four amphiphiles tested in Figure 6-S12.

Bin size, 1000 a.u..

Comparison of a Scatter Plot for Bipolar 5CB Droplets to the Scatter Plots Measured for Isotropic Oil-in-Water Emulsions

Figure 6-S14 below demonstrates that the scatter plots for each of the four isotropic oil-in-water emulsions possess a narrower distribution of SSCs at each FSC than the scatter plot obtained for a LC-in-water emulsion that contains bipolar LC droplets.

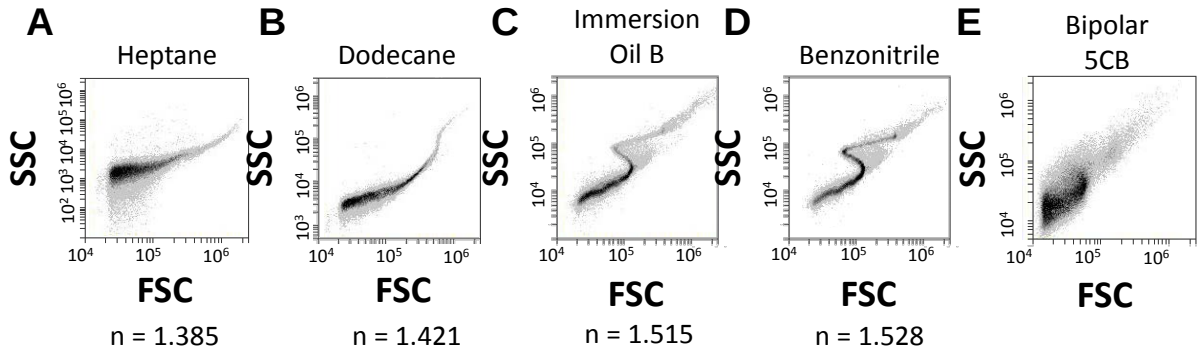

Figure 6-S14. Comparison of the scatter plot measured for bipolar 5CB droplets to those measured for droplets of isotropic oils.

(A-D) Scatter plots obtained by flowing (A) heptane, (B) dodecane, (C) immersion oil B, or (D) benzonitrile droplets dispersed in a 5.5 mM aqueous solution of SDS through a flow cytometer displayed in Figure 6-4A-D of the main text. (E) Scatter plot obtained by flowing nematic 5CB droplets in a bipolar configuration suspended in water through a flow cytometer. Note that different SSC axis scales were used for the isotropic oil-in-water emulsions because these emulsions led to lower values of SSC. Each scatter plot represents 50,000 events recorded at a flow rate of 14 μL/min.

Scatter Plot for Benzonitrile Droplets without SDS

Figure 6-S15 shows a scatter plot obtained by flowing benzonitrile droplets dispersed in water through a flow cytometer. The scatter plot is similar to the scatter plot measured for benzonitrile droplets dispersed in a 5.5 mM aqueous solution of SDS (Figure 6-S14D), supporting the conclusion that SDS does not contribute to the scattered light measured by the flow cytometer.

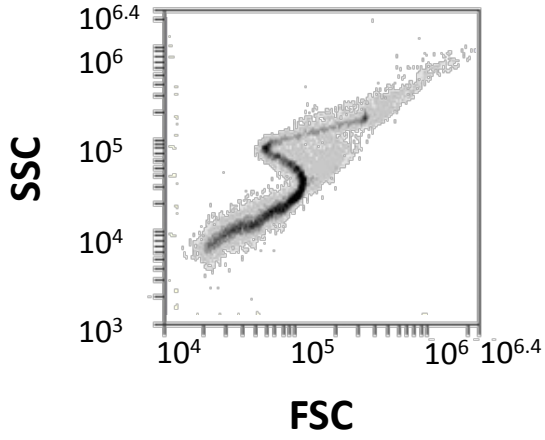

Figure 6-S15. Scatter plot obtained by flowing benzonitrile droplets dispersed in water through a flow cytometer.

The scatter plot represents 50,000 events recorded at a flow rate of 14 μL/min.

Calculation of the Percentage of Radial Droplets Contained in a LC Emulsion from Frequency Histograms of FSC

As described in the main text, the percentage of radial droplets contained in a LC emulsion can be quantified by comparing the number of light scattering events measured between ~30,000 a.u. and ~60,000 a.u. relative to the number of events measured within this region for an emulsion containing only radial droplets because this region of the scatter plot corresponds to the range of FSC values in which the S-shape characteristic of radial droplets is observed (Figure 6-2B of the main text). The following equation was used to calculate the percentage of radial LC droplets contained in an emulsion from the peak occurring between ~30,000 a.u. and ~60,000 a.u in frequency histograms of FSC values (see Figure 6-7A of the main text):

$$\Phi_{\mathrm{DPPC}}^{\mathrm{FC}} = \frac{\sum_{FSC=30,000}^{60,000} Count|_{\Phi_{\mathrm{DPPC}}^{\mathrm{PM}}} - \sum_{FSC=30,000}^{60,000} Count|_{\Phi_{\mathrm{DPPC}}^{\mathrm{PM}}=0\%}}{\sum_{FSC=30,000}^{60,000} Count|_{\Phi_{\mathrm{DPPC}}^{\mathrm{PM}}=100\%} - \sum_{FSC=30,000}^{60,000} Count|_{\Phi_{\mathrm{DPPC}}^{\mathrm{PM}}=0\%}} * 100\% \quad (6\text{-}11)$$

In equation 6-11 the area below the peak occurring at $\Phi_{\mathrm{DPPC}}^{\mathrm{PM}}$ = 0% is subtracted from the integrated area under each peak as a baseline. Then, the percentage of the corrected area under each peak relative to the area under the corrected peak occurring at $\Phi_{\mathrm{DPPC}}^{\mathrm{PM}}$ = 100% is calculated.

Heating of LC Droplets in a Flow Cytometer

As pointed out in the main text, all flow cytometry measurements were performed at room temperature (~25°C), which is below the nematic-to-isotropic transition temperature of 5CB (T_{NI} = 35°C).[59, 60] In an Accuri C6 flow cytometer, the power of the laser (50 mW)[40] is comparable to that used to optically trap LC droplets (*e.g.*, 70 mW)[61]. In an optical trap, the heating of an object in water is typically ~ 1°K/W,[62] and thus a 50 mW laser is predicted to generate a temperature increase of 0.05°K. Finally, we point out that we estimate LC droplets to pass through the laser within ~ 0.1 ms, corresponding to a very short period of illumination (heating).

6.6 References

*This chapter was prepared as a Full Paper reporting original research in the journal *Analytical Chemistry*. James Buchen performed preliminary measurements. Xiaoguang Wang performed the measurements on polymerized liquid crystal droplets and helped in development of our understanding of the scatter plots.

1. Bai, Y.; Abbott, N. L., Recent Advances in Colloidal and Interfacial Phenomena Involving Liquid Crystals. *Langmuir* **2011**, 27, 5719-5738.
2. Carlton, R. J.; Hunter, J. T.; Miller, D. S.; Abbasi, R.; Mushenheim, P. C.; Tan, L.; Abbott, N. L., Chemical and Biological Sensing Using Liquid Crystals. *Liquid Crystal Reviews* **2013**, 1-23.
3. Lockwood, N. A.; Gupta, J. K.; Abbott, N. L., Self-Assembly of Amphiphiles, Polymers and Proteins at Interfaces between Thermotropic Liquid Crystals and Aqueous Phases. *Surface Science Reports* **2008**, 63, 255-293.
4. Lowe, A. M.; Abbott, N. L., Liquid Crystalline Materials for Biological Applications. *Chemistry of Materials* **2012**, 24, 746-758.
5. Gupta, J. K.; Zimmerman, J. S.; de Pablo, J. J.; Caruso, F.; Abbott, N. L., Characterization of Adsorbate-Induced Ordering Transitions of Liquid Crystals within Monodisperse Droplets. *Langmuir* **2009**, 25, 9016-9024.
6. Lin, I. H.; Miller, D. S.; Bertics, P. J.; Murphy, C. J.; de Pablo, J. J.; Abbott, N. L., Endotoxin-Induced Structural Transformations in Liquid Crystalline Droplets. *Science* **2011**, 332, 1297-1300.
7. Miller, D. S.; Abbott, N. L., Influence of Droplet Size, Ph and Ionic Strength on Endotoxin-Triggered Ordering Transitions in Liquid Crystalline Droplets. *Soft Matter* **2013**, 9, 374-382.
8. Gupta, J. K.; Sivakumar, S.; Caruso, F.; Abbott, N. L., Size-Dependent Ordering of Liquid Crystals Observed in Polymeric Capsules with Micrometer and Smaller Diameter. *Angewandte Chemie, International Edition* **2009**, 48, 1652-1655.
9. Tjipto, E.; Cadwell, K. D.; Quinn, J. F.; Johnston, A. P. R.; Abbott, N. L.; Caruso, F., Tailoring the Interfaces between Nematic Liquid Crystal Emulsions and Aqueous Phases Via Layer-by-Layer Assembly. *Nano Letters* **2006**, 6, 2243-2248.
10. Alino, V. J.; Pang, J.; Yang, K. L., Liquid Crystal Droplets as a Hosting and Sensing Platform for Developing Immunoassays. *Langmuir* **2011**, 27, 11784-11789.
11. Alino, V. J.; Sim, P. H.; Choy, W. T.; Fraser, A.; Yang, K. L., Detecting Proteins in Microfluidic Channels Decorated with Liquid Crystal Sensing Dots. *Langmuir* **2012**, 28, 17571-17577.
12. Alino, V. J.; Tay, K. X.; Khan, S. A.; Yang, K. L., Inkjet Printing and Release of Monodisperse Liquid Crystal Droplets from Solid Surfaces. *Langmuir* **2012**, 28, 14540-14546.
13. Bi, X. Y.; Lai, S. L.; Yang, K. L., Liquid Crystal Multiplexed Protease Assays Reporting Enzymatic Activities as Optical Bar Charts. *Analytical Chemistry* **2009**, 81, 5503-5509.

14. Bera, T.; Fang, J. Y., Optical Detection of Lithocholic Acid with Liquid Crystal Emulsions. *Langmuir* **2013**, 29, 387-392.
15. Bera, T.; Fang, J. Y., Polyelectrolyte-Coated Liquid Crystal Droplets for Detecting Charged Macromolecules. *Journal of Materials Chemistry* **2012**, 22, 6807-6812.
16. Sivakumar, S.; Wark, K. L.; Gupta, J. K.; Abbott, N. L.; Caruso, F., Liquid Crystal Emulsions as the Basis of Biological Sensors for the Optical Detection of Bacteria and Viruses. *Advanced Functional Materials* **2009**, 19, 2260-2265.
17. Berggren, E.; Zannoni, C.; Chiccoli, C.; Pasini, P.; Semeria, F., Computer-Simulations of Nematic Droplets with Bipolar Boundary-Conditions. *Physical Review E* **1994**, 50, 2929-2939.
18. Drzaic, P. S., *Liquid Crystal Dispersions*. World Scientific: River Edge, NJ, USA, 1995.
19. Meyer, R. B., Piezoelectric Effects in Liquid Crystals. *Physical Review Letters* **1969**, 22, 918-921.
20. Ondris-Crawford, R.; Boyko, E. P.; Wagner, B. G.; Erdmann, J. H.; Zumer, S.; Doane, J. W., Microscope Textures of Nematic Droplets in Polymer Dispersed Liquid-Crystals. *Journal of Applied Physics* **1991**, 69, 6380-6386.
21. Prischepa, O. O.; Shabanov, A. V.; Zyryanov, V. Y., Transformation of Director Configuration Upon Changing Boundary Conditions in Droplets of Nematic Liquid Crystal. *JETP Letters* **2004**, 79, 257-261.
22. Volovik, G. E.; Lavrentovich, O. D., The Topological Dynamics of Defects - Boojums in Nematic Drops. *Zhurnal Eksperimentalnoi I Teoreticheskoi Fiziki* **1983**, 85, 1997-2010.
23. Lavrentovich, O. D., Topological Defects in Dispersed Liquid Crystals, or Words and Worlds around Liquid Crystal Drops. *Liquid Crystals* **1998**, 24, 117-125.
24. Prishchepa, O. O.; Shabanov, A. V.; Zyryanov, V. Y., Director Configurations in Nematic Droplets with Inhomogeneous Boundary Conditions. *Physical Review E* **2005**, 72, 031712-1-031712-11.
25. Kinsinger, M. I.; Buck, M. E.; Abbott, N. L.; Lynn, D. M., Immobilization of Polymer-Decorated Liquid Crystal Droplets on Chemically Tailored Surfaces. *Langmuir* **2010**, 26, 10234-10242.
26. Bao, N.; Zhan, Y. H.; Lu, C., Microfluidic Electroporative Flow Cytometry for Studying Single-Cell Biomechanics. *Analytical Chemistry* **2008**, 80, 7714-7719.
27. Gilman-Sachs, A., Flow-Cytometry. *Analytical Chemistry* **1994**, 66, A700-A707.
28. Givan, A. L., *Flow Cytometry : First Principles*. 2nd ed.; Wiley: New York, NY, USA, 2001.
29. McClain, M. A.; Culbertson, C. T.; Jacobson, S. C.; Ramsey, J. M., Flow Cytometry of Escherichia Coli on Nucrifluidic Devices. *Analytical Chemistry* **2001**, 73, 5334-5338.
30. Melamed, M. R.; Lindmo, T.; Mendelsohn, M. L., *Flow Cytometry and Sorting*. 2nd ed.; Wiley-Liss: New York, NY, USA, 1990.
31. Shapiro, H. M., *Practical Flow Cytometry*. 3rd ed.; Wiley-Liss: New York, NY, USA, 1995.
32. Simonnet, C.; Groisman, A., High-Throughput and High-Resolution Flow Cytometry in Molded Microfluidic Devices. *Analytical Chemistry* **2006**, 78, 5653-5663.
33. Hiemenz, P. C.; Lodge, T., *Polymer Chemistry*. 2nd ed.; CRC Press: Boca Raton, FL, USA, 2007.
34. Hiemenz, P. C.; Rajagopalan, R., *Principles of Colloid and Surface Chemistry*. 3rd ed.; Marcel Dekker: New York, NY, USA, 1997.

35. Zumer, S., Light-Scattering from Nematic Droplets - Anomalous-Diffraction Approach. *Physical Review A* **1988**, 37, 4006-4015.
36. Zumer, S.; Doane, J. W., Light-Scattering from a Small Nematic Droplet. *Physical Review A* **1986**, 34, 3373-3386.
37. Miller, D. S.; Carlton, R. J.; Mushenheim, P. C.; Abbott, N. L., Introduction to Optical Methods for Characterizing Liquid Crystals at Interfaces. *Langmuir* **2013**, 29, 3154−3169.
38. Terentjev, E. M., Stability of Liquid-Crystalline Macroemulsions. *Europhysics Letters* **1995**, 32, 607-612.
39. Brake, J. M.; Daschner, M. K.; Luk, Y. Y.; Abbott, N. L., Biomolecular Interactions at Phospholipid-Decorated Surfaces of Liquid Crystals. *Science* **2003**, 302, 2094-2097.
40. *Accuri Cytometers C6 Flow Cytometer Instrument Manual*. Accuri Cytometers Inc.: Ann Arbor MI.
41. Mondiot, F.; Wang, X.; de Pablo, J. J.; Abbott, N. L., Liquid Crystal-Based Emulsions for Synthesis of Spherical and Non-Spherical Particles with Chemical Patches. *Journal of the American Chemical Society* **2013**, 9972–9975.
42. Israelachvili, J. N., *Intermolecular and Surface Forces*. 2nd ed.; Academic Press London: San Diego, CA, USA, 1991.
43. Bodnar, V. G.; Lavrentovich, O. D.; Pergamenshchik, V. M., The Threshold for the Hedgehog - Ring Structural Transition in Nematic Drops in an Alternating Electric-Field. *Zhurnal Eksperimentalnoi I Teoreticheskoi Fiziki* **1992**, 101, 111-125.
44. Gartland, E. C.; Mkaddem, S., Instability of Radial Hedgehog Configurations in Nematic Liquid Crystals under Landau-De Gennes Free-Energy Models. *Physical Review E* **1999**, 59, 563-567.
45. Lavrentovich, O. D.; Terentiev, E. M., Phase-Transition with the Change of Symmetry of Topological Point-Defects (Hedgehogs) in a Nematic Liquid-Crystal. *Zhurnal Eksperimentalnoi I Teoreticheskoi Fiziki* **1986**, 91, 2084-2096.
46. Mkaddem, S.; Gartland, E. C., Fine Structure of Defects in Radial Nematic Droplets. *Physical Review E* **2000**, 62, 6694-6705.
47. Hsu, P.; Poulin, P.; Weitz, D. A., Rotational Diffusion of Monodisperse Liquid Crystal Droplets. *Journal of Colloid and Interface Science* **1998**, 200, 182-184.
48. Als-Nielsen, J.; McMorrow, D., *Elements of Modern X-Ray Physics*. 2nd ed.; Wiley: Hoboken, NJ, USA, 2011.
49. Meli, M. V.; Lin, I. H.; Abbott, N. L., Preparation of Microscopic and Planar Oil-Water Interfaces That Are Decorated with Prescribed Densities of Insoluble Amphiphiles. *Journal of the American Chemical Society* **2008**, 130, 4326-4333.
50. Bird, R. B.; Stewart, W. E.; Lightfoot, E. N., *Transport Phenomena*. Rev. 2nd ed.; J. Wiley: New York, NY, USA, 2007.
51. Taylor, G. I., The Formation of Emulsions in Definable Fields. *Proceeding of the Royal Society London A* **1934**, 146, 501-523.
52. Tsakalos, V. T.; Navard, P.; Peuvrel-Disdier, E., Deformation and Breakup Mechanisms of Single Drops During Shear. *Journal of Rheology* **1998**, 42, 1403-1417.
53. Fernandez-Nieves, A.; Link, D. R.; Marquez, M.; Weitz, D. A., Topological Changes in Bipolar Nematic Droplets under Flow. *Physical Review Letters* **2007**, 98, 087801-1-087801-4.
54. Crawford, G. P.; Polak, R. D.; Scharkowski, A.; Chien, L. C.; Doane, J. W.; Zumer, S., Nematic Director-Fields Captured in Polymer Networks Confined to Spherical Droplets. *Journal of Applied Physics* **1994**, 75, 1968-1971.

55. Gannon, M. G. J.; Faber, T. E., Surface-Tension of Nematic Liquid-Crystals. *Philosophical Magazine a-Physics of Condensed Matter Structure Defects and Mechanical Properties* **1978**, 37, 117-135.
56. Delabre, U.; Richard, C.; Cazabat, A. M., Some Specificities of Wetting by Cyanobiphenyl Liquid Crystals. *Journal of Physics-Condensed Matter* **2009**, 21, 1-11.
57. Raetz, C. R. H.; Whitfield, C., Lipopolysaccharide Endotoxins. *Annual Review of Biochemistry* **2002**, 71, 635-700.
58. Aurell, C. A.; Wistrom, A. O., Critical Aggregation Concentrations of Gram-Negative Bacterial Lipopolysaccharides (Lps). *Biochemical and Biophysical Research Communications* **1998**, 253, 119-123.
59. Luk, Y. Y.; Campbell, S. F.; Abbott, N. L.; Murphy, C. J., Non-Toxic Thermotropic Liquid Crystals for Use with Mammalian Cells. *Liquid Crystals* **2004**, 31, 611-621.
60. Shah, R. R.; Abbott, N. L., Coupling of the Orientations of Liquid Crystals to Electrical Double Layers Formed by the Dissociation of Surface-Immobilized Salts. *Journal of Physical Chemistry B* **2001**, 105, 4936-4950.
61. Humar, M.; Musevic, I., Surfactant Sensing Based on Whispering-Gallery-Mode Lasing in Liquid-Crystal Microdroplets. *Optics Express* **2011**, 19, 19836-19844.
62. Peterman, E. J. G.; Gittes, F.; Schmidt, C. F., Laser-Induced Heating in Optical Traps. *Biophysical Journal* **2003**, 84, 1308-1316.

Chapter 7. Rapid Detection of Endotoxin using Liquid Crystal Microdroplets in a Flow Focusing Device*

7.1 Introduction

Detection and quantification of bacterial endotoxin is critically important in a wide range of health-related contexts, including clinical and basic biomedical research,[1-6] public and occupational health,[7-12] and device and agent safety.[13-23] Endotoxin is a lipopolysaccharide (LPS) comprised of a glycophospholipid (called lipid A; Figure 7-1A) in addition to two polysaccharide domains, and it is found in the outer membrane of Gram-negative bacteria. Upon proliferation or death, Gram-negative bacteria shed endotoxin into the environment, thereby making the LPS available for detection. The most widely used method for detection of endotoxin is the so-called *Limulus* amoebocyte lysate (LAL) assay, which employs a labile mixture of enzymes obtained from the blood of horseshoe crabs that coagulate or clot in the presence of endotoxin. Although the LAL assay possesses the picogram per milliliter (pg/mL) sensitivity required for many applications,[13, 18, 24] the complexity and variation in activity of the LAL enzyme mixtures, which results from numerous interfering compounds (including synthetic surfactants, chelating agents and lipids) as well as season-dependent harvest and variation among crab species, leads to semi-quantitative results.[17, 18, 24-28]

As part of a study aimed at addressing the need for improved methods of detection of endotoxin, we recently reported that the internal configurations of micrometer-sized, water-dispersed droplets of (synthetic) thermotropic liquid crystal (LC) change in the presence of endotoxin (see Chapter 4).[29] Specifically, pg/mL aqueous concentrations of endotoxin from

Escherichia coli (EC) were observed to trigger a change in the internal ordering of the LC microdroplets (LCMDs) from a so-called bipolar configuration to a radial configuration (see Figure 7-1B for a schematic representation this change in configuration). Because LCs possess anisotropic optical properties (birefringence), the change in configuration of the LCMDs induced by interaction with endotoxin led to a distinct change in optical appearance, as imaged by polarized light microscopy (see insets in Figure 7-2). We also established that the mechanism of response of the LCMDs to endotoxin was strongly dependent on the size of the LCMDs (the optimal size was around 2 – 6 μm), and that the response was triggered by the interaction of 10^2 – 10^3 endotoxin molecules with each LCMD (see Chapter 5).[30] Significantly, because 10^7 molecules are required to form a monolayer over the entire surface of each MD,[29, 31] the mechanism by which the LPS triggers the change in the configurations of the LCMDs is not *via* a change in the anchoring energy of the LC (the energy that controls the preferred alignment of LC at an interface[32-34]) over the surface of a MD. Instead, a thermodynamic analysis revealed that the presence of endotoxin perturbs the free energies of the LCMDs by ~10^{-17} J/droplet, which is comparable to the standard free energy of self-association of ~10^3 endotoxin molecules.[30] These results, when combined with imaging that revealed localization of endotoxin at the center of LCMDs,[29] support the hypothesis that self-assembly of endotoxin at the sites of defects within micrometer-sized LC droplets provides the driving force for the ordering transitions.

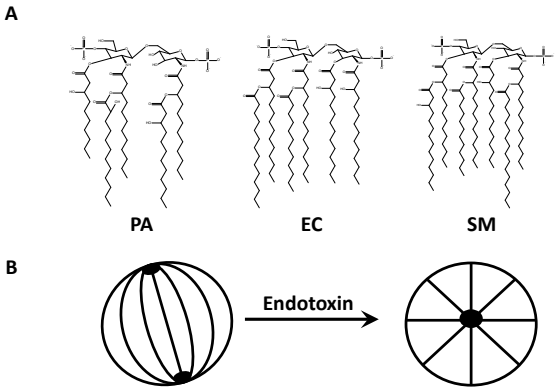

Figure 7-1. Bipolar-to-radial ordering transitions in water-dispersed liquid crystal microdroplets triggered by endotoxins.

(A) Chemical structures of the lipid A portion of endotoxin from *Pseudomonas aeruginosa* (PA; 5 tails), *Escherichia coli* (EC; 6 tails), and *Salmonella minnesota* (SM; 7 tails). (B) Schematic illustration of the bipolar-to-radial transformation in the internal configuration of water-dispersed MDs of thermotropic LC triggered by endotoxin. The black lines inside the MD boundaries represent the local orientation of the LC and the black circles represent topological defects (localized areas with lower liquid crystalline order).

While our initial studies have revealed the promise of LCMDs as the basis of a new analytical methodology for detection of endotoxin, the procedures for imaging the LCMDs, as used in our past studies, were tedious (several hours were required for analysis of hundreds of LCMDs).[29, 30] An additional technical challenge encountered in our prior studies was the sedimentation of LCMDs onto the coverslips used to support the endotoxin solution – it was necessary to avoid imaging LCMDs that had sedimented near the coverslips because interactions of the LCMDs with the glass perturbed the configurations of the MDs.[30, 35, 36] These issues necessitated the imaging of MDs that were diffusing in the bulk aqueous solution, and such MDs translate (at velocities greater than 1 μm/s) in and out of the plane of focus. While these technical challenges may be addressed by improved imaging methods, here we report that measurements of the scattering of light from LCMDs that are passing through a flow focusing device provides an alternative and rapid method for quantification of the response of LCMDs to endotoxin.

While the flow focusing device used in the current study was part of a commercial (low-end) flow cytometer, the principles established in our study are applicable to chip-based designs of flow focusing devices,[37-40] thus potentially providing low cost methods for rapid analysis of endotoxin.

Our use of a flow cytometer for analysis of endotoxin builds from our recent demonstration that low- and high-angle light scattering (so-called forward scattering (FSC) and side scattering (SSC)) from LCMDs dispersed in aqueous solutions can be analyzed to indicate the configurations of LCs within the MDs (see Chapter 6).[41] In particular, by using millimolar concentrations of synthetic surfactants to change the internal configurations of the LCMDs, which occurs as a result of adsorption of surfactant on the surfaces of the LCMDs, we showed that each configuration of the LC generated distinct light scatter plots.[41] Significantly, we demonstrated that the rapid rate of analysis of LCMDs that can be achieved by use of a flow focusing device permits characterization of each MD within a dispersion of 10,000 MDs in a few seconds. Whereas our past study established the feasibility of distinguishing between different configurations of LCMDs caused by surfactant-induced changes in surface anchoring energy (a consequence of formation of a monolayer of surfactant on the droplet surface), in the current study, we demonstrate that the methodology can be extended to detect endotoxin at the pg/mL level. We note that the balance of energetics underlying the response of the LCMDs to endotoxin is substantially finer than for surfactant-induced configurational transitions,[30] and thus it was not apparent to us, in advance of this study, that our prior results obtained using surfactants and flow cytometry[41, 42] would translate to detection of endotoxin. Significantly, the facile nature of the analytical methodology reported herein also enabled us to achieve a series of advances in our understanding of the interaction of endotoxin with LCMDs, which underlies the method.

Specifically, we reveal that endotoxin from three different organisms provide quantitatively similar responses when using the LCMDs, and we also establish that the response of the LCMDs to endotoxin can be used to obtain information about the state of aggregation of endotoxin in solution (which is relevant to the biological activity of the endotoxin[43]).

7.2 Experimental Section

Materials. Endotoxin from *Escherichia coli* (O127:B8), *Salmonella minnesota*, and *Pseudomonas aeruginosa*, lipid A from *Escherichia coli* F583 (Rd mutant; molecular weight = 1,800 Da), cardiolipin from *Escherichia coli* (CL), sodium dodecyl sulfate (SDS), triethylamine (TEA), and phosphate buffered saline (PBS) pouches (used to make PBS buffer used as the sheath fluid for flow cytometry) were purchased from Sigma-Aldrich (St. Louis, MO). 1,2-dipalmitoyl-*sn*-glycero-3-phosphocholine (DPPC), 1,2-di-(9Z-octadecenoyl)-*sn*-glycero-3-phosphoethanolamine (DOPE), 1,2-di-(9Z-octadecenoyl)-*sn*-glycero-3-phospho-L-serine (DOPS), 1,2-di-(9Z-octadecenoyl)-*sn*-glycero-3-phospho-(1'-myo-inositol) (DOPI), cholesterol (Chol), and phosphatidylcholines from an egg (egg PC) were purchased from Avanti Polar Lipids, Inc. (Alabaster, AL). Lipid X was obtained from the laboratory of Paul J. Bertics in the Department of Biomolecular Chemistry at the University of Wisconsin-Madison (Madison, WI). 4’-pentyl-4-cyanobiphenyl (5CB) was obtained from EM Sciences (New York, NY). EndoTrap® Red Equilibration Buffer (10 mM Na_2HPO_4/NaH_2PO_4, 80 mM NaCl, pH 7.2; certified to contain a concentration of endotoxin of less than 0.02 EU/mL (2 pg/ mL)) and EndoTrap® Red 1/1 chromatography columns for endotoxin removal were purchased from Hyglos GmbH (Regensburg, Germany). Neptune pipette tips (no detectable endotoxin) were purchased from Continental Lab Product, Inc. (San Diego, CA). Fisher’s Finest PremiumGrade cover glass,

Wheaton glass 20 mL scintillation vials, 1.5 mL FisherBrand micro-centrifuge tubes, 12 x 75 mm disposable glass culture tubes, 16 x 100 mm disposable glass culture tubes, and a 10 µL glass Hamilton blunt tipped syringe were obtained from Fisher Scientific (Pittsburgh, PA). Deionization of a distilled water source was performed with a Milli-Q system (Millipore, Bedford, MA) to give water with a resistivity of 18.2 MΩ cm.

Preparation of Aqueous Dispersions of Endotoxin or Lipid A. One mg of powdered endotoxin was dissolved in 1 mL of a 10 µM solution of SDS in EndoTrap® Red Equilibration Buffer at room temperature. The resulting solution was then subjected to two cycles of sonication for 5 s using a Branson Sonifier 250 (Emerson Electric Company, St. Louis, MO) and vortex mixing at 2,500 rpm for 1 minute. Following mixing, the 1 mg/mL stock solution was divided into 80 µL aliquots and stored in a freezer at – 80°C for future use.

Serial dilutions were performed by first removing an 80 µL aliquot of 1 mg/mL endotoxin from the freezer and allowing the solution to warm to room temperature. Next, the stock was vortexed at 2,500 rpm for 30 s. Finally, serial dilutions were performed to reach a final concentration of 0.5 pg/mL.

An identical protocol was followed to prepare aqueous dispersions of lipid A with the exception that TEA was added to the 10 µM SDS solution used to dissolve the 1 mg powdered lipid A at 0.2 v% to increase the solubility of the lipid. The serial dilutions were carried out in a 10 µM SDS solution free of TEA.

Preparation of Aqueous Dispersions of Phospholipids, CL, and Chol. Aqueous dispersions of DPPC, DOPE, DOPS, DOPI, Chol, CL, and egg PC were prepared according to previously

published methods.[44, 45] Briefly, for lipids initially dispersed in chloroform, the chloroform was evaporated under a stream of nitrogen and the vial containing the lipid was immediately placed under a vacuum for at least 1 hour. Afterwards, the dried lipid or lipid received as a powder was re-suspended in a 10 µM solution of SDS in EndoTrap® Red Equilibration Buffer to achieve a final concentration of 100 µg/mL and sonicated for 5 cycles of 1 minute at 12 W. Finally, serial dilutions were performed to reach a final concentration of 100 ng/mL.

Preparation of LC Emulsions and Dilution into Aqueous Dispersions of Amphiphiles. For experiments in which the volume of stock emulsion added to a sample was 70 µL or less, the emulsions were formed by first adding 6 µL 5CB to the bottom of a 12 x 75 mm disposable glass culture tube using a 10 µL blunt tipped syringe. Then, 3 mL of a 10 µM solution of SDS in EndoTrap® Red Equilibration Buffer was added to the tube, and the mixture was vortexed for 30 s at 3,000 rpm. A concentration of 10 µM SDS was selected because it led to reproducible formation of emulsions without influencing the configuration of the LCMDs. Next, the emulsions were allowed to incubate for 1 hour prior to dilution to allow measurable coalescence to arrest. For experiments in which the volume of stock added was above 70 µL, the emulsions were prepared in a similar fashion, with the exception that the volume of emulsion was increased from 3 to 10 mL. We confirmed that scale-up of the emulsion volume did not influence the response of the MDs (see Figure 7-S1 of the Supporting Information). As was the case for our previous studies,[29, 30, 36] the emulsification procedure resulted in polydisperse emulsions with MD sizes ranging between 1 and 20 µm-in-diameter. Finally, aliquots of the stock emulsions were diluted into a 700 µL volume of aqueous dispersions of lipid at a fixed volume, set to achieve a desired MD concentration, and the emulsion was allowed to incubate for 15 minutes

prior to measurement of light scattering by flow cytometry. A table with the average concentration of LCMDs resulting from each aliquot volume is available in the Supporting Information (Table 7-S1). An exception was experiments in which the volume of stock added to the samples was 400 µL because this volume of stock resulted in MD concentrations outside of the detection limit of our flow cytometer (see below). For these samples, 400 µL of stock was added and the samples were allowed to incubate for 15 minutes. Then, a twofold dilution of the samples was performed by adding 1.1 mL of 10 µM SDS and the samples were allowed to equilibrate for 30 minutes prior to measurement. We confirmed that a post-incubation twofold dilution did not influence the response of MDs to endotoxin by measuring dose-response curves for 70 and 200 µL of added stock before and after dilution (see Figure 7-S2 of the Supporting Information).

Flow Cytometry of LC Emulsions. Frequency histograms of the intensity of forward light scattering (FSC) were obtained for LC emulsions using a BD Accuri C6 flow cytometer (Ann Arbor, MI). FSC was measured at a detection angle of 0° ± 15°,[46] and all flow cytometry measurements were performed at room temperature. Emulsions were pumped through the flow cytometer at a flow rate of 14 µL/min and the histograms were constructed from the measurement of 5,000 LCMDs.

The percentage of radial MDs contained in a LC emulsion was quantified according to our previous procedure.[41, 42] Briefly, for a given emulsion the number of light scattering events measured between 3×10^4 and 6×10^4 a.u. was compared to the number of events measured within this region for an emulsion of LCMDs dispersed in 100 ng/mL endotoxin (positive control) because this concentration of endotoxin was found to lead to a pure population of radial

MDs. The following equation was used to calculate the percentage of radial LCMDs contained in an emulsion from the peak occurring between 3×10^4 and 6×10^4 a.u. in frequency histograms of FSC values:

$$\text{Percent Radial} = \frac{\sum_{FSC=30,000}^{60,000} Count|_{emulsion} - \sum_{FSC=30,000}^{60,000} Count|_{10\mu MSDS}}{\sum_{FSC=30,000}^{60,000} Count|_{\frac{100ng}{mL}} - \sum_{FSC=30,000}^{60,000} Count|_{10\mu MSDS}} \times 100\% \quad (7-1)$$

In equation 7-1, the area below the peak measured for an emulsion of LCMDs dispersed in a 10 μM aqueous solution of SDS (negative control; Figure 7-2A) is subtracted from the integrated area under each peak as a baseline. Then, the percentage of the corrected area under each peak relative to the area under the corrected peak measured for the positive control is calculated (Figure 7-2B).

Optical Characterization of LC Emulsions by Polarized Light Microscopy LC emulsions were characterized by polarized light microscopy according to previously published methods.[29, 30, 36] Briefly, a 40 μL volume of LC emulsion was dispensed onto a glass coverslip, and the configurations of the LCs within the emulsion MDs were determined by observation of the MDs under an Olympus IX71 inverted microscope (Center Valley, PA) using an objective magnification power of 100x (an oil-immersion lens). Polarized light micrographs of the LC emulsions were collected with a Hamamatsu 1394 ORCAER CCD camera (Bridgewater, NJ) connected to a computer and controlled through SimplePCI imaging software (Compix, Inc., Cranberry Twp., NJ). We characterized LCMDs that were located at least 50 μm above the surface of the coverslip and translating with velocities greater than 1 μm/s to avoid observation of LCMDs interacting with the surfaces of the coverslips.[35] Because the MDs were diffusing (translating and rotating), radial MDs exhibited an optical appearance that was invariant with

time when viewed between crossed polars, whereas bipolar MDs had a distinct, time-varying optical appearance.[36] Multiple images of each MD were taken to determine the time-dependent optical appearance of the MD, and thus the director configuration.

Dynamic Light Scattering. Dynamic light scattering measurements on endotoxin dispersions were performed on a Malvern Zetasizer Nano ZSP (Malvern Instruments, Malvern, UK). The samples were maintained at 25°C and the angle of the detector was 173°.

7.3 Results and Discussion

Our first experiments were performed to determine if it was possible to detect endotoxin from EC in aqueous solutions using FSC from MDs of nematic 5CB. We began by measuring FSC from LCMDs dispersed in either a 10 μM solution of sodium dodecyl sulfate (SDS) or the same solution spiked with endotoxin to a concentration of 100 ng/mL. The MD concentration used in these studies was ~5,000 LCMDs/μL (70 μL of stock emulsion diluted into 700 μL of sample; see above and Table 7-S1 of the Supporting Information for details). These concentrations of SDS and endotoxin were used because they were validated by optical microscopy to lead to populations of LCMDs in either bipolar or radial configurations, respectively (see insets of Figure 7-2 for representative polarized light micrographs). As detailed elsewhere, a bipolar configuration results, when LC is oriented tangential to the MD surface and is accompanied by two surface defects (*i.e.*, boojums) that form at diametrically opposite poles,[32, 45, 47-54] whereas the radial configuration arises when LC is oriented normal to the surface of a MD and it is accompanied by a single point (or small ring) defect present at the MD center (Figure 7-1B).[32, 45, 49, 51-55] Figure 7-2 shows histograms of the number of LCMDs giving rise to a

specific intensity of FSC, for the LC emulsions without (Figure 7-2A) and with (Figure 7-2B) endotoxin added. The data in the histograms were obtained at a rate of 1,250 MDs per second, and reveal that the radial configurations (but not the bipolar configurations) of the LCMDs generated a peak in the histogram of FSC for intensities measured between 3×10^4 and 6×10^4 a.u. (see the region indicated by the dashed red lines in Figure 7-2). The peak in Figure 7-2B is consistent with our prior measurements of LC emulsions with surfactant-induced radial configurations,[41, 42] and thus leads to the conclusion that the delicate balance of energetics that underlies endotoxin-triggered radial configurations is not perturbed during flow cytometry-based characterization of LCMD configurations (the combination of 100 ng/mL endotoxin and ~5,000 LCMDs/μL results in ~2×10^5 molecules/MD which is below the threshold ~10^7 molecules/MD required to cover the surfaces the LCMDs with a monolayer of endotoxin[29, 31,‡] (see Introduction)).

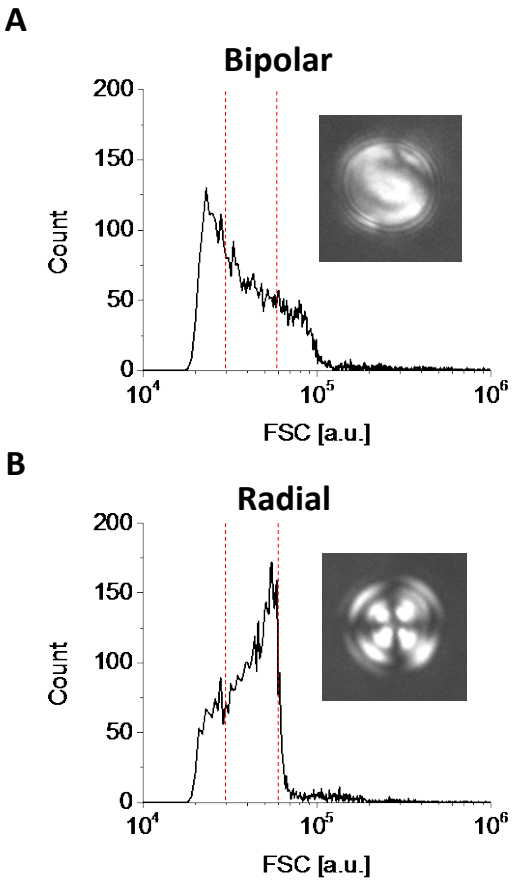

Figure 7-2. Frequency histogram of the intensity of forward light scattering (FSC) events generated by flowing aqueous dispersions of nematic LCMDs in either a (A) bipolar or (B) radial configuration through a flow cytometer.

The bipolar MDs were suspended in an aqueous buffer that contained 10 μM SDS, whereas the radial MDs were suspended in the same buffer to which endotoxin from EC was added to a concentration of 100 ng/mL. The concentration of MDs was ~5,000 LCMDs/μL and the histograms were constructed from analysis of 5,000 MDs. The insets in each scatter plot show a representative polarized light micrograph (crossed polars) of a 5 μm-in-diameter MD. The red dashed lines indicate the range of intensity values used for quantitative determination of the percentage of radial MDs.

Previously, we established that the peak characteristic of emulsions containing radial LCMDs (as shown in Figure 7-2) grows in height with increasing fraction of radial MDs contained in an emulsion comprised of a mixture of bipolar and radial MDs.[41] With the goal of brevity, we refer the reader to our past publication for an explanation of the origin of this peak

(see Chapter 6), and emphasize here that quantitation of the integrated area under the peak (relative to controls) can be used to quantify the fraction of radial MDs in a mixture of bipolar and radial MDs.[41, 42] To determine if the same methodology can be used to quantify the response of the LCMDs to endotoxins, we measured the FSC from LCMDs in a 100 pg/mL solution of endotoxin from EC at a droplet concentration of ~5,000 LCMDs/μL (black line in Figure 7-3A). The area of the peak measured for this emulsion was similar to that measured for the MDs in the 100 ng/mL endotoxin solution (see Figure 7-S3 of the Supporting Information for the two histograms displayed together), indicating that nearly all of the LCMDs assumed a radial configuration in the presence of 100 pg/mL of endotoxin (see below). We showed previously using optical microscopy that the response of LCMDs to endotoxin can be tailored by controlling the concentration of MDs in the emulsion.[29] Accordingly, we next increased the concentration of MDs introduced into the 100 pg/mL endotoxin solution to ~11,000 LCMDs/μL by increasing the volume of stock emulsion added to the sample to 200 μL. Figure 7-3A shows that this increase in LCMD concentration led to a decrease in the peak area of the histogram. By quantitatively comparing the areas of the peaks obtained at LCMD concentrations of ~5,000 and ~11,000 LCMDs/μL (see Experimental section for details), we determined the percentage of radial LCMDs in the two dispersions to be 98 ± 2 % and 78 ± 13 %, respectively.

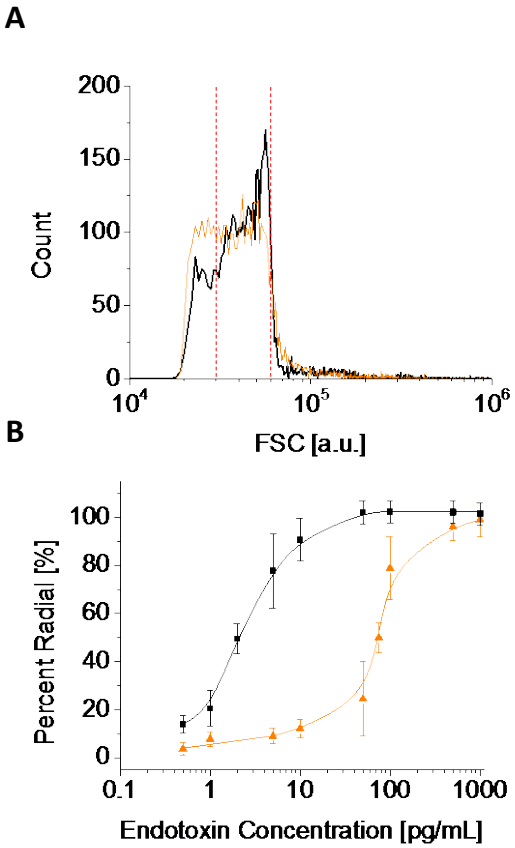

Figure 7-3. Dose-response curves of the percentage of LCMDs that underwent a bipolar-to-radial ordering transition in response to various concentrations of endotoxin from EC.

(A) Frequency histogram of FSC obtained by flowing nematic LCMDs suspended in aqueous solutions of 100 pg/mL endotoxin from EC through a flow cytometer. The concentration of MDs was ~5,000 (black line) or ~11,000 LCMDs/μL (orange line). The red dashed lines indicate the range of intensity values used for quantitative determination of the percentage of radial MDs. (B) Percentage of LCMDs that underwent a bipolar-to-radial ordering transition as a function of the concentration of endotoxin from EC. The average concentrations of MDs were (■) 5,100 ± 800 and (▲) 11,000 ± 2,000 LCMDs/μL. The lines are drawn to guide the eye.

Next, we quantified the fraction of radial MDs in LC dispersions exposed to various concentrations of endotoxin from EC for the above-described LCMD concentrations (Figure 7-3B). When using ~5,000 LCMDs/μL, the percentage of radial MDs was observed to increase significantly when the endotoxin concentrations exceeded 1 pg/mL endotoxin, and to saturate at

50 pg/mL. In contrast, when the concentration of LCMDs was ~11,000 LCMDs/μL, the response of the MDs to endotoxin was evident above 10 pg/mL and saturated at 500 pg/mL. While the dose-response curves shown in Figure 7-3B reveal that the concentration of endotoxin from EC in the aqueous solutions can be quantitatively determined by analysis of the FSC, an additional significant and unexpected finding that emerged from these measurements was that the approximately twofold increase in the concentration of LCMDs added to the samples led to a tenfold increase in the concentration at which the response of the MDs to endotoxin became saturated. Below we return to this observation and provide additional insight into its origins. We conclude our discussion of Figure 7-3 by noting that the time required to obtain the data in Figure 7-3 was greatly reduced relative to optical microscopy (~5 s was required to record FSC from 5,000 MDs; in contrast, it takes several days to acquire optical micrographs of an equivalent number of MDs).

To explore further the opportunity created by this new analytical methodology, and to advance our understanding of its capabilities for detection of endotoxin, we next investigated the response of the LCMDs to endotoxin obtained from bacteria other than EC. Specifically, we exposed LCMDs to endotoxin from either *Salmonella minnesota* (SM) or *Pseudomonas aeruginosa* (PA) (chemical structures of the lipid A portion shown in Figure 7-1A) to determine whether these endotoxins led to a similar response of LCMDs at pg/mL concentrations. Figure 7-4 shows that the endotoxins from SM and PA, which differ from the endotoxin from EC by the number of tails in lipid A (7 and 5, respectively, compared to 6 for endotoxin from EC), also triggered ordering transitions in LCMDs within the pg/mL concentration range. Additionally, the dose-response behavior of LCMDs to these two endotoxins was similar to that measured for endotoxin from EC at both MD concentrations (see Figure 7-5 below and Figure 7-S4 of the

Supporting Information). This result is important as it demonstrates that the LC-based methodology for detection of endotoxin is applicable to endotoxin obtained from at least three Gram-negative bacteria. In contrast, we note that the LAL assay for endotoxin can be strongly dependent on the bacterial source of endotoxin because different sources differentially activate the LAL enzyme mixture.[56, 57] Thus, for the LAL assay, the activity of each source of endotoxin must be established for quantitative determination of endotoxin concentration.

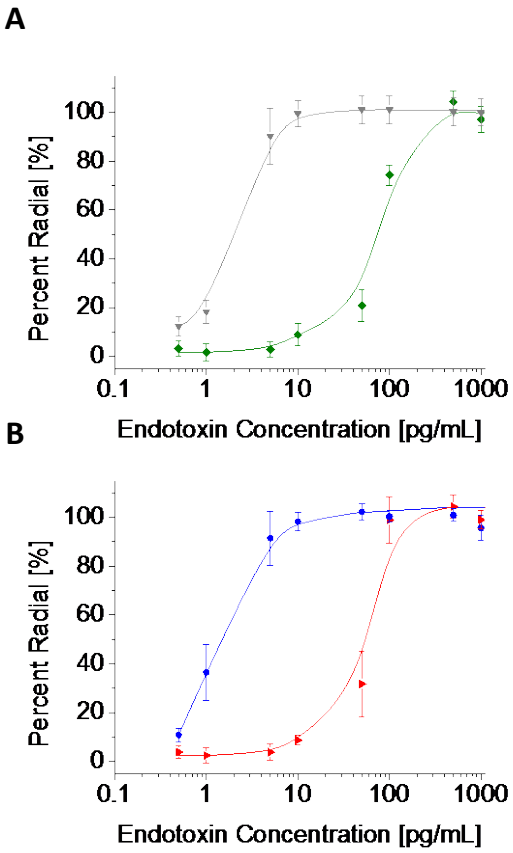

Figure 7-4. Dose-response curves for endotoxin from (A) SM or (B) PA.
The average concentrations of MDs were (▼) 5,000 ± 500, (●) 4,600 ± 400, (♦) 11,000 ± 2,000, and (►) 12,000 ± 2,000 LCMDs/μL.

We also note that by rescaling the dose-response curves shown in Figures 7-3 and 7-4 to show the percentage of LCMDs that underwent a bipolar-to-radial ordering transition in response

to the number of endotoxin molecules per LCMD (Figure 7-5), consistent with our previously reported model (see Chapter 5),[30] we find that the response of the LCMDs is complete in the presence of 10^2 – 10^3 endotoxin molecules per LCMD (on average).[‡] Additionally, we note that Figure 7-5 suggests that LCMDs respond to the presence of ~1 endotoxin molecule per LCMD in the dispersion. We caution, however, that the buffer used in these experiments is only validated to contain less than 2 pg/mL of endotoxin, and that the distribution of endotoxin across the MDs in the system is not expected to be uniform (see below). Overall, the results presented in Figure 7-5, when combined with those reported previously,[29, 30, 49] suggest that endotoxins trigger a bipolar-to-radial ordering transition in LCMDs at pg/mL aqueous concentrations *via* a mechanism that involves the assembly of 10^2 – 10^3 endotoxin molecules with each radial LCMD.

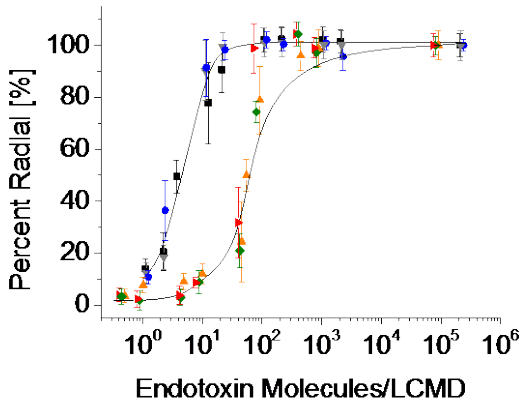

Figure 7-5. Dose-response curves for endotoxin from (■,▲) EC, (▼,♦) SM and (●,►) PA shown in Figures 7-3 and 7-4 rescaled to show the percentage of LCMDs that underwent a bipolar-to-radial ordering transition in response to the number of endotoxin molecules per MD.
The lines are drawn to guide the eye.

Although the order of magnitude of the number of endotoxin molecules measured to trigger the change in configuration of the LCMDs agrees with our previous studies,[29, 30, 49] an unexpected finding shown in Figure 7-5 is that the results obtained with ~5,000 or ~11,000

LCMDs/μL do not collapse onto the same curve (also see comments above regarding the effects of LCMD numbers on the response of the LCMDs to endotoxin). To gain further insight into the origin of this finding, we next measured dose-response curves for three additional concentrations of LCMDs added to solutions of endotoxin from EC (Figure 7-6A). For MD concentrations of ~500, ~2,500, and ~24,000 LCMDs/μL (see Table 7-S1 of the Supporting Information for details), the response of the MDs was observed to saturate at 5, 10, and 10^4 pg/mL of endotoxin, respectively (compared to 50 or 500 pg/mL for ~5,000 or ~11,000 LCMDs/μL, respectively). We note here that ~24,000 LCMDs/μL was outside of the detection limit of our flow cytometer (when emulsions become too concentrated, it is possible for multiple MDs to be reported by the flow cytometer as one droplet[46]). To address this issue, we lowered the MD concentration through a twofold dilution after incubating the MDs in the endotoxin solution for 15 minutes, a time that was sufficient for the endotoxin to interact with the LCMDs (see Experimental section). Interestingly, when the dose-response curves in Figure 7-6A were rescaled to show the response as a function of the number of endotoxin molecules per LCMD (Figure 7-6B), results obtained using samples with ~5,000 LCMDs/μL or less collapsed onto a single curve (the minor deviation evident in the results obtained with ~500 LCMDs/μL likely reflects the presence of background concentrations of endotoxin in the buffer (see above and Experimental section)), whereas the responses measured in samples with ~11,000 or ~24,000 LCMDs/μL did not collapse onto a universal curve.

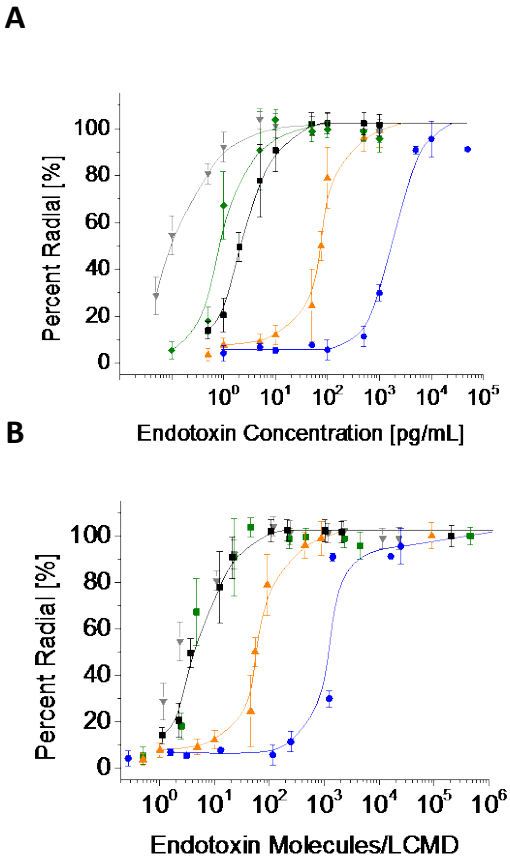

Figure 7-6. Dose-response and rescaled dose-response curves for endotoxin from EC at five different concentrations of LCMDs.

The average concentrations of MDs were (▼) 500 ± 50, (♦) 2,500 ± 200, (■) 5,100 ± 800, (▲) 11,000 ± 2,000 or (●) 24,000 ± 4,000 LCMDs/μL. (B) Dose-response curves in A rescaled to show the percentage of LCMDs that underwent a bipolar-to-radial ordering transition in response to the average number of endotoxin molecules per LCMD.

The observation reported above of a "threshold" concentration of endotoxin above which the rescaled dose-response curves no longer overlap hinted to us that the response of the LCMDs may reflect a concentration-dependent change in the state of aggregation of endotoxin. Here we comment that many properties of amphiphilic solutions exhibit such "threshold" behaviors associated with the onset of aggregation, including ionic conductivity, osmotic pressure, and turbidity.[58, 59] Specifically, for endotoxin, it has been reported that aggregates are present at

concentrations as low as 10 pg/mL,[60] and that aggregates formed at low concentrations associate into even more complex assemblies at higher concentrations (*e.g.*, ribbon-like structures, discs, or cubic and inverse hexagonal assemblies).[60-64] We hypothesized that the rescaled dose-response curves of samples containing more than ~5,000 LCMDs/μL did not collapse onto the other curves in Figure 7-6B because the endotoxin concentrations in the former samples exceeded 10 pg/mL, concentrations above which the aggregation of endotoxins changes.

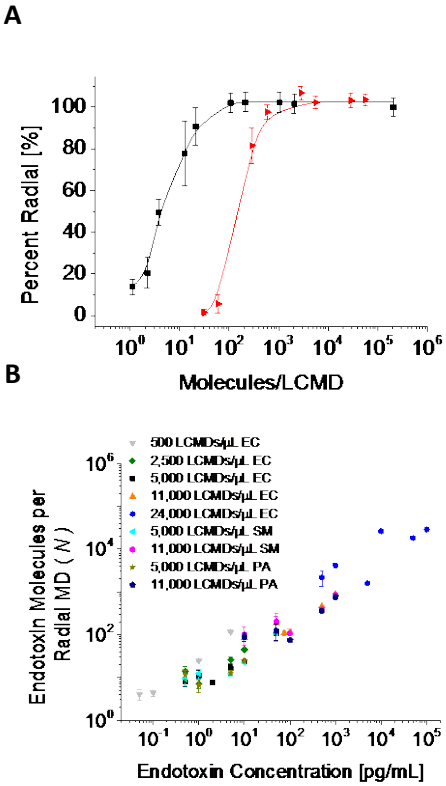

Figure 7-7. Dose-response curve for lipid A from EC and number of endotoxin molecules from EC, SM, or PA per radial LCMD (*N*) as a function of the concentration of endotoxin.

(A) Dose-response curve for (►) lipid A from EC and (■) endotoxin from EC. The curves are rescaled to show the percentage of LCMDs that underwent a bipolar-to-radial ordering transition in response to the number of molecules (lipid A or endotoxin) per LCMD. The average concentrations of MDs were (►) 5,600 ± 300 and (■) 5,100 ± 800 LCMDs/μL. (B) Number of endotoxin molecules from EC, SM, or PA per radial LCMD (*N*) as a function of the concentration of endotoxin. The plot was assembled from the data in Figures 7-3 through 7-6.

On the basis of the above-described hypothesis, we predicted that lipid A from EC, which does not contain the long polysaccharide domains of endotoxin and thus aggregates at lower concentrations,[62, 63, 65, 66] would require a higher number of molecules per LCMD to trigger a bipolar-to-radial ordering transition in LCMDs. Figure 7-7A compares the rescaled dose-response curves measured for lipid A and endotoxin from EC at concentration of MDs of ~5,000 LCMDs/μL (see Figure 7-S5 of the Supporting Information for the original dose-response curve for lipid A). Consistent with our hypothesis, lipid A required ten times the number of molecules per LCMD as compared to endotoxin (*e.g.*, 500 compared to 50 molecules per LCMD) to saturate the response of the LCMDs. Overall, the results shown in Figures 7-6 and 7-7A, when placed in the context of previous studies,[60-66] are consistent with the proposal that endotoxin undergoes a change in aggregation state above 10 pg/mL. Below we expand further regarding this hypothesis and discuss further the mechanism by which the state of aggregation of the endotoxin may impact the response of the LCMDs.

We hypothesized that the number of endotoxin aggregates that form in solution at concentrations of endotoxin above 10 pg/mL (which are larger than those that form below this concentration)[60-64] controls the number of LCMDs that can associate with the endotoxin. Specifically, our model assumes that an aggregate of endotoxin must associate with each LCMD in the dispersion to trigger the radial configuration. Thus, if the sizes of the endotoxin aggregates in solution increase with endotoxin concentration, the fraction of LCMDs that cannot associate with endotoxin will increase. A related prediction of this model is that the endotoxin does not associate uniformly with LCMDs in the dispersion. The above hypothesis led us to predict that the number of endotoxin molecules per *radial* LCMD (N) should increase with increase in endotoxin concentration. To test this prediction, we used the MD concentrations reported by our

flow cytometer to calculate *N* for each of the dose-response curves shown in Figures 7-3 through 7-6.‡ Figure 7-7B presents the results of this analysis for measurements involving a wide range of MD and endotoxin concentrations. Consistent with our hypothesis, the data collapsed onto a single curve and *N* is observed to increase with concentration of endotoxin.

The results shown in Figure 7-7 also provide a model-based prediction of the number of endotoxin molecules in aggregates present in solution at a given endotoxin concentration. For example, at a concentration of 100 ng/mL, Figure 7-7 predicts that ~30,000 endotoxin molecules are present in an aggregate. Using the density of endotoxin (1.4 g/cm^3)[67] and an approximate molecular weight of 50 kDa,‡ we estimate that a spherical aggregate composed of 30,000 molecules would be 150 nm-in-diameter. To test this prediction, we used dynamic light scattering to measure the average diameter of endotoxin aggregates in a 100 ng/mL solution. In agreement with the prediction, we measured the Z-average diameter of aggregates of endotoxin at this concentration to be 169 ± 33 nm.

Overall, both the analysis shown in Figure 7-7B and our dynamic light scattering measurement provide support for our proposal that the endotoxin aggregates that form in solution above 10 pg/mL limit the number of LCMDs that can associate with the endotoxin, and thus impact the response of the LCMDs to endotoxin. We note here that this implies that LCMDs are sensitive reporters of the aggregation state of endotoxins at low concentrations in aqueous solutions, and could offer a means to infer aggregation of endotoxin below the detection limits of current optical techniques (*e.g.*, dynamic light scattering, fluorescence, *etc.*). The capability to report the aggregation state at pg/mL concentrations is relevant to a range of contexts as it has been reported that endotoxin aggregates are responsible for initiation of cellular response to the

toxin.[43] However, until now, only atomic force microscopy has provided evidence of aggregation of endotoxin in the pg/mL concentration range.[60, 68]

In the final experiment reported in this chapter, we illustrate the power the LCMD-based methodology for endotoxin detection by screening a library of biological amphiphiles, thus providing additional characterization of the specificity of the LCMD ordering transition to endotoxins and lipid A. Specifically, we studied the influence of lipid X (an intermediate in the biological synthetic pathway for endotoxin with two aliphatic tails[18]), 1,2-dipalmitoyl-*sn*-glycero-3-phosphocholine (DPPC), 1,2-di-(9Z-octadecenoyl)-*sn*-glycero-3-phosphoethanolamine (DOPE), 1,2-di-(9Z-octadecenoyl)-*sn*-glycero-3-phospho-L-serine (DOPS), 1,2-di-(9Z-octadecenoyl)-*sn*-glycero-3-phospho-(1'-myo-inositol) (DOPI), cholesterol (Chol), cardiolipin from EC (CL), and phosphatidylcholines from an egg (egg PC) (see Figure 7-8A for chemical structures) on the ordering of bipolar LCMDs at bulk concentrations of lipid below 1 μg/mL. Above this threshold concentration amphiphiles are able to trigger an ordering transition within LCMDs *via* an adsorption induced change in MD surface energy (see Introduction).[29, 41, 45, 55, 69, 70] Figure 7-8B shows that, in contrast to the endotoxins and lipid A, the amphiphiles did not cause radial anchoring at 100 ng/mL in samples containing ~5,000 LCMDs/μL, and thus the ordering transition of MDs within the pg/mL concentration range is specific to endotoxin or lipid A relative to these other common biological amphiphiles. We note that the ordering transition was previously shown to be selective to endotoxin or lipid A from EC over 1,2-dilauroyl-*sn*-glycero-3-phosphatidylcholine (DLPC) and 1,2-dioleoyl-*sn*-glycero-3-phosphatidylcholine (DOPC) and the single-tailed synthetic surfactant sodium dodecylsulfate (SDS),[29] and that the flow focusing-based methodology for detection of endotoxin enabled us to rapidly screen additional amphiphiles of varying molecular architecture (Figure 7-8A).

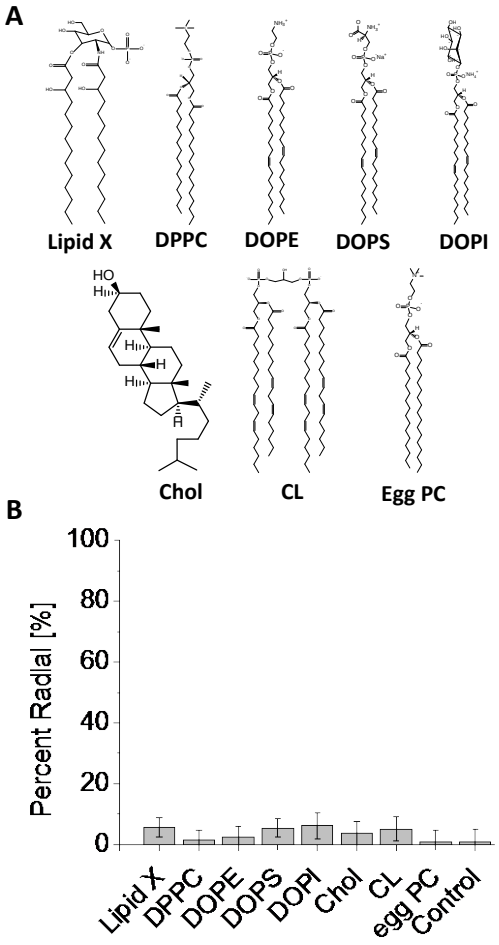

Figure 7-8. Specificity of the ordering transition of MDs within the pg/mL concentration range to endotoxin or lipid A.

(A) Chemical structures of lipid X, 1,2-dipalmitoyl-*sn*-glycero-3-phosphocholine (DPPC), 1,2-di-(9Z-octadecenoyl)-*sn*-glycero-3-phosphoethanolamine (DOPE), 1,2-di-(9Z-octadecenoyl)-*sn*-glycero-3-phospho-L-serine (DOPS), 1,2-di-(9Z-octadecenoyl)-*sn*-glycero-3-phospho-(1'-myo-inositol) (DOPI), cholesterol (Chol), cardiolipin from EC (CL), and the majority component of a mixture of phosphatidylcholines from an egg (egg PC). (B) Percentage of LCMDs that underwent a bipolar-to-radial ordering transition in the presence of 100 ng/mL of the indicated amphiphile. The control is a 10 μM aqueous solution of SDS. The concentration of MDs was ~5,000 LCMDs/μL.

7.4 Conclusions

The results reported in this chapter demonstrate a methodology for rapid and quantitative detection of bacterial endotoxins based on analysis of light scattered at low angles (< 15°) by LCMDs. The use of a flow focusing device allowed us to quantify the scattering of light from single LCMDs within a dispersion at rates of up to 10,000 MDs/second. Although we used the flow focusing component of a flow cytometer, the principles demonstrated in this chapter are general and should be readily translated to other microfluidic systems, including chip-based flow focusing systems fabricated, for example, by soft lithography. We note that several groups have already designed chip-based flow cytometers,[37-40] and flow cytometers with integrated microfluidics are commercially available.[38] Thus, we predict that the results of our investigation will enable fabrication of an on chip microfluidic light scattering detector for rapid detection of endotoxin.

In this chapter, we illustrate the capabilities of our new methodology for quantification of endotoxin by (i) demonstrating that LCMDs can be used to detect endotoxins from bacteria other than *Escherichia coli* (*Salmonella minnesota* and *Pseudomonas aeruginosa*) at pg/mL concentrations, (ii) screening other common biological amphiphiles for their influence on LCMDs, and (iii) characterizing further the analytic attributes of LCMDS in the presence of endotoxin. In the a latter context, we conclude that LCMDs can be used to probe aggregation of endotoxin at concentrations below the resolution limits of current techniques such as dynamic light scattering.

Acknowledgements

This work was primarily supported by NSF through DMR-1121288 (Materials Research Science and Engineering Center), the Army Research Office (W911NF-11-1-0251 and W911NF-10-1-0181), and the National Institutes of Health (CA108467 and CA105730). The authors would like to thank Xiaoguang Wang and Travis Nelson for helpful discussions.

7.5 Supporting Information

Additional dose-response curves, average concentrations of LC microdroplets (LCMDs), and frequency histograms

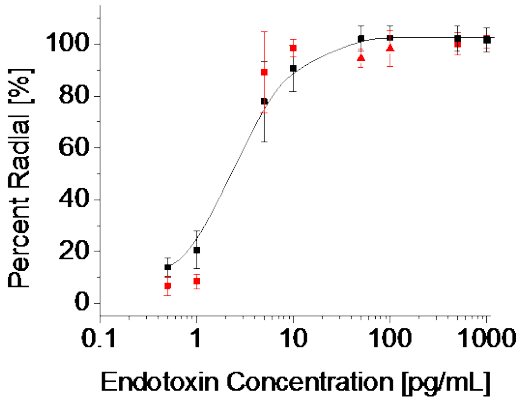

Figure 7-S1. Dose-response curves of the percentage of LCMDs that underwent a bipolar-to-radial ordering transition in response to various concentrations of endotoxin from EC.

The average concentration of MDs was ~5,000 LCMDs/μL. The samples were prepared from stock emulsions with a conserved volume ratio of 5CB to aqueous buffer, but with a total volume of (■) 3 mL or (▲) 10 mL (see Experimental section of the main text for details). The results show that scale-up of the emulsion volume did not influence the droplet response. The lines are drawn to guide the eye.

Table 7-S1. Average Concentrations of Liquid Crystal MDs

Strain of Bacteria	Volume of Stock Emulsion Added to Samples (µL)	Average MD Concentration (LCMDs/µL)
Escherichia coli	7	500 ± 50
	35	2,500 ± 200
	70	5,100 ± 800
	200	11,000 ± 2,000
	400	24,000 ± 4,000
Salmonella minnesota	70	5,000 ± 500
	200	11,000 ± 2,000
Pseudomonas aeruginosa	70	4,600 ± 400
	200	12,000 ± 2,000
Lipid A from *Escherichia coli*	70	5,600 ± 300

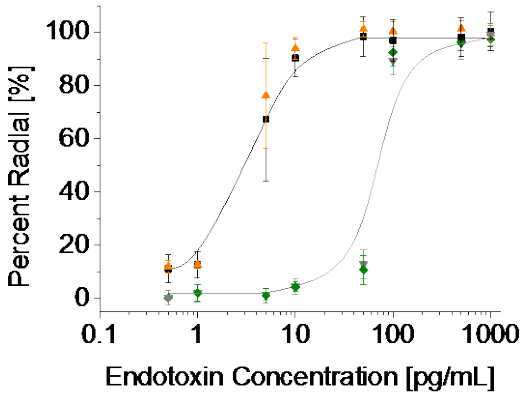

Figure 7-S2. Preservation of the dose-response behavior of LCMDs to endotoxin from EC following a twofold dilution of the samples.

Dose-response curves of the response of LCMDs to endotoxin from EC in which the average concentrations of LCMDs were (■,▲) ~5,000 and (▼,♦) ~11,000 LCMDs/µL (■,▼) before or (▲,♦) after dilution. The lines are drawn to guide the eye.

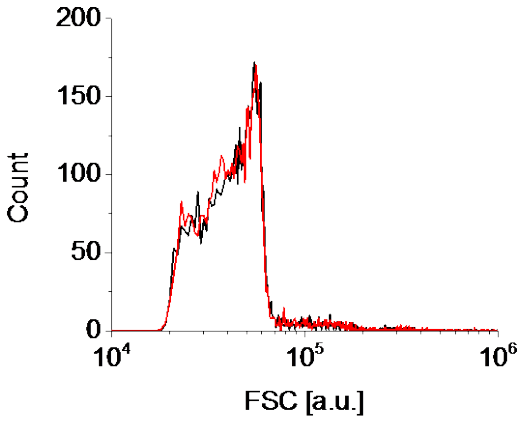

Figure 7-S3. Frequency histograms of FSC obtained by flowing nematic LCMDs suspended in aqueous solutions of 100 ng/mL (black line) or 100 pg/mL (red line) endotoxin from EC through a flow cytometer.

The average concentration of LCMDs was ~5,000 LCMDs/µL. The histograms are identical to those shown in Figures 7-2 and 7-3 of the main text.

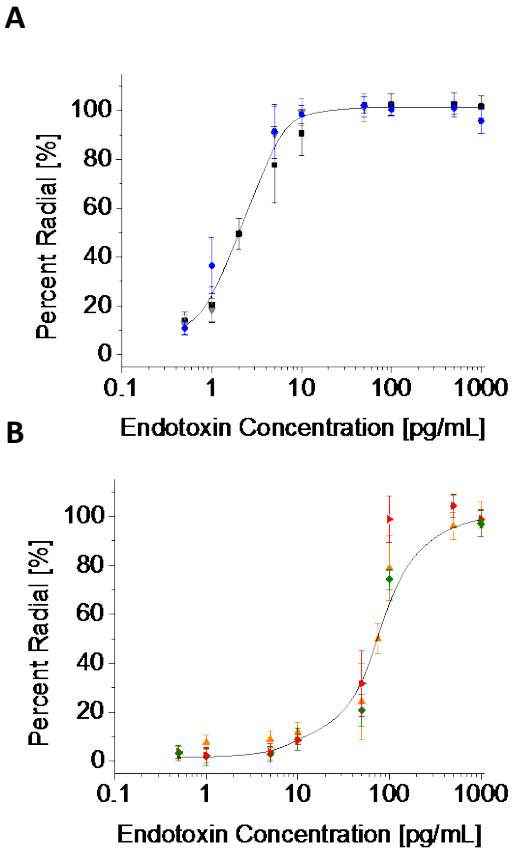

Figure 7-S4. Dose-response curves of the percentage of LCMDs that underwent a bipolar-to-radial ordering transition in response to various concentrations of endotoxin from (■,▲) EC, (▼,♦) SM or (●,►) PA.

The average concentrations of MDs were (■) 5,100 ± 800, (▲) 11,000 ± 2,000, (▼) 5,000 ± 500, (●) 4,600 ± 400, (♦) 11,000 ± 2,000, and (►) 12,000 ± 2,000 LCMDs/μL. The dose-response curves are identical to the curves plotted in Figures 7-3 and 7-4 of the main text, but grouped by droplet concentration for comparison. The lines are drawn to guide the eye.

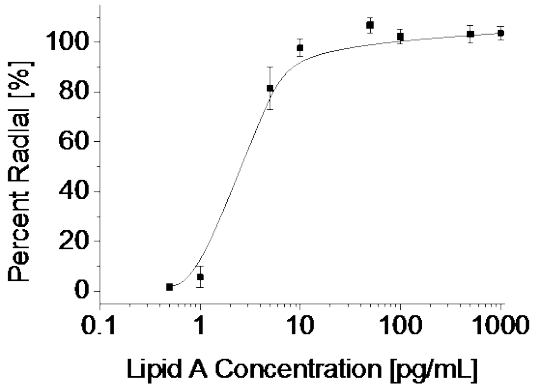

Figure 7-S5. Dose-response curves of the percentage of LCMDs that underwent a bipolar-to-radial ordering transition in response to various concentrations of lipid A from EC.

The average concentration of MDs was 5,600 ± 300. The lines are drawn to guide the eye.

Response of LCMDs upon exposure to a solution of 100 pg/mL endotoxin from EC or the same solution run thrice through an endotoxin removal column

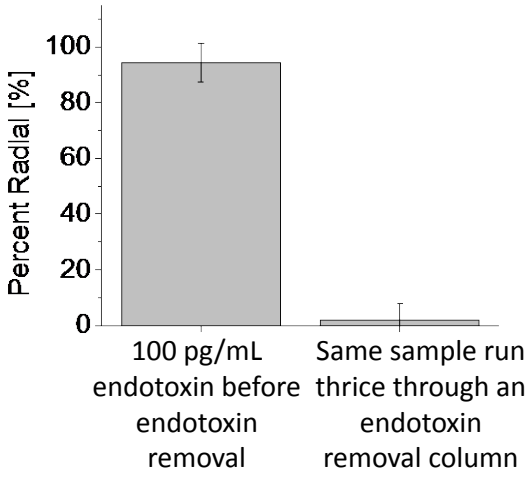

Figure 7-S6. Percentage of radial MDs in either a 100 pg/mL aqueous solution of endotoxin from EC or the same solution run thrice through an endotoxin removal column.

The average concentration of MDs was ~5,000 LCMDs/μL. The result confirms the bipolar-to-radial ordering transitions were induced by endotoxin.

7.6 References

*This chapter was prepared as a Full Paper reporting original research to be submitted the journal *Lab on a Chip*.

‡ As was done in reference [29] the molecular weights of the endotoxins were assumed to be 50 kDa.

1. Klevens, R. M.; Edwards, J. R.; Richards, C. L.; Horan, T. C.; Gaynes, R. P.; Pollock, D. A.; Cardo, D. M., Estimating Health Care-Associated Infections and Deaths in Us Hospitals, 2002. *Public Health Reports* **2007**, 122, 160-166.
2. Raymond, L. W.; Barkley, J. E.; Langley, R.; Sautter, R., Prolonged Respiratory Illness after Single Overnight Continuous Positive Airway Pressure Humidification: Endotoxin as the Suspect. *Southern Medical Journal* **2009**, 102, 1260-1262.
3. Dales, R.; Miller, D.; Ruest, K.; Guay, M.; Judek, S., Airborne Endotoxin Is Associated with Respiratory Illness in the First 2 Years of Life. *Environmental Health Perspectives* **2006**, 114, 610-614.
4. Stone, P. W.; Braccia, D.; Larson, E., Systematic Review of Economic Analyses of Health Care-Associated Infections. *American Journal of Infection Control* **2005**, 33, 501-509.
5. Safdar, N.; Dezfulian, C.; Collard, H. R.; Saint, S., Clinical and Economic Consequences of Ventilator-Associated Pneumonia: A Systematic Review. *Critical Care Medicine* **2005**, 33, 2184-2193.
6. Safdar, N.; Crnich, C. J.; Maki, D. G., The Pathogenesis of Ventilator-Associated Pneumonia: Its Relevance to Developing Effective Strategies for Prevention. *Respiratory Care* **2005**, 50, 725-739.
7. Bisgaard, H.; Hermansen, M. N.; Buchvald, F.; Loland, L.; Halkjaer, L. B.; Bonnelykke, K.; Brasholt, M.; Heltberg, A.; Vissing, N. H.; Thorsen, S. V.; Stage, M.; Pipper, C. B., Childhood Asthma after Bacterial Colonization of the Airway in Neonates. *New England Journal of Medicine* **2007**, 357, 1487-1495.
8. Gordon, T., Acute Respiratory Effects of Endotoxin-Contaminated Machining Fluid Aerosols in Guinea Pigs. *Fundamental and Applied Toxicology* **1992**, 19, 117-123.
9. O'Grady, N. P.; Preas, H. L.; Pugin, J.; Fiuza, C.; Tropea, M.; Reda, D.; Banks, S. M.; Suffredini, A. F., Local Inflammatory Responses Following Bronchial Endotoxin Instillation in Humans. *American Journal of Respiratory and Critical Care Medicine* **2001**, 163, 1591-1598.
10. Lim, C. H.; Yu, I. J.; Kim, H. Y.; Lee, S. B.; Kang, M. G.; Marshak, D. R.; Moon, C. K., Respiratory Effect of Acute and Subacute Exposure to Endotoxin-Contaminated Metal Working Fluid (Mwf) Aerosols on Sprague-Dawley Rats. *Archives of Toxicology* **2005**, 79, 321-329.
11. Lim, C. H.; Yu, I. J.; Kim, H. Y.; Lee, S. B.; Kang, M. G.; Marshak, D. R.; Moon, C. K., Inflammatory and Immunological Responses to Subchronic Exposure to Endotoxin-Contaminated Metalworking Fluid Aerosols in F344 Rats. *Environmental Toxicology* **2005**, 20, 212-218.
12. Lane, S. R.; Nicholls, P. J.; Sewell, R. D. E., The Measurement and Health Impact of Endotoxin Contamination in Organic Dusts from Multiple Sources: Focus on the Cotton Industry. *Inhalation Toxicology* **2004**, 16, 217-229.

13. Guideline on Validation of the Lal Test as an End-Product Endotoxin Test for Human and Animal Parenteral Drugs, Biological Products, and Medical Devices. *Maintained by: Division of Manufacturing and Product Quality, FDA* **1987**.
14. Gorbet, M. B.; Sefton, M. V., Endotoxin: The Uninvited Guest. *Biomaterials* **2005**, 26, 6811-6817.
15. Malyala, P.; Singh, M., Endotoxin Limits in Formulations for Preclinical Research. *Journal of Pharmaceutical Sciences* **2008**, 97, 2041-2044.
16. Nakagawa, Y.; Murai, T.; Hasegawa, C.; Hirata, M.; Tsuchiya, T.; Yagami, T.; Haishima, Y., Endotoxin Contamination in Wound Dressings Made of Natural Biomaterials. *Journal of Biomedical Materials Research, Part B: Applied Biomaterials* **2003**, 66B, 347-355.
17. Pearson III, F. C.; Weary, M.; Jorgensen, J. H., Pyrogens-Endotoxins, Lal Testing, and Depyrogenation. *Marcel Dekker, Inc, New York and Basel* **1985**.
18. Raetz, C. R.; Whitfield, C., Lipopolysaccharide Endotoxins. *Annual Review of Biochemistry* **2002**, 71, 635-700.
19. Ragab, A. A.; Van de Motter, R.; Lavish, S. A.; Goldberg, V. M.; Ninomiya, J. T.; Carlin, C. R.; Greenfield, E. M., Measurement and Removal of Adherent Endotoxin from Titanium Particles and Implant Surfaces. *Journal of Orthopaedic Research* **1999**, 17, 803-809.
20. Ross, V. C.; Twohy, C. W., Endotoxins and Medical Devices. In *Bacterial Endotoxins: Structure, Biomedical Significance and Detection with the Limulus Amebocyte Lysate Test*, Alan R Liss: New York, 1985; pp 267-268.
21. Dobrovolskaia, M. A.; Germolec, D. R.; Weaver, J. L., Evaluation of Nanoparticle Immunotoxicity. *Nature Nanotechnology* **2009**, 4, 411-414.
22. Dobrovolskaia, M. A.; Neun, B. W.; Clogston, J. D.; Ding, H.; Ljubimova, J.; McNeil, S. E., Ambiguities in Applying Traditional Limulus Amebocyte Lysate Tests to Quantify Endotoxin in Nanoparticle Formulations. *Nanomedicine* **2010**, 5, 555-562.
23. Hall, J. B.; Dobrovolskaia, M. A.; Patri, A. K.; McNeil, S. E., Characterization of Nanoparticles for Therapeutics. *Nanomedicine* **2007**, 2, 789-803.
24. Devleeschouwer, M. J.; Cornil, M. F.; Dony, J., Studies on the Sensitivity and Specificity of the Limulus Amebocyte Lysate Test and Rabbit Pyrogen Assays. *Applied and Environmental Microbiology* **1985**, 50, 1509-1511.
25. Harmon, P.; CabralLilly, D.; Reed, R. A.; Maurio, F. P.; Franklin, J. C.; Janoff, A., The Release and Detection of Endotoxin from Liposomes. *Analytical Biochemistry* **1997**, 250, 139-146.
26. Piluso, L. G.; Martinez, M. Y., Resolving Liposomal Inhibition of Quantitative Lal Methods. *PDA Journal of Pharmaceutical Science and Technology* **1999**, 53, 260-263.
27. Roslansky, P. F.; Novitsky, T. J., Sensitivity of Limulus Amebocyte Lysate (Lal) to Lal-Reactive Glucans. *Journal of Clinical Microbiology* **1991**, 29, 2477-2483.
28. Sakai, H.; Hisamoto, S.; Fukutomi, I.; Sou, K.; Takeoka, S.; Tsuchida, E., Detection of Lipopolysaccharide in Hemoglobin-Vesicles by Limulus Amebocyte Lysate Test with Kinetic-Turbidimetric Gel Clotting Analysis and Pretreatment of Surfactant. *Journal of Pharmaceutical Sciences* **2004**, 93, 310-321.
29. Lin, I. H.; Miller, D. S.; Bertics, P. J.; Murphy, C. J.; de Pablo, J. J.; Abbott, N. L., Endotoxin-Induced Structural Transformations in Liquid Crystalline Droplets. *Science* **2011**, 332, 1297-1300.

30. Miller, D. S.; Abbott, N. L., Influence of Droplet Size, Ph and Ionic Strength on Endotoxin-Triggered Ordering Transitions in Liquid Crystalline Droplets. *Soft Matter* **2013**, 9, 374-382.
31. Meli, M. V.; Lin, I. H.; Abbott, N. L., Preparation of Microscopic and Planar Oil-Water Interfaces That Are Decorated with Prescribed Densities of Insoluble Amphiphiles. *Journal of the American Chemical Society* **2008**, 130, 4326-4333.
32. Drzaic, P. S., *Liquid Crystal Dispersions*. World Scientific: River Edge, NJ, USA, 1995.
33. Gennes, P.-G. d.; Prost, J., *The Physics of Liquid Crystals*. 2nd ed.; Oxford University Press: New York, NY, USA, 1993.
34. Rapini, A.; Papoular, M., Distortion D'une Lamelle Nematique Sous Champ Magnetique Conditions D'ancrage Aux Parois. *Journal de Physique Colloques* **1969**, 30, C4-54-C4-56.
35. Kinsinger, M. I.; Buck, M. E.; Abbott, N. L.; Lynn, D. M., Immobilization of Polymer-Decorated Liquid Crystal Droplets on Chemically Tailored Surfaces. *Langmuir* **2010**, 26, 10234-10242.
36. Miller, D. S.; Carlton, R. J.; Mushenheim, P. C.; Abbott, N. L., Introduction to Optical Methods for Characterizing Liquid Crystals at Interfaces. *Langmuir* **2013**, 29, 3154-3169.
37. Miller, D. S.; Wang, X.; Buchen, J.; Lavrentovich, O. D.; Abbott, N. L., Analysis of the Internal Configurations of Droplets of Liquid Crystal Using Flow Cytometry. *Analytical Chemistry* **2013**, 85, 10296-10303.
38. Tan, L. N.; Wiepz, G. J.; Miller, D. S.; Shusta, E. V.; Abbott, N. L., Liquid Crystal Droplet-Based Amplification of Microvesicles That Are Shed by Mammalian Cells. *Analyst* **2014**, 139, 2386-2396.
39. Mueller, M.; Lindner, B.; Kusumoto, S.; Fukase, K.; Schromm, A. B.; Seydel, U., Aggregates Are the Biologically Active Units of Endotoxin. *Journal of Biological Chemistry* **2004**, 279, 26307-26313.
40. Brake, J. M.; Daschner, M. K.; Luk, Y. Y.; Abbott, N. L., Biomolecular Interactions at Phospholipid-Decorated Surfaces of Liquid Crystals. *Science* **2003**, 302, 2094-2097.
41. Gupta, J. K.; Zimmerman, J. S.; de Pablo, J. J.; Caruso, F.; Abbott, N. L., Characterization of Adsorbate-Induced Ordering Transitions of Liquid Crystals within Monodisperse Droplets. *Langmuir* **2009**, 25, 9016-9024.
42. Berggren, E.; Zannoni, C.; Chiccoli, C.; Pasini, P.; Semeria, F., Computer-Simulations of Nematic Droplets with Bipolar Boundary-Conditions. *Physical Review E* **1994**, 50, 2929-2939.
43. Meyer, R. B., Piezoelectric Effects in Liquid Crystals. *Physical Review Letters* **1969**, 22, 918.
44. Miller, D. S.; Wang, X.; Abbott, N. L., Design of Functional Materials Based on Liquid Crystalline Droplets. *Chemistry of Materials* **2013**, 26, 496–506.
45. Ondris-Crawford, R.; Boyko, E. P.; Wagner, B. G.; Erdmann, J. H.; Zumer, S.; Doane, J. W., Microscope Textures of Nematic Droplets in Polymer Dispersed Liquid-Crystals. *Journal of Applied Physics* **1991**, 69, 6380-6386.
46. Prischepa, O. O.; Shabanov, A. V.; Zyryanov, V. Y., Transformation of Director Configuration Upon Changing Boundary Conditions in Droplets of Nematic Liquid Crystal. *JETP Letters* **2004**, 79, 257-261.
47. Volovik, G. E.; Lavrentovich, O. D., The Topological Dynamics of Defects - Boojums in Nematic Drops. *Zhurnal Eksperimentalnoi I Teoreticheskoi Fiziki* **1983**, 85, 1997-2010.
48. Khan, W.; Choi, J. H.; Kim, G. M.; Park, S.-Y., Microfluidic Formation of Ph Responsive 5cb Droplets Decorated with Paa-B-Lcp. *Lab on a Chip* **2011**, 11, 3493-3498.

49. Khan, W.; Park, S.-Y., Configuration Change of Liquid Crystal Microdroplets Coated with a Novel Polyacrylic Acid Block Liquid Crystalline Polymer by Protein Adsorption. *Lab on a Chip* **2012**, 12, 4553-4559.
50. Gupta, J. K.; Sivakumar, S.; Caruso, F.; Abbott, N. L., Size-Dependent Ordering of Liquid Crystals Observed in Polymeric Capsules with Micrometer and Smaller Diameter. *Angewandte Chemie-International Edition* **2009**, 48, 1652-1655.
51. *Associates of Cape Cod Incorporated Limulus Amebocyte Lysate Chromo-Lal for the Detection and Quantitation of Gram Negative Bacterial Endotoxins (Lipopolysaccharides)*. East Falmouth, MA, USA, 2006.
52. Rietschel, E. T.; Kirikae, T.; Schade, F. U.; Mamat, U.; Schmidt, G.; Loppnow, H.; Ulmer, A. J.; Zähringer, U.; Seydel, U.; Di Padova, F., Bacterial Endotoxin: Molecular Relationships of Structure to Activity and Function. *FASEB Journal* **1994**, 8, 217-225.
53. Takayama, K.; Qureshi, N.; Raetz, C.; Ribi, E.; Peterson, J.; Cantrell, J.; Pearson, F.; Wiggins, J.; Johnson, A., Influence of Fine Structure of Lipid a on Limulus Amebocyte Lysate Clotting and Toxic Activities. *Infection and Immunity* **1984**, 45, 350-355.
54. Hiemenz, P. C.; Rajagopalan, R., *Principles of Colloid and Surface Chemistry*. 3rd ed.; Marcel Dekker: New York, NY, USA, 1997.
55. Israelachvili, J. N., *Intermolecular and Surface Forces*. 2nd ed.; Academic Press London: San Diego, CA, USA, 1991.
56. Aurell, C. A.; Hawley, M. E.; Wiström, A. O., Direct Visualization of Gram-Negative Bacterial Lipopolysaccharide Self-Assembly. *Molecular Cell Biology Research Communications* **1999**, 2, 42-46.
57. Brandenburg, K.; Koch, M.; Seydel, U., Phase Diagram of Deep Rough Mutant Lipopolysaccharide from *Salmonella Minnesota* R595. *Journal of Structural Biology* **1992**, 108, 93-106.
58. Santos, N. C.; Silva, A. C.; Castanho, M. A.; Martins-Silva, J.; Saldanha, C., Evaluation of Lipopolysaccharide Aggregation by Light Scattering Spectroscopy. *ChemBioChem* **2003**, 4, 96-100.
59. Sasaki, H.; White, S. H., Aggregation Behavior of an Ultra-Pure Lipopolysaccharide That Stimulates Tlr-4 Receptors. *Biophysical Journal* **2008**, 95, 986-993.
60. Seydel, U.; Schromm, A. B.; Blunck, R.; Brandenburg, K., Chemical Structure, Molecular Conformation, and Bioactivity of Endotoxins. *Chemical Immunology* **2000**, 74, 5-24.
61. Aurell, C. A.; Wistrom, A. O., Critical Aggregation Concentrations of Gram-Negative Bacterial Lipopolysaccharides (Lps). *Biochemical and Biophysical Research Communications* **1998**, 253, 119-123.
62. Bergstrand, A.; Svanberg, C.; Langton, M.; Nydén, M., Aggregation Behavior and Size of Lipopolysaccharide from *Escherichia Coli* O55: B5. *Colloids and Surfaces B: Biointerfaces* **2006**, 53, 9-14.
63. Ulevitch, R. J.; Johnston, A., The Modification of Biophysical and Endotoxic Properties of Bacterial Lipopolysaccharides by Serum. *Journal of Clinical Investigation* **1978**, 62, 1313.
64. Richter, W.; Vogel, V.; Howe, J.; Steiniger, F.; Brauser, A.; Koch, M. H.; Roessle, M.; Gutsmann, T.; Garidel, P.; Mäntele, W., Morphology, Size Distribution, and Aggregate Structure of Lipopolysaccharide and Lipid a Dispersions from Enterobacterial Origin. *Innate Immunity* **2011**, 17, 427-438.

65. Sivakumar, S.; Wark, K. L.; Gupta, J. K.; Abbott, N. L.; Caruso, F., Liquid Crystal Emulsions as the Basis of Biological Sensors for the Optical Detection of Bacteria and Viruses. *Advanced Functional Materials* **2009**, 19, 2260-2265.
66. Tjipto, E.; Cadwell, K. D.; Quinn, J. F.; Johnston, A. P.; Abbott, N. L.; Caruso, F., Tailoring the Interfaces between Nematic Liquid Crystal Emulsions and Aqueous Phases Via Layer-by-Layer Assembly. *Nano letters* **2006**, 6, 2243-2248.
67. Liu, P.; Meagher, R. J.; Light, Y. K.; Yilmaz, S.; Chakraborty, R.; Arkin, A. P.; Hazen, T. C.; Singh, A. K., Microfluidic Fluorescence in Situ Hybridization and Flow Cytometry (Mflowfish). *Lab on a Chip* **2011**, 11, 2673-2679.
68. Piyasena, M. E.; Graves, S. W., The Intersection of Flow Cytometry with Microfluidics and Microfabrication. *Lab on a Chip* **2014**, 14, 1044–1059.
69. Watts, B. R.; Zhang, Z.; Xu, C.-Q.; Cao, X.; Lin, M., Integration of Optical Components on-Chip for Scattering and Fluorescence Detection in an Optofluidic Device. *Biomedical Optics Express* **2012**, 3, 2784-2793.
70. Yun, H.; Bang, H.; Min, J.; Chung, C.; Chang, J. K.; Han, D.-C., Simultaneous Counting of Two Subsets of Leukocytes Using Fluorescent Silica Nanoparticles in a Sheathless Microchip Flow Cytometer. *Lab on a Chip* **2010**, 10, 3243-3254.
71. Fernández-Nieves, A.; Link, D.; Marquez, M.; Weitz, D. A., Topological Changes in Bipolar Nematic Droplets under Flow. *Physical Review Letters* **2007**, 98, 087801.

Chapter 8. Liquid Crystal Droplet-Based Amplification of Microvesicles that are Shed by Mammalian Cells*

8.1 Introduction

Microvesicles (MVs) are cell-derived membrane vesicles with sizes between 50 nm and 1 μm, and include exosomes released from multivesicular endosomes[1-3] and plasma membrane-shed vesicles.[4-6] MVs carry a host of cell-specific signaling proteins and nucleic acids, and have been recognized as important in cellular mechanisms underlying tumor progression, including intercellular transfer of specific biomolecules (*e.g.*, miRNA).[7-10] For example, Al-Nedawi and co-workers showed that U373 glioma cells that had been transfected with the gene for EGFRvIII, a mutant form of the epidermal growth factor receptor (EGFR) commonly associated with the glioblastoma multiforme (GBM), produced significantly more MVs than native U373 cells *in vitro*.[11] Recent studies also suggest that elevated levels of circulating MVs correlate to the presence of diseases, including cancers such as glioblastoma.[12-14] The use of MVs as potential biomarkers, in particular, has led to a growing interest in the development of analytical tools to quantify the presence of MVs in various biological fluids.[15, 16] In this chapter, we report new principles that employ microdroplets of thermotropic liquid crystals (LCs) for optical detection of MVs that have been specifically captured by immunobeads. A significant merit of the approach is that it can be performed using LC droplets and instrumentation that is routinely found in research and clinical laboratories.

As noted above, analysis of proteins associated with MVs (*e.g.*, cell-surface proteins) is important because it can provide information about the state (and processes) of the cells from

which the MVs originate.[5, 11] Current methods for analysis of the protein content of MVs, such as immunoblotting and enzyme-linked immunosorbent assay (ELISA), require large numbers of MVs (>10^8 MVs).[17-19] Characterization of MVs using flow cytometry (FC) across the size range of 100 nm to 1 μm is difficult in routine practice due to the weak scattering of light by the MVs and the wide variation in sizes of MVs.[20-22] A light scattering technique called nanoparticle tracking analysis (NTA) has also been reported for direct visualization of MVs, but it suffers from variability of background signals generated by serum particles.[15, 23] More recently, Shao and co-workers reported a technique that combines (i) immunotargeting of MVs with functionalized antibodies, (ii) covalent conjugation of superparamagnetic particles with the functionalized antibodies, (iii) a membrane filtration step for purification, and (iv) use of a miniaturized nuclear magnetic resonance system to detect the labeled MVs.[24] Relative to existing methods, they report a sensitivity of 10^5 MVs, surpassing methods such as NTA (10^7 MVs), FC (10^8 MVs) and immunoblotting (10^8 MVs) by at least two orders of magnitude.

While such methods are promising, techniques for molecular analysis of MVs that do not require use of covalent reactions in the presence of complex samples, do not require membrane purification steps, and use routine instrumentation found in basic biological and clinical laboratories have the potential to be quickly and widely adopted.

Herein we demonstrate principles for optical detection of MVs that utilize micrometer-sized LC droplets to report MVs that have been captured using antibodies targeted to proteins present in the MVs (Scheme 8-1). The LCs used in this study are nematic, thermotropic LCs and can be viewed as structured oils in which the molecules (mesogens) comprising the LC exhibit long-range orientational ordering. Our approach is enabled by two recent advances involving micrometer-sized droplets of LCs that are dispersed in aqueous solution (*i.e.*, LC-in- water

emulsions). First, the internal configurations of the LC droplets have been reported to be sensitive to the presence of lipids adsorbed to the surfaces of the droplets.[25-27] Specially, past studies have demonstrated that biological lipids and synthetic surfactants can change the orientations assumed by LCs at aqueous–LC interfaces (the so-called "anchoring" of LCs) through a mechanism that involves interactions between the aliphatic tails of the adsorbed amphiphiles and the mesogens of the LC.[28-30] In the absence of an adsorbate, the mesogens confined within the droplets arrange into a so-called bipolar configuration with two surface point defects (Figure 8-1a and 8-1b). Upon interaction with an amphiphile, however, the LC within the droplets transforms to a radial configuration with a single defect at the cores of the droplets (Figure 8-1d and 8-1e). The change in the configuration of the LC within the micrometer-sized LC droplet leads to a distinct change in optical properties of the droplets (see below for additional detail). Such observations have previously led to the development of LC droplet-based sensors to detect and differentiate between types of bacteria and viruses based on their cell-wall/envelope structure.[31]

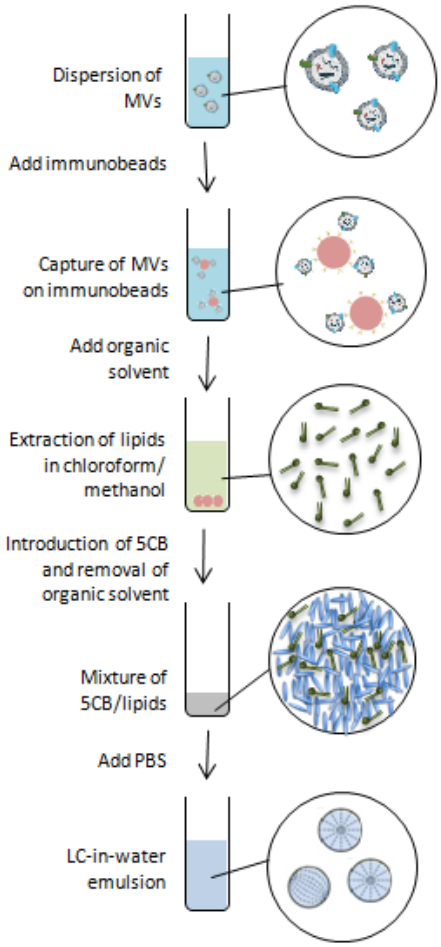

Scheme 8-1. Illustration of the experimental procedure.

MVs were first captured onto immunobeads *via* antibody—antigen recognition, and then extracted into the LC. Emulsification of the LC in PBS generated LC droplets, which were quantified using FC.

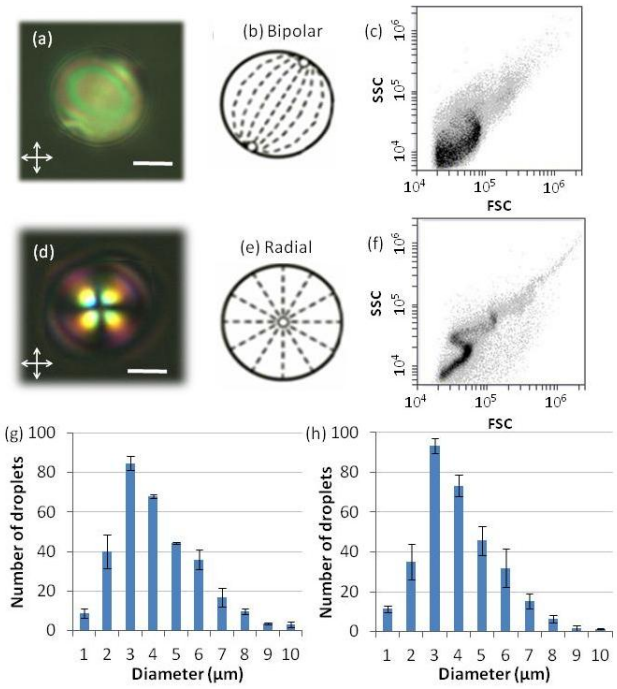

Figure 8-1. Characterization of aqueous dispersions of 5CB droplets with or without lipids extracted from MVs doped into the droplets by both polarized light microscopy and flow cytometry.

(a and d) Polarized light micrographs of a LC droplet in the (a) absence (bipolar) or (d) presence (radial) of lipids extracted from MVs (scale bar: 2 μm). (b and e) Schematic illustrations of the director configurations within the LC droplets corresponding to the micrographs shown in (a) and (d), respectively. Dashed lines represent the orientations of the LC, and open circles represent defects. (c and f) Light scatter plots of the intensity of side light scattering (SSC) versus forward light scattering (FSC) obtained by flowing LC droplets in the (c) absence (bipolar) or (f) presence (radial) of lipids extracted from MVs through a flow cytometer. (g and h) Size distributions of LC droplets in the (g) absence and (h) presence of lipids from MVs, as measured by optical microscopy.

The second recent advance that is leveraged in the approach to MV analysis that is reported herein revolves around the use of FC to read-out the configurational states of LC droplets. As noted above, while FC has been used to characterize MVs, the small sizes of MVs and the presence of background signal have presented a range of challenges that have not yet been resolved for routine analysis of MVs. In contrast, because LCs possess anisotropic optical

properties (birefringence), the scattering of light from micrometer-sized LC droplets is dependent on the internal configuration of the LC within the droplets and is easily characterized by FC. In particular, a recent study (see Chapter 6) has demonstrated that a population of LC droplets in the radial configuration generates a light scatter plot (Figure 8-1f) that is distinct from that measured for bipolar droplets (Figure 8-1c).[32] Specifically, when compared to bipolar droplets, radial droplets generate a narrower distribution of side scattering intensities (SSC, large angle light scattering) for a fixed intensity of forward light scattering (FSC, small angle light scattering). This difference in scatter plots arises from the different rotational symmetries of the refractive index profiles presented to the laser of the FC by the two configurations. Radial droplets present a spherically symmetric profile, whereas bipolar droplets do not. Furthermore, the FC-based method was demonstrated to be capable of rapidly quantifying the percentage of radial LC droplets (*i.e.*, within a few seconds) contained in a mixture of bipolar and radial droplets with high precision, as validated by parallel analysis of polarized light micrographs of the same emulsion. Finally, we emphasize that the FC-based method described above uses a simple flow cytometer (costing approximately US $15,000) that is operated only in light scattering mode.

Whereas the prior studies reported above establish that LC droplets are a promising analytical tool, they do not address detection of membrane vesicles from mammalian cells and they do not address quantification of MVs based on the presence of a specific protein target. The approach reported in this chapter was developed to address those challenges, specifically in the context of developing methods using LC droplets that rely only on instrumentation that is routinely found in biological and clinical laboratories. Our approach integrates the use of antibody-functionalized magnetic beads that capture MVs by recognition of key signaling

proteins present in the MVs along with the development of simple procedures that permit the transfer of the lipid component of the MVs into LC microdroplets. The experiments reported in this chapter used MVs derived from epidermoid carcinoma A431 cells and the capture of the MVs was achieved *via* the presence of epidermal growth factor receptor (EGFR) in the MVs. Our focus on EGFR was motivated in part by the observation that over-expression and mutation of EGFR has been associated with a number of cancers.[33] We demonstrate principles that result in facile detection of 10^6 MVs, which is better than NTA, FC, ELISA and immunoblotting, as well as a dynamic range of several orders of magnitude. With additional optimization of the LC-based method, higher sensitivity is envisaged.

8.2 Experimental Section

Materials. Dulbecco's modified Eagle's medium and penicillin–streptomycin solution were purchased from Mediatech (Herndon, VA). Cosmic calf serum was obtained from Hyclone (Logan, UT). Phosphate-buffered saline (PBS) (0.01 M phosphate; 0.138 M NaCl; 0.0027 M KCl; pH 7.4) and methanol was obtained from Sigma-Aldrich (St Louis, MO). Chloroform was purchased from Fisher Scientific (Pittsburgh, PA). Avidin-functionalized magnetic particles were obtained from Micromod (Rostock, Germany). Biotinylated anti-Epidermal Growth Factor Receptor (anti-EGFR) monoclonal antibody (111.6) was purchased from LifeSpan Biosciences (Seattle, WA). Biotinylated IgG1 isotype control was purchased from eBioscience (San Diego, CA). Anti-EGFR (1005, sc03) and horseradish peroxidase-conjugated secondary anti-rabbit IgG (sc-2054) were purchased from Santa Cruz Biotechnology (Dallas, TX). The nematic LC 4’-pentyl-4-cyanobiphenyl (5CB) was obtained from EMD Chemicals (Spring Valley, NY).

Deionization of a distilled water source was performed with a Milli-Q system (Millipore, Bedford, MA) to give water with a resistivity of 18.2 MΩ cm.

Cell Culture. A431 cells were cultured in Dulbecco's modified Eagle's medium with 10% cosmic calf serum and 100 U mL^{-1} penicillin/streptomycin. Cells were grown for 4 days to approximately 90% confluence in 15 mL of cell media in each T75 flask.

Isolation of MVs. Medium from the 4 day culture was collected and subjected to centrifugation at 8,000 × *g* for 30 min to eliminate cells and debris.[11] The MV fraction was obtained after centrifugation for 4 h at 40,000 × *g*, washing with PBS and centrifugation again for 4 h at 40,000 × *g*. MVs isolated from 30 mL of cell media (2 T75 flasks) were re-suspended in 700 μL PBS for analysis. The MV-associated protein and phospholipid recovered were quantified using the Bradford assay (Thermo Scientific, Rockford, IL) and the EnzyChrom phospholipid assay kit (BioAssay Systems, Hayward, CA), respectively, according to the manufacturers' instructions. Because the EnzyChrom phospholipid assay only measures choline-containing phospholipid, further verification of the concentration of MV-associated lipid was performed using fatty acid methylation and gas chromatography-mass spectrometry (GC-MS), according to published procedures.[34] The MVs isolated through the above-described procedure are anticipated to comprise mainly of cell membrane-derived vesicles (and not exosomes) because exosomes are much smaller (<100 nm) and thus only captured using a centrifugation speed (100,000 × *g*) that is higher than that employed here (40,000 × *g*).[15]

Dynamic Light Scattering. A 100 mW, 532 nm laser (Coherent Compass 315M-100) illuminated a temperature-controlled glass cell filled with a refractive-index matching fluid (decahydronaphthalene, Fisher Scientific, Pittsburgh, PA) maintained at 25°C. The angle of the detector was set at 90°. The autocorrelation function (ACF) was obtained using a BI-9000AT digital autocorrelator (Brookhaven Instruments Corporation, Holtsville, NY) and analyzed using the CONTIN[35] software package to yield a distribution of aggregate sizes of MVs.

Nanoparticle Tracking Analysis (NTA). NTA measurements were performed with a Nanosight LM10 (Nanosight, Amesbury, U.K.) equipped with a 405 nm laser. MV dispersions were prepared as described above and diluted until the concentration was acceptable for NTA measurements (1:40 dilution ratio was found to be optimal).[36] 400 µL of the diluted dispersion was injected into the sample chamber using a syringe. All measurements were collected at room temperature with the camera level set to the maximal value to allow for the detection of small particles. One 60 s video was taken for each dispersion. Data were captured and analyzed using NTA version 2.3.

Immunoblotting.[37, 38] MV-associated proteins were separated on 10% SDS-PAGE gels and then transferred to polyvinylidene difluoride membranes. The membrane was blocked with 5% nonfat dried milk/TBST (10 mM Tris, 150 mM NaCl, 0.05% Tween 20, pH 8) overnight at 4°C and then incubated with anti-EGFR primary antibodies (sc03, 0.4 µg mL^{-1}) in 5% nonfat dried milk/TBST for 1 h at 37°C. Subsequently, the membrane was washed three times in TBST, incubated with HRP-conjugated goat anti-rabbit IgG secondary antibodies (sc2054, 0.08 µg mL^{-1}) for 1 h at 37°C, and washed in TBST three times. The labeled proteins were visualized by the

enhanced chemiluminescence method (Luminata Crescendo, Billerica, MA). Detection was performed using a UVP Biochemi camera system (Upland, CA).

Atomic Force Microscope (AFM). AFM experiments were carried out with a Nanoscope III Multimode scanning probe microscope equipped with a "J" (120 μm) scanner (Veeco/Digital Instruments, Santa Barbara, CA). The images were acquired in tapping mode in solution using a commercially available liquid cell with oxide-sharpened silicon nitride V-shaped cantilevers at room temperature. The cantilever had a nominal spring constant of 0.32 Nm^{-1}. Imaging was performed at a scan rate of 2 Hz and at a resolution of 256 pixels per line. Images were flattened as required.

Capture of MVs using Functionalized Magnetic Beads. To functionalize the avidin-coated magnetic beads with antibodies, 10 μL of biotinylated antibody (200 μg mL^{-1}) was mixed with 20 μL of avidin-coated magnetic particles (10 mg mL^{-1}; this corresponds to ~10^7 magnetic particles in 20 μL) in a glass tube and placed on a shaker for 1 h. This ratio ensured that the antibody incubated against the magnetic particles was sufficient in quantity for monolayer coverage of the magnetic particles (two-fold excess of antibody was provided). The beads were subsequently rinsed by adding 500 μL of PBS to the tube and vortexing the mixture. The beads were collected using a magnet and the PBS was removed. This cycle was repeated thrice.

For capture of MVs using functionalized beads, a 100 μL dispersion of MVs was added to the 20 μL of functionalized beads and the mixture was vortexed for 30 s and placed on a shaker for 1 h. As above, three cycles of rinsing were performed to remove free, unbound MVs

from the solution mixture. PBS was removed from the collected beads prior to extraction of lipids.

Extraction of Lipids from MVs into LC droplets. To extract the lipids from MVs that were captured on the immunobeads, 100 µL of a chloroform—methanol (2 : 1) mixture was added to the beads (in a glass tube). The mixture was vortexed vigorously for 1 min and placed in a shaker for 15 min. The beads were then collected at the bottom of the vial by using a magnet. The organic overlayer was subsequently removed and transferred to a new glass tube. Next, 5CB of a prescribed volume was added to the organic phase (5CB is miscible with the organic solvent), and the solvent was evaporated under a stream of nitrogen gas. The dried sample containing 5CB was placed in a vacuum for 1 h to remove any residual chloroform.

LC emulsions (containing the lipids from the MVs) were formed by addition of 0.5 mL of PBS to the 5CB obtained from the above procedure, followed by sequential sonication (with a bath sonicator) and vortexing (3,000 rpm). The cycles of sonication and vortexing were performed until the emulsions started to appear slightly hazy. This procedure resulted in a polydisperse population of LC droplets with diameters ranging from 1 to 10 µm (Figure 8-1g and 8-1h). FC was used to establish that each emulsion contained between 7,000 and 15,000 LC droplets per mL.

Optical Characterization of LC Emulsions by Polarized Light Microscopy. Prior to characterization by FC, the LC emulsions were examined using a combination of bright field and polarized light microscopy to determine the ordering of the LC within the droplets. A 20 µL volume of the LC emulsion was dispensed onto a glass coverslip. The configurations of the LCs

within the emulsion droplets were determined by observation of the droplets under an Olympus IX71 inverted microscope (Center Valley, PA) using an objective magnification power of 100× (an oil-immersion lens). Polarized light micrographs of the LC emulsions were collected with a Hamamatsu 1394 ORCAER CCD camera (Bridgewater, NJ) connected to a computer and controlled through SimplePCI imaging software (Compix, Inc., Cranberry Twp., NJ). Bright field micrographs were collected by removing the polarizer from the optical path of the microscope.

Flow Cytometry of LC Droplets. Plots of the intensity of side light scattering (SSC) versus the intensity of forward light scattering (FSC) were obtained for LC-in-water emulsions using a BD Accuri C6 flow cytometer (Ann Arbor, MI). In the experiments described below, the emulsions were pumped through the flow cytometer at a flow rate of 14 μL min^{-1} and the scatter plots were constructed from the measurement of 50,000 LC droplets (typically, 5.1 ± 1.6 μL of the LC emulsion was flowed through to read 50,000 droplets).

8.3 Results

8.3.1 Characterization of MVs

Our initial experiments were performed to characterize the MVs shed by A431 cells into culture media. The results of these experiments enabled us to design and evaluate our LC droplet-based MV detection method. MVs (from cell media containing 10% serum) were separated from cells and cell debris by centrifugation using procedures described elsewhere[11] and resuspended in phosphate buffered saline (PBS) (see Experimental section). DLS measurements

revealed that the diameters of the MVs ranged from 100 nm to 1 μm (consistent with published literature[39]), with a number-average diameter of 320 ± 145 nm (Figure 8-2a). To verify that the isolated samples contained lipids consistent with the presence of MVs, the phospholipid content was quantified using an EnzyChrom phospholipid assay kit and gas chromatography-mass spectrometry (GC-MS). Based on the EnzyChrom assay, a phospholipid concentration of 9.8 ± 1.6 μM was measured from a dispersion of MVs which were prepared by reconstituting MVs isolated from ~4 mL of cell media in 100 μL of PBS. GC-MS measurements gave a phospholipid concentration (8.8 ± 1.8 μM) in close agreement with that measured using the EnzyChrom assay. GC-MS also revealed that the phospholipids of the MVs have tails that are typical of those found in mammalian cells (18-carbon aliphatic tails are the most common;[40] Figure 8-S1). From the total lipid concentration and average size of the vesicles, we estimated the concentration of MVs resuspended in the PBS to be 10^{10} MVs per mL (or 10^{8} MVs per mL of culture medium, which is a concentration similar to that reported by Shao *et al.*[24]). Finally, we note that the concentration of proteins in the dispersion of MVs was measured to be 63 ± 19 μg mL^{-1} by using the Bradford assay.

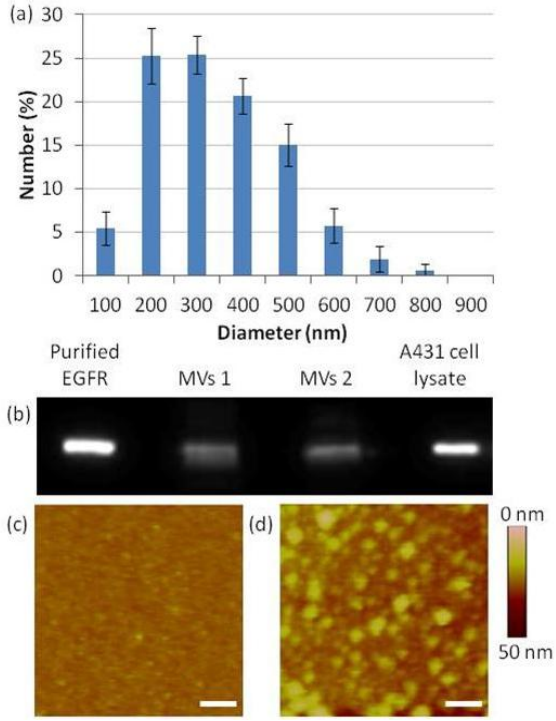

Figure 8-2. Characterization of MVs derived from A431 cells.

(a) Size distribution of MVs derived from A431 cells (suspended in PBS) as measured by dynamic light scattering (DLS). (b) Immunoblot analysis of two separate MV samples derived from two different batches of cells of A431 cells. Lysates were immunoblotted for EGFR. (c and d) AFM images of (c) a surface decorated with anti-EGFR 111.6 and (d) a surface decorated with anti-EGFR 111.6 and subsequently incubated with MVs derived from A431 cells (scale bar: 500 nm).

To provide additional confirmation of the number of MVs in our samples, we used NTA. A dilution of the above-described dispersion of MVs (with original lipid concentration of 9.8 ± 1.6 μM) was required to achieve the optimal concentration required for NTA. Specifically, a 1:40 dilution of the MV dispersion was performed (using PBS), which, when measured by NTA, gave a value of 4×10^8 particles per mL. Based on the earlier estimate of 10^{10} MVs per mL of PBS, this dilution step should result in a dispersion with a concentration of 2.5×10^8 MVs per mL PBS, which is a value that is in good agreement with that experimentally obtained by NTA.

We verified the presence of EGFR in the MVs obtained from the A431 cells by using immunoblotting (Figure 8-2b). The immunoblots were consistent with the presence of EGFR in the MVs, as evidenced by a band obtained from the MVs that coincided with purified EGFR (MW of 170 kDa). By comparison to bands of purified EGFR, the mass of EGFR in 10^8 MVs was estimated to be 14 ng. From this value, we estimate there to be approximately 500 EGFR molecules per MV. Here we note that past studies have reported that A431 cells can express ~10^6 EGFR molecules at the cell surface[41] and each cell has a typical size of approximately 40 μm.[42] We calculate, therefore, that a MV of diameter of 320 nm derived from an A431 cell will theoretically contain 250 EGFR molecules, which is of the same order of magnitude as our experimental value. However, we also note that MVs have been reported to be enriched in certain components of the cell membrane, in particular those that are associated with "lipid rafts".[10, 43] Since EGFR has been suggested to localize in lipid domains,[44] it is plausible that the concentration of EGFR may be enriched in MVs relative to that in the cell membrane.

Finally, we explored the use of surface-immobilized anti-EGFR 111.6 to capture EGFR-containing MVs derived from A431 cells. In this experiment, clean glass surfaces were initially decorated with avidin (according to previously reported procedures[45]), followed by functionalization with biotinylated anti-EGFR 111.6. Images obtained by using atomic force microscopy (AFM, in tapping mode) revealed that surfaces decorated only with antibody were smooth (Figure 8-2c, root-mean-squared (rms) roughness of 2.1 nm measured over an area of 2 μm × 2 μm) relative to the same surfaces incubated with EGFR-containing MVs, which exhibited circular features with diameters of ~150 nm (Figure 8-2d). Figure 8-S2 shows a measurement of the cross sectional height of the imaged surface. Notably, the size of these features (150 nm) is comparable to that measured by DLS (average at 320 nm). A control

experiment performed using a surface that was functionalized with a non-specific control IgG did not lead to capture of a comparable density of MVs (Figure 8-S3). These two results, when combined, are consistent with specific capture of MVs on surfaces presenting anti-EGFR 111.6 *via* antibody—antigen (EGFR) binding.

In summary, from the results presented above, we conclude that A431 cells shed membrane-bound MVs with an average diameter of 320 nm and that these MVs contain ~500 EGFR molecules. We also conclude that the A431 cells shed ~10^8 MVs per mL of culture media.

8.3.2 Interactions of Lipids from MVs with LC Droplets

Next, we performed a series of experiments to determine if lipids extracted from MVs shed by A431 cells would trigger ordering transitions in LC droplets. In this context, we note that past studies have shown that changes in the orientational ordering of LCs at aqueous interfaces (anchoring transitions) induced by amphiphiles are dependent on the structure and phase state of the amphiphiles.[46, 47] For example, it was shown that amphiphiles comprised of branched acyl chains do not cause LCs to assume a perpendicular or homeotropic orientation.[46] This was hypothesized to be due to frustrated packing of the branched amphiphiles, with branching preventing interdigitation (or coupling) of LC molecules with amphiphiles at the interface. Because MVs are derived from cell membranes, which are composed of a large variety of phospholipids (*e.g.*, with different tail lengths and degree of unsaturation, see Figure 8-S1) and other components of lipid rafts (*e.g.*, cholesterol, sphingomyelin), we characterized the response of LC droplets as a function of the number of MVs introduced into the LC.

Our initial experiments involved incubation of dispersions of MVs shed by A431 cells with LC droplets in PBS, a procedure that was reported previously to permit transfer of lipids

from model (or synthetic) vesicles, bacteria and viruses to LC droplets.[25-27] When using MVs shed by the A431 cells, however, we did not observe the LC droplets to undergo configurational transitions, consistent with a barrier to lipid transfer to the LC interface associated with the phase state of the lipid and/or proteins and carbohydrates associated with the outer surface of the MV membrane. This initial observation led us to explore an alternative procedure for transfer of the MV lipids to the LC droplets that employed an organic solvent. As described in the Methods section, a simple procedure that involved extraction of MV lipids into an organic solvent and subsequent introduction of the lipids into the LC was found to facilitate rapid transfer of lipids onto the LC interfaces. By using the EnzyChrom assay, we confirmed that >90% of the lipid in the MVs was extracted into a 100 μL mixture of chloroform—methanol (2 : 1).

Following emulsification, we characterized the ordering of the LC droplets with and without lipids extracted from MVs by using optical microscopy. Figure 8-1a shows a representative polarized light micrograph of a nematic LC droplet (in the absence of lipids) suspended in PBS. As detailed elsewhere, Figure 8-1a indicates the presence of two point defects (surface defects, called boojums) located at diametrically opposite ends, or “poles”, of the LC droplet and a bright appearance of a majority of the droplet.[48] From these observations and others (*e.g.*, performed using bright field microscopy), we conclude that the droplet is in a so-called bipolar configuration where the LC assumes a tangential orientation at the droplet surface (see Figure 8-1b for director profile). In contrast, following the transfer of lipids from MVs into the LC droplets, a distinct optical signature was observed. Figure 8-1d, with a single defect located at the droplet center and a characteristic dark cross, is consistent with a radial configuration where the LC is oriented perpendicular to the droplet surface (see Figure 8-1e for director profile). From these observations, we conclude that the presence of a sufficient quantity of MV-

derived lipid within the LC caused the droplets to assume a radial configuration, whereas in the absence of lipid, the configuration was bipolar.

While optical microscopy permits identification of the configuration of LC droplets, as discussed in the Introduction, FC provides a facile and quantitative method to characterize the size distributions of LC microdroplets as well as the percentage of radial and bipolar droplets within an emulsion.[32] Here we first address the use of FC to characterize the size distributions and more importantly changes in the size distributions due to coalescence of LC droplets during experiments. Specifically, we speculated that the presence of amphiphilic components of the MVs within the LC droplets could potentially influence the sizes and stability of the LC droplets formed by emulsification. To address this question, we used FC to measure the number of LC droplets formed by sonicating and vortexing 1 μL of 5CB (in 0.5 mL of PBS). In the absence of lipids extracted from MVs, we measured about 10^7 droplets (50,000 events counted for 5.1 ± 1.6 μL of the LC emulsion) to be formed. Assuming a monodisperse LC emulsion, we calculate that 1 μL of 5CB would produce 10^7 LC droplets with a diameter of 5.5 μm. To test this prediction, we measured the size of the 5CB droplets using optical microscopy. Our measurements reveal that the diameter of the LC droplets ranged from 1–10 μm, with an average diameter of 3.8 ± 1.7 μm (Figure 8-1g). Given the polydispersity of the emulsion drop size, we conclude that these two measurements are in reasonable agreement. In the presence of lipids from MVs in the 5CB droplets, the size distribution of the LC droplets determined by optical microscopy was similar to that obtained in the absence of lipids, with an average diameter of 3.6 ± 1.4 μm (Figure 8-1h). The number of lipid-containing LC droplets counted by FC was also similar to that measured above (50,000 events counted for 4.6 ± 1.3 μL of the LC emulsion).

To assess the stability of the LC droplets, the size distributions of the 5CB droplets, both in the absence and presence of lipids, were measured after 6 h. Inspection of Figure 8-S4 reveals that after 6 h, both distributions shifted to larger values, with an average diameter of 5.3 ± 1.6 μm and 5.2 ± 2.2 μm, respectively. This result suggests that the 5CB droplets have coalesced with time. In light of this result, as a precaution, we performed FC analysis within 1 h of preparation of the emulsions. However, we note that our current analysis of LC droplets using FC is based on a subpopulation of droplet sizes. The range of LC droplets selected for analysis (those which fall within FSC values of 30,000 to 60,000 a.u.) does not change significantly during the aging of the emulsion (Figure 8-S5). Indeed, a significant merit of using FC for analysis of LC droplets is that subpopulations of droplets (with a given range of size) can be selected for quantification.

Next we examined the FC scatter plots to analyze the internal configurations of the LC droplets. Figure 8-1c and f show FC scatter plots obtained using LC droplets free of lipids and containing MV lipids, respectively. As discussed in the Introduction, the characteristic features of these scatter plots are consistent with LC droplets in bipolar (Figure 8-1c) and radial (Figure 8-1f) configurations,[32] and they support our conclusion that the lipid components of MVs can induce ordering transitions in LC droplets. For FC-based methods of analysis of LC droplets to be useful for quantification of MVs, however, quantification of the number of radial droplets in a mixture of radial and bipolar droplets is needed. To this end, we varied the quantity of lipid introduced into the LC (by varying the number of MVs that were extracted into the organic solvent). Figure 8-3a–d show that as the number of MVs added to the LC was increased, a continuous evolution of the scatter plots from the broad distribution of SSC values at each FSC value (characteristic of emulsions containing bipolar LC droplets) to the distinct S-shape

(characteristic of emulsions containing radial LC droplets) was observed. To quantify the fraction of radial droplets within a sample of LC, guided by prior studies, we analyzed FSC values between 30 000 a.u. and 60 000 a.u.[32] Specifically, the number of light scattering events measured over this range of FSC values can be used to measure the percentage of radial droplets within a population of bipolar and radial droplets, a result that we found to be consistent with our measurements with MVs (Figure 8-S6). Figure 8-3e shows the percentage of radial droplets in the LC emulsions plotted as a function of the number of MVs that were transferred into the LC droplets.

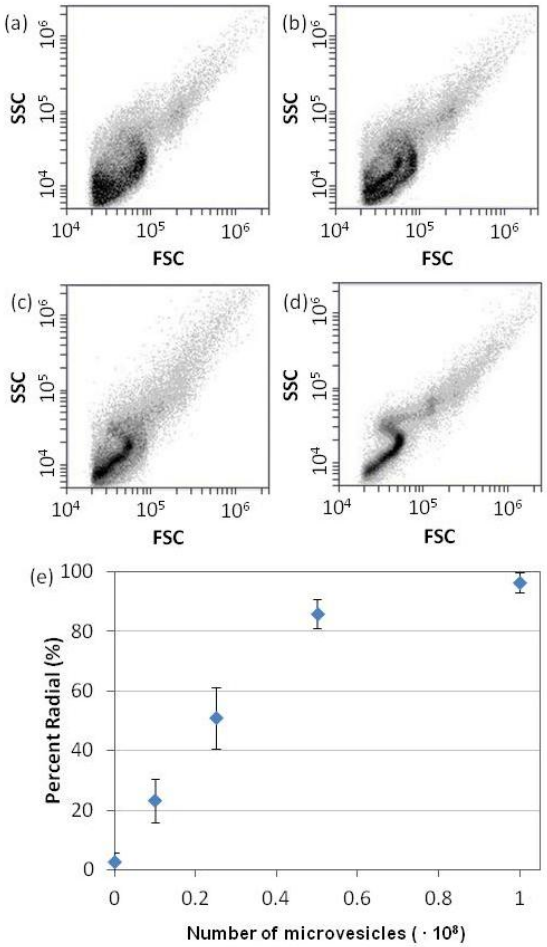

Figure 8-3. Dose-response behavior of the percentage of 5CB droplets that have undergone a bipolar-to-radial ordering transition in response to different numbers of MVs extracted into the LC.

(a–d) Scatter plots (intensity of side light scattering (SSC) versus forward light scattering (FSC)) obtained by FC-based analysis of LC emulsions obtained using LCs containing lipids extracted from A431-derived MVs. The total number of MVs extracted into the LC (1 μL 5CB) were (a) 0, (b) 1.25×10^7 (c) 2.5×10^7, (d) 10^8. (e) Percentage of LC droplets that exhibited a radial configuration, plotted as a function of number of MVs extracted into the LC (N = 3).

A key observation made regarding Figure 8-3 is that the response of the LC droplets to increasing concentrations of lipids from MVs is continuous. We attribute this continuous response to the variance of the size of the droplets (Figure 8-1g and h), which can influence the

balance of energetics that control the ordering within micrometer-sized LC droplets. Gupta and co-workers have demonstrated that the response of LC droplets to surfactants is dependent on the size of the LC droplets.[25] Specifically, the concentration of surfactants required to trigger a bipolar-to-radial ordering transition in LC droplets decreases with decreasing size of the droplets. This effect is due to size-dependent contributions of elastic and surface anchoring energies to the free energy of the LC droplets. To investigate the influence of LC droplet size on the response of the LC droplets to MVs, we quantified the percentage of droplets exhibiting the radial (or near-radial) configuration using optical microscopy. Inspection of Figure 8-S7 reveals that the percentage of LC droplets with a radial configuration decreased as the diameter of the droplets increased. This is consistent with previous observations[25] and supports our conclusion that the continuous response observed in Figure 8-3 is likely influenced by the range of LC droplet sizes in the emulsions used in our experiments.

8.3.3 Anchoring Transitions Induced by MVs Captured through Antigen–Antibody Recognition

The results described above demonstrate that LC droplets in combination with FC can be utilized to quantify the presence of MVs shed by A431 cells. As discussed in the Introduction, a key goal of the study reported in this chapter was to demonstrate quantification of MVs that contain key signaling proteins. To this end, we performed a series of experiments that targeted EGFR present in the MVs shed by A431 cells (as also noted in the Introduction, EGFR is used as an example of an important transmembrane signaling protein). Briefly, we incubated MVs with immunobeads presenting anti-EGFR 111.6, which were prepared using avidin-coated magnetic beads (1.5 mm) and biotinylated 111.6 (see Methods). Specificity of capture of the MVs was

established using a biotinylated non-specific IgG as an isotype control to the anti-EGFR 111.6. After functionalization of the beads (10^7 beads) with antibodies, they were rinsed with PBS and incubated with 100 µL of PBS containing 10^8 MVs for 1 h. The beads were then rinsed at least three times with PBS and then introduced into 100 µL of a chloroform–methanol organic mixture to extract MV lipids from the beads. The organic solvent was separated from the beads and contacted with 1 µL of 5CB. Following evaporation of the organic solvent, an LC emulsion was formed (see Methods).

Representative FC scatter plots obtained using the above-described procedures are shown in Figure 8-4a and 8-4b. When compared to the scatter plots obtained using beads with control IgGs (Figure 8-4a), the LC droplets with lipids extracted from anti-EGFR 111.6-functionalized beads generated scatter plots that had qualitative features characteristic of radial LC droplets (Figure 8-4b). Specifically, this latter plot has a narrower distribution of SSC values at each FSC value and the characteristic S-shape discussed earlier. Figure 8-4c shows the percentage of radial LC droplets in each sample, clearly demonstrating that the anti-EGFR 111.6-functionalized magnetic beads captured a significantly larger number of MVs than the beads presenting IgG controls. We note that our initial efforts suffered from false positives in control experiments performed with IgG-isotype functionalized beads, which we attributed to non-specific binding. To address this issue, the beads were subjected to a more stringent washing procedure that involved contact with a 1 µM SDS solution and three cycles of PBS rinsing. This additional step was found to eliminate the false positive signals from control IgG beads.

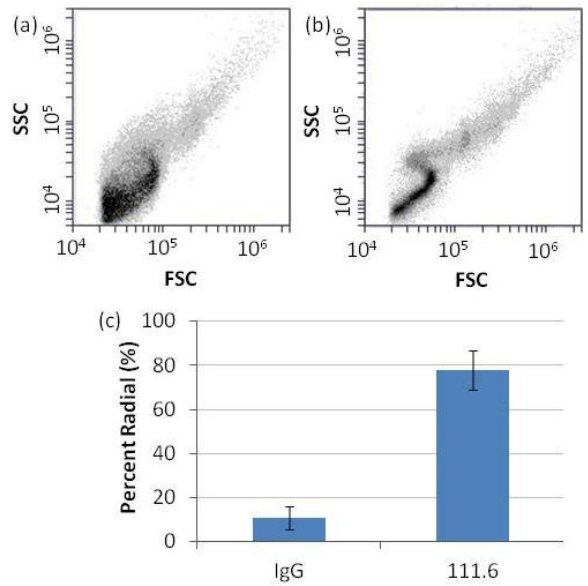

Figure 8-4. Bipolar-to-radial ordering transition triggered by MVs specifically captured through EGFR–anti-EGFR 111.6 recognition and subsequently extracted into 5CB prior to emulsification. Scatter plots of LC emulsions obtained after mixing of the LC with lipids extracted from magnetic particles that had been functionalized with (a) control IgG and (b) anti-EGFR 111.6 and subsequently incubated with A431-derived MVs. (c) Percentage of LC droplets that exhibited a radial configuration from IgG- or 111.6-functionalized magnetic particles (N = 5).

Next we quantified the response of the LC droplets as a function of the number of MVs contacted with the immunobeads. In this experiment, magnetic particles (functionalized with 111.6 or control IgG) were incubated against 100 μL dispersions that contained different numbers of MVs. Figure 8-5 shows a dose–response plot of the percentage of radial LC droplets as a function of the number of MVs present in the dispersion contacted with the immunobeads. The plots reveal that the percentage of radial LC droplets increased with the number of MVs that were incubated with the immunobeads. We interpret this response to reflect an increase in the number of MVs captured by the immunobeads and subsequently extracted into the LC, an interpretation that is supported by Figure 8-3. We also note the threshold number of MVs that

gave rise to 100% radial LC droplets was reported in Figure 8-3 to be 10^8. The experiments with immunobeads gave about 90% radial droplets when the immunobeads had been incubated with 10^8 MVs, suggesting that most of the MVs were captured by the beads and transferred to the LC. This conclusion was supported by quantification of MVs in the aqueous dispersion before and after contact with immunobeads.

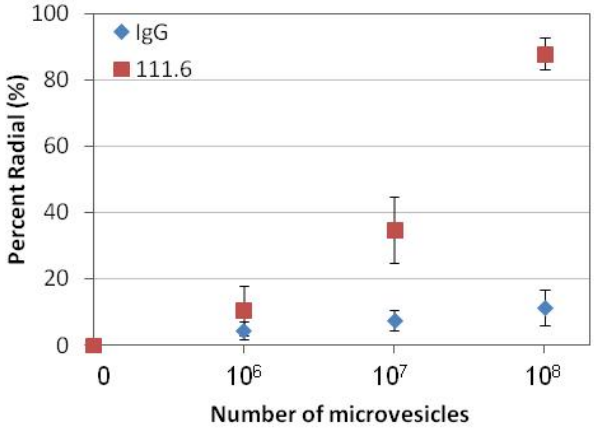

Figure 8-5. Percentage of LC droplets that exhibited a radial configuration, plotted as a function of number of MVs shed from A431 cells that were incubated against magnetic particles functionalized with anti-EGFR (111.6) or control (isotype) IgGs (N = 3).

Next we determined if the results in Figure 8-5 could be optimized further by reducing the number of LC droplets (by emulsification of less 5CB). In this optimization step, the number of MVs incubated with the magnetic particles was kept constant at 10^7 MVs (a concentration of MVs that resulted in mixed radial/bipolar configurations of LC droplets when using 1 µL of 5CB; see Figure 8-5). The results shown in Figure 8-6a reveal that the percentage of radial LC droplets increased with decrease in the amount of 5CB used. This observation is consistent with our conclusion that the internal ordering of the LC droplets is dependent on the amount of lipid in each droplet and that the use of smaller amounts of 5CB led to a higher concentration of lipid within each droplet (see Table 8-S1). Specifically, when the amount of 5CB used to prepare the

LC emulsion was decreased from 1 µL to 0.1 µL, the percentage of radial LC droplets increased from 35% (Figure 8-5) to 90% (Figure 8-6a).

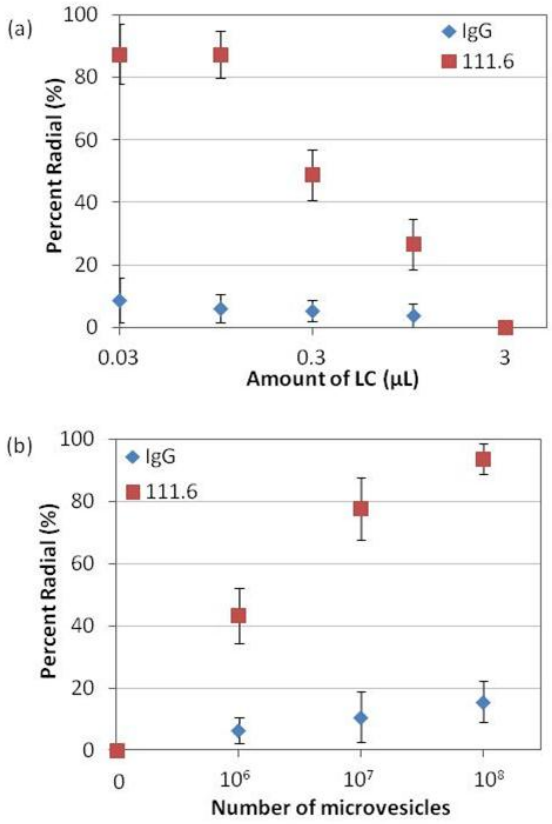

Figure 8-6. Dose-response behavior of the percentage of 5CB droplets that have undergone a bipolar-to-radial ordering transition in response to MVs specifically captured through EGFR–anti-EGFR 111.6 recognition as a function of the amount of LC used or the number of MVs extracted into the LC.

(a) Percentage of LC droplets that exhibited a radial configuration, plotted as a function of the amount of 5CB into which lipids from MVs captured on antibody-functionalized beads were introduced. The beads were incubated against 10^7 MVs. (b) Percentage of LC droplets that exhibited a radial configuration, plotted as a function of the number of MVs that were incubated against antibody-functionalized magnetic particles. The volume of LC used to form the emulsion was 0.03 µL.

Guided by the results above, Figure 8-6b shows the response of the LC droplets as a function of the number of MVs incubated with the immunobeads when 0.03 µL of 5CB was used

to prepare the LC emulsion. Inspection of Figure 8-6b reveals that the presence of 10^6 MVs can be readily quantified when using 0.03 μL of 5CB. As discussed above, the number of EGFR molecules per MV is estimated to be 500. This leads us to estimate that the current methodology permits detection of a concentration of EGFR in MVs in cell culture media of 5 fM.

8.4 Discussion

The key results reported in this chapter are two-fold. First, we have demonstrated that LC droplets in combination with FC can be used to quantify the presence of MVs shed by mammalian cells. In particular, we found spontaneous transfer of MVs shed from mammalian cells onto the interface of LC droplets to be very slow. This contrasts to past studies of model vesicles, viruses and bacteria (see above), and suggests that either the lipid composition/phase state of the membrane of the vesicles slows spontaneous transfer, or that proteins and polysaccharides that protrude from the surfaces of mammalian cells (and thus MVs) hinder contact of the membranes and the LC droplets. To overcome this barrier to transfer, we developed and validated a simple procedure that involves extraction of the MVs into the LC phase *via* use of an organic solvent. We demonstrated that the procedure permits quantitative reporting of MVs shed by cells by LC droplets (using FC).

A second key accomplishment reported in this chapter is the demonstration of a methodology that permits quantitation of MVs shed by cells that contain a target protein. In particular, we sought to demonstrate LC droplet-based methods that leverage protocols and instrumentation that are routinely found in biochemical laboratories. In this context, we found that capture of MVs *via* the use of antibody-functionalized beads provided a facile method to quantify the number of MVs in a sample that contained a targeted protein. While we have used

EGFR present in MVs shed by A431 cells as a model system with which to develop and validate the methodology reported in this chapter, we emphasize that EGFR is also an important target in cancer-related studies because its over-expression and mutation have been associated with some of the most aggressive forms of cancer. The methodology reported in this chapter was shown to permit detection of 10^6 MVs that contained EGFR in a sample. Our results and others[24] that have used immunoblotting to detect MVs have determined a sensitivity of 10^8–10^9 MVs, a value that is surpassed by the LC-based methods.

The high sensitivity of the LC-based detection method reported in this chapter arises in part because the binding of the MV-associated transmembrane protein is amplified by the high ratio of lipid to target protein in the MVs. The amplification that is inherent in the response of the LC droplets to the lipid component of the MVs provides a significant advantage over existing assays such as ELISA and immunoblotting. In addition, due to the lipid-driven ordering of LCs, the LC-based method does not require use of secondary antibodies, thus providing a cost advantage. Furthermore, methods such as immunoblotting and ELISA detect soluble antigens present in the sample and therefore, unlike the LC-based method, are not specific to MV-associated membrane proteins.

As mentioned in the Introduction, another technique that has been employed for direct detection of MVs is FC. While FC has been successful for routine cell sorting and cell counting, most conventional FC methods are not sufficiently sensitive to support detection of particles smaller than 500 nm, including MVs.[20-22] In contrast, LC-based FC reads out ordering transitions within micrometer-sized LC droplets induced by lipid-associated MVs and therefore it can readily detect MVs in the 100 nm-size range in a manner that is not strongly size-dependent. Also, the sensitivity of FC when used to probe directly for MVs was reported to be 10^8 MVs, a

value that is two orders of magnitude higher than the sensitivity of LC-based FC. Finally, we comment that fluorescent dyes have been used to label MVs in FC-based methods, but past studies have shown that the broad range of species present in complex mixtures (*e.g.*, free dyes, antibody aggregates, cell fragments with high levels of autofluorescence) give high background signal.[49]

In addition, we noted that NTA has also been used to detect MVs. Like FC, NTA analysis also suffers from false-positive signals that arise from aggregated serum proteins.[15] Also, because of statistical requirements,[36] the limit of detection of MVs in NTA is typically in the range of 10^8 particles per mL, a value that is surpassed by our current method. Here we emphasize that protein aggregates do not lead to false-positive signals in LC-based methods since the LC droplets respond specifically to lipids (main component of MVs) and not protein aggregates. This unique attribute of the LC-based method arises because adsorbate-induced anchoring of LCs is strongly dependent on the structure of the adsorbate.

Other techniques employed for analysis of MVs include electron microscopy[50] and AFM,[51] both of which require extensive sample preparation and do not provide quantitative information. One of the more sophisticated techniques developed thus far involves the use of a micro-NMR technique. In this technique, MVs are labeled with target-specific magnetic particles and introduced onto a microfluidic chip with a micro-NMR system.[24] This was used to profile circulating MVs from blood samples of glioblastoma patients and is proposed as a new way to monitor and predict response to disease therapies. While this technique surpasses our current method in terms of sensitivity (10^5 MVs), we note the complexity and extensive time requirement for sample preparation that accompanied this technique.

As mentioned above, the analytical attributes of the methodology reported in this chapter are closely tied to the response of the LC droplets to the lipid components of the MVs. We make an additional point regarding this topic in connection to the results in Figure 8-3. As noted above, past studies have shown that for a LC droplet to adopt a radial configuration as a result of adsorption of lipids at the droplet interface, close to saturation coverage of lipid is required at the LC interface.[25] To compare our results to these past studies, we calculated the number of lipid molecules introduced into each LC droplet from the MVs. For a LC droplet with a diameter of 5 μm, we calculate that a total of 10^8 lipid molecules are needed to saturate the interface of the LC droplet with lipid (the density of lipid at monolayer coverage is 1.7 molecules per nm^2).[30] For comparison, 10^8 MVs, which led to radial droplets prepared from 1 μL of 5CB, contain 10^{14} lipid molecules. Because 1 μL of 5CB generates about 10^7 droplets (see above), we calculate that the average number of lipid molecules per LC droplet is 10^7, which corresponds to 10% of the calculated saturation coverage.

We speculate that several factors may underlie our observation that the amount of lipid required to induce the radial configuration of LC droplets in our experiments is less than a monolayer coverage. First, the cell membrane (from which MVs are derived) contains a significant amount of cholesterol and sphingomyelin (up to 30 mol%, dependent on cell type[52]) that is not measured by the lipid assay used to quantify the lipid content of the MVs. These components may influence the phase states of the lipid monolayer and its interactions with the mesogens at the LC interface. In addition, the influence of lipids with acyl chains of varying lengths and degrees of unsaturation on LCs (see Figure 8-S1) has not been fully explored, and mixtures of such lipids may influence the ordering of LCs at sub-saturation coverage. We also note that our calculation above is approximate as it is based on the average droplet size, while in

practice the sizes of the LC droplets in the samples used in our experiments are polydisperse (see above for size effects).

We end this discussion by noting that a wide range of protein targets have now been detected in MVs shed into biological fluids: examples include EGFRs in MVs derived from pleural effusions of patients with non-small cell lung cancer[53] and detection of HER2/neu in MVs derived from blood of gastric cancer patients.[54, 55] CD147/EMMPRIN, a transmembrane protein, which is expressed at high levels by tumor cells, was found to be released from the surface of NCI-H460 cells *via* microvesicle shedding.[18, 56] AXL receptors, which have also been reported to be overexpressed in several types of human cancers, were detected in MVs circulating in plasma of chronic lymphocytic leukemia (CLL) patients.[57, 58] Overall, we note that the increased secretion of plasma membrane-derived MVs by cells in diseased states suggests that development of broadly applicable analytical platforms for MVs has the potential to impact basic biological research through to clinical diagnostics.

8.5 Conclusions

In summary, we have demonstrated principles for LC droplet-based quantification of MVs containing targeted proteins that are shed by mammalian cells. The approach uses micrometer-sized droplets of LCs to amplify MVs that are selectively captured *via* antibody-mediated interactions. The LC droplets are sufficiently large that they can be quantified *via* flow cytometry. The high lipid to protein ratio in the MVs leads to high sensitivity since LC droplets respond to the lipid component of the MVs. Specifically, we have validated the approach using MVs shed by A431 cells that contained EGFR. A significant merit of the approach is that the procedures and instrumentation that are combined with the LC droplets to create the

methodology are routinely found in basic biological and clinical laboratories. In these initial proof-of-concept experiments, we demonstrate that it is straightforward to quantify 10^6 MVs containing EGFR, a sensitivity that is better than immunoblotting, direct FC and NTA techniques. We also demonstrate a dynamic range of several orders of magnitude. Overall this chapter provides the framework for the use of LC droplets for detection of a broad range of MVs containing targeted proteins and lipids. With additional optimization, the analytical characteristics of the methodology can likely be improved further (*e.g.*, lower limit of detection).

Acknowledgements

This work was supported by the NSF under awards DMR-1121288 (MRSEC), by the National Institutes of Health (CA108467 and AI092004), and by the ARO (W911-NF-11-1-0251 and W911-NF-10-1-0181). We thank Dennis Yang and Professor Regina Murphy for their help with NTA measurements, and Daniel Mendez and Professor Brian Pfleger for their assistance with GC-MS measurements.

8.6 Supporting Information

lipid tails	mol %
C14:0	2.2
C16:1	4.7
C16:0	23.2
C18:2	20.6
C18:1	32.5
C18:0	16.7

Figure 8-S1. GC-MS analysis of the lipids tails of A431 cells-derived MVs.

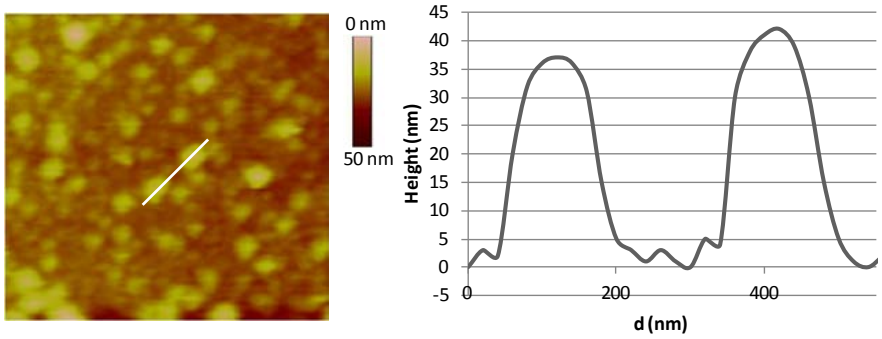

Figure 8-S2. AFM image of a surface decorated with anti-EGFR 111.6 and subsequently incubated with MVs derived from A431 cells.

The line corresponds to the location of the measurement of the cross sectional height (right plot).

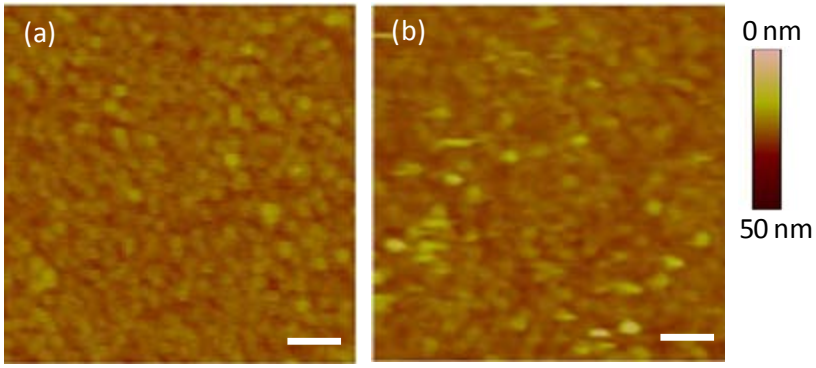

Figure 8-S3. AFM images of (a) a surface decorated with an isotype control IgG and (b) a surface decorated with isotype control IgG and subsequently incubated with MVs derived from A431 cells (scale bar: 500 nm).

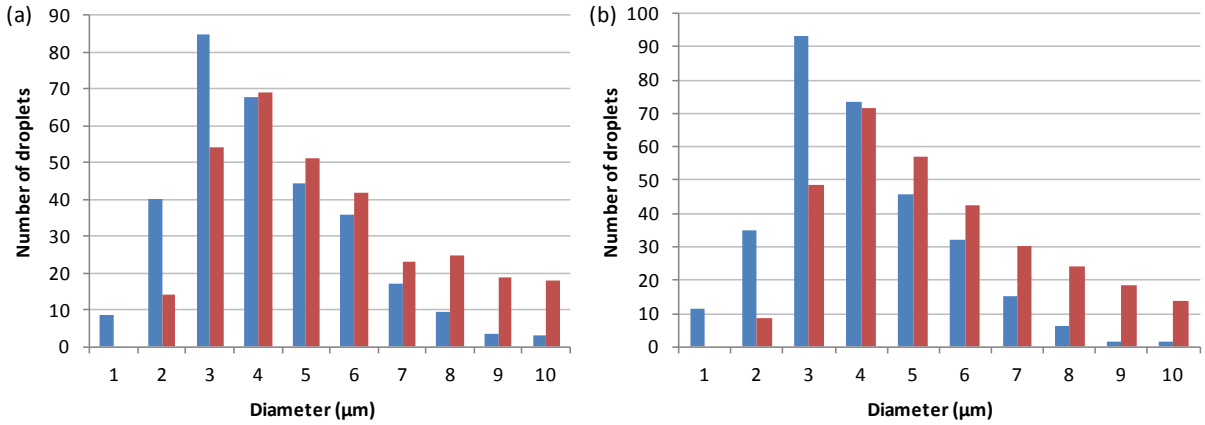

Figure 8-S4. Time-dependent size distributions of LC droplets in the (a) absence and (b) presence of lipids extracted from MVs (blue bars – 0 h and red bars – 6 h).

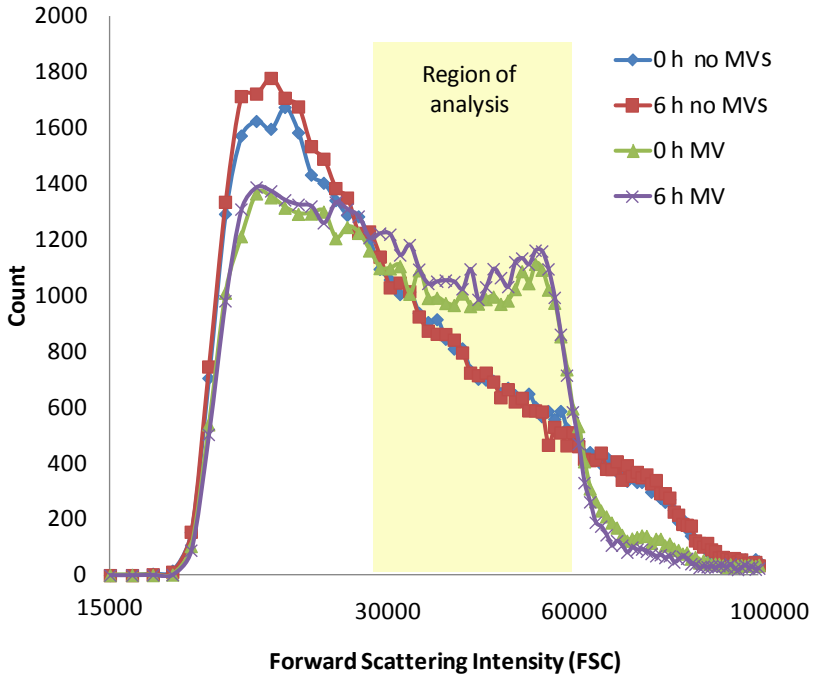

Figure 8-S5. Frequency histogram for FSC obtained for radial (with MVs) and bipolar (no MVs) LC droplets at t = 0 h and t = 6 h.

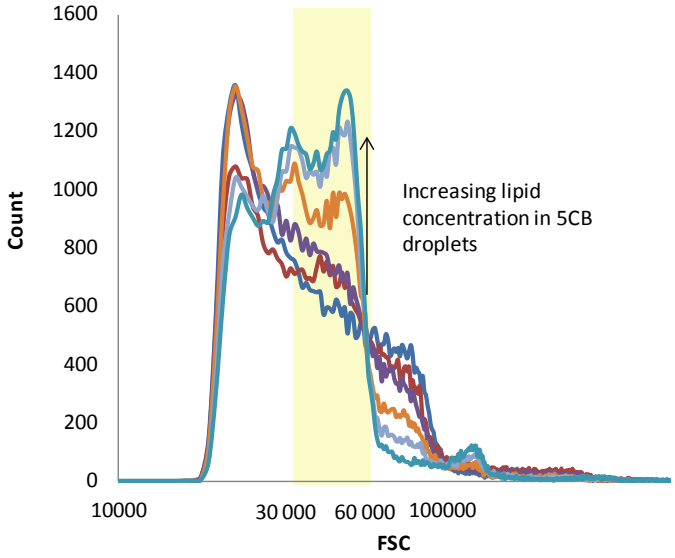

Figure 8-S6. Frequency histogram for FSC obtained with increasing concentration of lipids in 5CB droplets.

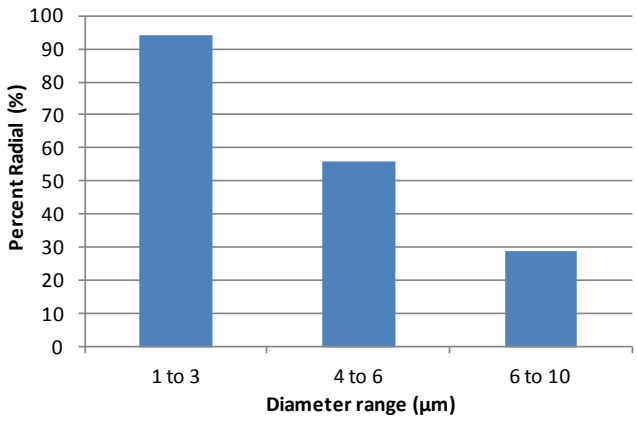

Figure 8-S7. Percentage of radial LC droplets as a function of diameter of LC droplets in the presence of lipids extracted from 5·107×MVs.

Table 8-S1. Theoretical amount of lipids in each droplet with a given amount of MVs and volume of 5CB used.

	# of lipids per droplet	
µL of 5CB	10^7 MVs	10^6 MVs
1	10^6	10^5
0.3	$3 \cdot 10^6$	$3 \cdot 10^5$
0.1	10^7	10^6
0.03	$3 \cdot 10^7$	$3 \cdot 10^6$

8.7 References

*This chapter was prepared as a Full Paper reporting original research in the journal *Analyst*. My contributions to the project were to assist in the development of the procedures for emulsifications and extraction of amphiphiles into LC droplets, to teach my co-authors the technique developed in Chapter 6 of this thesis for flow cytometry-based readout of LC droplet-based assays, and to consult on both the imaging of LC droplets and overall data analysis. I also assisted in the preparation of the manuscript.

1. Kahlert, C.; Kalluri, R., Exosomes in Tumor Microenvironment Influence Cancer Progression and Metastasis. *Journal of Molecular Medicine* **2013**, 91, 431-437.
2. Koga, K.; Matsumoto, K.; Akiyoshi, T.; Kubo, M.; Yamanaka, N.; Tasaki, A.; Nakashima, H.; Nakamura, M.; Kurok, S.; Tanaka, M.; Katano, M., Purification, Characterization and Biological Significance of Tumor-Derived Exosomes. *Anticancer Research* **2005**, 25, 3703-3707.
3. Théry, C.; Zitvogel, L.; Amigorena, S., Exosomes: Composition, Biogenesis and Function. *Nature Reviews Immunology* **2002**, 2, 569-579.
4. Camussi, G.; Deregibus, M. C.; Bruno, S.; Cantaluppi, V.; Biancone, L., Exosomes/Microvesicles as a Mechanism of Cell-to-Cell Communication. *Kidney International* **2011**, 78, 838-848.
5. Cocucci, E.; Racchetti, G.; Meldolesi, J., Shedding Microvesicles: Artefacts No More. *Trends in cell biology* **2009**, 19, 43-51.
6. Ratajczak, J.; Wysoczynski, M.; Hayek, F.; Janowska-Wieczorek, A.; Ratajczak, M. Z., Membrane-Derived Microvesicles: Important and Underappreciated Mediators of Cell-to-Cell Communication. *Leukemia* **2006**, 20, 1487-1495.
7. Balaj, L.; Lessard, R.; Dai, L.; Cho, Y. J.; Pomeroy, S. L.; Breakefield, X. O.; Skog, J., Tumour Microvesicles Contain Retrotransposon Elements and Amplified Oncogene Sequences. *Nature Communications* **2011**, 2, 180.
8. Ohno, S.-i.; Ishikawa, A.; Kuroda, M., Roles of Exosomes and Microvesicles in Disease Pathogenesis. *Advanced Drug Delivery Reviews* **2012**, 65, 398-401.
9. Valadi, H.; Ekstrom, K.; Bossios, A.; Sjostrand, M.; Lee, J. J.; Lotvall, J. O., Exosome-Mediated Transfer of Mrnas and Micrornas Is a Novel Mechanism of Genetic Exchange between Cells. *Nature Cell Biology* **2007**, 9, 654-659.
10. Al-Nedawi, K.; Meehan, B.; Kerbel, R. S.; Allison, A. C.; Rak, J., Endothelial Expression of Autocrine Vegf Upon the Uptake of Tumor-Derived Microvesicles Containing Oncogenic Egfr. *Proceedings of the National Academy of Sciences of the United States of America* **2009**, 106, 3794-3799.
11. Al-Nedawi, K.; Meehan, B.; Micallef, J.; Lhotak, V.; May, L.; Guha, A.; Rak, J., Intercellular Transfer of the Oncogenic Receptor Egfrviii by Microvesicles Derived from Tumour Cells. *Nature Cell Biology* **2008**, 10, 619-624.

12. Al-Nedawi, K.; Meehan, B.; Rak, J., Microvesicles Messengers and Mediators of Tumor Progression. *Cell Cycle* **2009**, 8, 2014-2018.
13. Martins, V. R.; Dias, M. S.; Hainaut, P., Tumor-Cell-Derived Microvesicles as Carriers of Molecular Information in Cancer. *Current Opinion in Oncology* **2013**, 25, 66-75.
14. van Doormaal, F. F.; Kleinjan, A.; Di Nisio, M.; Buller, H. R.; Nieuwland, R., Cell-Derived Microvesicles and Cancer. *Netherlands Journal of Medicine* **2009**, 67, 266-273.
15. Günter, M., Novel Tools for the Study of Cell Type-Specific Exosomes and Microvesicles. *Journal of Bioanalysis & Biomedicine* **2012**, 4, 46-60.
16. Jayachandran, M.; Miller, V. M.; Heit, J. A.; Owen, W. G., Methodology for Isolation, Identification and Characterization of Microvesicles in Peripheral Blood. *Journal of Immunological Methods* **2012**, 375, 207-214.
17. Osumi, K.; Ozeki, Y.; Saito, S.; Nagamura, Y.; Ito, H.; Kimura, Y.; Ogura, H.; Nomura, S., Development and Assessment of Enzyme Immunoassay for Platelet-Derived Microparticles. *Thrombosis and Haemostasis* **2001**, 85, 326-330.
18. Sidhu, S. S.; Mengistab, A. T.; Tauscher, A. N.; LaVail, J.; Basbaum, C., The Microvesicle as a Vehicle for Emmprin in Tumor–Stromal Interactions. *Oncogene* **2004**, 23, 956-963.
19. Théry, C., Boussac, M., Véron, P., Ricciardi-Castagnoli, P., Raposo, G., Garin, J., & Amigorena, S. , Proteomic Analysis of Dendritic Cell-Derived Exosomes: A Secreted Subcellular Compartment Distinct from Apoptotic Vesicles. *The Journal of Immunology* **2001**, 166, 7309-7318.
20. Gelderman, M. P.; Simak, J., Flow Cytometric Analysis of Cell Membrane Microparticles. *Methods Mol Biol* **2008**, 484, 79-93.
21. Kim, H. K.; Song, K. S.; Lee, E. S.; Lee, Y. J.; Park, Y. S.; Lee, K. R.; Lee, S. N., Optimized Flow Cytometric Assay for the Measurement of Platelet Microparticles in Plasma: Pre-Analytic and Analytic Considerations. *Blood Coagulation & Fibrinolysis* **2002**, 13, 393-397.
22. van der Vlist, E. J.; Nolte, E. N.; Stoorvogel, W.; Arkesteijn, G. J.; Wauben, M. H., Fluorescent Labeling of Nano-Sized Vesicles Released by Cells and Subsequent Quantitative and Qualitative Analysis by High-Resolution Flow Cytometry. *Nature Protocols* **2012**, 7, 1311-1326.
23. Soo, C. Y.; Song, Y.; Zheng, Y.; Campbell, E. C.; Riches, A. C.; Gunn-Moore, F.; Powis, S. J., Nanoparticle Tracking Analysis Monitors Microvesicle and Exosome Secretion from Immune Cells. *Immunology* **2012**, 136, 192-197.
24. Shao, H.; Chung, J.; Balaj, L.; Charest, A.; Bigner, D. D.; Carter, B. S.; Hochberg, F. H.; Breakefield, X. O.; Weissleder, R.; Lee, H., Protein Typing of Circulating Microvesicles Allows Real-Time Monitoring of Glioblastoma Therapy. *Nature Medicine* **2012**, 18, 1835-1840.
25. Gupta, J. K.; Sivakumar, S.; Caruso, F.; Abbott, N. L., Size-Dependent Ordering of Liquid Crystals Observed in Polymeric Capsules with Micrometer and Smaller Diameter. *Angewandte Chemie-International Edition* **2009**, 48, 1652-1655.
26. Gupta, J. K.; Zimmerman, J. S.; de Pablo, J. J.; Caruso, F.; Abbott, N. L., Characterization of Adsorbate-Induced Ordering Transitions of Liquid Crystals within Monodisperse Droplets. *Langmuir* **2009**, 25, 9016-9024.
27. Lin, I.-H.; Miller, D. S.; Bertics, P. J.; Murphy, C. J.; de Pablo, J. J.; Abbott, N. L., Endotoxin-Induced Structural Transformations in Liquid Crystalline Droplets. *Science* **2011**, 332, 1297-1300.

28. Brake, J. M.; Daschner, M. K.; Luk, Y.-Y.; Abbott, N. L., Biomolecular Interactions at Phospholipid-Decorated Surfaces of Liquid Crystals. *Science* **2003**, 5653, 2094-2097.
29. Hu, Q.-Z.; Jang, C.-H., Using Liquid Crystals to Report Molecular Interactions between Cationic Antimicrobial Peptides and Lipid Membranes. *Analyst* **2012**, 137, 567-570.
30. Meli, M. V.; Lin, I. H.; Abbott, N. L., Preparation of Microscopic and Planar Oil-Water Interfaces That Are Decorated with Prescribed Densities of Insoluble Amphiphiles. *Journal of the American Chemical Society* **2008**, 130, 4326-4333.
31. Sivakumar, S.; Wark, K. L.; Gupta, J. K.; Abbott, N. L.; Caruso, F., Liquid Crystal Emulsions as the Basis of Biological Sensors for the Optical Detection of Bacteria and Viruses. *Advanced Functional Materials* **2009**, 19, 2260-2265.
32. Miller, D. S.; Wang, X.; Buchen, J.; Lavrentovich, O. D.; Abbott, N. L., Analysis of the Internal Configurations of Droplets of Liquid Crystal Using Flow Cytometry. *Analytical Chemistry* **2013**, 85, 10296–10303.
33. Nicholson, R.; Gee, J.; Harper, M., Egfr and Cancer Prognosis. *European Journal of Cancer* **2001**, 37, 9-15.
34. Lennen, R. M.; Braden, D. J.; West, R. M.; Dumesic, J. A.; Pfleger, B. F., A Process for Microbial Hydrocarbon Synthesis: Overproduction of Fatty Acids in Escherichia Coli and Catalytic Conversion to Alkanes. *Biotechnology and Bioengineering* **2010**, 106, 193-202.
35. Provencher, S. W., *Comput. Phys. Commun* **1982**, 27, 213–242.
36. Filipe, V.; Hawe, A.; Jiskoot, W., Critical Evaluation of Nanoparticle Tracking Analysis (Nta) by Nanosight for the Measurement of Nanoparticles and Protein Aggregates. *Pharmaceutical Research* **2010**, 27, 796-810.
37. Bates, M. E.; Busse, W. W.; Bertics, P. J., Interleukin 5 Signals through Shc and Grb2 in Human Eosinophils. *American Journal of Respiratory Cell and Molecular Biology* **1998**, 18, 75-83.
38. Kim, Y.-N.; Wiepz, G. J.; Guadarrama, A. G.; Bertics, P. J., Epidermal Growth Factor-Stimulated Tyrosine Phosphorylation of Caveolin-1 Enhanced Caveolin-1 Tyrosine Phosphorylation Following Aberrant Epidermal Growth Factor Receptor Status. *Journal of Biological Chemistry* **2000**, 275, 7481-7491.
39. Lee, T. H.; D'Asti, E.; Magnus, N.; Al-Nedawi, K.; Meehan, B.; Rak, J. In *Microvesicles as Mediators of Intercellular Communication in Cancer—the Emerging Science of Cellular 'Debris'*, Seminars in immunopathology, 2011; Springer: 2011; pp 455-467.
40. Rohrer, G. A.; Pond, W.; Bell, A., Encyclopedia of Animal Science. In Taylor & Francis: 2004.
41. Krupp, M. N.; Connolly, D.; Lane, M., Synthesis, Turnover, and Down-Regulation of Epidermal Growth Factor Receptors in Human A431 Epidermoid Carcinoma Cells and Skin Fibroblasts. *Journal of Biological Chemistry* **1982**, 257, 11489-11496.
42. Terakawa, M.; Tsunoi, Y.; Mitsuhashi, T., In Vitro Perforation of Human Epithelial Carcinoma Cell with Antibody-Conjugated Biodegradable Microspheres Illuminated by a Single 80 Femtosecond near-Infrared Laser Pulse. *International Journal of Nanomedicine* **2012**, 7, 2653.
43. del Conde, I.; Shrimpton, C. N.; Thiagarajan, P.; Lopez, J. A., Tissue-Factor-Bearing Microvesicles Arise from Lipid Rafts and Fuse with Activated Platelets to Initiate Coagulation. *Blood* **2005**, 106, 1604-1611.

44. Couet, J.; Sargiacomo, M.; Lisanti, M. P., Interaction of a Receptor Tyrosine Kinase, Egf-R, with Caveolins Caveolin Binding Negatively Regulates Tyrosine and Serine/Threonine Kinase Activities. *Journal of Biological Chemistry* **1997**, 272, 30429-30438.
45. Tan, L. N.; Bertics, P. J.; Abbott, N. L., Ordering Transitions in Nematic Liquid Crystals Induced by Vesicles Captured through Ligand− Receptor Interactions†. *Langmuir* **2010**, 27, 1419-1429.
46. Lockwood, N. A.; de Pablo, J. J.; Abbott, N. L., Influence of Surfactant Tail Branching and Organization on the Orientation of Liquid Crystals at Aqueous-Liquid Crystal Interfaces. *Langmuir* **2005**, 21, 6805-6814.
47. Lockwood, N. A.; Gupta, J. K.; Abbott, N. L., Self-Assembly of Amphiphiles, Polymers and Proteins at Interfaces between Thermotropic Liquid Crystals and Aqueous Phases. *Surface Science Reports* **2008**, 63, 255-293.
48. Lavrentovich, O., Topological Defects in Dispersed Words and Worlds around Liquid Crystals, or Liquid Crystal Drops. *Liquid crystals* **1998**, 24, 117-126.
49. Aass, H. C. D., Reidun Øvstebø, Anne-Marie S. Trøseid, Peter Kierulf, Jens Petter Berg, and Carola Elisabeth Henriksson, Fluorescent Particles in the Antibody Solution Result in False Tf- and Cd14-Positive Microparticles in Flow Cytometric Analysis. *Cytometry Part A* **2011**, 79, 990-999.
50. Heijnen, H. F. G.; Schiel, A. E.; Fijnheer, R.; Geuze, H. J.; Sixma, J. J., Activated Platelets Release Two Types of Membrane Vesicles: Microvesicles by Surface Shedding and Exosomes Derived from Exocytosis of Multivesicular Bodies and Alpha-Granules. *Blood* **1999**, 94, 3791-3799.
51. Sharma, S.; Gillespie, B. M.; Palanisamy, V.; Gimzewski, J. K., Quantitative Nanostructural and Single-Molecule Force Spectroscopy Biomolecular Analysis of Human-Saliva-Derived Exosomes. *Langmuir* **2011**, 27, 14394-14400.
52. Pike, L. J.; Han, X.; Chung, K.-N.; Gross, R. W., Lipid Rafts Are Enriched in Arachidonic Acid and Plasmenylethanolamine and Their Composition Is Independent of Caveolin-1 Expression: A Quantitative Electrospray Ionization/Mass Spectrometric Analysis. *Biochemistry* **2002**, 41, 2075-2088.
53. Park, J. O.; Choi, D. Y.; Choi, D. S.; Kim, H. J.; Kang, J. W.; Jung, J. H.; Lee, J. H.; Kim, J.; Freeman, M. R.; Lee, K. Y., Identification and Characterization of Proteins Isolated from Microvesicles Derived from Human Lung Cancer Pleural Effusions. *Proteomics* **2013**, 13, 2125-2134.
54. Baran, J.; Baj-Krzyworzeka, M.; Weglarczyk, K.; Szatanek, R.; Zembala, M.; Barbasz, J.; Czupryna, A.; Szczepanik, A.; Zembala, M., Circulating Tumour-Derived Microvesicles in Plasma of Gastric Cancer Patients. *Cancer Immunology Immunotherapy* **2009**, 59, 841-850.
55. D'Souza-Schorey, C.; Clancy, J. W., Tumor-Derived Microvesicles: Shedding Light on Novel Microenvironment Modulators and Prospective Cancer Biomarkers. *Genes & development* **2012**, 26, 1287-1299.
56. Gabison, E. E.; Hoang-Xuan, T.; Mauviel, A.; Menashi, S., Emmprin/Cd147, an Mmp Modulator in Cancer, Development and Tissue Repair. *Biochimie* **2005**, 87, 361-368.
57. Ghosh, A. K.; Secreto, C. R.; Knox, T. R.; Ding, W.; Mukhopadhyay, D.; Kay, N. E., Circulating Microvesicles in B-Cell Chronic Lymphocytic Leukemia Can Stimulate Marrow Stromal Cells: Implications for Disease Progression. *Blood* **2010**, 115, 1755-1764.
58. Hong, C.-C.; Lay, J.-D.; Huang, J.-S.; Cheng, A.-L.; Tang, J.-L.; Lin, M.-T.; Lai, G.-M.; Chuang, S.-E., Receptor Tyrosine Kinase Axl Is Induced by Chemotherapy Drugs and

Overexpression of Axl Confers Drug Resistance in Acute Myeloid Leukemia. *Cancer letters* **2008**, 268, 314-324.

Chapter 9. Reversible Switching of Liquid Crystalline Order Permits Synthesis of Homogeneous Populations of Dipolar Patchy Microparticles*

9.1 Introduction

Nano-/microparticles with patterned surface properties (*e.g.*, patchy microparticles or Janus microparticles), when compared to their homogeneous counterparts, exhibit a range of physical properties that are enabling the design of new classes of functional materials.[1-3] For example, charged[4-6] or magnetic[7-9] dipolar patchy microparticles can be aligned or directed into self-assembled structures under the influence of an applied external electric or magnetic field, respectively. The responsiveness of these particles to external fields can be used for design of tunable electronic or photonic materials.[1] Additional applications of patchy microparticles include "electronic paper",[10, 11] self-propelled nano-/microparticles,[12] and biological detectors.[13, 14] Despite their potential utility, few methods exist for synthesis of patchy microparticles. Current methodologies include self-assembly of block copolymers, seeded emulsion polymerization, and microfluidics.[2] In this chapter, we advance a methodology for synthesis of homogeneous populations of dipolar patchy microparticles in which the long-range order of thermotropic liquid crystals (LCs) confined to micrometer-sized droplets dispersed in water is reversibly switched so as to direct colloidal microparticles to populate a unique location (patch) on the droplet surface. Subsequent photo-polymerization of the droplets is used to preserve the organization of the LC microparticles.

LCs combine properties commonly associated with crystalline solids (long-range orientational order) and isotropic liquids (high levels of molecular mobility).[15-18] When nematic

LCs are confined to water-dispersed microdroplets, the interfacial interactions of the LC set the orientation of the LCs at the droplet surface (*i.e.*, surface anchoring).[19-23] To accommodate the surface anchoring conditions, the LC within the interior of the droplet assumes a variety of configurations that involve elastic strain of the LC (*e.g.*, splay, bend, etc.)[23-27] and topological defects (localized regions where the LC effectively melts).[24, 25, 28-31] At equilibrium, the ordering of the LC within the microdroplets reflects minimization of the combined contributions of surface anchoring, bulk elastic deformations and topological defects to the free energy.[23-27] In the study reported in this chapter, we demonstrate that reversible manipulation of the surface anchoring of LC droplets decorated with colloids can be used to switch the configurations of LC droplets so as to sweep the colloids into unique locations on the droplet surface for the synthesis of homogeneous populations of patchy microparticles.[20, 23, 32, 33]

The use of reversible switching of LC microdroplet configurations, as described in this chapter for the synthesis of patchy microparticles, builds from our recent report of the use of LC droplets as templates for the synthesis of complex particles based on the LC-directed positioning of colloids (1 μm-in-diameter) adsorbed to the surfaces of the LC microdroplets.[34] In particular, for LC droplets with tangential surface anchoring that adopted a bipolar configuration (see below for additional discussion and Figure 9-1A), long-range elastic forces were observed to direct the colloids to preferentially locate at one of the two defects present at opposite poles of the bipolar droplets (*i.e.*, boojums)(see Appendix A).[34, 35] Because colloids with different compositions and properties can be positioned on the LC droplet surface (*e.g.*, polystyrene (PS) or silica colloids), the colloids can be used to introduce a desired functional property into the patchy microparticle (*e.g.*, surface chemistry or responsive to external field).[34] While this new generalizable technique for the synthesis of patchy microparticles offers the advantage of scalability over other

methods (described above) because synthesis occurs in a bulk aqueous phase, our previous publication reported heterogeneous populations of patchy microparticles because it was not possible to direct the colloids to a single pole of a LC droplet (*e.g.*, some LC droplets had colloids at both poles while others had colloids at only one pole).[34]

In the present study, we demonstrate that it is possible to take advantage of the above described internal switching of LC droplets to prepare populations of droplets with colloids adsorbed at *only one* location of the LC droplets. The configurations of the LC droplets are changed by either reversible adsorption of an amphiphilic species to the surfaces of the droplets or addition of salts. Characterization of the dynamics of both the internal switching and subsequent repositioning of the colloids to a single pole, in combination with a simple scaling argument, reveals the driving force for the repositioning is the long-range elasticity of the LC confined to the droplets. We illustrate the utility of this approach by synthesizing "Janus-like" microparticles and magnetically-responsive patchy droplets with either dipolar or quadrupolar symmetry for which the internal configuration of the LC leads to distinct optical responses upon application of an external magnetic field.

9.2 Experimental Section

Materials. Sodium dodecyl sulfate (SDS), sodium chloride (NaCl), sodium hydroxide (NaOH), and 2-dimethoxy-2-phenyl acetophenone (DMPAP) were purchased from Sigma-Aldrich (St. Louis, MO). 1 μm-in-diameter fluorescent polystyrene (PS) colloids (λ_{exc}=480 nm / λ_{em}=520 nm) were purchased from Bangs Laboratories (Fishers, IN). 4-cyano-4'-pentylbiphenyl (5CB) and 4-(3-acryloyoxypropyloxy) benzoic acid 2-methyl-1, 4-phenylene ester (RM257) were obtained from EM Sciences (New York, NY). 2.5 μm-in-diameter magnetic PS colloids were purchased

from Spherotech (Lake Forest, IL). Deionization of a distilled water source was performed with a Milli-Q system (Millipore, Bedford, MA).

Preparation of Liquid Crystal (LC)-in-Water Emulsions. LC-in-water emulsions were prepared according to previously published methods.[34, 35] Briefly, the emulsions were prepared by emulsifying 4 μL 5CB in 1.98 mL of an aqueous phase using a homogenizer (T25 digital ULTRA-TURRAX) equipped with a S25 N-10G dispersing element (IKA), for 30 s at 6,500 rpm. This procedure resulted in a homogeneous population of droplets in the bipolar configuration. The emulsions were contained in 19 mm-in-diameter, 51 mm high glass vials.

Adsorption of PS Colloids at the Surfaces of LC Droplets. The PS colloids were adsorbed at the surfaces of the LC droplets through addition of a 20 μL of a 1% wt/v PS colloid dispersion to 1.98 mL of a LC-in-water emulsion, followed by either a 30 or 300 s homogenization process at 6,500 rpm, for experiments with two or many adsorbed colloids, respectively.

Preparation of Preradial or Bipolar LC Droplets with Two PS Colloids Adsorbed at a Single Defect using Sodium Dodecyl Sulfate (SDS). For the experiments in which SDS was used to change the internal configuration from bipolar to preradial, 40 μL of a 100 mM aqueous solution of SDS was added to 2 mL of emulsions that contained bipolar LC droplets with two PS colloids adsorbed at the surface. The final concentration of SDS was 2 mM. The reverse (preradial-to-bipolar) ordering transition was achieved through dilution of 100 μL of an emulsion with preradial LC droplets into 2 mL pure water. The final concentration of SDS was below 0.1 mM.

Preparation of Preradial or Bipolar LC Droplets with Two PS Colloids Adsorbed at the Surface using Electrical Double Layer (EDL) Forces. For the experiments in which EDL forces were used to change the internal configuration from bipolar to preradial, 100 µL of an emulsion with bipolar LC droplets with two PS colloids adsorbed at the surface was added to 2 mL of a 1 M NaCl aqueous solution (with the pH adjusted to 12.7 using NaOH). Subsequently, to induce the reverse (preradial-to-bipolar) ordering transition, we added 100 µL of the emulsion to 2 mL pure water to decrease the concentration of NaCl below 100 mM.

Preparation of Polymerized LC Patchy Microparticles with "Janus-like" Surface Anisotropy. First, we prepared a photo-reactive RM257/DMPAP/5CB mixture to be used for formation of LC emulsions. The RM257 was mixed with 5CB at a wt/wt percentage of 10%. Then, the photo-initiator DMPAP was added at 5 % wt/wt based on the mass of RM257. After mixing, the experiments were performed in a fashion similar to those performed with two adsorbed PS colloids (see above). However, instead of 5CB, the RM257/DMPAP/5CB mixture was used, and multiple (more than two) colloids were adsorbed by increasing the homogenization time from 30 s to 300 s. Photo-polymerization of the 5CB/RM257/DMPAP mixture was performed using a UV lamp (365 nm) that delivered 2.5 mW/cm^2. The emulsion was exposed to UV light for 40 minutes.

Rotation of LC Patchy Droplets with Magnetic PS Colloids Adsorbed at the Surface. A magnetic field was introduced to a LC emulsion by placing a 1.9 cm-in-diameter, 1.3 cm thick magnetic disc (K&J Magnetics Inc., Pipersville, PA) ~15 cm away from the emulsion. The

strength of the magnetic field at the position of the LC emulsion was calculated by the magnet calculator on the website of K&J Magnetics.[36] The rotation of the magnetic patchy LC droplets was driven by an in-plane rotation of the magnetic disc.

Characterization of Patchy Microparticles by Bright Field (BF), Polarized Light (PL), and Fluorescence (Fluo) Microscopy. To characterize the LC patchy microparticles, a 50 μL volume of emulsion was first dispensed onto a glass coverslip. Next, the LC droplets were imaged using an Olympus IX71 inverted epifluorescence microscope (Center Valley, PA) equipped with a 100x oil-immersion objective, crossed polarizers, a mercury lamp, and a Chroma filter (457 nm $\leq \lambda_{exc} \leq$ 502 nm, and 510 nm $\leq \lambda_{em} \leq$ 562 nm). BF, PL, and Fluo micrographs of the droplets were collected with a Hamamatsu 1394 ORCAER CCD camera (Bridgewater, NJ) connected to a computer and controlled through SimplePCI imaging software (Compix, Inc., Cranberry Twp., NJ). BF micrographs were collected by removing the polarizer from the optical path of the microscope.

9.3 Results and Discussion

Emulsions of the nematic LC, 4-cyano-4'-pentylbiphenyl (5CB) in the bipolar configuration were prepared by dispersing 5CB in water, and homogenizing the mixture for 30 s. The left column of Figure 9-1A shows representative bright field (BF) and polarized light (PL) micrographs of a bipolar 5CB droplet obtained from our emulsification procedure. The bipolar droplet contains LC aligned tangential to the droplet surface and possesses two boojum defects at opposite poles.[23, 25, 31-33, 37-39] After formation of the bipolar droplets, 1 μm-in-diameter fluorescent PS colloids, at the surfaces of which the LC assumes a tangential anchoring, were

adsorbed to the surfaces of the droplets through addition of a 1 % (wt/v) dispersion of the PS colloids, followed by another 30 s of homogenization. Fluorescent PS colloids were used to permit the position of the colloids to be observed by fluorescence (Fluo) microscopy (Figure 9-1B). Consistent with our previous studies,[34, 35] this procedure led to a heterogeneous population of droplets with either two PS colloids located at a single boojum defect or one PS colloid at each boojum (Figure 9-1C). We comment here that our emulsification procedure resulted in LC droplets with diameters ranging from 1 to 40 μm and that we focus on LC droplets with diameters between 7 and 20 μm in the observations reported below. We also note that monodisperse LC emulsions can be prepared by various techniques (*e.g.*, microfluidics,[40] inkjet printing,[41] filling polymer microcapsules with LC,[42] *etc.*) and that advances reported below can be combined with these techniques.

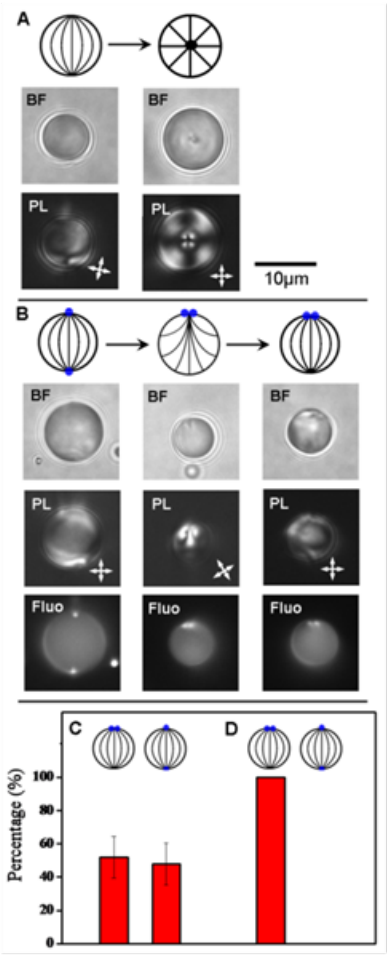

Figure 9-1. Adsorbate-driven switching of the internal configurations of LC droplets to sweep colloids to a single location on the LC droplet surfaces.

(A) Bipolar-to-radial ordering transition in a water-dispersed droplet of nematic 5CB without colloids adsorbed at the surface (triggered by adsorption of SDS). (B) Method utilized to direct 1 μm-in-diameter PS colloids initially at opposite boojums of a bipolar 5CB droplet to the same boojum *via* reversible adsorption of SDS. Schematic illustrations and the corresponding bright field (BF) and polarized light (PL) micrographs, and fluorescence (Fluo) micrographs (for B only) are shown from top to bottom for each equilibrium state of the LC droplets. In the schematics, the defects and colloids are represented by solid black or blue circles, respectively. The orientation of the crossed polarizers in PL micrographs is indicated by the white double-headed arrows. (C and D) Percentage of 5CB droplets in each two-colloid configuration (C) before or (D) after moving PS colloids to one defect of the bipolar LC droplets by using SDS to reversibly switch the LC order. The histograms were assembled from analysis of (C) 91 or (D) 48 droplets in 3 independent experiments.

Next, a small volume of a stock solution of 100 mM sodium dodecyl sulfate (SDS) was added to the aqueous phase of the emulsions to switch the internal configuration of the LC droplets (a so-called ordering transition) through adsorption of the surfactant at the LC droplet surface.[35] A final concentration of 2 mM SDS was selected to avoid formation of surfactant micelles, which can solubilize LC droplets.[43] After addition of the SDS solution, the droplets were observed to undergo a bipolar-to-preradial ordering transition. The preradial configuration involves LC aligned at an acute angle at the droplet surface (*e.g.*, tilted) and a single defect at a pole of the droplet (Figure 9-1B, middle column).[23, 25, 27, 31-33, 44] We comment that in the absence of the colloids, adsorption of SDS drives a bipolar-to-radial ordering transition (Figure 9-1A), and thus our observation of the preradial configuration suggests that the presence of the colloids results in an effective "pinning" of a topological defect to the droplet surfaces (see also Appendix A).[35] Importantly, independent of the positions of the colloids on the surfaces of bipolar droplets prior to addition of SDS (colloids adsorbed at single boojum or colloids adsorbed at each of the two boojums), after addition of SDS, the colloids were observed to locate at the site of the preradial defect (Figure 9-1B, middle column).

Finally, the reverse (preradial-to-bipolar) ordering transition was achieved through dilution of the surfactant to a final concentration of < 0.1 mM, and desorption of surfactant from the droplet surfaces (near-monolayer coverage of surfactant is required to change the orientation of the LC from tangential to normal).[21, 32, 45] Upon recovering the bipolar configuration, we did not observe LC droplets with colloids adsorbed at both boojum defects (Figure 9-1D). Instead, a homogeneous population of LC droplets with colloids adsorbed at a single boojum (Figure 9-1B, right column) was obtained. This state of the emulsion was found to persist over the duration of our observations (hours). Overall, the results of this experiment demonstrate that surfactant-

induced switching of the configurations of LC droplets can be used to synthesize homogeneous populations of bipolar droplets with colloids adsorbed at a single pole.

Next, we characterized the dynamics of the SDS-triggered bipolar-to-preradial ordering transition in 5CB droplets (with one PS colloid adsorbed initially at each boojum defect of the initial bipolar configuration) to provide insight into the mechanism driving the two colloids to the single defect of the preradial configuration. A representative example of the kinetic pathway for this process is shown in Figure 9-2. The initial time point (t = 0 s) displayed in Figure 9-2 represents the time at which the 100 mM SDS solution was added to the aqueous phase surrounding the 20 μm-in-diameter 5CB droplet (a drop of SDS solution was added to one end of the sample, and the sample was allowed to equilibrate). Following the addition, SDS was transported (*via* diffusion and convention) to the surface of the droplet. The first evidence of the LC ordering transition was observed at t = 77 s, at which point a disclination loop formed inside the 5CB droplet, consistent with a previously reported kinetic pathway.[31, 32, 46, 47] Subsequently (t = 77 - 81 s), the disclination loop migrated towards a site previously occupied by one of the two boojums, and shrank to a point to form the preradial configuration. Immediately following our observation of the bipolar-to-preradial ordering transition, we changed the imaging mode of the microscope from polarized light to fluorescence to determine the position of the PS colloids. Surprisingly, only one colloid was observed at the position of the defect of the preradial configuration, while the second colloid remained close to the location of the boojum of the initial bipolar configuration. Over the course of the next 40 s, the latter PS colloid was observed to migrate across the surface of the LC droplet and associate with the first colloid at the defect. From these results, we conclude that one PS colloid pinned the preradial point defect to the surface of the LC droplet, preventing escape of the defect into the core of the droplet (as would

be expected in the absence of adsorbed colloids; see Figure 9-1A),[35] and an additional long-range force drove the second colloid to join the first at the position of the point defect of the preradial configuration.

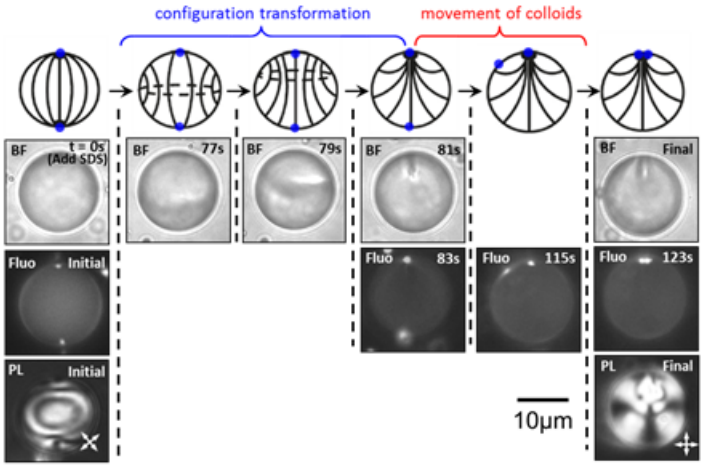

Figure 9-2. Representative micrographs for the kinetic pathway of a bipolar-to-preradial ordering transition in a nematic 5CB droplet with one 1 μm-in-diameter fluorescent PS colloid adsorbed at each of two boojum defects.

BF, Fluo and PL micrographs are shown from top to bottom for the initial and final state. BF or Fluo micrographs are shown for the intermediate states of the process to highlight the evolution of the LC configuration and movement of PS colloids, respectively. Corresponding schematic illustrations are shown at the top.

A key observation of the experiment described above is that the mobile PS colloid (*i.e.*, colloid not pinning the defect to the surface of the droplet) did not randomly diffuse over the surface of the droplet and arrest at the position of the preradial defect. Instead, it followed a nearly direct path from the position of the boojum of the initial bipolar configuration to the preradial defect. This observation led us to hypothesize that the driving force for the migration of the colloid was the elastic distortion of the LC induced by the presence of the colloid at the interface. To test this proposal, a simple scaling argument was formulated to compare the

magnitude of the elastic energy associated with the colloid-induced distortion of the LC to the energy dissipated by Stokes' drag during transport of the colloid across the surface of the LC droplet to the preradial defect. Here we comment that a colloid adsorbed at either the defect of a preradial LC droplet or at the opposite pole both distort the LC. Our experimental results reported above and recent coarse grain modelling (see Appendix A)[35] support, however, the proposition that elastic distortions (and defect core energies) are minimized by the partitioning of a colloid to a defect. Accordingly, we estimate the magnitude of the elastic forces driving the colloid to the defect as:[48-50]

$$E_{elastic}=Ka \qquad (9-1)$$

in which K is the elastic constant of the LC (using the "one constant" approximation), and a is the radius of the PS colloid (0.5 μm). Using a typical value for an elastic constant for a low molecular weight LC, $K=10^{-11}$ N,[29, 51] we calculate $E_{elastic} \approx 5\times10^{-18}$ J. As noted above, the force driving transport of the PS colloid across the surface of the LC droplet is opposed by a Stokes' drag force. Thus, the energy dissipated during the displacement of the colloid can be estimated as the product of this drag force and the distance that the PS colloid travelled to reach the preradial defect (d):[52, 53]

$$E_{transport}=6\pi\eta a v d \qquad (9-2)$$

in which η is the apparent dynamic viscosity experienced by the PS colloid at the aqueous—5CB interface, and v is the average velocity of the colloid. We estimate d to be $R\pi$, where R is the radius of the LC droplet (10 μm), and η to be 30 mPa s (for silica colloids at a planar aqueous—5CB interface, η was measured to fall between 25.8 and 34.9 mPa s[48]). In addition, v can be approximated as:

$$v=d/t \qquad (9-3)$$

in which *t* is the transit time for the PS colloid to reach the preradial defect (40 s, as shown in Figure 9-2). Combining equations 9-2 and 9-3, we calculate $E_{transport} \approx 7\times10^{-18}$ J, which is in close agreement with our estimate for the energy associated with the elastic distortion of the LC around the colloid (5×10^{-18} J). Overall, this simple scaling argument supports our hypothesis that the elastic forces generated by the LC droplet drive the colloid to the preradial defect.

The technique reported above for synthesis of homogeneous populations of patchy LC droplets used surfactants. Surfactants, however, are often difficult to remove following material synthesis, and their presence can hinder certain applications (*e.g.*, biological sensing[19-23]). Therefore, we sought to switch the internal configurations of the LC droplets through manipulation of the ionic strength and pH of the aqueous solution (without surfactant). Previously, we showed that it is possible to trigger bipolar-to-radial ordering transitions in LC droplets under conditions of high ionic strength (> 100 mM) and alkaline pH (> 12), due to the effects of an electrical double layer (EDL) that forms on the LC-side of the aqueous—LC interface.[54-56] To explore the use of salts and alkaline conditions for microparticle synthesis, we first formed emulsions of bipolar 5CB droplets with PS colloids adsorbed at either one or both boojums. Next, sodium chloride and sodium hydroxide (the final concentration of sodium chloride was 1 M and the pH was 12.7) were added to the aqueous phase of the emulsions. As was the case for the SDS-triggered ordering transition, addition of salt resulted in a homogeneous population of preradial LC droplets with both colloids adsorbed at the defect (Figure 9-S2 of Supporting Information). Finally, the reverse (preradial-to-bipolar) ordering transition, induced by dilution of the bulk aqueous concentration of sodium chloride to below 100 mM, resulted in a homogeneous population of bipolar droplets with two PS colloids trapped at a single boojum defect (Figure 9-S2 of Supporting Information). This experiment

demonstrates that simple adjustments of ionic strength and pH can also be used to switch the internal configurations of LC droplets to synthesize homogeneous populations patchy LC droplets. We comment here that in both methods described above for synthesis of homogeneous populations of patchy LC droplets (addition of surfactants or simple salts), the colloids remain trapped at a single boojum defect of the bipolar configuration (*i.e.*, do not return to the initial state of the system with one colloid located at each defect) because the colloids are located in a local free energy minimum.[35]

As described in the Introduction, there is a growing range of applications for Janus microparticles (*e.g.*, electronics, photonics, sensing), and thus we next sought to demonstrate how switching of LC droplets can be exploited to synthesize *solid* "Janus-like" microparticles (Janus microparticles are defined as patchy microparticles exhibiting an approximately 50:50 ratio of anisotropic surface coverage[2, 10]). We began by doping the LC with a small amount of the reactive mesogenic monomer 4-(3-acryloyloxypropyloxy) benzoic acid 2-methyl-1,4-phenylene ester (RM257) and the photo-initiator 2-dimethoxy-2-phenyl acetophenone (DMPAP) prior to formation of the LC-in-water emulsions. Next, the emulsions were formed and PS colloids were subsequently adsorbed to the surfaces of the LC droplets (see also the Experimental Section for more detail). We found that increasing the homogenization period from 30 s (used in the experiments reported above) to 300 s resulted in more than two PS colloids adsorbed to surfaces of the droplets. As was the case for two adsorbed PS colloids, we observed multiple colloids to adsorb at diametrically opposite boojums of bipolar LC droplets with equal probability (Figure 9-3A and B). We next added SDS to the emulsions to trigger a bipolar-to-preradial ordering transition, which was observed to sweep the colloids to a single pole of the droplets (the final concentration of SDS was again 2 mM). Finally, the emulsions were exposed

to UV light for 40 minutes to photo-polymerize the colloid-coated LC droplets in the preradial configuration.

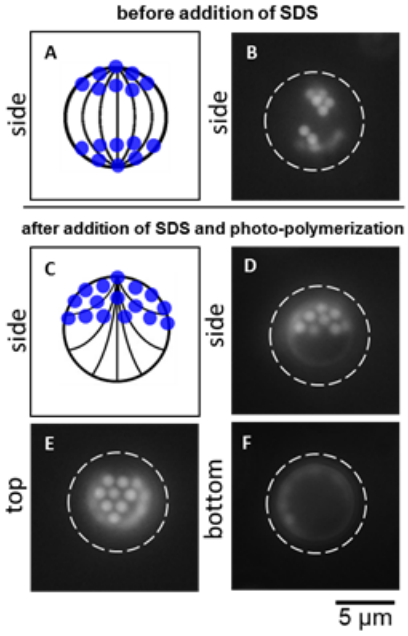

Figure 9-3. Synthesis of *solid* "Janus-like" microparticles *via* switching of LC droplets.
(A and B) Side view of the arrangement of PS colloids on the surface of a bipolar LC droplet prior to addition of SDS. A side view is shown to emphasize that colloids were adsorbed at both poles. (C-F) Solid "Janus-like" microparticles with an internal LC structure locked in the preradial configuration (adsorption of SDS) by a polymer network as viewed from the (D) side, (E) top, and (F) bottom. Each image was captured by allowing the microparticles to rotate and subsequently focusing on the apex of the newly oriented microparticle. The white dashed circles indicate the contour of the microparticle. The depth of focus was ~500 nm. Corresponding schematic illustrations viewed from the side are shown in (A) and (C).

Figure 9-3C-F shows Fluo micrographs of spherical *solid* "Janus-like" microparticles with an internal structure of LC locked in the preradial configuration by the polymer network (see Figure 9-S3 of the Supporting Information for the corresponding BF and PL micrographs, and Figure 9-S4 for additional examples). The colloids are located on approximately one half of the LC droplet. We note here that the depth of focus of the 100x oil-immersion objective used to

collect the images is ~500 nm. Therefore, PS colloids at different heights along the surface of the spherical “Janus-like” microparticles that fall within this depth of focus appear with similar intensity in Fluo micrographs. Interestingly, the packing arrangements of the colloids on the surfaces of the LC droplets follow a close-packed hexagonal pattern, which is distinct from the star structures recently reported to be formed by 4 μm-in-diameter silica particles, treated to induce a homeotropic anchoring of the LC, trapped at the surfaces of large (150 to 250 μm-in-diameter) bipolar LC droplets dispersed in an aqueous solution of polyvinyl alcohol.[57] Ongoing studies are investigating the origins of this hexagonal pattern, the results of which will be reported elsewhere (see Chapter 10). From the results displayed in Figure 9-3 and Figure 9-S3 of the Supporting Information, we conclude that our new methodology can be employed to synthesize solid spherical “Janus-like” microparticles with internal structuring characteristic of a LC droplet.

As described above, our methodology for synthesis of patchy microparticles and microparticles is generalizable because the LC droplets can be used to direct the assembly of a range of different organic or inorganic colloids on the droplet surfaces. In the final experiment reported in this chapter, we demonstrate synthesis of functional magnetic patchy LC droplets that can be rotated in weak magnetic fields. The patchy LC droplets were synthesized using paramagnetic, 2.5 μm-in-diameter PS colloids (the colloids contained dispersions of iron oxide nanoparticles). Prior to addition of any SDS, we observed bipolar LC droplets with multiple magnetic PS colloids distributed non-uniformly amongst their boojums. We comment here that although the larger size of the magnetic PS colloids (relative to the non-magnetic colloids) allowed the position of the colloids to be resolved in BF micrographs, the exact number of magnetic PS colloids adsorbed at the poles of the droplets could not be determined because the

colloids were not fluorescently labeled. When a permanent magnet was held ~15 cm away from the LC emulsion, the orientational response of the patchy bipolar LC droplets to the weak external magnetic field (~10^{-4} Tesla see below) depended on the location of the PS colloids on the surface of the droplets, as shown in Figure 9-4A. Specifically, bipolar LC droplets with magnetic PS colloids adsorbed at a single pole rotated to an equilibrium state in which the pole with the adsorbed colloids faced the location of the magnet. In contrast, bipolar LC droplets with colloids adsorbed at both poles were observed to align in a bimodal distribution of orientations with droplets oriented such that the two poles were aligned either parallel or perpendicular to magnet (see Figure 9-4A and 9-4B).

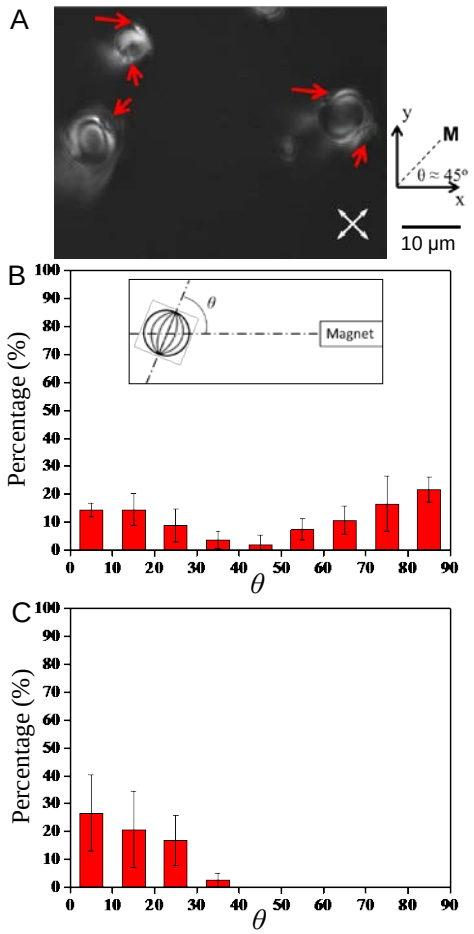

Figure 9-4. Influence of the positions of magnetic PS colloids adsorbed to the surfaces of bipolar LC droplets on the alignment of the patchy droplets in a weak external magnetic field.

(A) Representative PL micrographs of the orientation of droplets with colloids adsorbed at either a single pole (lower droplet on the left) or both poles (top droplet on the left and droplet on the right) in the vicinity of boojum defects. The magnet was held at a ~45^{o} angle with respect to x-axis and ~15 cm away from the sample. The red arrows indicate the location of the pole at which the magnetic PS colloids are adsorbed. (B and C) Distribution of rotational orientations observed for bipolar LC droplets in the presence of a magnetic field for droplets with magnetic PS colloids adsorbed at (B) either a single or both pole(s) prior to addition of SDS or (C) trapped at one pole by reversible adsorption of SDS. The rotational orientation is expressed as a function of the angle (θ, see inset in (B)) defined by the location of the magnetic disc relative to the orientation of a line that connects the boojum defects of bipolar LC droplets. The histograms were assembled from analysis of (B) 55 or (D) 39 droplets in 3 independent experiments.

The above observations show that the heterogeneous population of magnetic patchy LC droplets responds non-uniformly to the external magnetic field (Figure 9-4B). To overcome this drawback, homogeneous populations of LC droplets were prepared by reversible switching of the internal ordering of the LC using SDS (as described above). We note here that we prepared uniform populations of both bipolar and preradial dipolar patchy droplets because these configurations generate distinct optical appearances when viewed between crossed polarizers (Figure 9-1B). As shown in Figure 9-4C and Figure 9-S5A and 9-S5B of the Supporting Information, when the entire population of magnetic patchy LC droplets was in either the preradial or bipolar configuration, we observed a uniform orientational response of the LC droplets to the applied field. For example, Figure 9-5 shows a clock-wise 360° in-plane rotation of a LC droplet in either the preradial or bipolar configuration around an axis normal to the center of the droplets (see Supporting Information for corresponding videos). We end with two important comments. First, 0.1 - 1 Tesla magnetic fields have been shown to trigger ordering transitions in LC droplets in which the LC molecules (with a positive dielectric anisotropy) align parallel to the direction of the magnetic field (so-called Fredericks transitions).[25, 58] However, the magnetic field used here was much weaker (~10^{-4} Tesla), and the LC droplets were shown to rotate due to interactions between the adsorbed magnetic colloids and the field (rather than interactions between the field and LC). Second, two possible mechanisms exist for the observed rotation of magnetic patchy LC droplets: (i) the magnetic colloids and LC droplet rotate together or (ii) the magnetic colloids adsorbed at the surface rotate first, and the internal configuration of the LC droplet subsequently relaxes to its equilibrium state. We calculate the characteristic time for the LC to adopt the velocity of a magnetic colloid moving across the surface of the droplet ($\tau_v \sim R^2/v$, where v is the kinematic viscosity of 5CB and is of order 10^{-5} m^2/s)[59, 60] to be much

shorter than the time required for relaxation of the molecular orientational order within the LC droplet ($\tau_n \sim \eta_{5CB}R^2/K$, where $\eta_{5CB} \sim 10^{-2}$ Pa s is the dynamic viscosity of 5CB and $K \sim 10^{-11}$ N is the elastic constant (see above)).[29] For a 10 μm radius LC droplet $\tau_v \sim 10^{-5}$ s << $\tau_n \sim 0.1$ s, thus we conclude that viscous forces cause the LC to rotate with the magnetic colloid.

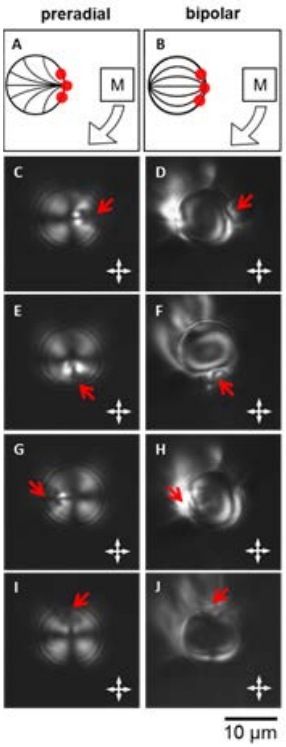

Figure 9-5. In-plane rotation of magnetically-responsive patchy microdroplets of LC.
PL micrographs of a clock-wise 360° in-plane rotation of a LC droplet in either a (A, C, E, G, I) preradial or (B, D, F, H, J) bipolar configuration around an axis normal to the center of the droplets. Magnet PS colloids were adsorbed at a single pole (indicated by the red arrow). The rotation was driven by a magnetic disc held ~15 cm away from the sample. The position of the magnet was to the (C and D) east, (E and F) south, (G and H) west, or (I and J) north of the sample in the plane of the stage. Corresponding schematic illustrations are shown in (A) and (B). Corresponding videos are available in the Supporting Information.

9.4 Conclusions

The experiments reported in this chapter demonstrate a generalizable approach to the synthesis of homogeneous dispersions of patchy LC microdroplets and microparticles. The approach uses reversible changes (*i.e.*, switching) of the internal ordering of the LCs to uniformly position colloids on the surfaces of the LC microdroplets. Specifically, a transformation from a bipolar to a preradial configuration, triggered by adsorption of surfactants or addition of simple salts to the aqueous phase of the LC emulsions, induces a long-range elastic force that sweeps adsorbed colloids to a unique location (the location of the single defect of the preradial configuration). The reverse ordering transition results in a homogeneous population of bipolar LC droplets with colloids remaining at the single location (one of the boojum defects) because the colloids are trapped in local free energy minimum on the surfaces of the droplets. We illustrate the utility of the methodology by demonstrating synthesis of solid “Janus-like” microparticles and also magnetically-responsive patchy bipolar or preradial LC droplets with dipolar symmetry. Because a range of colloidal materials can be positioned on the LC droplets using the methods reported in this chapter, and because the LC droplets can be polymerized to form patchy microparticles, the results presented in this chapter provide the basis of a general methodology for synthesis of complex multifunctional microparticles. Such microparticles have a range of potential applications, including in biological sensors, chemooptical transduction, directed self-assembly of mesoscopic materials, and drug delivery.

Acknowledgements

This work was primarily supported by NSF through DMR-1121288 (Materials Research Science and Engineering Center), the Army Research Office (W911NF-11-1-0251 and W911NF-10-1-0181), and the National Institutes of Health (CA108467, CA105730, AI092004.). Acknowledgment of support is also made to the Department of Energy, Basic Energy Sciences, Biomaterials Program (BESC0004025). The authors thank Professor Daniel J. Klingenberg, Professor Michael D. Graham, Dr. Jonathan K. Whitmer, Tyler F. Roberts, Dr. Rebecca J. Carlton, and Peter C. Mushenheim for helpful discussions.

9.5 Supporting Information

Additional Supporting Figures

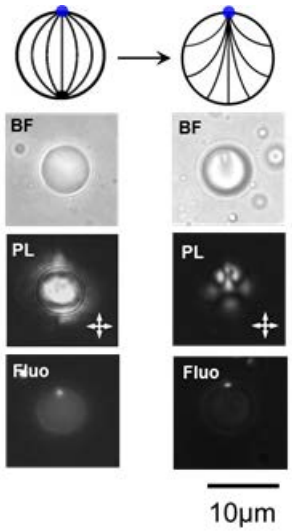

Figure 9-S1. SDS-induced bipolar-to-preradial ordering transition in water-dispersed droplets of nematic 5CB with a single 1 μm-in-diameter fluorescent PS colloid adsorbed at the surface.
The colloid pins the defect to the surface of the droplet. Schematic illustrations and the corresponding BF, PL and Fluo micrographs are shown from top to bottom. In the schematic, the defects and colloids are represented by solid black or blue circles, respectively. The orientation of the crossed polarizers in PL micrographs is indicated by the white double-headed arrows.

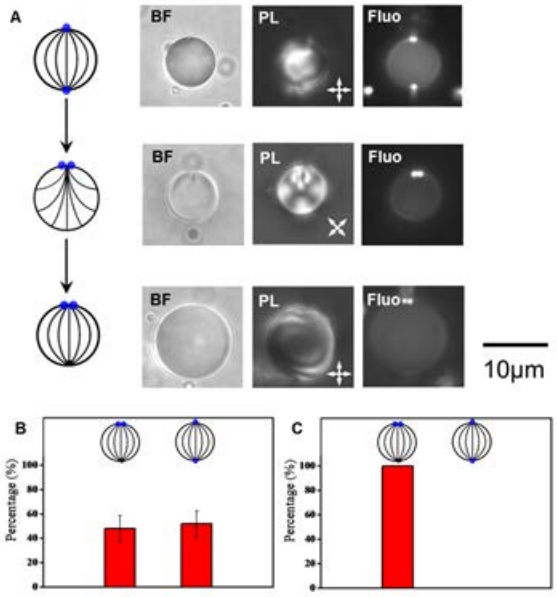

Figure 9-S2. Method utilized to direct 1 μm-in-diameter PS colloids at opposite boojums of a bipolar 5CB droplet to the same boojum *via* manipulation of electrical double layer forces through addition/dilution of salts.

(A) Schematic illustrations and the corresponding BF, PL, and Fluo micrographs are shown from left to right for each equilibrium state of the LC droplets. The orientation of the crossed polarizers in PL micrographs is indicated by the white double-headed arrows. (B and C) Percentage of 5CB droplets in each two-colloid configuration (B) before or (C) after moving PS colloids to one defect of bipolar 5CB droplets using sodium chloride solution. The histograms were assembled from analysis of (B) 49 or (C) 24 droplets in 3 independent experiments.

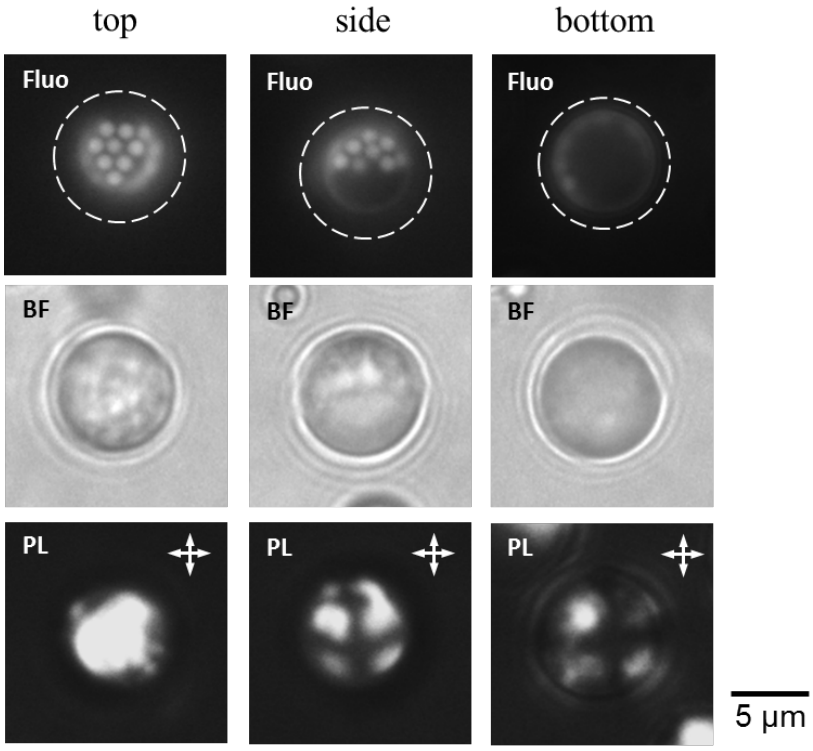

Figure 9-S3. Corresponding Fluo, BF, and PL micrographs of polymerized "Janus-like" preradial LC microparticles with multiple PS colloids adsorbed as viewed from top, side and bottom.

The Fluo micrographs are identical to those shown in Figure 9-3 of the main text.

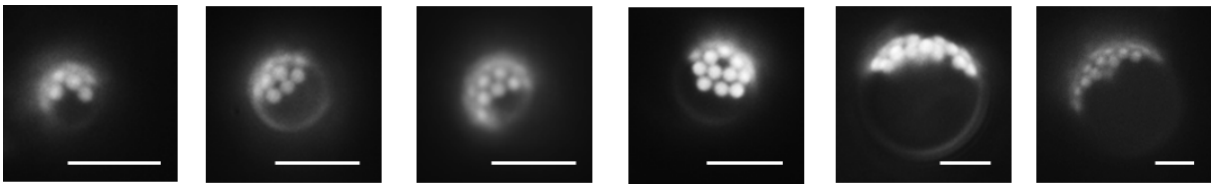

Figure 9-S4. Fluo micrographs of polymerized "Janus-like" preradial LC microparticles of various sizes with multiple PS colloids adsorbed as viewed from the side.

The scale bar is 5µm.

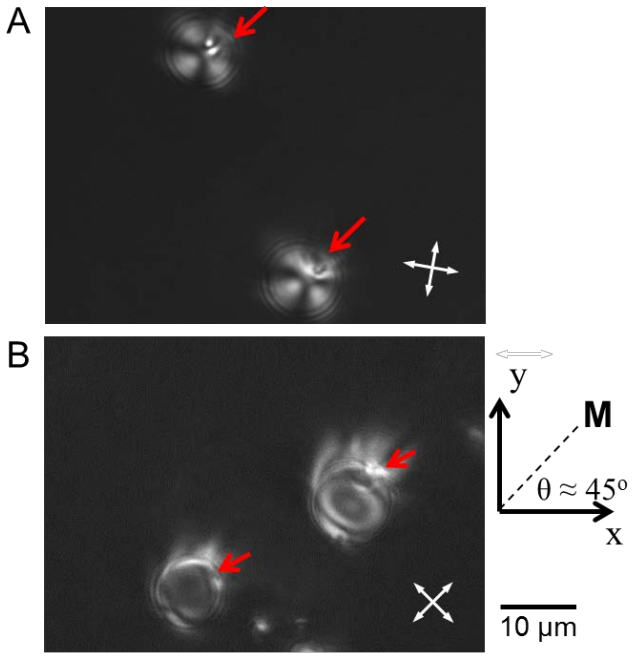

Figure 9-S5. Alignment of magnetically-responsive patchy microdroplets of LC in a magnetic field. (A) Representative PL micrographs of the orientation of patchy LC droplets with magnetic PS colloids adsorbed at the pole of the preradial configuration at which the point defect is located in the presence of magnetic field. (B) Representative PL micrograph of two bipolar LC droplets contained in a homogeneous population of droplets with magnetic colloids adsorbed at a single pole in the presence of magnetic field. The magnet was held at a ~45^{o} angle with respect to x-axis and ~15 cm away from the sample. The red arrows indicate the location of the pole at which the magnetic PS colloids are adsorbed.

9.6 References

*This chapter was prepared as a Full Paper reporting original research in the journal *Advanced Functional Materials*. Xiaoguang Wang and I worked together throughout the course of this project.

1. Pawar, A. B.; Kretzschmar, I., Fabrication, Assembly, and Application of Patchy Particles. *Macromolecular Rapid Communications* **2010**, 31, 150-168.
2. Walther, A.; Müller, A. H., Janus Particles: Synthesis, Self-Assembly, Physical Properties, and Applications. *Chemical Reviews* **2013**, 113, 5194–5261.
3. Yoshida, M.; Lahann, J., Smart Nanomaterials. *ACS Nano* **2008**, 2, 1101-1107.
4. Crowley, J. M.; Sheridon, N. K.; Romano, L., Dipole Moments of Gyricon Balls. *Journal of Electrostatics* **2002**, 55, 247-259.
5. Gangwal, S.; Cayre, O. J.; Velev, O. D., Dielectrophoretic Assembly of Metallodielectric Janus Particles in Ac Electric Fields. *Langmuir* **2008**, 24, 13312-13320.
6. Takei, H.; Shimizu, N., Gradient Sensitive Microscopic Probes Prepared by Gold Evaporation and Chemisorption on Latex Spheres. *Langmuir* **1997**, 13, 1865-1868.
7. Dyab, A. K.; Ozmen, M.; Ersoz, M.; Paunov, V. N., Fabrication of Novel Anisotropic Magnetic Microparticles. *Journal of Materials Chemistry* **2009**, 19, 3475-3481.
8. Erb, R. M.; Jenness, N. J.; Clark, R. L.; Yellen, B. B., Towards Holonomic Control of Janus Particles in Optomagnetic Traps. *Advanced Materials* **2009**, 21, 4825-4829.
9. Smoukov, S. K.; Gangwal, S.; Marquez, M.; Velev, O. D., Reconfigurable Responsive Structures Assembled from Magnetic Janus Particles. *Soft Matter* **2009**, 5, 1285-1292.
10. Nisisako, T.; Torii, T.; Takahashi, T.; Takizawa, Y., Synthesis of Monodisperse Bicolored Janus Particles with Electrical Anisotropy Using a Microfluidic Co-Flow System. *Advanced Materials* **2006**, 18, 1152-1156.
11. Sheridon, N.; Richley, E.; Mikkelsen, J.; Tsuda, D.; Crowley, J.; Oraha, K.; Howard, M.; Rodkin, M.; Swidler, R.; Sprague, R., The Gyricon Rotating Ball Display. *Journal of the Society for Information Display* **1999**, 7, 141-144.
12. Howse, J. R.; Jones, R. A.; Ryan, A. J.; Gough, T.; Vafabakhsh, R.; Golestanian, R., Self-Motile Colloidal Particles: From Directed Propulsion to Random Walk. *Physical Review Letters* **2007**, 99, 048102.
13. Xu, C.; Xie, J.; Ho, D.; Wang, C.; Kohler, N.; Walsh, E. G.; Morgan, J. R.; Chin, Y. E.; Sun, S., Au–Fe3o4 Dumbbell Nanoparticles as Dual-Functional Probes. *Angewandte Chemie International Edition* **2008**, 47, 173-176.
14. Yoshida, M.; Roh, K. H.; Mandal, S.; Bhaskar, S.; Lim, D.; Nandivada, H.; Deng, X.; Lahann, J., Structurally Controlled Bio-Hybrid Materials Based on Unidirectional Association of Anisotropic Microparticles with Human Endothelial Cells. *Advanced Materials* **2009**, 21, 4920-4925.
15. Chandrasekhar, S., *Liquid Crystals*. 2nd ed.; Cambridge University Press: New York, NY, USA, 1992.

16. Collings, P. J., *Liquid Crystals : Nature's Delicate Phase of Matter*. 2nd ed.; Princeton University Press: Princeton, NJ, USA, 2002.
17. Collings, P. J.; Hird, M., *Introduction to Liquid Crystals Chemistry and Physics*. Taylor & Francis: Bristol, PA, USA, 1997.
18. Gennes, P.-G. d.; Prost, J., *The Physics of Liquid Crystals*. 2nd ed.; Oxford University Press: New York, NY, USA, 1993.
19. Bai, Y.; Abbott, N. L., Recent Advances in Colloidal and Interfacial Phenomena Involving Liquid Crystals. *Langmuir* **2011**, 27, 5719-5738.
20. Carlton, R. J.; Hunter, J. T.; Miller, D. S.; Abbasi, R.; Mushenheim, P. C.; Tan, L.; Abbott, N. L., Chemical and Biological Sensing Using Liquid Crystals. *Liquid Crystal Reviews* **2013**, 1, 1-23.
21. Lockwood, N. A.; Gupta, J. K.; Abbott, N. L., Self-Assembly of Amphiphiles, Polymers and Proteins at Interfaces between Thermotropic Liquid Crystals and Aqueous Phases. *Surface Science Reports* **2008**, 63, 255-293.
22. Lowe, A. M.; Abbott, N. L., Liquid Crystalline Materials for Biological Applications. *Chemistry of Materials* **2012**, 24, 746-758.
23. Miller, D. S.; Wang, X.; Abbott, N. L., Design of Functional Materials Based on Liquid Crystalline Droplets. *Chemistry of Materials* **2013**, 26, 496–506.
24. Crawford, G. P.; Žumer, S., *Liquid Crystals in Complex Geometries: Formed by Polymer and Porous Networks*. Taylor & Francis Inc.: Bristol, PA, 1996.
25. Drzaic, P. S., *Liquid Crystal Dispersions*. World Scientific: River Edge, NJ, USA, 1995.
26. Lopez-Leon, T.; Fernandez-Nieves, A., Drops and Shells of Liquid Crystal. *Colloid and Polymer Science* **2011**, 289, 345-359.
27. Gupta, J. K.; Sivakumar, S.; Caruso, F.; Abbott, N. L., Size-Dependent Ordering of Liquid Crystals Observed in Polymeric Capsules with Micrometer and Smaller Diameter. *Angewandte Chemie-International Edition* **2009**, 48, 1652-1655.
28. Alexander, G. P.; Chen, B. G.-g.; Matsumoto, E. A.; Kamien, R. D., Colloquium: Disclination Loops, Point Defects, and All That in Nematic Liquid Crystals. *Reviews of Modern Physics* **2012**, 84, 497.
29. Kléman, M.; Lavrentovich, O. D., *Soft Matter Physics : An Introduction*. Springer: New York, NY, USA, 2003.
30. Lavrentovich, O. D., Topological Defects in Dispersed Liquid Crystals, or Words and Worlds around Liquid Crystal Drops. *Liquid Crystals* **1998**, 24, 117-125.
31. Volovik, G. E.; Lavrentovich, O. D., The Topological Dynamics of Defects - Boojums in Nematic Drops. *Zhurnal Eksperimentalnoi I Teoreticheskoi Fiziki* **1983**, 85, 1997-2010.
32. Gupta, J. K.; Zimmerman, J. S.; de Pablo, J. J.; Caruso, F.; Abbott, N. L., Characterization of Adsorbate-Induced Ordering Transitions of Liquid Crystals within Monodisperse Droplets. *Langmuir* **2009**, 25, 9016-9024.
33. Prischepa, O. O.; Shabanov, A. V.; Zyryanov, V. Y., Transformation of Director Configuration Upon Changing Boundary Conditions in Droplets of Nematic Liquid Crystal. *JETP Letters* **2004**, 79, 257-261.
34. Mondiot, F.; Wang, X.; de Pablo, J. J.; Abbott, N. L., Liquid Crystal-Based Emulsions for Synthesis of Spherical and Non-Spherical Particles with Chemical Patches. *Journal of the American Chemical Society* **2013**, 135, 9972–9975.

35. Whitmer, J. K.; Wang, X.; Mondiot, F.; Miller, D. S.; Abbott, N. L.; Pablo, J. J. d., Nematic-Field Driven Positioning of Particles in Liquid Crystal Droplets. *Physical Review Letters* **2013**, 111, 227801.
36. K&J Magnetics, I. http://www.kjmagnetics.com/calculator.asp (January, 2014).
37. Berggren, E.; Zannoni, C.; Chiccoli, C.; Pasini, P.; Semeria, F., Computer-Simulations of Nematic Droplets with Bipolar Boundary-Conditions. *Physical Review E* **1994**, 50, 2929-2939.
38. Meyer, R. B., Piezoelectric Effects in Liquid Crystals. *Physical Review Letters* **1969**, 22, 918.
39. Ondris-Crawford, R.; Boyko, E. P.; Wagner, B. G.; Erdmann, J. H.; Zumer, S.; Doane, J. W., Microscope Textures of Nematic Droplets in Polymer Dispersed Liquid-Crystals. *Journal of Applied Physics* **1991**, 69, 6380-6386.
40. Umbanhowar, P.; Prasad, V.; Weitz, D., Monodisperse Emulsion Generation Via Drop Break Off in a Coflowing Stream. *Langmuir* **2000**, 16, 347-351.
41. Alino, V. J.; Tay, K. X.; Khan, S. A.; Yang, K. L., Inkjet Printing and Release of Monodisperse Liquid Crystal Droplets from Solid Surfaces. *Langmuir* **2012**, 28, 14540-14546.
42. Sivakumar, S.; Gupta, J. K.; Abbott, N. L.; Caruso, F., Monodisperse Emulsions through Templating Polyelectrolyte Multilayer Capsules. *Chemistry of Materials* **2008**, 20, 2063-2065.
43. Peddireddy, K.; Kumar, P.; Thutupalli, S.; Herminghaus, S.; Bahr, C., Solubilization of Thermotropic Liquid Crystal Compounds in Aqueous Surfactant Solutions. *Langmuir* **2012**, 28, 12426-12431.
44. Prishchepa, O. O.; Zyryanov, V. Y.; Gardymova, A. P.; Shabanov, V. F., Optical Textures and Orientational Structures of Nematic and Cholesteric Droplets with Heterogeneous Boundary Conditions. *Molecular Crystals and Liquid Crystals* **2008**, 489, 84-93.
45. Brake, J. M.; Abbott, N. L., An Experimental System for Imaging the Reversible Adsorption of Amphiphiles at Aqueous-Liquid Crystal Interfaces. *Langmuir* **2002**, 18, 6101-6109.
46. Lin, I. H.; Miller, D. S.; Bertics, P. J.; Murphy, C. J.; de Pablo, J. J.; Abbott, N. L., Endotoxin-Induced Structural Transformations in Liquid Crystalline Droplets. *Science* **2011**, 332, 1297-1300.
47. Tomar, V.; Hernandez, S. I.; Abbott, N. L.; Hernandez-Ortiz, J. P.; de Pablo, J. J., Morphological Transitions in Liquid Crystal Nanodroplets. *Soft Matter* **2012**, 8, 8679-8689.
48. Abras, D.; Pranami, G.; Abbott, N. L., The Mobilities of Micro-and Nano-Particles at Interfaces of Nematic Liquid Crystals. *Soft Matter* **2012**, 8, 2026-2035.
49. Bresme, F.; Oettel, M., Nanoparticles at Fluid Interfaces. *Journal of Physics: Condensed Matter* **2007**, 19, 413101.
50. Stark, H., Physics of Colloidal Dispersions in Nematic Liquid Crystals. *Physics Reports* **2001**, 351, 387-474.
51. Joshi, A. A.; Whitmer, J. K.; Guzmán, O.; Abbott, N. L.; de Pablo, J. J., Measuring Liquid Crystal Elastic Constants with Free Energy Perturbations. *Soft Matter* **2014**, 10, 882-893.
52. Hiemenz, P. C.; Rajagopalan, R., *Principles of Colloid and Surface Chemistry*. 3rd ed.; Marcel Dekker: New York, NY, USA, 1997.
53. Israelachvili, J. N., *Intermolecular and Surface Forces*. 2nd ed.; Academic Press London: San Diego, CA, USA, 1991.
54. Carlton, R. J.; Gupta, J. K.; Swift, C. L.; Abbott, N. L., Influence of Simple Electrolytes on the Orientational Ordering of Thermotropic Liquid Crystals at Aqueous Interfaces. *Langmuir* **2012**, 28, 31-36.

55. Miller, D. S.; Abbott, N. L., Influence of Droplet Size, Ph and Ionic Strength on Endotoxin-Triggered Ordering Transitions in Liquid Crystalline Droplets. *Soft Matter* **2013**, 9, 374-382.
56. Carlton, R. J.; Ma, C. D.; Gupta, J. K.; Abbott, N. L., Influence of Specific Anions on the Orientational Ordering of Thermotropic Liquid Crystals at Aqueous Interfaces. *Langmuir* **2012**, 28, 12796-12805.
57. Gharbi, M. A.; Nobili, M.; Blanc, C., Use of Topological Defects as Templates to Direct Assembly of Colloidal Particles at Nematic Interfaces. *Journal of Colloid and Interface Science* **2014**, 417, 250-255.
58. Candau, S.; Le Roy, P.; Debeauvais, F., Magnetic Field Effects in Nematic and Cholesteric Droplets Suspended in a Isotropic Liquid. *Molecular Crystals and Liquid Crystals* **1973**, 23, 283-297.
59. Bird, R. B.; Stewart, W. E.; Lightfoot, E. N., *Transport Phenomena*. John Wiley & Sons: New York, NY, USA, 2007.
60. Miller, D. S.; Wang, X.; Buchen, J.; Lavrentovich, O. D.; Abbott, N. L., Analysis of the Internal Configurations of Droplets of Liquid Crystal Using Flow Cytometry. *Analytical Chemistry* **2013**, 85, 10296-10303.

Chapter 10. Organized Assemblies of Colloids Formed at the Poles of Micrometer-Sized Droplets of Liquid Crystal*

10.1 Introduction

Assemblies formed by colloids at liquid—liquid and liquid—gas interfaces can serve as models for a range of molecular phenomena,[1, 2] including molecular self-assembly.[3-7] They can also provide a means of stabilizing liquid—liquid emulsions[8-10] and synthesizing materials with tunable mechanical,[11, 12] optical,[13, 14] or electronic properties.[15, 16] When dealing with isotropic liquids, inter-colloid forces that act parallel to the interface include capillary,[17, 18] dipolar electrostatic,[19] and van der Waals forces.[6] If one of the liquids is a liquid crystal (LC), however, the elasticity of the LC phase as well as topological defects formed within the LC can generate additional types of inter-colloid interactions.[20-32] Significantly, LC-mediated interactions have unusual symmetries, including dipolar or quadrupolar symmetries,[20-25] which leads to the formation of chains or hexagonal arrays of colloids.[29, 30] In addition, inter-colloid interactions have been proposed to arise from a coupling between the elasticity of LCs and capillary interactions (so-called elastocapillary interactions).[26-28]

While ordered assemblies of colloids have been widely investigated at planar interfaces of LCs, only recently have assemblies of colloids on the curved interfaces of LC droplets been reported.[30-32] Specifically, we reported on the adsorption of pairs of colloids onto LC microdroplets (diameters ranging from 7 to 20 μm) in a bipolar configuration (see Figure 10-1 below) and found the colloids to adopt one of two arrangements – in one arrangement, a single colloid was positioned at each of the two diametrically opposed surface defects (*i.e.*, “boojums”);

in the second arrangement both colloids were localized at a single boojum (see Chapter 9).[31] We showed that it was also possible to polymerize the LC droplets with colloids positioned at their poles, thus leading to formation of "patchy" LC particles (spherical and non-spherical).[31] Through a combination of experiment and simulation, we confirmed that the colloids localized at the boojums to eliminate the energetic cost of the defect core as well as regions of high strain in the LC in the vicinity of the defect core (see Appendix A).[32] In this chapter, we move beyond our past studies to investigate formation of assemblies of larger numbers of colloids near the poles of LC droplets. In this context, we note that Gharbi and coworkers recently reported on assemblies formed by 4 μm-in-diameter silica colloids, treated to induce homeotropic anchoring of LC, on the surfaces of large (150 to 250 μm-in-diameter) bipolar LC droplets dispersed in an aqueous solution of polyvinyl alcohol.[30] Because the LC droplets used in their study were large compared to the colloid size, they observed organizations of the colloids that were closely related to those observed at planar LC interfaces (linear chains arising from dipolar interactions were reported).[29] In contrast, in the study reported in this chapter, we use 1 μm-in-diameter colloids and LC droplets that are less than 20 μm-in-diameter, and demonstrate that in this size range, the inter-colloid forces on the droplet interface lead to assemblies that are not observed to form on planar LC interfaces.

10.2 Experimental Section

Materials. 1 μm-in-diameter fluorescently labelled polystyrene (PS) colloids (λ_{exc} = 480 nm / λ_{em} = 520 nm) were purchased from Bangs Laboratories (Fishers, IN). Sodium chloride (NaCl) was purchased from Sigma Aldrich (St. Louis, MO). Polyimide (PI 2556) was purchased from HD Microsystems (Parlin, NJ). 4-cyano-4'-pentylbiphenyl (5CB) was obtained from EM

Sciences (New York, NY). Deionization of a distilled water source was performed with a Milli-Q system (Millipore, Bedford, MA).

Preparation of Liquid Crystal (LC)-in-Water Emulsions. LC-in-water emulsions were prepared according to previously published methods.[31, 32] Briefly, the emulsions were prepared by emulsifying 4 µL 5CB in 1.98 mL of an aqueous phase using a homogenizer (T25 digital ULTRA-TURRAX) equipped with a S25 N-10G dispersing element (IKA) for 30 s at 6,500 rpm. This procedure resulted in a population of droplets in the bipolar configuration. The emulsions were prepared in glass vials (diameter of 19 mm, height of 51 mm).

Adsorption of PS Colloids onto the Surfaces of LC Droplets. PS colloids were adsorbed onto the surfaces of the LC droplets through addition of 20 µL of a 1% wt/v PS colloids dispersion to 1.98 mL of a LC-in-water emulsion, followed by homogenization at 6,500 rpm. The duration of homogenization was 30 s, 45 s, 60 s, 90 s, or 300 s for experiments with two, three and four, five, six and seven, or many (more than seven) adsorbed colloids, respectively.

Preparation of PS Colloid-Decorated Planar Aqueous—5CB Interfaces. Glass slides coated with a PI film (rubbed) were prepared according to previous published methods.[29, 31] A film of 5CB with an approximately flat interface was prepared by filling the pores of a 20 µm-thick gold-coated specimen grid supported on a PI-treated glass slide. The system was then submerged in water. Finally, we added 2 mL of a 0.005% wt/v PS colloid dispersion to the aqueous phase above the LC films and allowed the colloids to sediment onto the aqueous—LC interface.

Bright field (BF), Polarized Light (PL), and Fluorescence (Fluo) Microscopy. To characterize assemblies of PS colloids that formed at the surfaces LC droplets, a 50 µL volume of the LC emulsion was dispensed onto a glass coverslip. Next, the LC droplets were imaged using an Olympus IX71 inverted epifluorescence microscope (Center Valley, PA) equipped with a 100x oil-immersion objective, crossed polarizers, mercury lamp, and Chroma filter (457 nm ≤ λ_{exc} ≤ 502 nm, and 510 nm ≤ λ_{em} ≤ 562 nm). BF, PL, and Fluo micrographs of LC-in-water emulsions were collected with a Hamamatsu 1394 ORCAER CCD camera (Bridgewater, NJ) connected to a computer and controlled through SimplePCI imaging software (Compix, Inc., Cranberry Twp., NJ). BF micrographs were collected by removing the polarizer from the optical path of the microscope. BF, PL, and Fluo micrographs of assemblies of PS colloids that formed at planar aqueous—5CB interfaces were captured using the same microscope.

10.3 Results

The goal of our first set of experiments was to characterize the packing arrangements exhibited by 1 µm-in-diameter fluorescent PS colloids adsorbed to the surfaces of droplets of nematic 5CB in the bipolar configuration. The 5CB-in-water emulsions with droplets in the bipolar configuration were prepared by dispersing 5CB in pure water, and homogenizing the mixture for 30 s. This procedure resulted in a polydisperse emulsion with LC droplets with diameters ranging from 1 - 40 µm. In our experiments, we focused our observations on LC droplets with diameters between 7 - 20 µm. After formation of the LC emulsions, the PS colloids, which induce a planar anchoring of nematic 5CB, were adsorbed to the surfaces of the LC droplets through addition of a 1 % wt/v dispersion of the colloids, followed by homogenization. We found that homogenization for 30 s led to a population of LC droplets

within which a significant number of droplets had two colloids adsorbed to their surfaces. Here we briefly summarize results obtained with two adsorbed colloids as context to our observations involving larger numbers of colloids.

Figure 10-1A shows Fluo, BF and PL micrographs of a bipolar 5CB droplet with two PS colloids adsorbed to the droplet surface. A schematic illustration of the configuration of the LC within the droplet is also shown to the right of the micrographs. In the bipolar configuration, LC is aligned tangential to the droplet surface, and two boojum defects are present at diametrically opposite ends of the droplet.[33-40] By comparing the Fluo micrograph to the BF and PL micrographs in Figure 10-1A, it is evident that the Fluo signal from the two adsorbed PS colloids coincides with the location of one of the two boojums (as we have previously reported;[31, 32] see Chapter 9).

Before describing results involving three or more colloids adsorbed to the surfaces of the LC droplets, we make four guiding statements. First, below we present only the Fluo micrographs of the colloid-decorated LC droplets because the Fluo micrographs clearly reveal the packing arrangements of the colloids. However, we emphasized that we captured BF and PL micrographs for all droplets to confirm that the colloids were localized in the vicinity of boojum defects of a bipolar configuration (*i.e.*, in the vicinity of a pole of the droplets). Second, although the colloids were observed to accumulate in the vicinity of the poles of the droplets, the scattering of light from the interfaces of the colloids and the optical resolution of our microscope (~500 nm) did not allow us to determine the exact positions of the colloids relative to the boojums. In the description of our experimental results below, for brevity, we state that the colloids accumulate at a pole of the droplets. Third, we observed assemblies of colloids to form at diametrically opposite poles of bipolar LC droplets with equal probability (see Figure 10-S1 of

Supporting Information). Finally, all packing arrangements of adsorbed colloids were observed to persist for at least six hours, and the colloids were not seen to rearrange into different packing arrangements over this duration.

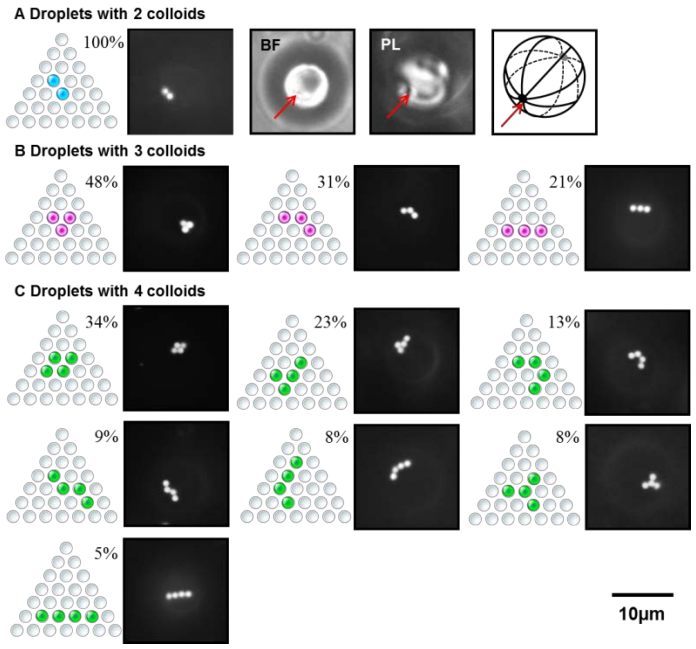

Figure 10-1. Packing arrangements observed for 1 μm-in-diameter, fluorescent PS colloids adsorbed to the poles of nematic 5CB droplets in bipolar configurations.

Arrangements are displayed for (A) two, (B) three and (C) four colloids. For each arrangement, we show a schematic illustration of the arrangement (left) and a fluorescence micrograph (right). For the two colloid arrangement bright field (BF) and polarized light (PL) micrographs, and a schematic illustration of the configuration of LC within the 5CB droplet are shown to demonstrate that the colloids are adsorbed at the site of a boojum defect. The red arrows indicate the location of the boojum defect at which the colloids are adsorbed. The percentages of droplets in each arrangement is expressed to the right of each schematic illustration, and was calculated from analysis of (A) 121, (B) 175 or (C) 180 droplets in 5 independent experiments. In Fluo micrographs, the contrast is enhanced to highlight the arrangements of colloids.

By increasing the duration of homogenization of the colloids and LC droplets to 45 s, we obtained an increasing population of droplets within each emulsion that had three or four colloids adsorbed to their surfaces. For droplets with three colloids adsorbed at a pole, we observed three

packing arrangements, each occurring with a different frequency, as shown in Figure 10-1B. When droplets with four colloids at their poles were observed, seven different arrangements were seen, again with different frequencies, as shown in Figure 10-1C. Inspection of Figure 10-1 reveals that, while extended assemblies were observed (*e.g.*, chain-like assemblies), the packing arrangement that maximized colloid—colloid contacts tended to be observed with the highest frequency. We return to this observation below.

Following characterization of droplets decorated with three and four adsorbed PS colloids, we increased further the homogenization period to 60 s, to increase the likelihood of obtaining 5CB droplets with five PS colloids adsorbed at a pole. For such droplets, twenty-one unique configurations were observed, as shown in Figure 10-2. Similar to the case of three or four adsorbed colloids, we observed compact assemblies with the highest frequency. Interestingly, the second most frequently observed arrangement was an arrangement that comprised a ring of colloids (top of the second column in Figure 10-2).

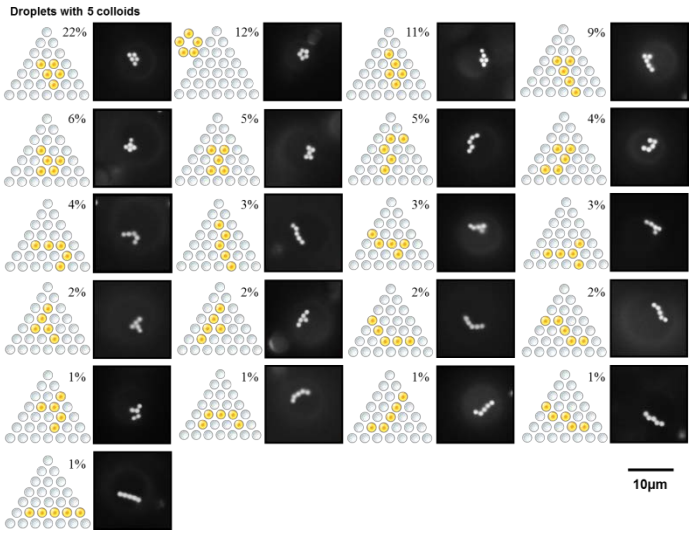

Figure 10-2. Packing arrangements observed for five PS colloids adsorbed to the poles of bipolar 5CB droplets.

The percentages were calculated from analysis of 287 droplets in 5 independent experiments. In Fluo micrographs, the contrast is enhanced to highlight the arrangements of colloids.

To characterize the symmetry of the packing arrangements of PS colloids on the surfaces of 5CB droplets, we next quantified the angles and spacings between adjacent PS colloids. The angles defined by adjacent colloids within the observed arrangements are shown in Figure 10-3A and 10-3B, respectively. Inspection of Figure 10-3 reveals that the angles are consistent with the geometry of a right hexagon and right pentagon, respectively. In addition, the center-to-center distance between adjacent colloids was measured to be 1.17 ± 0.06 μm, which indicates that the PS colloids with diameters of 1.01 ± 0.01 μm are not close packed (we note that we measured the diameters of 30 PS colloids in Fluo micrographs to obtain the average diameter and the error represents the standard deviation). From this analysis, we conclude that the packing arrangements of PS colloids shown in Figures 10-1 and 10-2 followed a hexagonal lattice, with the exception of the pentamer ring pattern observed for five colloids. We note here that the pentamer ring pattern has not been previously reported for assemblies of colloids at aqueous—LC interfaces.

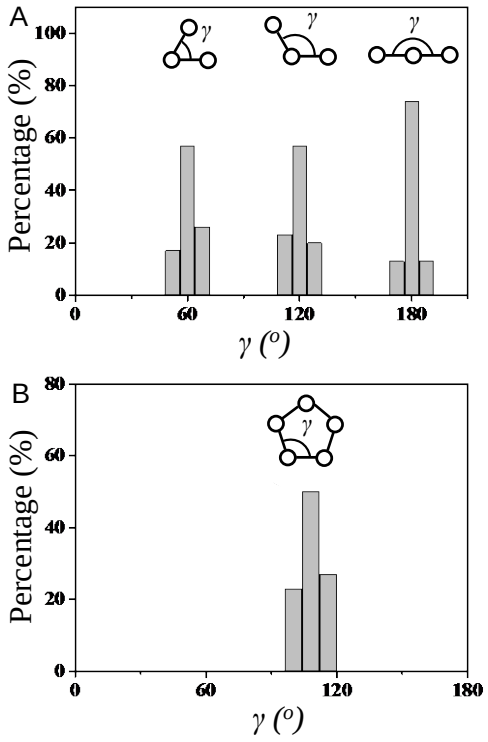

Figure 10-3. Distribution of angles (γ, see inset) defined by PS colloids adsorbed to droplets of 5CB in (A) hexagonal or (B) pentagonal arrangement.

The histograms were assembled from (A) 40 or (B) 15 droplets in 3 independent experiments.

We sought to provide insight into the relative stabilities of the various hexagonal and pentagonal packing arrangements by characterizing the frequency (*F*) with which we observed packing arrangements as a function of the total number of nearest neighbor colloid—colloid contacts (*N*) within each arrangement. To illustrate our analysis, we use LC droplets with five PS colloids (Figure 10-2) as a representative example. Four values of *N* (4, 5, 6 and 7) describe the arrangements shown in Figure 10-2. The frequency histogram for these *N* values, shown in Figure 10-4A, reveals that the arrangements corresponding to $N = 5$ are observed with the highest frequency. However, the results in Figure 10-4A do not directly predict the relative energies of the packing arrangements because a larger number of arrangements is possible for assemblies of colloids with low *N* (note that only one arrangement, a hexagonal array that

maximizes N, is observed for $N = 7$). To account for the multiplicity (M) of observed ways to arrange five colloids into an assembly with $N = 4$, 5, or 6, we normalized F by M. Figure 10-4B shows that F/M for $N = 7$ is at least three times larger than F/M for all other N values, which suggests that the assembly with $N = 7$ is the energetically most stable arrangement. We end this discussion by noting that we also attempted to estimate the relative energies of arrangements of five colloids of different N by assuming that the frequency distribution was described by a Boltzmann distribution (see Figure 10-S8 and the accompanying text of Supporting Information). Although the analysis supported our proposal that the assembly with $N = 7$ is the energetically most stable arrangement, it also predicted a small difference in energy between arrangements of different N (of order k_BT). We therefore conclude that the hexagonal packing arrangement of five colloids that maximizes N is the most stable arrangement, and that assemblies of five colloids with $N < 7$ are kinetically trapped states (they are likely a consequence of inter-colloid quadrupole—quadrupole elastic interactions as colloids partition to the poles of droplets (see below)).

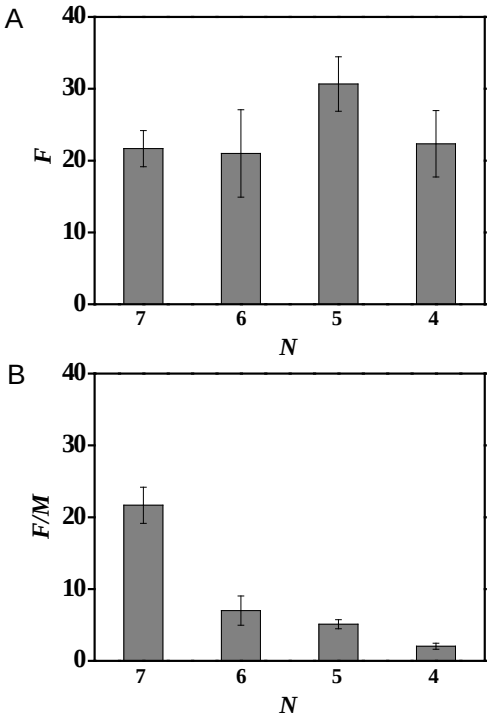

Figure 10-4. Frequency and normalized frequency histograms of the nearest neighbor colloid—colloid contacts (*N*) in packing arrangements with five PS colloids adsorbed to poles of bipolar 5CB droplets.

(A) Frequency (*F*) histogram of *N* in packing arrangements with five PS colloids adsorbed to poles of bipolar 5CB droplets. (B) *F* in A normalized by the multiplicity of arrangements possible for a given *N* (*M*). The plots were constructed from Figure 10-2.

Next, we investigated assemblies formed by higher numbers of PS colloids adsorbed at the surfaces of bipolar LC droplets. Here we comment that LC droplets decorated with many colloids are of potential technological interest because, as noted in the Introduction, colloids can stabilize LC-in-water emulsions (*i.e.*, LC Pickering emulsions), which have proven useful for chemical and biological sensing,[37, 41] or can lead to templated synthesis of Janus-like polymer microparticles, the surface chemistry of which could be tailored for a specific use.[31] Figure 10-5 shows some of the packing arrangements most frequently observed for droplets with six or seven adsorbed colloids. As was the case for fewer than six colloids, the most frequently observed

packing arrangements possess a hexagonal symmetry. Assemblies with more than seven adsorbed colloids are shown in Figure 10-5C. When many colloids were adsorbed to the LC droplets, we observed both the hexagonal array and pentamer ring pattern described above (both patterns are marked in Figure 10-5C). We note here that a uniform hexagonal array of PS colloids cannot form on the surface of a LC droplet at complete coverage due to the curvature of the surface of the LC droplet. In contrast, the Caspar and Klug “quasi-equivalence” principle often used to describe the packing of protein subunits on the spherical shells of viruses states that an icosahedral pattern constructed from pentamers and hexamers generates the maximum enclosed volume for a shell.[42-45] We speculate that complete coverage of the LC droplets by PS colloids may lead to an icosahedral packing arrangement analogous to that of viruses.

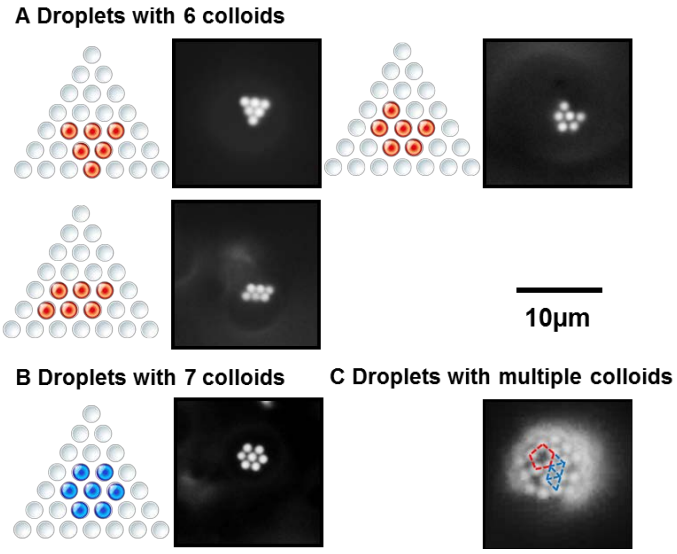

Figure 10-5. Packing arrangements most frequently observed for higher numbers of PS colloids adsorbed to the surfaces of bipolar 5CB droplets.

Packing arrangements most frequently observed for bipolar 5CB droplets with (A) six or (B) seven PS colloids adsorbed to their poles. (C) Packing arrangements observed for multiple PS colloids adsorbed at the surfaces of bipolar 5CB droplets. Colloids that follow a hexagonal or pentagonal pattern are marked by blue or red dashed lines, respectively. In Fluo micrographs, the contrast is enhanced to highlight the arrangements of colloids.

We performed three additional experiments to provide insight into the origin of the hexagonal arrays of colloids formed at the poles of bipolar LC droplets. First, we investigated the role of nematic order by heating the LC droplets into the isotropic phase. The PS colloids were observed to dissociate from the initial hexagonal array upon heating into the isotropic phase (see Figure 10-S5). We attribute the observed tendency of the colloids to move apart to electrostatic repulsion (see below). From this result, we conclude that the strained nematic phase of the LC plays a key role in driving the formation of hexagonal arrays of PS colloids at the poles of bipolar LC droplets.

Second, we investigated the role of interface curvature on array formation. Specifically, the PS colloids used in the droplet experiments described above were sedimented onto planar

aqueous—LC interfaces of 20 μm-thick films of 5CB (see Figure 10-S2 of Supporting Information for a schematic illustration of the film which was supported on rubbed PI to promote a uniform planar alignment of 5CB; the concentration of colloids added to the aqueous phase was 0.005 % wt/v). Surprisingly, and in contrast to LC droplets, the PS colloids did not spontaneously assemble into organized arrays at the planar aqueous—LC interface (even after several days; Figure 10-6A). At first we speculated that the lack of organization exhibited by the colloids was a consequence of weak anchoring of the LC on the surfaces of the colloids, thus preventing topological dipole—dipole or quadrupole—quadrupole interactions between colloids (see Introduction and below).[20-25] However, PL micrographs of isolated colloids revealed an optical signature consistent with quadrupolar symmetry and strain-induced formation of two diametrically opposite boojum defects at the surface of a colloid (see Figure 10-S2 of Supporting Information).[24, 31, 46] When combined, these various observations led us to conclude that the droplet geometry is necessary to obtain the hexagonal array of colloids (at the conditions reported above), and that a repulsive interaction kept the colloids separated at planar interfaces (preventing quadrupole—quadrupole elastic interactions from generating ordered assemblies of colloids).

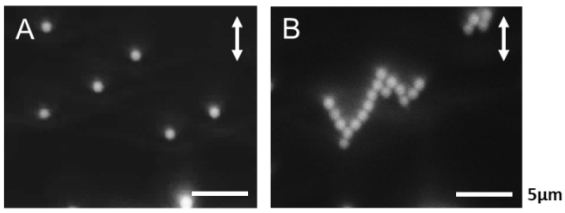

Figure 10-6. Packing arrangements observed for PS colloids adsorbed at the aqueous—LC interface of a planar 5CB film (A) in pure water or (B) in the presence of 1 mM NaCl supported on a rubbed polyimide-coated glass slide.

Double headed arrows indicate the rubbing direction of polyimide.

The absence of ordering exhibited by PS colloids adsorbed to the aqueous interfaces of isotropic 5CB droplets (Figure 10-S5B) and planar films of nematic 5CB (Figure 10-6A), when combined with the observed non-close packed arrangement of colloids on the surfaces of bipolar 5CB droplets, points to the existence of a repulsive interaction between PS colloids. We hypothesized that the origin of the repulsive interaction was an electrostatic repulsion between PS colloids. To test this hypothesis, 5CB droplets with PS colloids adsorbed at their surfaces were prepared in the presence of 1 mM NaCl. Consistent with screening of electrostatic repulsion between PS colloids at the droplet interface, the center-to-center distance between adjacent colloids on the LC droplets was measured to decrease from 1.17 ± 0.06 μm in the absence of salt to 1.07 ± 0.04 μm in the presence of NaCl (see Figure 10-S4 of Supporting Information). To summarize, the results of these three experiments led us to conclude that necessary conditions for formation of hexagonal arrays of colloids were: (i) nematic order of 5CB; and (ii) interfacial curvature (droplets).

10.4 Discussion

The experimental results reported above provide qualitative insight into the origin of the hexagonal arrays of PS colloids formed in the vicinity of boojum defects of water-dispersed bipolar 5CB microdroplets, and led us to hypothesize that three interactions dominate formation of the hexagonal arrays: (i) a long-range attraction of the PS colloids towards the boojum defects, at which splay distortions of the LCs are at a maximum (splay attraction); (ii) inter-colloid quadrupole—quadrupole elastic interactions (the result of a quadrupolar topological defect structure), and (iii) electrostatic repulsion between colloids. Here we present a simple model that accounts for each interaction, and we test predictions that emerge from the model against our

experimental observations. We comment here that our simple model focuses on pairwise interactions between colloids at these interfaces, although some studies suggest multibody effects may be important.[4, 27, 29]

The first term of our model captures splay attraction and is expressed as:

$$U_{splay} = -\frac{8}{3}\pi K \frac{a^3}{d^2} \qquad (10\text{-}1)$$

in which K is the elastic constant of the LC (10^{-11} N)[47] and a is the radius of the PS colloid (0.5 μm). Because we consider pairwise interactions between colloids, we take d to be the center-to-center distance between two PS colloids, one of which is fixed at the location of a boojum defect (*i.e.*, the location of maximum splay; see Figure 10-S6 of Supporting Information). Thus, equation 10-1 estimates the energy gain from replacement of strained LC as the second colloid moves towards a first colloid positioned at the boojum (see Supporting Information for the derivation).

The second term in our model is a quadrupole—quadrupole elastic interaction between adsorbed PS colloids and is evaluated as:

$$U_{quad} = \frac{\pi W^2 a^8}{30Kd^5}\left(1 - \frac{Wa}{56K}\right)(9 + 20\,cos(2\theta) + 35\,cos(4\theta)) \qquad (10\text{-}2)$$

in which W is the surface anchoring coefficient (10^{-4} J/m^2),[48, 49] and θ is the angle formed between the LC director and a line connecting the center of mass of each colloid.[25] We note here that the magnitude and sign of the quadrupole—quadrupole interaction depends on θ and that for the purposes of this chapter θ was fixed at 49.1° to obtain the maximum attractive interaction.

The third and final term in our model is an electrostatic repulsion between colloids, which is evaluated as:

$$U_{elec} = \frac{2\varepsilon_{5CB}\pi\alpha_w^2\sigma^2 a^2 sin2\gamma}{\varepsilon_o\varepsilon_w^2\kappa^4 d^3} \qquad (10\text{-}3)$$

in which ε_o is the permittivity of vacuum (8.85×10^{-12} $C^2/J\cdot m$),[50] ε_w is the dielectric constant of water (78),[50] ε_{5CB} is the average dielectric constant of 5CB (11),[51, 52] α_w is the extent of dissociation of surface charge groups (0.25), σ is the surface charge density (0.06 e^-/nm^2, see Supporting Information for details), γ is the contact angle at the aqueous—5CB interface (95^o, see Supporting Information for details), and κ is the Debye-Huckel parameter ($1/\kappa$ is the Debye screening length).[53] Equation 10-3 describes the effective dipole—dipole interaction between PS colloids at the aqueous—LC interface that results from the asymmetry of the ionic atmosphere surrounding the colloids in water.[53] For simplicity, in the above model, the anisotropy of the dielectric properties of 5CB is neglected.

Using the above-described model, we calculated the free energy as a function of the center-to-center distance between PS colloids adsorbed to either the aqueous—LC interface of a bipolar LC droplet (all three terms in the model) or a LC film (U_{quad} and U_{elec} only). Figure 10-7 shows the results of the calculation. Interestingly, for the case of colloids adsorbed at the planar aqueous—LC interface (solid line), our model predicts a ~1,000 k_BT energy barrier due to electrostatic repulsion. However, no such barrier was observed for colloids adsorbed at the surface of the bipolar LC droplet (dashed line) indicating that the electrostatic energy barrier for colloidal assembly on the planar interface was overcome by splay attraction on the LC droplet surface. Overall, this simple simulation captures a key difference in the behavior of PS colloids at the interfaces of LC droplets or films.

Next, we determined if the electrostatic energy barrier for colloidal assembly on a LC film, as shown in Figure 10-7, would vanish upon addition of salt to the aqueous phase (as was done to reduce the separation between colloids on the surfaces of droplets; Figure 10-S4 of Supporting Information). Figure 10-7 reveals that the energy barrier predicted by the model

indeed disappears in the presence of 1 mM NaCl (dotted line). To test this prediction in an experiment, we sedimented PS colloids onto the aqueous—LC interface of a 20 μm-thick film of 5CB with a uniform planar alignment in the presence of 1 mM NaCl. In agreement with our prediction, Figure 10-6B reveals that chain-like assemblies of PS colloids formed at the interface (see below). The result of this simple experiment further validates the ability of our simple model to capture key behaviors of colloids at aqueous—LC interfaces.

We end this discussion by commenting on an additional difference that we observe between the ordered assemblies of colloids formed on the surfaces of bipolar LC droplets and LC films. On planar LC interfaces, we observed chains of PS colloids at the planar interfaces of LC films (Figure 10-6B). In the absence of splay attraction, it has been shown previously that quadrupole—quadrupole elastic interactions between colloids, which result from two diametrically opposite colloid-associated boojum defects (that generate an optical signature between crossed polarizers that is consistent with the signatures that we observed for PS colloids at planar aqueous—LC interfaces; see Figure 10-S2 of Supporting Information), lead to chain-like assemblies.[25] In contrast, on droplets we did not observe chains, but rather hexagonal assemblies of colloids that maximized colloid—colloid contacts. The difference between the assemblies observed on the aqueous—LC interfaces of planar films and bipolar LC droplets further highlights the importance of splay attraction in defining colloidal assembly on the surfaces of LC microdroplets, as hexagonal assemblies form to maximize strain reduction in the LC.

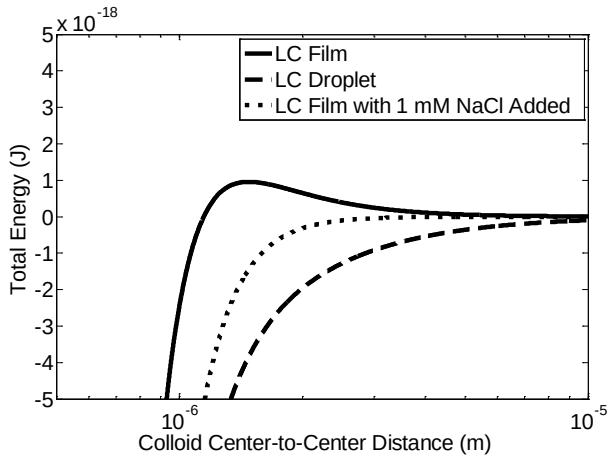

Figure 10-7. Dependence of total free energy on the center-to-center distance between PS colloids adsorbed at the aqueous—LC interface of (solid line) a planar LC film in pure water, (dashed line) a bipolar LC droplet in pure water, or (dotted line) a planar LC film in the presence of 1 mM NaCl.

10.5 Conclusions

Overall, the results reported in this chapter reveal that three key interactions underlie the organized assemblies formed by 1 μm-in-diameter PS colloids at the surfaces of water-dispersed nematic LC microdroplets in the bipolar configuration: (i) a long-range attraction of the adsorbed colloids to boojums at which splay distortion of the LC is at a maximum (splay attraction), (ii) inter-colloid quadrupole—quadrupole elastic interactions (the result of a quadrupolar topological defect structure), and (iii) electrostatic repulsion between colloids. These three interactions promote formation of hexagonal arrays of colloids in the vicinity of boojum defects. In contrast, for the case of colloids at the aqueous—LC interface of a LC film with a uniform planar alignment, the splay attraction is absent and the electrostatic repulsion keeps colloids separated under conditions of low ionic strength of the aqueous phase. However, addition of simple salt to the aqueous phase can screen the repulsion and leads to chaining of colloids at the interface. Thus, the influence of splay attraction is two-fold. It both overcomes repulsive interactions to

promote the ordering of colloids on the surfaces of LC droplets, and plays a key role in determining the morphology of the assembly formed.

The results reported in this chapter provide fundamental insights into inter-colloid interactions at liquid crystalline interfaces, thus providing guidance to design of a novel class of functional soft materials. In particular, our study reveals that several additional arrangements of colloids are possible on the surfaces of bipolar LC droplets (*e.g.*, open hexagonal or pentamer ring structures), and likely reflect kinetically trapped states of the system. This phenomenon will be explored in a future study, but we point out here that the observation of a pentamer ring pattern suggests that a synthetic version of the shells of sphere-like viruses might be realized through the use of colloid adsorption to the surfaces of LC droplets.

Acknowledgements

This work was primarily supported by NSF through DMR- 1121288 (Materials Research Science and Engineering Center), the Army Research Office (W911NF-11-1-0251 and W911NF-10-1-0181), and the National Institutes of Health (CA108467, CA105730, AI092004.). Acknowledgment of support is also made to the Department of Energy, Basic Energy Sciences, Biomaterials Program (DESC0004025). The authors thank Dr. Jonathan K. Whitmer, Tyler F. Roberts, Reza Abbasi, and Emre Bukusoglu for helpful discussions.

10.6 Supporting Information

Distribution of the Positions of Adsorbed Polystyrene Colloids between the Two Boojums of the Bipolar Configuration of LC Droplets

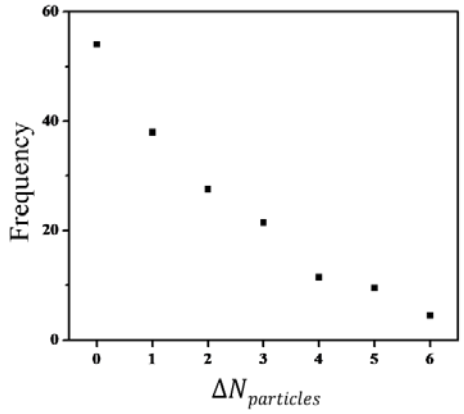

Figure 10-S1. Distribution of the difference in the number of colloids adsorbed at the two boojums of bipolar 5CB droplets.

The figure shows that colloids adsorbed at both boojum defects of the bipolar configuration with equal probability.

Optical Characterization of the Anchoring of LC on PS Colloids Adsorbed to Planar Aqueous—LC Interface

As shown in Figure 10-S2, isolated PS colloids sedimented onto LC films with a uniform planar director profile revealed quadrupolar symmetry of the optical signature generated by the colloids, which suggests the presence of two boojum defects at the surface of a colloid and existence of elastic quadrupole—quadrupole interactions between PS colloids.[24, 31, 46]

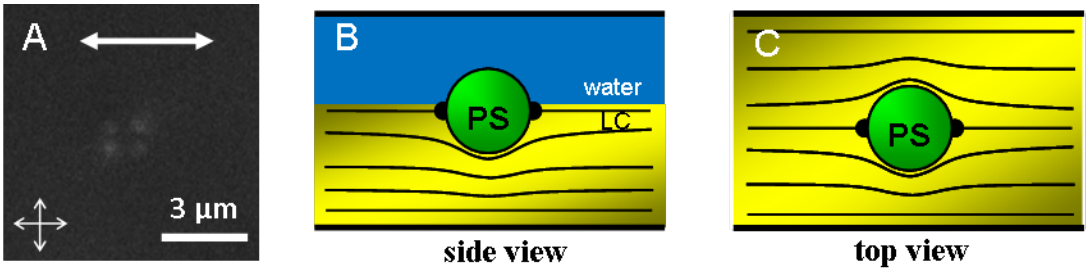

Figure 10-S2. Anchoring of LC on PS colloids adsorbed to planar aqueous—LC interfaces.
(A) PL micrograph and schematic illustrations of a (B) side or (C) top view of a single 1 µm-in-diameter PS colloid adsorbed to the planar aqueous—5CB interface of a 5CB film supported on a polyimide-coated glass slide. Double headed arrow in (A) indicates the rubbing direction of polyimide.

Effect of Contrast Enhancement on Fluorescence Images

In the main text, the contrast of Fluo images is enhanced to highlight the arrangements of colloids. A typical Fluo image after contrast enhancement is shown in Figure 10-S3A. The original image is shown in Figure 10-S3B. Comparison of the two micrographs reveals that the spacing between colloids is larger in original images than enhanced images. Therefore, the measurement of spacing between colloids was conducted using original images.

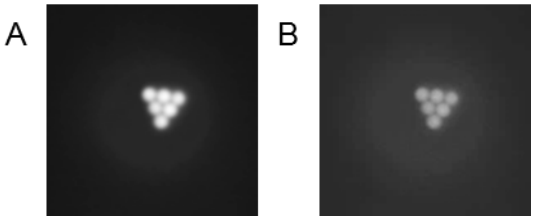

Figure 10-S3. Fluo micrograph of bipolar 5CB droplets with six colloids adsorbed to a pole (A) after or (B) before contrast enhancement.
(A) is identical to that shown in Figure 10-2 of the main text.

Spacing between PS Colloids Adsorbed to the Surface of LC Droplets in the Presence of Salt

We prepared 5CB droplets with PS colloids adsorbed to their surfaces in the presence of 1 mM sodium chloride (NaCl). The ratio of the center-to-center distance between adjacent colloids on LC droplets in the presence of NaCl was measured to be 1.07 ± 0.04, indicating that the addition of salt screened the electrostatic repulsion between PS colloids.

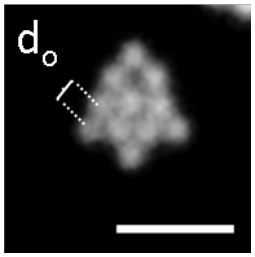

Figure 10-S4. Representative packing arrangements observed for 1 μm-in-diameter PS colloids adsorbed to a pole of nematic 5CB droplets in bipolar configuration in the presence of 1 mM NaCl.

Role of Nematic Order in the Formation of Arrays of Colloids Adsorbed to the Surface of LC Droplets

We investigated the role of nematic order in the formation of the arrays by heating the LC droplets with colloids adsorbed to the isotropic phase. Figure 10-S4 shows representative Fluo micrographs of a LC droplet with three PS colloids adsorbed to the surface both before (Figure 10-S5A) and after (Figure 10-S5B) heating. The PS colloids were observed to break from the initial hexagonal array and separate from one another on the surface upon heating to the isotropic phase. We note here that the fluorescence signal of PS colloids decreased upon heating because the dye is soluble in isotropic phase. This result leads us to conclude that the elastic energy from

a strained nematic phase of the LC drives the formation of hexagonal arrays of PS colloids to the poles of bipolar LC droplets.

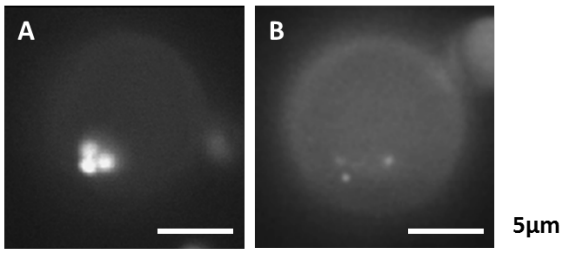

Figure 10-S5. Packing arrangements observed for PS colloids adsorbed to the surfaces of 5CB droplets (A) in nematic phase or (B) 30 s after heating into isotropic phase.

Derivation of the Expression for Splay Attraction

Both in our previous studies (see Chapter 9 and Appendix A)[31, 32, 54] and the experiments reported in the main text, we observed colloids adsorbed to the surfaces of bipolar LC droplets to partition to the surface defects to eliminate the energetic penalty associated with high-splay distortion of the LC within these regions. Here we derive a simple order of magnitude estimate for this so-called "splay attraction". We focus on a case in which one colloid is located at the center of a splay field where splay is at a maximum, and a second colloid subsequently introduced into the field is also attracted to this location (Figure 10-S6).

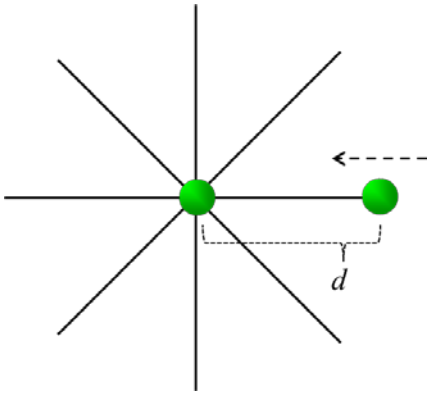

Figure 10-S6. Schematic illustration of splay attraction.
First, a single colloid is attracted to the region of maximum splay. A second colloid introduced into the field is also attracted to this high-splay region.

The elastic energy density of the splay field can be estimated from the splay term in the Frank–Oseen equation[55]:

$$f_e = \frac{1}{2}[K(\nabla \cdot \bar{n})^2] \qquad (10\text{-}4)$$

in which K is the splay elastic constant, and $\bar{n}$ is a vector of order unity that represents the local orientation of the LC (the so-called nematic director). In spherical coordinates $\nabla \cdot \bar{n} = \frac{1}{r^2}\frac{d}{dr}(r^2 n_r)$. Thus, equation 10-4 scales as:

$$f_e = \frac{2K}{d^2} \qquad (10\text{-}5)$$

in which d is distance of a colloid from the boojum defect occupied by another colloid (Figure 10-S6). From equation 10-5 we estimate the splay attraction energy as:

$$E_{splay} = -\left(\frac{4}{3}\pi a^3\right)\left(\frac{2K}{d^2}\right) = -\frac{8}{3}\pi K\frac{a^3}{d^2} \qquad (10\text{-}6)$$

in which a and $\frac{4}{3}\pi a^3$ are the radius and volume of a PS colloid, respectively. Equation 10-6 estimates the energy gain as a function of the position of the second colloid (d). The smallest d

is the experimentally observed center-to-center spacing between PS colloids in the vicinity of the boojum defect. Equation 10-6 is equation 10-1 of the main text.

Contact Angle for PS Colloids Adsorbed to the Surfaces of LC Droplets

We used 4 μm-in-diameter PS colloids (instead of 1 μm-in-diameter) to measure the contact angle for PS colloids adsorbed to the aqueous—LC interface of a LC droplet, as shown in Figure 10-S7. 4 μm-in-diameter PS colloids were used so that the colloids could be resolved in bright field micrographs. The contact angle is measured to be ~ 95^{o}.

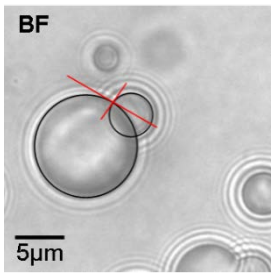

Figure 10-S7. Contact angle for a 4 μm-in-diameter PS colloid adsorbed to the surface of nematic LC droplet.
The contact angle is measured to be ~ 95^{o}.

Measurement of Surface Charge Density of PS Colloids

The surface charge density of PS colloids was calculated based on the zeta-potential measurement using the following equation:

$$\sigma = \frac{2\varepsilon_0\varepsilon_w \kappa kT}{ze}\sinh\left(\frac{ze\zeta}{2kT}\right)\left[1+\frac{1}{\kappa a}\frac{1}{\left(\cosh\frac{ze\zeta}{4kT}\right)^2}\right] \qquad (10-7)$$

in which σ is surface charge density, ε_0 is the permittivity of vacuum (8.85×10^{-12} $C^2/J \cdot m$), ε_w is dielectric constant of water (78), κ is Debye-Huckel parameter ($1/\kappa$ is Debye screening length), k is the Boltzmann constant, T is the temperature, z is the valence number, e is the electronic charge, ζ is the zeta potential, and a is the radius of PS colloid (0.5 μm).[56] κ can be calculated as:

$$\kappa = \left(\frac{e^2 \sum_i c_i z_i^2}{\varepsilon_0 \varepsilon_w kT} \right)^{\frac{1}{2}} \qquad (10 - 8)$$

in which c is the concentration of ions per m^3. The results are summarized in Table 9-S1. The average charge density is calculated to be 0.06 e^-/nm^2.[56]

Table 9-S1. Calculation of surface charge density on PS colloids based on zeta-potential measurement.

zeta potential (mV)	salt concentration (mM)	Debye length (nm)	surface charge density (e^-/nm^2)
-5.8	1000	0.30	0.08
-11.7	100	0.96	0.05
-15.1	75	1.11	0.06
-18.7	50	1.36	0.06

Analysis of the Relative Stabilities of Packing Arrangements of Five PS Colloids on the Surfaces of Bipolar LC Droplets

To estimate the relative energies of the packing arrangements of five PS colloids on the surfaces of bipolar LC droplets (Figure 10-2 of the main text), we assume that the frequency distribution (Figure 10-4 of the main text) is described by a Boltzmann distribution ($F(N) \propto M(N)e^{-E(N)}$; where M and E are the multiplicity of arrangements and energy (in units of k_BT) for a given N, respectively). Therefore, we plot $-\ln(F/M)$ as a function of N in Figure 10-S8.

The analysis predicts that the energy of the system is lowered by increasing N within an arrangement of five colloids (a line fit to the data predicts an energy gain of ~0.8 k_BT per N), and that $N = 7$ is the energetically most stable arrangement. However, we note that the difference in energy between arrangements of different N is small (of order k_BT), suggesting that the frequency distribution is not described by a Boltzmann distribution. Instead, energy barriers must exist between each N, or else thermal fluctuations would lead to rearrangement of the colloids. From this analysis, we conclude that the hexagonal packing arrangement of five colloids that maximizes N is the most stable arrangement, and that assemblies of five colloids with $N < 7$ are kinetically trapped states.

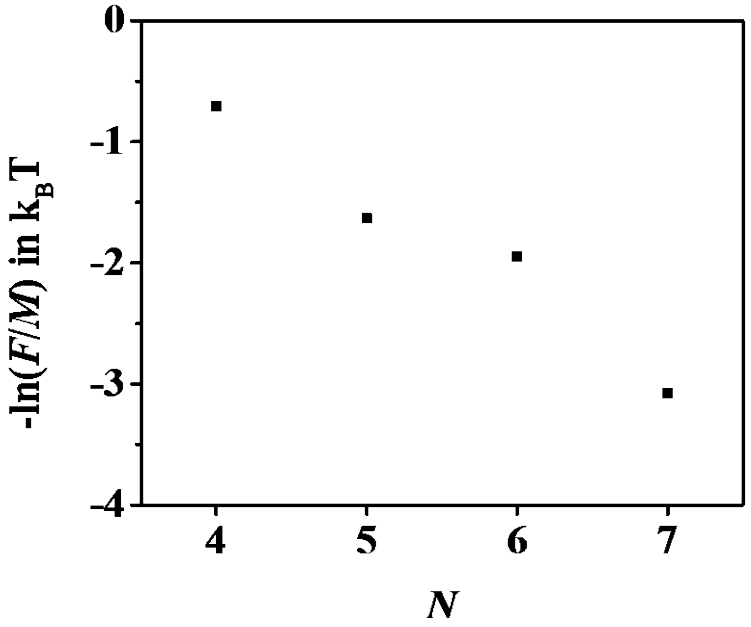

Figure 10-S8. Negative natural logarithm of frequency (F) over the multiplicity of arrangements possible for a given N (M) in units of k_BT plotted as function of N.

The plots were constructed from Figure 10-2 of the main text.

10.7 References

*This chapter was prepared as a Full Paper reporting original research submitted to the journal *Soft Matter*. Xiaoguang Wang and I worked together throughout the course of this project. Adapted with permission from: Wang, W.; Miller, D. S.; de Pablo, J. J.; Abbott, N. L. Organized Assemblies of Colloids Formed at the Poles of Micrometer-Sized Droplets of Liquid Crystal. *Soft Matter* 2014 (Submitted).

1. Assoud, L.; Ebert, F.; Keim, P.; Messina, R.; Maret, G.; Löwen, H., Ultrafast Quenching of Binary Colloidal Suspensions in an External Magnetic Field. *Physical Review Letters* **2009,** 102, 238301.
2. Bowden, N. B.; Weck, M.; Choi, I. S.; Whitesides, G. M., Molecule-Mimetic Chemistry and Mesoscale Self-Assembly. *Accounts of Chemical Research* **2001,** 34, 231-238.
3. Nazarenko, V. G.; Nych, A. B.; Lev, B. I., Crystal Structure in Nematic Emulsion. *Physical Review Letters* **2001,** 87, 075504.
4. Nych, A. B.; Ognysta, U. M.; Pergamenshchik, V. M.; Lev, B. I.; Nazarenko, V. G.; Musevic, I.; Skarabot, M.; Lavrentovich, O. D., Coexistence of Two Colloidal Crystals at the Nematic-Liquid-Crystal-Air Interface. *Physical Review Letters* **2007,** 98, 057801.
5. Oettel, M.; Dietrich, S., Colloidal Interactions at Fluid Interfaces. *Langmuir* **2008,** 24, 1425-1441.
6. Onoda, G. Y., Direct Observation of Two-Dimensional, Dynamic Clustering and Ordering with Colloids. *Physical Review Letters* **1985,** 55, 226.
7. Park, B. J.; Pantina, J. P.; Furst, E. M.; Oettel, M.; Reynaert, S.; Vermant, J., Direct Measurements of the Effects of Salt and Surfactant on Interaction Forces between Colloidal Particles at Water-Oil Interfaces. *Langmuir* **2008,** 24, 1686-1694.
8. Binks, B. P.; Murakami, R., Phase Inversion of Particle-Stabilized Materials from Foams to Dry Water. *Nature Materials* **2006,** 5, 865-869.
9. Giermanska-Kahn, J.; Schmitt, V.; Binks, B.; Leal-Calderon, F., A New Method to Prepare Monodisperse Pickering Emulsions. *Langmuir* **2002,** 18, 2515-2518.
10. Vignati, E.; Piazza, R.; Lockhart, T. P., Pickering Emulsions: Interfacial Tension, Colloidal Layer Morphology, and Trapped-Particle Motion. *Langmuir* **2003,** 19, 6650-6656.
11. Aussillous, P.; Quéré, D., Liquid Marbles. *Nature* **2001,** 411, 924-927.
12. Meeker, S.; Poon, W.; Crain, J.; Terentjev, E., Colloid–Liquid-Crystal Composites: An Unusual Soft Solid. *Physical Review E* **2000,** 61, R6083.
13. Hosoki, K.; Tayagaki, T.; Yamamoto, S.; Matsuda, K.; Kanemitsu, Y., Direct and Stepwise Energy Transfer from Excitons to Plasmons in Close-Packed Metal and Semiconductor Nanoparticle Monolayer Films. *Physical Review Letters* **2008,** 100, 207404.
14. Kim, B.; Tripp, S. L.; Wei, A., Tuning the Optical Properties of Large Gold Nanoparticle Arrays. *Materials Research Society Symposium Proceedings* **2002,** 676, Y6. 1-Y6. 4.
15. Kim, J.; Lee, D., Electron Hopping Dynamics in Au38 Nanoparticle Langmuir Monolayers at the Air/Water Interface. *Journal of the American Chemical Society* **2006,** 128, 4518-4519.
16. Velev, O. D.; Kaler, E. W., Structured Porous Materials via Colloidal Crystal Templating: From Inorganic Oxides to Metals. *Advanced Materials* **2000,** 12, 531-534.

17. Kralchevsky, P. A.; Nagayama, K., Capillary Interactions between Particles Bound to Interfaces, Liquid Films and Biomembranes. *Advances in Colloid and Interface Science* **2000,** 85, 145-192.
18. Botto, L.; Lewandowski, E. P.; Cavallaro, M.; Stebe, K. J., Capillary Interactions between Anisotropic Particles. *Soft Matter* **2012,** 8, 9957-9971.
19. Pieranski, P., Two-Dimensional Interfacial Colloidal Crystals. *Physical Review Letters* **1980,** 45, 569-572.
20. Poulin, P.; Stark, H.; Lubensky, T.; Weitz, D., Novel Colloidal Interactions in Anisotropic Fluids. *Science* **1997,** 275, 1770-1773.
21. Lubensky, T.; Pettey, D.; Currier, N.; Stark, H., Topological Defects and Interactions in Nematic Emulsions. *Physical Review E* **1998,** 57, 610.
22. Ruhwandl, R.; Terentjev, E., Long-Range Forces and Aggregation of Colloid Particles in a Nematic Liquid Crystal. *Physical Review E* **1997,** 55, 2958.
23. Musevic, I.; Skarabot, M.; Tkalec, U.; Ravnik, M.; Zumer, S., Two-Dimensional Nematic Colloidal Crystals Self-Assembled by Topological Defects. *Science* **2006,** 313, 954-958.
24. Stark, H., Physics of Colloidal Dispersions in Nematic Liquid Crystals. *Physics Reports* **2001,** 351, 387-474.
25. Smalyukh, I. I.; Lavrentovich, O. D.; Kuzmin, A. N.; Kachynski, A. V.; Prasad, P. N., Elasticity-Mediated Self-Organization and Colloidal Interactions of Solid Spheres with Tangential Anchoring in a Nematic Liquid Crystal. *Physical Review Letters* **2005,** 95, 157801.
26. Smalyukh, I. I.; Chernyshuk, S.; Lev, B. I.; Nych, A. B.; Ognysta, U.; Nazarenko, V. G.; Lavrentovich, O. D., Ordered Droplet Structures at the Liquid Crystal Surface and Elastic-Capillary Colloidal Interactions. *Physical Review Letters* **2004,** 93, 117801.
27. Oettel, M.; Domınguez, A.; Tasinkevych, M.; Dietrich, S., Effective Interactions of Colloids on Nematic Films. *The European Physical Journal E* **2009,** 28, 99-111.
28. Gharbi, M. A.; Nobili, M.; In, M.; Prévot, G.; Galatola, P.; Fournier, J.-B.; Blanc, C., Behavior of Colloidal Particles at a Nematic Liquid Crystal Interface. *Soft Matter* **2011,** 7, 1467-1471.
29. Koenig, G. M.; Lin, I. H.; Abbott, N. L., Chemoresponsive assemblies of microparticles at liquid crystalline interfaces. *Proceedings of the National Academy of Sciences of the United States of America* **2010,** 107, 3998-4003.
30. Gharbi, M. A.; Nobili, M.; Blanc, C., Use of Topological Defects as Templates to Direct Assembly of Colloidal Particles at Nematic Interfaces. *Journal of Colloid and Interface Science* **2014,** 417, 250-255.
31. Mondiot, F.; Wang, X.; de Pablo, J. J.; Abbott, N. L., Liquid Crystal-Based Emulsions for Synthesis of Spherical and Non-Spherical Particles with Chemical Patches. *Journal of the American Chemical Society* **2013,** 135, 9972–9975.
32. Whitmer, J. K.; Wang, X.; Mondiot, F.; Miller, D. S.; Abbott, N. L.; Pablo, J. J. d., Nematic-Field Driven Positioning of Particles in Liquid Crystal Droplets. *Physical Review Letters* **2013,** 111, 227801.
33. Berggren, E.; Zannoni, C.; Chiccoli, C.; Pasini, P.; Semeria, F., Computer-Simulations of Nematic Droplets with Bipolar Boundary-Conditions. *Physical Review E* **1994,** 50, 2929-2939.
34. Drzaic, P. S., *Liquid Crystal Dispersions*. World Scientific: River Edge, NJ, USA, 1995.
35. Gupta, J. K.; Zimmerman, J. S.; de Pablo, J. J.; Caruso, F.; Abbott, N. L., Characterization of Adsorbate-Induced Ordering Transitions of Liquid Crystals within Monodisperse Droplets. *Langmuir* **2009,** 25, 9016-9024.

36. Meyer, R. B., Piezoelectric Effects in Liquid Crystals. *Physical Review Letters* **1969,** 22, 918.
37. Miller, D. S.; Wang, X.; Abbott, N. L., Design of Functional Materials Based on Liquid Crystalline Droplets. *Chemistry of Materials* **2013,** 26, 496–506.
38. Ondris-Crawford, R.; Boyko, E. P.; Wagner, B. G.; Erdmann, J. H.; Zumer, S.; Doane, J. W., Microscope Textures of Nematic Droplets in Polymer Dispersed Liquid-Crystals. *Journal of Applied Physics* **1991,** 69, 6380-6386.
39. Prischepa, O. O.; Shabanov, A. V.; Zyryanov, V. Y., Transformation of Director Configuration upon Changing Boundary Conditions in Droplets of Nematic Liquid Crystal. *JETP Letters* **2004,** 79, 257-261.
40. Volovik, G. E.; Lavrentovich, O. D., The Topological Dynamics of Defects - Boojums in Nematic Drops. *Zhurnal Eksperimentalnoi I Teoreticheskoi Fiziki* **1983,** 85, 1997-2010.
41. Carlton, R. J.; Hunter, J. T.; Miller, D. S.; Abbasi, R.; Mushenheim, P. C.; Tan, L.; Abbott, N. L., Chemical and Biological Sensing Using Liquid Crystals. *Liquid Crystal Reviews* **2013,** 1, 1-23.
42. Berger, B.; Shor, P. W.; Tucker-Kellogg, L.; King, J., Local Rule-Based Theory of Virus Shell Assembly. *Proceedings of the National Academy of Sciences* **1994,** 91, 7732-7736.
43. Marzec, C. J.; Day, L. A., Pattern Formation in Icosahedral Virus Capsids: The Papova Viruses and Nudaurelia Capensis Beta Virus. *Biophysical Journal* **1993,** 65, 2559-2577.
44. Zandi, R.; Reguera, D.; Bruinsma, R. F.; Gelbart, W. M.; Rudnick, J., Origin of Icosahedral Symmetry in Viruses. *Proceedings of the National Academy of Sciences of the United States of America* **2004,** 101, 15556-15560.
45. Caspar, D. t.; Klug, A. In *Physical Principles in the Construction of Regular Viruses*, Cold Spring Harbor Symposia on Quantitative Biology, 1962; Cold Spring Harbor Laboratory Press: 1962; pp 1-24.
46. Poulin, P.; Weitz, D., Inverted and Multiple Nematic Emulsions. *Physical Review E* **1998,** 57, 626.
47. Kléman, M.; Lavrentovich, O. D., *Soft Matter Physics : An Introduction*. Springer: New York, NY, USA, 2003.
48. Rapini, A.; Papoular, M., Distortion d'une Lamelle Nematique sous Champ Magnetique Conditions d'Ancrage aux Parois. *Journal de Physique Colloques* **1969,** 30, C4-54-C4-56.
49. Seo, D.-S.; Muroi, K.-i.; Isogami, T.-r.; Matsuda, H.; Kobayashi, S., Polar Anchoring Strength and the Temperature Dependence of Nematic Liquid Crystal(5 CB) Aligned on Rubbed Polystyrene Films. *Japanese Journal of Applied Physics* **1992,** 31, 2165-2169.
50. Israelachvili, J. N., *Intermolecular and Surface Forces*. 2nd ed.; Academic Press London: San Diego, CA, USA, 1991.
51. Carlton, R. J.; Gupta, J. K.; Swift, C. L.; Abbott, N. L., Influence of Simple Electrolytes on the Orientational Ordering of Thermotropic Liquid Crystals at Aqueous Interfaces. *Langmuir* **2012,** 28, 31-36.
52. Miller, D. S.; Carlton, R. J.; Mushenheim, P. C.; Abbott, N. L., Introduction to Optical Methods for Characterizing Liquid Crystals at Interfaces. *Langmuir* **2013,** 29, 3154-3169.
53. Aveyard, R.; Binks, B.; Clint, J.; Fletcher, P.; Horozov, T.; Neumann, B.; Paunov, V.; Annesley, J.; Botchway, S.; Nees, D., Measurement of Long-Range Repulsive Forces between Charged Particles at an Oil-Water Interface. *Physical Review Letters* **2002,** 88, 246102.

54. Wang, X.; Miller, D. S.; Pablo, J. J. d.; Abbott, N. L., Reversible Switching of Liquid Crystalline Order Permits Synthesis of Homogeneous Populations of Dipolar Patchy Microparticles. *Advanced Functional Materials* **2014 (In Press)**.
55. Frank, F. C., I. Liquid Crystals. On the Theory of Liquid Crystals. *Discussions of the Faraday Society* **1958,** 25, 19-28.
56. Makino, K.; Ohshima, H., Electrophoretic Mobility of a Colloidal Particle with Constant Surface Charge Density. *Langmuir* **2010,** 26, 18016-18019.

Chapter 11. Chemical Control over the Shape and Surface Morphology of Spherical and Non-Spherical Particles Synthesized from Liquid Crystalline Microdroplets*

11.1 Introduction

Development of facile and scalable methodologies for synthesis of particles of anisotropic shape is an important challenge because this class of particles has proven useful in a range of applications including intracellular delivery,[1, 2] emulsion stabilization,[3] and catalysis.[4, 5] Recently, we reported such a technique for synthesis of non-spherical polymer particles with chemical patches.[6] The methodology exploited the long-range order of a thermotropic liquid crystal (LC) in the nematic phase to align polymer chains during synthesis (*i.e.*, serve as a template). The LC was confined to millions of micrometer-sized droplets dispersed in aqueous solution which both led to confinement-induced elastic stresses that directed chemically-treated colloids adsorbed to the droplet surfaces to well-defined positions, thus enabling chemical patches to be engineered on the surfaces of the particles,[6-8] and made the method highly scalable. After polymerization, the LC was extracted to yield the polymer microparticles. While promising, this methodology has only been utilized to synthesize polymer particles from LC droplets in a bipolar configuration, which resulted in ellipsoidal (lemon-shaped) particles.

Herein, we report an experimental investigation of the dependence of the shape and surface morphology of polymer particles synthesized from LC microdroplets on the internal configuration of the LC droplet templates. We reveal that the LC droplets are a rich palette of

templates that allow remarkable control over the shape and surface morphology of the polymer particles. The unique configurations of the LC droplets are accessed through a range of chemical methodologies (*e.g.*, surfactant adsorption in the presence or absence of adsorbed colloids or variation of the chemical composition of the LC/monomer mixture) that result in homogeneous populations of LC droplets in a particular configuration.

11.2 Experimental Section

Materials. Sodium dodecyl sulfate (SDS), glycerol, and 2-dimethoxy-2-phenyl acetophenone (DMPAP) were purchased from Sigma-Aldrich (St. Louis, MO). 1 μm-in-diameter fluorescent polystyrene (PS) colloids (λ_{exc} = 480 nm / λ_{em} = 520 nm) were purchased from Bangs Laboratories (Fishers, IN). 4-cyano-4'-pentylbiphenyl (5CB) and 4-(3-acryloyoxypropyloxy) benzoic acid 2-methyl-1, 4-phenylene ester (RM257) was obtained from EM Sciences (New York, NY). Deionization of a distilled water source was performed with a Milli-Q system (Millipore, Bedford, MA). The liquid crystalline phase consisted of 5CB containing 10 - 40 % wt/wt of RM257. The photo-initiator DMPAP was added at 5 wt % based on the mass of RM257.

Preparation of the Bipolar LC-in-Water Emulsions. The LC-in-water emulsions were prepared according to previously published methods.[6-8] Bipolar LC droplets were prepared by homogenizing 4 μL LC mixture in 2 mL 90 v % glycerol/water using a homogenizer (T25 digital ULTRA-TURRAX) equipped with a S25 N-10G dispersing element (IKA), for 30 seconds at 6,500 rpm. The emulsions were prepared in glass vials (19 mm-in-diameter, 51 mm-in-height).

Preparation of the Radial LC-in-Water Emulsions. Radial LC droplets were prepared by homogenizing 4 µL LC mixture in 2 mL water for 30 seconds at 6,500 rpm. After emulsification, a small volume of a stock solution of 100 mM SDS was added to the emulsions to change the internal configuration of the LC droplets from bipolar to radial. The final concentration of SDS was 2 mM.

Preparation of the Axial LC-in-Water Emulsions. Axial LC droplets were prepared by homogenizing 4 µL LC mixture in 2 mL pure water for 30 seconds at 6,500 rpm.

Preparation of the Preradial LC-in-water Emulsions. Preradial LC droplets were prepared according to previously publish methods.[8, 9] Briefly, 4 µL LC mixture in 2 mL water with 1 µm-in-diameter fluorescent PS colloids added (0.01 wt % / v based on emulsion) was homogenized for 30 seconds at 6,500 rpm. After emulsification, a small volume of a stock solution of 100 mM SDS was added to the emulsions to change the internal configuration of the LC droplets to preradial. The final concentration of SDS was 2 mM.

Photo-Polymerization of the LC Droplets. Photo-polymerization of 5CB/RM257/DMPAP mixture was performed using a UV lamp (365 nm) that delivered 2.5 mW/cm^2. The emulsion was exposed to UV light for 30 minutes.

Bright Field (BF), Polarized Light (PL), and Fluorescence (Fluo) Microscopy. A 50 µL volume of the polymerized LC emulsion was dispensed onto a glass coverslip. Next, the polymeric microparticles were imaged using an Olympus IX71 inverted epifluorescence

microscope (Center Valley, PA) equipped with a 100x oil-immersion objective, crossed polarizers, mercury lamp, and Chroma filter (457 nm $\leq \lambda_{exc} \leq$ 502 nm, and 510 nm $\leq \lambda_{em} \leq$ 562 nm). BF, PL, and Fluo micrographs of LC-in-water emulsions were collected with a Hamamatsu 1394 ORCAER CCD camera (Bridgewater, NJ) connected to a computer and controlled through SimplePCI imaging software (Compix, Inc., Cranberry Twp., NJ). BF micrographs were collected by removing the polarizer from the optical path of the microscope.

SEM Characterization of Surface Morphology of Polymer Microparticles. Scanning electron micrographs of polymer microparticles were captured on a Hitachi S-2600N Scanning electron microscope.

11.3 Results and Discussion

In the first set of experiments, we sought to demonstrate that the shape of polymer microparticles synthesized from water-dispersed LC microdroplets can be tuned by controlling the internal configuration of the LC droplets. Before describing the results, we introduce the configurations of LC droplets that were utilized as templates for microparticle synthesis by describing the states encountered during an adsorbate-driven change in the surface anchoring of a LC droplet (the surface anchoring sets the preferred alignment of LC at the surface of a droplet and the LC within arranges into an equilibrium configuration that minimizes elastic strain[10-12]). Figure 11-1 shows a schematic illustration of an adsorbate-induced ordering transition in a water-dispersed LC droplet, driven, for example, by sodium dodecyl sulfate (SDS). Initially, the droplet dispersed in water exhibits a bipolar configuration,[11, 13-16] in which the average orientation of LC (so-called director, ***n***) is tangential at the droplet interface and two diametrically opposite surface point defects (so-called boojums) are present at the poles (Figure

11-1A).[11, 12, 14, 17-21] After addition of adsorbate, the first transition of configuration is a bipolar-to-axial transition,[11, 12, 14, 15, 21] evidenced by the disappearance of the two boojums and simultaneous appearance of a disclination ring near the droplet equator (Figure 11-1A-B). With further increase in bulk adsorbate concentration (and thus concentration of adsorbate at the aqueous—LC interface), this ring defect moves towards a pole and shrinks to a surface point defect, forming a preradial configuration (Figure 11-1C). Finally, at saturation coverage of the droplet surfaces by adsorbate the point defect migrates from the surface of the droplet to the center, passing through an escaped radial configuration prior settling in the final radial structure (Figure 11-1D).[11, 12, 14, 15, 21] In the experiments below, we investigate the shape of polymer microparticles synthesized from LC droplets in the bipolar, axial, preradial, or radial configuration. We note here that although the axial and preradial configuration can be accessed by controlling the amount of adsorbate added to the aqueous phase, the configuration of LC droplets is dependent on droplet size.[11, 13, 16] Because we used polydisperse LC-in-water emulsions with droplet diameters ranging from 1 to 40 μm a homogeneous population of axial or preradial configurations could not be obtained *via* the use of an adsorbate. To overcome this challenge we devised other methods to obtain emulsions with axial or preradial droplets, as detailed below.

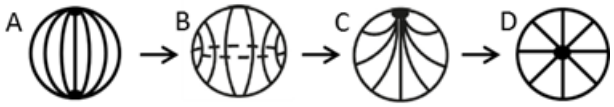

Figure 11-1. Schematic illustration of concentration-dependent equilibrium director configurations induced by increasing surface coverage of a droplet by adsorbate.
Only configurations used as templates for the synthesis of polymer microparticles in this study are shown: (A) bipolar, (B) axial, (C) preradial, and (D) radial configuration. In between the preradial and radial configuration a droplet exhibits a so-called escaped radial configuration.

First, we investigated the shape of polymer microparticles templated by a bipolar configuration of LC microdroplets. The LC mixture used in our experiments was comprised of 4-cyano-4'-pentylbiphenyl (5CB) into which the reactive liquid crystalline monomer 4-(3-acryloyoxypropyloxy) benzoic acid 2-methyl-1,4-phenylene ester (RM257) was doped at 20% wt/wt. Bipolar LC droplets were prepared by homogenizing 4 µL of the LC mixture dispersed in 2 mL of a 90 % v/v glycerol/water mixture for 30 seconds at 6,500 rpm. Subsequently, the emulsions were photo-polymerized *via* exposure to UV light for 30 minutes. The left column in Figure 11-2A reveals that the polymerized bipolar LC droplets remained in the bipolar configuration indicating that the backbone of the polymer chains followed the local director of the LC within the droplets. After polymerization, 200 µL of emulsion was added to 1.8 mL ethanol to extract 5CB from the polymerized LC droplets. The solutions were then centrifuged for 20 minutes at 4,500 rpm, after which the ethanol was removed and the extraction step was repeated. Following extraction, 500 µL water was added to re-disperse the pellet. Extraction of 5CB from the polymeric LC microparticles resulted in deswelling of microparticles in a direction normal to the line connecting the poles of the bipolar configuration, and generated ellipsoidal (or lemon-shaped) particles (right column in Figure 11-2A). Such lemon-shaped particles were also observed in our previous study with the exception that polystyrene (PS) or silica particles were

present at the poles of those particles.[6] We comment here that the backbone of the polymer chains is oriented along the long axis of the ellipsoidal particles, and thus the mechanical properties of the anisotropic polymer network is much stronger along the backbone of the polymer.

We next characterized polymer microparticles synthesized from radial LC microdroplets. The emulsions were prepared as described above. After emulsification, a small volume of a stock solution of 100 mM SDS was added to achieve a final concentration of 2 mM and trigger a change in the internal configuration of the LC droplets from bipolar to radial. As was observed for bipolar droplets, subsequent polymerization of radial LC droplets preserved the internal configuration of the LC (Figure 11-2B). However, in contrast to the polymer particles templated by bipolar droplets, extraction of 5CB from the polymeric LC microparticles led to spherical particles (rather than lemon-shaped particles; right column in Figure 11-2B). As described above, preservation of the internal configuration of the LC following polymerization of the monomer implies that the polymer backbone follows the local director within the droplets. The observation of spherical particles templated from radial LC droplets is consistent with this conclusion, as the orientation of the polymer chains is perpendicular to the surface of particles so that deswelling occurs in a uniform fashion that is spherically symmetric (in contrast to the anisotropic deswelling behavior of microparticles templated from bipolar droplets).

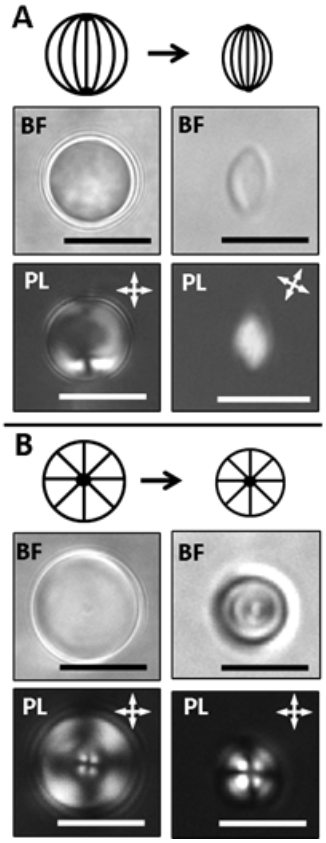

Figure 11-2. Templated synthesis of (A) ellipsodal (lemon-shaped) or (B) spherical polymeric microparticles from 5CB droplets in the bipolar or radial configuraiton, respectively.
The droplets were doped with the reactive mesogenic monomer RM257 (20 % wt/wt based on the mass of LC phase), photo-polymerized, and the 5CB was subsequently extracted. The left and right columns show schematic illustrations and the corresponding bright field (BF) and polarized light (PL) micrographs of polymerized LC droplets before or after extraction of the LC, respectively. The orientation of the crossed polarizers in PL micrographs is indicated by the white double headed arrows. Scale bars: 10 μm.

The above results reveal that the shape of the polymer microparticles can be tailored *via* changes in the internal configuration of the LC droplets utilized as templates. Building on this discovery, we next prepared polymer particles from LC droplets in the axial or preradial configuration. As described above, emulsions containing homogeneous populations of these configurations cannot be obtained by the methods used in our study due to size-dependent ordering of the LC droplets.[11, 13, 16] Instead, we formed emulsions with axial droplets by

dispersing the LC mixture in water, instead of the 90 % v/v glycerol/water mixture, prior to photo-polymerization. Whereas dispersing droplets of LC mixed with 20% wt/wt RM257 in a 90 % v/v glycerol/water mixture resulted in a bipolar configuration (Figure 11-2A), dispersion of the droplets in water was observed to lead to a homogenous population of droplets in the axial configuration (left column in Figure 11-3A). We speculate that the axial configuration was the result of a tilted alignment of the LC mixture at the aqueous—LC interface caused by RM257 (in the absence of RM257 5CB droplets adopt a bipolar configuration in water). This observation is consistent with a report that showed that lecithin-coated LC droplets dispersed in glycerol must be heated to transition from a bipolar to the radial configuration,[21] whereas other reports show that similar droplets adopt a radial configuration without heating when dispersed in water[14, 15, 22, 23] (although we note here that the LCs were different in these studies and that temperature can also influence adsorption of surfactant from bulk solution to the droplet surfaces[24]). It also implies that glycerol leads to a tangential anchoring of LC at a droplet surface that is stronger than that of water (*i.e.*, a higher anchoring energy (*W*)), which is the subject of an on-going investigation to be reported elsewhere. After polymerization of the axial droplets and extraction of 5CB, rod-shaped particles were obtained (right column in Figure 11-3A).

To form emulsions with homogeneous populations of preradial droplets we exploited our recent observation that colloids adsorbed at the surfaces of LC droplets with normal anchoring effectively ‘pin’ the topological defect of the radial configuration (preferred in the absence of adsorbed colloids) to the surface, resulting in a preradial configuration (see Chapter 9 and Appendix A).[7, 8] Based on these findings, preradial LC droplets were prepared by first homogenizing 4 µL LC mixture in 2 mL water for 30 seconds at 6,500 rpm, in the presence of 1 µm-in-diameter fluorescent PS colloids (0.01% wt/v based on emulsion) to adsorb the colloids to

the droplet surfaces. After emulsification, a small volume of a stock solution of 100 mM SDS was added to the emulsions to change the internal configuration of the LC droplets to preradial. The final concentration of SDS was 2 mM. Consistent with our previous observation, this procedure led to emulsions with a homogeneous population of preradial LC droplets (left column in Figure 11-3B). Upon extraction of 5CB, we observed that polymerized preradial LC particles led to pear-shaped polymer microparticles, as shown in the right column in Figure 11-3B.

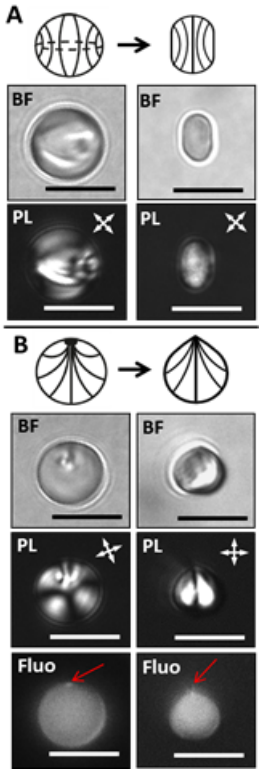

Figure 11-3. Templated synthesis of (A) rod-shaped or (B) pear-shaped polymeric microparticles from 5CB droplets in the axial or preradial, respectively.

The left and right columns show schematic illustrations and the corresponding BF, PL and fluorescence (Fluo) micrographs (for B only) of polymerized LC droplets before or after extraction of the LC, respectively. The concentration of RM257 was 20 % wt/wt based on the mass of LC phase. The orientation of the crossed polarizers in PL micrographs is indicated by the white double headed arrows. The position of the PS colloid adsorbed at the particle surface is indicated by red arrow. Scale bars: 10 μm.

The above results demonstrate the remarkable level of control over the shape of polymer microparticles synthesized from LC droplets that can be achieved *via* manipulation of the internal configuration of droplets prior to polymerization. We next sought to achieve an even greater level of control by changing the composition of the LC mixture, which we hypothesized would influence the aspect ratio (AR; defined as the ratio of the major to minor axis of the particles) of the microparticles. For this purpose, we focused on synthesis of microparticles

templated by bipolar or radial droplets because of the drastically different deswelling behavior observed upon extraction of 5CB for these two configurations. Figure 11-4A shows that the shape of polymeric microparticles formed from bipolar droplets changed from ellipsoidal to spherical with increase in the composition of RM257. We attribute this to a decrease in deswelling during the process of extraction of 5CB caused by the higher density of polymer chains (and cross-links) within the droplets. In contrast, the shape of the particles remained spherical after removal of 5CB for polymerized radial droplets at all compositions of RM257. The aspect ratio of the polymeric microparticles as a function of the percentage of RM257 in the LC mixture for particles with a major axis between 5 and 10 μm templated from bipolar or radial droplets is shown in Figure 11-4B. Consistent with our interpretation above, we observed a decrease in aspect ratio with increase in reactive monomer for microparticles formed from bipolar droplets. In contrast, the aspect ratio was constant with increase in reactive monomer for particles formed from radial droplets. These results led us to conclude that the shape and aspect ratio of microparticles can be finely tuned by varying the composition of the reactive monomer RM257 doped into the LC droplets.

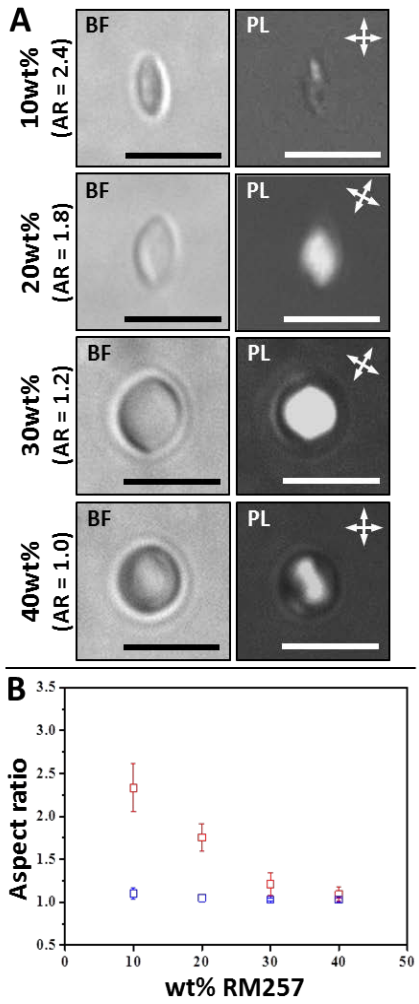

Figure 11-4. Control over the aspect ratios (AR) of polymer microparticles by the amount of RM257 doped into the LC used as templates.

(A) Optical micrographs of ellipsoidal particles formed from polymerized bipolar particles of different RM257 composition following extraction of 5CB. Corresponding BF and PL micrographs are shown on the left and right, respectively, for each composition. The aspect ratio (AR) of each microparticle is indicated. The orientation of the crossed polarizers in PL micrographs is indicated by the white double headed arrows. Scale bars: 10 μm. (B) Aspect ratio of particles with a major axis between 5 and 10 μm as a function of percentage of RM257. Red and blue represent particles templated by the bipolar and radial configuration, respectively.

In the final experiment reported in this chapter, we characterized the surface morphology of polymer microparticles templated from bipolar or radial LC droplets by scanning electron

microscopy (SEM) to determine if this property of particles is also correlated to the internal configuration of the LC template. These two LC droplet templates were selected because the surface anchoring of LCs for the two droplet configurations is in maximum contrast. Figure 11-5 reveals that the surface morphology of ellipsoidal particles is smooth, whereas the surface morphology of spherical particles formed from radial droplets is rough. This observation is consistent with our above conclusion that the alignment of the polymer chains is along the director of the LC, and reveals yet another property of the polymer particles which can be tailored by manipulation of the configuration of the LC droplet from which the particles are templated.

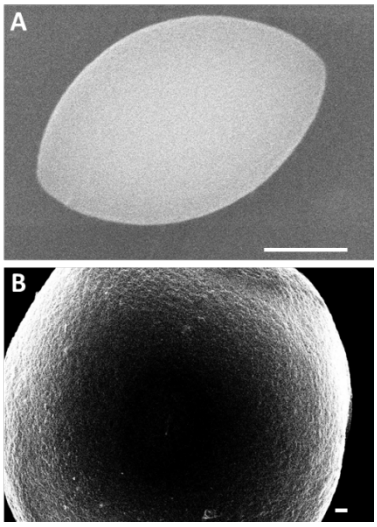

Figure 11-5. SEM images of (A) an ellipsoidal (lemon-shaped) microparticle or (B) a spherical microparticle.

The concentration of RM257 was 20 % wt/wt based on the mass of LC phase. Scale bars: 2 μm.

11.4 Conclusions

The results reported in this chapter reveal that water-dispersed LC microdroplets represent a rich palette of templates for synthesis polymer particles. Remarkable control over the

shape and surface morphology of the polymer particles was achieved through chemical manipulation of the surface anchoring of LC, which led to transformations in the internal configurations of the droplets. Bipolar, radial, axial, or preradial configurations of the droplets led to lemon-shaped, spherical, rod-shaped, or pear-shaped particles, respectively. The shape of particles was further manipulated by changes in the amount of monomer from which the particles were synthesized doped into the LC. Overall, the set of design rules that emerged from this study will guide synthesis of polymer particles of anisotropic shape which might be useful in applications ranging from intracellular delivery to biocatalysis.

11.5 References

*This chapter is presents the results of a collaborative research project. I worked together on the project with Xiaoguang Wang, Emre Bukusoglu, Marco A. Bedolla Pantoja, and Nicholas L. Abbott and Jie Xiang and Oleg D. Lavrentovich from Kent State Unversity. My contribution to the project was in performing the experiments with Xiaoguang Wang to obtain the data for Figures 11-1 through 11-4. The chapter is prepared for submission to the journal *Chemistry of Materials*.

1. Chithrani, B. D.; Ghazani, A. A.; Chan, W. C., Determining the Size and Shape Dependence of Gold Nanoparticle Uptake into Mammalian Cells. *Nano Letters* **2006,** 6, 662-668.
2. Muro, S.; Garnacho, C.; Champion, J. A.; Leferovich, J.; Gajewski, C.; Schuchman, E. H.; Mitragotri, S.; Muzykantov, V. R., Control of Endothelial Targeting and Intracellular Delivery of Therapeutic Enzymes by Modulating the Size and Shape of ICAM-1-Targeted Carriers. *Molecular Therapy* **2008,** 16, 1450-1458.
3. Madivala, B.; Vandebril, S.; Fransaer, J.; Vermant, J., Exploiting Particle Shape in Solid Stabilized Emulsions. *Soft Matter* **2009,** 5, 1717-1727.
4. Tian, N.; Zhou, Z.-Y.; Sun, S.-G.; Ding, Y.; Wang, Z. L., Synthesis of Tetrahexahedral Platinum Nanocrystals with High-Index Facets and High Electro-Oxidation Activity. *science* **2007,** 316, 732-735.
5. Cui, C.; Gan, L.; Heggen, M.; Rudi, S.; Strasser, P., Compositional Segregation in Shaped Pt Alloy Nanoparticles and Their Structural Behaviour During Electrocatalysis. *Nature Materials* **2013,** 12, 765-771.
6. Mondiot, F.; Wang, X.; de Pablo, J. J.; Abbott, N. L., Liquid Crystal-Based Emulsions for Synthesis of Spherical and Non-Spherical Particles with Chemical Patches. *Journal of the American Chemical Society* **2013,** 135, 9972–9975.
7. Whitmer, J. K.; Wang, X.; Mondiot, F.; Miller, D. S.; Abbott, N. L.; Pablo, J. J. d., Nematic-Field Driven Positioning of Particles in Liquid Crystal Droplets. *Physical Review Letters* **2013,** 111, 227801.
8. Wang, X.; Miller, D. S.; Pablo, J. J. d.; Abbott, N. L., Reversible Switching of Liquid Crystalline Order Permits Synthesis of Homogeneous Populations of Dipolar Patchy Microparticles. *Advanced Functional Materials* **2014 (In Press)**.
9. Whitmer, J. K.; Wang, X.; Mondiot, F.; Miller, D. S.; Abbott, N. L.; Pablo, J. J. d., Nematic-Field Driven Positioning of Particles in Liquid Crystal Droplets. *Physical Review Letters* **2013,** 111, 227801.
10. Gennes, P.-G. d.; Prost, J., *The Physics of Liquid Crystals*. 2nd ed.; Oxford University Press: New York, NY, USA, 1993.
11. Miller, D. S.; Wang, X.; Abbott, N. L., Design of Functional Materials Based on Liquid Crystalline Droplets. *Chemistry of Materials* **2013,** 26, 496–506.
12. Drzaic, P. S., *Liquid Crystal Dispersions*. World Scientific: River Edge, NJ, USA, 1995.
13. Gupta, J. K.; Sivakumar, S.; Caruso, F.; Abbott, N. L., Size-Dependent Ordering of Liquid Crystals Observed in Polymeric Capsules with Micrometer and Smaller Diameter. *Angewandte Chemie-International Edition* **2009,** 48, 1652-1655.

14. Gupta, J. K.; Zimmerman, J. S.; de Pablo, J. J.; Caruso, F.; Abbott, N. L., Characterization of Adsorbate-Induced Ordering Transitions of Liquid Crystals within Monodisperse Droplets. *Langmuir* **2009,** 25, 9016-9024.
15. Lin, I. H.; Miller, D. S.; Bertics, P. J.; Murphy, C. J.; de Pablo, J. J.; Abbott, N. L., Endotoxin-Induced Structural Transformations in Liquid Crystalline Droplets. *Science* **2011,** 332, 1297-1300.
16. Miller, D. S.; Abbott, N. L., Influence of Droplet Size, pH and Ionic Strength on Endotoxin-Triggered Ordering Transitions in Liquid Crystalline Droplets. *Soft Matter* **2013,** 9, 374-382.
17. Berggren, E.; Zannoni, C.; Chiccoli, C.; Pasini, P.; Semeria, F., Computer-Simulations of Nematic Droplets with Bipolar Boundary-Conditions. *Physical Review E* **1994,** 50, 2929-2939.
18. Meyer, R. B., Piezoelectric Effects in Liquid Crystals. *Physical Review Letters* **1969,** 22, 918.
19. Ondris-Crawford, R.; Boyko, E. P.; Wagner, B. G.; Erdmann, J. H.; Zumer, S.; Doane, J. W., Microscope Textures of Nematic Droplets in Polymer Dispersed Liquid-Crystals. *Journal of Applied Physics* **1991,** 69, 6380-6386.
20. Prischepa, O. O.; Shabanov, A. V.; Zyryanov, V. Y., Transformation of Director Configuration upon Changing Boundary Conditions in Droplets of Nematic Liquid Crystal. *JETP Letters* **2004,** 79, 257-261.
21. Volovik, G. E.; Lavrentovich, O. D., The Topological Dynamics of Defects - Boojums in Nematic Drops. *Zhurnal Eksperimentalnoi I Teoreticheskoi Fiziki* **1983,** 85, 1997-2010.
22. Carlton, R. J.; Hunter, J. T.; Miller, D. S.; Abbasi, R.; Mushenheim, P. C.; Tan, L.; Abbott, N. L., Chemical and Biological Sensing Using Liquid Crystals. *Liquid Crystal Reviews* **2013,** 1, 1-23.
23. Miller, D. S.; Wang, X.; Buchen, J.; Lavrentovich, O. D.; Abbott, N. L., Analysis of the Internal Configurations of Droplets of Liquid Crystal Using Flow Cytometry. *Analytical Chemistry* **2013,** 85, 10296-10303.
24. Hiemenz, P. C.; Rajagopalan, R., *Principles of Colloid and Surface Chemistry*. 3rd ed.; Marcel Dekker: New York, NY, USA, 1997.

Chapter 12. Summary and Recommendations for Future Directions

12.1 Summary

The studies reported in this thesis revealed physiochemical principles for the design of functional materials based on water-dispersed microdroplets of thermotropic liquid crystal (LC). The materials fall under two categories: (i) LC-in-water emulsion-based biological sensors; and (ii) spherical and non-spherical microparticles with or without chemical patches synthesized from the droplets of LC-in-water emulsions. Below, the principles elucidated for design of these materials are summarized.

12.1.1 Principles for Design of Biological Sensors based on Nematic LC-in-Water Emulsions

The first five studies reported in this thesis revealed principles for design of biological sensors based on nematic LC-in-water emulsions. In the first study, a fundamentally new mechanism for transformations of the internal structure of LC microdroplets (ordering transitions) was discovered that involved an ordering transition from a bipolar state of the droplets to a radial one triggered by addition of picogram per milliliter (pg/mL) concentrations of bacterial endotoxin (or lipid A) to the surrounding aqueous medium. In contrast to previous studies in which such ordering transitions were driven by adsorption of ~10^7 lipid molecules to the surfaces of droplets,[1-5] endotoxin triggered the transitions *via* a localized interaction of ~10^3 molecules with topological defects present within the droplets. In the second study, several

important design rules to achieve the exquisite sensitivity of LC droplets to endotoxin were unveiled. Significantly, it was found that the ordering transition requires a delicate balance of surface anchoring and bulk elastic energies of LC droplets which can be achieved by tuning both droplet size and solution conditions (ionic strength or pH) of the confining aqueous medium.

Two additional key findings reported in the first study include: (i) the ordering transitions triggered by endotoxin are selective to its molecular architecture relative to other common amphiphiles; and (ii) fluorescently labeled endotoxin was observed to localize within the core defect of radial LC droplets. When combined with the prediction of a thermodynamic model presented in the second study that the influence of endotoxin on the free energy of a LC droplet is consistent with the energetics of self-assembly of 10^3 endotoxin molecules (~10^{-17} J), these findings strongly suggest that endotoxin formed an inverted assembly within the core defect of the final radial configuration to stabilize it relative to the initial bipolar configuration.

The third study revealed a novel methodology for rapid determination of configurations of water-dispersed LC microdroplets based on measurement of light scattered by droplets as they are passed through the flow focusing device in a flow cytometer. The method relied on differences in the rotational symmetry of the refractive index environments of bipolar and radial droplets. The spherically symmetric environment characteristic of radial droplets caused them to scatter light as droplets of isotropic oils, whereas the rotational anisotropy of the environment of bipolar droplets led to more complex light scattering. The light scattering behavior of radial droplets, which was predicted by a form factor analysis that accounted for interference effects, gave rise to a peak in frequency histograms of low angle light scattering (< 15° away from incidence) measured for dispersions of radial droplets relative to those measured for bipolar droplets. In dispersions that contained a mixture of bipolar and radial droplets, the peak grew

with increase in concentration of radial droplets and its integrated area relative to the area under a peak measured for a dispersion of only radial droplets was found to be directly correlated to optical microscopy measurements of the percentage of radial droplets (coefficient of determination of 0.98). When compared to optical microscopy, this new method for determination of the percentage of radial droplets in LC emulsions provides the basis of a more rapid and statistically robust method of analysis (droplets are measured at rates of up to 10,000 droplets per second compared to ~100 droplets per hour). Thus, the method should streamline readout of chemical and biological assays based on the response of LC microdroplets to external stimuli.

In the fourth study, the facile nature of the analytical methodology reported in the third enabled fundamental insights into interaction of endotoxin with LC droplets. First, the methodology was used to demonstrate that endotoxin from *Escherichia coli*, *Salmonella minnesota* or *Pseudomonas aeruginosa* all lead to quantitatively similar responses in the LC droplets, which suggests a conserved molecular level mechanism for these three endotoxins. Second, by varying the number of LC droplets in a dispersion containing endotoxin, it was demonstrated that the LC droplets respond to the state of aggregation of the endotoxin in solution. This key insight both will enable further optimization of LC-in-water emulsions for detection of biological species that aggregate in solution, and suggests a novel methodology to probe the aggregation state of endotoxin in solution at concentrations below current optical techniques. The latter has important implications for public health as aggregation of endotoxin has been proposed previously to play a role in cellular responses to endotoxin.[6]

In the final study, the flow cytometry-based readout for LC droplet order was exploited for quantitative detection of membrane-derived microvesicles (MVs) shed by cells that were

selectively captured via antibody-mediated interactions. Detection of MVs is important because they are being investigated for their role in intercellular communication and as potential biomarkers of disease.[7-9] The technique reported in the study was substantially more sensitive than techniques such as immunoblotting (limit of detection of 10^6 MVs compared to $>10^8$)[10-12] because the lipid-component of the MVs served to amplify the antibody-mediated capture of the target proteins in the MVs.

The principles defined in the first series of investigations should have a twofold impact on future designs of stimuli responsive LC droplets. First, they provide a guide to engineer LC emulsions to maximize the sensitivity of LC droplets to external stimuli. Second, they reveal a rapid methodology for readout of chemical and biological assays based on ordering transitions in LC droplets which could enable the design of low cost commercial sensors based on these materials. In addition, the studies demonstrate that LC-in-water emulsions can be utilized for quantitative determination of the amount of two medically important species in aqueous solutions – bacterial endotoxins and cell-shed MVs. With further optimization, the systems reported in the studies may develop into low cost alternatives for current sensors of these species.

12.1.2 Principles for Design of Spherical and Non-Spherical Polymer Microparticles with or without Chemical Patches Synthesized from LC-in-Water Emulsions

The last three studies reported in this thesis revealed principles for the design of spherical and non-spherical polymer microparticles with or without chemical patches synthesized from LC-in-water emulsions. The results of these three studies are summarized below.

First, a technique was presented to overcome the existence of multiple local energetic minima for the positions of colloids on the surfaces of LC droplets (corresponding to surface

defects) which generate kinetic traps for the colloids and result in heterogeneous populations of patchy microparticles. It used adsorbate-driven switching of the internal configurations of LC droplets to sweep colloids to a single location, thus resulting in the synthesis of homogeneous populations of patchy microparticles. The utility of the technique was illustrated through synthesis of “Janus-like” microparticles and magnetically-responsive patchy microdroplets of LC with either dipolar or quadrupolar symmetry that exhibited distinct optical responses upon application of an external magnetic field.

Second, forces that govern organized assemblies of colloids that induce tangential anchoring of LC formed at the poles of micrometer-sized droplets of LC in a bipolar configuration were revealed. Through a combination of experiments and an analytical model it was found that the assemblies, which most frequently mapped onto a local (non-close packed) hexagonal lattice, were the result of: (i) a long-range attraction between the adsorbed colloids due to the increasing rate of strain (splay) of LC near the surface defects (splay attraction), (ii) a shorter-range attractive interaction that reflects the quadrupolar symmetry of the strain in the LC around the adsorbed colloids, and (iii) a repulsive interaction between colloids that reflects the presence of an electrical double layer at the aqueous interface of the sulphate-terminated colloids.

Finally, it was revealed that different configurations of LC microdroplets allow a remarkable level of control over the shape and surface morphology of polymer microparticles synthesized from the droplets. The configurations were accessed in a highly controlled manner by chemical manipulation of the surface anchoring of LC droplets. Further control over particle shape was permitted by changes in the amount of monomer doped into the LC from which the particles were synthesized.

The results of the second series of investigations defined principles for control over the synthesis of an exciting new class of soft materials based on LC-in-water emulsions. The full potential of the materials has yet to be realized as they might become useful in applications ranging from intracellular delivery to biocatalysis. Therefore, the physiochemical principles presented in this thesis should enable design of not only biosensors or polymer microparticles based on LC-in-water emulsions, but also a broad range of functional soft materials. I end this summary by noting that the systems studied in this thesis also provide important insights into complex phenomena observed in biological membranes where elastic stresses associated with membrane curvature lead to concentration of lipids and/or proteins within areas of high curvature.[13-15]

12.2 Recommendations for Future Directions

An important finding in this thesis was that water-dispersed microdroplets of LC are exquisitely sensitive reporters of bacterial endotoxins. Several experimental observations support that endotoxin triggers a bipolar-to-radial ordering transition of the droplets *via* formation of an inverted self-assembly within the core defect of radial droplets. This conclusion elicits many questions regarding the phenomenon of self-assembly of amphiphiles within liquid crystalline systems. First, what types of assemblies do other amphiphiles form in these systems? Second, will assemblies of other amphiphiles also localize within the cores of defects present in LCs? Finally, can the self-assembled structures formed by amphiphiles in LCs be correlated to molecular architecture, as is the case for molecular self-assembly in isotropic media?[16] To address these questions and others my colleague Xiaoguang Wang is conducting several experimental investigations.

The remarkable selectivity of the bipolar-to-radial ordering transition in LC microdroplets within the pg/mL range of adsorbate to the molecular architecture of endotoxins and lipid A relative to other amphiphiles also raises an important question: Is it possible to synthesize a mimic of endotoxin or lipid A that will also trigger the transition? If a mimic could successfully be synthesized, the freedom to engineer the properties of the molecule could open the door to a new range of sensors based on LC microdroplets. Recently, under the direction of Professor David M. Lynn, Matthew C. D. Carter has synthesized a molecule able to trigger the transition within the pg/mL range. Together, Matthew, Xiaoguang Wang, and I have begun to characterize its molecular architecture relative to that of lipid A to understand the mechanism by which it drives the transition. In the future, this avenue of investigation should lead to the discovery of molecules which are both fundamentally intriguing and could enable new designs of materials based on LC-in-water emulsions.

Another interesting future direction would be to extend the work in the second series of investigations to more complex phases of LCs. For example, the complex arrays of topological defects presented by droplets of LC in smectic, chiral, or blue phases could enable design of several novel soft materials.[17, 18] In addition, the fast optical responses of blue phases to external stimuli compared to the nematic phase (microseconds compared to milliseconds)[19] could make materials based on droplets of LC in blue phases superior to those based on the droplets studied in this thesis for optical applications.

Finally, as mentioned above, I believe that the principles defined by the second series of experimental investigations will enable designs of several functional materials based on LC-in-water emulsions. For example, it should be possible to localize nanoparticles or self-assembled structures within the core defect of radial droplets, and trigger their release by adsorption of

micrometer-sized colloids at the droplet surfaces. Additionally, this idea could be extended to release of materials within cells (*e.g.*, therapeutics) if current investigations on internalization of LC droplets by living cells prove to be successful. I end by noting that the ability to prepare faceted droplets of chromonic LCs has recently been demonstrated.[20] If these droplets can also be used as templates for material synthesis, I predict that they will enable synthesis of catalysts based on LC droplets, as facets often act as catalytic hotspots.[21, 22]

12.3 References

1. Prischepa, O. O.; Shabanov, A. V.; Zyryanov, V. Y., Transformation of Director Configuration upon Changing Boundary Conditions in Droplets of Nematic Liquid Crystal. *JETP Letters* **2004,** 79, 257-261.
2. Volovik, G. E.; Lavrentovich, O. D., The Topological Dynamics of Defects - Boojums in Nematic Drops. *Zhurnal Eksperimentalnoi I Teoreticheskoi Fiziki* **1983,** 85, 1997-2010.
3. Brake, J. M.; Daschner, M. K.; Luk, Y. Y.; Abbott, N. L., Biomolecular Interactions at Phospholipid-Decorated Surfaces of Liquid Crystals. *Science* **2003,** 302, 2094-2097.
4. Meli, M. V.; Lin, I. H.; Abbott, N. L., Preparation of Microscopic and Planar Oil-Water Interfaces that are Decorated with Prescribed Densities of Insoluble Amphiphiles. *Journal of the American Chemical Society* **2008,** 130, 4326-4333.
5. Sivakumar, S.; Wark, K. L.; Gupta, J. K.; Abbott, N. L.; Caruso, F., Liquid Crystal Emulsions as the Basis of Biological Sensors for the Optical Detection of Bacteria and Viruses. *Advanced Functional Materials* **2009,** 19, 2260-2265.
6. Mueller, M.; Lindner, B.; Kusumoto, S.; Fukase, K.; Schromm, A. B.; Seydel, U., Aggregates are the Biologically Active Units of Endotoxin. *Journal of Biological Chemistry* **2004,** 279, 26307-26313.
7. Martins, V. R.; Dias, M. S.; Hainaut, P., Tumor-cell-derived microvesicles as carriers of molecular information in cancer. *Current Opinion in Oncology* **2013,** 25, 66-75.
8. van Doormaal, F. F.; Kleinjan, A.; Di Nisio, M.; Buller, H. R.; Nieuwland, R., Cell-derived microvesicles and cancer. *Netherlands Journal of Medicine* **2009,** 67, 266-273.
9. Al-Nedawi, K.; Meehan, B.; Rak, J., Microvesicles Messengers and mediators of tumor progression. *Cell Cycle* **2009,** 8, 2014-2018.
10. Günter, M., Novel Tools for the Study of Cell Type-Specific Exosomes and Microvesicles. *Journal of Bioanalysis & Biomedicine* **2012,** 4, 46-60.
11. Osumi, K.; Ozeki, Y.; Saito, S.; Nagamura, Y.; Ito, H.; Kimura, Y.; Ogura, H.; Nomura, S., Development and assessment of enzyme immunoassay for platelet-derived microparticles. *Thrombosis and Haemostasis* **2001,** 85, 326-330.
12. Sidhu, S. S.; Mengistab, A. T.; Tauscher, A. N.; LaVail, J.; Basbaum, C., The microvesicle as a vehicle for EMMPRIN in tumor–stromal interactions. *Oncogene* **2004,** 23, 956-963.
13. Oliver, P. M.; Crooks, J. A.; Leidl, M.; Yoon, E. J.; Saghatelian, A.; Weibel, D. B., Localization of Anionic Phospholipids in Escherichia Coli Cells. *Journal of Bacteriology* **2014**, JB. 01877-14.
14. Renner, L. D.; Weibel, D. B., Cardiolipin Microdomains Localize to Negatively Curved Regions of Escherichia Coli Membranes. *Proceedings of the National Academy of Sciences* **2011,** 108, 6264-6269.
15. Renner, L. D.; Weibel, D. B., MinD and MinE Interact with Anionic Phospholipids and Regulate Division Plane Formation in Escherichia Coli. *Journal of Biological Chemistry* **2012,** 287, 38835-38844.
16. Israelachvili, J. N., *Intermolecular and Surface Forces*. 2nd ed.; Academic Press London: San Diego, CA, USA, 1991.

17. Lopez-Leon, T.; Fernandez-Nieves, A., Drops and Shells of Liquid Crystal. *Colloid and Polymer Science* **2011,** 289, 345-359.
18. Fukuda, J.; Zumer, S., Novel Defect Structures in a Strongly Confined Liquid-Crystalline Blue Phase. *Physical Review Letters* **2010,** 104, 017801.
19. Xu, D.; Rao, L.; Tu, C.-D.; Wu, S.-T., Nematic Liquid Crystal Display with Submillisecond Grayscale Response Time. *Journal of Display Technology* **2013,** 9, 67-70.
20. Jeong, J.; Davidson, Z. S.; Collings, P. J.; Lubensky, T. C.; Yodh, A., Chiral Symmetry Breaking and Surface Faceting in Chromonic Liquid Crystal Droplets with Giant Elastic Anisotropy. *Proceedings of the National Academy of Sciences* **2014,** 111, 1742-1747.
21. Tian, N.; Zhou, Z.-Y.; Sun, S.-G.; Ding, Y.; Wang, Z. L., Synthesis of Tetrahexahedral Platinum Nanocrystals with High-Index Facets and High Electro-Oxidation Activity. *science* **2007,** 316, 732-735.
22. Cui, C.; Gan, L.; Heggen, M.; Rudi, S.; Strasser, P., Compositional Segregation in Shaped Pt Alloy Nanoparticles and Their Structural Behaviour During Electrocatalysis. *Nature Materials* **2013,** 12, 765-771.

Appendix A. Nematic-Field-Driven Positioning of Particles in Liquid Crystal Droplets*

A.1 Introduction

Liquid crystals (LCs) exhibit thermodynamic and structural properties that are intermediate between those expected from ordinary solid and liquid states. Though structurally liquid, molecules within LCs can adopt distinct orientations, resulting in a new palette of technologically useful phases. Spherical confinement of LCs results in two primary morphologies. Bipolar droplets are formed when LCs prefer to order tangent to the interface (planar anchoring), creating two point defects (boojums) on their surfaces as a consequence of the Poincaré–Hopf theorem.[1] Radial morphologies appear when LC molecules are oriented perpendicular to the interface (homeotropic anchoring). A single ring- or pointlike defect is formed in the center of the droplet, with molecules outside the core aligning with the local radial vector. Uniform, axial, and uniaxial morphologies can also be achieved by tuning the anchoring strength.[2, 3]

Recent work has demonstrated that the tight interplay between the interface of a droplet interface and its interior can lead to the formation of new ordered phases.[4] In such phases, the droplet interior organizes adsorbates at the interface, while the adsorbates also influence the order adopted by the LC. When a critical adsorbate concentration is reached, not only does the interior morphology of the droplet change from bipolar to homeotropic, but spherical or striped adsorbate domains also self-organize on the surface due to the interplay of enthalpy and elastic stresses. The question addressed in this appendix, which from a practical perspective is more

intriguing, is whether the interior morphology of a LC droplet can be used to control the positioning of small particles at its interface. If possible, the resulting nanoparticle-decorated droplets would provide a promising new route for templated assembly of functional patchy particles,[5] as well as for development of primed sensing devices, whose morphology is balanced on the edge of a knife to be swayed by vanishing concentrations of analyte.[6]

A.2 Results and Discussion

Small particles or impurities in a nematic LC are known to exhibit a preference for phase boundaries and defect regions.[7] In pioneering experiments on bulk LC emulsions, optical traps were utilized to demonstrate the affinity between colloidal particles and a locally melted nematic phase.[8, 9] Further work has shown colloidal particles to have an affinity for disclination lines, useful in templated nanowire assembly.[7, 10-14] Defect affinity, combined with self-assembly of surfactant molecules, is thought to be partly responsible for the exquisite sensitivity of droplet biosensors.[6, 15] While recent investigations of nematic double-emulsions[16] also indicate that an intricate interplay exists between defects on the interior and exterior droplets, studies of nanoparticles at LC droplet interfaces are not available.

Experimentally, we observe this behavior for larger droplet–particle combinations. Figure A-1 shows a series of micrographs for bare (Figure A-1(a) and A-1(b)) 5CB droplets and those decorated with one (Figure A-1(f)–A-1(h)) or two (Figure A-1(k)–A-1(m)) fluorescent polystyrene particles. Additional details regarding the experimental system are provided in the Supporting Information. Images generated using bright field, polarized light, and fluorescence microscopy reveal the interior morphology of the droplet and the presence of particles at the

defects. The forces holding these particles are strong — particles never leave their adopted defect unless the LC is heated through the clearing point.

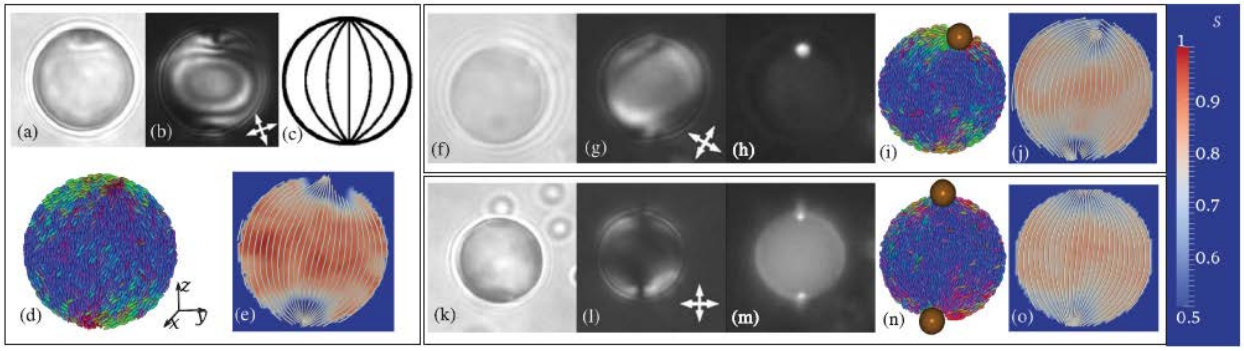

Figure A-1. Partitioning of polystyrene colloids to the boojums of bipolar LC droplets. Experimental images of 5CB droplets in water emulsions with zero (a),(b), one (f)–(h), or two (k)–(m) adsorbed polystyrene particles. Bright field, polarized light and fluorescence images (particle cases only) are shown alongside simulated systems depicting a $\sigma = 10\sigma_o$ particle adsorbed onto a Gay-Berne droplet of radius $R = 25\sigma_o$. Mesogens are colored by an (r, g, b) value representing their (*x*, *y*, *z*) orientation. The cartoon in (c) depicts the field lines expected in a bipolar morphology. (d) Snapshot of a bare droplet with planar anchoring, alongside a plot of the scalar order parameter (*S*) and field lines within the droplet (e). The axes are given next to this plot for clarity; subsequent views are rotated, but preserve the (r, g, b) color mapping. The boojum defects are clearly visible for their low value of *S* and as confluence points for the field lines. For clarity, field lines are projected onto the viewing plane. Importantly, it can be seen that the defect is $\approx 5\sigma_o$ in radius. Simulation results for a single adsorbed particle (i),(j), and two adsorbed particles (n),(o) are also shown. The region of disorder within these droplets (prior to the adsorption of particles) coincides exactly with the particle positions. Overall nematic ordering is similar in each case, suggesting each configuration minimizes the LC elastic cost. In both simulation and experiment, the particles are approximately the size of the defect core. The order parameter scale for maps (e), (j), (o) is given on the right panel.

To address the origin and strength of these forces, we implement a molecular model utilizing a Gay–Berne (GB) representation of the LC,[17-20] with particles modeled by spheres of varying diameter. As the GB ellipsoids represent single molecules, this necessarily examines smaller length scales than those accessible in the experiments, and serves to provide a

comprehensive view of particles in LC droplets that encompasses mesoscopic and microscopic length scales. Comparison between the two is justified provided the two systems exhibit the same morphology, as the driving forces in colloidal aggregation will be elastic stresses associated with the presence of defects. In the following discussion, lengths are reduced by the ellipsoid minor diameter σ_o, energies by the Gay–Berne interaction strength ε, and masses by the mesogen mass m;[21] this sets a natural timescale at $t_o = \sqrt{m{\sigma_o}^2/\varepsilon}$. Anchoring and particle confinement inside a drop of radius $R = 25$ are handled by a modified 9-3 Lennard-Jones wall,[22] which enforces a spherical shape to mimic that of larger aqueous droplets. Our approach differs from that in recent investigations of LC droplets in equilibrium with their own vapor, which adopt tactoid shapes.[23, 24] We explicitly aim to avoid these geometries, and use our results for spherical geometries to connect with experiments on spherical droplets an order of magnitude larger,[25] which are prohibitive to molecular simulation. Note that past work has indeed shown that results for GB systems at small length scales can be mapped onto those of continuum models at much longer length scales.[26] Additional details are provided in the Supporting Information.

After evolving the droplet interior to its equilibrium nematic configuration through *NVT* molecular dynamics simulations, we place a particle near the surface, at a radius $r = 23$, deleting any overlapping mesogens. This is done for two types of configurations: polar placement (where the particle is placed at a boojum defect), and equatorial placement (between the two boojums). Following this, two types of simulations are performed to probe dynamic and thermodynamic behavior. The dynamics are monitored for $2 \times 10^5 t_o$ in standard *NVT* molecular dynamics. Slow diffusion renders simple MD insufficient to sample free energies, hence, free energies are calculated through a biased molecular dynamics approach.

Representative configurations for particles of diameter $\sigma = 10$ placed on the surface of a droplet are given alongside the experimental images in Figure A-1.[27] Mixing rules for the GB potential[28, 29] imply planar anchoring is energetically preferred, though the actual anchoring for large particles ($\sigma \in \{8,10\}$) is closer to homeotropic (*cf.*, Figure A-1(i) and A-1(n)). High-splay regions are eliminated (*cf.*, Figure A-1(e)) when a particle is located at a boojum defect, indicating that a strong preference should exist for this region. When a particle occupies this state, the disorder and elastic stress associated with the defect are eliminated. Importantly, for the $\sigma = 10$ particle depicted in the figure, the particle and boojum sizes are nearly equal. The competition in boundary conditions between particle LC and surface LC may even be enough to deform the droplet into a more elongated object to balance surface tension,[30] though the rigid boundaries here prevent this. Smaller particles exhibit more planarlike orientation.[28, 31] A combination of entropic and anchoring effects also limits configurations available to the particle. In simulation, larger particles ($\sigma \in \{8,10\}$) were observed primarily at the droplet interface, while smaller particles roamed the entire droplet volume.

This behavior is apparent from results shown in Figure A-2(a), where a histogram of particle positions (obtained from standard *NVT* molecular dynamics simulations of length $2 \times 10^5 t_o$) is plotted. Simulations were prepared by placing a particle at the interface of the droplet and allowing it to diffuse around the droplet. Note that a uniform distribution over the volume of the droplet would be proportional to $(R^2 - z^2)$, which corresponds to the dotted line. These histograms are averaged over a set of six independent simulations; three having initial conditions near the equator, and three starting at the poles. The smallest particles examined here, $\sigma = 2$, roam throughout the droplet and do not exhibit a preferred location. Increasing the particle size brings segregation toward the poles of the droplet. To study the segregation dynamics, we follow

the alignment of the normalized position vector $\hat{\boldsymbol{r}}$ of each particle relative to the nematic ordering vector $\hat{\boldsymbol{n}}$ for the two largest particles considered here. The results are plotted in Figure A-2(b) and A-2(c). Each particle exhibits a pronounced preference for the interfacial boojum defect. In the case of particles having $\sigma = 10$, particles placed at a polar region have a strong tendency to remain there, while particles placed at the equator segregate to the defect. This can be clearly seen in Figure A-2(c), where the green equatorial trajectories segregate toward the poles over the duration of a simulation despite slow diffusive motion of the particle in dense nematic LC. The polar trajectories retain configurations where the nematic axis is aligned with the particle position vector (though occasional fluctuations away from this alignment are observed). This behavior is suggestive of the presence of deep attractive wells for particles to the boojums.

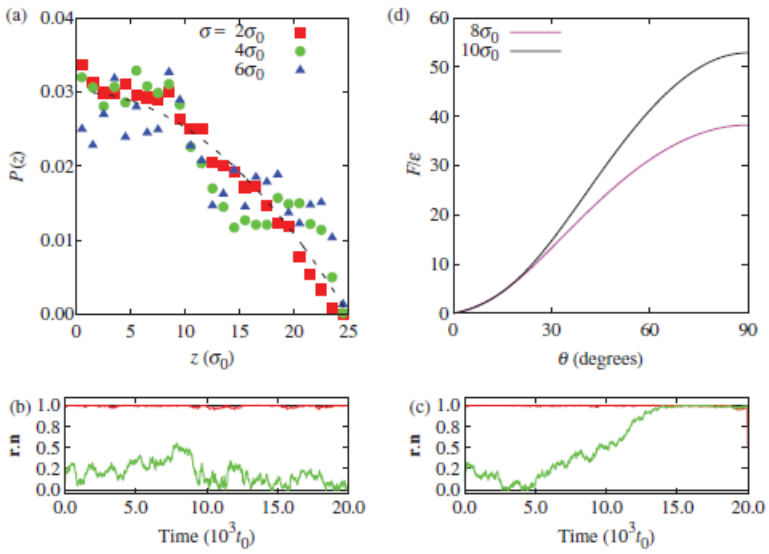

Figure A-2. Influence of colloid size on the partitioning of polystyrene colloids to boojums.
(a) Probability distribution for particles as a function of distance along the nematic axis $\hat{\boldsymbol{n}} = \hat{\boldsymbol{z}}$ from standard *NVT* simulation trajectories. The poles of the droplet are located at z = 25 and z = -25, respectively. The distribution trends toward polar regions as the particle size is increased. Statistics are coarsened by slow diffusion for large particles, which are not shown for clarity. The dashed line corresponds to a uniform volume distribution. (b),(c) Representative trajectories from simulations with (b) $\sigma = 8\sigma_o$ and (c) $\sigma = 10\sigma_o$. Red lines denote trajectories which start at a boojum defect, while green lines denote trajectories originating from the equator of the droplet. A distinct preference for the boojum region is observed in both cases. The $\sigma = 10\sigma_o$ particle segregates to one of the boojums through rotation of the nematic vector, while the $\sigma = 8\sigma_o$ particle remains in its initial misaligned configuration. (d) Potential of mean force for particles of size $\sigma = 8\sigma_o$ and $\sigma = 10\sigma_o$ as a function of the angle θ formed by the radial position of the particle and the nematic axis. As the particle size increases, a deep minimum develops at the location of the boojum defects.

In Figure A-2(d), we plot the free energy of interaction (or potential of mean force (PMF)), normalized by ε, between single particles and boojum defects for larger adsorbed colloids. These simulations are performed at temperature $k_{\mathrm{B}}T/\varepsilon = 1.44$, so the PMF may be converted to thermal units dividing by this factor. Here, the nematic director has been constrained to lie along the z axis, and bias is applied to sample particle positions along this axis.

In agreement with the results in Figure A-2(a), we observe a monotonic deepening of the free energy well with increasing particle size. Though small particles are ambivalent to their surroundings, significant free energetic gains of order several tens of $k_{\mathrm{B}}T$ occur as particles are grown to the largest size considered here. As the origin of this free energetic, gain resides in the alleviation of elastic stress. Scaling our results to larger systems such as those amenable to experiment, we expect that only the elastic stress should play a role, as in the segregation of colloidal particles to nematic-isotropic phase boundaries.[32] Importantly, the minima observed for large particles are deep, and may be exploited for robust particle assembly.

Though in Figure A-1 we show the results of ideal two-particle placement, such robust assembly is not always the case. Indeed, as shown in Figures A-3(a)–A-3(d), particles often located near the same defect. As particles are themselves larger than a boojum, this is a suboptimal condition. To quantify this effect, in Figure A-3(e) we plot results of simulations for the free energy of two nanoparticles as a function of separation. These simulations proceed similarly to the one-particle calculations, except that here one particle is fixed in space at $z = 25$, and the nematic axis is free to reorient. This has the effect of fixing one particle at a boojum defect while the other particle is driven around the surface. In this case, the free energy exhibits two minima. Focusing on the free energy curve for $\sigma = 10$, the first minimum occurs when two particles share the same boojum defect, and has a depth of $\approx -25k_{\mathrm{B}}T$ relative to the maximum free energy for $\sigma = 10$ particles where we have utilized $k_{\mathrm{B}}T/\varepsilon = 1.44$. This minimum develops as the nanoparticles are pushed close together, until it is mitigated by the repulsive interactions between overlapping nanoparticles. In the cross-sectional view depicted in Figure A-3(h), one can see that the defect has been annihilated by the presence of the two particles. The second minimum occurs for particles at opposing boojums, and has depth $\approx -50k_{\mathrm{B}}T$, comparable with

the energy found in the one-particle case. The interior structure of the defect is modified when two particles are present at one pole, as evidenced by Figure A-3(i). The central repulsive region ($\theta \approx 90°$ in Figure A-3) contains contributions from strong elastic deformations of the nematic order, bringing the two boojum defects closer together, and from conformations where the driven nanoparticle has escaped the primary boojum, alleviating the elastic cost, but creating further stress associated with its surface anchoring. In metadynamics trajectories,[33, 34] we find that the boojum defect will detach when the particle is driven just past the equator of the droplet (taking the fixed particle and droplet center to define the polar axis). This observation correlates extremely well with the quantitative free energy results of Figure A-3(e), which show a plateau in the free energy when the droplet is near the equator, before presenting a strong second minimum for adjacent particles. This is further elucidated by Figure. A-3(f) and A-3(g), which show the two particles to interact through a region with nematic orientation which differs from the overall director, and which exhibits substantially more orientational disorder.

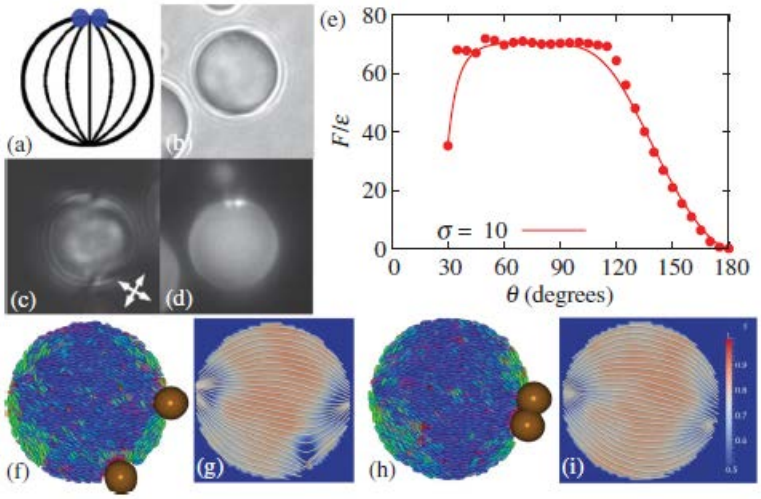

Figure A-3. Local free energy minima on the surfaces of bipolar LC droplets at the site of boojums. (a) Cartoon of two particles located at the same boojum defect, complemented by experimental images from bright field (b), polarized light (c), and fluorescence (d) microscopy. (e) Potential of mean force for two particles of size $\sigma = 10\sigma_o$ one of which is restricted to lie at the position of a boojum defect. The coordinate θ defines the angle between the position vector a particle (relative to the droplet center) and the nematic axis $\hat{\boldsymbol{n}}$. Two minima are observed, with particles either located near the same pole or segregating to opposing poles. The latter case is thermodynamically favorable for the large particle, as particle anchorings and steric effects prevent elastic relaxation within the droplet. Dots represent the computed potential, while the solid line is a Bezier curve approximation to the data. (f)–(i) Instantaneous morphology, order parameter maps, and field lines for two representative configurations of $\sigma = 10\sigma_o$ spheres. (f),(g) Particles separated by a 70° angle in the plane coincident with the center of the droplet. The field lines in (g) show three defect regions, corresponding to the positions of the two particles and the free boojum. The region between the two particles is disordered relative to the bulk; this can be alleviated by the particle proceeding to the occupied boojum as in (h), or by migrating to the free boojum. (g),(h) Two particles sharing the same boojum defect. Interestingly, the field lines depicted in (i) appear to show an additional defect occupying the region between the two interacting particles.

Finally, in Figure A-4, we consider the effects of droplet morphology on particle positioning. Here, surfactant (8 mM sodium dodecyl sulfate (SDS)) is added to the aqueous dispersion to induce homeotropic anchoring on the droplet. Normally, this results in a radial droplet morphology. However, the presence of one (Figure A-4(a)–A-4(c)) or two (Figure A-

4(d)– A-4(f)) particles pins the radial defect. This has the further effect of selecting a single two-particle arrangement from the two competing bipolar arrangements. A similar effect is predicted in simulations by preparing a radial state, and then adjusting the surface anchoring toward the bipolar–radial transition to mimic the addition of surfactant. Here, the radial defect moves from the center of the droplet to the surface and attaches preferentially to the nanoparticle. The presence of these stable states implies that a few adsorbed nanoparticles are sufficient to create morphological changes in LC droplets, which could be utilized in a reversible sequestration process.

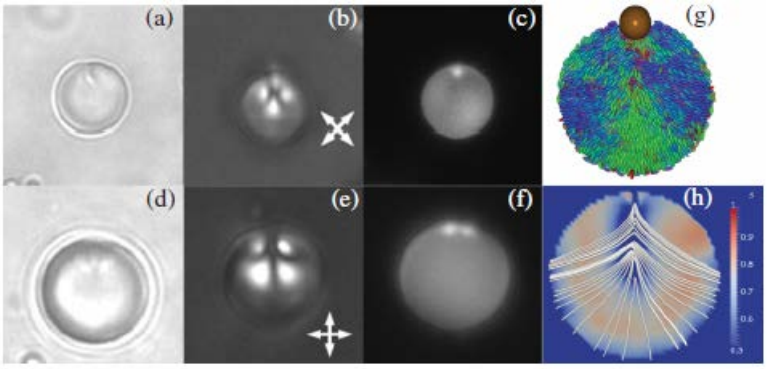

Figure A-4. 'Pinning' of the radial defect to the surface of LC droplet by an adsorbed polystyrene colloid results in a preradial configuration.

(a)–(c) Addition of 8 mM SDS to a droplet with one adsorbed particle results in a pinned preradial defect. Formation of this morphology is robust against the order of surfactant and particle adsorption. (d) – (f) The same method can be used to robustly select morphologies with two particles sharing the preradial defect. (g),(h) Simulations with an adsorbed nanoparticle ($\sigma = 10\sigma_o$) quenched from a radial morphology predict such a structure to occur at the transition from a bipolar to a radial droplet.

A.3 Conclusions

The results reported in this appendix demonstrate the size-dependent segregation of nanoparticles to defect regions in LC droplets. While the droplet sizes examined here are small,

past work has shown that they can be safely extrapolated to longer length scales, more amenable to experimental characterization.[4, 6] The results reported here indicate that nematic droplets can indeed be used to create dipolar functional particles, where the particle on each pole could have different chemical characteristics, and thereby, offer unique possibilities for hierarchical assembly of ordered structures. They also demonstrate that single particles can be used for active displacement of defects and release of a radial defect to an interface. Droplet formation is simple and robust, facilitating the creation of such particles in the laboratory. Extensions of these results to larger surface coverages by nanoparticles are underway.

Acknowledgements

The authors acknowledge support from the Department of Energy, Basic Energy Sciences, Biomaterials Program under Grant No. DE-SC0004025. J.K.W. was partially supported by a NHGRI training grant to the Genomic Sciences Training Program, No. T32HG002760. We gratefully acknowledge the computing resources provided on ‘‘Fusion,’’ a 320-node computing cluster operated by the Laboratory computing Resource Center at Argonne National Laboratory. We acknowledge the University of Chicago Research Computing Center for use of the Midway cluster and support of this work. A portion of this research was performed using resources and the computing assistance of the UW-Madison Center For High Throughput Computing (CHTC), an active member of the Open Science Grid, which is supported by the National Science Foundation and the U.S. Department of Energy’s Office of Science. J. K.W. acknowledges support from UChicago Argonne, LLC, Operator of Argonne National Laboratory (‘‘Argonne’’). Argonne, a U.S. Department of Energy Office of Science laboratory, is operated under Contract No. DE-AC02-06CH11357.

A.4 Supporting Information

This supplementary information contains details of the experimental and simulation techniques used.

A.4.1 Experimental

Nematic droplets are obtained by homogenizing 4 μL 5CB nematogen in 1.98 mL water for 30 seconds at 6,400 rpm. The emulsification is performed by a T25 digital ULTRATURRAX homogenizer equipped with a S25 N-10G dispersing element. The resulting droplets exhibit a bipolar morphology. To prepare particle–droplet configurations, 20 μL of a 1 %wt solution of fluorescent polystyrene particles (Bangs Laboratories, Inc.) are added to the dispersed LC droplets. The mixture is then homogenized for another 30 seconds at 6,400 rpm, which transfers polystyrene particles to the LC surfaces. After homogenization, the size distribution is broad; in the current study, we focus on a subset of droplets having size ≈ 10μm.

The contact angle of the water–5CB–polystyrene interfaces is measured to be approximately 85° by observing the adsorption of a much larger 4.2 μm diameter polystyrene particle (Bangs Laboratories, Inc.). Particles are thus located on the surface of the droplet, approximately half-in and half-out of the nematic phase. The adsorption energy may be estimated from the immersed area of the 5CB droplet, and the energy densities of 5CB–water, PS–water, and 5CB—PS interfaces.[35, 36] This estimate gives a preference of 1.7×10^{-14} J for interfacial adsorption over encapsulation within the droplet, and 2.4×10^{-14} J for adsorption versus aqueous dispersion.

Addition of surfactant creates a transition from the bipolar morphology to a radial morphology in the absence of adsorbed nanoparticles.[6, 15] An intermediate state between bipolar

and radial, identified as preradial, is observed in the transition process. Here, 8mM sodium dodecyl sulfate (SDS) is added to the droplet dispersion to induce homeotropic anchoring on the droplets. Such a concentration is sufficient to transform a bare droplet from a bipolar to radial conformation.[2, 37-40] Addition of polystyrene colloids either before or after the process creates the stable preradial configurations observed for one- and two-particle droplets in the text.

A.4.2 Simulation Model

Our simulations include N = 19,250 particles in a droplet of size $R = 25\sigma$, resulting in a density $\rho = 0.294$. Mesogens are represented as prolate spheroids with an aspect ratio $\kappa = 3$. Our model satisfies the prescription $(\kappa, \kappa', \mu, \nu)$ = (3, 5, 1, 2) in the notation of Bates and Luckhurst.[17] This is closely related to the well-studied (3, 5, 2, 1) model (*e.g.*, Ref [19]). Importantly for our model, at the temperature and density considered in this work, our droplets are nematic. Nanoparticles are represented by spheres of varying diameter, with interactions described through a standard prescription[28, 31] corresponding to the limit of the Gay–Berne interaction when one of the species becomes spherical. Excluding steric repulsions, nanoparticle–mesogen interactions are very weak. Due to entropic effects, this will result in homeotropic anchoring at the surface of the particle for large enough mesogens. In units of the mesogen–mesogen energy scale ε_{o}, mesogen–sphere and sphere–sphere interactions have prefactor $1.44\varepsilon_{\mathrm{o}}$. The simulations are carried out in a modified version of LAMMPS[29] with a timestep $\delta t = 10^{-3} t_{\mathrm{o}}$. All simulations take place at temperature $T = 1.44\varepsilon_{\mathrm{o}}/k_{\mathrm{B}}$, which is below the isotropic-nematic transition at that density. The interparticle potentials for the mesogen–mesogen interactions are given in Figure AS-1. It should be noted that, though energetic mixing rules[28, 31] prescribe a slight preference for planar anchoring homeotropic anchoring results for

larger particles, as this increases the free volume accessible to GB particles. This is evidenced by the length scale separation of steric barriers for the $\sigma = 10\sigma_o$ particle in Figure AS-2 for mesogen–sphere interactions, which is $\approx \sigma/2 < (\kappa - 1)\,\sigma/2$.

A.4.2.1 Confinement

The experimental systems considered here have free boundaries. Such free boundaries, however, cannot be described explicitly in our simulations because comparably sized simulated nematic droplets in equilibrium with their vapor would adopt tactoid shapes, which do not permit comparison to experiment. We thus adopt a model in which the droplet shape and the anchoring preference are enforced simultaneously. The wall is similarly useful to mimic liquid crystal droplets encapsulated by a polyelectrolyte multilayer,[2, 41-43] though this situation presents a more complicated environment for particle dynamics than the experiments of interest in this work.

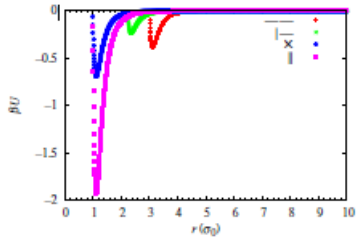

Figure AS-1. Interaction potential for Gay–Berne mesogens using the parameters $(\kappa, \kappa', \mu, \nu)$ = (3, 5, 1, 2) in the notation of Ref. [17].

The configurations correspond to end-to-end (− −), end to side (| −), crossed (×) and side-to-side (| |) arrangements. Crossed mesogens have an interaction equivalent to Lennard-Jones spheres with $\varepsilon = 1$ and $\sigma = 1$.

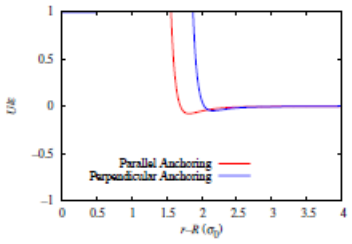

Figure AS-2. Surface anchoring potential of Gay–Berne mesogens to nanoparticle surfaces. This potential is plotted for $\sigma = 10\sigma_o$ particles. Though the interactions are tuned to have effectively no anchoring preference, large particles experience homeotropic anchoring, as this configuration gains free volume near the nanoparticle interface.

Mesogens are confined to a spherical droplet of radius R = 25. Regarding σ_o as 1 nm, a typical minor diameter for the ellipsoid of revolution surrounding mesogens such as 5CB, this system size corresponds to a droplet of diameter 50 nm by a 9–3 Lennard-Jones wall.[22] The implementation of boundaries within our Gay–Berne simulations is simple, but nontrivial. Due to orientationally dependent excluded volume interactions, prolate ellipsoids such as those considered in our work experience an entropically driven homeotropic anchoring when in the presence of a free boundary. In order to access the normal twist mode, it is then necessary to implement a boundary condition on the curved cylindrical surface which constrains the director to orient within the tangent plane.

We implement a variation of the colloidal potential of Antypov and Cleaver[44] to obtain this dependence. In that work, a colloid interaction with a small spherical particle is represented by integration of the Lennard-Jones potential over the colloidal volume. An orientationally dependent function,

$$\tilde{\Gamma}\left(\omega, \hat{\boldsymbol{u}}_j, \hat{\boldsymbol{r}}_j\right) = \frac{1-\omega}{1-\omega\left[1-\left(\hat{\boldsymbol{r}}_j \cdot \hat{\boldsymbol{u}}_j\right)^2\right]} \qquad (A-1)$$

is used in the excluded volume and energy modulation terms. Within this function the vectors $\hat{\boldsymbol{u}}_j$ and $\hat{\boldsymbol{r}}_j$ are the orientation of Gay–Berne particle *j* and the unit normal pointing from the nearest point on the wall to particle *j*. Noting the surface-to-surface distance

$$\xi = r - \sigma_o \tilde{\Gamma}\left(\chi, \hat{\boldsymbol{u}}_j, \hat{\boldsymbol{r}}_j\right)^{-1/2} + \sigma_o \qquad (\text{A - 2})$$

we may write the full potential as

$$U_{\text{surface}}\left(\hat{\boldsymbol{u}}_j, \hat{\boldsymbol{r}}_j\right) = \varepsilon_{\text{surface}} \tilde{\Gamma}\left(\chi'_{\text{surface}}, \hat{\boldsymbol{u}}_j, \hat{\boldsymbol{r}}_j\right) \left[\frac{2}{15}\left(\frac{\sigma_o}{\xi}\right)^9 - \left(\frac{\sigma_o}{\xi}\right)^3\right] \qquad (\text{A - 3})$$

The remaining unspecified parameter, χ'_{surface} depends on the ratio of side-on (s) to end-on (e) mesogen–surface interactions,

$$\chi'_{\text{surface}} = 1 - \left(\frac{\varepsilon_{\text{s}}}{\varepsilon_{\text{e}}}\right)^{-1/\mu} \qquad (\text{A - 4})$$

We utilize $\chi(\kappa) = (\kappa^2 - 1)/(\kappa^2 + 1)$ with κ = 3, μ = 2, and ν = 1. Two adjustable parameters then remain, $\varepsilon_{\text{surface}}$ and $\varepsilon_{\text{s}}/\varepsilon_{\text{e}}$, which we set to 1.0 and 10.0, respectively. These parameters favor parallel over perpendicular orientations, resulting in degenerate planar anchoring. A plot of this potential is given in Figure AS-3, showing how it strongly favors planar over homeotropic orientations. To obtain preradial states, ($k_{\text{B}}T$, $\varepsilon_{\text{surface}}$, $\varepsilon_{\text{s}}/\varepsilon_{\text{e}}$) were adjusted to achieve a radial nematic morphology (1.72, 0.5, 0.25), and then quenched to (1.44, 0.5, 0.256). Moderately weaker homeotropic anchorings were observed to result in bipolar morphologies.

A.4.2.2 Order Parameter

Order within simulated nematic droplets is characterized by the unit nematic vector $\hat{\boldsymbol{n}}$ and scalar order parameter *S*, each as a function of position within the droplet. Globally, a tensor order parameter may be defined as

$$\boldsymbol{Q} = \langle \frac{3}{2}\hat{\boldsymbol{u}}_i\hat{\boldsymbol{u}}_i - \frac{1}{2} \rangle \qquad (A - 5)$$

from which S is derived as the largest eigenvalue, and $\hat{\boldsymbol{n}}$ its normalized eigenvector. The average runs over all mesogens i in the system. A local analog of this, $\boldsymbol{Q}(\mathbf{x})$, is utilized in our order parameter maps and may be obtained by choosing a location **x** within the droplet, and performing the average over all mesogens i within a cutoff radius r_c, a value we set to $2\kappa\sigma_o$.

A.4.2.3 Free Energies

The free energies reported in this work were calculated using umbrella biases on particle positions. Particles in this part of the simulation were confined to move near the surface of the droplet. For single particle simulations, the orientation of the nematic was fixed, and a stiff umbrella ($10^5\varepsilon/\sigma_o^2$) was placed on the adsorbed macroparticle. From the resulting simulation, we obtained the equilibrium position and force on the macroparticle, and thus the gradient of the free energy. This was integrated along a path in θ, the angle between the position vector of the particle and the nematic (z) axis. Two-particle simulations proceeded similarly, with the global nematic axis unrestricted, and the position of one boojum fixed at a stationary macroparticle. The position of the remaining particle was varied and the energies calculated analogously to the single-particle case. We performed similar calculations using umbrella sampling[45] on initial conditions that had been prepared using metadynamics,[33, 34] with the particles free to move away from the droplet surface. The energies obtained using these two methods were found to be consistent with each other.

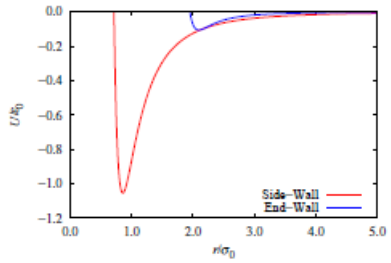

Figure AS-3. A plot of the wall anchoring potential used to impose degenerate planar anchoring. See equations A-1–A-4 for the functional form of the potential. Wall interaction parameters $\varepsilon_{\text{surface}} = 1.0$ and $\varepsilon_{\text{s}}/\varepsilon_{\text{e}} = 10.0$ are used.

A.5 References

*This appendix was prepared as a Letter reporting original research in the journal *Physical Review Letters*. My contribution to the project was in conducting the experiments to obtain the data shown in Figure A-4, proofreading the manuscript, and participating in conversations regarding the details of the experiments and theory of liquid crystals.

1. Kamien, R. D., The Geometry of Soft Materials: A Primer. *Reviews of Modern Physics* **2002**, 74, 953.
2. Gupta, J. K.; Sivakumar, S.; Caruso, F.; Abbott, N. L., Size-Dependent Ordering of Liquid Crystals Observed in Polymeric Capsules with Micrometer and Smaller Diameter. *Angewandte Chemie-International Edition* **2009**, 48, 1652-1655.
3. Hernández, S.; Moreno-Razo, J.; Ramírez-Hernández, A.; Díaz-Herrera, E.; Hernández-Ortiz, J.; de Pablo, J., Liquid Crystal Nanodroplets, and the Balance Between Bulk and Interfacial Interactions. *Soft Matter* **2012**, 8, 1443-1450.
4. Moreno-Razo, J. A.; Sambriski, E. J.; Abbott, N. L.; Hernandez-Ortiz, J. P.; de Pablo, J. J., Liquid-Crystal-Mediated Self-Assembly at Nanodroplet Interfaces. *Nature* **2012**, 485, 86-89.
5. Solomon, M. J., Directions for Targeted Self-Assembly of Anisotropic Colloids from Statistical Thermodynamics. *Current Opinion in Colloid & Interface Science* **2011**, 16, 158-167.
6. Lin, I. H.; Miller, D. S.; Bertics, P. J.; Murphy, C. J.; de Pablo, J. J.; Abbott, N. L., Endotoxin-Induced Structural Transformations in Liquid Crystalline Droplets. *Science* **2011**, 332, 1297-1300.
7. Voloschenko, D.; Pishnyak, O. P.; Shiyanovskii, S. V.; Lavrentovich, O., Effect of Director Distortions on Morphologies of Phase Separation in Liquid Crystals. *Physical Review E* **2002**, 65, 060701.
8. Muševič, I.; Škarabot, M.; Babič, D.; Osterman, N.; Poberaj, I.; Nazarenko, V.; Nych, A., Laser Trapping of Small Colloidal Particles in a Nematic Liquid Crystal: Clouds and Ghosts. *Physical Review Letters* **2004**, 93, 187801.
9. Škarabot, M.; Ravnik, M.; Babič, D.; Osterman, N.; Poberaj, I.; Žumer, S.; Muševič, I.; Nych, A.; Ognysta, U.; Nazarenko, V., Laser Trapping of Low Refractive Index Colloids in a Nematic Liquid Crystal. *Physical Review E* **2006**, 73, 021705.
10. Coursault, D.; Grand, J.; Zappone, B.; Ayeb, H.; Lévi, G.; Félidj, N.; Lacaze, E., Linear Self-Assembly of Nanoparticles Within Liquid Crystal Defect Arrays. *Advanced Materials* **2012**, 24, 1461-1465.
11. Fleury, J.-B.; Pires, D.; Galerne, Y., Self-Connected 3D Architecture of Microwires. *Physical Review Letters* **2009**, 103, 267801.
12. Pires, D.; Fleury, J.-B.; Galerne, Y., Colloid Particles in the Interaction Field of a Disclination Line in a Nematic Phase. *Physical Review Letters* **2007**, 98, 247801.
13. Ravnik, M.; Alexander, G. P.; Yeomans, J. M.; Zumer, S., Mesoscopic Modelling of Colloids in Chiral Nematics. *Faraday Discussions* **2010**, 144, 159-169.

14. Ravnik, M.; Alexander, G. P.; Yeomans, J. M.; Žumer, S., Three-Dimensional Colloidal Crystals in Liquid Crystalline Blue Phases. *Proceedings of the National Academy of Sciences* **2011**, 108, 5188-5192.
15. Miller, D. S.; Abbott, N. L., Influence of Droplet Size, pH and Ionic Strength on Endotoxin-Triggered Ordering Transitions in Liquid Crystalline Droplets. *Soft Matter* **2013**, 9, 374-382.
16. Fernández-Nieves, A.; Vitelli, V.; Utada, A. S.; Link, D. R.; Márquez, M.; Nelson, D. R.; Weitz, D. A., Novel Defect Structures in Nematic Liquid Crystal Shells. *Physical Review Letters* **2007**, 99, 157801.
17. Bates, M.; Luckhurst, G., Computer Simulation Studies of Anisotropic Systems. XXX. The Phase Behavior and Structure of a Gay–Berne Mesogen. *The Journal of Chemical Physics* **1999**, 110, 7087-7108.
18. Cleaver, D. J.; Care, C. M.; Allen, M. P.; Neal, M. P., Extension and Generalization of the Gay-Berne Potential. *Physical Review E* **1996**, 54, 559.
19. de Miguel, E.; Rull, L. F.; Chalam, M. K.; Gubbins, K. E.; Van Swol, F., Location of the Isotropic-Nematic Transition in the Gay-Berne Model. *Molecular Physics* **1991**, 72, 593-605.
20. Gay, J.; Berne, B., Modification of the Overlap Potential to Mimic a Linear Site–Site Potential. *The Journal of Chemical Physics* **1981**, 74, 3316-3319.
21. Allen, M. P.; Tildesley, D. J., *Computer Simulation of Liquids*. Oxford University Press: Oxford, UK, 1987.
22. Abraham, F. F.; Singh, Y., The Structure of a Hard-Sphere Fluid in Contact with a Soft Repulsive Wall. *The Journal of Chemical Physics* **1977**, 67, 2384-2385.
23. Rull, L.; Romero-Enrique, J.; Fernandez-Nieves, A., Computer Simulations of Nematic Drops: Coupling between Drop Shape and Nematic Order. *The Journal of Chemical Physics* **2012**, 137, 034505.
24. Vanzo, D.; Ricci, M.; Berardi, R.; Zannoni, C., Shape, Chirality and Internal Order of Freely Suspended Nematic Nanodroplets. *Soft Matter* **2012**, 8, 11790-11800.
25. Mondiot, F.; Wang, X.; de Pablo, J. J.; Abbott, N. L., Liquid Crystal-Based Emulsions for Synthesis of Spherical and Non-Spherical Particles with Chemical Patches. *Journal of the American Chemical Society* **2013**, 135, 9972–9975.
26. Kim, E. B.; Guzman, O.; Grollau, S.; Abbott, N. L.; de Pablo, J. J., Interactions Between Spherical Colloids Mediated by a Liquid Crystal: A Molecular Simulation and Mesoscale Study. *The Journal of Chemical Physics* **2004**, 121, 1949-1961.
27. The order parameter and field line maps in this Letter were created using PARAVIEW V. 3.98.1, published by Kitware, Inc. http://www.paraview.org. In.
28. Brown, W. M.; Petersen, M. K.; Plimpton, S. J.; Grest, G. S., Liquid Crystal Nanodroplets in Solution. *The Journal of Chemical Physics* **2009**, 130, 044901.
29. Plimpton, S., Fast Parallel Algorithms for Short-Range Molecular Dynamics. *Journal of Computational Physics* **1995**, 117, 1-19.
30. Israelachvili, J. N., *Intermolecular and Surface Forces*. 2nd ed.; Academic Press London: San Diego, CA, USA, 1991.
31. Berardi, R.; Costantini, A.; Muccioli, L.; Orlandi, S.; Zannoni, C., A Computer Simulation Study of the Formation of Liquid Crystal Nanodroplets from a Homogeneous Solution. *The Journal of Chemical Physics* **2007**, 126, 044905.
32. Meeker, S.; Poon, W.; Crain, J.; Terentjev, E., Colloid–Liquid-Crystal Composites: An Unusual Soft Solid. *Physical Review E* **2000**, 61, R6083.

33. Laio, A.; Gervasio, F. L., Metadynamics: A Method to Simulate Rare Events and Reconstruct the Free Energy in Biophysics, Chemistry and Material Science. *Reports on Progress in Physics* **2008**, 71, 126601.
34. Singh, S.; Chopra, M.; de Pablo, J. J., Density of States-Based Molecular Simulations. *Annual Review of Chemical and Biomolecular Engineering* **2012**, 3, 369-394.
35. Delabre, U.; Richard, C.; Cazabat, A., Some Specificities of Wetting by Cyanobiphenyl Liquid Crystals. *Journal of Physics: Condensed Matter* **2009**, 21, 464129.
36. Wu, S., Surface and Interfacial Tensions of Polymer Melts. II. Poly (methyl methacrylate), Poly (n-butyl methacrylate), and Polystyrene. *The Journal of Physical Chemistry* **1970**, 74, 632-638.
37. Brake, J. M.; Mezera, A. D.; Abbott, N. L., Effect of Surfactant Structure on the Orientation of Liquid Crystals at Aqueous-Liquid Crystal Interfaces. *Langmuir* **2003**, 19, 6436-6442.
38. Gupta, J. K.; Zimmerman, J. S.; de Pablo, J. J.; Caruso, F.; Abbott, N. L., Characterization of Adsorbate-Induced Ordering Transitions of Liquid Crystals within Monodisperse Droplets. *Langmuir* **2009**, 25, 9016-9024.
39. Lockwood, N. A.; Cadwell, K. D.; Caruso, F.; Abbott, N. L., Formation of Polyelectrolyte Multilayer Films at Interfaces between Thermotropic Liquid Crystals and Aqueous Phases. *Advanced Materials* **2006**, 18, 850-854.
40. Tjipto, E.; Cadwell, K. D.; Quinn, J. F.; Johnston, A. P. R.; Abbott, N. L.; Caruso, F., Tailoring the Interfaces Between Nematic Liquid Crystal Emulsions and Aqueous Phases via Layer-by-Layer Assembly. *Nano Letters* **2006**, 6, 2243-2248.
41. Zou, J.; Fang, J., Director Configuration of Liquid-Crystal Droplets Encapsulated by Polyelectrolytes. *Langmuir* **2009**, 26, 7025-7028.
42. Zou, J. H.; Bera, T.; Davis, A. A.; Liang, W. L.; Fang, J. Y., Director Configuration Transitions of Polyelectrolyte Coated Liquid-Crystal Droplets. *Journal of Physical Chemistry B* **2011**, 115, 8970-8974.
43. Bera, T.; Fang, J. Y., Polyelectrolyte-Coated Liquid Crystal Droplets for Detecting Charged Macromolecules. *Journal of Materials Chemistry* **2012**, 22, 6807-6812.
44. Antypov, D.; Cleaver, D. J., The Effect of Spherical Additives on a Liquid Crystal Colloid. *Journal of Physics: Condensed Matter* **2004**, 16, S1887.
45. Frenkel, D.; Smit, B., *Understanding Molecular Simulation*. Academic Press: San Diego, CA, USA, 2002.